Surfactant Adsorption and Surface Solubilization

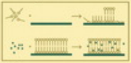

EDITED BY
Ravi Sharma

ACS Symposium Series 615

Downloaded by 89.163.35.42 on October 11, 2012 | http://pubs.acs.org
Publication Date: May 5, 1996 | doi: 10.1021/bk-1995-0615.fw001

Surfactant Adsorption and Surface Solubilization

Downloaded by 89.163.35.42 on October 11, 2012 | http://pubs.acs.org
Publication Date: May 5, 1996 | doi: 10.1021/bk-1995-0615.fw001

ACS SYMPOSIUM SERIES **615**

Surfactant Adsorption and Surface Solubilization

Ravi Sharma, EDITOR
Eastman Kodak Company

Developed from a symposium sponsored
by the Division of Colloid and Surface Chemistry
at the 208th National Meeting
of the American Chemical Society,
Washington, DC,
August 21–26, 1994

American Chemical Society, Washington, DC 1995

Downloaded by 89.163.35.42 on October 11, 2012 | http://pubs.acs.org
Publication Date: May 5, 1996 | doi: 10.1021/bk-1995-0615.fw001

TP 994 .S82 1995 Copy 1

Surfactant adsorption and surface solubilization

Library of Congress Cataloging-in-Publication Data

Surfactant adsorption and surface solubilization / Ravi Sharma, editor.

p. cm.—(ACS symposium series, ISSN 0097–6156; 615)

"Developed from a symposium sponsored by the Division of Colloid and Surface Chemistry at the 208th National Meeting of the American Chemical Society, Washington, D.C., August 21–25, 1994."

Includes bibliographical references and indexes.

ISBN 0–8412–3333–0

1. Surface active agents—Congresses. 2. Adsorption—Congresses.

I. Sharma, Ravi, 1956– . II. American Chemical Society. Division of Colloid and Surface Chemistry. III. American Chemical Society. Meeting (208th: 1994: Washington, D.C.) IV. Series.

TP994.S82 1995
541.3'3—dc20

95–44680
CIP

This book is printed on acid-free, recycled paper.

Copyright © 1995

American Chemical Society

All Rights Reserved. The appearance of the code at the bottom of the first page of each chapter in this volume indicates the copyright owner's consent that reprographic copies of the chapter may be made for personal or internal use or for the personal or internal use of specific clients. This consent is given on the condition, however, that the copier pay the stated per-copy fee through the Copyright Clearance Center, Inc., 222 Rosewood Drive, Danvers, MA 01923, for copying beyond that permitted by Sections 107 or 108 of the U.S. Copyright Law. This consent does not extend to copying or transmission by any means—graphic or electronic—for any other purpose, such as for general distribution, for advertising or promotional purposes, for creating a new collective work, for resale, or for information storage and retrieval systems. The copying fee for each chapter is indicated in the code at the bottom of the first page of the chapter.

The citation of trade names and/or names of manufacturers in this publication is not to be construed as an endorsement or as approval by ACS of the commercial products or services referenced herein; nor should the mere reference herein to any drawing, specification, chemical process, or other data be regarded as a license or as a conveyance of any right or permission to the holder, reader, or any other person or corporation, to manufacture, reproduce, use, or sell any patented invention or copyrighted work that may in any way be related thereto. Registered names, trademarks, etc., used in this publication, even without specific indication thereof, are not to be considered unprotected by law.

PRINTED IN THE UNITED STATES OF AMERICA

American Chemical Society
Library
1155 16th St., N.W.
Washington, D.C. 20036

Downloaded by 89.163.35.42 on October 11, 2012 | http://pubs.acs.org
Publication Date: May 5, 1996 | doi: 10.1021/bk-1995-0615.fw001

Downloaded by 89.163.35.42 on October 11, 2012 | http://pubs.acs.org
Publication Date: May 5, 1996 | doi: 10.1021/bk-1995-0615.fw001

1995 Advisory Board

ACS Symposium Series

Robert J. Alaimo
Procter & Gamble Pharmaceuticals

Mark Arnold
University of Iowa

David Baker
University of Tennessee

Arindam Bose
Pfizer Central Research

Robert F. Brady, Jr.
Naval Research Laboratory

Mary E. Castellion
ChemEdit Company

Margaret A. Cavanaugh
National Science Foundation

Arthur B. Ellis
University of Wisconsin at Madison

Gunda I. Georg
University of Kansas

Madeleine M. Joullie
University of Pennsylvania

Lawrence P. Klemann
Nabisco Foods Group

Douglas R. Lloyd
The University of Texas at Austin

Cynthia A. Maryanoff
R. W. Johnson Pharmaceutical
Research Institute

Roger A. Minear
University of Illinois
at Urbana–Champaign

Omkaram Nalamasu
AT&T Bell Laboratories

Vincent Pecoraro
University of Michigan

George W. Roberts
North Carolina State University

John R. Shapley
University of Illinois
at Urbana–Champaign

Douglas A. Smith
Concurrent Technologies Corporation

L. Somasundaram
DuPont

Michael D. Taylor
Parke-Davis Pharmaceutical Research

William C. Walker
DuPont

Peter Willett
University of Sheffield (England)

Downloaded by 89.163.35.42 on October 11, 2012 | http://pubs.acs.org
Publication Date: May 5, 1996 | doi: 10.1021/bk-1995-0615.fw001

Foreword

THE ACS SYMPOSIUM SERIES was first published in 1974 to provide a mechanism for publishing symposia quickly in book form. The purpose of this series is to publish comprehensive books developed from symposia, which are usually "snapshots in time" of the current research being done on a topic, plus some review material on the topic. For this reason, it is necessary that the papers be published as quickly as possible.

Before a symposium-based book is put under contract, the proposed table of contents is reviewed for appropriateness to the topic and for comprehensiveness of the collection. Some papers are excluded at this point, and others are added to round out the scope of the volume. In addition, a draft of each paper is peer-reviewed prior to final acceptance or rejection. This anonymous review process is supervised by the organizer(s) of the symposium, who become the editor(s) of the book. The authors then revise their papers according to the recommendations of both the reviewers and the editors, prepare camera-ready copy, and submit the final papers to the editors, who check that all necessary revisions have been made.

As a rule, only original research papers and original review papers are included in the volumes. Verbatim reproductions of previously published papers are not accepted.

Downloaded by 89.163.35.42 on October 11, 2012 | http://pubs.acs.org
Publication Date: May 5, 1996 | doi: 10.1021/bk-1995-0615.pr001

Preface

SURFACTANT ADSORPTION is a widely studied phenomenon, encompassing several scientific and technological disciplines, including wetting, adhesion, emulsions, foams, separation science, polymer blends and composites, and stabilization of colloidal dispersions, to name a few. Many new surfactants (particularly polymer surfactants and sugar-based surfactants) that have been developed have led to improved performance and new applications. Surfactant usage and surfactant design would benefit if synthetic chemists, physical scientists, and engineers could have a clearer understanding of the molecular and structural parameters that control surfactant adsorption. These scientists are presented with an enormous challenge to understand the behavior of surfactants at various interfaces and how surfactant adsorption and surfactant structure relate to technological performance.

The chapters in this book discuss information in the area of surfactant adsorption relating to structure, characterization, new methodologies, and new theories, and how these would augment our understanding of surfactant adsorption and surface solublization. Many of the chapters are contributions from participants of the "Kodak Symposium on Surfactant Adsorption and Surface Solubilization," upon which this book is based.

I am grateful to the organizing committee of the Division of Colloid and Surface Chemistry for allowing me to organize the symposium and to Eastman Kodak Company for sponsoring the symposium. I thank the following people for helping me run the symposium by acting as session chairpersons: Claude Treiner, Terry Cosgrove, Paul Luckham, Maria Santore, Ponesseril Somasundaran, Luuk Koopal, and Les Fina. I also thank the authors for submitting their manuscripts for publication in this book, and I thank the reviewers for their efforts.

RAVI SHARMA
Materials Science and Engineering Division
Eastman Kodak Company
Rochester, NY 14650–2158

August 15, 1995

In Surfactant Adsorption and Surface Solubilization; Sharma, R.;
ACS Symposium Series; American Chemical Society: Washington, DC, 1996.

Downloaded by 89.163.35.42 on October 11, 2012 | http://pubs.acs.org
Publication Date: May 5, 1996 | doi: 10.1021/bk-1995-0615.ch001

Chapter 1

Small-Molecule Surfactant Adsorption, Polymer Surfactant Adsorption, and Surface Solubilization: An Overview

Ravi Sharma

Materials Science and Engineering Division, Eastman Kodak Company, Rochester, NY 14650–2158

The importance of surfactant adsorption and surface solubilization to a variety of technologies is well known and continues to be studied. Small molecule surfactants and polymer surfactants form a variety of structures when adsorbed to an interface. This is particularly true for adsorbed surfactants at the solid/liquid interface. For polymer surfactants, however, a variety of structures are also possible at the air/liquid interface. The structure of surfactant aggregates on surfaces and their correlation with the shape of adsorption isotherms, and with technologically important processes such as wettability, friction, adhesion, and surface solubilization will no doubt continue to be a subject of research for many years.

General

Surfactants are employed in a variety of technologies. Detergency, emulsification, dispersion, coating, wetting, flotation, petroleum recovery, lubrication and adhesion are some examples that depend on the ability of surfactants to adsorb at an interface and on their ability to solubilize hydrocarbon materials in micelles and/or in adsorbed layers (*1-5*). For many years researchers have investigated surfactant behavior at various interfaces and in solution (*1-6*). The interfaces usually studied are the solid/liquid interface, liquid/liquid interface, and the liquid/air interface. More recently, segregation at polymer/polymer interfaces has also been studied (see later in this paper). It is abundantly apparent that some surfactants are better than others for a given application. Barring nonequilibrium effects and transport-related effects, this difference ultimately depends on the amount of adsorption and on the structure of the adsorbed layer (configuration of the adsorbed surfactant). The relationship between the structure of a surfactant and its adsorption capacity is much sought after. To this

0097–6156/95/0615–0001$12.00/0

extent there has been a large volume of published data on adsorption at the air/water and liquid/liquid interfaces (*1b*). Surfactant effectiveness and efficiency for adsorption at the liquid/gas and liquid/liquid interfaces for surface tension reduction has been discussed by Rosen (*1b*). Recently, an adsorption map relating adsorption of surfactants to surface energetics has been presented by Vogler (*7*).

Surfactants may be classified according to the type of head group (*1,3,8*). Surfactants containing a negatively charged head group, such as carboxylic acids and salts, and alkyl benzene sulfonates are called anionic surfactants; cationic surfactants have a positively charged head group (e.g., quaternary ammonium salts and amines) and nonionic surfactants have a hydrophilic head group that is not charged (e.g., ethers, alcohol ethoxylates, and carboxylic acid esters). Another important subset of nonionic surfactants are zwitterionic surfactants (*9*). These electrically neutral compounds possess formally charged groups that are separated by intervening atoms. A zwitterionic compound that bears both an acidic group and a basic group is amphoteric. In addition, acidic, basic and nonamphoteric zwitterionic surfactants exist. Another increasingly important class of nonionic surfactants are the so-called "sugar surfactants," which contain either cyclic or linear oligomeric saccharides (*10,11*).

Downloaded by 89.163.35.42 on October 11, 2012 | http://pubs.acs.org
Publication Date: May 5, 1996 | doi: 10.1021/bk-1995-0615.ch001

For every type of surfactant, substitution of the usual hydrocarbon hydrophobic component by other hydrophobic groups is possible. Hydrophobic groups that are commonly incorporated into a hydrocarbon backbone, either as spacers or as pendants, include fluorinated groups and dimethylsiloxane groups. The degree of substitution ranges from partial to complete. Fluorinated surfactants and poly(dimethylsiloxane) or PDMS-based surfactants are an important class of surfactants with applications in the coating, textile, molding, and lubrication industries. A major component of nonionic surfactants include polymerized blocks of polar groups (e.g., polyethyleneoxide) and hydrophobic groups (e.g., polydimethylsiloxane) in a variety of arrangements called nonionic block copolymers (*12*). In this overview, small molecule surfactants are surfactants that do not contain large polymerized segments. Polymer surfactants consist of polymer segments such as poly(dimethylsiloxane), poly(ethyleneoxide), and poly(propyleneoxide).

Adsorption Properties

The adsorption properties of surfactants is a much studied phenomenon, both with regard to the amount of adsorption and to the structure of the adsorbed layer. Certain aspects of adsorption behavior to solid surfaces are clear. For example, anionic surfactants adsorb readily owing to electrostatic interactions on positively charged surfaces and vice versa (*13*). A characteristic feature of surfactant adsorption at concentrations below the CMC is that adsorbed surfactants form local aggregates on the surface. These aggregates have been referred to as hemimicelles, admicelles, and surface micelles, implying a micelle-like structure (*13-15*). Recently, the term "solloid" has been coined to represent a surfactant and polymer aggregates on a surface (*13c,d,e*). Another important aspect of surfactant adsorption is the effect of surfactant chain length, particularly with respect to distinction between adsorption on hydrophobic or hydrophilic surfaces (*16,17a*). Koopal and Ralston have applied a modified version of the Scheutjens and Fleer theory for polymer adsorption to flexible long-chain surfactants. They demonstrate the importance of segment-surface interactions and lateral chain-chain interactions, and how these interactions lead to various limiting adsorption equations depending on solvent quality (*17*).

Downloaded by 89.163.35.42 on October 11, 2012 | http://pubs.acs.org
Publication Date: May 5, 1996 | doi: 10.1021/bk-1995-0615.ch001

The structure of surface aggregates continues to be controversial (*15f,j,18,19*). Harwell and co-workers suggest that the term admicelle should be reserved for local bilayer structure, and hemi-micelle for monolayer aggregates (*15f,j*). Furthermore, Harwell et al. (*15j*) propose that at higher surfactant concentration, a more-or-less continuous bilayer forms, and this has the effect of reversing the original charge on the surface; e.g., an anionic substrate is converted to a positively charged surface due to a second layer of cationic surfactant that adsorbs with its charge group outermost (*13,19-23*). A different structure of the surface aggregates at the solid/liquid interface is proposed by others (*18,19*). In Somasundaran's model, a gradual change from monolayer aggregates (hemimicelle) to hemimicelles with reverse orientation with increasing adsorption density is postulated based on a variety of spectroscopic studies (*18*). The reverse orientation model has the tails of top-most surfactant molecules interpenetrating the tails of the bottom layer, thus creating a polar surface as in the bilayer model case but with a difference in layer thickness - it is expected to be thinner because of interpenetration of the hydrophobic tails. In Gu's model (*19*), individual surface aggregates, rather than Harwell's patchy bilayer structure, is depicted. Several adsorption models for the adsorption of ionic surfactants on charged solids have been proposed (*15j,18-26* and references therein). Stilbs et al. report on the aggregation of adsorbed surfactants as studied by NMR (*27*). The adsorption of cationic surfactants on a variety of hydrophilic and hydrophobic substrates is reviewed in an article by Ingram and Ottewill (*24*). Cases has published several papers dealing with the surfactant adsorption at the solid/liquid interface

(*15d,28*). He has provided a theory for surfactant adsorption by assuming surface heterogeneity, and identifying different adsorption behavior for short chain-length surfactants (n < 8) and long chain-length surfactants, coupled with whether temperature is below or above the Krafft temperature. Above the Krafft temperature, and for adsorption on hydrophilic surfaces, two limiting cases consistent with the theory of two-dimensional condensation on a heterogeneous surface can be described: 1) at relatively low surfactant concentration, ionic surfactants with aliphatic chain (n > 8), which have a high affinity for the surface, hemimicelles (monolayer aggregates) form whose sizes are limited by domain size of the heterogeneity, and 2) at high relative concentration, bilayer formation (admicelle) is possible if the surface is hydrophobic because of hemimicelle formation. In the case of adsorption on a hydrophilic surface, surfactants having a weak affinity for the surface (i.e., nonionic surfactants and similarly charged ionic surfactants) form surface micelles that are reminiscent of bulk solution micelles. Surface aggregation in the weak surface affinity limit has recently been studied by Manne et al. (*29*) for an ionic surfactant adsorbing on an uncharged hydrophobic surface (see below). Below the Krafft temperature, two-dimensional aggregates only are formed (the aliphatic chains are always in a condensed state), and again the theory of two-dimensional condensation on a heterogeneous surface can be applied. Cases (*28f*) and Narkiewicz-Michalek (*30*) have presented an insightful review on surfactant adsorption.

Downloaded by 89.163.35.42 on October 11, 2012 | http://pubs.acs.org
Publication Date: May 5, 1996 | doi: 10.1021/bk-1995-0615.ch001

A controversy exists for the adsorption mechanism of ionic surfactants on uncharged hydrophobic surfaces (primarily graphite) at surfactant concentration close to the critical micelle concentration (CMC) (*29*). In one model, a gradual change from a parallel to a perpendicular adsorption configuration occurs as the concentration approaches the critical micelle formation (*31*). Cooperativity effects between the hydrophobic tails enhance the adsorption there by increasing the adsorption close to the CMC. In a second model, hemimicelle formation due to micelle collapse near the surface is responsible for the increase in adsorption close to the CMC (*32*). Recent AFM work supports neither of these models, rather that hemimicelles are templated by a epitaxially bound monolayer consisting of chains parallel to the graphite surface (*29*). Note that in the case of adsorption to a hydrophobic surface, the hemicelles consist of surfactants with their hydrophilic portions outermost, which is in contrast to the hemicelles depicted on mineral oxides with hydrophobic tails outermost (*14c*). Nonionic surfactants adsorb on surfaces, the adsorption mechanism being one of the following: a) adsorption by hydrogen bonding, b) adsorption by polarization of π electrons (attractive interaction between electron-rich aromatic nuclei of the adsorbate and positive sites located on the substrate), c) adsorption by van der Waals dispersion forces, and d) adsorption by alternating hydrophobic bonding. Because of the absence of ionic interactions the shape of the adsorption isotherm is different to that observed between an ionic surfactant and an oppositely charged surface (*33*). Presumably, the shape of the isotherm would reflect the variety of structures inferred from AFM data on the adsorption of poly(oxyethylene) nonionic surfactant on colloidal silica (*34*).

The interfacial properties of a solution of two or more surfactants exhibit synergistic and antagonistic effects. A solution of mixed surfactants is said to exhibit synergism if it shows greater interfacial activity (e.g., lower interfacial tension) than that demonstrated by any of the individual components at the same concentration.(*1*) Synergy depends on the attraction between the surfactants such that one surfactant attracts the other with the net effect of reducing the concentration of surfactant required for one of the following applications: 1) lowering interfacial tension to a given value, 2) achieving a given amount of surfactant adsorption at the solid/liquid interface and 3) formation of micelles. When surfactants in a mixed solution repel each other (e.g., due to electrical repulsions), negative synergism results (*9c*). An example of negative synergism for total surfactant adsorption for C8E4 and sodium dodecylsulfate (SDS) on graphitized carbon has been reported (*35*). The adsorption of SDS and ethoxylated nonylphenol (NP12) from their mixed solutions on TiO_2 exhibits synergistic effects when the SDS content is low, but antagonistic effects (negative synergism) at higher SDS concentrations (*36*). Similar synergistic effects and antagonistic effects were observed in the case of adsorption studies on silica gel from cetytrimethylammonium bromide (CTAB)-Triton X-100 and CTAB-Triton X-305. The mixed adsorption becomes more complicated when silica gel is replaced with methylated silica gel (*37*). Esumi et al. have studied the adsorption of poly(styrenesulfonate) or PSS, sodium dodecyl sulfate (SDS), and hexadecyltrimethylammonium chloride (HTAC) from single solutions and PSS-SDS and PSS-HTAC binary mixed solutions on alumina. They found that SDS decreases PSS adsorption, while HTAC enhances PSS adsorption due to formation of a complex of PSS-HTAC on alumina (*38*).

Harwell et al. have studied the adsorption of SDS and polyethoxylated nonylphenol (NPEO10) and their mixtures on gamma alumina(*14b*). The individual adsorption isotherm indicate that SDS adsorbs significantly, while NPEO10 does not. In fact, there is doubt that NPEO10 admicelles form from pure NPEO10 solutions. However,

Downloaded by 89.163.35.42 on October 11, 2012 | http://pubs.acs.org
Publication Date: May 5, 1996 | doi: 10.1021/bk-1995-0615.ch001

there is a dramatic change when a mixture of SDS and NPEO10 is used; e.g., 20/80 mixture of SDS/NPEO10 results in the formation of surface aggregates that are 75% NPEO10. This behavior is attributed to the high degree of nonideality of the system, in that the composition of the surface aggregates do not follow an ideal mixing rule. It is also shown that the nonideality does not conform to regular solution behavior either. Thus, in some instances and in particular, adsorption to the solid/liquid interface, application of bulk solution thermodynamics does not appear to be successful (*39*). Real solution theories may be appropriate in these instances.

An important aspect of adsorbed layer is their interaction dynamics and the evolution of their structure over time. Couzis and Gulari have studied *in situ* the dynamics and structure of sodium laurate adsorbed onto alumina surfaces by infrared attenuated total reflectance spectroscopy (*40*). They show that the laurate ion does not adopt its final structure immediately - a few hours are required for an "equilibrium" structure to form. The structure and mechanism of laurate-alumina interactions is dependent on pH.

Downloaded by 89.163.35.42 on October 11, 2012 | http://pubs.acs.org
Publication Date: May 5, 1996 | doi: 10.1021/bk-1995-0615.ch001

Adsorption at the liquid/air and liquid/liquid interfaces has been studied by measuring surface or interfacial tension. The dependence of surface tension on surfactant concentration can be used to determine the amount adsorbed by application of the Gibbs equation (*4*). Radiotracer methods have also been used with some success, and have been especially useful in studies with mixed surfactants in order to determine the adsorbed amounts of each component (*20,24*). Surface tension reduction at fluid interfaces by the adsorption of soluble ionic and nonionic surfactants has been discussed by Ingram and Ottewill (*24*).

Neither of the above mentioned approaches yield structural information to the degree as by a recently developed technique called neutron reflectivity (*41*). Polymer conformation for a number of copolymers at the hexane/water interface has been studied by neutron reflection (*42*). In the case of poly(ethyleneoxide)-poly(propyleneoxide)-poly(ethyleneoxide) or PEO-PPO-PEO triblock, the adsorbed layer was diffuse and thicker than the micellar radius, suggesting some stretching of the molecule. In contrast, a random copolymer of poly(vinyl alcohol-co-acetate) was shown to adsorb in an all-train configuration. Apparantly, hexane is a poor solvent for the hydrophobic moieties of both of these polymers, and in the case of the PEO-PPO-PEO, hexane does not appear to notably alter the conformation adopted at the air/water interface. Hexane is, however, a good solvent for the PDMS segment of the

PDMS-PVPO diblock, and as expected, it is drawn out of the water and forms a dense layer between the two phases (*42*). Using another reflection technique, Fina has attempted to obtain structural information on water-soluble surfactant at the air/water interface with *in situ* external reflection infrared spectroscopy (*43*).

Poly(dimethylsiloxane) with various functionally-terminated groups have been studied at the air/water interface (*44*). It appears that most of the difunctional oligomers stand up with one group at the air/water interface and the other away from the surface. Only in the case of di-NH2-PDMS (with PDMS mol wt = 1970) was there evidence that both end-functionalities were at the air/water interface with the intervening PDMS chain forming loops. Other end-functionalized polymer have also been studied [see references cited in ref. *44b*]. Block polyelectrolytes have been shown to form surface micelles (*45*). The shape of the micelle (e.g., circular and rod-like), depends on the relative size of the hydrophobic block and the charged block. Recently, surface micelles were also observed at the air/water interface in studies involving a variety of nonionic diblocks (*46*). A review of some interesting observations on the spreadability of polymers at the air/water interface has been presented by Gaines (*44a*).

Neutron reflectivity measurements have been used to study monolayers of derivatives of styrene-maleic anhydride copolymers at the air/water interface. For derivatives prepared using long-chain alcohols (dodecyl or undecyl alcohol) as pendants, the alkyl chains are completely out of the water subphase at high surface pressure at the expense of the phenyl groups. At lower surface pressure, about 50% of the phenyl groups are out of the water and approximately 30% of the alkyl chains are submerged. The thickness of the alkyl chains and of the backbone and phenyl group layer was also determined, and used to infer the structure of the layer (*47,48*). Neutron reflectivity measurements have also been employed to study the structure of hydroxyl-terminated 1,4-polyisoprene (PIP-OH) at the air/water interface(*46*). Interestingly, it is inferred that films of PIP-OH consist of closely packed chains in a monolayer coexisting with multilayers, even at low surface pressure (well before the collapse point indicated on the surface compression isotherm). In another approach, second harmonic generation (SHG) was used to study molecular arrangement of a poly(acrylonitrile-co-4-vinylpyridine) monolayer at the air/water interface (*49*). The SHG data indicated that the pyridine groups were solvated, with nearly a vertical orientation on average at the interface, and the nitrile groups coiled up in the chain above the water surface. Polymer adsorption at the solid/liquid interface has been

Downloaded by 89.163.35.42 on October 11, 2012 | http://pubs.acs.org
Publication Date: May 5, 1996 | doi: 10.1021/bk-1995-0615.ch001

Downloaded by 89.163.35.42 on October 11, 2012 | http://pubs.acs.org
Publication Date: May 5, 1996 | doi: 10.1021/bk-1995-0615.ch001

studied with increasing activity over the past 10 years or so. Earlier studies indicated that the configuration of adsorbed polymers may be different to that in bulk solution (*50*). The configuration of adsorbed diblock copolymers has been studied experimentally (*51*) and theoretically (*52*). Because of the preferential solubility of one block in the surrounding medium, the more soluble component extends out into the solvent while the insoluble blocks anchor the molecule to a surface (*53*). It is predicted that terminally attached polymers will have segment density profiles that depend on coil radius of the chain, R, and the distance between grafting sites on the surface, D (*50a,e,52g*). The adsorbed layers are termed "mushrooms" (when D >> R) or "brushes" (when D << R). According to the Alexander-de Gennes theory, the brush layer thickness (L) scales with number of monomer units in the brush (N_b) to a power = 1 or 3/5 when the grafting density is high or low respectively (*50a,52g*). Surface force apparatus studies have established that the adsorbed layers formed by block copolymers are highly extended (up to six times the radius of gyration), and that L scales with N_b to a power between 0.7-1.0 depending on composition (*51g-i*). The nonlinear dependance of L on N_b between the limiting cases set out by Alexander and de Gennes is consistent with theoretical predictions by Munch et al., Evers et al., and Whitmore et al. (*54*) In an extreme case of one anchor unit per chain (endfunctionalized polystyrene), the scaling relationship $L \sim N_b^{0.6}$ was found, which is in good agreement with the Alexander-de Gennes model when the grafting density is low (*51j,h,55b*). Small angle neutron scattering has been used to characterize chemically grafted PDMS chains on silica (*56*). At high grafting density and in good solvent, the chains are stretched such that $L \sim N_b$ (*51h,k,56*). Another important theoretical prediction is that a maximum in L should occur at a particular block size. This has been corroborated by a number of experiments (*51i*). Thus, there is a significant amount of data that shows good agreement between theory and experiment, although a notable exception is the case of poly(2-vinylpyridine-*b*-styrene) adsorbed onto porous mica (*51i*). Polymer brushes can also form at fluid interfaces, as found by Factor et al. (*57*).

Recent neutron reflectivity measurements probing the structure of adsorbed layers of a symmetric diblock copolymer of polystyrene and poly(methylmethacrylate) or P(S-*b*-MMA) indicated that the the PMMA segments anchor to a quartz surface forming a dense layer. However, the segmental concentration of PS was too low to be detected (*58*). Very recently, evanescent wave ellipsometry was used to study the adsorbed amount at the glass-polymer solution [P(S-*b*-MMA) in carbon tetrachloride) interface. Significantly, the adsorbed amount exhibited a maximum suggesting that the solubility of the P(S-*b*-MMA) diblock in CCl_4 increased with increasing molecular weight, which in turn caused a reduction in the amount adsorbed. Kim et al. (*58*) conclude that the variable solvation of the adsorbed layer (CCl_4 coadsorbs with the PMMA layer at the glass surface) must be taken into account to describe the segment density profiles of diblocks adsorbed onto a surface. Recently there has been considerable interest in understanding the behavior of anchored chains in various solvents (*55*), including mixed solvents (*59*). Interestingly, under certain solvent conditions, preferential solvation of one of the solvents has been observed in polystyrene brushes with significant changes in the segment density profile (*59*). The preferential partitioning of one of the solvents into the adsorbed diblock is similar to the surface solubilization (see below) of non-polar solutes into surfactant aggregates found on solid surfaces.

Downloaded by 89.163.35.42 on October 11, 2012 | http://pubs.acs.org
Publication Date: May 5, 1996 | doi: 10.1021/bk-1995-0615.ch001

The structure of adsorbed layers formed by a series of PEO-PPO-PEO triblock copolymers has recently been investigated using sedimentation field-flow fractionation and electron spin resonance (*53*). In these studies it was found that the motion of the PEO segments depended on the radius of the particle (polystyrene latex) on which they were adsorbed and the chain length of the PEO segment. In addition, the thickness of the adsorbed layer depended on the PEO chain length and on the radius of the particle on which they were adsorbed. Further, for a given particle radius, the PPO chain length only affected the amount adsorbed. Recent self-consistent field theory has been applied to the problem of diblock polymer adsorption on small particles. It is found that the adsorbed amount and the hydrodynamic layer thickness depend on particle size (*60*). Conformation of polymers has also been examined by fluorescence and NMR (*61*).

The adsorption of copolymers at the interface between two immiscible polymers and polymer-nonpolymer interface has been studied. It has been shown that segregation of a A-B diblock can be used to enhance the interfacial strength between homopolymers A and B (*62*). Similarly, mechanical strength of a polymer/nonpolymer interface has also been improved by the adsorption of diblocks at the interface (*63*) and by using self-assembled monolayers (*64*). There are a number of theories describing the segregation of A-B block copolymers at the interface between immiscible A and B homopolymers (*65,66*). Leibler's theory for the segregation of copolymers at the A-B interface describes two different regimes of segregation: the wet brush and dry brush models (*65*). When the degree of polymerization of the A homopolymer (N_A) is greater than the degree of polymerization of the A block of the copolymer (N_{cA}), then the homopolymer chains do not significantly penetrate the copolymer brush at the interface; i.e, a dry brush persists at the interface. When $N_A < N_{cA}$, the homopolymer chains penetrate the copolymer brush creating a wet brush. Shull and Kramer have developed a self-consistent mean field theory that determines the adsorption of an A-B diblock to an interface between immiscible A and B homopolymers (*66*). Good agreement between experiment and the mean field theory was observed in the case of dPS-PVP adsorption at the polystyrene-poly(2-vinylpyridine) interface (*67a*) and at the polystyrene-poly(styrene-r-parahydroxystyrene) interface (*67b*). In addition to diblocks, copolymers exist as random copolymers, perfectly alternating copolymers, and as ABA triblocks. The adsorption of random copolymers and triblocks has been discussed by Marques and Joanny (*68*) and by Balazs et al. (*69*), respectively.

Shull has also developed a self-consistent mean field theory for end-functionalized polymers segregating to an impenetrable wall (*70*). The segregation of poly(deuterostyrene-b-2-vinyl pyridine) [dPS-PVP] to alkylsilanated silicon oxide surfaces has recently been studied (*71*). It was observed that the segregation of dPS-PVP diblock was much weaker to the alkylsilanated SiO_2- polystyrene interface than to the polystyrene-SiO_2 interface. Furthermore, the abrupt onset of segregation above a critical chemical potential suggested the formation of surface micelles. The bulk concentration of dPS-PVP at this surface transition was lower than the critical micelle concentration. Surface micelles are predicted when the attractive interactions between a copolymer and a surface is weak - as is the case for PVP blocks interacting with the alkylsilanated surface (*72*). These surface structures are not to be confused with "bulk" micelles, which exist preferentially at the interface (*73,74*). In another study, dPS-PVP segregation to an immiscible interface between polystyrene and a random copolymer of polystyrene (70%) and poly(parahydroxystyrene) [PS-PHSS] was monitored (*67b,74*). The adsorption of the dPS-PVP was accompanied by emulsification of one of the phases; i.e., a dramatic increase in copolymer adsorption beyond a critical copolymer concentration was attributed to an increase in interfacial area resulting from a vanishing interfacial tension between the two bulk phases. The tentative picture is one of a dispersion of small spheres of PS-PHSS random copolymer surrounded by a diblock shell (dPS block outermost) and dispersed in a PS matrix (*67b*). Recently, the segregation of dPS-PVP at the interface between polystyrene and [PS-PHSS] with 30% PS content has been studied. Cross-section transmission electron microscopy micrographs indicate that "hair-pin" structures exist. These undulating interfaces have not pinched off to create spherical domains

Downloaded by 89.163.35.42 on October 11, 2012 | http://pubs.acs.org
Publication Date: May 5, 1996 | doi: 10.1021/bk-1995-0615.ch001

(*75*). As to whether these hair-pin structures are a precursor to spherical domains, it is not known. On one hand, the kinetics for pinch off to spherical domains may be very slow and further, work on lower molecular weight copolymers will be required to test this hypothesis. Alternatively, the hair-pin structures may indeed be stable phase and it may be one of a variety of complicated structures that are known to exist for microemulsions.

Adsorption Kinetics

Studies in dynamic interfacial phenomena, such as adsorption kinetics and how quickly an interface recovers its interfacial tension, viscosity, and elasticity following a surface perturbation, have helped understand various technological processes such as foaming (*76,77*), emulsification (*76,78*), demulsification (*79*), and high-speed film coating (80). Adsorption kinetics of small molecule surfactants have mostly related to the air/water interface. At surfactant concentration below the CMC, adsorption kinetics follow a simple diffusion model (*81-83*). However, at surfactant concentration above the CMC, an additional complications because of the rate at which micelles dissociate is introduced (*84-87*). Other complications include electrostatic interactions, orientation effects, and mixed surfactant-macromolecule systems (*83,86*). Adsorption kinetics to liquid/liquid interfaces has additional complication due to the transport of solvent molecules across the interface (*82*). Almost invariably, adsorption kinetics has been measured by monitoring surface tension as a function of time and surface rheology at different rates of surface perturbation. Methods such as oscillating jets, ring and plate techniques, meniscus shapes, drop volume, surface potential, surface relaxation, surface quasi-elastic light scattering, and the bubble pressure method have been used to obtain adsorption kinetics (*83,87-92*). Recently, *in situ* ellipsometry has been used to study adsorption-desorption kinetics of nonionic polyethylene glycol monoethers at the silica-water interface (*93*). In addition, a phenomenogical study on the very early stages of polymer adsorption has been reported by Somasundaran and Sivakumar (*94*). In this study, the attachment of silica particles is used to decorate the polymer that has adsorbed.

The kinetics of block copolymer adsorption has been treated theoretically (*95*). In the initial stage of the adsorption kinetics, micelle relaxation is negligible and the adsorption is diffusion limited. The surface coverage increases as $\sigma \sim t^{1/2}$, where σ = surface coverage and t = time. This stage of adsorption is dominated by free chains. At larger times, micelle relaxation is important and a steady state is reached where all

Downloaded by 89.163.35.42 on October 11, 2012 | http://pubs.acs.org
Publication Date: May 5, 1996 | doi: 10.1021/bk-1995-0615.ch001

the chains released by the micelles adsorb on the surface. In this regime, surface coverage increases as $\sigma \sim t$. During this process, the outer brush of the adsorbed layer builds up and the energy barrier against adsorption increases. The theory compares quite well to experimental data when applied to the adsorption kinetics for polystyrene-polyvinylpyridine on silver, although in an apparent contradiction with the Leibler model, it is claimed that adsorption is initiated by micelle adsorption (*95c,96d*). On the other hand, there is good qualitative agreement between Liebler's theory and experiments by Motschmann et al. (*96c*). Recently, Xu et al. have studied the adsorption kinetics of polystyrene-poly(ethylene oxide) copolymer on dispersed polystyrene latex particles (*96e*). They conclude that the adsorption process is a three-step mechanism that is initiated by direct adsorption of micelles (step 1), followed by surface rearrangement (step 2), and lastly, formation of a final adsorbed layer by disruption of the micelle structure and wetting of the polystyrene particle by the polystyrene core (step 3). The kinetics of surface rearrangement (step 2) was most sensitive to the curvature of the particle, it being slower for less curved particles (larger particles). Direct adsorption by micelles has also been deduced by Munch and Gast (*51e*), and scanning electron microscopy images of adsorbed micelles have been presented by Cao et al. (*97*).

Downloaded by 89.163.35.42 on October 11, 2012 | http://pubs.acs.org
Publication Date: May 5, 1996 | doi: 10.1021/bk-1995-0615.ch001

Surface Solubilization

By analogy with solubilization phenomena in micellar solutions, it is expected that surfactant aggregates present at solid surfaces would likewise be capable of solubilizing nonpolar molecules (*98-103*). The surfactant aggregates could be present as hemimicelles, bilayers, or isolated surfactant clusters with a relatively small aggregation number (*19h*). Solubilization by adsorbed surfactant layers has been termed surface solubilization (*99,100*), coadsorption (*101,102*), or adsolubilization (*15f,103,104*). Surface solubilization is often taken as proof that the adsorbed surfactant aggregates are micelle-like (*19h*). To this effect, some early work verifying the existence of hemimicelles relied on visual evidence (*99,100*), and later spectroscopic evidence (*98*), of a dye staining solid particles at a surfactant concentration where hemimicelles exist; i.e., the surfactant concentration corresponding to the steep part of the adsorption isotherm. More recently, electron spin resonance (ESR) measurements on adsorbed surfactant aggregates indicate a hydrophobic microenvironment in the adsorbed aggregate, similar to that found in bulk micelles (*105*). Structural information about adsorbed surfactant aggregates has been obtained by fluorescence decay measurements and ESR measurements (*106*). See also ref. *106e* in which a unique study on the surfactant aggregation process by time-resolved resonance Raman spectroscopy has been described. Adsolubilization of a series of alcohols and alkanes into SDS admicelles on alumina were measured and compared to solubilization by micelles (*104*). For alkanes, the standard free energy of transfer of the alkanes into the admicelles was similar to that found with transfer of alkanes into micelles. Interestingly, however, for alcohols, the ratio of adsolubilized alcohol-SDS was much larger than in bulk micelles; i.e., the partition coefficient for the alcohol into admicelles was greater than the partition coefficient into micelles. Lee et al. (*104*) explain this unexpected behavior by invoking a two-site adsolubilization model; i.e., the alcohol is adsolubilized in the core of the admicelle (as in the case of the alkanes) and additionally at the perimeter of the micelle. Similarly, it was found that the two-site adsolubilization model was applicable to the naphthol-SDS admicelle system, but not to naphthalene-SDS admicelle system (*107*). A two-site solubilization model in bulk micelles has been postulated by Mukerjee and Cardinal (*108*).

Downloaded by 89.163.35.42 on October 11, 2012 | http://pubs.acs.org
Publication Date: May 5, 1996 | doi: 10.1021/bk-1995-0615.ch001

Another possibility for an increased solubilization capacity by admicelles in the alcohol-SDS admicelle systems (on a per surfactant molecule basis) could be due to a lower curvature of the surface aggregates compared to micelles (*108,109*). The (higher) internal pressure of the micelle would increase the chemical potential of solubilizate and therefore reduce its partition coefficient on a concentration basis into the micelle. A counter to this argument would be the similar free energy of transfer found for the alkanes partitioning into admicelles and micelles (*104*). However, the counter argument is only valid if the alkane did not transform the admicelles (~zero curvature) to highly curved small surface aggregates postulated by Zhu and Gu. (*19g*) Clearly, direct evidence rather than inferences about the shape of the surface aggregates, and the shape of surface aggregates in the presence of various adsolubilized solutes, such as alkanes and alcohols would be desirable. As in the case of solubilization of solutes by bulk micelles, surface solubilization also depends on the kinds of surfactants adsorbed, including mixed surfactant bilayers (*110*). Recently, adsolubilization (coadsorption) of decane by nonionic surfactant adsorbed at the silica-water interface has been studied by *in situ* ellipsometry (*93d*).

Adsolubilization is at the core of some novel applications and technologies. It is the basis for a separation process called admicellar chromatography (*107,111*) and for the removal of organic contaminants by surfactant aggregates on solid supports (*107,112*). Adsolubilization of styrene monomer into surfactant aggregates at an alumina surface enables *in situ* polymerization resulting in an ultra-thin coating of polystyrene over inorganic particles [Fe_2O_3, TiO_2 (*103*), and alumina (113)] and over a flat alumina coating (*99*). In related work, Esumi et al. (*113*) and Glatzhofer et al. (*114*) have polymerized styrene adsolubilized in a polymerizable surfactant bilayer on alumina. The resulting product is a mixture of different molecular weight polystyrene, possibly copolymerized with the surfactant. Similarly, polymer-encapsulated TiO_2 pigment particles have been prepared (*115*). Recently, tetrafluoroethylene gas partitioned into perfluoroheptanoate admicelles on alumina powder has been polymerized to poly(tetrafluoroethylene) (*116*). Methane and butane coadsorbed with surfactant at the mineral oxide/water interface (or possibly adsolubilized by adsorbed surfactant) was found to increase the flotation of alumina, but not of quartz. This difference could potentially be used to separate certain mineral ores by selective flotation (*117*). Nonionic surfactants adsorbed on γ-alumina (*118*) or polyacrylate nanoparticles (*119*) are capable of adsolubilizing various drugs suggesting the possible use of adsolubilization for drug delivery and drug formulation.

Conclusion

The adsorption of small molecule surfactants and polymer surfactants at various interfaces is complex and continues to be extensively studied. A variety of surfactant aggregates have been postulated based on theoretical arguments and inferences from experiments. These are admicelles (bilayers), surface micelles, and hemimicelles (monolayer aggregates, and reverse orientation model). It is likely that each type of surface aggregate exists depending on specific circumstances. Also possible is that a number of structures could coexist if the adsorbate is heterogeneous. A similar variety of rich structures are expected for polymeric surfactants, although well defined limiting structures (mushroom and brush structures) have been assigned in the case of diblock copolymers. Additionally, diblocks form a variety of two-dimensional micelles at the air/water interface. However, much more work needs to be carried out to achieve a global relationship between chemical structure and adsorption. The structure of surfactant aggregates on surfaces and their correlation with the shape of adsorption isotherms and with technologically important processes, such as wettability, friction, adhesion, and surface solubilization, will no doubt continue to be the subject of research for many years.

Downloaded by 89.163.35.42 on October 11, 2012 | http://pubs.acs.org
Publication Date: May 5, 1996 | doi: 10.1021/bk-1995-0615.ch001

References

1. (a) Rosen, M. J. *Surfactants and Interfacial Phenomena*; Wiley-Interscience: New York, NY, 1989 (2nd edition). (b) *ibid*, pp 69 onwards and pp 212 onwards.
2. *Surfactants in Emerging Technologies*; Rosen, M. J., Ed.; Surfactant Science Series; Marcel Dekker, Inc: New York, NY, 1987: Vol. 26.
3. Myers, D. *Surfactant Science and Technology*; VCH:New York, NY, 1988.
4. Adamson, A. W. *Physical Chemistry of Surfaces*; Wiley-Interscience: New York, NY, 1990 (5th Edition).
5. *Industrial Applications of Surfactants III*; Karsa, D. R., Ed.; Royal Society of Chemistry: London, 1990.
6. Miller, C. A.; Neogi, P. *Interfacial Phenomena*; Surfactant Science Series, Marcel Dekker, Inc: New York, NY, 1985, Vol. 17.
7. Vogler, E. A.; Martin, D. A.; Montgomery, D. B.; Graper, J.; Sugg, H. W. *Langmuir* **1993**, *9*, 497.
8. Everett, D. H. *Basic Principles of Colloid Chemistry*; Royal Society of Chemistry: London, 1988; pp 156.
9. (a) Osborne, D. W. and Ward, A. J. I. *Langmuir* **1991**, *7*, 840. (b) Laughlin, R. G. *ibid*, 842. (c) Rosen, M. J. *ibid*, 885.
10. (a) Eastoe, J.; Rogueda, P; Harrison, W. J.; Howe, A. M.; Pitt. A. R. *Langmuir* **1994**, *10*, 4429-4433. (b) Morley, W. G.; Tiddy, G. J. *J. Chem. Soc. Faraday Trans.* **1993**, *89*, 2823.
11. Shinoda, K.; Kamanaka, T.; Kinoshita, K. *J. Phys. Chem.* **1959**, *63*, 648.
12. (a) Piirma, I. *Polymeric Surfactants*, Surfactant Science Series, Marcel Dekker, Inc: New York, NY, 1992, Vol. 42. (b) Kissa, E. *Fluorinated Surfactants: Synthesis - Properties - Applications*, Surfactant Science Series, Marcel Dekker, Inc: New York, NY, 1994, Vol. 50. (c) Tadros, T. F. *Surfactants in Agrochemicals*, Surfactant Science Series, Marcel Dekker, Inc: New York, NY, 1995, Vol. 54.
13. (a) Somasundaran, P.; Feurstenau, D. W. *J. Phys. Chem.* **1966**, *70*, 90.
    (b) Feurstenau, D. W.; Jang, H. M. *Langmuir* **1991**, *7(12)*, 3138-43.
    (c) Kunjappu, J. T; Somasundaran, P. *Colloids Surf.* **1989**, *38*, 305-311.
    (d) Somasundaran, P.; Kunjappu, J. T. *Colloids Surf.* **1989**, *37*, 245-268.
    (e) Wirth, M. J.; Piaseck-Coleman, D. A.; Montgomery, M. E., Jr. *Langmuir* **1995**, *11*, 990.
14. (a) Harwell, J. H.; Bitting, D. *Langmuir* **1987**, *3*, 500. (b) Harwell, J. H.; Roberts, B. L.; Scamehorn, J. F. *Colloids Surf.* **1988**, *32*, 1-17.
15. (a) Gaudin, A. M.; Feurstenau, D. W. Trans. *Am. Inst. Min., Metall. Pet. Eng.* **1955**, *202*, 66. (b) Gaudin, A. M.; Feurstenau, D. W. Trans. *Am. Inst. Min., Metall. Pet. Eng.* **1955**, *202*, 958. (c) Somasundaran, P.; Healy, T. W.; Fuerstanau, D. W. *J. Phys. Chem.* **1964**, *68*, 3562. (d) Goujon, G.; Cases, J. M.; Mutaftschiev, B. *J. Colloid Interface Sci.* **1976**, *56*, 587. (e) Scamehorn, J. F.; Schecter, R. S.; Wade, W. H. *J. Colloid Interface Sci.* **1982**, *85*, 463. (f) Harwell, J. H.; Hoskins, J. C.; Schecter, R. S.; Wade, W. H. *Langmuir* **1985**, *1*, 251. (g) Bisio, P. D.; Carteledge, J. G.; Keesom, W. H.; Radke, C. J. *J. Colloid Interface Sci.* **1980**, *78*, 225. (h) Chander, S.; Feurstenau, D. W.; Stigter, D. In *Adsorption From Solution*; Ottewill, R. H.; Rochester, C. H.; Smith, A. L., Eds.; Academic: London, 1985; p917. (i) Chander, S.; Somasundaran, P.; Turro, N. J.; *J. Colloid Interface Sci.* **1987**, *117*, 31. (j) Yeskie, M. A.; Harwell, J. H. *J. Phys. Chem.* **1988**, *92*, 2346-2352.
16. Feurstenau, D. W., In *The Chemistry of Biosurfaces*; M. L. Hair, Ed.; Dekker: New York, NY, 1971, Vol. 1, pp 143.
17. (a) Koopal. L.; Ralston, J. *J. Colloid Interface Sci.* **1986**, *112*, 362.
    (b) Koopal. L.; Wilkinson, G. T.; Ralston, J. *J. Colloid Interface Sci.* **1988**, *126*, 493.

Downloaded by 89.163.35.42 on October 11, 2012 | http://pubs.acs.org
Publication Date: May 5, 1996 | doi: 10.1021/bk-1995-0615.ch001

18. Kunjappu, J. T.; Somasundaran, P. *J. Phys. Chem.* **1989**, *93*, 7744-5.
19. (a) Gao, Y.; Du, J.; Gu, T. *J. Chem Soc., Faraday Trans. 1* **1987**, *83*, 2671. (b) Gu, T.; Gao, Y.; He, L. *J. Chem Soc., Faraday Trans. 1* **1988**, *84*, 4471. (c) Gu, T.; Huang, Z. *Colloids Surf.* **1989**, *40*, 71. (d) Gu, T.; Zhu, B.-Y.; *Colloids Surf.* **1990**, *44*, 81. (e) Zhu, B.-Y.; Gu, T. *J. Chem Soc., Faraday Trans. 1* **1989**, *85*, 3813. (f) Zhu, B.-Y.; Gu, T.; Zhao, X. *J. Chem Soc., Faraday Trans. 1* **1989**, *85*, 3819. (g) Rupprecht, H.; Gu, T. *Colloid Polym. Sci.* **1991**, *269*, 506-522. (h) Gu, T.; Rupprecht, H.; Zhu, B.-Y. *Progr. Colloid Polym. Sci.* **1992**, *88*, 74.
20. (a) Corkill, J. M.; Goodman, J. F.; Ogden, C. P.; Tate, J. R. *Proc. Roy. Soc.* **1963**, *A273*, 84. (b) Jayson, G. G.; Thomson, G. *J. Colloid Interface Sci.* **1986**, *111*, 65.
21. Recently, dipolar amphiphiles have been used to construct self-assembled monolayers. Unlike monopolar surfactants, adsorption of a single molecular layer of the ionic bolaform amphiphiles cause charge reversal due to their dipolar structure. See for example: (a) Decher, G.; Hong, J. D. *Makromol. Chem. Macromol. Symp.* **1991**, *46*, 321. (b) Decher, G.; Hong, J. D.; Schmidt, J. *Thin Solid Films* **1992**, *210/211*, 831. (c) Decher, G.; Hong, J. D. *Ber. Bunsen-Ges. Phys. Chem.* **1991**, *95*, 1430. (d) Mao, G.; Tsao, Y.; Tirrell. M; Davis, T. D.; Hessel, V; Ringsdorf, H. *Langmuir* **1993**, *9*, 3461-70.
22. Billet, D. F.; Ottewill, R. H. In *Wetting*, Society of Chemical Industry: London, 1967, Vol. 25; pp 253.
23. Carmona-Ribeiro, A. M.; Midmore, B. R. *Langmuir* **1992**, *8*, 801.
24. Ingram, B. T.; Ottewill, R. H. In *Cationic Surfactants: Physical Chemistry*, Surfactant Science Series, Rubingh, D. N.; Holland, P. M., Eds.; Marcel Dekker, Inc: New York, NY, 1991, Vol. 37; pp 173-216.
25. Koopal, L. K.; Keltjens, L. *Colloids Surf.* **1986**, *17*, 371-388.
26. Lajtar, L.; Narkiewicz-Michalek, J.; Rudzinski, W.; Partyka, S. *Langmuir* **1994**, *10*, 3754-64.
27. Söderland, E.; Stilbs, P. *Langmuir* **1993**, *9*, 2024. (b) Söderland, E.; Stilbs, P. *Langmuir* **1993**, *9*, 1678. (c) Söderland, E.; Stilbs, P. *J. Colloid Interface Sci.* **1991**, *143*, 586.
28. (a) Cases, J. M.; Mutaftschiev, B. *Surface Sci.* **1968**, *9*, 57-72. (b) Cases, J. M. *Bull, Minér.* **1979**, *102*, 684-707. (c) Cases, J. M.; Canet, D.; Doerler, N.; Poirier, J. E. In *Adsorption at the Gas -Solid and the Liquid-Solid Interface*, Rouqerol, J. and Sing, K. S. W., Eds.; Elsevier/North Holland: Amsterdam, 1982; pp 21-53. (d) Cases, J. M.; Poirier, J. E.; Canet, D. In *Solid-Liquid Interactions in Porous Media*, Technip: Paris, 1985, pp. 335-370. (e) Cases, J. M.; Levitz, P.; Poirier, J. E.; Van Damme, H. In *Advances in Mineral Processing*, Somasundaran, P., Ed.; SME Publishers: Littleton, 1986; pp 171-181. (f) Cases, J. M. In *Influence Removal Org. Drinking Water*; Mallevialle, J.; Suffet, I. H.; Chan, U. S., Eds.; Lewis: Boca Raton, Fl., 1992; pp 1-17.
29. Manne, S.; Cleveland, J. P.; Gaub, H. E.; Stucky, G. D.; Hansma, P. K. *Langmuir* **1994**, *10*, 4409.
30. Narkiewicz-Michalek, J. *Ber. Bunsen-Ges. Phys. Chem.* **1991**, *95*, 85-95.
31. (a) Zettlemoyer, A. C. *J. Colloid Interface Sci.* **1968**, *28*, 343. (b) Greenwood, F. G.; Parfitt, G. D.; Picton, N. H.; Wharton, D. G. In *Adsorption from Aqueous Solutions*; Weber, W. J., Matejevic, E., Eds.; American Chemical Society: Washington DC, 1968; pp 135-144.
32. Koganovskii, A. M. *Colloid J. USSR*, **1962**, *24*, 702-708.
33. von Rybinski, W.; Schwuger, M. J. In *Nonionic Surfactants: Physical Chemistry*; Schick, M. J., Ed.; Surfactant Science Series; Marcel Dekker, Inc: New York, NY, 1987, Vol. 23, pp 45.
34. Rutland, M. W.; Senden, T. J. *Langmuir* **1993**, *9*, 412.

Downloaded by 89.163.35.42 on October 11, 2012 | http://pubs.acs.org
Publication Date: May 5, 1996 | doi: 10.1021/bk-1995-0615.ch001

35. Hey, M. J.; MacTaggart, J. W.; Rochester, C. H. *J. Chem. Soc., Faraday Trans. 1*, **1986**, *82*, 1805.
36. Ma, C.; Xia, Y. *Colloids Surf.* **1992**, *68*(3), 171-7.
37. Huang, Z; Gu, T. *Colloids Surf.* **1987**, *28*(2-4), 159-68.
38. Esumi, K.; Masuda, A.; Otsuka, H. *Langmuir* **1993**, *9*, 284.
39. (a) Somasundaran, P.; Xu, Q. *Langmuir* **1992**, *8*, 1065. (b) Xu, Q; Vasudevan, T. V.; Somasundaran, P.; *J. Colloid Interface Sci.* **1991**, *142*, 528.
40. Couzis, A; Gulari, E. *Langmuir* **1993**, *9*, 3414.
41. (a) Hayter, J. B.; Highfield, R. R.; Pullman, B. J.; Thomas, R. K.; McMullen, A. I.; Penfold, J. *J. Chem. Soc. Faraday Trans. 1* **1981**, *77*, 1437. (b) Bradley, J. E.; Lee, E. M.; Thomas, R. K.; Willat, A. J.; Gregory, D. P.; Penfold, J.; Ward, R. C.; Waschkowski, W. *Langmuir* **1988**, *4*, 821. (c) Lee, E. M.; Thomas, R. K.; Penfold, J.; Ward, R. C.; *J. Phys. Chem.* **1989**, *93*, 381. (d) Lee, E. M.; Thomas, R. K.; Rennie, A. R. *Prog. Colloid Polym. Sci.* **1990**, *81*, 203.
42. Phipps, J. S.; Richardson, R. M.; Cosgrove, T.; Eaglesham, A. *Langmuir* **1993**, *9*, 3530-3537.
43. Fina, L. J., see contribution in this book.
44. (a) Gaines, Jr. G. L. *Langmuir* **1991**, *7*, 834-39. (b) Lenk, T. J.; Lee, D. H. T.; Koberstein, J. T. *Langmuir* **1994**, *10*, 1857.
45. (a) Zhu, J.; Eisenberg, A.; Lennox, R. B. *J. Am. Chem. Soc.* **1991**, *113*, 5583; (b) Zhu, J.; Lennox, R. B.; Eisenberg, A. *Langmuir* **1991**, *7*, 1579; (c) Zhu, J.; Eisenberg, A.; Lennox, R. B. *Makro. Chem* (Macro. Symp.) **1992**, *53*, 211.; (d) Zhu, J.; Lennox, R. B.; Eisenberg, A. *J. Phys. Chem.* **1992**, *96*, 4727.; (e) Zhu, J.; Eisenberg, A.; Lennox, R. B. *Macromolecules* **1992**, *25*, 6547.; (f) Zhu, J.; Eisenberg, A.; Lennox, R. B., *Macromolecules* **1992**, *25*, 6556.
46. Li, S.; Hanley, S.; Kahn, I.; Varshney, S. K.; Eisenberg, A.; Lennox, R. B. *Langmuir* **1993**, *9*, 2243.
47. Hodge, P; Towns, C. R.; Thomas, R. K.; Shackelton, C. *Langmuir* **1992**, *8*, 585.
48. Gentle, I. R.; Saville, P. M.; White, J. W.; Penfold, J. *Langmuir* **1993**, *9*, 646.
49. Frysinger, G. S.; Barnoski, A. A.; Gaines, G. L., Jr.; *Langmuir* **1994**, *10*, 2277.
50. (a) Alexander, S. *J. Phys.* (Paris) **1977**, 38, 983. (b) Killmann, E.; Maier, H.; Baker, J. A. *Colloids and Surfaces* **1988**, *31*, 51. (c) Tadros, TH. F.; Vincent, B. J. *J. Colloid Interface Sci.* **1989**, *72*, 505. (d) Cohen Stuart, M. A.; Cosgrove, T.; Vincent, B. *Adv. Colloid Interface Sci.* **1986**, *24*, 143. (e) de Gennes, P-G. *Adv. Colloid Interface Sci.* **1987**, *27*, 189. (f) Scheutjens, J. M.; Fleer, G. J. *J. Phys. Chem* **1979**, *83*, 1619. (g) Scheutjens, J. M.; Fleer, G. J. *J. Phys. Chem* **1980**, *84*, 178. (h) Milner, S. T.; Witten, T. A.; Cates, M. E. *Macromolecules* **1991**, *24*, 1987.
51. (a) Parsonage, E.; Tirrell, M; Watanabe, H.; Nuzzo, R. G.; *Macromolecules* **1991**, *24*, 1987. (b) Satija, S. K.; Majkrzak, C. F.; Russell, T. P.; Sinha, S. K.; Sirota, E. B.; Hughes, G. J. *Macromolecules* **1990**, *23*, 3860. (c) Guzonas, D.; Boils, D.; Hair, M. L. *Macromolecules* **1991**, *24*, 3383. (d) Guzonas, D.; Boils, D.; Tripp, C. P.; Hair, M. L. *Macromolecules* **1992**, *25*, 2434. (e) Munch, M. R.; Gast, A. P. *Macromolecules* **1990**, *23*, 2313. (f) Blum, F. D.; Sinha, B. R.; Schwab, F. C. *Macromolecules* **1990**, *23*, 3592. (g) Patel, S.; Tirrell. M.; Hadziioannou, G. *Colloids Surf.* **1988**, *31*, 157.(h) Ansarifar, M. A.; Luckham, P. F. *Polymer* **1988**, *29*, 329. (i) Taunton, H. J.; Toprakcioglu, C.; Fetters, L. J.; Klein, J. *Macromolecules* **1988**, *21*, 3336.(j) Taunton, H. J.; Toprakcioglu, C.; Fetters, L. J.; Klein, J. *Nature* **1988**, *332*, 712. (k) Hadziioannou, G.; Patel, S.; Granick, S.; Tirrell, M. *J. Am. Chem. Soc.* **1986**, *108*, 2869. (l) Webber, R. M.; Anderson, J. L. *Langmuir* **1994**, *10*, 3156.
52. (a) Marques, C.; Joanny, J. F.; Leibler, L. *Macromolecules* **1988**, *21*, 1051. (b) Marques, C.; Joanny, J. F. *Macromolecules* **1989**, *22*, 1054 and references therein. (c) de Gennes, P-G. *Macromolecules* **1981**, *14*, 1637. (d) Evers, O. A.; Scheutjens, J. M. H. M.; Fleer, G. J. *Macromolecules* **1990**, *23*, 5221. (e) Milner, S. T.; Witten, T. A.; Cates, M. E. *Macromolecules* **1988**, *21*, 2610. (f)

Downloaded by 89.163.35.42 on October 11, 2012 | http://pubs.acs.org
Publication Date: May 5, 1996 | doi: 10.1021/bk-1995-0615.ch001

Cosgrove, T.; Heath, T.; van Lent, B.; Leermarkers, F.; Scheutjens, J. M. *Macromolecules* **1987**, *20*, 1692. (g) de Gennes, P-G. *Macromolecules* **1980**, *13*, 1069.

53. Li, J-T.; Caldwell, K; Rapoport, N. *Langmuir* **1994**, *10*, 4475-4482.
54. (a) Munch, M. R.; Gast, A. P. *Macromolecules* **1988**, *21*, 1366. (b) Evers, O. A.; Scheutjens, J. M. H. M.; Fleer, G. J. *Macromolecules* **1990**, *23*, 5221. (c) Whitmore, M; Noolandi, J. *Macromolecules* **1990**, *23*, 3321.
55. Dhoot, S. M. Ph.D. Thesis, University of Minnesota, 1994. (b) McKenzie, P. F.; Webber, R. M.; Anderson, J. L. *Langmuir* **1994**, *10*, 1539.
56. (a) Auroy, P.; Auvray, L.; Léger, L. *Phys. Rev. Lett.* **1991**, 66, 719 and references therein. (d) Auroy, P.; Auvray, L.; Léger, L. *Physica A* **1991**, *172*, 269.
57. Factor, B. J.; Lee, L.-T.; Kent, M. S.; Rondalez, F. Paper No. 307 Presented at the 67th Colloid and Surface Science Symposium, University of Toronto, June 21-23, 1993.
58. Kim, M, W.; Russell, T. P.; Moses, T.; Chen, W.; Shen, Y. R. *Macromolecules* **1994**, *27*, 7490.
59. Auroy, P.; Auvray, L. *Langmuir* **1994**, *10*, 225.
60. Wijmans, C. M.; Leermarkers, F. A. M.; Fleer, G. J. *Langmuir* **1994**, *10*, 1331.
61. (a)Tjipangandjara, K. J.; Huang, Y.-B.; Somasundaran, P.; Turro, N. J. *Colloids and Surfaces* **1990**, *44*, 229. (b) Garces, F. O.; Sivadasan, K.; Somasundaran, P.; Turro, N. J. *Macromolecules* **1994**, *27*, 272. (c) Maltesh, C.; Xu, Q.; Somasundaran, P.; Benton, W. J.; Nguyen, H. *Langmuir* **1992**, *8*, 1511. (d) Maltesh, C.; Somasundaran, P. *Colloids and Surfaces* **1992**, *69*, 167. (e) Kiefer, J. J.; Somasundaran, P.; Ananthapadmanabhan, K. P. *Langmuir* **1993**, *9*, 1187. (f) Sivadasan, K.; Somasundaran, P. *J. Polym. Sci. Part A: Polym. Chem.* **1991**, *29*, 911. (g) Maltesh, C.; Somasundaran, P.; Pradip; Kulkarni, R. A.; Gundiah, S. *Macromolecules* **1991**, *24*, 5775. (h) Pradip; Maltesh, C.; Somasundaran, P.; Kulkarni, R. A.; Gundiah, S. *Langmuir* **1991**, *7*, 2108.
62. (a) Creton, C.; Kramer, E. J.; Hui, C. Y.; Brown, H. R. *Macromolecules* **1992**, *25*, 3075. (b) Brown, H. R. *Macromolecules* **1989**, *22*, 2859. (c) Washiyama, J.; Creton, C.; Kramer, E. J. *Macromolecules* **1992**, *25*, 4751. (d) Washiyama, J.;Kramer, E. J.; Hui, C-Y. *Macromolecules* **1993**, *26*, 2928. (e) Janarthanan, V.; Stein, R. S.; Barrett, P. D. *Macromolecules* **1994**, *27*, 4855. (f) Brown, H. R.; Char, K.; Deline, V. R. In *Integration of Fundamental Polymer Science and Technology*, Lemstra, P. J. Ed; Elsevier: Amsterdam, Vol. 5, pp 51. (g) Willet, J. L.; Wool, R. P. *Macromolecules*,**1993**, *26*, 5336. (h) Brown, H. R; Deline, V. R.; Green, P. F. *Nature* **1989**, *341*, 221.
63. (a) Smith, J. W.; Kramer, E. J.; Mills, P. *J. Polym. Sci.- Poly. Phys.* **1994**, *B 32*, 1731. (b) Smith, J. W.; Kramer, E. J.; Xiao, F.; Hui, C-Y.; Reichert, W.; Brown, H. R. *J. Mater. Sci.* **1993**, *28*, 4234.
64. Plueddeman, E. P. *Silane Coupling Agents*, Plenum Press: New York, NY, **1991**.
65. (a) Leibler, L. *Makromol. Chem. Macromol. Symp.* **1988**, *16*, 1. (b) Leibler, L. *Physica A*, **1991**, *172*, 258.
66. Shull, K. R.; Kramer, E. J. *Macromolecules* **1990**, *23*, 4769.
67. (a) Shull, K. R.; Kramer, E. J.; Hadziioannou, G.; Tang, W. *Macromolecules* **1990**, *23*, 4780. (b) Shull, K. R.; Kelock, A. J.; Deline, V. R.; MacDonald, S. A. *J. Chem .Phys.* **1992**, *97*, 2095.
68. Marques, C. M.; Joanny, J. F. *Macromolecules* **1990**, *23*, 268.
69. (a) Balazs, A. C.; Lewandowski, S. *Macromolecules* **1990**, *23*, 839. (b) Balazs, A. C.; Huang, K.; Lantman, C. W. *Macromolecules* **1990**, *23*, 4641.
70. Shull, K. R. *J. Chem. Phys.* **1991**, *94*, 5723.
71. Calistri-Yeh, M, Kramer, E. J.; Shull, K. R.; Sharma, R., in preparation.
72. Shull, K. R. *Macromolecules* **1993**, *26*, 2343.

Downloaded by 89.163.35.42 on October 11, 2012 | http://pubs.acs.org
Publication Date: May 5, 1996 | doi: 10.1021/bk-1995-0615.ch001

73. Jones, R. A. L.; Kramer, E. J.; Rafailovich, M. H.; Sokolov, J.; Schwarz, S. A. *Phys. Rev. Lett.* **1989**, *62*, 280.
74. Shull, K. R.; Winey, K. I.; Thomas, E. L.; Kramer, E. J. *Macromolecules* **1991**, *24*, 2748.
75. Jandt, K. D.; Xu, Z.; Kramer, E. J.; Edgecombe, B. D.; Frechet, J. M. J. presented at APS meeting (San Diego), March, 1995. See also, Materials Science Centre, Report # 7913, Cornell University, 1995.
76. Kragel, J.; Siegel, S. Miller, R; Born, M.; Schano, K.-H. *Colloids Surf. A* **1994**, *91*, 169 and references therein.
77. (a) Lucassen, J. In *Anionic Surfactants - Physical Chemistry of Surfactant Acton;* Lucassen-Reynders, *E. H.*, Ed.; Surfactant Science Series, Marcel Dekker: New York, NY, 1981, Vol. 11; pp 217-265 (b) Edwards, D. A.; Brenner, H.; Wasan, D. T. *J. Colloid Interface Sci.* **1989**, *130*, 266. (c) Wasan, D. T.; Nikolov, A. D.; Lobo, L. A.; Koczo, K.; Edwards, D. A. *Prog. Surf. Sci.* **1992**, *40*, 119.
78. (a) Sherman, P. *J. Colloid Sci.* **1953**, *8*, 35. (b) Lucassen-Reynders, E. H.; Kuijpers, K. A. *Colloids Surf.* **1992**, *63*, 175. (c) Doi, M.; Ohta, T. *J. Chem Phys.* **1991**, *95*, 1242. (d) Dickinson, E,; Murray, B. S.; Sainsby, G. *J. Chem Soc. Faraday Trans. 1* **1988**, *84*, 871.
79. (a) Krawczyk, M. A.; Wasan, D. T.; Shetty, C. S. *Ind. Eng. Chem. Res.* **1991**, *30*, 367. (b) Thompson, D. G.; Taylor, A. S.; Graham, D. E. *Colloids Surf.* **1985**, *15*, 175. (c) Jones, T. J. Neustadter, E. L.; Whittingham, K. P. *J. Can. Pet. Technol.* **1978**, *April-June*, 100. (d) Sjöblom, J.; Söderlund, H.; Lindblad, S; Johansen, E. J.; Skjärvo, I. M. *Colloid Polym. Sci.* **1990**, *268*, 389. (e) Shetty, C. S.; Nikolov, A. D.; Wasan, D. T. *J. Disp. Sci. Tech.* **1992**, *13*, 121. (f) Breen, P. J., in this book.
80. (a) Fruhner, H.; Krägel, J.; Kretzschmar, G. *J. Inf. Rec. Mater.* **1991**, *19*, 45. (b) Kretzschmar, G.; Fruhner, H.; Krägel, J. *Tenside* **1993**, *30*, 110.
81. Ward, A. F. H.; Tordai, L. *J. Chem. Phys.* **1946**, *14*, 543.
82. Miller, R. *Colloids Surf.* **1990**, *46*, 75 and references therein
83. Kochurova, N. N.; Rusanov, A. I. *Colloids Surf. A* **1993**, *76*, 1.
84. Fainerman, V. B. *Usp. Khim.* **1985**, *54*, 1613; English Translation in *Russ. Chem. Rev.* **1985**, *54*, 948.
85. Dunn, A. S. *Poly. Mater. Sci. Eng.* **1991**, *64*, 221.
86. Miller, R.; Kretzschmar, G. *Adv. Colloid Interface Sci.* **1991**, *37*, 97 and references therein.
87. Geeraerts, G.; Joos, P. *Colloids Surf. A* **1994**, *90*, 149.
88. Fainerman, V. B.; Makievski, A. V.; Joos, P. *Colloids Surf. A* **1994**, *90*, 213.
89. (a) van Voorst Vader, F.; Erkens, T. F.; van den Tempel, M. *Trans. Faraday Soc.* **1964**, *60*, 1170. (b) Lucassen-Reynders, E. H.; Lucassen, J. *Colloids Surf. A* **1994**, *85*, 211.
90. Miller, R.; Loglio, G.; Tesei; U.; Schano, K.-H. *Adv. Colloid Interface Sci.* **1991**, *37*, 73.
91. (a) Sauer, B.; Yu, H. *Macromolecules* **1989**, *22*, 786. (b) Langevin, D.; Meunier, J.; Chatenay, D. In *Surfactants in Solution*; Mittal, K. L., Ed.; Plenum Press: New York, NY, 1984, Vol. 3; pp 1991.
92. Hua, X. Y.; Rosen, M. J. *J. Colloid Interface Sci.* **1988**, *124*, 652.
93. (a) Tiberg, F.; Lindman, B.; Langdgren, M. *Thin Solid Films* **1993**, *234*, 478. (b) Tiberg, F.; Jönsson, B.; Lindman, B. *Langmuir* **1994**, *10*, 3714. (c) Tiberg, F.; Jönsson, B.; Tang, J.; Lindman, B. *Langmuir* **1994**, *10*, 2294. (d) Tiberg, F.; Brink, J., in this book.
94. Somasundaran, P.; Sivakumar, A. *Colloids Surf.* **1988**, *30*, 401.
95. (a) Ligoure, Ch.; Leibler, L. *J. Phys. F.* **1990**, *51*, 1313. (b) Johner, A.; Joanny, J. F. *Macromolecules* **1990**, *23*, 5299. (c) Johner, A.; Joanny, J. F.; Marques, C. *Physica A* **1991**, *172*, 285. (d) Kislenko, V. N.; Berlin, Ad. A.; Moldovanov, M. A. *Kolloidn. Zh.* **1993**, *55(1)*, 83.

Downloaded by 89.163.35.42 on October 11, 2012 | http://pubs.acs.org
Publication Date: May 5, 1996 | doi: 10.1021/bk-1995-0615.ch001

96. (a) Munch, M. R.; Gast, A. *J. Chem. Soc., Faraday Trans.* **1990**, *86*, 1341. (b) Munch, M. R.; Gast, A. *Macromolecules* **1990**, *23*, 2313. (c) Motschmann, H.; Stamm, M.; Toprakcioglu, Ch. *Macromolecules* **1991**, *24*, 3681. (d) Tassin, J. F.; Siemens, R. L.; Tang, W. T.; Hadziioannou, G.; Swalen, J. D.; Smith, B. A. *J. Phys. Chem.* **1989**, *93*, 2106. (e) Xu, R; D'Unger, G.; Winnik, M. A.; Martinho, J. M. G.; d'Oliveira, J. M. R. *Langmuir* **1994**, *10*, 2977, and references therein.
97. Cao, T.; Yin, W.; Armstrong, J. L.; Webber, S. E. *Langmuir* **1994**, *10*, 1841.
98. Zhu, B.-Y.; Gu, T. *Adv. Colloid Interface Sci.* **1991**, *37(1-2)*, 1-32. (b) Zhu, B.-Y.; Zhao, X.; Gu, T. *J. Chem Soc., Farday Trans. 1* **1988**, *84*, 3957.
99. Stigter, O.; Williams, R. J.; Mysels, K. J. *J. Phys. Chem.* **1955**, *59*, 330.
100. Nunn, C. C.; Schecter, R. S.; Wade, W. H. *J. Phys. Chem.* **1982**, *86*, 3271.
101. Monticone, V.; Treiner, C. *J. Colloid Interface Sci.* **1994**, *166*, 394.
102. Koganovski, A. M.; Klimenko, N. A.; Tryasorakova, A. A. *Kolloidn Zh.* **1974**, *36*, 861; **1976**, *38*, 165.
103. Wu, J.; Harwell, J. H.; O'Rear, E. A. *Langmuir* **1987**, *3*, 531; *Colloids Surf.* **1987**, *26*, 155.
104. Lee, C.; Yeskie, M. A. Harwell, J. H.; O'Rear, E. A. *Langmuir* **1990**, *6*, 1758.
105. Esumi, K.; Sugimura, A.; Yamada, T. *J. Jpn. Soc. Colour Mater. (SHIKIZAI)* **1993**, *66(3)*, 142.
106. (a) Somasudaran, P; Chander, P.; Turro, N. J. *J. Colloid Interface Sci.* **1987**, *117*, 31. (b) Somasudaran, P; Chander, P.; Turro, N. J. *Colloids Surf.* **1986**, *20*, 415. (c) Waterman, K. C. Turro, N. J.; Chander, P; Somasundaran, P. *J. Phys. Chem.* **1986**, *90*, 6829. (d) Chander, P.; Somasundaran, P; Waterman, K.; Turro, N. J. *J. Phys. Chem.* **1987**, *91*, 148 and references therein. (e) Somasundaran, P.; Kunjappu, J. T.; Kumar, C. V.; Turro, N. J.; Barton, J. K. *Langmuir* **1989**, *5*, 215. (f) Sivakumar, A.; Somasundaran, P. *Langmuir* **1994**, *10*, 131 and references therein.
107. Nayyar, S. R.; Sabatini, D. A.; Harwell, J. H. *Environ. Sci. Technol.* **1994**, *28*, 1874.
108. Mukerjee, P.; Cardinal, J. R. *J. Phys. Chem.* **1978**, *82*, 1620.
109. Mukerjee, P. *Ber. Bunsenges. Phys. Chem.* **1978**, *82*, 931; *Kolloid. Z. Z. Polym.* **1970**, *76*, 236; In *Solution Chemistry of Surfactants*; Mittal, K. L., Ed.; Plenum Press: New York, NY,1984, Vol. 1; pp 153.
110. Esumi, K.; Sakamoto, Y.; Nagahama, T.; Meguro, K. *Bull. Chem. Soc. Jpn.* **1989**, *62*, 2502-6.
111. (a) Barton, J. W.; Fitzgerald, T. P.; Lee, C.; O'Rear, E. A.; Harwell, J. H. *Sep. Sci. Technol.* **1988**, *23*, 637. (b) Grout, R. C. M. S. Thesis, University of Oklahoma, 1987.
112. (a) Klumpp, E; Heitmann, H.; Lewandowski, H.; Schwuger, M. J. *Prog. Colloid Polym. Sci.* **1992**, *89*, 181. (b) Klumpp, E; Heitmann, H.; Schwuger, M. J. *Colloids and Surfaces A* **1993**, *78(1-3)*, 93. (c) Valsaraj, K. T. *Sep. Sci. Technol.* **1992**, *27(12)*, 1633; **1989**, *24*(13), 1191.
113. Meguro, K.; Yabe, T.; Ishioka, S.; Kato, K.; Esumi, K. *Bull. Chem. Soc. Jpn.* **1986**, *59*, 3019.
114. Glatzhofer, D. T.; Cho, G, Lai, C. L.; O'Rear, E. A.; Fung, B. M. *Langmuir* **1993**, *9(11)*, 2949.
115. Caris, C. H. M.; Herk, A. M. V.; German, A. L. *FATIPEC-Kongr.* **1990**, *20th*, 325-9.
116. Lai, C.-L.; Harwell, J. H.; O'Rear, E. A. *Langmuir* **1995**, *11*, 905-911.
117. Somasundaran, P.; Moudgil, B. M. *J. Colloid Interface Sci.* **1974**, *47*, 290.
118. Jansen, J.; Treiner, C.; Vaution, C.; Puisieux, F. *Int. J. Pharm.* **1994**, *103*, 19.
119. Harmia, T.; Speiser, P.; Kreuter, J. *Int. J. Pharm.* **1986**, *33*, 45.

RECEIVED September 1, 1995

Downloaded by 89.163.35.42 on October 11, 2012 | http://pubs.acs.org
Publication Date: May 5, 1996 | doi: 10.1021/bk-1995-0615.ch001

Chapter 2

Adsorption of Surfactants and Solubilization in Adsorbed Layers

Pasupati Mukerjee[1], Ravi Sharma[2], Richard A. Pyter[3], and Michael J. Gumkowski[4]

[1]School of Pharmacy, University of Wisconsin, Madison, WI 53706
[2]Materials Science and Engineering Division, Eastman Kodak Company, Rochester, NY 14650–2158
[3]Abbott Laboratories, Department 493, North Chicago, IL 60064
[4]Pfizer Central Research, Building 156, Eastern Point Road, Groton, CT 06340

Sodium decyl sulfate and sodium perfluorooctanoate have similar critical micellization concentrations but behave differently in adsorption to Graphon. Monomeric perfluorooctanoates have a weaker affinity for the surface, reflecting some fluorocarbon-hydrocarbon antipathy, but show stronger, cooperative, lateral interactions in adsorbed layers. Electrolyte effects can be represented simply: the isotherm is uniquely determined by the mean activity of the surfactants. The observed differences in adsorption to solid-liquid and liquid-vapor interfaces provide rationalization for different wetting properties. Micelles tagged by the dye Orange OT have given direct evidence of the exclusion of ionic micelles from charged surfaces. Comparison has been made with co-ion exclusion. Adsorbed bilayers of surfactants solubilize Orange OT more effectively than coexisting micelles. A two-state model of solubilization is used to describe and compare uptake in micelles and bilayers.

This presentation gives an account of some of the findings of our research in this laboratory on (a) adsorption of fluorocarbon and hydrocarbon surfactants to Graphon, which is a graphitized carbon with a fairly homogeneous surface, (b) the relation of interfacial adsorption to contact angles and wetting, (c) the negative adsorption of micelles from charged surfaces, and (d) the comparison of solubilization in adsorbed bilayers to solubilization in micelles in terms of the two-state model of solubilization in lipid assemblies. Much of the research on items (a), (b), and (c) is as yet unpublished. The material presented here has been chosen to illustrate some important points. Although some published work is reviewed, no attempt has been made to give a comprehensive review of the literature, the emphasis being on work done in this laboratory.

0097–6156/95/0615–0022$12.00/0

Experimental

Materials. The surfactant material used is similar to the material described in previous publications from this laboratory (*1,2*). Orange OT (1-o-tolylazo-2-naphthol) was a synthetic preparation and was recrystallized from acetone-water mixtures and ethanol (*3*). Alon was obtained from Degussa Inc.

Methods. The adsorption of the anionic surfactants, lithium tetradecyl sulfate (LiTDS), sodium decyl sulfate (SDeS) and sodium perfluorooctanoate (SPFO) were measured by using analytical procedures based on a two-phase equilibration method in which the surfactants are extracted into chloroform as salts of the cationic dye methylene blue (*4,5*). Dodecyl pyridinium chloride (DPC) and cetyl pyridinium chloride (CPC) were analyzed by ultraviolet spectrophotometry based on the pyridinium chromophore. In all experiments time-dependence was investigated to assure equilibration. The solubilization of Orange OT was estimated by using a dialysis equilibrium method (*3*).

Adsorption to Graphon

The adsorption of surfactants from aqueous solutions to different interfaces often involves quite different expressions of the hydrophobicity of amphiphilic molecules which also leads to their self-association to produce micelles and other lipid assemblies (*1,6-8*). The comparison of the behavior of fluorocarbon and hydrocarbon surfactants has been of considerable interest in this connection (*1,7,8*). Remarkable differences have been found in the adsorption of surfactants to air-water, heptane-water, and perfluoroheptane-water interfaces from dilute aqueous solutions, particularly in comparison to the formation of micelles in solution. The net expression of hydrophobicity depends not only upon the interactions of the hydrophobic moieties of these surfactants with water but also on their interactions at different interfaces or with each other where self-association is involved.

The work presented here is a part of a study of the nature of the adsorption of fluorocarbon and hydrocarbon surfactants to Graphon (*9*). Graphon is a graphitised carbon exhibiting a nearly homogeneous surface. The study was designed to explore the differences in the expression of hydrophobicity of the two classes of surfactants in their adsorption to a relatively simple hydrophobic solid surface, and to compare adsorption to solid surfaces to adsorption to fluid interfaces.

Results and Discussion. Figure 1 shows the adsorption isotherms of SDeS and SPFO. The critical micellization concentrations (c.m.c.) of these two substances are very similar, 0.032 M for SDeS (*11*) and 0.031 M for SPFO (*12*). Figure 1 indicates that SDeS shows greater adsorption than SPFO from dilute aqueous solutions, i.e., at the initial stages of adsorption. Previous work has indicated that SPFO adsorbs some 6.4 times more effectively than SDeS at the air/water interface, when surfactant concentrations are low (*1,7*). The Graphon-water interface shows a reversal which is also seen at the hexane/water interface where

SDeS adsorbs from dilute aqueous solutions nearly twice as effectively as SPFO (*1,7*). Thus the adsorption data from dilute solutions in Figure 1 suggests strongly that the unfavorable interactions between fluorocarbons and hydrocarbons reflected in the hexane/water interface data (*1,7,8*) are also important for Graphon-water interface.

With increasing concentrations, however, Figure 1 shows a pronounced difference in the adsorption isotherms of SDeS and SPFO. The SDeS isotherm is much closer to a simple Langmuir-type isotherm than the SPFO isotherm. The latter shows a considerable degree of cooperativity and at higher concentrations the adsorption of SPFO exceeds that of SDeS. A number of model isotherms, such as those carrying the names of Langmuir, Davies and Rideal (*12*), Fowler and Guggenheim (*13*), have been examined. None appears to be satisfactory. Qualitatively we believe the high degree of cooperativity exhibited by the SPFO isotherm arises from attractive lateral interactions between the fluorocarbon chains. These are probably hydrophobic in origin. Arguments have been summarized recently to show that fluorocarbon chains are more hydrophobic than hydrocarbon chains (*7*) and a major part of the difference arises from the greater contributions of water-structure effects in the case of fluorocarbons (*7,14*).

The comparison between adsorption to the solid-water interface and to the liquid-vapor interface is of fundamental interest. It is also important in the understanding of wetting properties of surfactants, as discussed later. Figure 2 shows plots of the ratios of the adsorption of SDeS and SPFO to the Graphon-water interface, Γ_{SL}, and to the liquid-vapor interface, Γ_{LV}, from an earlier publication (*15*). The Γ_{SL}/Γ_{LV} ratios are plotted against the reduced concentration, C/c.m.c., of SPFO and SDeS. For SDeS Γ_{SL} is much higher than Γ_{LV} in dilute solutions suggesting that the Graphon-water interface allows additional attractive interactions of the hydrocarbon chain when compared to the air-water interface. With increasing concentration, however, the Γ_{SL}/Γ_{LV} ratio decreases to a value of somewhat less than unity. In comparison, the Γ_{SL}/Γ_{LV} ratio is much less than unity for dilute solutions of SPFO, suggesting strongly that the interactions of individual fluorocarbon chains at the Graphon-water interface are less attractive than at the air/water interface. With increasing concentration, however, the Γ_{SL}/Γ_{LV} ratio increases and becomes close to unity near the c.m.c., exceeding the ratio for SDeS. These results can be attributed to a greater degree of cooperative chain-chain interactions in the adsorbed layer of SPFO at the Graphon-water interface (*8,9*).

Effect of Added Electrolytes on Adsorption. The adsorption of ionic surfactants to initially neutral surfaces involves the uptake of the surfactant in presence of an electrostatic potential produced by the adsorbed layer. It is well known that when inert inorganic electrolytes are added, with a common counterion, surfactant adsorption is facilitated because the repulsive electrostatic interactions in the adsorbed layer are reduced when electrolyte concentrations are higher and the thickness of the electrical double layer is lower (*12,13*). In the case of surfactant adsorption at the air/water and oil/water interfaces it has been found that these electrolyte effects can usually be treated in a simple

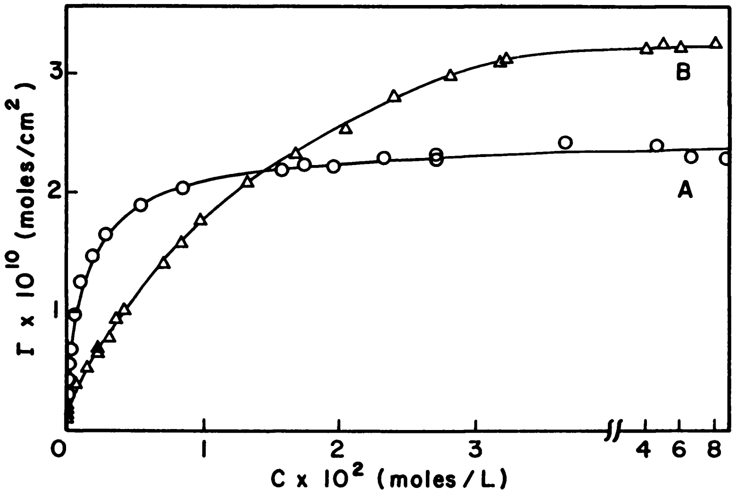

Figure 1. Surfactant adsorption, Γ, to Graphon. ○ - SDeS, Δ - SPfO.

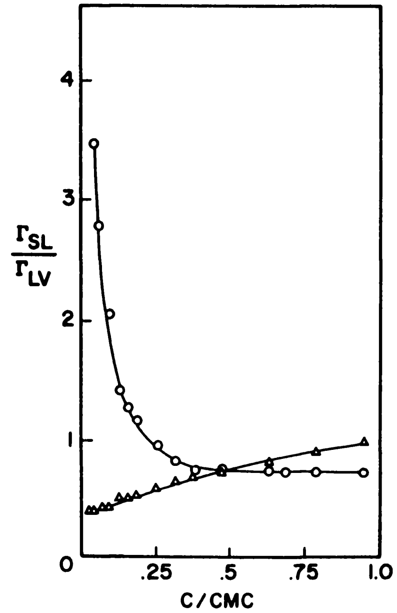

Figure 2. Γ_{SL}/Γ_{LV} as a function of reduced surfactant concentration, C/c.m.c., on Graphon. ○ - SDeS, Δ - SPfO. Reproduced with permission from ref. 15. Copyright 1982, Academic Press.

manner (*16,17*). Thus surface and interfacial tension data for these interfaces at various salt concentrations can be represented by single plots if the mean ionic activity of the surfactant is used instead of its concentration. Thermodynamic approaches in support of this treatment have been presented (*16*).

Surfactant adsorption to solid surfaces is expected to differ greatly from adsorption to fluid surfaces. Nevertheless, in our study on the effect of added sodium chloride on the adsorption of anionic surfactants to Graphon (*9*), we have found that the effect of the inert electrolyte on adsorption can be represented very well by the effect of the inert electrolyte on the calculated mean ionic activity, $a_\pm$, of the surfactant salt. Equation 1 is used to calculate the value of $a_\pm$.

$$a_\pm = \gamma_\pm \left[(C_{Na} + C_s)C_s\right]^{1/2} \qquad (1)$$

$C_{Na}+$ represents the concentration of added NaCl, C_s is the concentration of the surfactant, a sodium salt, and $\gamma_\pm$ is assumed to equal to mean ionic activity coefficient of sodium chloride at the ionic strength involved (*18*). Figure 3 shows a representative plot for SPFO. Added NaCl concentration was varied from zero to 0.15 M. The adsorption data fall on the same curve when plotted against $a_\pm$ of SPFO. Similar results were also obtained for sodium decyl and dodecyl sulfates. These results and their significance will be reported later in full (*9*).

An important practical application of the results of the type shown in Figure 3 is that the effect of electrolytes on the adsorption at any concentration of a surfactant can be easily predicted by calculating the effect on $a_\pm$ of the surfactant if the adsorption isotherm is available at one salt concentration.

Wetting of Solids. It has been shown that the relative absorbability of a surfactant to the solid-liquid and to the liquid-vapor interfaces has a very important implication for the wetting of relatively low-energy solids by surfactant solutions (*15*). If a surfactant solution with a surface tension γ_{LV} produces a contrast angle Θ on such a solid, Lucassen-Reynders (*19*) showed that

$$\frac{d(\gamma_{LV}\cos\theta)}{d\gamma_{LV}} = \frac{\Gamma_{SV}-\Gamma_{SL}}{\Gamma_{LV}} \qquad (2)$$

where Γ_{SV}, Γ_{SL}, and Γ_{LV} represent the surface excesses or adsorption of the surfactant at the solid-vapor, solid-liquid, and liquid-vapor interfaces. For neutral surfaces Γ_{SV} can be assumed to be zero. A plot of $\gamma_{LV}\cos\Theta$ against γ_{LV} then has a slope of $-(\Gamma_{SL}/\Gamma_{LV})$. Figure 4, taken from an earlier publication (*15*), shows the range of expected behavior of surfactants for the wetting of paraffin for which $\cos\Theta$ has the value of -0.276 in water (*15*). The wetting line is the line represented by $\cos\Theta = 1$. The line obtained by assuming Γ_{SL}/Γ_{LV} is zero does not meet the wetting line at any value of γ_{LV}, i.e., complete wetting is impossible. On the other hand, if Γ_{LV}/Γ_{SL} is zero, wetting may occur

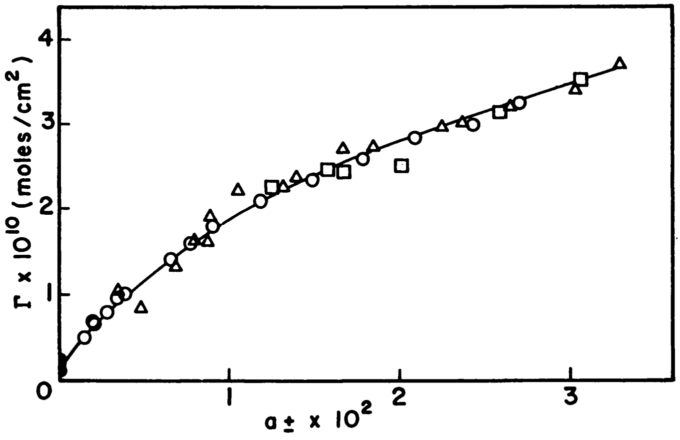

Figure 3. SPFO adsorption to Graphon in the presence of various NaCl concentration plotted against the mean activity of SPfO. ○ - No NaCl, Δ - 0.1 M NaCl, ☐ NaCl concentrations 0.02 M, 0.05 M, 0.08 M, 0.15 M. All equilibrium concentrations are below the c.m.c.

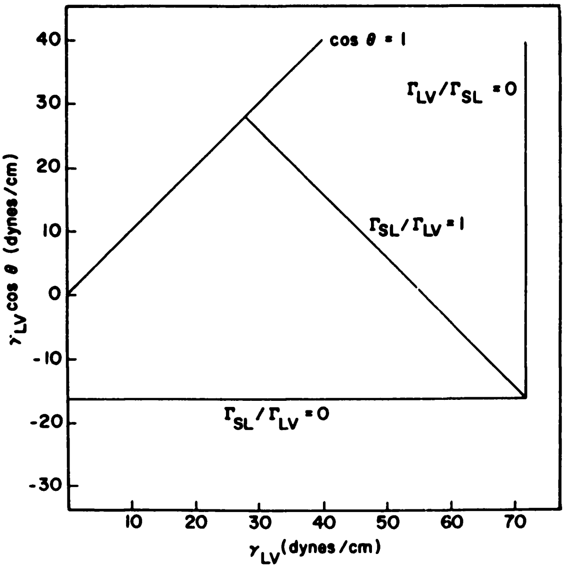

Figure 4. Theoretical γ_{LV} cosΘ versus surface tension plots for surfactant solutions on paraffin assuming Γ_{SL}/Γ_{LV} equal to zero, one, or infinity. Reproduced with permission from ref. 15. Copyright 1982, Academic Press.

without any change in γ_{LV}. Johnson and Dettre (*20*) proposed that Γ_{LV}/Γ_{SL} be taken as unity for wetting by surfactants. For this curve the critical surface tension for wetting is 28 ergs cm^{-2} (Figure 4).

The above considerations have provided good qualitative explanations for some unusual wetting properties of surface active agents. Thus fluorocarbon surfactant solutions tend to show higher contact angles on nonpolar solids such as paraffin and polyethylene when compared to solutions of hydrocarbon surfactants which have the same surface tension values. The critical surface tensions needed for wetting are thus often significantly lower (*15*). These kinds of phenomena can be readily explained qualitatively by the different kinds of Γ_{SL}/Γ_{LV} curves represented in Figure 2. These considerations have been examined in detail using a number of examples (*15*).

Exclusion of Micelles from Charged Surfaces

In 1975 a proposal was made that ionic micelles can show negative adsorption to surfaces which bear the same charge as the ionic micelles (*2*). This can be ascribed to the exclusion of micelles from the electrical double layers of the charged surfaces (*2*) resulting from repulsive interactions similar to what causes the well-known co-ion exclusion from double layers (*21*). Aside from its intrinsic interest micellar exclusion may have some interesting implications for other kinds of studies. For example, when surfactant adsorptions to solid surfaces are estimated from the usual experiments based on measurements of the loss of surfactant in the supernatant liquid, any estimate of the adsorption of the surfactant monomer to the solid surface is affected by the negative adsorption of micelles above the c.m.c. As a result there may be an underestimate of monomeric adsorption. Under some circumstances there may even be an apparent maximum in the adsorption isotherm. These points can be illustrated by some experimental data presented in 1975 (*2*) on the adsorption of sodium dodecyl sulfate and sodium tetradecyl sulfate (Figure 5) to a sample of Bio-Glass 200, which is a porous glass with an average pore-diameter of 18.5 nm and a surface area of about 140 m^2/g. Because of the hydrophilic nature of the glass surface and its negative charge, the adsorption of the anionic monomers of SDS was very small. As a result, above the c.m.c. value of about 8.5 mM (*10*), the net adsorption of SDS was essentially negative as a result of micellar exclusion. With sodium tetradecyl sulfate the adsorption of the monomer up to the c.m.c. of about 2 mM was significant although it was an order of magnitude lower than the adsorption of cationic surfactants to the same substrate (*2*). Above the c.m.c., however, the apparent adsorption decreased with increase in concentration, as expected from the combination of monomer adsorption and micellar exclusion. As a result a maximum was exhibited by the adsorption isotherm near the c.m.c.

Although a thermodynamic analysis supporting the possibility of micellar exclusion of the kind described above has been published (*22*), it has also been suggested that a maximum in an adsorption isotherm is thermodynamically impossible (*23*). In view of the controversial nature of this finding we have studied the exclusion of micelles from solid suspensions bearing the same charge

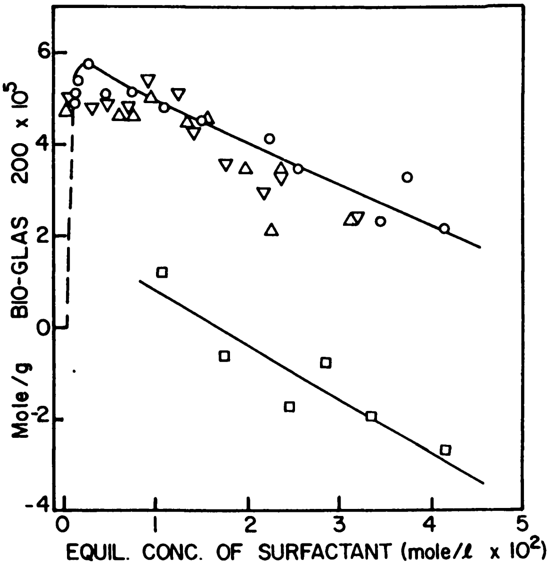

Figure 5. Adsorption of sodium tetradecyl sulfate (STDS) and sodium dodecyl sulfate (SDS) to Bio-GLas 200 at 35°C. ○ - STDS, Δ - STDS in 0.01 M NaCl, ∇ - STDS in 0.03 M NaCl, □ - SDS. Reproduced with permission from ref. 2. Copyright 1975, American Chemical Society.

as the micelles using a direct method (*24*). In this the micelles are tagged by the solubilization of Orange OT, an uncharged dye molecule which has a negligibly low solubility, about 10^{-7} M, in water. The solubilization of Orange OT has frequently been used to determine c.m.c. values of surfactants (*10*). The negative adsorption of micelles can be directly determined from the exclusion of the tagged micelles from the solid surface. This results in an increase in the absorbance of Orange OT in the supernatant liquid when an appropriate finely divided solid is added to the system. We have also compared the negative adsorption of Orange OT in a micellar solution with the negative adsorption of the surfactant itself from the same solution and the negative adsorption of a similar surfactant below the c.m.c. as a co-ion.

Table I. Negative Adsorption to Alon

		Vex ($\frac{\text{ml}}{\text{g}}$)	δ (Å)
1.	Surfactant Exclusion, Micellar, CPC, Ci = 0.0985 M	0.73 ± 0.015	64 ± 1.3
2.	Orange OT Exclusion, Micellar, CPC, Ci = 0.0985 M, A_i = 0.944	0.71 ± 0.025	60 ± 2.1
3.	Monomer Exclusion, DPC, Ci = 4.41 x 10^{-3} M	0.67	57

Results and Discussion. Table I shows a typical set of data using Alon, a nonporous aluminum oxide powder with a surface area of 117 sq m/g, and two cationic surfactants. At the supernatant equilibrium pH of about 5.1 Alon is known to have a positively charged surface. The exclusion of monomeric dodecyl pyridinium chloride (DPC), well below its c.m.c. value, from the double layer of Alon was measured by adding about 0.14-0.15 g of Alon per ml of a DPC solution in water. At equilibrium the concentration of DPC in the supernatant increased by about 10% over the initial concentration, C_i, when Alon was added. This increase indicates a negative adsorption of DPC to Alon arising from the exclusion of the cationic surfactant from the electrical double layers around the alumina particles. For the particular experiment reported in Table I, assuming that the exclusion arises entirely from complete exclusion from a region of thickness δ around each Alon particle, the value of δ can be estimated to be 57 Å, corresponding to an excluded volume, Vex, of 0.67 ml/g. The thickness of the double layer at the final ionic strength of the solution is about 43 Å. It is possible to use the exclusion data and the Gouy-Chapman theory for planar electric double layers (*21*) to estimate a surface potential of about 55 mv which appears to be of reasonable magnitude.

Similar experiments using micellar solutions of cetyl pyridinium chloride (CPC) at a high initial concentration of 0.0985 M were performed to study micellar exclusion. These solutions contained the dye Orange OT at a trace concentration. The CPC concentration was about 100 times higher than its c.m.c., which is about 0.0010 M (*10*). When Alon was added to this solution the CPC concentration increased by about 13% whereas the absorbance of Orange OT also increased by about 13% from initial value, A_i (Table I). The mean values of δ and V_{ex} from duplicate experiments are shown in Table I. The δ values of 64 ± 1.3 Å from the surfactant exclusion measurements and 60 ± 2.1 Å from Orange OT exclusion measurements are quite similar, suggesting very strongly that the effects here are almost entirely due to the exclusion of micelles, the adsorption of monomeric CPC, positive or negative, being of little consequence.

The data in Table I show that the direct estimate of micellar exclusion from the increase in absorbance of solubilized Orange OT is in good agreement with the exclusion estimated from the negative adsorption of the micellar surfactant. It should be noted that the CPC concentration used was high. The exclusion of micelles is expected to be lower at high micellar concentrations because extensive intermicellar repulsions in solution counteract to some extent the repulsive interactions the micelles experience in the electrical double layers of the charged surfaces. Thus, although the δ values for the micelles are similar to the δ-value exhibited by the monomer exclusion of DPC, a more detailed analysis is needed to show that micelles are probably excluded more effectively than monomers (*24*).

We note that the exclusion of micelles, other such colloidal species, and polyelectrolytes from surfaces may arise from a combination of steric and electrostatic interactions (*2*). Under appropriate circumstances such exclusion effects may be useful for probing the roughness and charge characteristics of surfaces.

Solubilization in Adsorbed Layers

It is well known that cationic surfactants at high concentrations, above the c.m.c., produce bilayers on glass (*25*). The uptake of the surfactants from dilute solutions, below the c.m.c., involves ion-exchange (*25*) and a lowering of the pH in the supernatant was reported for the adsorption of tetradecyl pyridinium bromide to porous glass (*2*). At higher concentrations bilayers form at the surface.

An early observation on the ability of such bilayers to solubilize uncharged, hydrophobic, molecules was made by Stigter, Williams, and Mysels in 1955 (*26*). They noted the adsorption of Orange OT to the surface of glass when a cationic surfactant was present well above the c.m.c. They ascribed this adsorption to solubilization in the bilayers which they described as equivalent to giant lamellar micelles proposed by McBain (*27*). In 1976, some preliminary unpublished work done in this laboratory by R.T. Cataldi confirmed this uptake of Orange OT in adsorbed bilayers. In addition, there were indications that the solubilizing power of the adsorbed bilayers was actually greater than that of micelles in the case of Orange OT. Subsequently, a number of studies from this laboratory have examined the nature of solubilization in micelles (*3,28-32*). The findings from these studies provide a rationale for solubilization in bilayers in relatively simple cases such as the uptake of Orange OT (*33*).

Solubilization of Orange OT in Micelles and Bilayers. Solubilization of hydrophobic molecules in micelles and other lipid assemblies is due primarily to the presence of the hydrocarbon core of the micelles. As pointed out in a number of studies (*3,28-32*), for nonpolar aliphatic hydrocarbons the solubilization capacity of micelles is much less than that of bulk hydrocarbons. On the other hand, for many polar molecules, the solubilization capacity of micelles is much larger. We define the micelle-water distribution coefficient, $K_{m/w}$, and the hydrocarbon-water distribution coefficient, $K_{h/w}$, as

$$K_{m/w} = X_m/X_w; \; K_{h/w} = X_h/X_w \tag{3}$$

where X_m, X_w, and X_h are the mole-fractions in micelles, water, and hydrocarbon, respectively. It is found that the ratio of $K_{m/w}$ to $K_{h/w}$ in the case of sodium dodecyl sulfate (SDS) micelles is only about 0.1 for decane but the ratio can be much higher for somewhat polar molecules such as butanol, the value for propionamide being as high as 3.7 x 10^5 (*3*).

A 2-state model of micellar stabilization that gives a reasonable account of this range of behavior exhibited by different solubilizates has been advanced in recent years (*3,28-32*). Solubilizates are assumed to be distributed between a "dissolved" state associated with the micelle core and an "adsorbed" state in which the solubilizate resides at the micelle-water interface. The relative amounts in the two states depends greatly upon the interfacial activity of the solubilizate, i.e., its tendency to adsorb at the micelle-water interface. In addition, it has been proposed that the interfacial tension at the micelle-water interface produces an intramicellar Laplace pressure (*34*) which reduces the solubility of any solute dissolving in the micelle core (*3,28-32*). This last factor gives a ready qualitative explanation of the low solubility of hydrocarbons such as decane in SDS micelles. Decane is not expected to show any significant interfacial activity at a hydrocarbon-water interface and the "adsorbed" state is not expected to be important. On the other hand, interfacial tension data in hydrocarbon-water systems show that substances such as butanol or propionamide are highly interfacially active (*3*). Such molecules can "adsorb" at the micelle-water interface and because of the very high surface area of the small micelles, about 4 x 10^5 m^2/mole for SDS micelles, this "adsorbed" state can be responsible for the major part of the uptake by micelles.

On the basis of the above picture, the solubility of Orange OT in micelles can be represented (*3*) by the equation

$$X_m = X_h e^{-(\Delta P)\bar{V}/RT} \left[1 + \frac{1}{RT}\left(-\frac{d\gamma}{dX}\right) A \, B\right] \ldots \tag{4}$$

Here X_m is mole fraction in micelles and X_h is the mole fraction in a representative liquid hydrocarbon, both at saturation, ΔP is the Laplace pressure of micelles, $\overline{V}$ is the partial molal volume of Orange OT, R is the molar gas constant, T is the absolute temperature, $d\gamma/dX$ is the rate of change of the interfacial tension of a decane-water interface with the mole fraction, X, of Orange OT in decane, and A is the micelle-water interfacial area of a mole of micellized surfactant. The $1/RT(-d\gamma/dX)$ term represents the expected adsorption per unit area of a hydrocarbon-water interface from the Gibbs adsorption equation. The micelle-water interface contains polar groups, however, which reduces the available area. The term B represents a correction factor for taking this into account (*3,31*).

The solubility of Orange OT in SDS micelles can be analyzed by the above approach in some detail because this micellar system has been studied in some detail (*3,31*). The Laplace pressure, estimated from gas-solubility data is 440 atm (*3*). Using the estimated molar volume of Orange OT, the value of the term $\exp[(-\Delta P)\overline{V}/RT]$ was calculated to be 1/89. The solubility of Orange OT in bulk decane gives a mole fraction of 5.6×10^{-3} (*35*), which can be used as the value of X_h. The Laplace pressure effect, by itself, should make X_m 89 times lower than X_h. Interfacial tensions of the decane-water interface were measured as a function of the mole fraction, X, of Orange OT in order to estimate interfacial adsorption (*3*). A linear curve was obtained, from which the value of $-d\gamma/dX$ was calculated to be 2150 erg cm^{-2}. Estimating the interfacial area of micelles from geometry, the term $1/RT\ (-d\gamma/dX)A$ was calculated to be 361. The correction factor B was estimated using a thermodynamic theory based on competitive adsorption (*3*). The details will be published later. The value of B was calculated to be 0.35. It agrees roughly with a geometric estimate of the fraction of the surface of micelles which is not covered by polar groups. The interfacial adsorption factor is thus expected to increase X_m over X_h by the factor $(1 + 361 \times 0.35)$, i.e., 127. The value of X_m calculated from this theory is thus 8.0×10^{-3}, not very different from X_h because the Laplace pressure effect and the interfacial adsorption effect counteract each other quite effectively. The theoretical estimate of X_m agrees very well with the experimental number of 7.9×10^{-3} estimated from reported solubilization data at concentrations close to the c.m.c. (*3*) and a value of 8.35×10^{-3} estimated in this laboratory at a high concentration, 0.2 M SDS (*3*). Similarly good agreement between calculated $K_{m/w}$ and X_m values and experimental values for many solubilizates have been observed and will be reported later (*3*).

For comparing the solubilizing powers of adsorbed layers and coexisting micelles, the partition of Orange OT at lower concentrations between the adsorbed layers and micelles have been determined experimentally (*33*). Here porous and nonporous silica were used to study the bilayers of cationic surfactants and the alumina Alon was used to study bilayers of lithium tetradecyl sulfate (LiTDS). In all cases the bilayers were found to be more efficient solubilizers than micelles. A complete report on this interesting finding with be presented later. Here we present data for LiTDS.

For LiTDS micelles, the solubility of Orange OT determined from solubilization experiments gave an X_m value of 2.17×10^{-2}. This value is about

2.7 times higher than for SDS. Chain length effects on X_h, i.e., the solubility in hydrocarbons, is much less (*35*). This large factor, however, is consistent with a lowering of the Laplace process expected for the larger micelles of LiTDS. In the experiments where Orange OT partitions between LiTDS micelles and the bilayers of LiTDS on Alon, it was found that Orange OT-LiTDS ratio is higher for the bilayer by a factor of 3.0 at 0.0102 M NaCl concentration and 3.3 at 0.102 M NaCl concentration. Thus, in 0.0102 M NaCl, the mole fraction in LiTDS bilayers at saturation should be 3.0 times the X_m value above, i.e., 6.4×10^{-2}. This value is more than 10 times higher than the X_h value of 5.6×10^{-3}. It seems that interfacial adsorption is responsible for this increase even for the bilayers.

With respect to the higher solubilizing capacity of the bilayer compared to that of the micelle, we note that the surface area per mole of surfactant is expected to be much less for the planar bilayer than for the spherical micelles, particularly because one face of the bilayer is expected to be in contact with the solid. Similarly, because of closer head-group packing, the hydrocarbon fraction of the bilayer-water interface available for interfacial adsorption is expected to be lower. The competitive adsorption model (*3*) leads to the same conclusion. Thus the net interfacial adsorption effect arising from lower values of A and B in Equation 3 should be lower. On the other hand, the Laplace pressure effect is likely to be much reduced or absent for the planar bilayer. This factor is expected to increase X_m by a factor of 89 for SDS bilayers over SDS micelles. Similarly, large factors are expected for LiTDS and other systems as well. The superior solubilizing power of bilayers as compared to micelles is, thus, likely to be mainly due to the abolition of the Laplace pressure effects.

Acknowledgments

The research from this laboratory reported here received primary support from the National Science Foundation, Grants ENG-78-16860 and CPE8216450, and the Public Health Services.

Literature Cited

(1) Mukerjee, P.; Handa, T. *J. Phys. Chem.* **1981**, *85*, 2298.
(2) Mukerjee, P.; Anavil, A. In *Adsorption at Interfaces*; Mittal, K. L., Editor; ACS Symp. Ser. 8; American Chemical Society: Washington, D.C., pp 107-128.
(3) Mukerjee, P.; Gumkowski, M. J. *Unpublished Work*; Gumkowski, M.J.; Ph.D. Dissertation, Univ. of Wisconsin, 1986.
(4) Mukerjee, P. *Anal. Chem.* **1956**, *28*, 870.
(5) Sharma, R.; Pyter, R. A.; Mukerjee, P. *Anal. Letters* **1989**, *22*, 999.
(6) Mukerjee, P. *Adv. Coll. Interf. Sci.* **1967**, *1*, 241.
(7) Mukerjee, P. *Coll. Surf.* **1994**, *84*, 1-10.
(8) Mukerjee, P. *J. Am. Oil Chem. Soc.* **1982**, *59*, 573.

(9) Mukerjee, P.; Pyter, R. A. *Unpublished Work*; Pyter, R.A. 1980 *Ph.D. Dissertation, University of Wisconsin.*

(10) Mukerjee, P.; Mysels, K. J. *Critical Micelle Concentrations of Aqueous Surfactant Systems*; NSRDS-NBS 36, Superintendent of Documents: Washington, D.C., 1971.

(11) Mukerjee, P.; Gumkowski, M. J.; Chan, C. C.; Sharma, R. *J. Phys. Chem.* **1990**, *94*, 8832.

(12) Davies, J. T.; Rideal, E. K. *Interfacial Phenomena*; Academic Press: New York, N.Y., 1963.

(13) Aveyard, R.; Haydon, D. A. *An Introduction to the Principles of Surface Chemistry*; Cambridge Press: London, U.K., 1973.

(14) Mukerjee, P.; Korematsu, K.; Ōkawauchi, M.; Sugihara, G. *J. Phys. Chem.* **1985**, *89*, 5308.

(15) Pyter, R. A.; Zografi, G.; Mukerjee, P. *J. Coll. Interf. Sci.* **1982**, *89*, 144.

(16) Lucassen-Reynders, E. H. *J. Phys. Chem.* **1966**, *70*, 1977.

(17) Mukerjee, P.; Handa, T. *Unpublished work.*

(18) Robinson, R. A.; Stokes, R. H. *Electrolyte Solutions*; Butterworths: London, U.K., 1968.

(19) Lucassen-Reynders, E. H. *J. Phys. Chem.* **1963**, *67*, 969.

(20) Johnson, R. E.; Dettre, R. H. In *Surface and Colloid Sciences*; Matijevic, E., Ed.; Wiley-Interscience: New York, N.Y., 1969.

(21) Loeb, A. L., Overbeek, J. Th. G.; Wiersema, P. H. *The Electrical Double Layer Around a Spherical Colloid Particle*; The M.I.T. Press: Cambridge, MA, 1960.

(22) Hall, D. G. *J. Chem. Soc. Faraday I* **1980**, *76*, 386.

(23) Adamson, A. W. *Physical Chemistry of Surfaces*; Fourth Edition, Interscience Publishers: New York, NY, 1980.

(24) Sharma, R.; Mukerjee, P. Unpublished Work, paper presented at the 196th National Meeting of the American Chemical Society, 1988.

(25) *Cationic Surfactants*; Jungermann, E., Ed.; Surfactant Science Series; Marcel Dekker: New York, N.Y., 1970.

(26) Stigter, D.; Williams, R. J.; Mysels, K. J. *J. Phys. Chem.* **1955**, *59*, 330.

(27) McBain, J. W. *Colloid Science*; D.C. Heath & Co.: Boston, MA, 1950.

(28) Mukerjee, P.; Cardinal, J. R. *J. Phys. Chem* **1978**, *82*, 1620.

(29) Mukerjee, P. In *Solution Chemistry of Surfactants*; Mittal, K. L., Ed.; Plenum Press: New York, N.Y., 1979, Vol. 1; p 153.

(30) Mukerjee, P. *Pure Appl. Chem.* **1980**, *52*, 1317.

(31) Pyter, R. A.; Ramachandran, C.; Mukerjee, P. *J. Phys. Chem.* **1982**, *86*, 3206.

(32) Mukerjee, P.; Ko J-S. *J. Phys. Chem.* **1992**, *96*, 6090.

(33) Mukerjee, P.; Sharma, R. Unpublished work, paper presented at the 196th National Meeting of the American Chemical Society, 1988.

(34) Mukerjee, P. *Koll. Zeit. Zeit. Polym.* **1970**, *236*, 76.

(35) Kolthoff, I. M.; Graydon, W. F. *J. Phys. Coll. Chem.* **1951**, *66*, 699.

(36) Schott, H. *J. Phys. Chem.* **1966**, *70*, 2966.

RECEIVED September 6, 1995

Downloaded by NORTH CAROLINA STATE UNIV on October 14, 2012 | http://pubs.acs.org
Publication Date: May 5, 1996 | doi: 10.1021/bk-1995-0615.ch003

Chapter 3

Porosity Effects on the Adsorption of Cationic Surfactants and the Coadsorption of 2-Naphthol at Various Silica–Water Interfaces

C. Treiner and V. Monticone

Laboratoire d'Electrochimie, Unité de Recherche Associé au Centre National de la Recherche Scientifique 430, Université Pierre et Marie Curie, 4 Place Jussieu, Bâtiment 74, Paris 75005, France

The formation of surfactant aggregates at solid/liquid interfaces may induce the coadsorption of hydrophobic molecules. This phenomenon has been investigated in the case of 2-naphthol coadsorbed with cationic surfactants on the surface of four porous and on nonporous silicas in aqueous solutions. The uptake of solute from the aqueous solution may be almost complete at a surfactant equilibrium concentration close to the critical micelle concentration (cmc). At surfactant concentrations above the cmc, the solute is partitioned between the surface adsorbed aggregates and the free micelles. Coadsorption and micellar solubilization partition coefficients have been calculated.The corresponding standard free energies indicate that the former effect is favored over the latter. A most probable interpretation of this observation is suggested which takes into account the difference in microviscosity between adsorbed and free surfactant aggregates and the specific interaction which occurs in water between aromatic solutes and cationic surfactants.

The adsorption of surfactants from aqueous solutions onto various solid surfaces is a field of continous interest, which has made recent progress especially on an experimental viewpoint by using new methods such as neutron reflection *(1)* or ellipsometry *(2)*. The presence of surfactant ions or molecules on solid particles may induce the adsorption of molecules or ions, which otherwise would not be adsorbed onto the solid surface. This phenomenon has been coined surface solubilization, in reference to the classical solubilization effect, adsolubilization *(3,4)* or coadsorption *(5)*. This coadsorption effect has bearings in various research areas such as micellar chromatography (6), drug carriers *(7,8)* and more generally to environmental situations (soil-remediation) *(9-11)*. The influence of various physicochemical parameters such as pH, temperature, ionic strength, specific surface and porosity on the adsorption of surfactants on oxide minerals have been thoroughly studied. However, the effect of these parameters on the coadsorption effect is not known. One of the questions asked in the present investigation is the following: is the coadsorption effect only dependent upon the amount of surfactant adsorbed, the latter quantity being dependent on the above stated variables, or are there any other parameters involved in this effect.

0097–6156/95/0615–0036$12.00/0

The aim of the present investigation was an attempt to answer this question in the case of the coadsorption of a model solute, 2-naphthol, in the presence of a cationic surfactant, hexadecylpyridinium chloride adsorbed on two different silicas, a nonporous and a very porous one. Additional surfactant adsorption experiments on silicas of various properties were also performed using another cationic surfactant: dimethylbenzyltetradecylammonium chloride.

Material and Methods

The surfactants, hexadecylpyridinium chloride (CPC), and dimethylbenzyltetradecylammonium chloride (TBzCl) from Sigma and the naphthalene derivative, 2-naphthol, from Aldrich (99 % pure) were used as received. The critical micelle concentrations (cmc) of the surfactants were determined with the conductivity method using an automatic Wayne Kerr conductivity bridge (model 6542); the cell had platinized electrodes. The cmc agreed well with literature values. In the presence of 0.01 $mol.L^{-1}$ of NaCl, the cmc was equal to 2.3×10^{-4} $mol.L^{-1}$ for CPC and 6.3×10^{-4} $mol.L^{-1}$ for TBzCl.

The nonporous silicas were Aerosil 200 and Aerosil OX50 both being gifts from Degussa-France. The porous silicas were Sorbsil C30 from Rhone-Poulenc (France), with an average pore volume of 0.6 $ml.g^{-1}$ and Sipernat 50S from Degussa-France with a pore volume of 0.003 $ml.g^{-1}$. The Table presents the BET surfaces of the silicas used. The values were communicated by the manufacturers. The adsorption experiments were performed in the presence of 0.01 $mol.L^{-1}$ sodium chloride, at two equilibrium pH values: 3.6 and 6.5. The pH were adjusted with sodium hydroxyde. As the isoelectric point (IEP) of both silicas is around 3.2, the solid surfaces are negatively charged. However, a full bilayer seems to be obtained only at the highest of the two pH values *(5)*. The pK of 2-naphthol being equal to 9.51, only the neutral form of the phenol derivative was present at both pH values investigated. Water was purified on exchange membranes, passed over graphite and over 0.25 micron filters.

The batch-method was used. 0.1 g. of solid was equilibrated with 10 ml of aqueous solution for 24 hrs at 25.00 ± 0.05°C. After ultracentrifugation at 10,000 rpm, the concentrations of surfactant and solute were determined independently on the supernatant solutions using a double-beam UV spectrophotometer (Cary 1E).

The wavelengths chosen for the analysis were 259 nm and 328 nm for CPC and 2-naphthol respectively. The total concentration of 2-naphthol was constant and equal to 4×10^{-4} $mol.L^{-1}$ in all experiments. Note that all concentrations have been expressed in the molar basis ($mol.L^{-1}$) because solute partition coefficients between aggregates and aqueous solutions will be calculated from the adsorption data using that concentration scale. The concentrations refer implicitely to 1 g. of solid.

Results and Discussion

Adsorption of cationic surfactants on various silicas

Adsorption of TBzCl on various silicas. Figure 1 shows the variation of TBzCl adsorption with equilibrium (free) surfactant concentration on the four silicas investigated. Classical sigmoid curves are obtained. An adsorption plateau appears in all cases for the same surfactant concentration which corresponds well with the cmc of that surfactant in the presence of 0.01 $mol.L^{-1}$ of added salt with a common ion. On figure 2, the plateau values are plotted as a function of the BET surfaces. It appears

Downloaded by NORTH CAROLINA STATE UNIV on October 14, 2012 | http://pubs.acs.org
Publication Date: May 5, 1996 | doi: 10.1021/bk-1995-0615.ch003

Downloaded by NORTH CAROLINA STATE UNIV on October 14, 2012 | http://pubs.acs.org
Publication Date: May 5, 1996 | doi: 10.1021/bk-1995-0615.ch003

Table.

Some characteristic parameters of the four silicas used and the maximum adsorption of TBzCl at two added salt concentrations.

silica type	pore volume ml.g^{-1}	BET surface m^2.g^{-1}	Γ_{max}* mol.L^{-1}	Γ_{max}** mol.L^{-1}
Aerosil OX50	0	50 ± 15	0.00118	-
Aerosil 200	0	200 ± 25	0.0044	0.0075
Sipernat 50S	0.003	450	0.0090	0.0130
Sorbsil C30	0.60	700	0.0055	0.0075

* NaCl = 0.01 mol.L^{-1}; ** NaCl = 0.1 mol.L^{-1}

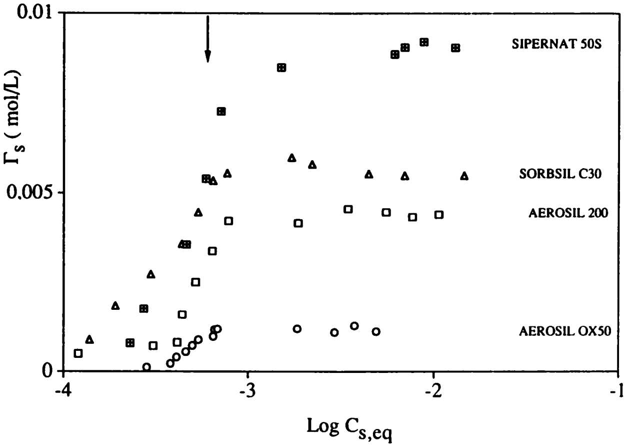

Figure 1. Isotherm of TBzCl on various silicas in a 0.01 mol.L^{-1} NaCl aqueous solution at pH = 3.6. On all the isotherms the arrow indicates the cmc.

Downloaded by NORTH CAROLINA STATE UNIV on October 14, 2012 | http://pubs.acs.org
Publication Date: May 5, 1996 | doi: 10.1021/bk-1995-0615.ch003

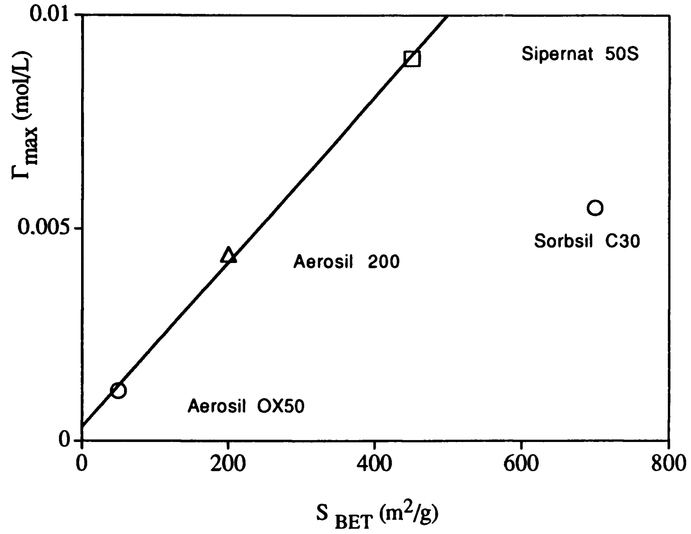

Figure 2. Variation of the plateau values of TBzCl adsorption isotherms on various silicas as a function of their BET surfaces.

clearly that Sorbsil C30 does not fit with the other three silicas. It must be stressed that the straight line passing through the plateau values for the three Degussa silicas goes through zero only at low salt concentration. This point will be addressed further below.

The large deviation of the porous Sorbsil C30 from the other silicas is most certainly related to the size of the pores. In order to discard the possibility of an obstruction effect due to the large size of the Debye ionic atmosphere at low solution ionic strength which could prevent the surfactant ions to penetrate the pores, a number of adsorption experiments were performed at a larger ionic strength with 0.1 $mol.L^{-1}$ of added NaCl. Also, increasing the ionic strength increases surfactant adsorption by screening the repulsion of like charges at the silica surface; thus, more surfactant ions are able to pack onto the solid surface, while the Debye length is decreased. If the obstruction effect was of an electrostatic origin, the increase of surfactant adsorption should be more important for the porous material than for the nonporous one as it would let more surfactant ions to penetrate the pores. The Table presents the maximum adsorption of TBzCl at the plateau at two salt concentrations. The increase of surfactant adsorption is essentially the same for the porous and for the nonporous materials. It may be concluded then, that the obstruction effect, which is most certainly nonexistent for nitrogen gas (which is used for the BET surface determinations) is important and of a geometric origin and not of an electrostatic one. It suggests that the diameter of the pores at the solid surfaces is rather large for Sipernat 50S and small for Sorbsil C30, even if the reverse situation is true as far as the pore volumes are concerned.

From the plateau adsorption values obtained on Aerosil OX50, Aerosil 200 and Sipernat 50S in the presence of 0.01 mol.L^{-1} of added salt, an average surface area per surfactant monomer may be evaluated. One obtains: $A_S = 0.83$ nm^2. It is interesting to compare the present findings to the results obtained by Giordano et.al. *(12)* for the adsorption of a nonionic surfactant, Triton X-100, on various silicas with well characterized pore radii. These authors showed that as the BET surfaces increased, the pore radii decreased and the plateau adsorption decreased. For example, as the BET surface increased from 47 to 557 m^2.g^{-1}, the pore radii decreased from 30 to 2.6 nm. These results are in qualitative agreement with the present ones concerning, for example, Sipernat 50S and Sorbsil C30 which BET surfaces are equal respectively to 450 and 700 m^2.g^{-1}. For Sipernat 50S, the pore volume is large (80 %) but so are also the pore radii so that there is no interference between surfactant adsorption and the presence of the pores. Hence, the Sipernat 50S result fits with the nonporous values but not Sorbsil SC30. In this latter case, taking into account the pore volume and the surface area, a rough calculation leads to an average pore radius of 1.2 nm, a small value indeed.

The fact that the linear plot shown on figure 2 goes through zero deserves some further comments. The same linear relationship has been noted before for anionic surfactants adsorbed on polystyrene particles (13). Figure 3 shows the variation of the plateau values for a cationic surfactant with properties similar to those of TBzCl, namely CPC, on Aerosil 200, in the presence of various concentrations of added NaCl, at pH = 3.6. The left coordinate indicates the number of surfactant molecules which may be accomodated at the silica surface per nm^2. It may be concluded that the increase of adsorption must level off at the highest salt concentrations and therefore, cannot be proportional to salt concentration. Thus, the line passing through the three experimental points of figure 3 may, or may not go to nonzero (positive) values as the BET surface goes to zero, depending upon the solution ionic strength. Nevertheless, the linearity does imply that the same surfactant surface area is found at the three silica/water interfaces, i.e. 0.83 nm^2.

Adsorption of CPC on Sorbsil C30 and on Aerosil 200. The two silicas chosen for the coadsorption investigation of 2-naphthol were the nonporous Aerosil 200 and the highly porous Sorbsil C30. As discussed above and displayed on figure 1 for TBzCl, these two silicas differ widely in BET surfaces but the maximum surfactant adsorption is only marginally different. Figures 4 and 5 show the isotherms for CPC at the two pH values of 3.6 and 6.5 in the presence of 0.01 mol.L^{-1} NaCl. The plateau values are attained at the cmc. Again, the adsorption on Sorbsil C30 is only slightly higher than for Aerosil 200. Note however, that the adsorption begins to increase at a lower surfactant concentration for the former than for the latter silica. It may also be pointed out that the two isotherms run almost parallel to each other in the whole surfactant concentration range.

Coadsorption of 2-naphthol on CPC adsorbed aggregates: Aerosil 200 and Sorbsil C30 as solid substrates.

The coadsorption of 2-naphthol on the silicas is extremely small or nil in the absence of surfactant under the present experimental conditions as far as ionic strength and pH are concerned. As CPC adsorbs on silica, 2-naphthol molecules are incorporated in the surfactant structures formed at the silica/water interface. This effect has been described previously *(5)*. It may be recalled that polar as well as non polar solutes may adsorb from aqueous solutions onto mineral oxides in the absence of surfactant. It is the case, for example, of a nonpolar molecule such as naphthalene on Sorbsil C30 *(14)*.

Figures 6 and 7 show the results obtained with Aerosil 200 *(4)* and Sorbsil C30 *(14)*. 2-naphthol coadsorption is plotted as a function of CPC equilibrium

Downloaded by NORTH CAROLINA STATE UNIV on October 14, 2012 | http://pubs.acs.org
Publication Date: May 5, 1996 | doi: 10.1021/bk-1995-0615.ch003

Downloaded by NORTH CAROLINA STATE UNIV on October 14, 2012 | http://pubs.acs.org
Publication Date: May 5, 1996 | doi: 10.1021/bk-1995-0615.ch003

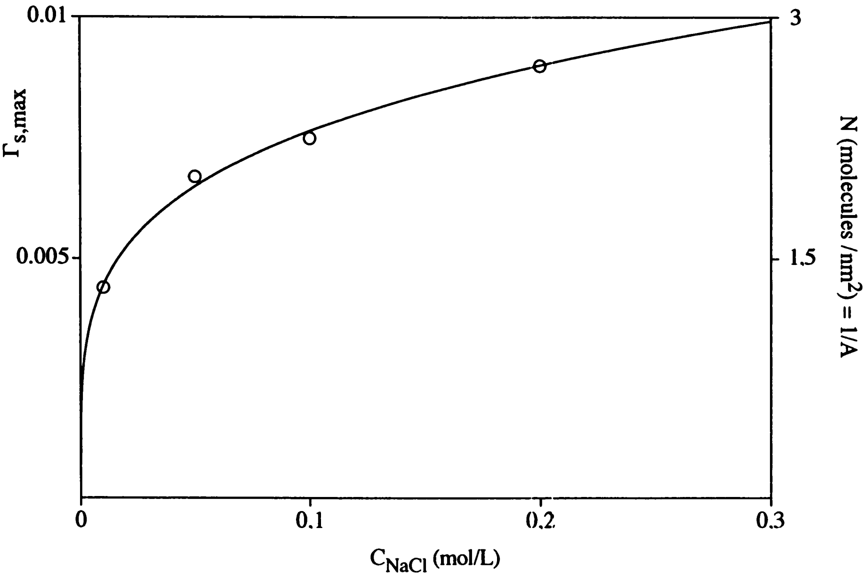

Figure 3. Variation of the plateau values for CPC adsorption isotherm on nonporous Aerosil 200 as a function of added sodium chloride concentration.

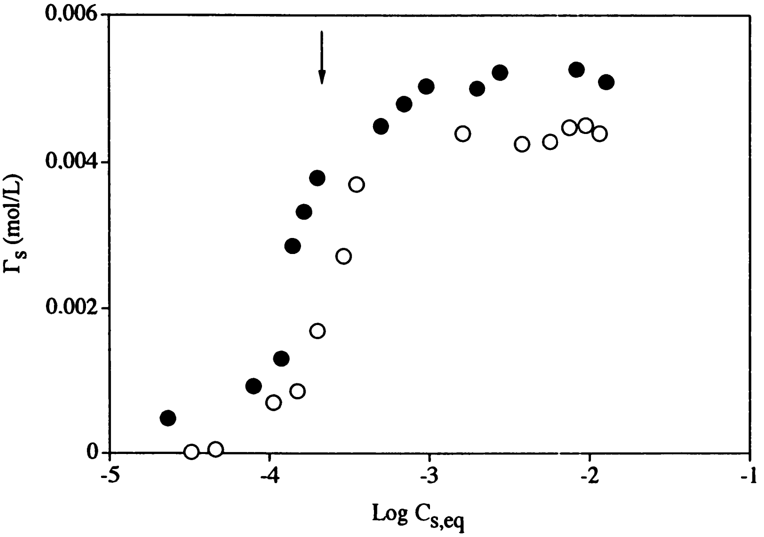

Figure 4. Adsorption isotherm for CPC on (m) Aerosil 200 and on Sorbsil C30 (l) at pH = 3.6 and NaCl concentration of 0.01 mol.L^{-1}.

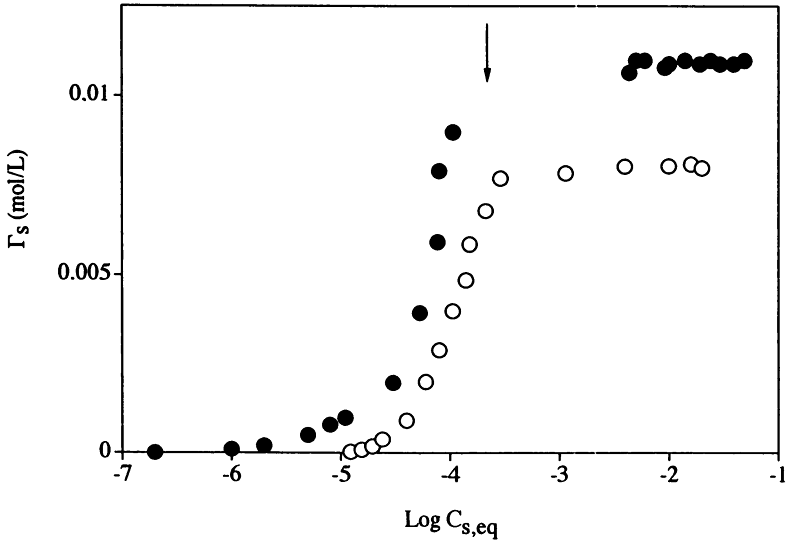

Figure 5. Adsorption isotherm for CPC on (m) Aerosil 200 and on Sorbsil C30 (1) at pH = 6.5 and NaCl concentration of 0.01 $mol.L^{-1}$.

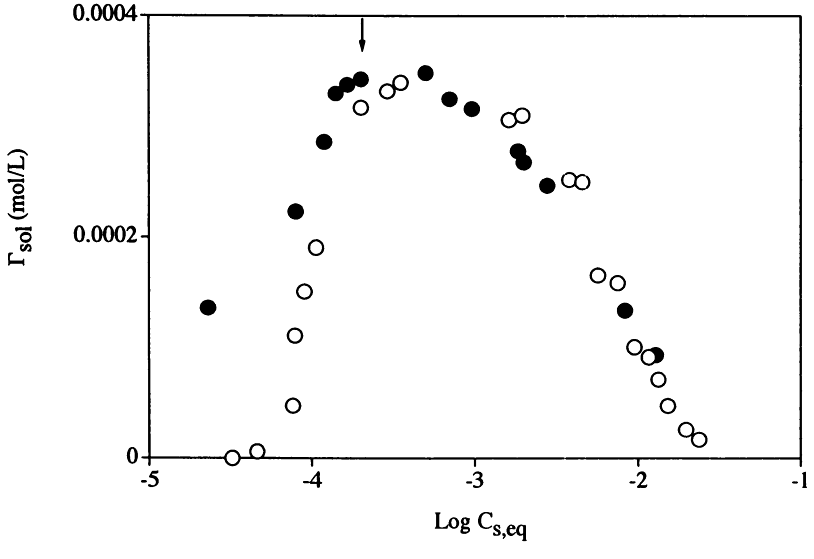

Figure 6. Coadsorption of 2-naphthol and CPC on (m) Aerosil 200 and on Sorbsil C30 (1) at pH = 3.6 and NaCl concentration of 0.01 $mol.L^{-1}$

Downloaded by NORTH CAROLINA STATE UNIV on October 14, 2012 | http://pubs.acs.org
Publication Date: May 5, 1996 | doi: 10.1021/bk-1995-0615.ch003

Downloaded by NORTH CAROLINA STATE UNIV on October 14, 2012 | http://pubs.acs.org
Publication Date: May 5, 1996 | doi: 10.1021/bk-1995-0615.ch003

concentration. The solute coadsorption increases with surfactant adsorption up to the cmc. In the case of Sorbsil C30, 97 % of the total 2-naphthol concentration is then incorporated in the adsorbed surfactant layers. As free micelles are formed above the cmc, coadsorption and micellar solubilization compete for incorporating the solute molecules. Eventually, at very high CPC concentration, the solute is completely partitioned into the free micelles.

Before attempting an interpretation of the results obtained it is instructive to calculate the degree of solute incorportation with respect to adsorbed surfactant aggregates. Figure 8 shows the isotherm of 2-naphthol in an aqueous silica/CPC system, at a constant equilibrium surfactant concentration just below the cmc, at the adsorption plateau ($C_s = 5 \times 10^{-3}$ mol.L^{-1}) at pH = 3.6 in the presence of 0.01 mol.L^{-1} of NaCl. A straight line was drawn through the linear portion of the curve, showing the ideal domain with respect to solute concentration. The profile of the whole curve suggests a Langmuir-type isotherm. The end-point of the linear domain is approximately equal to a solute concentration of 1×10^{-3} mol.L^{-1} i.e. to a maximum solute mole fraction $x_{sol} = 0.2$. Thus, below this limiing value, 2-naphthol should be considered as infinitely dilute with respect to the adsorbed pseudo-phase. Above this concentration, solute/solute interactions appear. As a constant solute concentration of 4×10^{-4} mol.L^{-1} was used throughout this investigation, one may consider that the conditions of dilute solutions were respected for the solute/surfactant ratios studied, except for the most diluted surfactant concentrations. It is interesting to note that the same solute mole fraction x_{sol} of 0.20 has been observed to correspond to the maximum value beyond which interactions between solubilized alcohols molecules appear in classical micellar solutions *(15,16)*.

The comparison of the solute coadsorption at the two pH values with the two silicas reveals a number of expected observations but also some unexpected ones. Firstly, the coadsorption is higher with Sorbsil C3O than with Aerosil 200 below the cmc and the difference is larger the lower the surfactant concentration. Furthermore the coadsorption begins at a lower surfactant concentration with Sorbsil C30 than with Aerosil 200. These results were expected as they follow from the behavior of CPC on the mineral surfaces. Secondly, the difference between the two curves is nil at the cmc. The effect was expected at pH = 6.5 because almost all of the 2-naphthol was already coadsorbed on Aerosil 200 and this effect could obviously not be further increased on the porous material. Such was not the case at pH = 3.6. Thirdly, the rate of the change of the solute micellar solubilization with micelle concentration are equal at pH = 3.6 but slightly different at pH = 6.5 for the two silicas.

Partition coefficients. In order to present these observations on a more quantitative basis, it may be useful to analyze the data using the pseudo-phase model as in the case of micellar solubilization. The following relationship has be suggested *(14)*:

$$P_{ads} = \frac{C_t - C_f}{C_f C_{s,ads}} \qquad (1)$$

where C_t and C_f are respectively the total and the free solute concentrations and $C_{s,ads}$ the adsorbed surfactant concentration. The index sol, for solute, has been omitted on equations (1) and (2) for the sake of clarity, but are indicated on the corresponding figures. A similar equation has been used by others *(17)*. If the decrease of coadsorption is solely the consequence of a preferential micellar solubilization phenomenon, the following relation applies:

$$P_{des} = \frac{C_t - C_{ads} - C_f}{C_f (C_{s,t} - cmc)} \qquad (2)$$

Downloaded by NORTH CAROLINA STATE UNIV on October 14, 2012 | http://pubs.acs.org
Publication Date: May 5, 1996 | doi: 10.1021/bk-1995-0615.ch003

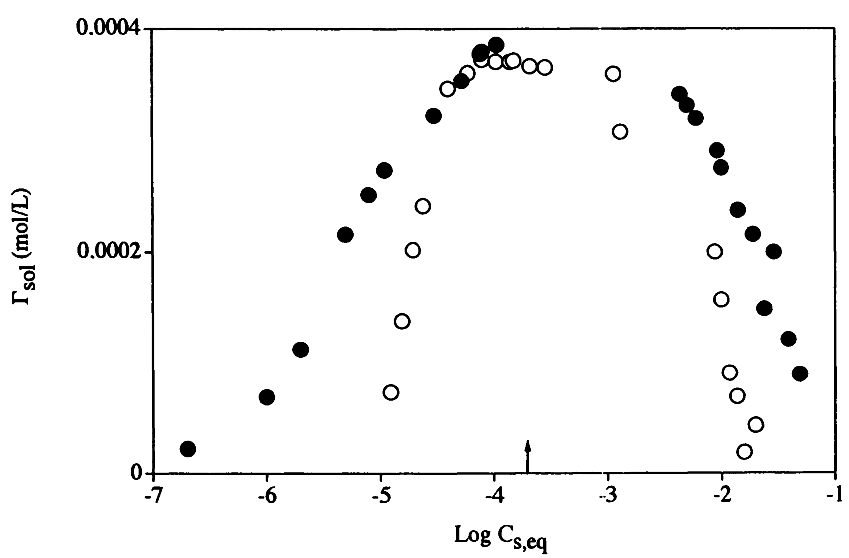

Figure 7. Coadsorption of 2-naphthol and CPC on (m) Aerosil 200 and on Sorbsil C30 (m) at pH = 6.5 and NaCl concentration of 0.01 mol.L^{-1}.

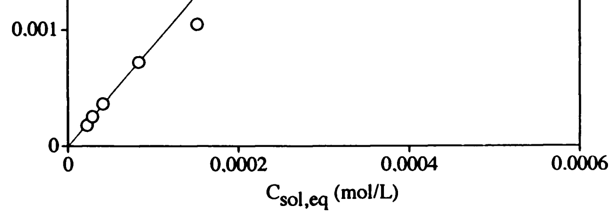

Figure 8. Adsorption isotherm of 2-naphthol on Sorbsil C30 in the presence of 4.8 x 10^{-3} mol.L^{-1} of adsorbed CPC concentration on Sorbsil C30 at pH = 3.6 and NaCl concentration of 0.01 mol.L^{-1}.

where $C_{s,t}$ is the total surfactant concentration and C_{ads} is the concentration of adsorbed solute. P_{des} is a micellar solubilization partition coefficient, the subscript emphasizing the fact that the constant corresponds to a state of competition with the coadsorption phenomenon.

Taking the average values obtained for 2-naphthol with CPC on Aerosil 200 and Sorbsil C30, one gets, using a CPC standard partial molar volume of 0.35 $L.mol^{-1}$, on the molar basis: for the coadsorption effect, $P_{ads} = 4650 \pm 150$ and 8950 ± 1200, at pH = 3.6 and pH = 6.5 respectively; for the micellar solubilization process, the corresponding partition coefficients are: $P_{des} = 1535 \pm 400$ and 1925 ± 150 at the same respective two pH values. The main conclusion which may be drawn from the examination of these data is that the coadsorption effect is independent from the type of silica used provided that there is no adsorption of the solute on the bare solid surfaces. The independency of the P_{ads} values upon the type of silica used in this study could be the consequence of the very similar surfactant adsorption isotherms on both silicas at each pH value. Interestingly, it may be pointed out that the coadsorption coefficients do not provide the information displayed on figures 6 and 7: the coadsorption begins at a lower surfactant concentration for Sorbsil C30 than for Aerosil 200. Note also that the decrease of coadsorption is identical for the two silicas at the lower pH value (figure 6) but the solubilization partition coefficients are different. This is due to the fact that, as the solute micellar solubilization is independent upon the type of silica and CPC adsorption is larger for Sorbsil C30, P_{des} must be smaller than for Aerosil 200.

Incidently, an adsorption partition coefficient may also be derived from the linear portion of the 2-naphthol isotherm of figure 8. P_{ads}, is here defined as ratio of the initial slope divided by the concentration of adsorbed surfactant, which is constant and equal to 4.8×10^{-3} $mol.L^{-1}$ in that case (the total surfactant concentration is 5×10^{-3} $mol.L^{-1}$). The value of P_{ads} is equal to 5100 in the molar basis, to be compared to 4650 ±150 obtained from equation (2). The agreement is very satisfactory as it is deduced from different sets of data and different calculation procedures.

The variation of P_{ads} with pH for both silicas is surprising. It should not be due to a partial dissociation of 2-naphthol because the pK value of that phenol is three orders of magnitude higher than the solution pH, as mentioned above. More experiments would be necessary on other phenols to interpret this result.

One of the main observations which may be derived from the present investigation is the large difference between the coadsorption and the so-called desorption (solubilization) partition constants. If, in the presence of an excess of micelle, the solute is preferentially solubilized in the free micelles as a consequence of a difference in chemical potentials, the standard chemical potential is in favor of the coadsorption phenomenon. From the above partition coefficient values, the differences between the coadsorption and the micellar solubilization effects can be calculated in terms of molar standard free energies. One finds - 2.75 $kJ.mol^{-1}$ at pH = 3.6 and - 3.80 $kJ.mol^{-1}$ at pH = 6.5.

The interpretation of the behavior reported above can only be of a speculative nature. The first point to be stressed is that the difference observed should not be primarily due to a chemical effect. Arenes and other aromatic molecules seem to interact specifically with ammonium cationic groups *(18,19)*. Viscoelastic effects have also been described as the result of mixing cationic surfactants with some aromatic ions or molecules *(20)*. Both of these chemical effects should be common to the micellar solubilization and to the coadsorption effects. It seems therefore that any interpretation should take into account the difference in the structure of the surfactant aggregates or to their physicochemical properties.

A first suggestion may be put forward with emphasis on the respective microviscosity of adsorbed and free aggregates. It has been deduced from fluorescence measurements using dinaphthylpropane as a probe and water+glycerol mixtures as the

Downloaded by NORTH CAROLINA STATE UNIV on October 14, 2012 | http://pubs.acs.org
Publication Date: May 5, 1996 | doi: 10.1021/bk-1995-0615.ch003

reference system, that the microviscosity of an anionic surfactant monolayer is much higher than that of a micelle *(21)*. In the case of sodium dodecylsulfate either adsorbed on alumina or as free micelles in the bulk solution, the microviscosities are evaluated as 90-120 cp for the former and 8 cp for the latter structure. A range of values between 20 to 40 cp has been also published for sodium dodecylsulfate using another reference system (22). If it is assumed that the kinetics of transfer of the solute from the bulk to the surfactant aggregates is essentially dependent upon the viscosity of the bulk, the difference of the partition constants (assimilated to equilibrium constants for the purpose of the discussion) noted above should be depending upon the kinetics of transfer from the surfactant structure to the bulk. If the solute diffusion coefficient may be considered, as a first approximation, as dependent upon the viscosity of the media, the ratio of microviscosities should be equal to the ratio of diffusion coefficients which in turn would then be directly related to the kinetics of solute transfer from the structure to the bulk. A factor between 5 and 10 as noted above for the microviscosity ratio is in global agreement with the partition coefficient ratios. Note also that the microviscosities need not be the same for sodium dodecylsulfate on alumina and for CPC aggregates adsorbed on silica. It must be stressed however that the suggested microviscosity effect rests upon the hypothesis that the solute penetrates the surfactant aggregates. If the coadsorption is only a surface effect, then the rigidity of the system should play a minor role in the whole process.

An alternative interpretation of the effect observed would be to invoke the difference in the geometry of the two media, spherical tridimentional micelles versus bidimentional bilayers, to interpret the difference in the energetics of micellar solubilization and of coadsorption. Mukerjee had suggested long ago *(23)* that the reason for the larger solubility of a nonpolar gas in a hydrocarbon than in a micellar solution (on a mole/mole basis) could be the Laplace pressure which opposes the penetration of a particle of spherical symetry of very small dimensions. This hypothesis has been repeatedly invoked with some success *(24,25)* and seems difficult to refute *(26)*. Although the order of magnitude is about right (for propane, a factor of about 4 is observed between sodium dodecylsulfate and hydrocarbon solubilities *(25)* as compared to factors of 2 to 5, depending upon the pH of the solution, between P_{ads} and P_{des} in the present case) the main problem lies with the extension of Mukerjee's hypothesis to polar hydrophobic molecules. This is questionable as these molecules should adsorb onto the surfactant structures (whether spherical or bidimentional) and not penetrate them, at least at high dilution. However, it may be pointed out again that the same hypothesis is involved in the interpretation based upon the rigidity effect.

The assumption of a solute penetration deserves some further comments. Neutron reflection studies on cationic aggregates adsorbed on a hydrophilic silica surface have suggested that double-layer stuctures appear at a surfactant coverage, as low as 20 % *(1)*. If that is the case, then the 2-naphthol molecules have the possibility of interacting with the cationic head-groups of either the first layer of surfactants (turned towards the solid surface) or the second layer (with the head-groups turned outwards). This second layer should be preferred for steric reasons. The first layer of surfactants may therefore structure as the concentration of adsorbed surfactant increases without the necessity of a true penetration. This possibility does not exist with regular micelles. The rigidity effect could then be the most probable interpretation of the difference in the standard free energies of the solute with adsorbed versus micellar aggregates. This effect implies some specific interaction between the aromatic solute and the cationic head-groups of the type which has been recalled above *(19)*. The consequence of this interpretation is that the fraction of solute residing, as an average, within the structure would then depend upon the degree of interaction between solute and surfactant head-group. This effect would reintroduce the specificity of the solute in an otherwise hydrophobic effect which dominates almost entirely the micellar solubilization phenomenon.

Downloaded by NORTH CAROLINA STATE UNIV on October 14, 2012 | http://pubs.acs.org
Publication Date: May 5, 1996 | doi: 10.1021/bk-1995-0615.ch003

Incidently the interpretation of neutron reflection studies in terms of surfactant aggregates at low surfactant coverage finds some confirmation in the uptake of 2-naphthol even at very low surfactant concentrations. It also provides some support to the use of a single partition coefficient describing the solute/aggregate interaction in the whole surfactant/solute domain studied.

Finally, it should be noted that the comparison between the coadsorption and the micellar solubilization processes on the same experimental run adopted here, avoids the use of different techniques for micellar coefficients evaluation which, being usually dependent upon some particular assumption, would introduce an uncertainty in the calculated values and therefore on the validity of the comparison.

Conclusions

2-naphthol is coadsorbed in the presence of CTAB below the cmc both on porous or nonporous silicas. Above the cmc, free micelles compete for the solubilization of the neutral solute. The coadsorption effect, in the case of 2-naphthol, as calculated using the pseudo-phase model is dependent upon the pH of the system and the concentration of adsorbed surfactant but not on the type of silica. The main observation of the present investigation is the larger energetics of solute coadsorption as compared to the classical micellar solubilization effect. It is suggested that this observation may be due, at least in part, to the very different microviscosities of the adsorbed and the free surfactant aggregates and to the formation of bilayered surfactant aggregates at low surfactant coverage. An alternative interpretation based upon the Laplace pressure effect, also involves some solute penetration within the surfactant structures. Curiously, the first hypothesis implies a physical effect which decreases the solute ability to leave the interface, whereas the second hypothesis suggests a force which increases the ability of the solute to penetrate the interface. However, both models imply some solute penetration of the solute in the surfactant layers. This remains an open question. More experiments are needed with solute of different size and polar moieties in order to test these various hypothesis.

Literature cited

1. Rennie, A. R.; Lee, E. M.; Simister, E. A.; Thomas, R. K. *Langmuir* **1990**, *6*, 1031.
2. Wangnerund, P.; Olofsson, G. *J. Colloid Interf. Sci.* **1992**,*153*,392.
3. Esumi, K.; Meguro, K. *Langmuir* **1990**, *6*, 826.
4. Wu, J.; Harwell, J. H.; O'Rear, E. A. *Langmuir* **1987**, *3*, 351.
5. Esumi, K.; Shibayama, M; Meguro, K. *Langmuir* **1990**, *6*, 826.
6. Monticone, V.; Treiner, C. *Langmuir* **1994**,*10*, 2395.
7. Armstrong, D.W.; Borme, F. *Anal. Chem.* **1981**, *53*, 1662.
8. Harma,T.; Speiser, P.; Kreuter, J. *J. Pharmaceutics* **1986**, *33*, 45.
9. Zimmer, A. K.; Maincent, P.; Thouvenot, P.; Kreuter, J. *Int. J. Pharma.* **1994**, *110*, 211.
10. Wagner, J.; Chen, H.; Brownawel, B.J.; Westwall, J. C. *Environ. Sci. Technol.* **1994**, *28*, 231.
11. Rav-Acha, C. H.; Rebhun, M.*Wat.Res.***1992**, *26*, 1645.
12. Pankow, J. F.; McKenzie, S. W. *Environ. Sci. Technol.* **1991**, *25*, 2046.
13. Giordano, F.; Desnoyel, R.; Rouquerol, J. *Colloids and Surf.* A **1993**, *71*, 293.
14. Piirma, I.; Chen, S. R. *J. Colloid Interf. Sci.* **1980**, *74*, 90.
15. Monticone, M.; Treiner, C. *Langmuir* (in press)
16. Abuin, E. B.; Lissi, E. A. *J.Colloid Interf. Sci.* **1983**, *95*, 183.
17. Treiner, C.; Khodja, A. A.; Fromon, M.; Chevalet, J. *J. Solution Chem.* **1989**, *18*, 217.

Downloaded by NORTH CAROLINA STATE UNIV on October 14, 2012 | http://pubs.acs.org
Publication Date: May 5, 1996 | doi: 10.1021/bk-1995-0615.ch003

18. Schieder, D.; Dobias, B.; Klumpp, E.; Schwuger, M. J.*Colloids and Surf.* A **1994**, *88*, 103.
19. Almgren, M.; Grieser, F.; Thomas, J. K. *J. Am. Chem. Soc.* **1979**, *101*, 279.
20. Viaene, K.; Verbeek, A.; Geladé, E.; De Shryver, F. C. *Langmuir* **1986**, *3*, 456.
21. Bayer, O.; Hoffmann, H.; Ulbricht, W.; Thurn, H. *Adv. Colloid Interf. Sci.* **1981**, *26*, 177.
22. Chandar, M.; Somasundaran, P.; Turro, N. J. *J. Colloid Interf. Sci.* **1987**, *117*, 31.
23. Singer, L. A. In *Solution Behavior of Surfactants;* Mittal, K. L.; Fendler, E. J., Eds.; Plenum Press: New York, N.Y., 1978, Vol. 1; pp 73.
24. Mukerjee, P. *Kolloid Z. Z. Polym.* **1970**, *236*, 76.
25. Matheson, I. B. C.; King Jr., A. D. *J. Colloid Interf. Sci.* **1978**, *66*, 464.
26. Prapaitrakul, W.; King Jr., A. D. *J. Colloid Interf. Sci.* **1985**, *106*, 186.
27. Oates, J. D.; Schechter, R. S. *J. Colloid Interf. Sci.* **1989**, *131*, 307.

RECEIVED May 3, 1995

Downloaded by NORTH CAROLINA STATE UNIV on October 14, 2012 | http://pubs.acs.org
Publication Date: May 5, 1996 | doi: 10.1021/bk-1995-0615.ch003

Chapter 4

Adsolubilization: Some Expected and Unexpected Results

John H. O'Haver and Jeffrey H. Harwell

School of Chemical Engineering and Materials Science and Institute of Applied Surfactant Research, University of Oklahoma, 100 East Boyd, Norman, OK 73019

Surfactants adsorbed at the solid/liquid interface can form aggregates that are similar in nature to micelles. Recent studies have reinforced the idea of an adsorbed micelle, or admicelle, which is capable of solubilizing solutes much as micelles do. The phenomenon of adsolubilization, solubilization in adsorbed surfactant bilayers, is just beginning to be explored. Data presented here show that while some systems of solute and surfactant exhibit trends similar to those seen in solubilization, others do not. These similarities and differences, and the reasons for them, are just beginning to be explored.

The phenomenon of solubilization has been recognized, studied, and utilized for much of this century. Likewise, the idea that surfactants adsorbed at a solid/liquid interface could form aggregates that are similar in nature to micelles has been recognized for over 30 years[1]. In contrast, that admicelles should be capable of solubilizing organics, in a surface analog to solubilization, has only been recognized in the literature for the last two decades or so[2], and has only been seriously studied within the past decade. This paper takes a brief look at some of the similarities and differences between the two phenomena.

SURFACTANT ADSORPTION

In order to fully understand the concept of adsolubilization, one must have an understanding of the formation and structure of admicelles. Figure 1 is a schematic of a typical surfactant adsorption isotherm. Such isotherms are frequently seen for the adsorption of ionic surfactants on oppositely charged surfaces, while similar isotherms are sometimes found for the adsorption of nonionic surfactants.

0097–6156/95/0615–0049$12.00/0

These isotherms are commonly divided into 4 regions[3,4]. Region 1, sometimes referred to as the Henry's Law region, is a region of low surfactant adsorption densities. In this region surfactants adsorb as individual molecules with little interactions; it is generally assumed that no aggregates are formed in region 1. The surfactant concentrations in which this region occurs may be so low that measurement of adsorption is not possible. Region 2 is characterized by a sharp increase in the slope of the isotherm. All investigators have attributed this to the formation of surfactant aggregates on the surface[3-14], whether local monolayers (hemimicelles), local bilayers (admicelles), or something in between. The micelle-like nature of these aggregates has been reinforced by several spin probe and dye studies[2]. It should be pointed out that these aggregates form at adsorption densities which may be lower than 1/100th of a monolayer coverage. There is little agreement on the mechanism for the change in slope which begins region 3. Investigators have proposed that it may be due to increasing competition for the remaining surface area[15,16], a more complete transition from monolayer to bilayer[17-19], or heterogeneities in the substrate surface[4,13]. Recent studies indicate that the aggregates have a micelle like nature throughout regions 2 and 3[2,20]. The transition from region 3 to 4 occurs near the critical micelle concentration (CMC). Region 4 is called the plateau region[14], and for many surfactants the adsorption in this region is nearly constant for all concentrations above the CMC.

ADSOLUBILIZATION: THE PHENOMENON

Surfactant aggregates called micelles have the ability to preferentially absorb organic solutes from solution, a process called solubilization. Adsolubilization is the surface analog to solubilization, with adsorbed surfactant bilayers playing the role of micelles (Figure 2). Organic solutes, with limited solubilities in water, preferentially partition into the interior of the admicelle.

The studies of adsolubilization to date have predominantly been in the area of exploring the nature of the adsorbed surfactant layer, although new technologies based upon adsolubilization are beginning to emerge[2]. These applications include admicellar chromatography, admicellar catalysis, and surface modification processes. The surface modification process has proven to be an flexible, effective means of modifying the nature of mineral oxide surfaces[22,23,24]. Modified silicas have been shown to make improved reinforcing-fillers for use in tire rubber compounding[25].

ADSOLUBILIZATION STUDIES: EXPECTED RESULTS[21]

The adsolubilization of alkanes into sodium dodecyl sulfate (SDS) admicelles was determined by a solute vapor pressure method, which is explained fully in the reference[21]. The basic experimental procedure is given below:

1. Add alumina, SDS and pH adjusted deionized water to a vessel of known volume, seal and evacuated it to the vapor pressure of the slurry. The feed was designed so that the bulk surfactant concentration at equilibrium was below the CMC.

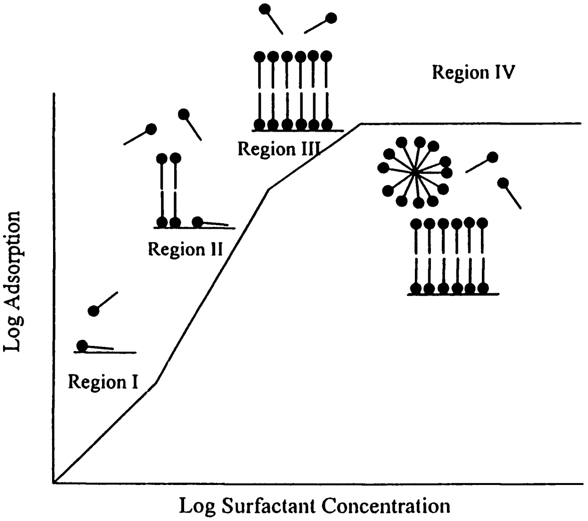
Region IV
Region III
Region II
Region I
Log Adsorption
Log Surfactant Concentration

Figure 1. A typical surfactant adsorption isotherm.

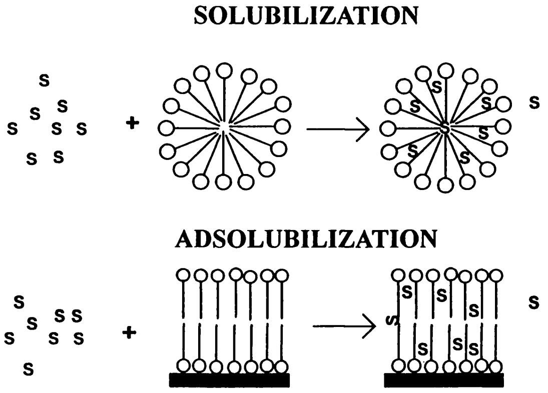
SOLUBILIZATION
s
s s
s s s
s s
+
s
s
s
s
s
s
ADSOLUBILIZATION
s
s s s
s s s
s
+
s
s
s
s
s
s
s
s

Figure 2. A comparison of solubilization to adsolubilization.

In Surfactant Adsorption and Surface Solubilization; Sharma, R.;
ACS Symposium Series; American Chemical Society: Washington, DC, 1996.

2. Incremental amounts of alkane were flashed to the system and allow to equilibrate.
3. The pressure of the system was read by means of a transducer.
4. From the pressure data, and appropriate blank runs, the amount of adsolubilized alkane could be calculated by performing a mass balance.

A series of n-alkanes, C5 to C7, were analyzed.

The results for the adsolubilization of the three alkanes are shown in Figure 3. A reduced pressure, $P_i/P_o = 1$, represents the saturation concentration of the alkane in the water, where P_i is the partial pressure of the alkane and P_o is the vapor pressure of the alkane at this temperature. As would be expected, the adsolubilization increases with increasing alkane reduced pressure. Extrapolating the data to a reduced pressure of 1 gives saturation adsolubilizations of 333, 263, and 212 µmoles of solute per gram of substrate for n-pentane, n-hexane, and n-heptane, respectively. Evaluation of bulk surfactant concentration before adsolubilization and at maximum adsolubilization indicated no appreciable increase in surfactant adsorption due to adsolubilization. As alkane carbon chain length increased the adsolubilization was seen to decrease for a given reduced pressure. This implies that, just as there are differing capacities for the solubilization of various compounds in surfactant micelles, so there are differing capacities in the admicelle. As the molecular weight of the adsolubilizate increases, the adsolubilization capacity [(micromoles of adsolubilized solute)/(micromoles of adsorbed surfactant) at saturation] in a given surfactant admicelle apparently decreases.

The partitioning of the alkane between the admicelle aggregate and the bulk solution can be described by Kapp, which is defined as [(moles of alkane in the admicelle)/(moles alkane in the admicelle + moles adsorbed surfactant) / mole fraction of alkane in the bulk solution]. The Kapp value at varying alkane adsolubilizations is shown in Figure 4. The values of Kapp for the three alkanes at saturation, as well as literature values for the Kapp of n-hexane and n-heptane in SDS micelles, are shown in Table I. The data show that the partitioning of alkanes between the bulk phase and admicelles or micelles is similar in magnitude and exhibits the same trends.

Yeskie also looked at the incremental change in standard state free energy per methyl group in the series. The value he obtained, in the presence of .15 M NaCl, was -0.79 kcal/mole. This compares favorably with the literature values for alkanes in SDS micelles of -0.62 kcal/mole for no added salt[26], and -0.72 kcal/mole for .1 M NaCl[27]. This again reinforces the similarities between solubilization and adsolubilization.

Table I. Kapp for alkanes at saturation in SDS admicelles and micelles. (.15 M added NaCl)

ALKANE	**Kapp in SDS admicelles on alumina**	**Kapp in SDS micelles[26]**
n-pentane	$4.3 * 10^4$	N/A
n-hexane	$1.8 * 10^5$	$3.5 * 10^5$
n-heptane	$5.9 * 10^5$	$1.0 * 10^6$

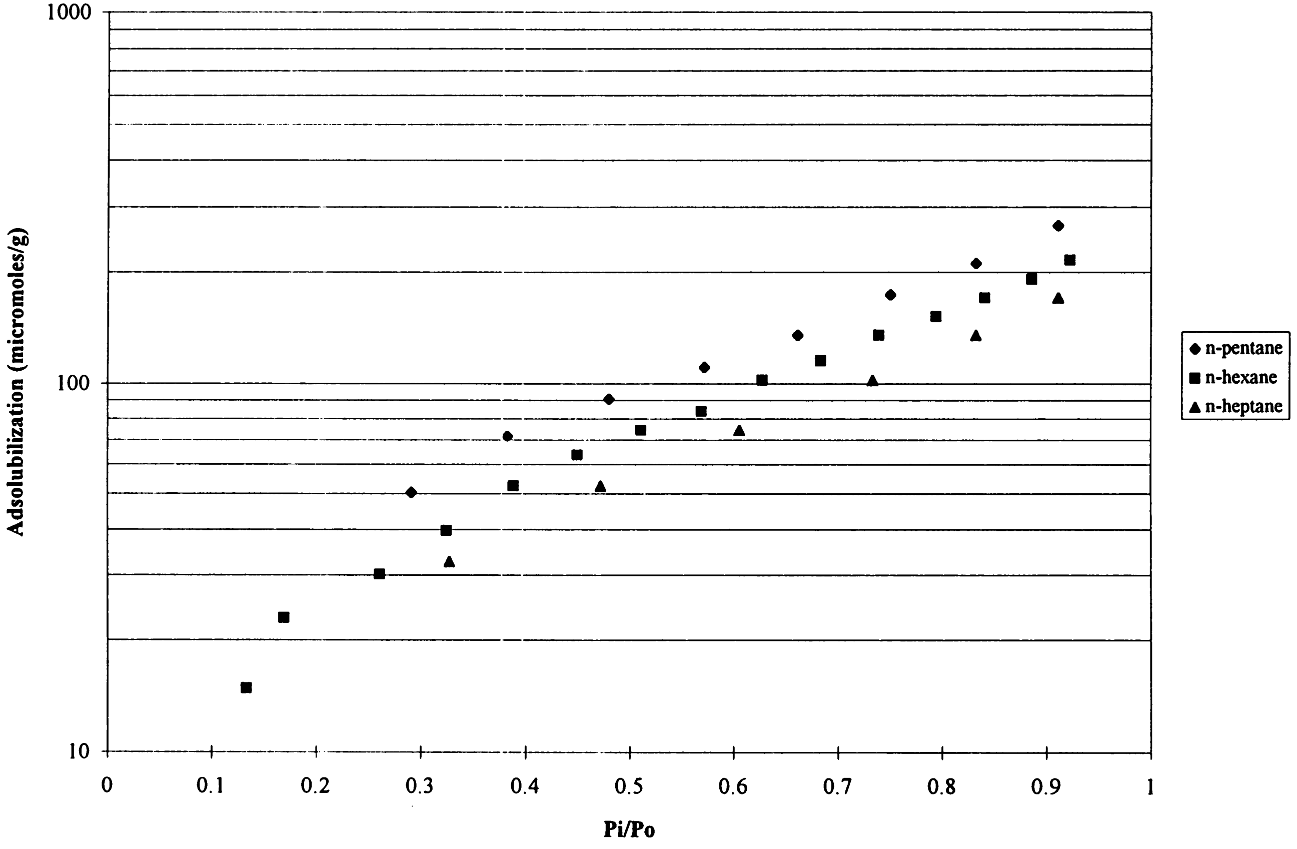

Figure 3. Alkane adsolubilization as a function of reduced pressure.

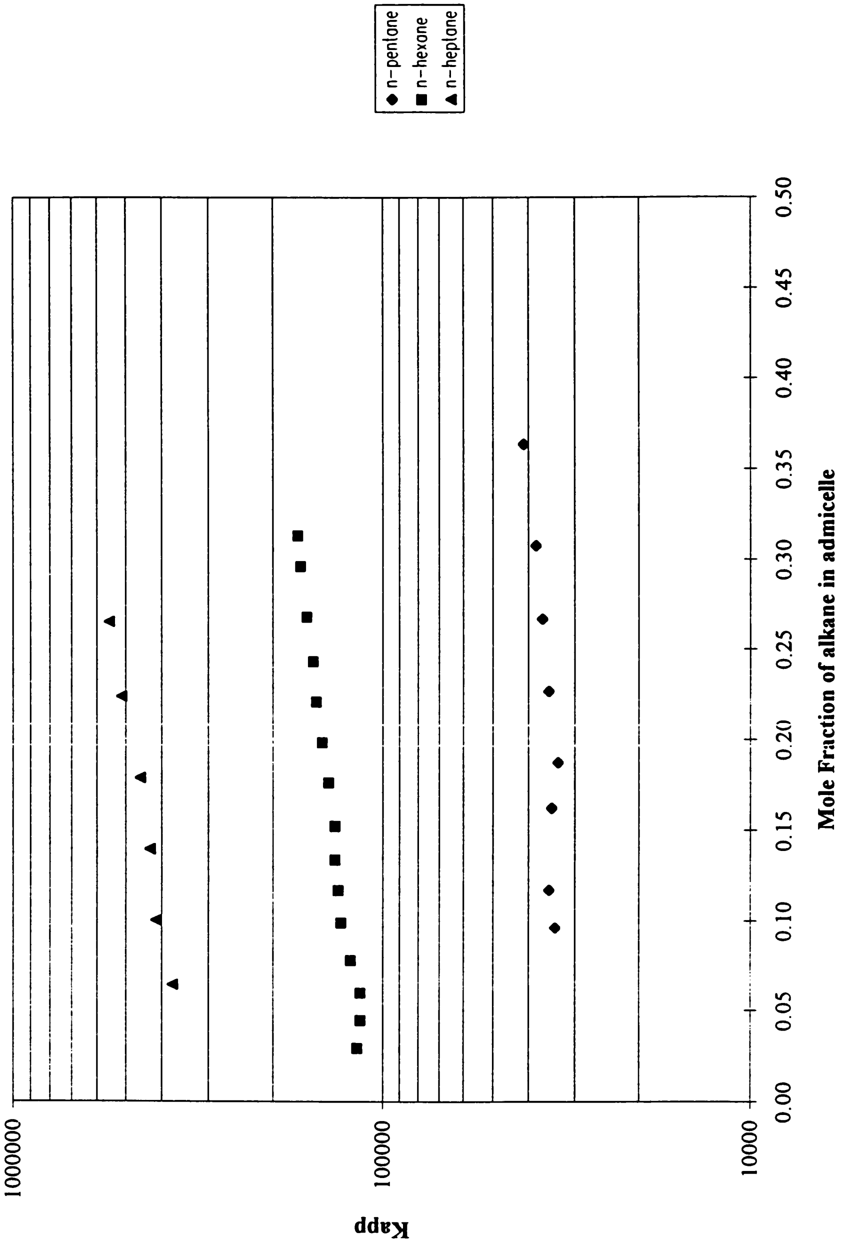

Figure 4. Kapp as a versus the mole fraction of the alkane in the admicelle.

Another interesting observation can be made by comparing the ratio of adsolubilized solute to adsorbed surfactant. Defining a partition coefficient, K, as (moles adsolubilized solute / moles adsorbed surfactant), we find that in the case of n-alkanes, increasing equilibrium bulk surfactant concentration, and therefore adsorbed surfactant, causes an increase in the partition coefficient (Table II). Yeskie hypothesized that alkanes, because of their nonpolar nature, would adsolubilize only in the core of an admicelle. Therefore, if admicelles start as small surface aggregates at low adsorption, and form larger and larger aggregates as the CMC is approached, then the ratio of exterior surfactant molecules to interior ones would decrease with increasing coverage (Figure 5). Because of this, as the surface aggregates increase in size, the core volume increases, and more solute can partition there per surfactant molecule. It should be noted, however, that similar trends in K have been observed for alkanes in micelles.

Table II. The partition coefficient for n-hexane at saturation for increasing levels of surfactant adsorption

Adsorbed Surfactant (micromoles/g)	**Adsolubilization Capacity: K at saturation (moles adsolubilized n-hexane / moles adsorbed surfactant)**
93	.411
473	.556

ADSOLUBILIZATION STUDIES: UNEXPECTED RESULTS[21]

Similar studies were conducted for the adsolubilization of the series of alcohols isopropyl, n-butanol, n-pentanol, n-hexanol and n-heptanol. The work began by looking at the adsorption of SDS onto alumina, both with and without the presence of alcohols. Contrary to the alkane study, where surfactant adsorption was a weak function of alkane concentration, the results showed that the presence of high concentrations of alcohol in the system greatly increased the adsorption of surfactant onto the alumina surface in regions 1, 2 and 3 of the adsorption isotherm, in Figure 6. At an equilibrium concentration of 150 μM SDS, the adsorption is approximately 0.8 micromoles/g in the absence of any alcohol and 10 micromoles/g in the presence of 0.5 M isopropanol. These results implied a higher Henry's Law constant for the surfactant in the presence of high concentrations of alcohol. This is surprising as surfactant monomers are considered to be at infinite dilution in this region, and therefore the surfactant adsorption was not expected to change. This suggests the co-adsorption of small surfactant monomer-alcohol aggregates of unknown size in Region 1. The co-adsorption is not surprising in itself, but it does imply that because the bulk concentration of alcohol is not measurably lowered, that the number of alcohols molecules taking part in the aggregates is small. Another interesting result was that, although adsorption was increased in Regions 1 to 3, plateau adsorption in Region 4 was decreased by approximately 15% for all alcohols tested. Since the extent to which the alumina surface was completely filled with alcohol saturated admicelle-layer is unknown, it is not possible to determine whether the decrease is due

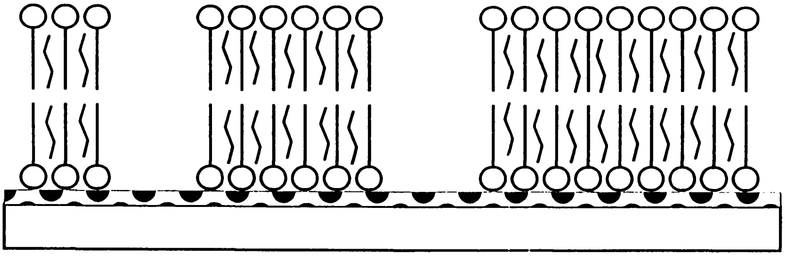

Figure 5. A schematic of alkane adsolubilization in SDS admicelles.

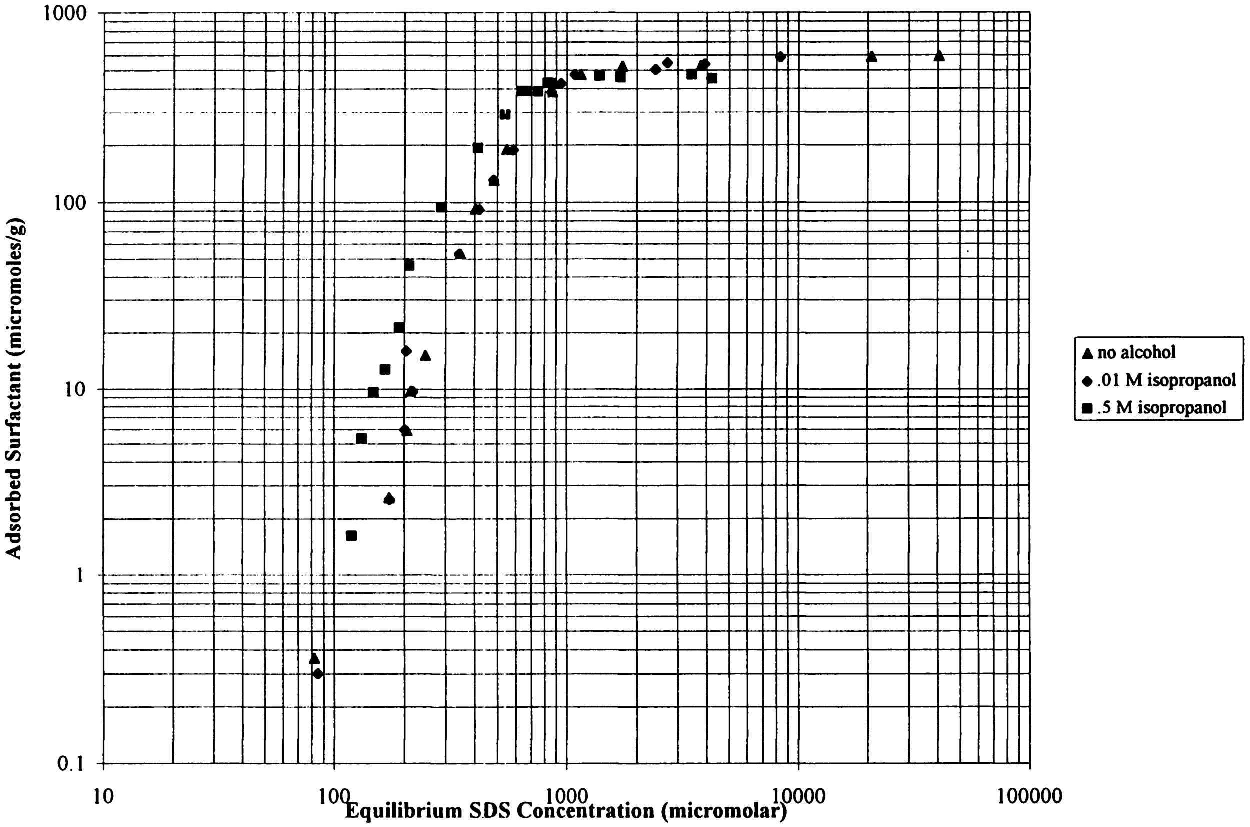

Figure 6. Surfactant adsorption in the presence of increasing isopropanol feed concentrations.

to swollen-admicelle interactions at the surface, or due to the competition with the swollen micelles in the bulk. The results for the adsorption of SDS in the presence of each alcohol in the series (at .1 M feed concentration) is shown in Figure 7. Because of the varying solubilities of these alcohols in water, a more meaningful analysis was to plot surfactant adsorption for the various alcohols at the same relative concentrations, that is, at concentrations representing the same fraction of saturation. These results are given in Figure 8, and show that at the same relative concentrations, all of the alcohols impact surfactant adsorption approximately the same.

The study focused extensively on the adsolubilization of the alcohols at varying levels of surfactant adsorption. Yeskie proposed a two-site model for the adsolubilization of alcohols. He hypothesized that alcohols, because of the polar -OH group, would adsolubilize not only on the interior of an admicelle aggregate, but also along the edges of the aggregates, which are pictured as disk-like in structure (Figure 9). Therefore, at very low surfactant adsorption levels, where the surface aggregates were small, the effect of alcohol adsorption along the edges of aggregates on the partition coefficient would be large. As the aggregates increased in size with increasing levels of surfactant adsorption, the impact of these "edge effects" would be lessened, and the partition coefficient would decrease. The data show that the value of K decreases for increasing levels of surfactant adsorption. Therefore, for compounds which are very hydrophobic and adsolubilize almost exclusively in the interior of the admicelle, the partition coefficient will increase with increasing levels of adsorbed surfactant. For compounds which are more hydrophilic in nature and can adsolubilize not only in the interior of the admicelle but also on the edges, we expect to see a decreasing partition coefficient with increasing levels of adsorbed surfactant. These results should not cloud the fact that the total amount of adsolubilized alcohol increases with increasing levels of adsorbed surfactant. The data probably follow a Langmuir-type adsorption isotherm for solubilization in the palisade layer, but this could not be tested because of the strong edge effects.

The study also showed that there was no appreciable adsorption of alcohols in the absence of surfactant. There was also no measurable amount of alcohol adsolubilization in the Henry's Law region of the surfactant adsorption isotherm, although the previously discussed results showed that there were surfactant / alcohol interactions at the interface in this region. A reasonable explanation of this is that a small amount of adsolubilizing alcohol molecules allows the surfactant to adsorb to a significantly higher degree in region 1, even though the change in alcohol bulk concentration is at or below detection limits. This could also be viewed as the presence of a few co-adsorbed alcohols allowing significantly larger surfactant aggregates to form due to the dipole-induced dipole interactions between the surfactant and alcohol molecules.

As with the alkanes, for a given level of surfactant adsorption, alcohol adsolubilization increases with increasing equilibrium alcohol concentration (Figure 10). Figure 11 shows that for a given level of surfactant adsorption, comparing the alcohol adsolubilization for the same relative concentrations of the alcohols, one sees almost identical behavior for the whole series.

Recent studies in this area have shown some additional differences between solubilization and adsolubilization. In looking at the maximum mole fraction of solute

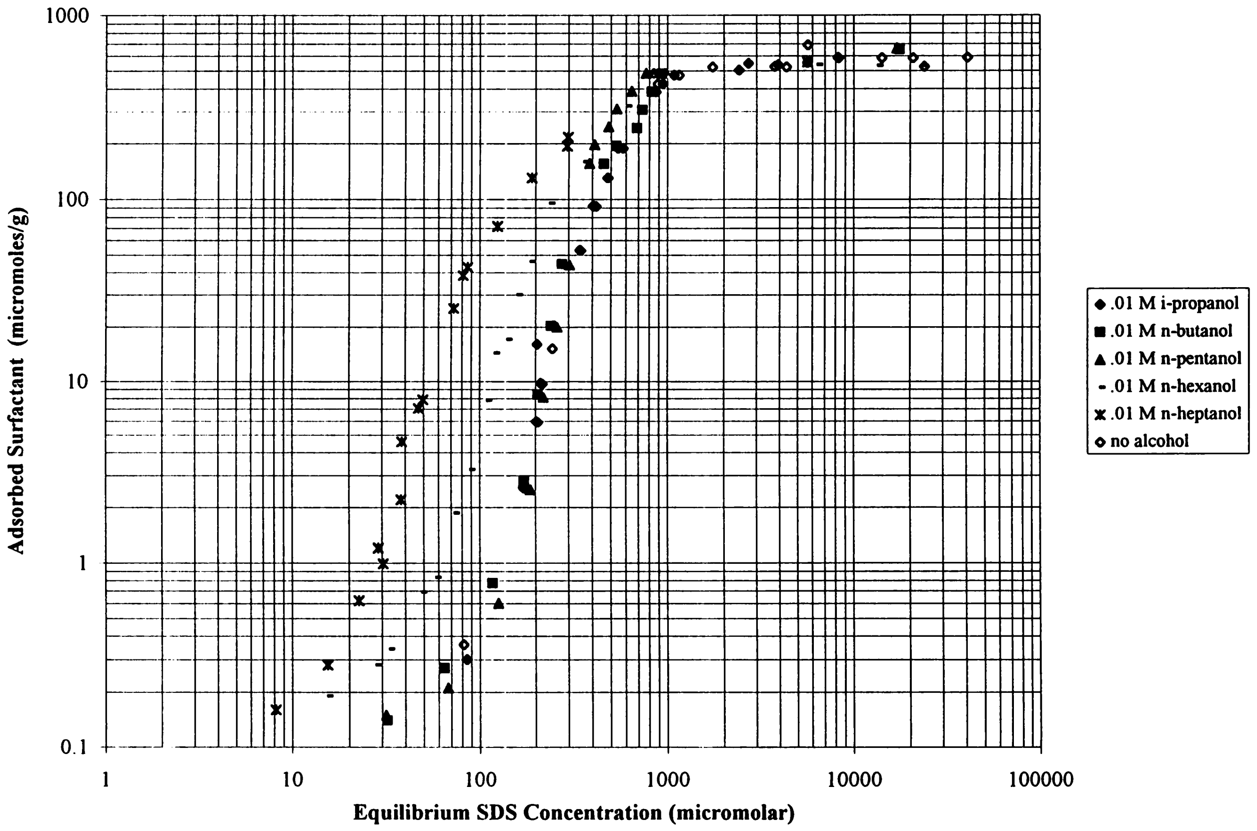

Figure 7. Surfactant adsorption in the presence of .01 M concentrations of various alcohols.

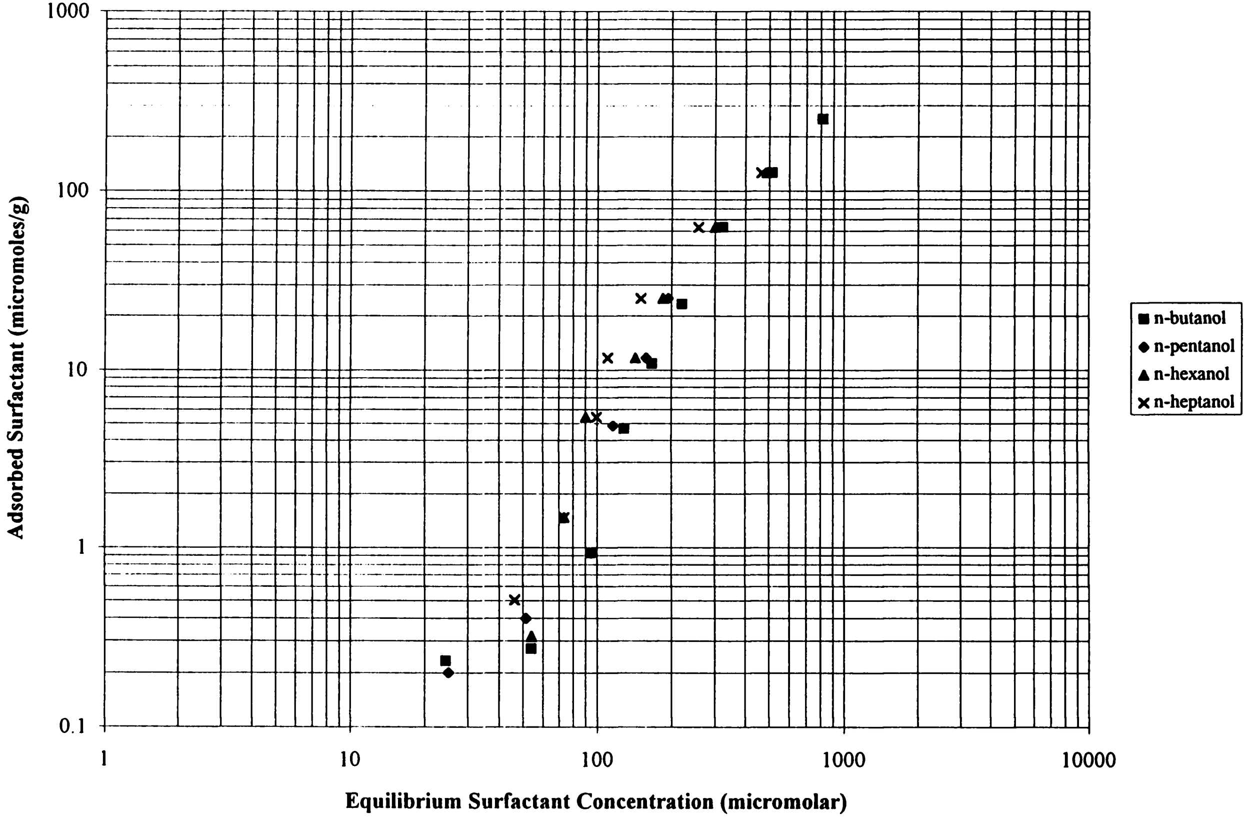

Figure 8. Surfactant adsorption in the presence of four alcohols, all at the same reduced concentration.

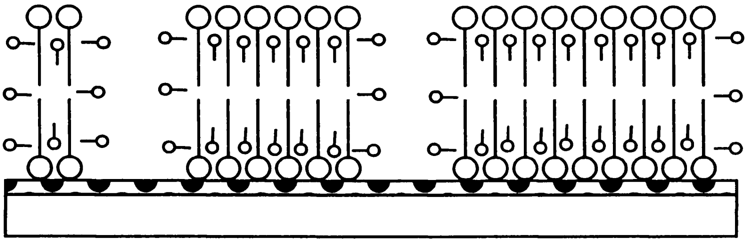

Figure 9. A schematic of alcohol adsolubilization in SDS admicelles.

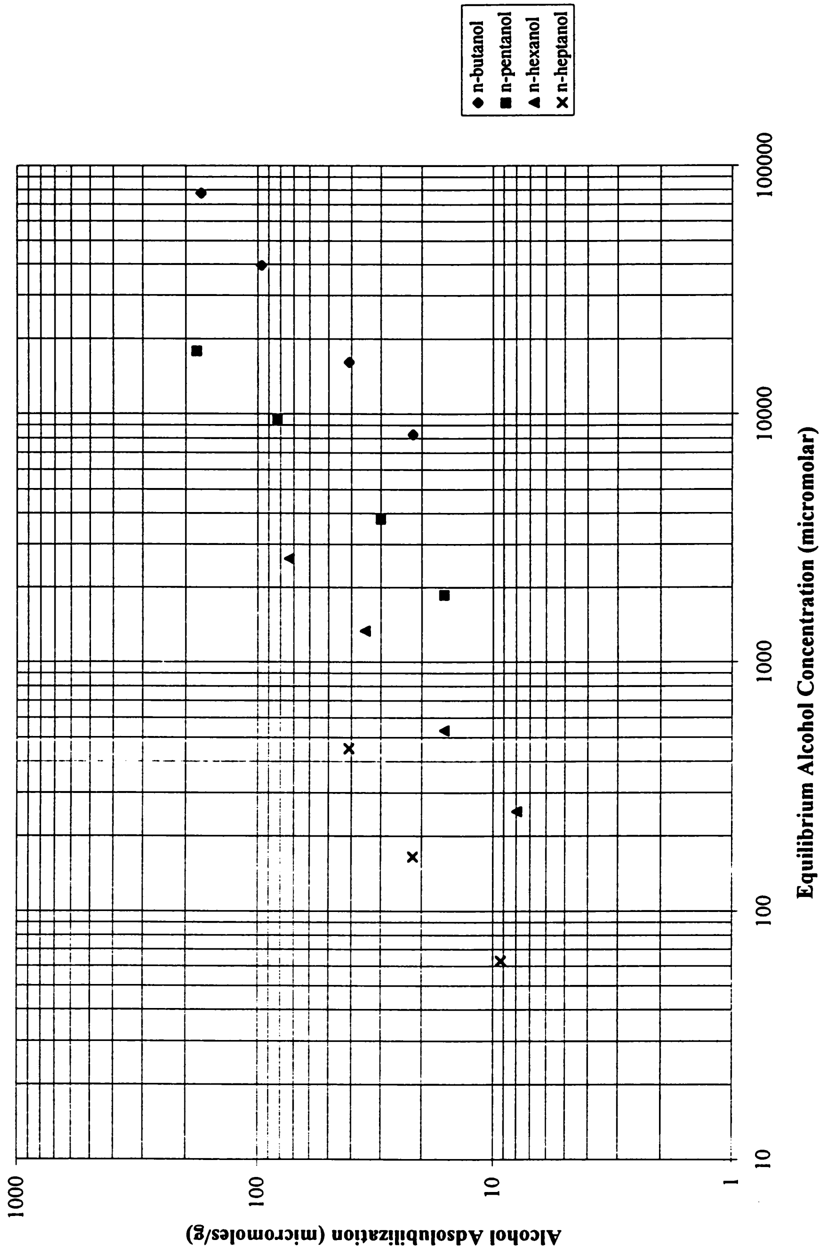

Figure 10. Alcohol adsolubilizations as functions of equilibrium alcohol concentrations.

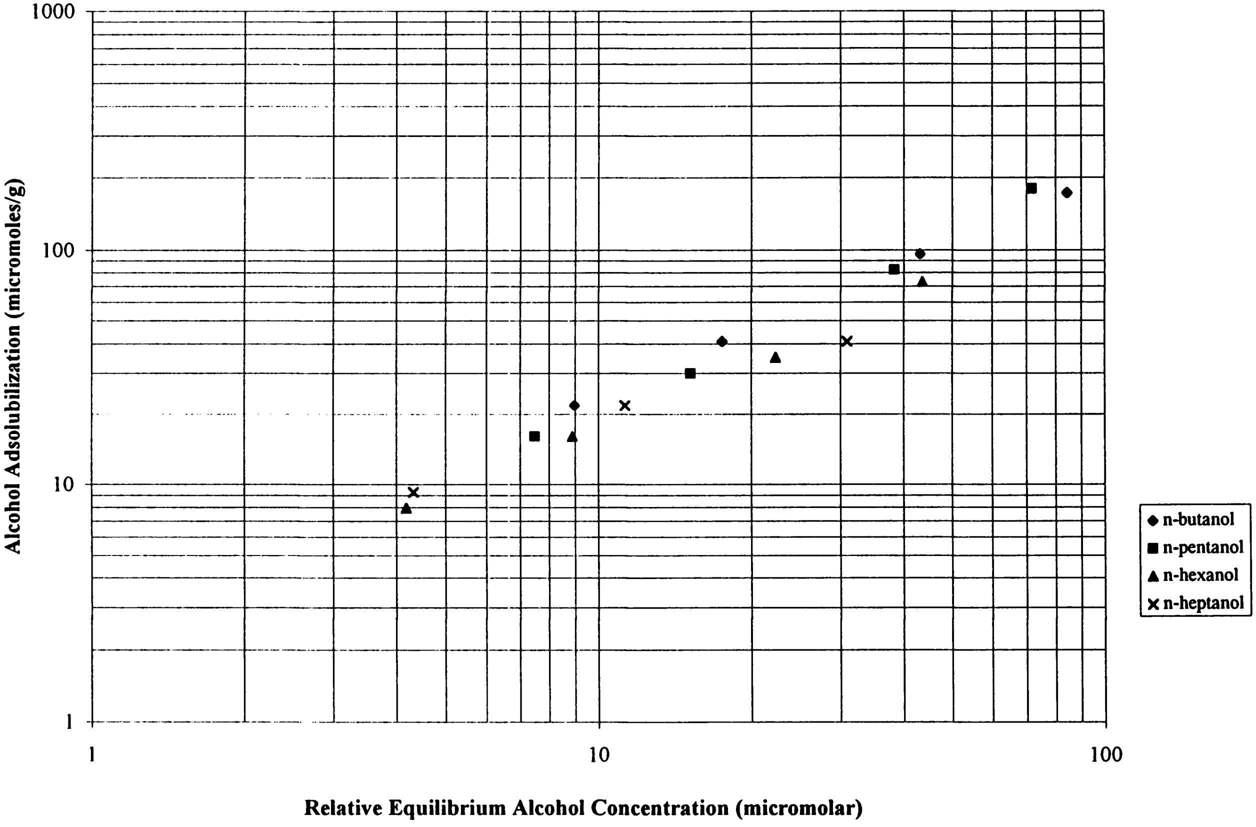

Figure 11. Alcohol adsolubilizations as functions of relative equilibrium alcohol concentrations.

in a micelle, the values are generally less than 0.3, even when the solution is saturated with solute. Recently, studies were made of the adsolubilization of 1,3-butadiene in cetyltrimethylammonium bromide admicelles on amorphous silica[28]. Data show that at relatively high partial pressures of butadiene, the mole fraction of adsolubilizate in the admicelle [moles adsolubilized solute / (moles adsolubilized solute + moles adsorbed surfactant)] can reach values as high as 0.7 (Table III). These higher values, representing higher solubilizing capacities, may be due to the differing geometries of micelles and admicelles (Figure 12). Using an idealized spherical micelle, the "volume available for solubilization" per molecule can be thought of as the volume of a cone. For an admicelle, where the surfaces are relatively smooth on a molecular level, the "volume available for adsolubilization" can be thought of as a circular cylinder. For solubilization within the core, perhaps including the last half of the surfactant alkane chain, the volume for the cylinder divided by the volume of the cone is $\pi r^2 h/(1/3\pi r^2 h)$, or 3. This ratio is constant, whatever fraction of the alkane chain you choose to use in order to make the calculation. This calculated ratio of adsolubilizing volume in admicelles to solubilizing volume in micelles is close to the ratio of adsolubilization to solubilization capacities observed experimentally.

Table III. Mole fraction of adsolubilized monomer in the admicelle at various monomer partial pressures

1,3-Butadiene Partial Pressure	**Ratio of Adsolubilized Monomer to Adsorbed Surfactant**
0.0	0.00
6.4	.27
12.6	.42
18.5	.52
24.0	.59
29.9	.63
34.3	.66

CONCLUSIONS

Adsolubilization can be seen as the surface analog to solubilization, with admicelles playing the role of micelles. The data presented here, from just a few studies, show that although the phenomenon of adsolubilization has many similarities to solubilization, it also has several distinctive characteristics. Similarities include: the adsolubilization of various solutes increases with increasing solute concentration; increasing the molecular weight of the solute in a homologous series decreases the capacity of the admicelle and the micelle to take up that compound; the increase in partition coefficient with increasing surfactant loading; similar incremental free energies per methyl group; decreasing partition coefficients for alcohols at increasing surfactant concentrations; and nonpolar compounds tend to partition into the admicelle core, while polar compound tend to partition into the palisade layer and by the head groups. Differences include; "edges" to admicelles which allow for areas of

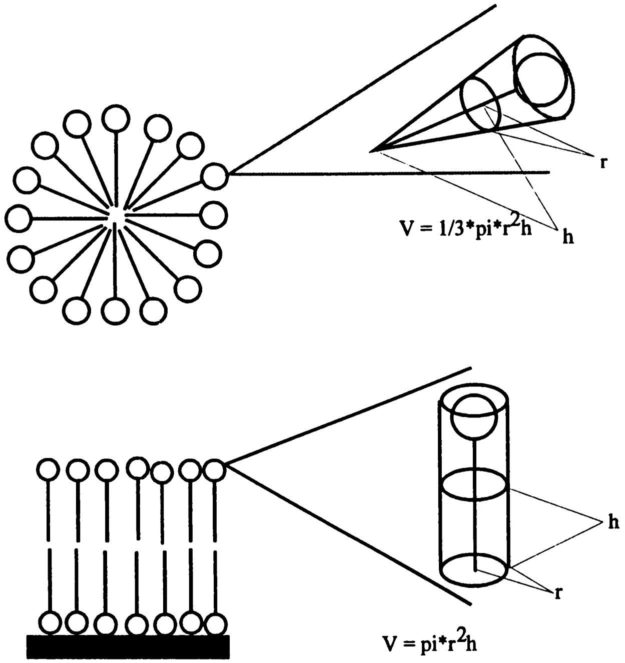

Figure 12. A schematic showing the relative volumes available for solubilization in a micelle versus adsolubilization in an admicelle.

greatly changing polarity in the admicelle; solubilization by surfactant monomers; and apparently higher solubilizing capacities on a mole fraction basis. The impact of the presence of another interface, that of the solid, is only now being explored. The possibilities of capillary condensation within small pores on some substrates could increase apparent adsolubilization, as well as adsorption due to the hydrophobic effect. All of these interactions must be taken into account in future studies.

Some of the many possible applications of adsolubilization, as well as the fundamental nature of the phenomenon itself, are just beginning to be explored. The ability to concentrate compounds in a surfactant layer at the solid/liquid interface opens up possibilities in surface modification, admicellar catalysis, structuring of nanoscale materials, and many other as yet unthought of areas. The authors believe that adsolubilization, and applications utilizing it, may well end up being as significant a discovery as solubilization has proven to be.

REFERENCES

1. Iler, R.K. "Colloid Chemistry of Silica and Silicates", Cornell University Press, Ithaca, New York, 1955.
2. O'Haver, J.H.; Harwell, J.H.; Lobban, L.L.; E.A. O'Rear, "Adsolubilization", in *Solubilization in Surfactant Solutions*, Christian, S.D.,

and Scamehorn, J.F. Eds; Surfactant Science Series Vol. 55; Marcel Dekker, New York, 1995.

3. Somasundaran, P.; Fuerstenau, D.W. *J. Phys. Chem.*, **79**:90 (1982).
4. Scamehorn, J.F.; Schechter, R.S.; Wade, W.H. *J. Colloid Interface Sci.*, **85**:463 (1982).
5. Gaudin, A.M.; Fuerstenau, D.W. *Min. Eng.*, **7**:958 (1955).
6. Gaudin, A.M.; Fuerstenau, D.W. *Trans. AIME*, **202**:66 (1966).
7. Somasundarun, P.; Healy, T.W.; Fuerstenau, D.W. D.W. *J. Phys. Chem.*, **68**:3562 (1964).
8. Cases, J.M.; Villierras, F. *Langmuir*, **8**:1251 (1992).
9. Böhmer, M.R.; Koopal, L.K. *Langmuir*, **8**:1594 (1992).
10. Böhmer, M.R.; Koopal, L.K.; Jannssen, R.; Lee, E.M.; Thomas, R.K.; Remie, A.R. *Langmuir*, **8**:228 (1992).
11. Yeskie, M.A.; Harwell, J.H. *J. Phys. Chem.*, **92**:2346 (1988).
12. Bitting, D.; Harwell, J.H. *Langmuir*, **3**:531 (1987).
13. Harwell, J.H.; Hoskins, J.; Schechter, R.S.; Wade, W.H. *Langmuir*, **1**:251 (1985).
14. Trogus, F.J.; Schechter, R.S.; Wade, W.H. *J. Colloid Interface Sci.*, **70**:293 (1979).
15. Levitz, P.; Van Damme, H.; Keravis, D. *J. Phys. Chem.*, **88**:2228 (1984).
16. Levitz, P.; Van Damme, H. *J. Phys. Chem.*, **90**:1302 (1986).
17. Waterman, K.C.; Turro, N.J.; Chandar, P.; Somasundaran, P. *J. Phys. Chem.*, **90**:6828 (1987).
18. Chandar, P.; Somasundaran, P.; Waterman, K.C.; Turro, N.J. *J. Phys. Chem.*, **91**:148 (1987).
19. Chandar, P.; Somasundaran, P.; Turro, N.J. *J. Colloid Interface Sci.*, **117**:31 (1987).
20. Kung, K.S.; Hayer, K.F. *Langmuir*, **9**:263 (1993).
21. Yeskie, M.A. Ph.D. Dissertation, University of Oklahoma, 1988.

22 Wu, J. Ph.D. Dissertation, University of Oklahoma, 1987.

23 Lai, C-L. Ms. Thesis, University of Oklahoma, 1993.

24 O'Haver, J.H.; Harwell, J.H.; O'Rear, E.A.; Snodgrass, L.J.; Waddell, W.H. *Langmuir*, **10**, 2588, (1994).

25 O'Haver, J.H.; Waddell, W.H.; Evans, L.R.; Harwell, J.H. accepted for publication in Journal of Applied Polymer Science.

26 Hoiland, H.; Ljosland, E.; Backlund, S. *Journal of Colloid and Interface Science*, **101**, 467, (1984).

27 Wishnia, A. Journal of Physical Chemistry, 67, 2079 (1963).

28 O'Haver, J.H. Ph.D. Dissertation, University of Oklahoma, 1995.

RECEIVED May 3, 1995

Chapter 5

Admicellar Catalysis

Chung-Ching Yu and Lance L. Lobban

**School of Chemical Engineering and Materials Science,
University of Oklahoma, Norman, OK 73019**

Our earlier study has demonstrated the catalysis by sodium dodecyl sulfate (SDS) surfactant adsorbed on solid surfaces (admicellar catalysis). The adsorbed SDS aggregates have catalytic activity comparable to that of SDS micelles for the acidic hydrolysis of trimethyl orthobenzoate (TMOB). In the present study we investigate pH and buffer concentration effects on the admicellar catalysis of the same reaction. At constant surfactant adsorption, the reaction rate increases as the pH or buffer concentration decreases. A significant change is observed in the dependence of rate constant on surfactant adsorption. The transition may be due either to a higher packing density of the surfactant aggregates or to an adsorbed aggregate structure change. The solubilization of organic solute into admicelles (adsolubilization) is also measured. Adsolubilization constants of reactant TMOB and product methyl benzoate (MB) are roughly constant (164 M^{-1} and 80 M^{-1}, respectively) at SDS adsorption levels below 300 μmol/g. As SDS adsorption increases beyond 380 μmol/g, the adsolubilization constants of both species decrease.

Reactions catalyzed by surfactant micelles have been extensively studied for decades (*1-4*). In spite of the great rate enhancement observed for many reactions, few practical applications of micellar catalysis have been developed due to the difficulties of product isolation (*5*). This major shortcoming can render micellar catalysis ineffective or disadvantageous even for lab scale organic synthesis (*6*). For industrial scale application, these difficulties are even more prohibitive. Thus, development of techniques to solve this problem while maintaining or improving the rate enhancement is required for practical employment of catalysis by surfactant aggregates.

An alternative technique of catalysis comprises using surfactant aggregates adsorbed on a solid surface to facilitate the surfactant/product separation step. Surfac-

0097–6156/95/0615–0067$12.00/0

tant aggregates adsorb onto mineral oxide surfaces at bulk phase concentrations significantly below the critical micelle concentration (cmc) (*7-8*), making the catalysis by adsorbed surfactant (admicelles) possible at very low aqueous phase surfactant concentration.

There is continuing debate in the literature about whether the adsorbed surfactants on solid surface are monolayered aggregates, called ***hemimicelles*** (*9*) or bilayered aggregates, called ***admicelles*** (*10-11*). However, for ionic surfactant adsorption on charged hydrophilic surfaces, studies of the aggregate structure using fluorescence probe (*12*), electron spin resonance and fluorescence spectra (*13*), ^{2}H NMR spectroscopy (*14*), neutron reflection (*15-16*) or theoretical predictions (*17*) have indicated that at sufficiently high surface coverage the surfactant aggregates are bilayers.

Analogous to micelles, adsorbed surfactant aggregates solubilize organics into the hydrophobic environment of the hydrocarbon chains (*11-12, 18-19*). Solubilization of organic substrates into admicelles (adsolubilization) has been studied to investigate admicellar chromatography (*20*) and the polymerization of styrene in admicelles which serve as reaction solvents (*21-23*). Recently, O'Haver and coworkers (*24*) have reported a study on *in situ* formation of polystyrene in admicelles to modify the surface properties of inorganic powders.

In our earlier study (*25*), we demonstrated catalysis by adsorbed anionic sodium dodecyl sulfate (SDS) surfactant on high surface area solid supports. The results showed adsorbed SDS aggregates have catalytic activity comparable to that of micelles (*26-27*) in the acidic hydrolysis of trimethyl orthobenzoate (TMOB). In our laboratory, admicellar catalysis in a continuous flow packed bed reactor was also demonstrated (*28*).

In this study, we investigate pH and buffer concentration effects on the catalytic activity of admicelles in the TMOB hydrolysis reaction. We also discuss how the morphology of adsorbed surfactant aggregates may be affected by the pH and buffer concentration and how the morphology is related to the catalytic activity of the admicelles.

Experimental Section

Materials. Anionic sodium dodecyl sulfate (SDS) surfactant was electrophoresis grade from the Eastman Kodak Company and was employed without further purification since there is no surface tension minimum in plots of surface tension versus concentration. TMOB and methyl benzoate (MB) from Aldrich Chemical Company were used as received. Sodium acetate from Fisher Scientific and acetic acid from Mallinckrodt Inc. were used for the buffer solution. Porous activated acidic alumina from Aldrich Chemical Company was sieved before use. A particle size distribution of 37-100 microns was obtained and a BET surface area of 173 m^2/g was measured. All the solutions were prepared with deionized distilled water.

Adsorption Measurements. 500 mL of aqueous SDS solution was mixed with 20 g of the alumina particles in a 600 mL beaker. The room temperature solutions were buffered to various pH at different acetate buffer concentrations and occasionally agitated over a period of at least 4 days to allow equilibrium adsorption of SDS. The aqueous phase SDS concentration was determined using a Perkin-Elmer high performance liquid chromatograph (HPLC) with a Wescan conductivity detector and a 5 cm C18 reversed-phase silica column. Peak areas were calculated on a Varian 4270 integrator. A simple mass balance then gave the amount of SDS adsorbed on the alumina, from which the adsorbed SDS per gram of alumina (μmol/g) was calculated.

Adsolubilization Measurements. Methyl benzoate (MB) was mixed with methanol at a volume ratio of 1:2. An MB solution was prepared by adding 25 μL of the MB/methanol mixture to 50 mL of water. Then 1 mL of the MB solution was injected into a 15 cm-long glass test tube containing 10 mL of SDS solution and 0.4 g of alumina. After manually agitating the test tube for 2 minutes, samples were withdrawn from the solution by syringe filtration. Samples were put in a quartz cuvette and the MB concentration was measured using a Hewlett-Packard 8452A diode array UV/Vis spectrophotometer. Absorbance at λ_{max} = 230 nm was used to determine the concentration. The concentration of MB in the admicelles was obtained by subtracting that in the aqueous phase from the total concentration. The partition coefficient, K_m, of MB is defined as the ratio of MB concentration in the admicelles (defined as moles adsolubilized MB per unit total volume) to that in the aqueous phase. The adsolubilization constant, K_{ads}, is then expressed as

$$K_{ads} = \frac{K_m}{[D]_{ads}}$$

where $[D]_{ads}$ is the adsorbed surfactant concentration (M), i.e., moles of adsorbed surfactant per liter of total solution volume. K_{ads} has units of M^{-1}. TMOB adsolubilization measurements were carried out in a similar fashion. The 208 nm absorbance peak was used to determine the aqueous phase TMOB concentration.

Kinetics Measurements. To initiate the reaction, 5 μL of TMOB (the resulting initial concentration was 5.82×10^{-5} M) were injected into the beaker containing admicelles. The reaction mixture was constantly mixed using a magnetic stirring bar. The reaction mixture was continuously sampled through a 5 micron filter placed in the beaker by pumping a side stream to a flowcell of the UV spectrophotometer and measuring the absorbance at 230 nm, an absorbance maximum of the reaction product methyl benzoate (MB). The filter prevented removal of the adsorbed surfactant from the beaker and precluded alumina particles' interference with the UV measurements. After passage through the UV flowcell, the sample was returned to the 600 mL beaker.

At some conditions when air bubbles formed and interfered with the UV measurements, an alternative batch method was used to measure the reaction rate. The reaction was initiated by injecting 1 μL of TMOB into a 100 mL reactor. This reactor contained 4 g of alumina and adsorbed SDS. Periodically, samples were withdrawn and put in a quartz cuvette to measure the absorbance of MB. From the MB concentration versus reaction time, the observed first-order rate constant was calculated through a simple kinetic fit.

Results and Discussion

Critical Micelle Concentration (cmc). It is important to determine the cmc to avoid micellar catalysis contributions. The cmc of the SDS solutions was measured using a du Noüy ring tensiometer or a bubble tensiometer. We noted that, at constant aqueous phase surfactant concentration, the surface tension of surfactant solution after contacting with alumina is lower than that of a solution of the same surfactant concentration not in contact with alumina (as shown in Figure 1). Moreover, the cmc of a surfactant solution in contact with alumina is lower than that of a solution in the absence of alumina. The cmc's at various acetate buffer concentrations are listed in Table I. In the surfactant solution after adsorption, some of the sodium ions in the admicellar phase dissociate from adsorbed SDS bilayers, causing an increase of sodium ions in the aqueous phase and a decrease of the cmc. Organic solute has also been reported to shift the cmc of surfactant solutions (*11, 29*). In our study, the effect of TMOB or MB on the cmc is assumed to be negligible since the concentration of TMOB or MB is very low (~10^{-5} M).

Table I. cmc of Various SDS Solutions in a Buffered System (μM)

Acetate buffer concentration	0.01 M	0.05 M	0.10 M	0.15 M
SDS solution in the absence of alumina*	5500	2500	1900	1000
SDS solution in contact with alumina*	3100	1900	1500	900
SDS solution in contact with alumina†	2900	1700	1300	800

* using a bubble pressure tensiometer † using a du Noüy ring tensiometer

Adsolubilization. For the adsolubilization measurements, we used syringe filtration to obtain a clear supernatant solution. The method of sampling did not affect the results. All the data shown in Figures 2 and 3 are at aqueous phase SDS concentrations below the cmc so that no micelles are present. Figure 2 shows that the partition coefficient of MB and TMOB between phases varies linearly with adsorbed SDS concentration below 0.015 M (400 μmol/g). The partition coefficient of MB starts to decrease as the adsorbed SDS concentration increases above 0.015 M. Figure 3 shows the plots of adsolubilization constant versus SDS adsorption. Since the adsolubilization constant is calculated by dividing the partition coefficient by the adsorbed SDS concentration, the deviation of the data points is larger due to the small value of the denominator.

The results indicate that at high SDS adsorption level, the admicelles become less effective at adsolubilizing MB, possibly due to the blocking of some small pores in alumina particles by the second surfactant layer. When the SDS bilayer is forming, the

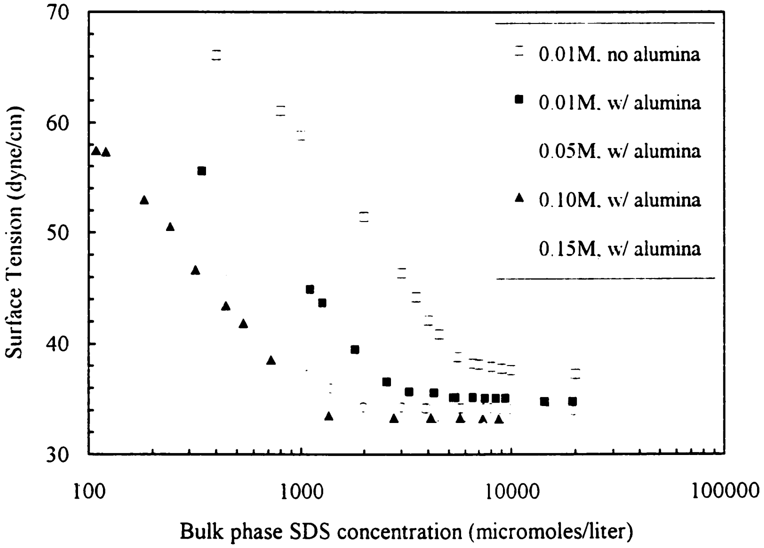

Figure 1. Solution Surface Tension at Various Buffer Concentrations.

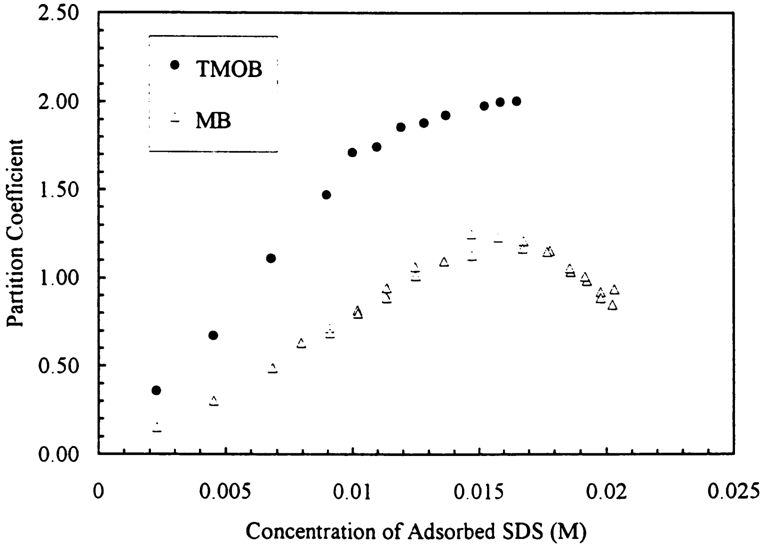

Figure 2. Partition Coefficients of TMOB and MB.

In Surfactant Adsorption and Surface Solubilization; Sharma, R.;
ACS Symposium Series; American Chemical Society: Washington, DC, 1996.

long alkyl chain could sterically block MB molecules from penetrating the pore as bilayers from the opposite walls approach each other (*24*). Another possible explanation could be that the tighter packing of the surfactant molecules in the aggregates hinders the incorporation of solutes into the admicelles. Therefore, in this range of adsorbed SDS concentration, the available sites to adsolubilize MB decrease as the SDS adsorption increases.

For adsorbed SDS concentration from 0 to 0.017 M, TMOB adsolubilization shows a trend similar to MB adsolubilization, the partition coefficient increasing with increasing adsorbed SDS concentration (see Figure 2). Below 0.011 M (300 μmol/g), the slope gives a TMOB adsolubilization constant 164 M^{-1}, about two times that of MB, i.e., 80 M^{-1}. Above 0.011 M, the partition coefficient increases slowly with increasing adsorbed SDS concentration, while the adsolubilization constant decreases as shown in Figure 3. To avoid the interference of MB with TMOB adsolubilization measurements, the solution pH was kept above 7 to inhibit the reaction. At high pH, the maximum SDS adsorption was reduced, therefore no adsolubilization constant for TMOB was obtained above the adsorption level of 450 μmol/g.

In this study, no experiment was conducted for the adsorption of solutes on alumina. But from the extrapolation of the partition coefficient shown in Figure 2, it is reasonable to assume that alumina has no capability of adsorbing organic solutes in the absence of SDS. This assumption agrees with other studies on adsolubilization which stated no appreciable adsorption of alcohols in the absence of surfactant (*11*) and no styrene adsorption on solid substrate (*21*).

pH Effect on the Rate Constant. Figure 4 shows the solution pH effect on the apparent first-order rate constant. As can be seen in Figure 4, at constant SDS adsorption, the apparent rate constant increases as the pH decreases. As the pH decreases, the concentration of free hydrogen ions in the aqueous phase increases. The higher aqueous phase concentration leads to more hydrogen ions bound to the opposite-charged head groups of the top layer of the admicelles. Since the hydrolysis of TMOB is an acid catalyzed reaction, an increase in hydrogen ions bound to the admicelles will enhance the reaction rate. As aqueous phase pH is increased, the concentration of hydrogen ions bound to the admicelles decreases, decreasing the admicelle-catalyzed reaction rate.

Also in Figure 4, at surfactant adsorption below 380 μmol/g, the rate constant depends only weakly on pH. Above 380 μmol/g, the pH effect on rate constant becomes more significant. The results seem to indicate that the binding of hydrogen ions becomes more important at high surfactant adsorption, suggesting a change in the surfactant aggregate morphology from monolayer to bilayer. An alternative explanation, however, is that tighter packing density of admicelles at higher adsorption level (resulting in higher charge density) leads to a higher hydrogen ion concentration bound to the exposed head groups. At sufficiently high pH (see Figure 4 at pH = 6.1), no transition is observed. Perhaps at high pH the change in slope is very small due to the low hydrogen ion concentration.

We are presently developing a pseudophase kinetic model which we hope will enable us to better determine whether the transition in reaction rate in Figure 4 represents a change in morphology, or merely an increase in packing density of the bilayer.

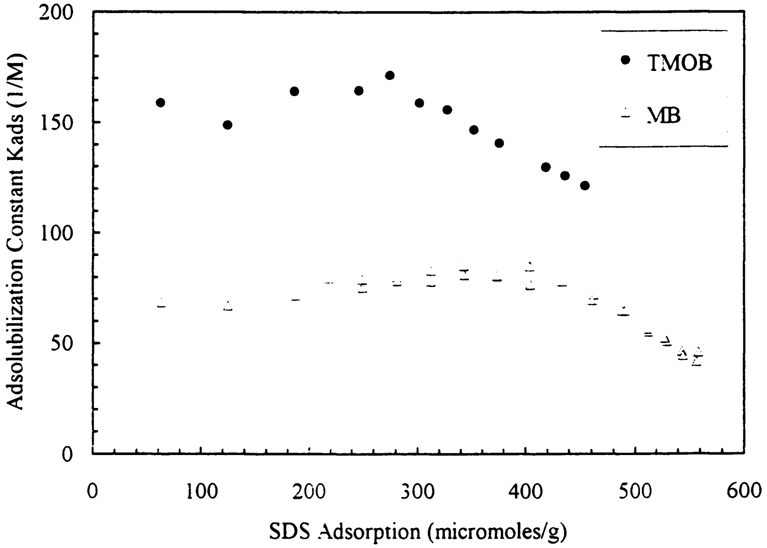

Figure 3. Adsolubilization Constant Versus SDS Adsorption.

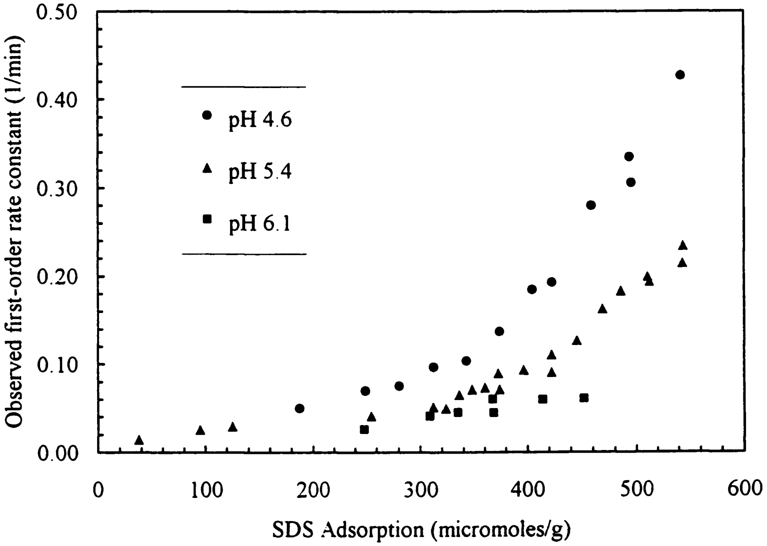

Figure 4. Effect of Solution pH on the Rate Constant at 0.01M Acetate Buffer.

Buffer Concentration Effect on the Rate Constant. The relationship between rate constant and acetate buffer concentration is shown in Figure 5. As expected, at constant buffer concentration, the rate constant increases with increasing surfactant adsorption. At constant adsorption and nearly constant pH, however, an increase in buffer concentration decreases the reaction rate. As the buffer concentration increases, the concentration of sodium ions in the system increases. Higher sodium ion concentration in the aqueous phase will cause sodium ions to replace hydrogen ions bound to the admicelle charged head groups, i.e., there is a competition between sodium ions and hydrogen ions in the region of the charged admicelle head groups. Therefore, when a swamping salt is applied, virtually all the hydrogen ions bound to the admicelles could be replaced by the competitive counterion. In that case, the admicelles will not enhance the reaction rate, instead the reaction should be inhibited by the surfactant admicelles.

At the highest buffer concentration used in our study (0.15 M), the rate constant increases only very slowly as the adsorption increases. If a much higher buffer concentration were used, the rate constant would probably remain constant or even decrease with increasing SDS adsorption. Since inhibition by admicelles was not our objective, no experiments were conducted for the rate inhibition.

Particularly at the lowest buffer concentration of 0.01 M, the break in the slope of rate versus surfactant adsorption can be observed. However, it remains unclear from these data whether a transition in morphology occurs, or whether the slope gradually increases as, for example, admicelle packing density increases.

Adsolubilization Effect on the Rate Constant. Since at higher adsorption level there is lower TMOB local concentration in the admicellar phase (see Figure 3), the apparent first-order rate constant should also decrease. But our data show the opposite trend. We postulate that at higher adsorption either the bilayer forms or the packing density of admicelles increases, either one leading to higher charge density. The greater charge density attracts hydrogen ions from the bulk phase to the admicelles. Therefore, the reaction rate increases with increasing surfactant adsorption, i.e., the rate enhancement due to increased hydrogen ion concentration overcomes the effect of the poorer adsolubilization.

Conclusions

Admicellar catalyzed hydrolysis reaction of TMOB at various pH and buffer concentrations has been demonstrated. At constant SDS adsorption, the reaction rate increases with decreasing solution pH and buffer concentration. A significant transition was observed in the plots of reaction rate versus SDS adsorption, except at pH 6.1 and at the buffer concentration of 0.15 M. The adsolubilization results also showed that TMOB is more hydrophobic than MB. Below SDS adsorption of 300 μmol/g, the adsolubilization constant of MB is half that of TMOB, 80 M^{-1} versus 164 M^{-1}. At high levels of SDS adsorption, adsolubilization may be hindered by pore blockage or tighter packing density, causing the adsolubilization constants to decrease.

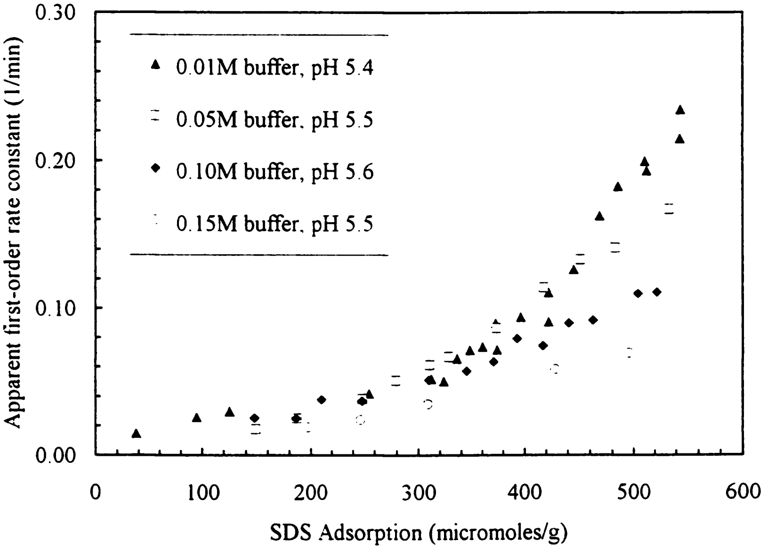

Figure 5. Effect of Buffer Concentration on the Rate Constant.

Acknowledgment

Acknowledgment is made to the Donors of The Petroleum Research Fund, administered by the American Chemical Society, and to the National Science Foundation, for support of this research.

Literature Cited

1. Bunton, C. A. In *Surfactants in Solution*; Mittal, K. L., Fendler, E. J., Eds.; Plenum Press: New York, NY, 1991, Vol. 11, pp 17.
2. Romsted, L. S. In *Surfactants in Solution*; Mittal, K. L., Lindman, B., Eds.; Plemun Press: New York, NY, 1984, Vol. 2, pp 1015.
3. Chaimovich, H.; Aleixo, F. M. V.; Cuccovia, I. M.; Zanette, D.; Quina, F. H. In *Solution Behavior of Surfactants*; Mittal, K. L., Fendler, E. J., Eds.; Plenum Press: New York, NY, 1982, Vol. 2, pp 949.
4. Berezin, I. V.; Martinek, K.; Yatsimirski, *Russ. Chem. Rev.* **1973**, *42*, 787.
5. Bunton, C. A. *Pure Appl. Chem.* **1977**, *49*, 969.
6. Menger, F. M.; Rhee, J. U.; Rhee, H. K. *J. Org. Chem.* **1975**, *40*, 3803.
7. Goujon, G.; Cases, J. M.; Mutaftschiev, B. *J. Colloid Interface Sci.* **1976**, 56, 587.
8. Lopata, J. J.; Harwell, J. H.; Scamehorn, J. F., In *Surfactant-Based Mobility Control*, Smith, D. H., Ed.; ACS Symp. Ser.; 1988, Vol. 373, pp 205.

9. Somasundaran, P; Fewrstenau, D. W. *J. Phys. Chem.* **1966**, 70, 90.

10. Harwell, J. H.; Hoskins, J. C.; Schechter, R. S.; Wade, W. H. *Langmuir* **1985**, *1*, 251.

11. Yeskie, M. A.; Harwell, J. H. *J. Phys. Chem.* **1988**, *92*, 2346.

12. Chandar, P.; Somasundaran, P.; Turro, N. J. *J. Colloid Interface Sci.* **1987**, *117*, 31.

13. Esumi, K.; Nagahama, T.; Meguro, K. *Colloids Surfaces* **1991**, 57, 149.

14. Söderlind, E. and Stilbs, P. *Langmuir* **1993**, *9*, 2024.

15. Rennie, A. R.; Lee, E. M.; Simister, E. A.; Thomas, R. K. *Langmuir* **1990**, *6*, 1031.

16. McDermott, D. C.; McCarney, J.; Thomas, R. K.; Rennie, A. R. *J. Colloid Interface Sci.* **1994**, *162*, 304.

17. Scamehorn, J. F.; Schechter, R. S.; Wade, W. H. *J. Colloid Interface Sci.* **1982**, *85*, 463.

18. Levitz, P.; Van Damme, H; Kervis, D. *J. Phys. Chem.* **1984**, *88*, 2228.

19. Chandar, P.; Somasundaran, P.; Waterman, K. C.; Turro, N. *J. Phys. Chem.* **1987**, *91*, 148.

20. Fitzgerald, T. and Harwell, J. H. In *Recent Advances in Separation Technique—III*, AIChE Symp. Ser.; 1986, Vol. 82, pp 142.

21. Wu, J.; Harwell, J. H.; O'Rear, E. A. *Langmuir*, **1987**, *3*, 531.

22. Wu, J.; Harwell, J. H.; O'Rear, E. A. *J. Phys. Chem.* **1987**, *91*, 623.

23. Esumi, K.; Watanabe, N.; Meguro, K. *Langmuir* **1991**, *7*, 1775.

24. O'Haver, J.; Harwell, J. H.; O'Rear, E. A.; Snodgrass, L. J.; Waddell, W. H. *Langmuir* **1994**, *10*, 2588.

25. Yu, C.-C.; Wong, D. W.; Lobban, L. L. *Langmuir* **1992**, *8*, 2582.

26. Dunlap, R. B.; Cordes, E. H. *J. Am. Chem. Soc.* **1968**, *90*, 4395.

27. Dunlap, R. B.; Cordes, E. H. *J. Phys. Chem.* **1969**, *73*, 361.

28. Wong, D. W. Master's Thesis, University of Oklahoma, **1994**.

29. Morgan, M. E.; Uchiyama, H.; Christian, S. D.; Tucker, E. E.; Scamehorn, J. F. *Langmuir* **1994**, *10*, 2170.

RECEIVED May 3, 1995

Downloaded by NORTH CAROLINA STATE UNIV on October 13, 2012 | http://pubs.acs.org
Publication Date: May 5, 1996 | doi: 10.1021/bk-1995-0615.ch006

Chapter 6

Self-Assembly of Ionic Surfactants Adsorbed on Mineral Oxides: Surface Charge and Salt Effects

Luuk K. Koopal and Tanya Goloub[1]

Department of Physical and Colloid Chemistry, Wageningen Agricultural University, Dreyenplein 6, 6703 HB Wageningen, Netherlands

Adsorption of ionic surfactants on mineral oxides is studied by comparing calculated results with experimental data for the sodium nonyl benzene sulphonate - rutile (SNBS-TiO_2) and the dodecyl pyridinium chloride - silica (DPC-SiO_2) system. In the calculations a distinction is made between constant charge and constant potential surfaces. Experimental (SNBS-TiO_2) and calculated isotherms for a constant potential surface at different salt concentrations show a common intersection point (cip) where the electrostatic interactions vanish. The cip marks the transition from "head-on" adsorbed surfactant molecules (hemi-micelles) to bilayer structures (ad-micelles). The course of the surface charge adjustment upon surfactant adsorption supports this conclusion. Constant potential surfaces like rutile promote surfactant self-assembly in hemi-micelles and ad-micelles. For constant charge surfaces theory also predicts a cip coinciding with the charge equivalence point. The transition from head-on adsorbed molecules to ad-micelles is more distinct than for the constant potential surfaces. The shapes of the DPC-SiO_2 isotherms reflect the constant charge case. Yet, the surface charge of SiO_2 adjusts to DPC adsorption. This adjustment hardly promotes surfactant self-assembly and self-assembly of DPC in hemi-micelles does not occur at low salt concentration.

The adsorption of ionic surfactants on solid surfaces is of both practical and academic interest. This interest has led to a large number of studies. Adsorption of cationic surfactants is often studied on negative silicas (*1-9*),

---

[1] Current address: Faculty of Chemistry, Saint Petersburg State University, Saint Petersburg, Russia

0097–6156/95/0615–0078$13.50/0

Downloaded by NORTH CAROLINA STATE UNIV on October 13, 2012 | http://pubs.acs.org
Publication Date: May 5, 1996 | doi: 10.1021/bk-1995-0615.ch006

and that of anionic surfactants on positive metal hydroxide surfaces (*10-19*), but also the adsorption on a variety of other surfaces has been investigated (e.g. *20-25*). The generally accepted view is that surfactant self-assembly in the adsorbed layer may contribute to the adsorption. Aggregate structures termed hemi-micelles (*5,6,10,12,13,19,20*) and ad-micelles (*16,17,19*) or more generally solloids (*27*) are suggested. Micro polarity and micro viscosity of surfactant layers has been studied by ESR, Raman and luminescence spectroscopy (*27-31*). Neutron reflection (*7,32,33*), small angle neutron scattering (*34,35*) and NMR spectroscopy (*36,37*) are used to give insight in the distribution of the surfactant molecules at the interface. However, the fact that the nature of the aggregates may depend on factors like pH, salt concentration and surface type is often not clearly recognised.

With ionic surfactants both coulombic and non coulombic interactions are important, this leads to a more complicated situation than often realised. For instance: (a) the charge density of the surface may be more important than the nature of the surface, (b) surfaces may change their surface charge upon surfactant adsorption, (c) the salt concentration determines the magnitude of the coulombic interaction and (d) specific interactions may occur between the surfactant ion and its counter ion and between the surface and its counter ion. A good understanding of these and the more common factors affecting the amount adsorbed and the structure of the adsorbed layer is important in optimising the use of surfactants.

Based on the experimental studies several models for the isotherm and the adsorbed layer structure have been proposed. Most models have an *ad hoc* character, i.e. *a priori* assumptions are made with respect to the structure of the adsorbed layer. A review of extended Langmuir and Frumkin (Fowler-Guggenheim) type models has been given by Koopal (*39*). Models not mentioned in ref. *39* that also presume the structure of the adsorbed layer are the bilayer model of Scamehorn et al. (*15*) and Mehrian et al. (*25*), the hemi-micelle models of Chander et al. (*12*), Gu and co-workers (*6,26,40,41*) and Lajtar et al. (*42*) and the model suggested by Narkiewicsz-Michalek et al. (*43*). All these models cannot independently resolve questions about the structure of the adsorbed layer, because the structure itself is characteristic for the model. Yet, they may help to unravel the adsorption behaviour as a function of the solution conditions.

Koopal et al. (*8,18,19,44,45,46*) have shown that with the self consistent field lattice theory for association and adsorption (SCFA) there is no need to make assumptions about the adsorbed layer structure. The SCFA theory can be used to study micellization (*47*) or adsorption of surfactants (*8,18,19,44,45,46*). For ionic surfactants near surfaces the equilibrium distribution of segments in the direction perpendicular to the surface (1D-SCFA) can be calculated. In the case of non ionic surfactants it is also possible to consider local surface aggregates of which the structure follows from the calculation (2D-SCFA) (*44*). For ionic surfactants with their electrostatic interactions it is not yet possible to do this. In this case the theory can therefore not give accurate insight in the surfactant concentrations at which the local surface aggregates are formed. However, trends predicted with respect to the surfactant orientation are relevant.

Downloaded by NORTH CAROLINA STATE UNIV on October 13, 2012 | http://pubs.acs.org
Publication Date: May 5, 1996 | doi: 10.1021/bk-1995-0615.ch006

Results obtained with the SCFA theory show that the shape of the isotherms is quite complex, even if the surface is homogeneous. Therefore, invoking heterogeneity as sole source to explain the complex shape of surfactant isotherm, as is done by some authors (e.g., *15,16,21,43*), is certainly overestimating the role of surface heterogeneity. As soon as self-assembly of surfactant molecules dominates the adsorption process surface heterogeneity is of secondary importance. This is especially true for surfaces with a random heterogeneity. On patchwise heterogeneous surfaces heterogeneity may be important for adsorption at high electrolyte concentrations, but at low electrolyte concentrations, when the characteristic dimension of a patch is smaller than the Debye screening length, patchwise surfaces resemble random surfaces (*38*) and the heterogeneity is relatively unimportant.

To review and further investigate surfactant adsorption the trends observed in the isotherms calculated with the SCFA theory will be compared with experimental results. Specifically the differences between surfactant adsorption on silica and metal oxides, like Al_2O_3, TiO_2 and Fe_2O_3, will be critically examined. To this aim the adsorption of sodium nonyl benzene sulfonate (SNBS) on rutile will be compared with that of dodecyl pyridinium chloride (DPC) on Aerosil, a pyrogenic silica. Results for SNBS adsorption on rutile are taken from previous work (*18,19*), those for DPC on silica are new. It will be shown that both the surface type and salt concentration are very important with respect to surfactant self-assembly at the surface. To discriminate between different structures we will call aggregates of "head-on" adsorbed molecules hemi-micelles and local bilayer structures ("head-on" + "head-out" adsorbed molecules) ad-micelles.

Materials

Surfactants. Pure sodium para 3-nonyl benzene sulphonate (SNBS) and dodecyl pyridinium chloride (DPC) are used as surfactants. The critical micelle concentrations or cmc's of these surfactants in various NaCl solutions are reported in (*45*) and in good agreement with existing literature values (*48,49*).

Solids. Rutile (TiO_2) with a BET surface area of 52 m^2/g is used. The rutile is synthesised according to the method described by Bérubé and De Bruyn (*50*). Aerosil Ox-50 is a pyrogenic silica (SiO_2), obtained from Degussa, with a BET area of 50 m^2/g. Before use the silica is washed several times with pure water. The surface charge of both rutile and Aerosil is characterised by means of potentiometric titrations at different salt concentrations. For rutile the charging behaviour is found to agree with previous measurements (*51*). The point of zero charge (pzc) equals 5.8. The charge - pH curves of Aerosil Ox-50 reflect those of a "hard" surface SiO_2 (*52,53*). The pzc is approached asymptotically at low pH values and it may be assumed that at pH 3 the surface charge is negligible.

Chemicals. All other chemicals used were of pro-analyse quality, and the water was deionised and purified using an Elgastat UHP unit.

Experimental Techniques

Surfactant Adsorption Isotherms. Adsorption isotherms were measured at constant pH and ambient room temperature, 21°±1°C, using a depletion method which has been described in detail elsewhere (*18,45*). The initial and final pH values were matched by repeated additions of OH^- or H^+ to restore the pH to its initial value. UV spectrophotometry is used to determine the surfactant concentration in the supernatant, and thus the amount adsorbed.

Surface Charge Adaptation. A method of following the response of the surface charge on adsorption throughout the isotherm has been described by Böhmer and Koopal (*18*). During the surfactant adsorption measurements the number of moles of H^+ or OH^- required to maintain the pH at its fixed level are measured. The amount of OH^- or H^+ added is a direct measure of the change of surface charge per unit area due to surfactant adsorption. At each point of the surfactant isotherm the surface charge of the mineral can now be calculated from its value in the absence of surfactant, obtained by potentiometric titration, and the surface charge adjustment at the given pH and surfactant load.

Downloaded by NORTH CAROLINA STATE UNIV on October 13, 2012 | http://pubs.acs.org
Publication Date: May 5, 1996 | doi: 10.1021/bk-1995-0615.ch006

SCFA Theory

Outline. A detailed account of the self-consistent field theory for adsorption and association of surfactants and its extension with electrostatics can be found elsewhere (*8,18,19,46,54-57*). The equilibrium distribution of segments perpendicular to the surface is calculated by minimising the free energy of the system (1D-SCFA). In the 1D-SCFA theory the molecules are placed in a lattice that facilitates the counting of the conformations of the molecules. The lattice consists of M lattice layers numbered $z=1,......,M$ parallel to the surface. Layer $z=1$ is adjacent to the solid (layer $z=0$).

The surfactant is modelled as a chain of r segments and water and ions as monomers. Every lattice site in the system is filled with one of these segments or monomers. The conformational statistics of the chains are calculated using the rotational isomeric state (RIS) scheme of Leermakers et al. (*54,55*). The RIS scheme prevents conformations in which backfolding of segments occurs and allows for an energetic distinction between trans and gauche conformations in the chains. These restrictions are intended to give the chain a realistic flexibility.

In the calculations the surfactant ion is assumed to be a linear $A_{12}B_3$ chain, viz. the tail section consists of 12 aliphatic A segments and the head group of 3 hydrophilic B segments. The difference between CH_2 and CH_3 segments is neglected. The head group segments each carry 1/3 of a unit of charge, i.e. each head group (B_3) is monovalent. In addition to the surfactant, water and a fully dissociated monomeric salt CD is included: C defined as the surfactant co-ion and D its counter ion.

For the electrostatic interactions, the charges are assumed to be located on the mid-planes between lattice layers and the intervening space is free of charge. Consequently two neighbouring planes can be treated as a charged condensor and their potential difference can be calculated using basic electrostatics. The potential on the solid surface serves as a reference point for the calculation of the electrostatic potentials (*8,57*).

The contact interactions between the various segments and between segments and the surface are accounted for using Flory-Huggins χ parameters.

Choice of Parameters. For the lattice layer spacing, l, we take 0.31 nm, l^2 is the area and l^3 the volume of a lattice cell. The present choice corresponds with 55.5 moles of lattice sites per dm^3 indicating that each of the lattice cells has about the same size as a H_2O molecule or a CH_2 segment. The dielectric constants are taken as $2\varepsilon_0$ for the aliphatic A segments and $80\varepsilon_0$ for the remaining segments.

The χ parameters between the aliphatic A segments and the hydrophilic segments, W, B, C, and D are taken as 2 reflecting the mutual hydrophobic repulsion between the aliphatic segments and all other segment types. A value of about 2 for χ_{Ax} (x= W, B, C, D) is required to correctly predict the aliphatic chain length dependence of the cmc. The remaining solution χ parameters are set to zero unless specifically stated. Therefore water, W, is a perfect solvent for B, C, and D. The latter species interact with each other only through coulombic forces and differ only in their valency. These conditions are comparable to those underlying the Gouy-Chapman theory. The choice for χ equal to zero implies that the ions and ionic head segments are not preferentially hydrated. The present values of the parameters give for micelles of ionic surfactants a fair agreement between calculated and measured aggregation numbers and cmc's as a function of chain length and salt concentration (*47*).

The specific (non-coulombic) interactions of the segments with the surface are also expressed as χ parameters. Only one non-zero surface χ parameter is used, that between the surface and the head group segments, χ_{BS} =-10. This value of χ_{BS} amounts to a Gibbs energy of adsorption (an exchange quantity) of -2.5 kT per segment. The head group is therefore modelled as having a strong specific interaction with the surface. That in general a fairly strong non coulombic attraction exists between the ionic head group and an oxide surface can be deduced from the surface charge adjustment that is caused by the surfactant adsorption (see Figures 7 and 9). Although χ_{AS}=0 the tail segments have a weak attraction (-0.5 kT) for the surface due to the fact that the number of unfavourable water/A contacts is diminished upon adsorption.

To introduce a distinction between surface types calculations will be presented for constant potential (variable charge) and constant charge (variable potential) surfaces. Most crystalline metal oxide surfaces can be considered as constant potential surfaces, amorphous SiO_2 is neither constant potential nor constant charge (*39*). In the constant potential case the surfactant ion $A_{12}B_3$ is allowed to adsorb on an oppositely charged surface with a surface potential of $|100|$ mV, unless stated otherwise. For a crystalline metal oxide surface a surface potential of $|100|$ mV is attained at a pH slightly less than 2 pH units from the pristine pzc of the oxide (*39*). In the constant charge case a charge of 0.1 charges per lattice site is assumed. This value corresponds

Downloaded by NORTH CAROLINA STATE UNIV on October 13, 2012 | http://pubs.acs.org
Publication Date: May 5, 1996 | doi: 10.1021/bk-1995-0615.ch006

with a charge density of 0.17 C/m^2 and is about the same as the initial charge of the constant potential surface.

Remarks. The choice of parameters intends to give a fairly realistic representation of the system and yet not to overburden the calculation with unnecessary detail. The aim is not to fit data, but to investigate the qualitative effect that salt concentration and surface properties have on the isotherms and related properties. The calculations are used to aid the interpretation and understanding of effects observed in the experimental data. As mentioned above the 1D-SCFA theory cannot give accurate insight in the concentration at which local aggregates are formed nor about their size. This type of information can only be obtained from measured isotherms (*19*) and/or specific experiments (*27-31*). Nevertheless, the SCFA predictions made with respect to the orientation of the surfactant molecules in the different regions of the isotherm will represent the orientation of the surfactant molecules in the centre of the local aggregates very well if the aggregates are not too small.

Theoretical Results: Constant Potential Surfaces

Adsorption Isotherms. Calculated adsorption isotherms for a surface potential of 100 mV are given on log-log and lin-log scales in Figure 1 for three salt concentrations. The adsorbed amount is expressed as n^{exc}, the excess number of surfactant molecules per surface site. On the horizontal axis the total volume fraction is shown, below the cmc it is equal to the bulk volume fraction and above the cmc it is the average volume fraction of free surfactant and surfactant in micelles. The critical micelle volume fractions at different salt concentrations have been calculated using a lattice of spherical geometry (*8,47*).

The log-log isotherms are presented in Figure 1a, they emphasise the lower part of the isotherms. The isotherms show four regimes. In region I the slope is unity and the adsorption follows Henry's law. In region II theory predicts a phase transition or condensation step caused by surfactant self-assembly. The phase transition indicates that two coexisting phases are present on the surface at a given bulk solution volume fraction. Region III has a slope much smaller than region II, the coulombic attraction changes to a coulombic repulsion. Region IV starts where a plateau is reached slightly above the cmc.

The four regions can also be seen in the lin-log isotherms that show more clearly the upper part of the isotherm, see Figure 1b. The plateau adsorption increases only slightly with increasing salt concentration.

The adsorption isotherms as a function of salt concentration show a common intersection point (cip). The cip marks the point where the salt effect inverses, i.e. the point where the coulombic interactions vanish. As the potential in the plane (or region) where the surfactant head groups adsorb is zero, the adsorption does not depend on the salt concentration. Before the cip coulombic attraction between surface and surfactant occurs and an increase of the salt concentration increases the screening and thus decreases the adsorption. Beyond the cip the coulombic repulsion between the surfactant head groups dominates and salt addition has the opposite effect, a better

Downloaded by NORTH CAROLINA STATE UNIV on October 13, 2012 | http://pubs.acs.org
Publication Date: May 5, 1996 | doi: 10.1021/bk-1995-0615.ch006

Downloaded by NORTH CAROLINA STATE UNIV on October 13, 2012 | http://pubs.acs.org
Publication Date: May 5, 1996 | doi: 10.1021/bk-1995-0615.ch006

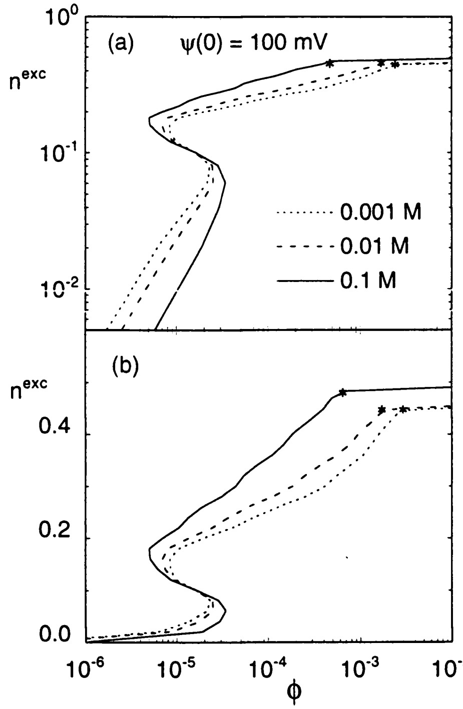

Figure 1. Calculated adsorption isotherms for the model surfactant $A_{12}B_3$ on a surface with a fixed potential of 100 mV at three salt (CD) concentrations.

The following χ parameters are used: $\chi_{AW}=\chi_{AB}=\chi_{AC}=\chi_{AD}=2$, other χ parameters in solution are zero. The χ parameters for the interaction with the surface are $\chi_{BS}=-10$ and $\chi_{AS}=\chi_{CS}=\chi_{DS}=0$. The relative dielectric constants are 80 for W, B, C and D and 2 for A; the lattice layer thickness l equals 0.31 nm and the cross section of a site is l^2. The cmc's are indicated with a marker. Results are shown in a log-log plot, Figure 1a, and in a lin-log plot, Figure 1b.

screening enhances the adsorption. In the absence of specific interactions of the salt ions with the other components the cip coincides with the overall iso electric point (iep). This has been proven on a thermodynamic basis also (60).

Structure of the Adsorbed Layer. Segment volume fractions as a function of the layer number z give information on the structure of the adsorbed layer. Results for four surface coverages, corresponding with three regions (I, II and III) in the isotherm are shown in Figure 2 for a salt concentration of 0.01 M. In the panels at the right the volume fractions are plotted on a logarithmic scale to be able to show the surfactant co-ions and counter ions more clearly.

In region I (n^{exc}=0.01) the adsorbed molecules are fairly flat on the surface, see Figure 2a. Besides the coulombic and specific interaction between the head groups and surface the tails are squeezed out of the water because of the high value for χ_{AW}. The surface charge is screened by both surfactant (B) and salt ions. The head group segments are almost all located in the first layer. The distribution of the CD ions is shown in the semi logarithmic plot. The D ions are attracted by the surface charge, the C ions expelled.

At the end of region II (n^{exc}=0.2, see Figure 2b) mainly a head-on adsorbed monolayer is on the surface, the surface is hydrophobized by the A segments, but some B segments appear at the solution side of the adsorbed layer. The surface charge is almost completely neutralised by B segments in layer 1. The profile of the surfactant counter ions C follows that of the B segments. The D ions are excluded from the surfactant rich regions. Beyond about layer 7 the C and D ions follow the diffuse layer pattern.

In region III (n^{exc}=0.3, see Figure 2c) the density of the head-on adsorbed molecules still increases, but the main effect is that a second layer of head-out adsorbed molecules is assembling on the first layer. In region III the surface becomes gradually more hydrophilic until the cmc is reached (region IV). In regions III and IV the segment distribution is basically the same. Further adsorption leads to an increase in layer thickness with most of the additionally adsorbing molecules in a head-out orientation. The head group charges at the solution side are mainly compensated by accumulation of C ions in between the head groups, the residual surfactant charge is compensated by the ions in the diffuse layer in the solution. Some counter ions C intercalate between the head groups at the surface side of the bilayer, see the semi logarithmic part of Figure 2c. The D ions are excluded from the surfactant layer, but the excluded amount hardly contributes to the charge balance.

Near the cmc the hydrocarbon core of the adsorbed surfactant bilayer separates two net uncharged parts of the system. On the surface side the sum of the surface charge and the charge of the surfactant head groups B plus some intercalated salt ions C equals zero and on the solution side the head groups B, the C ions in between them and salt ions in the diffuse layer have a total charge of zero. The head group segments at the solution side of the adsorbed layer are distributed over about six lattice layers. This distribution strongly resembles the distribution in the head group region of a micelle (47). The fact that the head segments are not in the same plane makes it very difficult for the D ions (surfactant co ions) to contribute to the charge balance.

Downloaded by NORTH CAROLINA STATE UNIV on October 13, 2012 | http://pubs.acs.org
Publication Date: May 5, 1996 | doi: 10.1021/bk-1995-0615.ch006

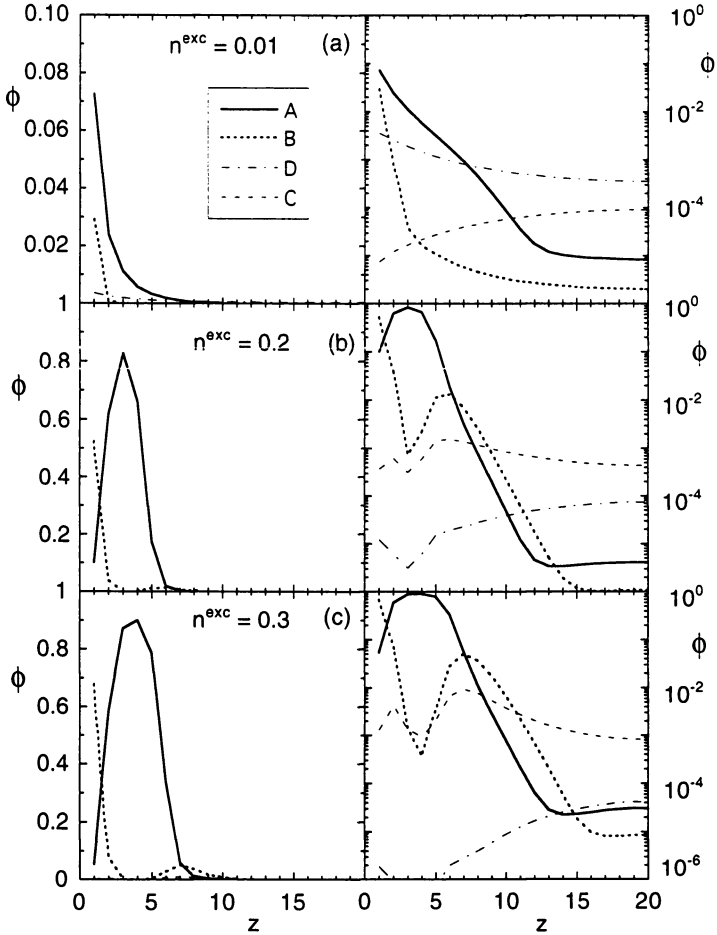

Figure 2. Calculated adsorbed layer structure for $A_{12}B_3$. Volume fraction profiles of the A and B segments and the ions C and D near a surface of constant potential of | 100 | mV in a 0.01 M CD solution are shown for four values of n^{exc} (panels a to d) The volume fractions of C and D are sometimes too small to be seen in the normal plots, therefore at the right results are replotted using a semi logarithmic scale. See Figure 1 for the parameters, z is the layer number.

Downloaded by NORTH CAROLINA STATE UNIV on October 13, 2012 | http://pubs.acs.org
Publication Date: May 5, 1996 | doi: 10.1021/bk-1995-0615.ch006

Downloaded by NORTH CAROLINA STATE UNIV on October 13, 2012 | http://pubs.acs.org
Publication Date: May 5, 1996 | doi: 10.1021/bk-1995-0615.ch006

Surface Charge Adaptation. As a constant potential surface is able to adjust its charge upon surfactant adsorption this effect is also investigated. In Figure 3 the surface charge, expressed in number of charges per lattice site, $\sigma_0 a_s/e$, and the adsorbed amount of surfactant, Γ_S, are plotted as a function of the volume fraction of surfactant for two different salt concentrations and three values of the surface potential. Initially the surface charge adjusts strongly to neutralise the adsorbed surfactant charge (the arrow marks the initial surface charge). At higher coverages the adjustment of the surface charge levels off, whereas the surfactant adsorption still increases considerably. The plateau value of the surface charge decreases with decreasing surface potential. For a given surface potential the plateau value of $\sigma_0 a_s/e$ is mainly determined by the surfactant adsorption and only weakly dependent on the salt concentration. The small difference between the plateau values is due to the fact that at high salt concentration more positive salt ions intercalate between the head-on adsorbed surfactant molecules.

In general the calculations are in qualitative agreement with experimental results (*18,19,45,46*). In the section "SNBS adsorption on rutile" a more detailed comparison will be made.

Theoretical Results: Constant Charge Surfaces

Adsorption Isotherms. Figure 4 shows calculated adsorption isotherms of $A_{12}B_3$ at three salt concentrations for a surface with a fixed charge of 0.1 charges per lattice site, panel a shows the double logarithmic plots, panel b the semi-logarithmic isotherms. Similarly to Figure 1 the initial adsorption decreases with increasing salt concentration, whereas at high adsorption this effect is reversed. The distinction between the two regions is again marked by a cip of the isotherms. Also in this case the log-log isotherms show about four regions. In contra-distinction with the constant potential case the adsorption isotherms at low salt concentrations show two steps, this is very clear in the lin-log plot. Both steps are caused by surfactant self-association.

Region I is composed of a Henry region followed by a steep increase. The steepness of this first step is depending on the surface charge and the magnitude of χ_{BS} and χ_{AW}. For low charge densities and weak interactions the slope will be more gradual. The first plateau corresponds with region II in the log-log isotherm.

The cip and the first plateau in the adsorption isotherm exist at a coverage of 0.1 molecule per surface site. This corresponds with the neutralisation of the surface charge by surfactant. Unlike with the constant potential surface the charge can not adapt to the situation and once the surface charge has been compensated there is no electrostatic driving force for surfactant adsorption anymore. Further adsorption may still occur because the tail segments dislike the aqueous environment and they can reduce the number of contacts with water by association with the adsorbed layer. Moreover, the lead segments have a specific affinity for the surface. However, at low salt concentration and adsorption values slightly larger than σ_0/F an electrostatic repulsion between the head groups occurs. This repulsion is so strong that the adsorption hardly increases with increasing equilibrium surfactant volume fraction. As a consequence the slope of region II in the log-

Downloaded by NORTH CAROLINA STATE UNIV on October 13, 2012 | http://pubs.acs.org
Publication Date: May 5, 1996 | doi: 10.1021/bk-1995-0615.ch006

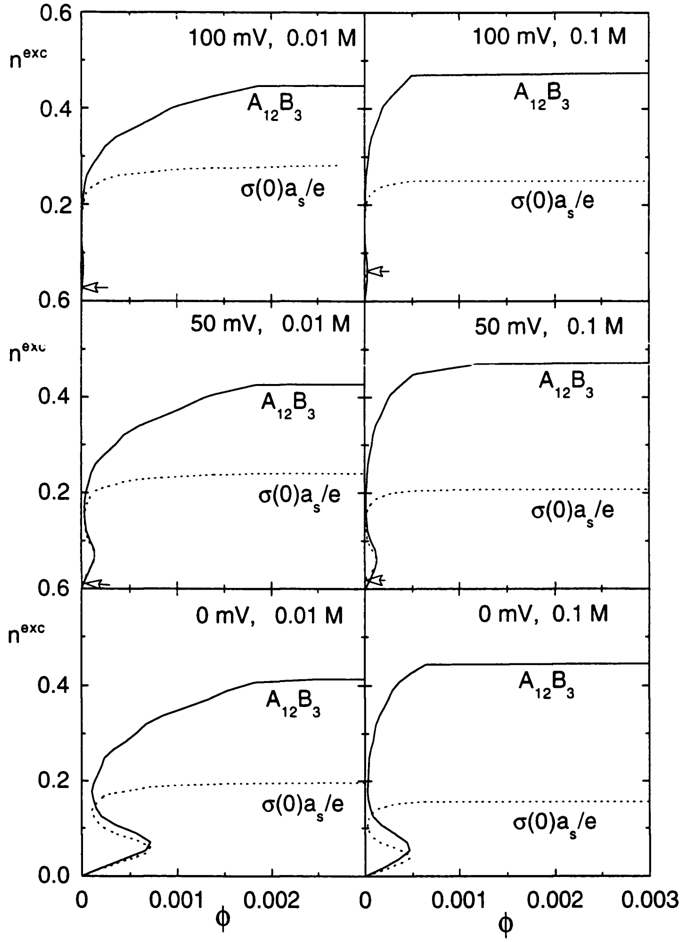

Figure 3. Surface charge adjustment of a constant potential surface upon surfactant adsorption. Both the adsorption of $A_{12}B_3$ and surface charge (expressed in the same units) are plotted as function of the volume fraction $A_{12}B_3$ in solution. The surface potential and the salt concentration are indicated. See Figure 1. for parameters.

Downloaded by NORTH CAROLINA STATE UNIV on October 13, 2012 | http://pubs.acs.org
Publication Date: May 5, 1996 | doi: 10.1021/bk-1995-0615.ch006

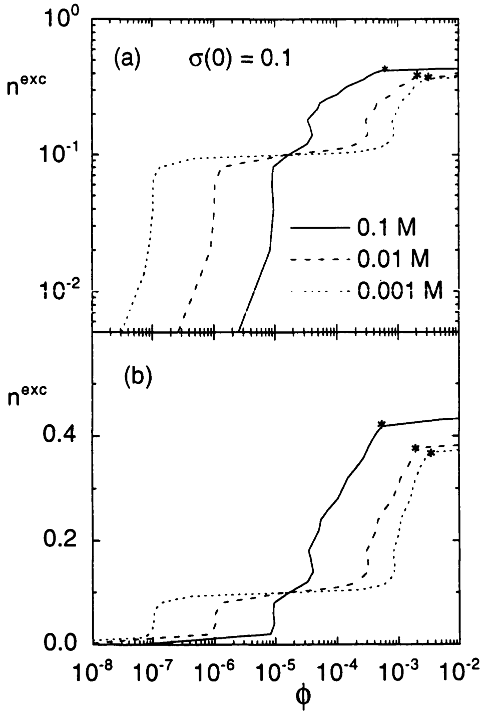

Figure 4. Calculated adsorption isotherms for the model surfactant $A_{12}B_3$ on a surface with a fixed charge of 0.1 charge per lattice site at three salt (CD) concentrations. Results are shown in a log-log plot, panel a, and in a lin-log plot, panel b. See for parameters Figure 1.

log plot is smaller than that in region I. At about a factor of 10 before the cmc region III starts (the second step in the isotherm) the adsorption increases substantially and a bilayer is formed due to surfactant self-assembly.

At high salt concentrations (0.1 M) both the coulombic surface / surfactant attraction and the surfactant / surfactant repulsion are much weaker and the first and the second step in the isotherm are so close that the two steps can hardly be distinguished.

Region IV starts, as before, when the cmc is reached. At high salt concentration the adsorbed amount beyond the cmc is somewhat higher than at low salt concentrations, see Figure 4b. The decreasing repulsion between the head groups with increasing ionic strength causes more adsorption as well as a lower cmc. The decrease of the cmc with increasing salt concentration partly cancels the effect of the salt concentration on the adsorbed amount so that the differences in the plateau of the isotherm are relatively small.

The calculated isotherms are in fair agreement with those found for surfactant adsorption on carbon black (*61*), biotite and fluorite (*21*), polystyrene latex (*62*) and PTFE latex (*63*).

Structure of the Adsorbed Layer. Volume fractions of the different segments or ions as a function of the layer number z are shown in Figure 5 for three adsorbed amounts of surfactant and 0.001 M salt. To be able to see the profiles of ions C and D more clearly the results are also plotted on a semi logarithmic volume fraction scale. When the surface excess of surfactant is low (n^{exc} = 0.006, Figure 5a) adsorption will make the surface somewhat hydrophobic. The amount of head segments near the surface is still rather small. The surface charge is mainly compensated by positive adsorption of ions D and some negative adsorption of ions C.

At n^{exc} = 0.1, Figure 5b, the surface charge is exclusively compensated by surfactant ions. Almost all surfactant molecules are head-on adsorbed and they largely compensate the surface charge. A few surfactant molecules are adsorbed with their head group towards the solution. As the surface charge is balanced by the surfactant charge the volume fractions of C and D equal their bulk values. The A segments accumulate at the solution side of the adsorbed layer and the surface has become most strongly hydrophobic at the charge neutralisation point.

At coverages above the cip (n^{exc} = 0.3, Figure 5c) a surfactant bilayer is present on the surface and the system becomes more hydrophilic again. In general the bilayer is asymmetric; the head groups near the surface are distributed over about two lattice layers, whereas at the solution side the head group distribution is much wider. Moreover, the second step of the isotherm is larger than the first one, but not all additionally adsorbing surfactants orient with their hydrophilic heads to the solution side. At both sides of the surfactant layer counter ions C accumulate between the head group segments B. The surfactant co-ions D are excluded from the adsorbed layer region. The dip in the A and B segment profiles near layer number 15 shows that also the surfactant ions are expelled from the diffuse layer.

Downloaded by NORTH CAROLINA STATE UNIV on October 13, 2012 | http://pubs.acs.org
Publication Date: May 5, 1996 | doi: 10.1021/bk-1995-0615.ch006

Downloaded by NORTH CAROLINA STATE UNIV on October 13, 2012 | http://pubs.acs.org
Publication Date: May 5, 1996 | doi: 10.1021/bk-1995-0615.ch006

Nonyl Benzene Sulphonate Adsorption on Rutile

Adsorption Isotherms. In Figure 6 adsorption isotherms of SNBS on rutile at pH 4.1±0.1 at three salt concentrations are shown as log-log (panel a) and lin-log (panel b) plots. Similarly as in the theoretical isotherms four regions can be distinguished in the double logarithmic plots. The initial part of the log-log

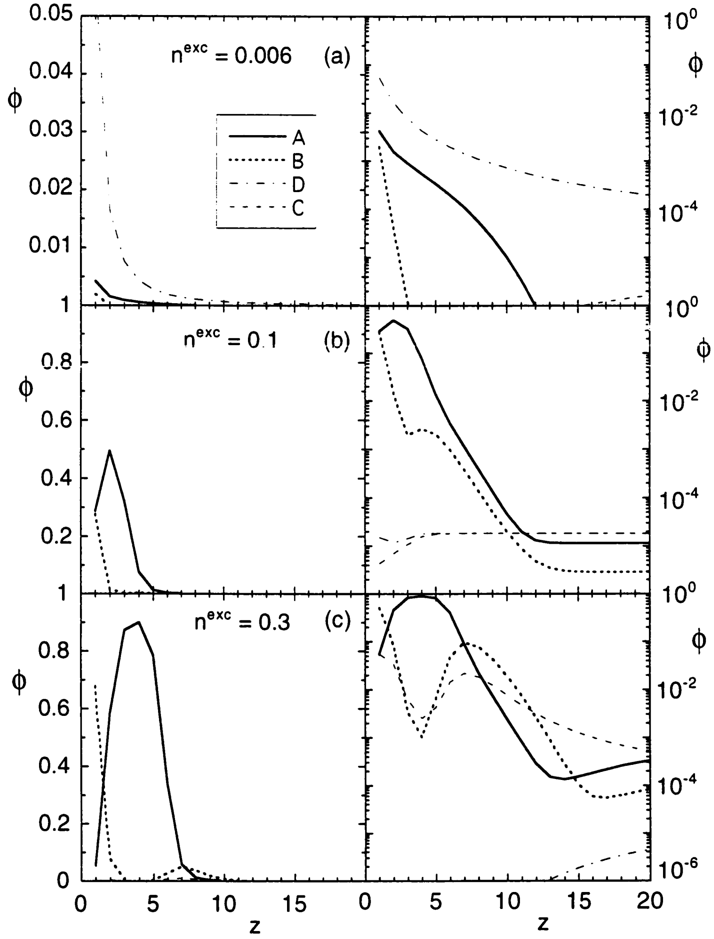

Figure 5. Calculated adsorbed layer structure for $A_{12}B_3$ on a constant charge surface. Volume fraction profiles of A, B, C and D near a surface in a 0.001 M CD solution are shown at three values of the adsorbed amount, n^{exc}, as indicated. The figures on the left hand side are lin-lin plots, they match the semi logarithmic plots on the right hand side. See Figure 1 for the parameters, z is the layer number.

Downloaded by NORTH CAROLINA STATE UNIV on October 13, 2012 | http://pubs.acs.org
Publication Date: May 5, 1996 | doi: 10.1021/bk-1995-0615.ch006

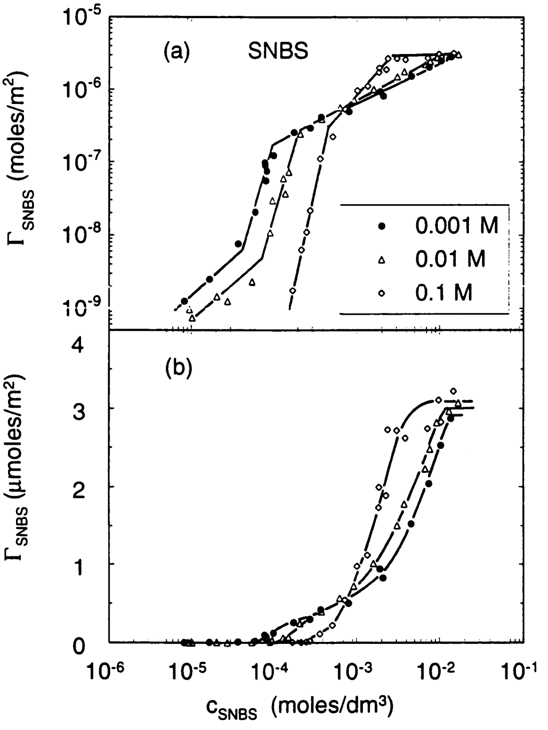

Figure 6. Experimental isotherms of SNBS adsorption on rutile at pH = 4.1 and three electrolyte concentrations as indicated. The data is shown on both log-log (a) and lin-log (b) scales.

plots can be understood by considering the empirical proportionality $\Gamma_S \sim c_S^n$ where n expresses the local co-operativity of the adsorption process. For n>1 a positive and for n<1 a negative co-operativity is observed, whereas the Henry limit (ideality) gives n=1. In region I the coverage is too low for the adsorbed molecules to interact with each other, the slope is about unity.

Mutual interaction starts in region II, where the coverage is still very low: roughly between 0.03 and 3% of the maximum coverage. The transition point between regions I and II is often called the critical hemi-micelle concentration. A straight line with a slope of about four fits the data points in region II, indicating a strongly positive co-operativity of the adsorption and proof for surfactant self-assembly.

The slope in region III is considerably lower than that of region II and it depends notably on the salt concentration. It is less than unity for low salt concentrations and somewhat higher than unity for 0.1M salt. Salt addition promotes the adsorption in region III by screening the head group repulsion. The transition between regions II and III is more pronounced for low salt concentrations, which also indicates that at low salt concentrations the repulsion between head groups becomes important in region III. The cmc marks the transition to region IV, where the plateau is reached.

The main difference between the experimental and calculated isotherms is situated in region II. The calculations over-exaggerate region II both with respect to range and steepness. This is due to the fact that in reality molecules adsorb in local aggregates, whereas in the calculations 2D condensation occurs in at least one entire lattice layer. Therefore 2D condensation starts at relatively high coverage and proceeds till a dense monolayer of surfactant has been formed. As the calculated range of region II is too large, the slope of region III becomes relatively small compared with experimental results.

An important similarity between calculated and measured isotherms is the cip of the isotherms obtained at different salt concentrations and the inversion of the salt effect.

In Figure 6b, the lin-log plot, the strong co-operativity present at the low coverages is evident at low salt concentrations as a weak shoulder in the isotherms. The lin-log isotherms show much better than the log-log isotherms that the "bulk" of the adsorption occurs in region III. Also the existence and the position of the (near) cip is clearly shown. The cip is located at $\Gamma \approx 0.6$ μmol/m^2 where the equilibrium concentration is about 0.6 mmol/dm^3. It is shown in ref. (*18*) that the cip corresponds to the iep. In agreement with the theory the plateau values reached in region IV are about the same for the different salt concentrations.

Surface Charge Adjustment and Layer Structure. To study the surface charge adjustment experiments were done at pH 4, 5 and 6 and two salt concentrations. In Figure 7 the adsorption of SNBS and surface charge are

Downloaded by NORTH CAROLINA STATE UNIV on October 13, 2012 | http://pubs.acs.org
Publication Date: May 5, 1996 | doi: 10.1021/bk-1995-0615.ch006

Downloaded by NORTH CAROLINA STATE UNIV on October 13, 2012 | http://pubs.acs.org
Publication Date: May 5, 1996 | doi: 10.1021/bk-1995-0615.ch006

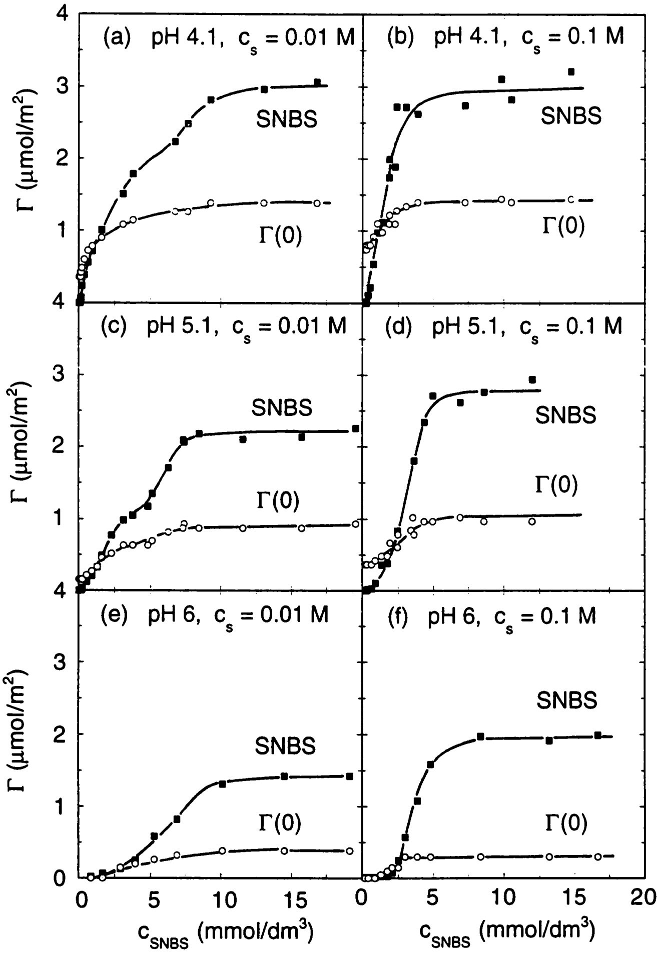

Figure 7. Experimental isotherms of SNBS adsorption and (absolute) surface "charge" Γ(0) (both in μmol/m^2) on rutile at three pH values and two electrolyte concentrations as indicated in each panel.

Downloaded by NORTH CAROLINA STATE UNIV on October 13, 2012 | http://pubs.acs.org
Publication Date: May 5, 1996 | doi: 10.1021/bk-1995-0615.ch006

shown as function of the surfactant concentration. To facilitate the comparison surface charge and adsorbed amount are both expressed in $\mu mol/m^2$. That is, the surface "charge" is expressed as $\Gamma(0) = \sigma_0/F$. Information about the structure of the adsorbed layer can be obtained by comparing $\Gamma(0)$ and Γ_S. Head-on adsorption may either cause a new charge to be formed at the surface to couter balance its own charge, or it may be exchanged with an adsorbed Cl^- ion. Head-out adsorption will not affect the surface charge. Hence, as long as the surface charge adjusts to the surfactant adsorption head-on adsorption occurs. The difference between Γ_S and $\Gamma(0)$ is due to head-out adsorption plus some head-on adsorption of molecules that are accompanied by a counter ion. Therefore, head-out adsorption is about proportional to Γ_S-$\Gamma(0)$ but not necessarily equal to this difference.

The proton uptake due to surfactant adsorption is the strongest at low surfactant adsorption and low salt concentrations: with almost every adsorbing surfactant molecule a proton is adsorbed, indicating that all surfactant molecules will be adsorbed head-on. At higher salt concentrations the initial slope is less, partly the surfactant ions cause proton adsorption, partly a displacement of Cl^- ions at the surface by NBS^- ions takes place. At high adsorbed amounts the surface charge becomes almost independent of the salt concentration: the surfactant is responsible for the screening of the surface charge.

In general the proton adsorption tends to level off after the point where the surface charge and the surfactant charge balance, the equivalence point. This point corresponds for SNBS with the cip in the isotherms and with the iep (*18*). The strong surface charge adjustment before the cip in combination with the observed steep slope of region II of the isotherms indicates that hemi-micelles are formed at the surface. Hemi-micelle formation is promoted by the "flexibility" of the surface charge. Changes in surface charge due to SNBS adsorption still occur beyond the cip. This demonstrates that the head-on adsorption is not completed at the cip. The substantial difference between Γ_S and $\Gamma(0)$ beyond the cip indicates that a large part of the additionally adsorbing molecules is oriented with its head groups towards the solution: after the cip the formation of ad-micelles starts. The rate of transition from hemi-micelles to ad-micelles depends strongly on the salt concentration, the higher c_s the sharper becomes the transition. At all three pH values the SNBS adsorption around the cmc depends only weakly on the salt concentration, increasing c_s increases the adsorption somewhat due to the better screening of the head group charges.

The effect of pH on the adsorption is also relatively weak in region IV but present. The pH effect is most strongly observed at the initial part of the isotherm (region I and II): the higher the pH the lower is the affinity of the surfactant for the surface. At pH=6 the bare rutile surface has the same charge sign as the surfactant. The specific affinity of the head group for the surface is, however, sufficient to overcome the coulombic repulsion and the adsorption induces a positive charge on the surface.

For a further discussion of surfactant adsorption on rutile or the metal hydroxides in general we refer to refs. *18,19,45,46*. In ref. *45* and *46* the adsorption of SNBS on positive rutile is compared with that of DPC on negative rutile and an extensive discussion is given on the adsorbed layer

Downloaded by NORTH CAROLINA STATE UNIV on October 13, 2012 | http://pubs.acs.org
Publication Date: May 5, 1996 | doi: 10.1021/bk-1995-0615.ch006

structure in each of the four regions of the isotherm. For the weakly adsorbing DP^+ ion the situation is considerably more complicated than for the strongly adsorbing NBS^- ion. However, the cip remains the transition point for hemi- and ad-micelle formation.

Dodecyl Pyridinium Chloride Adsorption on Aerosil

Adsorption isotherms. The adsorption isotherms for DPC, measured at pH 9 and two salt concentrations are shown in Figure 8a as log-log plot and in Figure 8b as lin-log plot. To make comparison with older results easy also a lin-lin plot is included, Figure 8c. The isotherms at low and high salt concentrations have different shapes. At low salt concentration the lin-lin plot shows clearly a two step isotherm, but the "hesitation" in the adsorption is also evident in the lin-log and log-log plot. The type of adsorption isotherm shown in Figure 8c is usually observed for adsorption of cationic surfactants on silica at low salt concentrations (2-6). At high salt concentration the isotherm is of the S-type in all three plots.

At both low and high salt concentrations four regions may be distinguished in the log-log plots. For low salt concentration the different regions can also be observed in the other plots. The initial slope (region I) of the DPC isotherms in the double logarithmic plot is equal to unity within experimental error. In this region specific and coloumbic interactions between charged surface groups and surfactant ions take place, but the adsorbed molecules cannot interact with each other. In region II, the slope of isotherms, measured at low salt concentration, is less than unity. This indicates that the electrostatic repulsion between head groups is important and it demonstrates that surfactant self-assembly does not occur! This behaviour deviates strongly from that observed for adsorption on the crystalline metal oxides like rutile. On silica surfactant molecules adsorb, at low salt concentration, without appreciable lateral interaction up to the end of region II. The surfactant concentration has to increase to about 0.1 of the cmc before the aggregation starts and region III begins. Due to lateral hydrophobic attraction the slope of the isotherm in region III is steeper than that in II.

Increasing the salt concentration increases the slope of region II considerably due to a better screening of head group repulsion. Consequently head groups can be adsorbed relatively close together and surfactant self-assembly occurs. The slope in region III depends only weakly on the salt concentration. Consequently at high salt concentration this slope is smaller than in region II, whereas at low salt concentration the situation is reversed. The transition to region IV is observed at the cmc. An increase in the salt concentration leads to a rise of the plateau value and small decrease of concentration (cmc), where plateau is reached: diminishing the lateral repulsion allows a closer packing of the molecules and/or a higher aggregate density.

The isotherms show a cip in region II, the concentration at which the intersection occurs, corresponds well with the point where the surfactant charge and the surface charge balance, the equivalence point, see Figure 9. The reasons for the cip are the same as those mentioned for SNBS adsorption

Downloaded by NORTH CAROLINA STATE UNIV on October 13, 2012 | http://pubs.acs.org
Publication Date: May 5, 1996 | doi: 10.1021/bk-1995-0615.ch006

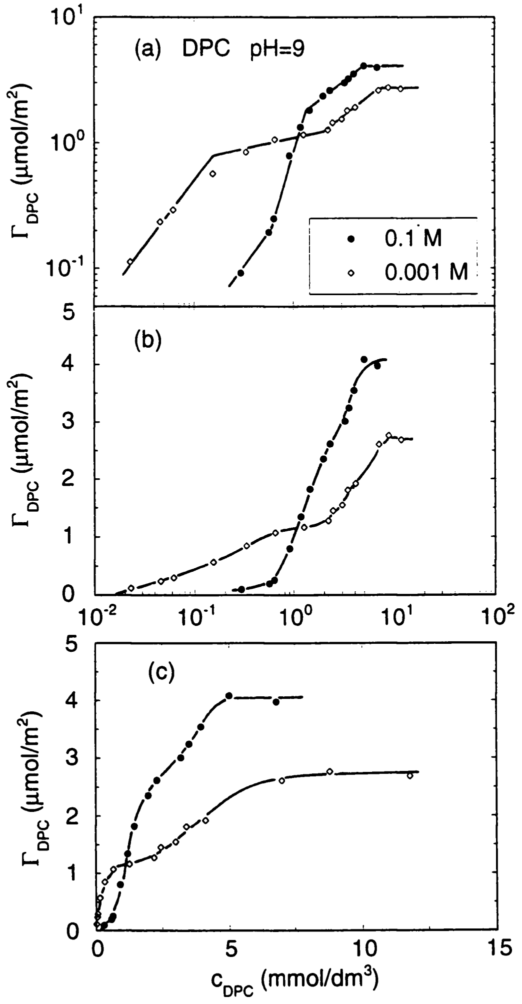

Figure 8. Experimental isotherms of DPC on Aerosil Ox-50 at pH=9 and two electrolyte concentrations as indicated. The data is shown on log-log (a), lin-log (b) and lin-lin (c) scales.

Downloaded by NORTH CAROLINA STATE UNIV on October 13, 2012 | http://pubs.acs.org
Publication Date: May 5, 1996 | doi: 10.1021/bk-1995-0615.ch006

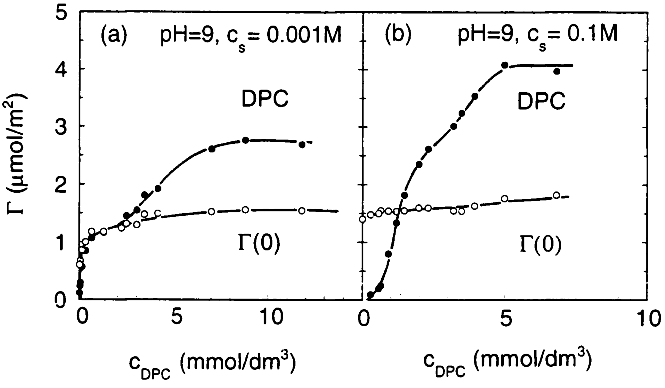

Figure 9. Experimental isotherms of DPC adsorption and absolute surface charge Γ(0) (both in μmol/m^2) on Aerosil Ox-50 at pH=9 and two electrolyte concentrations (panel a: 0.001M, panel b: 0.1M).

Downloaded by NORTH CAROLINA STATE UNIV on October 13, 2012 | http://pubs.acs.org
Publication Date: May 5, 1996 | doi: 10.1021/bk-1995-0615.ch006

on rutile. The difference with the SNBS-rutile case is that the cip is located in region II instead of in region III of the isotherm.

In general, the experimental isotherms, with their low slope in region II for the low salt concentrations and the presence of the cip in this region, resemble those of the calculated isotherms for a constant charge surface at low and high salt concentration more closely than those of the constant potential surface. The fact that the charging of silica differs from that of rutile also follows from modeling studies on the charging behaviour of the solids (*39,58,59*). Böhmer and Koopal (*8*) have suggested that silica could be approximated as a constant charge surface. In the next section it will be shown however, that the surface charge of silica adapts significantly to surfactant adsorption. The correct conclusion is that silica is neither a constant charge nor a constant potential surface but a "regulating" surface. This type of surface charge behaviour can in principle also be described with the SCFA theory, but at present such calculations are not yet made.

Surface Charge Adjustment and Adsorbed Layer Structure. The effect of DPC adsorption on the surface charge of Aerosil at pH 9 is shown in Figure 9 for two salt concentrations (0.001 M and 0.1M). For the comparison the surface "charge" ($\Gamma(0)=\sigma_0/F$) and adsorbed amount of surfactant are both expressed in μmol/m^2. The maximum change in surface charge occurs at low surfactant and low salt concentrations, where the adsorption and surface charge isotherms almost coincide. It means, that at low salt concentrations with almost every adsorbing surfactant ion a proton is desorbed and practically all adsorbed surfactant ions will adsorb head-on. After compensation of the surface charge by surfactant (the equivalence point) the surface charge continues to increase weakly whereas the surfactant adsorption increases substantially. This indicates that locally adsorption of surfactant in a second layer starts, i.e. with its head group directed to the solution. The weak increase of $\Gamma(0)$ shows that some of the additionally adsorbing molecules are still head-on adsorbed. On top of this some other surfactant ions may adsorb head-on if they are accompanied with a counter ion. In general, one may conclude that small ad-micelles are formed around the initially head-on adsorbed (isolated) molecules. This representation of the surface aggregate corresponds with that suggested by Zhu et al. (*40,41*).

At high salt concentration the changes in surface charge due to the surfactant adsorption are much less, evidently DP^+/Na^+ exchange is important. The high salt concentration screens the surface charge fairly well and it is difficult for the surfactant to start its adsorption. Once the adsorption starts it increases strongly over a rather small concentration range and a sharp intersection point with the $\Gamma(0)$ isotherm is found. This equivalence point corresponds with the cip of the DPC isotherms. Before the equivalence point DP^+ adsorption occurs by exchange of Na^+, beyond the equivalence point the adsorbing surfactant ions bring their "own" counter ions to compensate their charge. The latter effect has been stressed before by Bijsterbosch (*4*). The super equivalent adsorption indicates again ad-micelle formation. The effect of a high salt concentration is twofold: (1) before the cip hemi-micelles are formed (compare the steep slope of region II of the log-log isotherm) and (2) the transition from head-on adsorbed molecules to ad-micelles becomes very sharp. In summary, below the cip head-on adsorption occurs: at low salt concentration as isolated molecules, at high salt concentration as hemi-micelles, above the cip ad-micelle formation occurs at all salt concentrations.

Increasing the salt concentration increases the packing density of the adsorbed surfactants, but the values of the $\Gamma(0)$ at the cmc hardly depend on the salt concentration. This indicates that the bilayer becomes more asymmetric and that around the cmc the screening of the surface charge is almost entirely done by surfactant.

Conclusions

The SCFA isotherms for homogeneous surfaces resemble measured surfactant adsorption isotherms with their four regions if plotted as log adsorption versus log concentration. So far no other theory could do this unless ad hoc assumptions were made about surface heterogeneity and the structure of the adsorbed layer. Nevertheless for the constant potential surfaces a typical difference appears with the experimental isotherms: region II is over exaggerated. In practice local aggregates (hemi-micelles) are formed so that region II will both start and end at lower surfactant concentrations than predicted theoretically. The phase separation in the mean field approximation is postponed and exaggerated as it can only occur in at least one entire lattice layer.

Both SCFA theory and experiments show that the course of the isotherms is dependent on the salt concentration and the charge characteristics of the surface. Isotherms obtained at different salt concentration show a common intersection point or cip. The cip marks the point where the coulombic interaction vanishes and the surfactant orientation of the newly adsorbing molecules changes form mainly "head-on" to predominantly "head-out".

For constant potential (variable charge) surfaces, like the crystalline metal oxides (*39*), the adsorption increases gradually at all salt concentrations. The surface charge tends to follow the surfactant adsorption up to the cip. New charges at the surface are created in the vicinity of the sites that are already occupied with head-on adsorbed surfactant molecules. As a result hemi-micelle formation is promoted. Beyond the cip the head-on adsorption still increases somewhat, but most of the newly adsorbed surfactant is adsorbing head-out and ad-micelles are formed.

For constant charge (variable potential) surfaces and at low ionic strength the calculated isotherm shows an adsorption "plateau" at an adsorption level corresponding to the surface charge density. Approaching concentrations close to the cmc the adsorption increases again and reaches a final plateau value at the cmc. At high salt concentration this "hesitation" in the isotherm disappears. The reason for the hesitation is the coulombic repulsion between the surfactant head groups, this repulsion is minimised at high salt concentration. Isotherms on silica resemble this behaviour, yet silica is not a constant charge surface. Measurements show that at low salt concentration the surface charge of silica increases significantly due to surfactant adsorption. In the case of silica this charge adjustment does not promote hemi-micelle formation, at low salt concentration isolated head-on

Downloaded by NORTH CAROLINA STATE UNIV on October 13, 2012 | http://pubs.acs.org
Publication Date: May 5, 1996 | doi: 10.1021/bk-1995-0615.ch006

Downloaded by NORTH CAROLINA STATE UNIV on October 13, 2012 | http://pubs.acs.org
Publication Date: May 5, 1996 | doi: 10.1021/bk-1995-0615.ch006

adsorbed molecules are present on the surface. Apparently the new charges at the silica surface cannot be created in the near vicinity of the charged sites occupied with a head-on adsorbed surfactant molecule. In this respect the silica surface is much less "flexible" than that of the crystalline metal oxides. Further arguments for this difference in behaviour can be found in refs. *39, 58* and *59*. At high salt concentration the charge adjustment is much smaller, but in this case the initial surface charge is larger and the head group repulsion is smaller than at low salt concentration. As a result hemi-micelles are formed before the cip. After passing the cip ad-micelles are formed both at low and high salt concentrations. The size of the ad-micelles is however determined by the salt concentration: at low concentration the ad-micelles are significantly smaller than at high concentration.

The surfactant orientations in the adsorbed layer as deducted from the present analysis relate very well to experimentally observed maximums in hydrophobicity (*14,64-66*) and flotation recovery (*67,68*) of particles as a function of surfactant concentration: at low adsorbed amounts the particles are hydrophobized, whereas at high adsorbed amounts the presence of head groups at the solution side make the particles more hydrophilic again. The results also indicate that around the cip the colloidal stability will be at its minimum, not only because the particles plus adsorbed layer are uncharged, but also because the particles are hydrophobized.

In general we conclude that although the 1D-SCFA theory is not perfect, it definitely is of use in helping to understand surfactant adsorption and to design experiments to gain further insight in the adsorption behaviour.

Acknowledgments

The co-operation between the department of Physical and Colloid Chemistry of Wageningen University and the Colloid Chemistry group of the State University of St. Petersburg is supported by the EU-INTAS project 93-3372.

Literature Cited

1. Ball, B.; Fuerstenau, D. W. *Discuss. Faraday Soc.* **1971,** *52,* 361.
2. Rupprecht, H.; Ullmann, E.; Thoma, K. *Fortschritte Kolloide Polymere* **1971,** *55,* 45.
3. Rupprecht, H. *J. Pharm. Sci.* **1972,** *61,* 700.
4. Bijsterbosch, B. H. *J. Colloid Interface Sci.* **1974,** *47,* 186.
5. Gao, Y.; Du, J.; Gu, T. *J. Chem. Soc. Faraday Trans.* I, **1987,** *83,* 2671.
6. Gu, T.; Huang, Z. *Colloids Surf.* **1989,** *40,* 71.
7. Rennie, A. R.; Lee, E. M.; Simister, E. A.; Thomas, R. K. *Langmuir* **1990,** *6,* 1031.
8. Böhmer, M. R.; Koopal, L. K. *Langmuir* **1992,** *8,* 1594.
9. Wängnerud, P.; Olofsson, G. *J. Colloid Interface Sci.* **1992,** *153,* 392.
10. Fuerstenau, D. W.; Modi, H. J. *J. Electrochemical Soc.* **1959,** *106,* 336.
11. Fuerstenau, D.W.; Wakamatsu, T. *Discuss. Faraday Soc.* **1975,** *59,* 157.
12. Chander, S.; Fuerstenau, D. W.; Stigter, D. In *Adsorption from Solution;* Ottewill, R. H.; Rochester, C. H.; Smith, A. L., Eds.; Academic Press: London, 1983; pp 197.

13. Somasundaran, P.; Fuerstenau, D. W. *J. Phys. Chem.* **1966**, *70*, 90.
14. Moudgil, B. M.; Soto, H.; Somasundaran, P. In *Reagents in Mineral Technology*; Somasundaran, P.; Moudgil, B., Eds.; Surfactant Science Series; M. Dekker, New York **1988**, *27*, Chap. 3; p 79.
15. Scamehorn, J. F.; Schechter, R. S.; Wade, W. H. *J. Colloid Interface Sci.* **1982**, *85*, 463.
16. Harwell, J. H.; Hoskins, J. C.; Schechter, R. S.; Wade, W. H. *Langmuir* **1985**, *1*, 251.
17. Bitting, D.; Harwell, J. H. *Langmuir* **1987**, *3*, 500.
18. Böhmer, M. R.; Koopal, L. K. *Langmuir* **1992**, *8*, 2649.
19. Böhmer, M. R.; Koopal, L. K. *Langmuir* **1992**, *8*, 2660.
20. Jaycock, M. J.; Ottewill, R. H.; Rastogi, M. C. *Proc. 3rd Int. Congress Surface Activity*, 1960, Vol. 2; pp 283.
21. Cases, J. M.; Villieras, F. *Langmuir* **1992**, *8*, 1251.
22. Dobias, B. In *Coagulation and Flocculation*; Dobias, B. Ed.; Surfactant Science Series; M. Dekker: New York, 1993, Vol. 47, Chap. 12; pp 539.
23. Herder, P. C.; Claesson, P. M.; Herder, C. E. *J. Colloid Interface Sci.* **1987**, *119*, 155.
24. Mehrian, T.; De Keizer, A.; Lyklema, J. *Langmuir* **1991**, *7*, 3094.
25. Mehrian, T.; De Keizer, A.; Korteweg, A. J.; Lyklema, J. *Colloids Surf. A: Physicochem. Eng. Aspects* **1993**, *73*, 133.
26. Gu, T.; Gao, Y.; He, L. *J. Chem. Soc. Faraday Trans.* I, **1988**, *84*, 4471.
27. Somasundaran, P.; Kunjappu, J. T. *Colloids Surf.* **1989**, *37* 245.
28. Chandar, P.; Somasundaran, P.; Waterman, K. C.; Turro, N. J. *J. Colloid Interface Sci.* **1987**, *91*, 148.
29. Chandar, P.; Somasundaran, P.; Turro, N. J. *J. Colloid Interface Sci.* **1987**, *117*, 31.
30. Esumi, K.; Nagahama, T.; Meguro, K. *Colloids Surf.* **1991**, *57*, 149
31. Esumi, K.; Sugimura, A.; Yamada, T.; Meguro, K. *Colloids Surf.* **1992**, *62*, 249.
32. McDermott, D. C.; Lu, J. R.; Lee, E. M.; Thomas, R. K.; Rennie, A. R. *Langmuir*, **1992**, *8*, 1204.
33. McDermott, D. C.; Kanelleas, D.; Thomas, R. K.; Rennie, A. R.; Satija, S. K.; Majkrzak, C. F. *Langmuir*, **1993**, *9*, 2404.
34. Cummins, P. G.; Stapels, E.; Penfold, J. *J. Phys. Chem.* **1990**, *94*, 3740.
35. Cummins, P. G.; Stapels, E.; Penfold, J. *J. Phys. Chem.* **1991**, *95*, 5902.
36. Söderlind, E.; Stilbs, P. *Langmuir* **1993**, *9*, 1678.
37. Söderlind, E.; Stilbs, P. *Langmuir* **1993**, *9*, 2024.
38. Koopal, L. K.; Van Riemsdijk, W. H. *J. Colloid Interface Sci.* **1989**, *128*, 188.
39. Koopal, L. K. In *Coagulation and Flocculation*; Dobias, B. Ed.; Surfactant Science Series; M. Dekker, New York **1993**, *47*, Chap. 4; p 101.
40. Zhu, B-Y.; Gu, T. *J. Chem. Soc. Faraday Trans.* I, **1989**, *85*, 3813.
41. Zhu, B-Y.; Gu, T.; Zhao, X. *J. Chem. Soc. Faraday Trans.* I, **1989**, *85*, 3819.
42. Lajtar, L.; Narkiewicz-Michalek, J.; Rudzinski, W.; Partyka, S. *Langmuir* **1994**, *10*, 3754.
43. Narkiewicz-Michalek, J.; Rudzinski, W.; Partyka, S. *Langmuir* **1993**, *9*, 2630.

Downloaded by NORTH CAROLINA STATE UNIV on October 13, 2012 | http://pubs.acs.org
Publication Date: May 5, 1996 | doi: 10.1021/bk-1995-0615.ch006

44. Böhmer, M. R.; Koopal, L. K.; Janssen, R.; Lee, E. M.; Thomas, R. K.; Rennie, A.R. *Langmuir* **1992**, *8*, 2228.
45 Koopal, L. K.; Lee, E. M.; Böhmer, M. R. *J. Colloid Interface Sci.* **1995**, *175*, 85.
46. Lee, E. M.; Koopal, L. K. *J. Colloid Interface Sci.* **1995**, submitted.
47. Böhmer, M. R.; Koopal, L. K.; Lyklema J. *J. Phys. Chem.* **1991**, 95, 9569.
48. Mukerjee, P.; Mysels K. J. **1971** *Critical Micelle Concentrations of Aqueous Surfactant systems* NSRDS-NBS 36, U.S. Government Printing Office, Washington D.C.
49. Van Os, N. M.; Haak, J. R.; Rupert, L. A. M. **1993** *Physico-chemical properties of selected anionic, cationic and nonionic surfactants;* Elsevier Science Publishers, Amsterdam.
50. Bérubé, Y. G.; De Bruyn, P. L. *J. Colloid Interface Sci.* **1968**, *27*, 305.
51. Gibb, A. W.; Koopal, L. K. *J. Colloid Interface Sci.* **1990**, *134*, 122.
52. Bolt, G. H. *J.Phys. Chem.* **1957**, *61*, 1166.
53. Abendroth, R. P. *J. Colloid Interface Sci.* **1970**, *34*, 591; *J. Phys. Chem.* **1972**, *761*, 2547.
54. Evers, O. A.; Scheutjens, J. M. H. M.; Fleer, G. J. *Macromolecules* **1990**, *23*, 5221.
55. Leermakers, F. A. M.; Scheutjens, J. M. H. M. *J. Chem. Phys.* **1988**, *89*, 3264.
56. Leermakers, F. A. M.; Scheutjens, J. M. H. M. *J. Phys. Chem.* **1989**, *93*, 7417.
57. Böhmer, M. R.; Evers, O. A.; Scheutjens, J. M. H. M. *Macromolecules* **1990**, *23*, 2288.
58. Hiemstra, T.; De Wit, J. C. M.; Van Riemsdijk, W. H. *J. Colloid Interface Sci.* **1989**, *133*, 105.
59. Hiemstra, T.; Van Riemsdijk, W. H. *Colloids Surf.* **1991**, *59*, 7.
60. De Keizer, A.; Böhmer, M. R.; Mehrian, T.; Koopal, L. K. *Colloids Surf.* **1990**, *51*, 339.
61. Day, R. E.; Greenwood, F. G. Parfitt, G. D. *Proc. 4th Int. Congress Surface Active Substances*, 1967, Vol.*2B*; pp 1005.
62. Connor, P.; Ottewill, R. H. *J. Colloid Interface Sci.* **1971**, *37*, 642.
63. Bee, H. E.; Ottewill, R. H.; Rance, D. G.; Richardson, R. A. **1983**, in *Adsorption from solution;* Ottewill, R. H.; Rochester, C. H.; Smith, A. L., Eds.; Academic Press: London, 1983; pp 155.
64. Pashley, R. M.; Israelachvilli, J. N. *Colloids Surf.* **1981**, *2*, 169.
65. Herder, P. *J. Colloid Interface Sci.* **1990**, *135*, 346.
66. Menezes, J. L.; Yan, J.; Sharma, M. M. *Colloids Surf.* **1989**, *38*, 365.
67. Mishra, S. K. In *Reagents in Mineral Technology;* Somasundaran, P.; Moudgil, B., Eds.; Surfactant Science Series; M. Dekker: New York, 1988, Vol. 27, Chap. 7; pp 195.
68. Novich, B. E. *Colloids Surf.* **1990**, *46*, 255.

RECEIVED May 3, 1995

Downloaded by NORTH CAROLINA STATE UNIV on October 13, 2012 | http://pubs.acs.org
Publication Date: May 5, 1996 | doi: 10.1021/bk-1995-0615.ch006

Chapter 7

Spectroscopic Characterization of Surfactant and Polymer Solloids at Solid–Liquid Interfaces

P. Somasundaran, S. Krishnakumar, and Joy T. Kunjappu

Langmuir Center for Colloids and Interfaces, Henry Krumb School of Mines, Columbia University, New York, NY 10027

Adsorbed surfactant and polymer layers play a major role in several key industrial operations such as flocculation/dispersion,ceramic processing, lubrication flotation and detergency. Much work has been done to understand the physico-chemical interactions that govern the formation of colloidal layers adsorbed on surfaces (*solloids*). The structure of these layers plays a critical role in determining interfacial properties and information on such structures, particularly at microscopic and molecular levels , can be helpful for controlling the behavior of the systems. We have recently adapted fluorescence, electron spin resonance, Fourier transform infrared, and excited-state resonance Raman spectroscopic techniques to obtain information on microstructure of adsorbed layers on a molecular level. In-situ characterization techniques that have been used recently for examining the adsorbed layers at the solid-liquid interface are reviewed here. Effects of surfactant and polymer structure, pH, and their synergistic effects on the evolution and properties of the adsorbed layer are discussed.

Adsorption of surfactants and polymers at the solid-liquid interface is a key phenomena in many important processes such as flocculation, flotation, dispersion, and stabilization *(1)*. These applications are a sequel to the modification of the solid surface by the adsorbates in terms of the electrical and allied processes. Optimum performance of these processes is possible by a detailed understanding of the adsorbates at the solid-liquid interface and the related structure-performance relationship of these species.

In this article, we discuss some of the advanced techniques and methodologies that we have used recently for investigating the microstructure of the adsorbed monomeric and polymeric aggregates at the solid-liquid interface, which are known

0097–6156/95/0615–0104$15.50/0

as solloids (surface colloids). We have investigated the complex dependence of the adsorbed layer structures on the processes of dispersion, flocculation and flotation. We have used mainly the techniques of fluorescence emission, electron spin resonance, Fourier transform infrared, and excited state Raman spectroscopy to delineate the microstructure of the adsorbed layers of surfactant and polymeric aggregates.

We first give a description of the basic principles of the above spectroscopic techniques as used in our studies. This description is followed by a discussion of the individual systems comprising of surfactants, polymers, mixed surfactants and surfactant-polymer aggregates at various solid-solution interfaces. These interfaces include alumina and silica in aqueous and non-aqueous media.

Techniques

Fluorescence Spectroscopy. Fluorescence emission is the radiative emission of light by an excited molecule returning to its ground state energy level. This phenomenon bears a wealth of information on the environment of the light absorbing species and has been exploited for a long time for exploring the solution behavior of surfactants. Parameters of fundamental importance in fluorescence emission are 1) emission maximum (wavelength of maximum intensity), 2) quantum yield of fluorescence (emission efficiency measured as intensity) and 3) fluorescence life-time (time taken by the excited state to decay to 1/e of its initial value).

The fluorescence measurements are generally carried out by a steady state fluorescence spectrofluorometer and lifetime of fluorescence by time resolved fluorescence lifetime instrument *(2)*. The dependence of fluorescence intensity and life-time on the physicochemical environment of the fluorescing molecule has been well documented *(3)*. Such data for micellar photochemistry has been used to understand the microenvironment within micelles *(4)*. We have recently adapted this technique as a tool to investigate the adsorbed layer structures of surfactants on solids to obtain information on the *micropolarity, microviscosity* of the probe environment and the *aggregation number* of the surfactant adsorbed at the interface. To determine the micropolarity, a fluorescent molecule like pyrene, which possesses a highly structured fluorescence spectrum whose vibrational lines are susceptible to intensity fluctuations brought on by polarity changes of the medium, is used. This empirical knowledge has been found to be of universal applicability and used widely to investigate the micropolarity of micelles. A properly resolved fluorescence spectrum of pyrene in fluids exhibits five vibronic bands in the region from 370 to 400 nm. The intensities of the first (I_1) and the third (I_3) are found to be particularly sensitive to the changes in the probe environment. The ratio of these peaks (I_3/I_1), sometimes referred to as the polarity parameter, changes from ~ 0.6 in water to a value greater than unity in hydrocarbon media.

The dynamics of fluorescence emission of pyrene has been previously studied in homogeneous and micellar solutions using time resolved fluorescence spectrometry *(5)*. While the decay kinetics of monomer and excimer emission may be derived directly for a homogeneous solution (continuous medium), statistical methods are to be applied to arrive at similar kinetics in aggregated micellar ensembles. This stems from a need to recognize the possibility of random multiple occupancy of the probe in the aggregates which affects the excimer forming probability within the aggregate. If the micellar system is viewed as a group of individual micelles with n probes, P_n the average number of probes per micelle, may be related to n, by Poisson statistics through the relation

$$P_n = n^n \exp(-n)/n! \tag{1}$$

This model yields the following relation for the time dependence of monomer emission

$$I_{m[t]} = I_{m[0]} \exp\,[-k_o t + n(\exp\,(-k_e t)-1)] \tag{2}$$

where k_0 is the reciprocal lifetime of excited pyrene in the absence of excimer formation, k_e is the intra micellar encounter frequency of pyrene in excited and ground states, and $I_{m[0]}$ and $I_{m[t]}$ represent the intensity of monomer emissions at time zero and time t respectively. Knowing n, one can calculate aggregation number N using the expression

$$n = [P]/[Agg] = [P]\,N/\,([S] - [S_{eq}]) \tag{3}$$

where [P] is the total pyrene concentration, [Agg] is the concentration of the aggregates and [S] - $[S_{eq}]$ is the concentration of the adsorbed surfactant.

Electron Spin Resonance Spectroscopy (ESR). Molecular species with a free electron possesses intrinsic angular momentum (spin), which in an external magnetic field undergoes Zeeman splitting. For a system with S=1/2, two Zeeman energy levels are possible whose energy gap (Δ E) is given by

$$\Delta E = h\nu = gBH_o \tag{4}$$

where ν is the frequency of the electromagnetic radiation corresponding to ΔE, g is a proportionality constant, B is the Bohr magneton (natural unit of the magnetic moment of the electron), and H_0 is the applied magnetic field.

The magnetic moment of the free electron is susceptible also to the secondary magnetic moments of the nuclei and thus the Zeeman splitting will be superimposed by the hyperfine splitting which brings about further splitting of the absorption signal. The hyperfine splitting pattern depends on the spins and the actual number of the neighboring nuclei with spins. If the electron is in the field of a proton (s=1/2, where s is the spin quantum number) then the ESR spectrum would yield two lines of equal intensity and similar interaction with a nucleus, as in nitrogen (s=1), would produce a triplet of equal intensity. The line shapes of ESR signals are subject to various relaxation processes (spin lattice and spin-spin relaxations) occurring within the spin system as well as anisotropic effects due to the differentially oriented paramagnetic centers being acted upon by an external magnetic field *(6)*. These effects result in a broadening of the absorption lines. Three types of ESR studies can be applied to probe surfactant microstructures - spin probing, spin labeling and spin trapping *(7)*. In the spin-probing technique, a molecule with a spin is externally added to the system, whereas in spin labeling a spin bearing moiety forms a part of the molecule through covalent bonding. The spin trapping technique is mainly used for the identification of radicals produced thermally, photochemically or radiolytically by trapping the radical through chemical reactions with a spin trap (like butyl nitroxide) and converting the radical to a free radical which can be examined by ESR. This technique has been used widely to study micellization of different surfactants in both aqueous and non-aqueous media *(8)*,*(9)*,*(10)*. This has also been used to study the exchange kinetics and solubilization sites in water-in-oil microemulsions *(11)* . ESR studies as applied to micellar systems rely on the sensitivity of a free radical probe to respond to its microenvironment.

Information on micropolarity and microviscosity can be obtained by measuring the hyperfine splitting constant A_N and the rotational correlation time τ. The latter is the time required for a complete rotation of the nitroxide radical about its axis. Its value can be defined as the time required for the nitroxide to rotate through an angle of one radian. The rotational correlation time (τ) measured from the ESR spectrum is reflective of the probe mobility and can be used to monitor the changes in microviscosity of the adsorbed layer brought about as a result of adsorption followed by close packing of molecules in the adsorbed layer. The hyperfine splitting constant (A_N) that can also be measured from the spectrum, changes as a function of the environment polarity and hence yields information on the formation of different microdomains at the interface as a result of adsorption. In the case of slow anisotropic motion the observed changes in the spectrum can be quantified by using the concept of order parameter S which can be calculated from the spectrum using the following equation

$$S = 1.66\frac{(A_{//}-(A_1(meas)+C))}{(A_{//}+2(A_1(meas)+C))} \quad \textit{where} \quad C = (1.45-0.019(A_{//}-A_1(meas))) \quad \textit{gauss} \qquad (5)$$

and $A_{//}$ and A_1 are the hyperfine splittings measured from the spectra. The order parameter is usually a parameter of molecular motion and varies between 0 (low order) and 1(high order).

Infrared Spectroscopy (IR). The vibrational frequencies of bonds in a molecule correspond to the infrared region of the electromagnetic spectrum. Different groups in a molecule possess characteristic absorption frequencies which serve as their identification marks. Moreover, these frequencies are related to the bond strength, bond energy and other related parameters. In the case of a diatomic molecule, the stretching frequecy ν is expressed as,

$$\nu = 1/(2\pi c)\sqrt{(k/\mu)} \qquad (6)$$

where k is the force constant, c the velocity of light, and μ, the reduced mass which is equal to$(m_1+m_2)/m_1m_2$, m_1 and m_2 being the masses of the atoms forming the bond *(12)*.

A prerequisite for the absorption of infrared radiation by a molecule is that the concerned vibration should cause a change in its dipole moment. Both the stretching and bending vibrations are useful for the identification of the bonding characteristics. The frequency positions and the frequency intensities help in the qualitative detection and the quantitative estimation respectively.

The common IR sampling methods such as KBr pelletting, nujol mulling, etc. cannot be applied to an aqueous environment. The analysis of solid samples has been accelerated by the use of attenuated total reflectance technique (ATR). In this mode, the powdered sample or the slurry is smeared on an internal reflection element (IRE). The evanescent field of the IR light undergoing multiple internal reflections samples the material adhering onto the IRE and gets attenuated collecting information on the vibrational aspects of the material. Equations are available which relate the adsorption density (Γ) of surfactants quantitatively to the parameters of IRE and IR light exemplified as follows *(13)*,

$$\Gamma = [\{A/(l/\cot\theta) - \varepsilon C_b d_e\}] / 1000\varepsilon\ (2d_e/d_p) \tag{7}$$

where A = integrated absorbance (cm^{-1}), l = IRE length, t = IRE thickness, ε = molar absorptivity of surfactant ($l/(cm^2.mol)$), C_b = surfactant bulk concentration (mol/l), d_p = depth of penetration, d_e = effective depth, and θ = incident angle of light on IRE (degrees).

Raman Spectroscopy. Raman spectroscopy is essentially a scattering technique giving information on the vibrational modes of a molecule. Those vibrations causing a polarizability change of a molecule are Raman active. Raman spectroscopy has an edge over infrared spectroscopy since it is ideal in an aqueous environment and versatile in its ease of sample handling.

The Raman process (inelastic scattering) is inherently weak in sensitivity due to its low cross section ($\sim 10^{-6}$). An inelastic impact of the molecule with the light quantum results in transferring the vibrational energy from the light quantum to the molecule (Stokes process) or from the molecule to the light quantum (anti-Stokes process). The electric field of the light induces in the molecule a dipole moment μ' which is related to the field strength E and polarizability α of the molecule according to the equation

$$\mu' = \alpha E \tag{8}$$

The directional dependence of the polarizability is described by a tensor which becomes symmetrical for a non-chiral molecule. Quantum mechanical treatment provides a good estimate of the intensities of the Stokes and anti-Stokes lines, though the classical picture does not provide a resonable estimate.

The earlier Raman studies have been carried out under continuous wave light. With the advent of lasers, both continuous wave and pulsed lasers are used for collecting Raman spectra. To enhance the intensity of Raman lines, the excitation can be localized to a narrow absorption band (Resonance Raman Scattering). The intensity problem is overcome in a few cases by the Surface Enhanced Raman Spectroscopy

(SERS). Another approach to circumvent this problem involves the use of Excited State Resonance Raman Spectroscopy in which the scattering property of a molecule in the excited state is utilized. The excited state produced by a laser pulse is scattered by the same pulse or another pulse in a one-color or two-color laser pump-probe experiment *(14)*. The potential of this process to study interfacial phenomena is discussed in this account.

Surfactant/Solid Systems

Adsorption of Sodium Dodecyl Sulfate on Alumina. The adsorption of sodium dodecyl sulfate on alumina from aqueous solutions has been studied extensively and used as a model system here to illustrate the different stages in the mechanisms of adsorption of an ionic surfactant on a charged solid. A systematic analysis of such an isotherm was first done by one of us in 1964 *(15)* and is referred to as the S-F isotherm *(16)*. A typical example of an S-F isotherm is shown in Figure 1, where the adsorption of SDS on alumina at pH 6.5 under constant ionic strengh conditions is shown. This isotherm is divided into four regions. Mechanistically, these regions may be viewed as follows.

-Region I which has a slope of unity under constant ionic strength conditions results from the electrostatic interactions between the ionic surfactant species and the oppositely charged solid surface.

-Region II is marked by a conspicuous increase in adsorption which is attributed to the onset of surfactant aggregation at the surface through lateral interactions between hydrocarbon chains. The aggregates formed on the surface, in general, between surfactant and/or polymer species are referred to as *solloids* (surface colloids)*(17)*. In the case of simple ionic surfactants it has also been called hemi-micelles, admicelles, surface micelles and surfactant self assemblies.*(18)*,*(19)*,(16)

-Region III shows a decrease in the slope of the isotherm and this is ascribed to the increasing electrostatic hindrance to the surfactant adsorption following interfacial charge reversal caused by the adsorption of the charged species. In Region III and beyond, both the adsorbent species and the adsorbate are similarly charged.

-Region IV and the plateau in it correspond to the maximum surface coverage as controlled by the micelle formation in the bulk or monolayer coverage whichever is attained at the lowest surfactant concentration; further increase in surfactant concentration does not alter the adsorption density.

The application of spectroscopic techniques to study these systems gives a better insight into the internal structure of Al_2O_3/SDS solloid system. I_3/I_1 values for pyrene were determined using fluorescence spectroscopy for alumina/sodium dodecylsulfate/water systems for various regions of the adsorption isotherm *(20)*. Figure 2 indicates an abrupt change in local polarity of the probe from an aqueous environment to a relatively non-polar micelle type environment as the SDS adsorbs on to the alumina surface. It is to be noted that this abrupt change occurs in a region that is well below the critical micelle concentration (CMC) and coincides approximately with the transition in the adsorption isotherm from Region I to Region II. In the plateau region I_3/I_1 value coincides with the maximum value for SDS micellar solutions indicating completion of aggregation on the surface. It can also be seen that the polarity

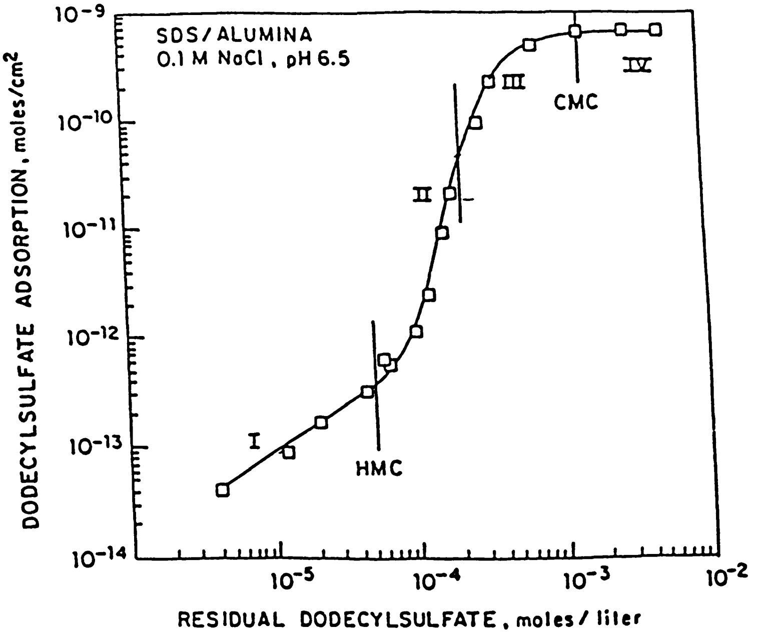

Figure 1. Adsorption isotherm of sodium dodecylsulfate (SDS) on alumina at pH 6.5 in 10^{-1} kmol/m^3 NaCl.

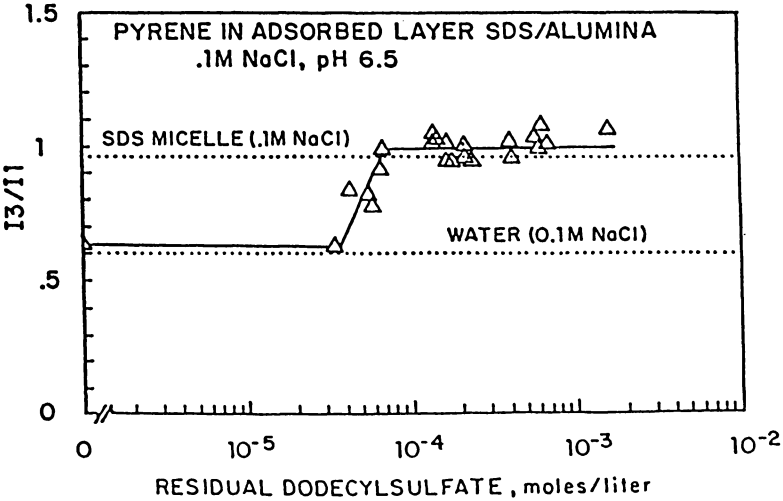

Figure 2. I_3/I_1 fluorescence parameter of pyrene in sodium dodecylsulfate (SDS) in alumina slurries. (Reproduced with permission from ref. 20. Copyright 1987, Academic Press)

parameter is fairly constant throughout most of the Region III and above and hence seems to be independent of the surface coverage.

Information on microviscosity of the adsorbed layer is obtained by studying the excimer (exci̲ted di̲mer̲) forming capabilities of suitable fluorescent molecules like 1,3-dinaphthyl propane. The excimer, which is a complex of a ground state and an excited state monomer, has a characteristic emission frequency. The intramolecular excimer formation is a sensitive function of the microviscosity of its local environment. This property, expressed as the ratio of the monomer to excimer yield (I_m/I_e) for 1,3-dinaphthyl propane, is determined (Figure 3) for the solution and for the adsorbed layer for the various regions of the adsorption isotherm *(21)*. These are then compared to the I_m/I_e values of DNP in mixtures of ethanol and glycerol of known viscosities. Based on the I_m/I_e values of DNP for ethanol-glycerol mixtures, a microviscosity value of about 100 cP is obtained for the adsorbed layer compared to a value of 8 cP for micelles. A higher value of microviscosity in the solloid as reported by DNP is indicative of a highly condensed surfactant assembly.

A kinetic analysis based on the relation of the decay profiles of pyrene in the adsorbed layer for different regions of the alumina/dodecylsulfate adsorption isotherm yielded the aggregation numbers marked in Figure 4 for dodecyl sulfate solloids (20). These results yield a picture of the evolution of the adsorbed layer. The aggregates in Region II appear to be of relatively uniform size while in Region III there is a marked growth in the aggregate size. In Region II, the surface is not fully covered and some positive sites are still available for further adsorption. Since the aggregation number is fairly constant in Region II, further adsorption in this region can be considered to occur by the formation of more aggregates but of the same size. The transition from Region II to III corresponds to the isoelectric point of the solid, and adsorption in region III is proposed to occur through the growth of existing aggregates rather than the formation of new ones due to lack of positive adsorption sites. This is possible by the hydrophobic interaction between the hydrocarbon tails of the already adsorbed surfactant molecules and the adsorbing ones. The new molecules adsorbing at the solid-liquid interface can be expected to orient with their ionic heads towards the water, as supported by the hydrophobicity studies*(22)*, since the solid particles possess a net negative charge under these conditions. A schematic representation of the adsorption by lateral interactions is given in Figure 5.

These studies were complemeted by using ESR to further investigate changes in microviscosity within the adsorbed layer using three isomeric stable free radicals 5-, 12- and 16- doxyl stearic acids as the spin labels. These spin labels were co-adsorbed individually on the alumina along with the main adsorbate, sodium dodecylsulfate, and the main regions of the isotherm were investigated. The hyperfine splitting constants of 16-doxyl stearic acid measured in dodecyl sulfate solloids (15.0G) are indicative of a less polar environment in comparison to its value for water (16.0G) and SDS micelles (15.6G). Similarly microviscosities were estimated from τ measurements and calibrated against τ measured in ethanol-glycerol mixtures (Figure 6). These give reasonably high values for the solloids in reference to the values for water. Three different microviscosities were obtained using different probes indicating that the nitroxide group in each case experienced a different viscosity within the solloid. These observations may be explained by assuming a model for the adsorption of the probe in

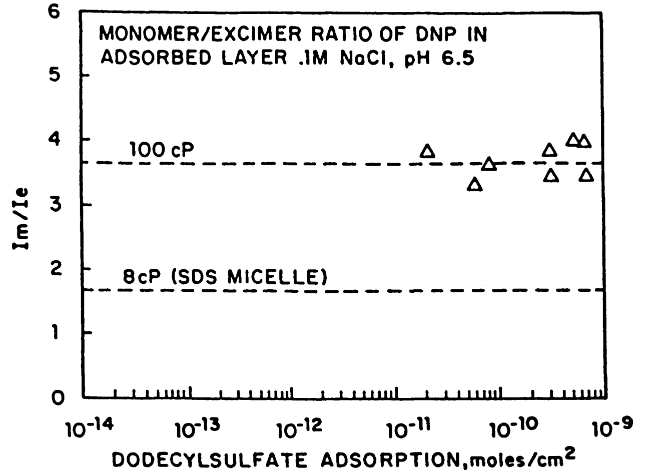

Figure 3. Monomer to excimer ratio (I_m/I_e) of dinaphthyl propane (DNP) in SDS-alumina slurries as a function of SDS adsorption density. The viscosities refer to those of ethanol-glycerol mixtures which give a similar I_m/I_e ratio for DNP. (Reproduced with permission from ref. 20. Copyright 1987, Academic Press)

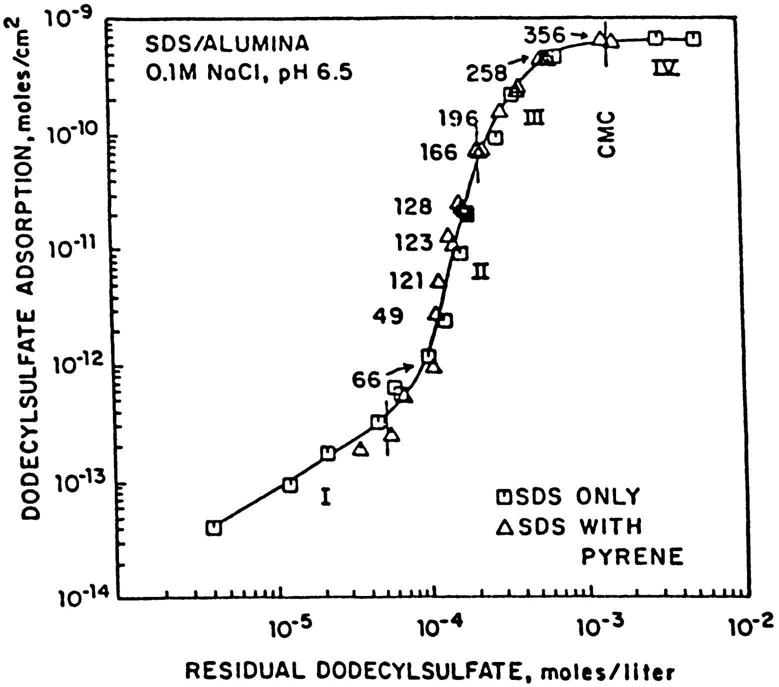

Figure 4. Surfactant aggregation numbers determinined for various adsorption densities (average number is indicated). (Reproduced with permission from ref. 20. Copyright 1987, Academic Press)

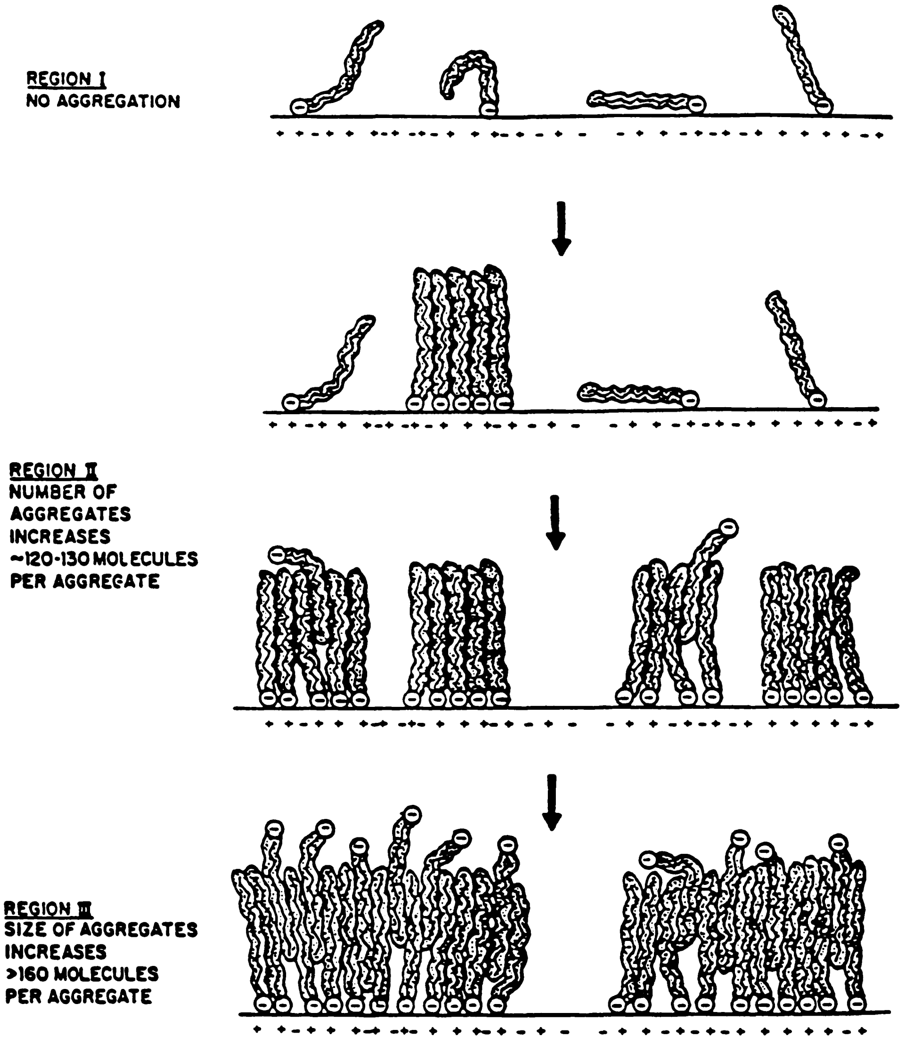
REGION I
NO AGGREGATION
REGION II
NUMBER OF AGGREGATES INCREASES
~120-130 MOLECULES PER AGGREGATE
REGION III
SIZE OF AGGREGATES INCREASES
>160 MOLECULES PER AGGREGATE

Figure 5. Schematic representation of the correlation of surface charge and the growth of aggregates for various regions of the adsorption isotherm depicted in Figure 1. (Reproduced with permission from ref. 20. Copyright 1987, Academic Press)

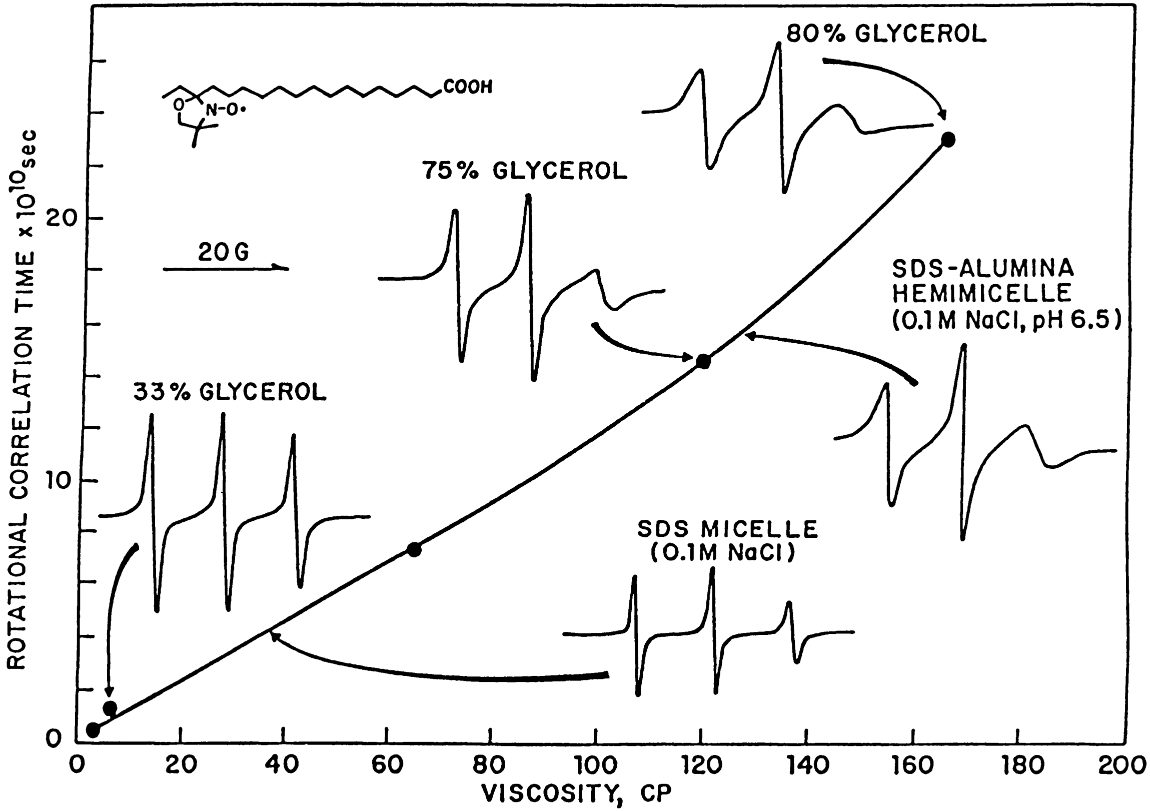

Figure 6. Comparison of ESR spectra of 16-doxyl stearic acid in solloids, micelles and ethanol-glycerol mixtures and corresponding rotational correlation times and viscosities. (Adapted from ref. 23)

which the carboxylate group is bound to the alumina surface. Such a model would require greater mobility of the nitroxide moiety near the SDS/H_2O interface (as in the 16-doxyl stearic acid case) and less mobility of the 12-doxyl and 5-doxyl probes *(23),(24)*. This work is the first reported indication of variations in microviscosity within a surfactant solloid as estimated by any known technique.

The alumina/dodecylsulfate system has also been probed by excited state resonance Raman Spectroscopy using Tris(2,2'-bipyridyl) ruthenium (II) chloride [$Ru(bpy)_3^{2+}$] as a reporter molecule*(25)*. It has been shown that ruthenium polypyridyl complexes serve as excellent photophysical probes for biopolymers like nucleic acids. The excited state of $Ru(bpy)_3^{2+}$ shows strong resonance enhanced Raman transitions when probed at 355 nm. Furthermore, it has been shown that binding of this ion to clay particles results in substantial changes in the ground-state transitions of the excited state-resonance Raman spectrum. For these reasons this probe was chosen to study the solloids formed at the alumina-water interface with excited-state resonance Raman spectroscopy. The third harmonic of a Nd-YAG laser excited and scattered the $Ru(bpy)_3^{2+}$ molecules at a pulse energy of 5 mJ, pulse width of 6 ns, and a wavelength of 354.5 nm. The excited state Raman spectrum of $Ru(bpy)_3^{2+}$consisting of 14 lines (7 lines each from the ground and the excited states) was calibrated using an authentic spectrum.

Raman spectra of $Ru(bpy)_3^{2+}$ above the CMC show frequency shifts as well as intensity changes as compared to its spectrum in water. These transitions can be attributed to the perturbation of the excited state by the SDS micelles. Excited state resonance Raman spectrum of this probe in various regions of adsorption isotherm for the alumina/SDS system is shown in Figure 7. The spectrum of $Ru(bpy)_3^{2+}$ on alumina in the absence of SDS is very much similar to its spectrum in water both in terms of frequencies and relative intensities. This trend is continued into region II, where the solloid aggregation process begins. In regions III and IV, the Raman spectrum shows significant changes. The frequency shifts are more pronounced than in the case of micelles. A plot of change in wave numbers for some of the lines in the four different regions of the adsorption isotherm is shown in Figure 8. The changes in Raman frequency and intensity assume substantial significance in the transition regions II and III onwards only. This could be due to the change of net charge on the alumina surface from positive to negative. The favorable net negative charge enhances the adsorption of the probe at the solid-liquid interface. Accordingly, no adsorption of $Ru(bpy)_3^{2+}$ was observed when the supernatants were analyzed in Region I and Region II or in the absence of SDS. These results indicate that adsorption of $Ru(bpy)_3^{2+}$ onto alumina becomes significant only close to the isoelectric point. The transitions at 1213, 1286 and 1428 cm^{-1} show significant increments and these trends clearly suggest the probe adsorption on to the solloids. Also it was seen that the 1286 peak shifted to 1281 in the presence of solloids while it was practically unchanged in the sodium dodecylsulfate micelles. It may be speculated that $Ru(bpy)_3^{2+}$ may be sensing different environments within the SDS micelles and the alumina/SDS solloids. Implicit in these results is also the potential of the time resolved Raman spectroscopy as a powerful diagnostic tool to explore the solid - liquid interface.

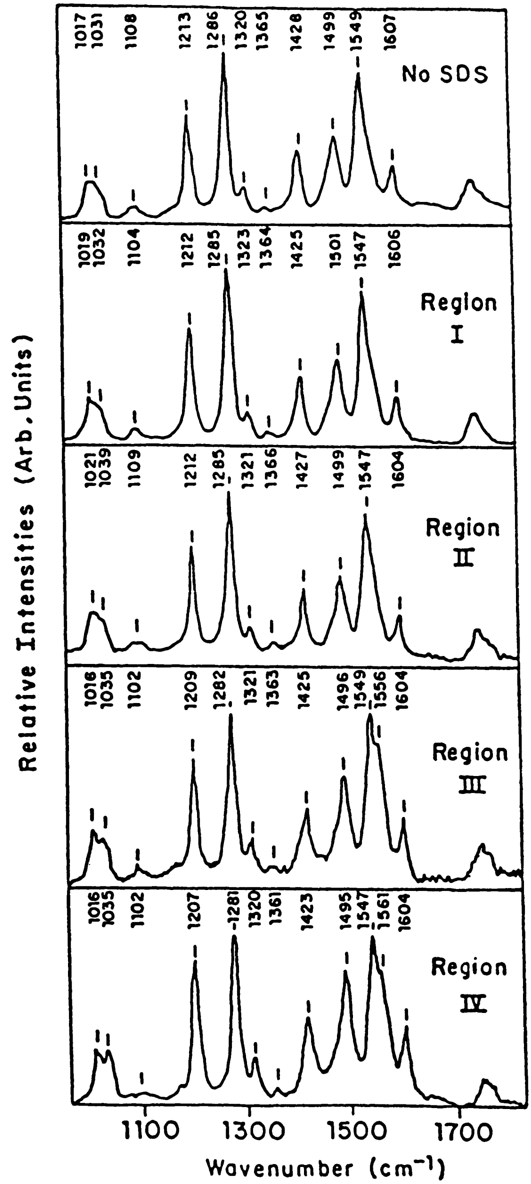

Figure 7. Resonance Raman spectrum of $Ru(bpy)_3^{2+}$ for various regions of the alumina/SDS adsorption system. (Adapted from ref. 25)

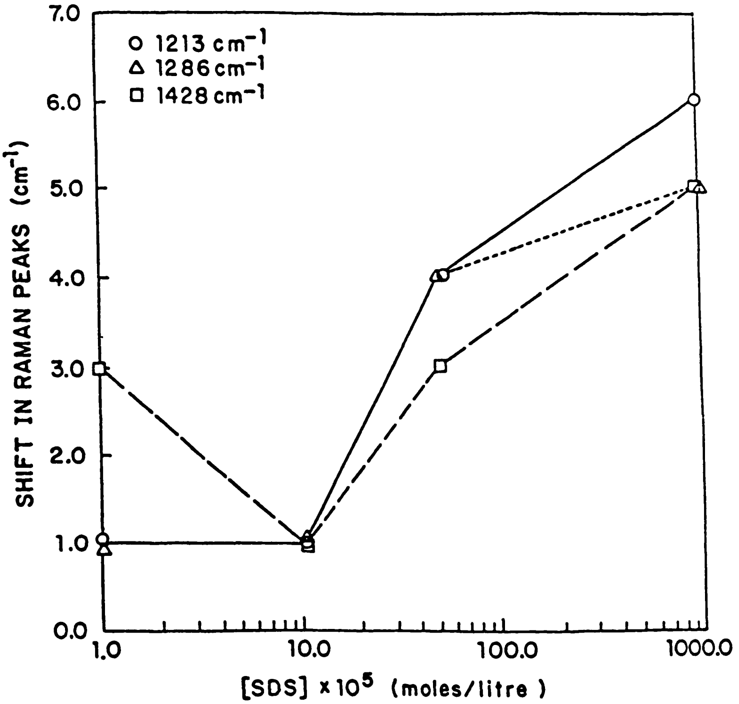

Figure 8. Frequency shifts of resonance Raman lines of $Ru(bpy)_3^{2+}$ as a function of SDS concentration for the alumina/SDS system. (Adapted from ref. 25)

Isomeric Surfactants at an Interface *(26)*. Studies of changes in the position of the sulfonate and the methyl groups on the aromatic ring of alkylxylenesulfonate showed a marked effect of such changes on the micellization and adsorption at the alumina/water interface. Fluorescence spectroscopy was used to probe the microstructure of the adsorbed layers in these systems. Adsorption isotherms for 4-(4-undecyl)-2,6-dimethylbenzenesulfonate (Para-1), 4-(4-undecyl)-2,5-dimethylbenzene sulfonate (Para-2) and 5-(4-undecyl)-2,4-dimethylbenzenesulfonate (Meta) on alumina from water and the I_3/I_1 values along various regions of the isotherm are shown in Figure 9 and 10 respectively. At low adsorption densities the value of the polarity parameter, I_3/I_1, is ~ 0.6 and once the solloids form the value goes up to about 1. It can also be seen that there is no measurable difference among the polarities of the adsorbed layers of the three surfactants indicating that these layers in all three cases are structurally similar with minimum water penetration. Average aggregation numbers (determined using fluorescence decay) of the solloids increase from 17 to 76 with increase in adsorption in all the three cases (Figure 11). The aggregation numbers of the two paraxylene sulfonates are similar throughout the range studied. However, at higher adsorption densities, the aggregation number of the metaxylenesulfonate is lower than those of the paraxylenesulfonates. This suggests higher steric hindrance to the packing of the surfactant molecules in the solloids of the metaxylenesulfonate. Based on this evidence, the effect of change of functional groups on the aromatic ring of the alkylxylenesulfonates on adsorption can be attributed to the steric constraints to the packing of surfactant molecules in their aggregates.

Conformation of Aerosol-OT at Alumina-Cyclohexane Interface *(27),(28)*. Colloidal dispersions in non-aqueous media have a number of technological applications, but water is present in most of these cases and plays a major role in determining the dispersion behavior. The adsorption of Aerosol-OT, sodium bis(2-ethylhexyl) sulfosuccinate, on alumina was investigated using Infrared spectroscopy *(29)*. Figure 12 shows the IR spectrum of AOT adsorbed on alumina in cyclohexane along with the spectra for alumina and AOT. The spectrum does not show any new absorption bands or shifts in the existing bands on alumina or AOT due to the adsorption. This suggests that the adsorption proceeds via weak physical interaction. The effect of water on the stability of a colloidal suspension of alumina in cyclohexane in the presence of surfactant, Aerosol-OT is shown in Figure 13. A succession of flocculated, dispersed and flocculated states are observed as the amount of water added to the suspensions is increased. ESR studies were conducted using 7-doxyl stearic acid as a probe to get structural information on the adsorbed layer.

Figure 14 shows some of the spectra obtained at different water concentrations with 7-doxyl stearic acid coadsorbed with a full monolayer of Aerosol-OT on the alumina surface. The changes observed in the ESR line shape correspond to an increase in the probe mobility consistent with a decrease in the ordering of the probe environment. The calculated order parameter (eqn. 5) plotted as a function of water concentration is shown in Figure 15. It can be seen that as more water is added to the suspension the order parameter decreased until it reached a constant value of 0.75. These results are interpreted in terms of an increase in the probe lateral diffusion within the adsorbed surfactant layer. Such an increase in the probe lateral diffusion is realistic,

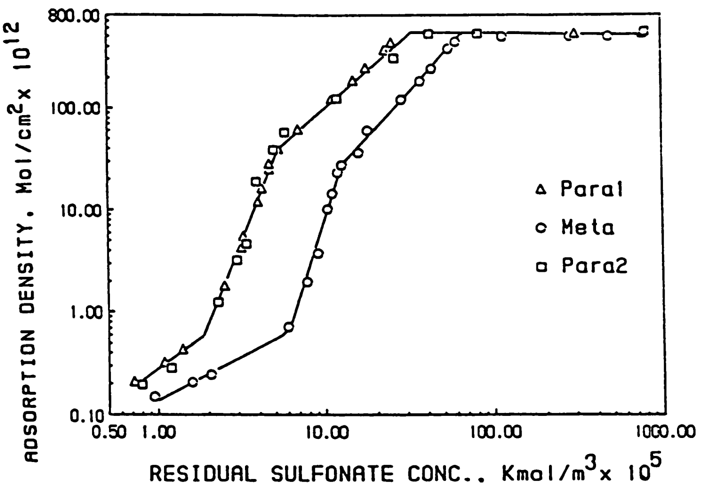

Figure 9. Adsorption of alkylxylene sulfonates on alumina. (Adapted from ref. 26)

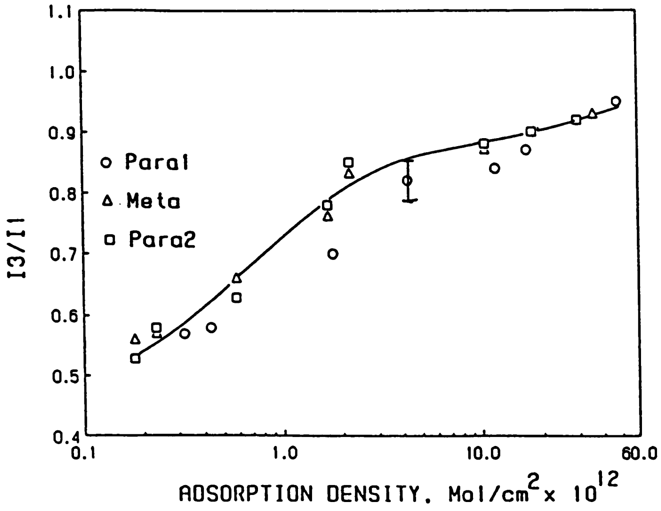

Figure 10. Polarity of adsorbed layers of alkylxylenesulfonates in terms of I_3/I_1 as a function of surfactants adsorption density. (Adapted from ref. 26)

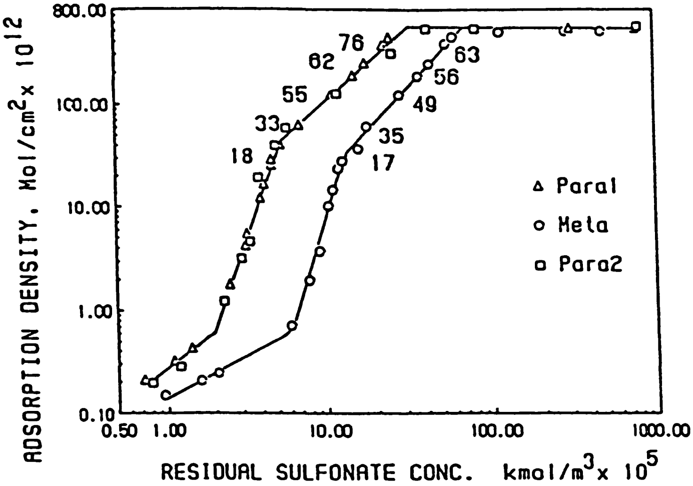

Figure 11. Aggregation numbers determined at different adsorption densities shown along the isotherm. (Adapted from ref. 26)

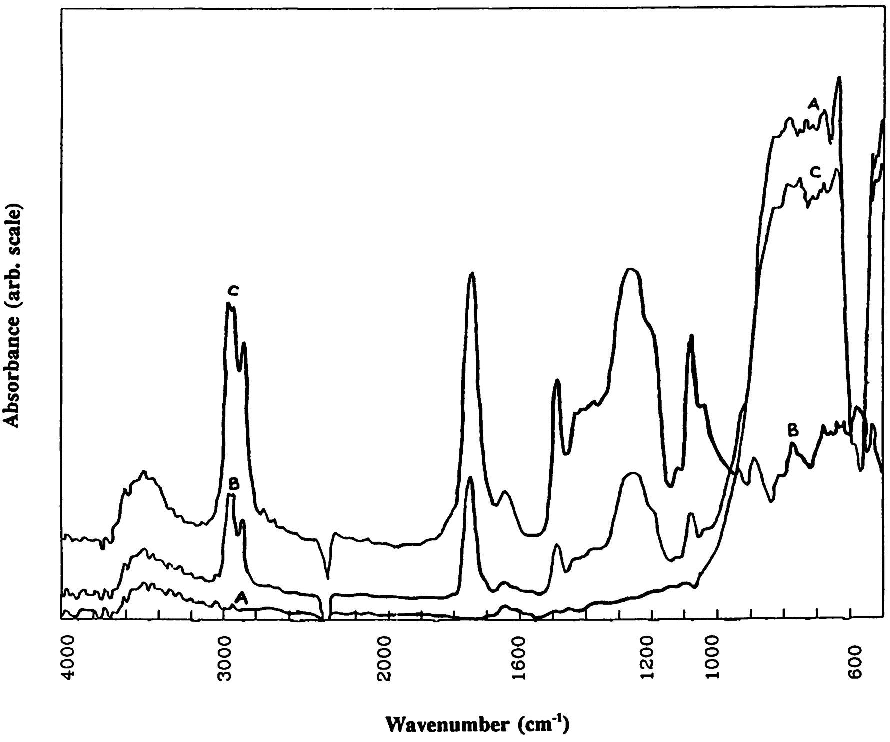

Figure 12. Infrared spectrum of (a) pure alumina (b) pure AOT and (c) AOT adsorbed on alumina. (Adapted from ref. 29)

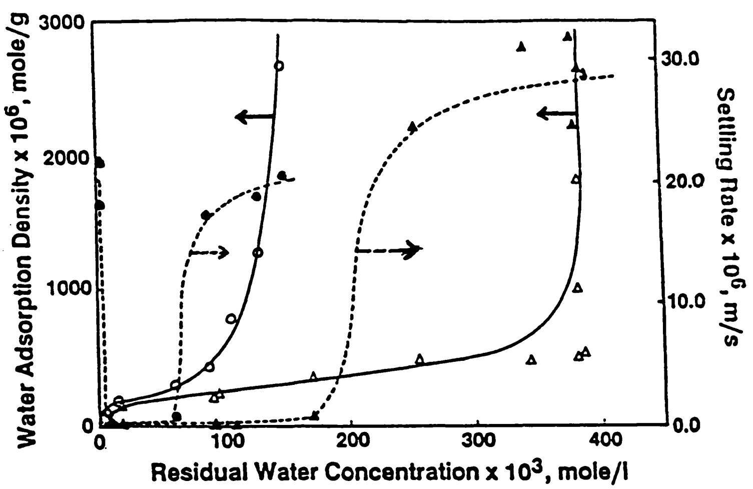

Figure 13. Effect of water on the alumina suspension stability at two different surfactant concentrations; solid symbols [AOT] = 8.5 x10^{-3} M/l and hollow symbols [AOT] = 26.5 x 10^{-3} M/l (dotted line): The corresponding water adsorption densities are also shown (solid line). (Adapted from ref. 28)

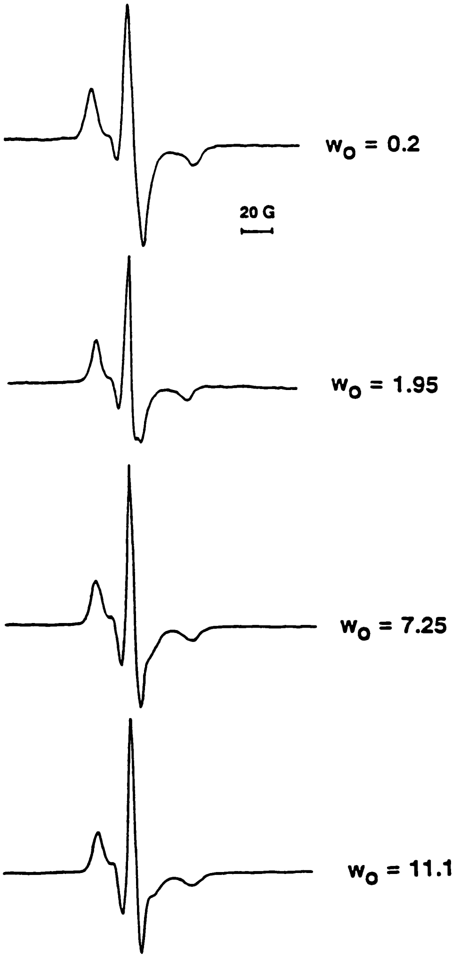

Figure 14. Effect of water on the ESR spectra of 7-doxyl stearic acid coadsorbed with a monolayer of Aerosol-OT at the alumina/cyclohexane interface. (Adapted from ref. 28)

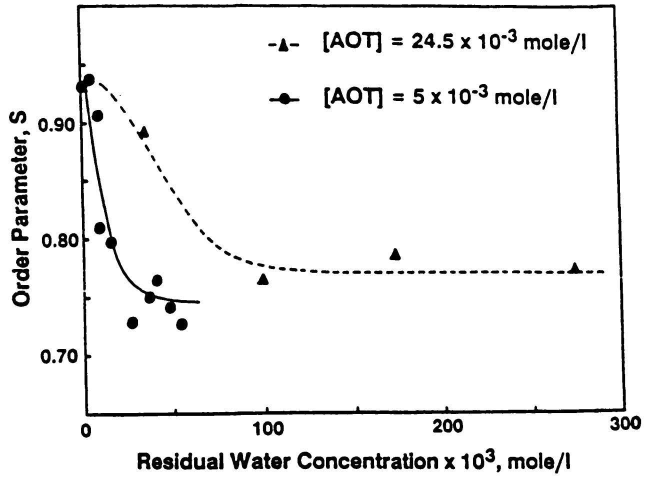

Figure 15 .Effect of water on the order parameter, S, calculated from the ESR spectra of 7-doxyl stearic acid coadsorbed with Aerosol OT at the alumina/cyclohexane interface.(Adapted from ref. 28) considering the structural reorganization of the complex adsorbed layer when water is present at the interface. At low water concentrations, water molecules bind the carboxylic groups of the stearic acid molecules and the polar groups of Aerosol OT, directly to the hydroxyl groups of the alumina surface. This binding limits the ability of the probe to move within the adsorbed layer and is consistent with a model of localized adsorption where the adsorbed molecules have limited degrees of freedom. As the water adsorption density increases, the carboxylic groups of the probe molecules interact with water molecules not bound directly to the hydroxyl groups of the mineral surface. Similar interactions between the polar groups of Aerosol OT and water molecules are most likely, as a result of which the adsorbed layer can become loosely bound to the mineral surface. The molecular diffusion limited by the binding of the surfactant molecules at low water concentrations thus increases markedly as water adsorbs on particles.

Oleate on Dolomite and Francolite. FTIR spectroscopy in the ATR mode has been employed to investigate the surface precipitation phenomenon during the adsorption of oleate on Francolite and Dolomite. Near total flotation of the individual minerals could be achieved with oleate collector, a reagent used to induce surface hydrophobicity. Based on that, the flotation of binary mixtures attempted under restricted conditions of pH deemed to provide excellent selectivity based on the data for individual minerals. It was conjectured that the loss in selectivity of flotation of the above mixed minerals could be due to the alteration of the surface properties of the minerals due to the interactions between dissolved mineral species and the oleate resulting in surface and bulk precipitation. An FTIR experiment was performed in a Harrick's ATR liquid prism assembly with dolomite/oleate system. Dolomite shows a strong C=O stretching frequency of the carbonate group at 1488 cm^{-1}. Figure 16 shows the FTIR spectra of dolomite mixed with oleate at various concentrations of the latter. The dolomite peak is seen to diminish with increasing oleate concentration and a new peak characteristic of the oleate appears at a lower frequency. The decrease in the dolomite peak is attributed to direct oleate adsorption, formation of Ca and Mg oleate precipitates on the mineral surface and/or to the masking of carbonate groups on the mineral surface. This observation was in agreement with the results from depletion isotherms of the oleate and the dependence on the concentrations of the dissolved Ca^{2+} and Mg^{2+} species at the interface and in solution *(30)*.

Mixed Surfactants on Alumina. Most of the practical situations related to industrial processes such as enhanced oil recovery deal with mixed surfactant systems *(31)* arising either as contaminants or as deliberately added components to tune the surface properties. Mixed surfactants are considerably less expensive and readily available than pure components. Moreover, in mixed systems comprising ionic and non-ionic surfactants, the problem of precipitation is abated and greater salt tolerance is achieved.

While the solution properties of mixed surfactant systems have been addressed recently *(32)*, the nature of aggregation of mixed suractants on solids has been only scantly investigated. We have attempted recently to elucidate the microstructural properties of adsorbed layers of mixed surfactants on solids like alumina, silica and kaolinite by spectroscopic techniques to supplement the information gathered from

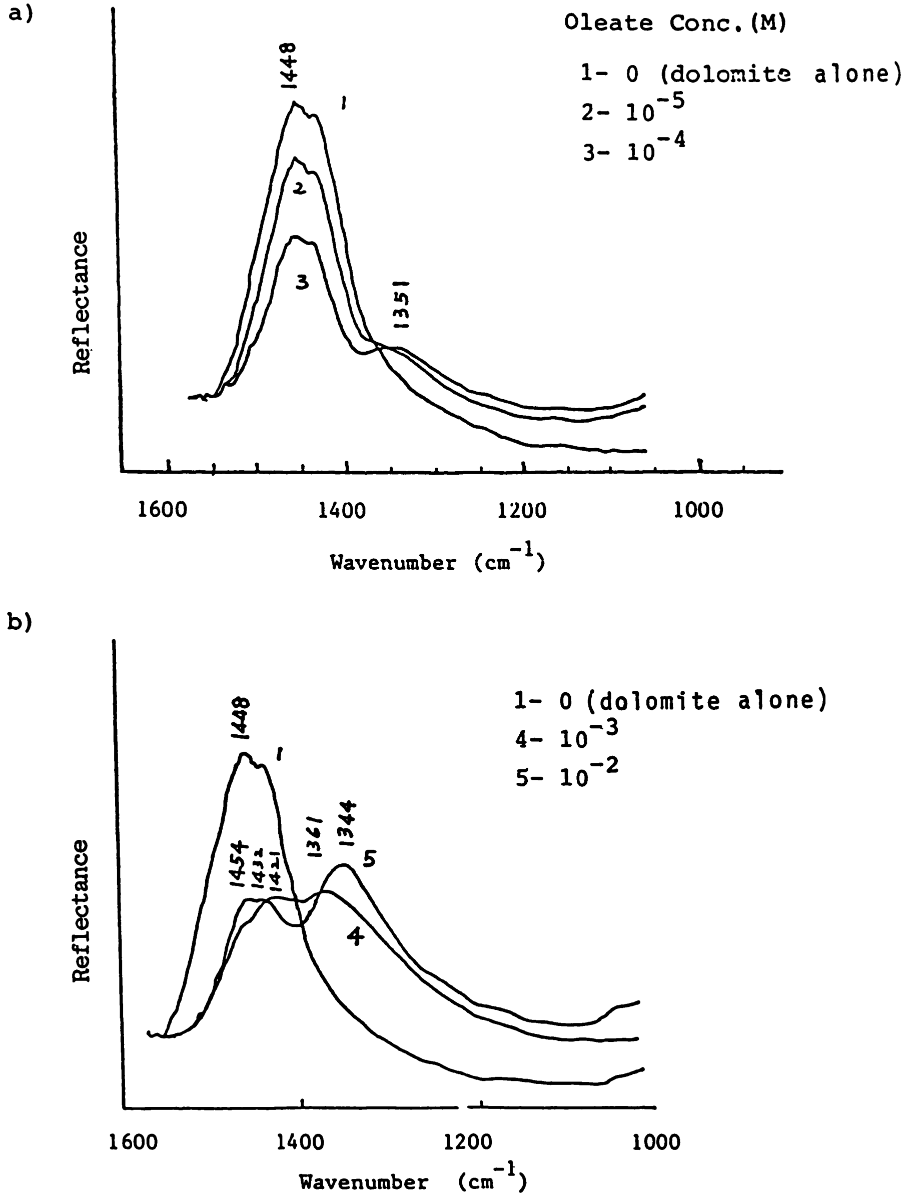

Figure 16. ATR spectra of dolomite slurry at different concentrations of oleate; (a) low concentration region, (b) high concentration region.

adsorption, microcalorimetry and allied studies *(33)*. The microstructures of sodium dodecylsulfate and dodecyloxyheptaethoxyl ethyl alcohol ($C_{12}EO_8$) layers on alumina were probed with pyrene. The polarity parameter measured at various points on the isotherm is shown in Figure 17. It is seen that the polarity parameter is nearly a constant along the isotherm, while the value in dodecylsulfate micelles is lower than that obtained for it at the alumina-water interface. This throws light on the compact nature of the adsorbed layers. Pyrene probing of the $C_9\phi EO_{40}$ (nonylbenzene derivative) aggregates on silica showed that no hydrophobic aggregates were formed at the solid-liquid interface.

Polymer/Solid Systems

Polymer Conformation in the Adsorbed State. Polymers can exist in different conformations both in solution and in the adsorbed state. The adsorption of polymeric materials onto solid surfaces can be quite different from the adsorption of small molecules in that the polymer adsorption is greatly influenced by the multifunctional groups that it possesses *(34)*. This stems from the widely varying sizes and configurations available for the polymer. In addition, macromolecules usually possess many functional groups each having a potential to adsorb on one or more given surfaces.

Among the polymeric materials, polyelectrolytes are the most important because of their participation in many biological processes and their utility in processes like dispersion, flocculation, adhesion and rheology. Polyacrylic acid (PAA) is chosen here as a model polyelectrolyte to gain insight into the adsorption behavior of polyelectrolytes in general. Such an understanding is important in acquiring effective control over processes of colloidal stabilization and flocculation.

Polyacrylic acid can exist in different conformations depending on the solvent, pH, and ionic strength conditions *(35)*. Such a flexibility also influences its adsorption characteristics on solids and in turn affects the subsequent suspension behavior. Using a fluorescent labelled polymer and by monitoring the extent of excimer formation it was shown that the polymer at the interface could have a stretched or coiled conformation at the interface depending on the pH. The rationale behind the use of this technique is the observation that the extent of excimer formation which depends on the interaction of an excited state pyrene pendant group of the polymer with another pyrene group in the ground state and therefore depends on the polymer conformation. This may be understood by examining Figure18 which shows that at low pH, there is a better probability for intramolecular excimer formation between pyrene groups resulting from a favorable coiled conformation. Similarly a low probability for the excimer formation at high pH may be understood as a consequence of the repulsion between the highly ionized carboxylate groups in the polymer and the subsequent stretching of the polymer chain. This difference is reflected in the nature of their fluorescence spectra as seen in Figure 19 where at low pH the intensity due to the excimer emission is larger than at higher pH.

We have also performed a detailed investigation on the flocculation behavior of alumina particles with and without added polymer under fixed and shifted pH conditions. The polymer conformation was shown to be a controlling factor of the

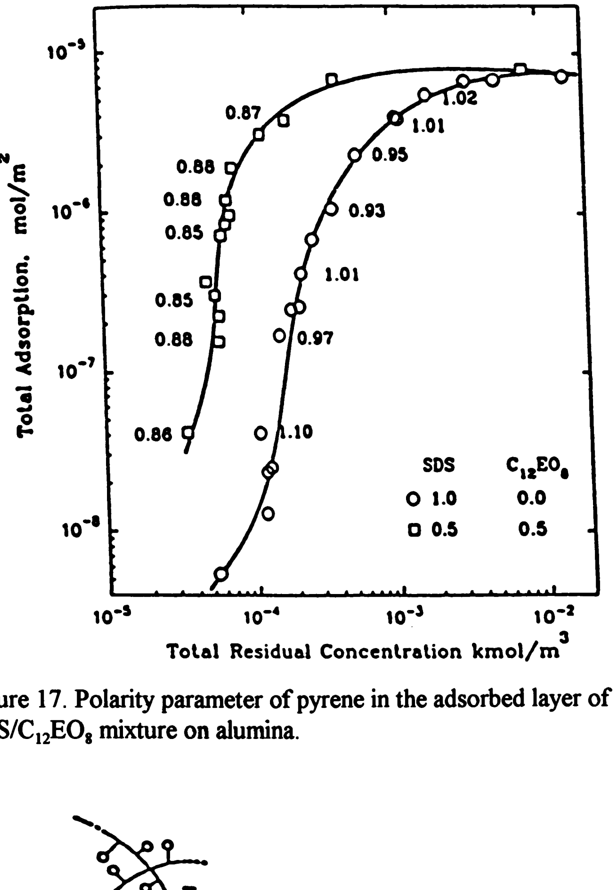

Figure 17. Polarity parameter of pyrene in the adsorbed layer of 1:1 $SDS/C_{12}EO_8$ mixture on alumina.

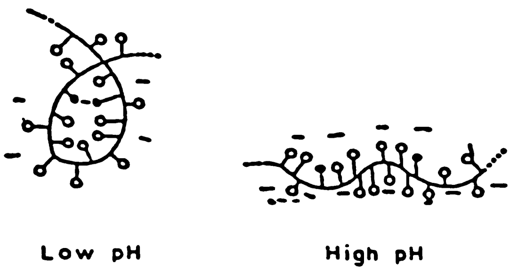

Figure 18. Schematic representation of the conformation of polyacrylic acid at different pH values. (Adapted from ref. 36)

flocculation process in this case. The results of fluorescence emission studies using pyrene labelled PAA in the adsorbed state under shifted pH conditions i.e. adsorbing the polymer at a fixed pH and then changing the pH to a desired value showed that the excimer fluorescence emission intensity of the polymer at the solid/liquid interface after adsorption at high pH values remains the same even after changing the pH to lower values (Figure 20). From this observation the variation of polyacrylic acid conformation at the solid-liquid interface under shifted pH conditions may be represented as shown in Figure 21. It may be inferred that the polymer conformation at a given pH may be manipulated by controlling the adsorption conditions *(36)*. In contrast, the polymer adsorbed in the coiled form at low pH did stretch out when the pH was increased.

Dapral at Solid-Liquid Interface. Hydrophobically modified polymers have been increasingly used nowadays to increase the viscosity and elasticity of solutions as they can undergo interesting intramolecular and intermolecular association by hydrophobic interactions. These polymers are also promising as steric stabilizers as well as flocculating agents for hydrophilic and hydrophobic surfaces in both aqueous and non-aqueous media. We have studied the stabilization effects of Dapral GE 202 (maleic anhydride α-olefin copolymer with both hydrophobic and hydrophilic side chains) which is a hydrophobically modified comb-type polymer whose structure is as indicated in Figure 22. The observed changes in suspension stability cannot be explained in terms of the corresponding changes in electrokinetic properties *(37)*. Fluorescence studies were conducted using free pyrene as the probe and the polarity parameter measured at different levels of Dapral adsorption (Figure 23). At low concentrations the I_3/I_1 value for pyrene is similar to that in water but with increase in concentration this increases reaching upto a value of 1 at a Dapral concentration of 500 ppm. These suggest the formation of aggregates at the interface with the creation of hydrophobic microdomains into which the pyrene partitions preferentially. Such an aggregation can explain the continued adsorption of Dapral even after the reversal of surface charge. The formation of such hydrophobic aggregates would now render the surfaces hydrophilic since the ethylene oxide chains will be dangling into solution and stabilization of the suspension in this case is attributed to a combination of electrostatic repulsion and steric hindrance of the adsorbed molecules.

Fluorescence spectroscopy was also used to detect the orientation of Dapral on alumina particles in non-aqueous media*(38)*. 7-dimethylamino-4-methyl coumarin which is a relatively hydrophilic molecule was used to probe the adsorbed layer of DAPRAL at the alumina/toluene interface. The spectrum for the probe in the absence of DAPRAL is similar to that obtained in water solution (maximum emission at 470 nm, Figure 24). This is attributed to the hydrophilicity of the bare alumina surface. With an increase in polymer adsorption, the maximum wavelength shifts towards the shorter wavelength range reaching the value for hydrocarbon solvents (390 nm) at 500 mg/l of DAPRAL (Figure 25). This observation supports the mechanism of polymer adsorption through the interaction between the ethylene oxide chains and the hydroxyl groups on the alumina surface with the hydrocarbon side chains dangling towards the solution and the alumina particles eventually fully covered to become totally hydrophobic. This is supported by the fact that the alumina suspensions are stabilized significantly by the adsorption of DAPRAL.

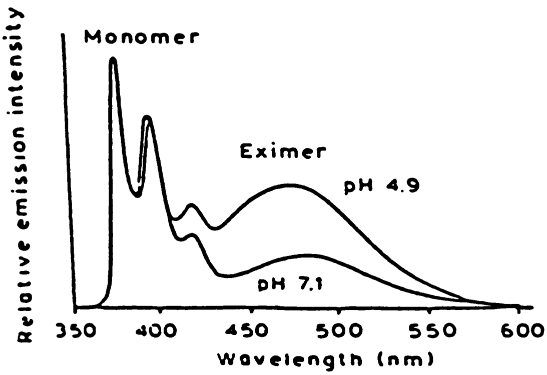

Figure 19. Schematic representation of the correlation of the extent of excimer formation and intrastrand coiling of pyrene labeled polyacrylic acid. (Adapted from ref. 36)

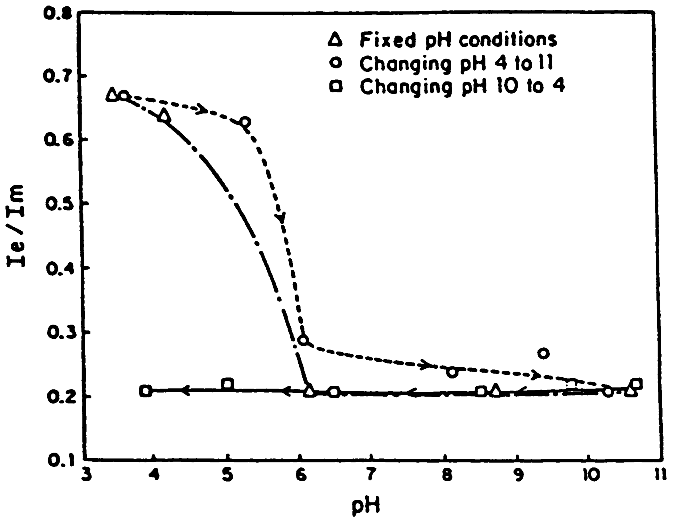

Figure 20. Excimer to monomer ratio, I_e/I_m for alumina with 20 ppm PAA as a function of final pH under changing pH conditions.

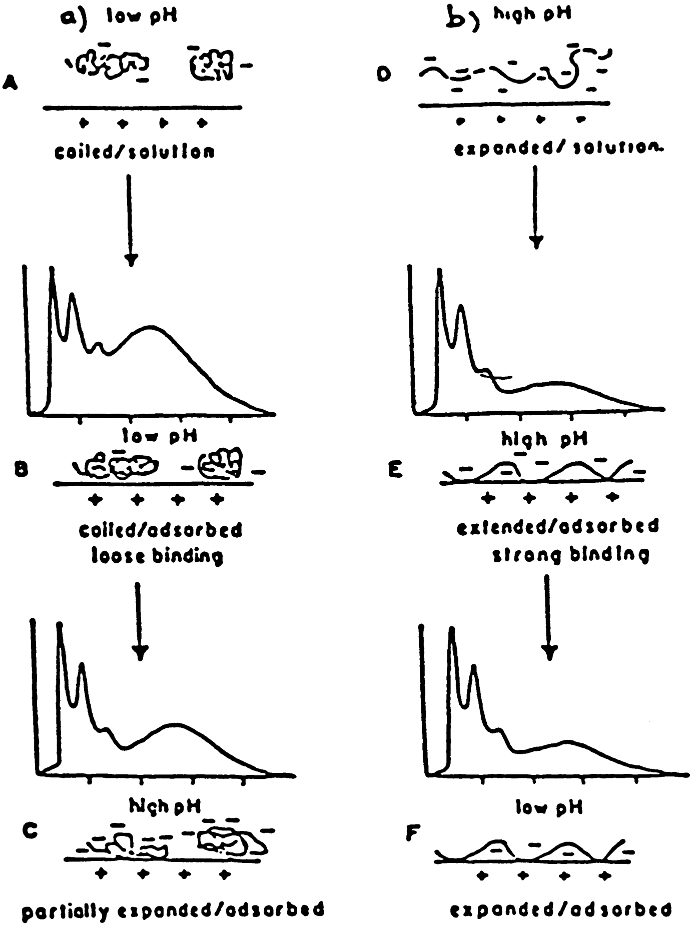
a) low pH
A
coiled/solution
low pH
B
coiled/adsorbed
loose binding
high pH
C
partially expanded/adsorbed
b) high pH
D
expanded/solution
high pH
E
extended/adsorbed
strong binding
low pH
F
expanded/adsorbed

Figure 21. Schematic representationof the adsorption process of pyrene-labeled polyacrylic acid on alumina A) At low pH polymer is coiled in solution which leads to B) adsorption in coiled form. C) Subsequent raising of the pH causes some expansion of the polymer D) Polymer at high pH in solution is extended and binds E) strongly to the surface in this conformation F) Subsequent lowering of pH does not allow for sufficient intrastrand interactions for coiling to occur. (Adapted from ref. 36)

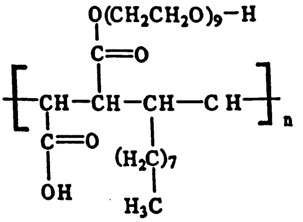

$$\left[-\underset{\underset{OH}{|}}{\underset{C=O}{|}}{CH}-\overset{\overset{O(CH_2CH_2O)_9-H}{|}}{\overset{C=O}{|}}{CH}-\underset{\underset{H_3C}{|}}{\underset{(H_2C)_7}{|}}{CH}-CH-\right]_n$$

Figure 22. Molecular structure of DAPRAL.

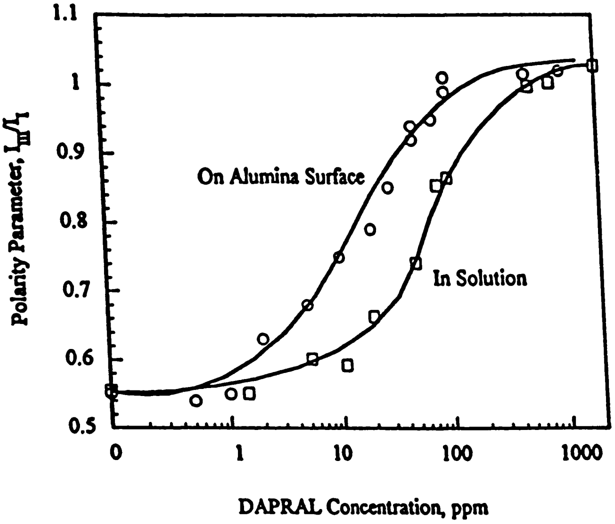

Figure 23. Aggregation of Dapral in solution and at the alumina-water interface (pH 8):(a) in solution, (b) at the interface. (Reproduced with permission from ref. 38. Copyright 1994, Elsevier)

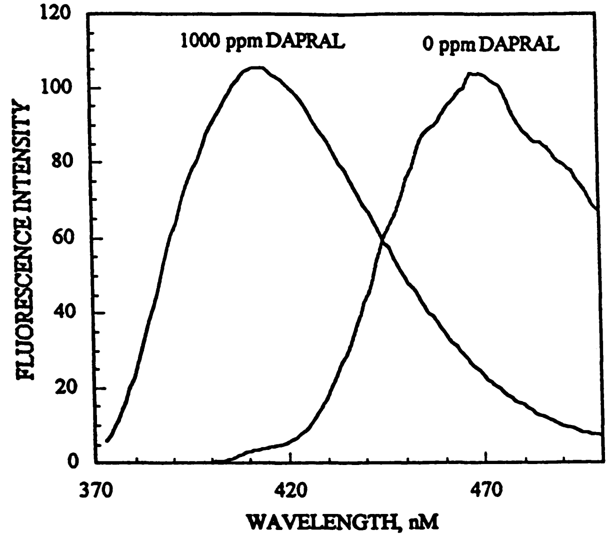

Figure 24. Fluorescence spectrum of 7-amino 4-methyl coumarin at the alumina toluene interface in the presence of 0 ppm DAPRAL and 1000 ppm DAPRAL. (Reproduced with permission from ref. 38. Copyright 1994, Elsevier)

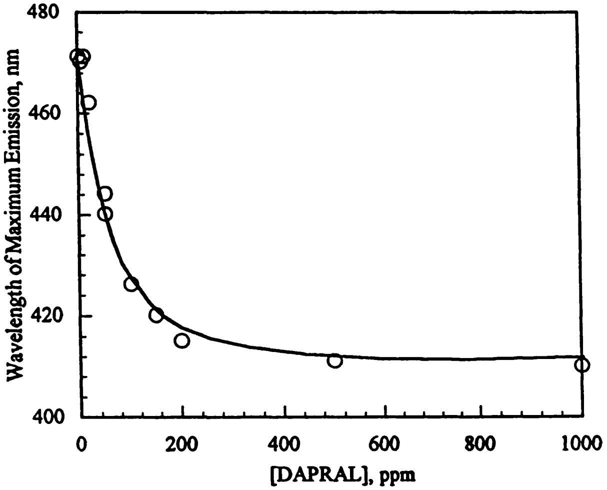

Figure 25. Diagaram illustrating the shift in maximum emission wavelength of coumarin at the alumina-toluene interface with adsorption of DAPRAL. (Reproduced with permission from ref. 38. Copyright 1994, Elsevier)

Polymer/Surfactant/Solid System

Polymer-Surfactant Aggregates at an Interface. Investigations on polymer-surfactant aggregates are of importance owing to the use of these mixed systems in areas related to enhanced oil recovery, colloidal stability, flotation and flocculation. The conformation of polyethylene oxide (PEO) mixed with sodium dodecysulfate at alumina-water interface was measured using pyrene-labeled polymer. Figure 26 shows the I_e/I_m values of the PyPEO on alumina surface preadsorbed with SDS. Interestingly, the conformation of the co-adsorbed PEO was markedly influenced as a result of its interaction with SDS *(39)*. Thus PEO could be force-adsorbed onto alumina. This experiment demonstrates the potential of fluorescence spectroscopy to investigate the conformational aspects of polymers and surfactants adsorbed together at a solid-liquid interface.

Concluding Remarks

A new insight has been obtained on the structure and evolution of surfactant and polymer aggregates at solid-liquid interfaces both in aqueous and non-aqueous media by the application of spectroscopic and classical methods. These findings have been correlated with the performance parameters of the individual systems. The aggregation number of sodium dodecylsulfate on alumina was determined at various points of the solloid evolution and the variation of the micro-viscosity within the solloid layer was determined along the isotherm using ESR and Raman spectroscopy. Fluorescence spectroscopic studies also indicate that steric hindrance to packing in the adsorbed layers controls the solloid formation of the alkyl xylenesulfonates. Also infrared spectroscopy has been used to study the adsorption of surfactants such as oleate on mineral surfaces. Pyrene probing revealed the solloidal structure of mixed surfactants. The effect of pH dependent conformational equilibria of polyacrylic acid on the adsorption process and its implications to flocculation have been explored to suggest reasonable conformational structures for the polymer solloid. The spectroscopic techniques were also useful in studying adsorption processes in non-aqueous media. Thus, the role of water in controlling the dispersion properties of alumina dispersed in cyclohexane by increasing the lateral diffusion of the adsorbed surfactant molecules was depicted using ESR technique. A rare insight has been gained on the stabilization of solids by the hydrophobically modified polymer Dapral in aqueous and non-aqueous media. Furthermore, spectroscopic methods were adopted to interrogate more complex systems consisting of surfactants and polymers. It is clear that there is a variety of techniques now becoming available to examine structures insitu at levels smaller than ever before and one can obtain valuable equilibrium and kinetic information on a molecular level by adapting these techniques suitably.

Acknowledgments. We wish to acknowledge the financial support from National Science Foundation, Department of Energy, Unilever Research and Nalco.

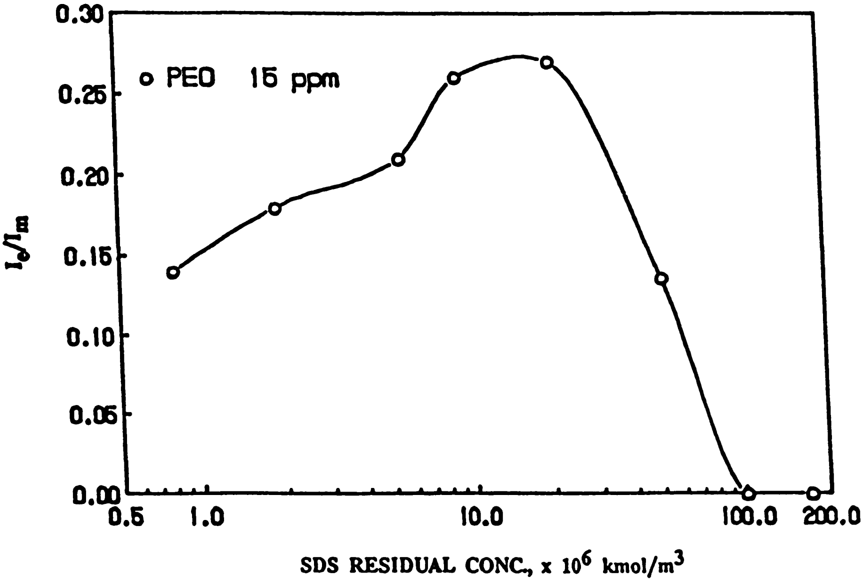

Figure 26. PEO conformation on the alumina surface preadsorbed with SDS expressed as coiling index. (Reproduced with permission from ref. 39. Copyright 1990, John Wiley & Sons)

Literature Cited

1. Hanna, H.S.; and Somasundaran, P., In D.O. Shah and R.S. Scheter (Eds.), Improved Oil Recovery by Surfactant and Polymer Flooding, Academic Press, New York, **1977**, p 253.

2. Lakowicz, J.R.; "Principles of Fluorescence Spectroscopy", Plenum Press, New York, **1983**.

3. Thomas, J.K.; "The Chemistry of Excitation at Interfaces", *American Chemical Society Monograph*, **1984**.

4. Turro, N.J.; Cox, G.S.; Paczkowski, M.A.; "Photochemistry in Micelles", *Topics in Current Chemistry*, **1985**, *129*, p 57

5. Demas, J.N.; "Excited State Lifetime Measurements", Academic Press, New York, **1983.**

6. Wertz, J.H.; Bolton, J.R.; "Electron Spin Resonance - Elementary Theory and Practical Applications", Chapman and Hall, New York, **1986** .

7. Ranby, B.; "ESR Spectroscopy in Polymer Research", Rabek and Springer (eds), Berlin, **1977**.

8. Francesca Ottaviani. M.; Baglloni. P.; and Martini. G.; *J. Phys. Chem.*, **1983,** *87,* p 3146.

9. Lim. Y.Y.; and Fendler. J.H.; *J. Am. Chem. Soc.*, **1978**, *24*, p 7490.

10. Krishnakumar, S.; Somasundaran, P.; *J. Coll. & Int. Sci.*, **1994,** *162*, p 425.

11. Barelli, A.; and Eicke, H. F.; *Langmuir*, **1986**, *2*, p 780.

12. "Laboratory Methods in Vibrational Spectroscopy", Wills, H.A.; vander Maas, J.H.; Miller, R.C.G.;(Eds), John Wiley & Sons, New York, **1987**.

13. Kellar, J.J.; Cross, W.M.; Miller, J.D.; *Applied Spectroscopy*, **1990**, *44*, p 1508.

14. Kunjappu, J.T.; Somasundaran, P.; *J. Indian Chem. Soc.*, **1989**, *66*, p 639.

15. Somasundaran, P.; PhD Thesis, University of California, Berkeley, **1964**.

16. Somasundaran, P.; Feurstenau, D.W.; *J. Phys. Chem.*, **1966**, *70*, p 90.

17. Somasundaran, P.; Kunjappu, J.T.; *Colloids & Surfaces*, **1989**, *37*, p 245.

18. Harwell, J.H.; Bitting, D.; *Langmuir*, **1987**, *3* , p 500.

19. Gaudin, A.M.; Feurstenau, D.W.; *Min. Eng.*, **1955**, *7*, p 66.

20. Somasundaran, P.; Chandar, P.; Turro, N.J.; , *J. Coll. & Interface Sci.*, **1987**, *117*, p 31.

21. Somasundaran, P.; Chandar, P.; Turro, N.J.; *Colloids & Surfaces*, **1986**, *20*, p 145.

22. Somasundaran, P.; Chandar, P.; Chari. K.; *Colloids & Surfaces*, **1983**, *8*, p 121.

23. Waterman, K.C.; Turro, N.J.; Chandar, P.; Somasundaran, P.; *J. Phys. Chem.*, **1986**, *90*, p 6829.

24. Chandar, P., Somasundaran, P.; Waterman, K.C.; Turro, N.J.; *J. Phys. Chem.*, **1986**, *91*, p 150.

25. Somasundaran, P.; Kunjappu, J.T. ; Kumar, C.V.; Turro, N.J.; Barton, J.K.; *Langmuir,* **1989**, *5*, p 215.

26. Sivakumar, A.; Somasundaran, P.; *Langmuir*, **1994,** *10*, p 131.

27. Malbrel, C.A.; D. Eng Sci. Thesis, Columbia University, **1991**

28. Malbrel, C.A.; Somasundaran, P.; *Langmuir*, **1992**, *8*, p 1285.

29. Krishnakumar, S.; Somasundaran, P.; *Langmuir*, **1994**, *10*, p 2786.

30. Xiao, L.; Viswanathan, K.V.; Somasundaran, P.; In Extractive Metallurgy and Material Science, S. Li (ed.), Changhsha, China, **1987**, p 110.

31. Harwell, J.H.; Scamehorn, J.F.; In Mixed Surfactant Systems, Ogino,K., Abe, M., (eds), Surfactant Science Series, Vol 33, Marcel Dekker, New York, **1993,** p 263.

32. Ogino, K.; Abe, M.; *J. Coll. & Interface . Sci.*, **1985**, *107*, p 509.

33. Sivakumar, A.; Somasundaran, P.; Thach, S.; *Colloids & Surfaces*, **1993**, *70*, p 69.

34. Morawetz, H.; "Macromolecules in Solution", John Wiley & Sons, New York, **1975**.

35. Arora, K.S.; Turro, N.J.; *J. Polymer Science*, **1987**, *25* , p 243.

36. Chandar, P.; Somasundaran, P.; Waterman, K.C.; Turro, N.J.; *Langmuir,* **1987**, *3* , p 298.

37. Somasundaran, P.; Li, C.; XiangYu ; *Colloids & Surfaces*, **1992**, *69*, p 155.

38. Somasundaran, P.; Xiang Yu; *Colloids & Surfaces*, **1994**, *89*, p 277.

39. Maltesh, C.; Somasundaran, P.; Ramachandran, R.; *J. Applied Polymer Science*, **1990**, *45*, p 329.

RECEIVED July 27, 1995

Downloaded by NORTH CAROLINA STATE UNIV on October 13, 2012 | http://pubs.acs.org
Publication Date: May 5, 1996 | doi: 10.1021/bk-1995-0615.ch008

Chapter 8

Adsorption of Polymer and Surfactant from Their Binary Mixtures on Alumina

Kunio Esumi

Department of Applied Chemistry and Institute of Colloid and Interface Science, Science University of Tokyo, Kagurazaka, Shinjuku-ku, Tokyo 162, Japan

The adsorption of water-soluble polymers and surfactants on positively charged alumina has been investigated. In the case of same charged adsorbates, such as sodium poly (styrenesulfonate) (PSS) and sodium dodecyl sulfate (SDS), the competitive adsorption between PSS and SDS on alumina occurs, where the adsorption strength of SDS is much greater than that of PSS. The adsorption from opposite charged adsorbates of PSS and hexadecyltrimethylammonium chloride (HTAC) shows enhancement of HTAC adsorption by PSS due to a formation of their complexes on alumina surface, which provides a lower micropolarity compared with those of respective adsorbates. In the case of neutral polymer and anionic surfactants, such as poly(vinylpyrrolidone) (PVP) and lithium dodecyl sulfate (LiDS), lithium perfluorooctanesulfonate (LiFOS), and sodium bis (2-ethylhexyl)sulfosuccinate(AOT), the adsorption of anionic surfactants enhances remarkably the adsorption of PVP at low surfactant concentrations due to a formation of PVP-surfactant complexes. However, at high surfactant concentrations, the adsorption of PVP decreases where the magnitude in the adsorption of PVP is still higher than that in the absence of the surfactants. In particular, the adsorption of PVP is most enhanced by the adsorption of AOT. In addition, the conformation of PVP adsorbed on alumina takes predominantly as train segments even in a wide range of PVP adsorption: the PVP-LiFOS system shows a larger train portion for PVP conformation in comparison with PVP-LiDS and PVP-AOT systems.

Interactions between polymers and surfactants in aqueous solutions have been intensively investigated by many techniques (1-3). The strength of interactions depends on the kinds of both polymer and surfactant. It has been shown that the binding of ionic surfactants to neutral polymers occurs mainly by hydrophobic interactions, while a combination of electrostatic and hydrophobic interactions is involved in the binding of oppositely charged polymers and surfactants.

Adsorption of polymers, on the other hand, has recently received much attention, both experimentally and theoretically (4-7). Adsorption and orientation of polymers and surfactants, however, have not been extensively studied at the solid/liquid interface (8-12), although it is important to the understanding of the mechanisms of stabilization and flocculation of dispersions and emulsions. It has been reported (9) that poly (vinyl alcohol) adsorption increased significantly in the presence of preadsorbed

0097–6156/95/0615–0138$12.00/0

cationic surfactant on silica at high pH, while at low pH the cationic surfactant adsorbed to a great extent in the presence of preadsorbed poly(vinyl alcohol). However, adequate information on the conformation of nonionic polymers adsorbed on particles in the presence of surfactants is not yet available, whereas the conformation of polymers alone adsorbed at the solid/liquid interface has been studied using many methods. These include small neutron scattering, neutron and X-ray reflectivity, NMR, ellipsometry, internal reflection spectroscopy, electron spin resonance(ESR), and various other techniques (7,13).

The objective of this paper was to investigate the interaction between polymers and surfactants on solid particles in aqueous solution. In addition, the conformation of polymers adsorbed on particles in the presence of surfactants was also investigated by ESR measurements. Five systems were studied as follows: sodium poly(styrene sulfonate) (PSS)-sodium dodecyl sulfate (SDS)-alumina (14), PSS-hexadecyltrimethyl ammonium chloride(HTAC)-alumina (15), poly(vinyl pyrrolidone)(PVP)-lithium dodecyl sulfate (LiDS), lithium perfluorooctane sulfonate (LiFOS)-alumina (16), and PVP-sodium bis(2-ethylhexyl)sulfosuccinate (AOT)-alumina (17).

Downloaded by NORTH CAROLINA STATE UNIV on October 13, 2012 | http://pubs.acs.org
Publication Date: May 5, 1996 | doi: 10.1021/bk-1995-0615.ch008

Experimental

Materials. PSS and PVP were obtained from Aldrich Chemical Co Inc., and Wako Chemical Ltd., where the former was purified by dialysis and the latter was used without further purification. The molecular weights of PSS and PVP were 10000 and 40000, respectively. The spin-labeled PVP was prepared (18) by polymerizing N-vinylpyrrolidone and allylamine using tert-butyl perbenzoate as initiator and ethanol as solvent, followed by a reaction with 4-isothiocyanato-2,2,6,6-tetramethylpiperidine-1-oxyl in dichloromethane at 40°C. The spin-labeled PVP thus obtained was purified with ethyl ether. The molar ratio of N-vinylpyrrolidone to allylamine in the spin-labeled PVP was about 100:3 as determined by NMR, and its molecular weight was about 16000 as determined by measurement of static light scattering.

SDS, LiDS, and LiFOS were synthesized in our laboratory and used after purification. HTAC was obtained from Tokyo Kasei Industries and purified with acetone. AOT supplied by Nikko Chemical Co. was purified as follows. AOT was dissolved in benzene and then water was added. After the sample was vigorously stirred, the water phase was eliminated. This procedure was repeated three times. Finally, AOT was obtained by evaporating the benzene solution. The purity of all the surfactants used was ascertained by the absence of a minimum in the surface tension-surfactant concentration curves.

α-Alumina of 99.995% purity was supplied by Showa Denkou K.K.. The particle diameter and specific surface area were 500 nm and 10.0 m^2g^{-1}, respectively.

Methods. The adsorption of surfactants and polymers on alumina was calculated by measuring their concentrations in solutions before and after adsorption at 25°C. All experiments were performed in glass vials with caps. The glass vials containing suspensions in the presence of 10 mmol dm^{-3} electrolyte were equilibrated by shaking 24 h in a 25°Cwater bath. After equilibration, the solids were separated by centrifugation and the supernatant was analyzed. The pH of the suspensions was adjusted to 3.5.

Measurements. The concentrations of PSS and spin-labeled PVP were determined by means of UV-Vis spectrophotomety and ESR, and the concentrations of the surfactants by the Abott method(19). The other measurements have been described in detail elsewhere (14,15).

Downloaded by NORTH CAROLINA STATE UNIV on October 13, 2012 | http://pubs.acs.org
Publication Date: May 5, 1996 | doi: 10.1021/bk-1995-0615.ch008

Results and Discussion

PSS-SDS-alumina system

The adsorption of PSS alone increased sharply and then reached a plateau with increasing PSS concentration, indicating a high affinity between PSS and the alumina surface. This adsorption mainly occurs due to an electrostatic attraction force since PSS is negatively charged and alumina surface is positively charged (14).

Figure 1 shows the adsorption of PSS and SDS on alumina from the mixed solutions at a fixed initial concentration of PSS (0.4 g dm^{-3}) as a function of SDS concentration. The adsorption isotherm of SDS obtained from the solutions in the presence of PSS is obviously different from that obtained in the absence of PSS. In the presence of PSS there is a considerable decrease in the amount of SDS adsorbed at low SDS concentrations. However, at 5 mmol dm^{-3} SDS or above the amount of SDS adsorbed is almost the same in the presence or absence of PSS. The adsorbed amount of PSS, on the other hand, decreased linearly until 5 mmol dm^{-3} SDS and then became almost zero. This suggests that the adsorbed PSS is replaced by SDS with an increase of SDS concentration.

Figure 2 shows the adsorption of PSS and SDS from the mixed solutions at a fixed initial concentration of SDS (5 mmol dm^{-3}) as a function of PSS concentration. The adsorbed amount of PSS increased, while that of SDS remained constant with increasing PSS concentration. The adsorbed amount of SDS corresponds to bilayer adsorption of SDS on alumina. Both figures suggest that the adsorption of SDS on alumina is much stronger than that of PSS. It is noteworthy that for both the systems the dispersion stability of alumina is good and the z potential of alumina ranges between -50 and -55 mV.

The microenvironmental properties of the adsorbed layer of SDS and PSS were estimated by using fluorescence and ESR techniques. It is well known (20) that the maximum fluorescence wavelength of pyrene-1-carboxaldehyde (PCA) is very sensitive to solvent polarity; the maximum fluorescence wavelegnth decreases with decreasing polarity of the solvents. This concept was applied to estimate polarity in the adsorbed layer on alumina. Figure 3 shows that in the presence of PSS (0.4 g dm^{-3}) the maximum fluorescence wavelength of PCA incorporated in the adsorbed layer shifts gradually from 464 nm to 450 nm, while that in the supernatant solutions shifts gradually and becomes constant (458 nm) at 7 mmol dm^{-3} SDS or above. This indicates that the environment sensed by PCA in the adsorbed layer of PSS and SDS is less polar than that in the adsorbed layer of PSS alone. Further, the change in the maximum fluorescence wavelength of PCA in the adsorbed layer corresponds to the ratio of the adsorbed amounts of SDS and PSS: The maximum fluorescence wavelength of PCA decreases with decreasing ratio of PSS to SDS. This result can be easily understood in that SDS is strongly oriented on the positively charged alumina surface with its hydrophobic chain to aqueous solution, whereas PSS is less packed on the alumina due to an intra-repulsion force between negatively charged groups of PSS. This may lead to a different compactness between SDS and PSS in the adsorbed layer on alumina. On the other hand, in the presence of SDS (5 mmol dm^{-3}), the maximum fluorescence wavelength of PCA in the adsorbed layer was predominantly reflected by the SDS adsorbed layer.

The microviscosity of the adsorbed layer was also estimated using 2,2,6,6-tetramethylpiperidinyl-1-oxy (TEMPO). Generally, an isotropic three-line spectrum of TEMPO is affected markedly with an adsorbed layer and relative anisotropy in the ESR spectra can be related to the rotational mobility of TEMPO (21). The rotational mobility is proportional to the microviscosity in which the probe is located. Figure 4

Downloaded by NORTH CAROLINA STATE UNIV on October 13, 2012 | http://pubs.acs.org
Publication Date: May 5, 1996 | doi: 10.1021/bk-1995-0615.ch008

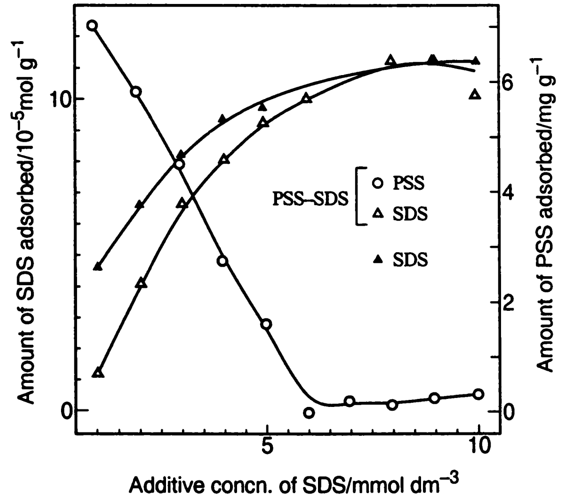

Figure 1 Adsorption of PSS and SDS on alumina from their mixtures; fixed initial concentration of PSS, 0.4 g dm^{-3}.

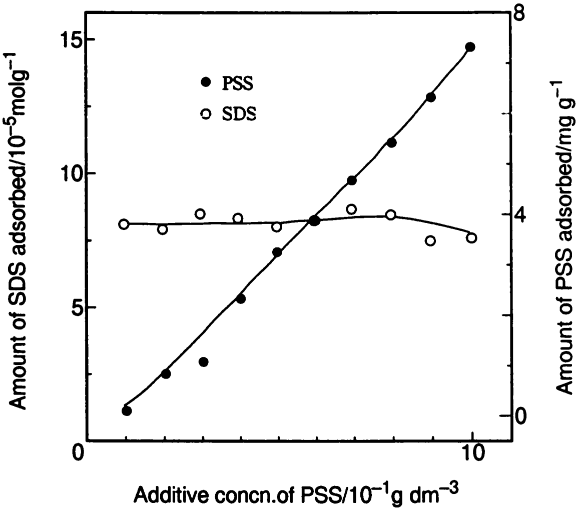

Figure 2 Adsorption of PSS and SDS on alumina from their mixtures; fixed initial concentration of SDS, 5 mmol dm^{-3}.

In Surfactant Adsorption and Surface Solubilization; Sharma, R.;
ACS Symposium Series; American Chemical Society: Washington, DC, 1996.

Downloaded by NORTH CAROLINA STATE UNIV on October 13, 2012 | http://pubs.acs.org
Publication Date: May 5, 1996 | doi: 10.1021/bk-1995-0615.ch008

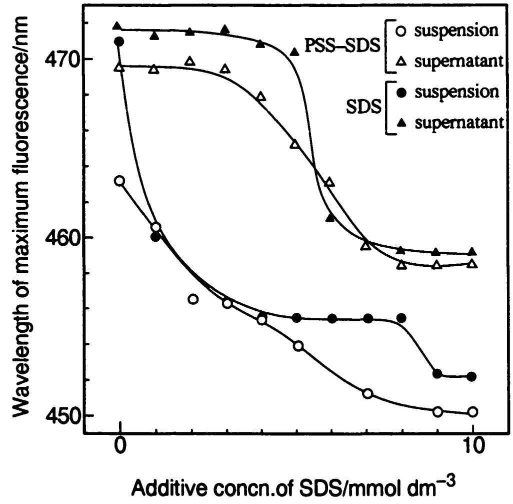

Figure 3 Changes in maximum fluorescence wavelength of PCA for PSS-SDS-alumina system; fixed initial concentration of PSS, 0.4 g dm^{-3}.

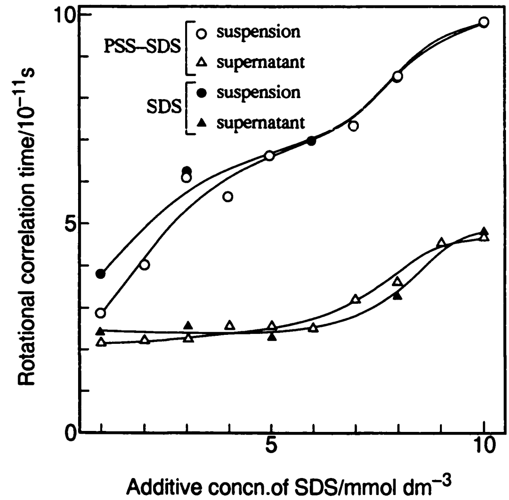

Figure 4 Changes in rotational correlation time of TEMPO for PSS-SDS-alumina system; fixed initial concentration of PSS, 0.4 g dm^{-3}.

shows that in the presence of PSS (0.4 g dm^{-3}) the rotational correlation time of TEMPO in the adsorbed layer increases gradually with an increase of SDS concentration. The fact (22) that most of the TEMPO solubilized in the micelles is located at the micelle-water interface would suggest that TEMPO resides in high polarity sites in the adsorbed layer of SDS and PSS on alumina. The feature in the rotational correlation time of TEMPO against SDS concentration is very similar to that of PCA. It seems likely that TEMPO molecules reside mainly at the polar region of the adsorbed layer of SDS and PSS and the microviscosity sensed by TEMPO is significantly affected by the adsorbed amount of SDS. Actually, in the presence of SDS (5 mmol dm^{-3}) the rotational correlation time of TEMPO is hardly altered, indicating that this result is also reflected by the SDS adsorption.

Downloaded by NORTH CAROLINA STATE UNIV on October 13, 2012 | http://pubs.acs.org
Publication Date: May 5, 1996 | doi: 10.1021/bk-1995-0615.ch008

PSS-HTAC-alumina system

When PSS and HTAC were mixed in aqueous solutions, precipitation often occurred due to formation of a complex by hydrophobic as well as electrostatic attractive forces between PSS and HTAC. In this study, an adsorption experiment was done where the mixed aqueous solutions showed no precipitation.

Figure 5 shows the adsorption of PSS and HTAC on alumina from the mixed solutions at a fixed initial concentration of PSS (0.4 g dm^{-3}). The adsorbed amount of PSS increased gradually, while that of HTAC increased above some concentration of HTAC. A similar result has been observed on adsorption of oppositely charged surfactants on solids (23-25). In the absence of PSS, the adsorption of HTAC is small on alumina because of an electrostatic repulsion force between positively charged HTA^+ and positively charged sites on alumina. On the other hand, since PSS and HTAC can form a complex due to an electrostatic attraction force between oppositely charged PSS and HTAC in aqueous solution and a hydrophobic force between PSS and HTAC, it is reasonable to assume that a similar complex of PSS and HTAC forms on the surface of alumina. In particular, above 10 mmol dm^{-3} HTAC, a formation of the complex on the alumina surface occurs remarkably. This adsorption may influence microenvironmental properties in the adsorbed layer.

The maximum fluorescence wavelength of PCA in the adsorbed layer of PSS and HTAC shifted from 464 nm to 445 nm with an increase of HTAC concentration (Fig.6). This low micropolarity may be due to a great compactness of the complex between PSS and HTAC which corresponds to the coiling of PSS chains with HTAC, since formation of the PSS-cationic complex accompanying coiling of PSS has been confirmed from viscosity and fluorescence measurements (26,27).

The microviscosity sensed by TEMPO in the PSS-HTAC adsorbed layer on alumina was almost the same as that in the supernatant solutions. A similar feature was observed for the microviscosity in the HTAC adsorbed layer alone. These results indicate that TEMPO molecules reside at adsorbed HTAC molecules or in solution, as the microviscosity scarcely changes.

In addition, from the comparison in the adsorption of PSS-HTAC and PSS-cationic fluorocarbon surfactant (28) on alumina, it has been found that the adsorption of PSS is appreciably greater in PSS-HTAC system than in PSS-cationic fluorocarbon surfactant system, while the adsorption of HTAC is almost the same as that of the cationic fluorocarbon surfactant.

PVP-LiDS, LiFOS-alumina system

Figures 7 and 8 show the adsorption of LiDS, LiFOS and PVP on alumina from their mixed aqueous solutions at fixed initial concentrations of PVP (0.2 and 0.5 g dm^{-3}) as a function of the surfactant concentration. In both systems, the amount of PVP

Downloaded by NORTH CAROLINA STATE UNIV on October 13, 2012 | http://pubs.acs.org
Publication Date: May 5, 1996 | doi: 10.1021/bk-1995-0615.ch008

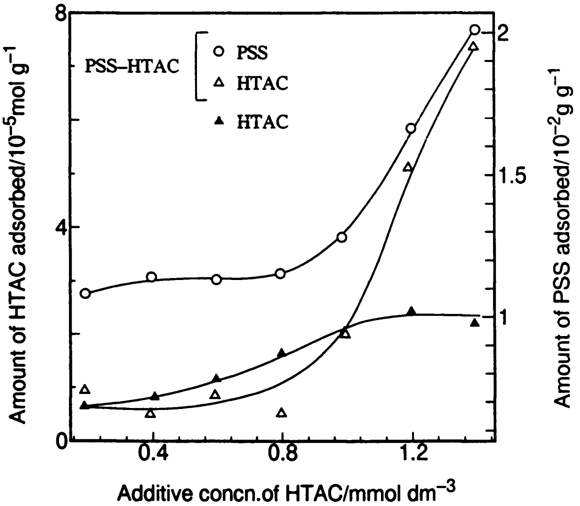

Figure 5 Adsorption of PSS and HTAC on alumina from HTAC/PSS-HTAC mixtures; fixed initial concentration of PSS, 0.4 g dm^{-3}.

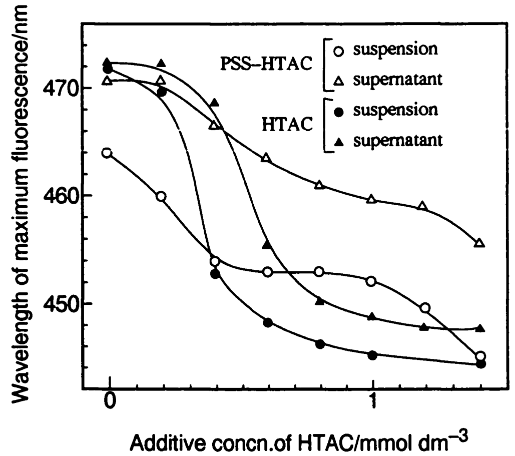

Figure 6 Changes in maximum fluorescence wavelength of PCA for PSS-HTAC-alumina system; fixed initial concentration of PSS, 0.4 g dm^{-3}.

Downloaded by NORTH CAROLINA STATE UNIV on October 13, 2012 | http://pubs.acs.org
Publication Date: May 5, 1996 | doi: 10.1021/bk-1995-0615.ch008

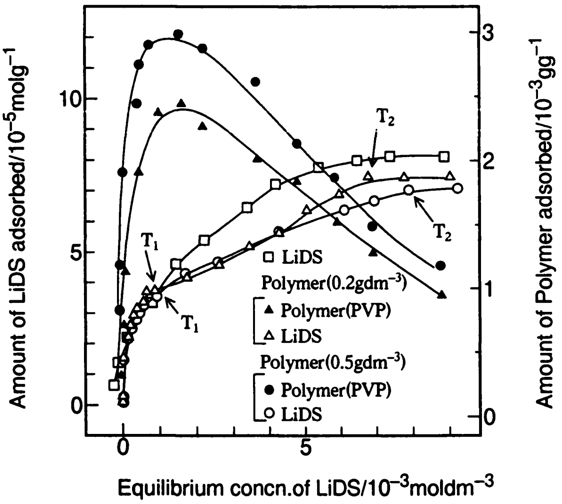

Figure 7 Adsorption of PVP and LiDS on alumina from their mixtures; fixed initial concentrations of PVP, 0.2 and 0.5 g dm^{-3}.

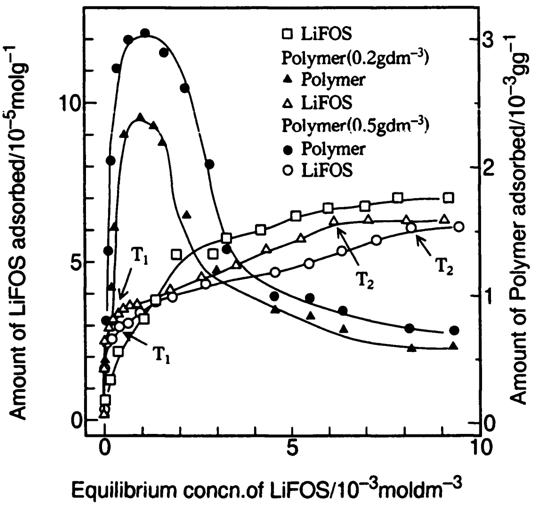

Figure 8 Adsorption of PVP and LiFOS on alumina from their mixtures; fixed initial concentrations of PVP, 0.2 and 0.5 g dm^{-3}.

adsorbed increased markedly with the surfactant concentration and showed a maximum, then decreased. On the other hand, the adsorption of the surfactant also increased with the surfactant concentration and reached a plateau in the absence of PVP, whereas in the presence of PVP the adsorbed amount of the surfactant was less compared with that of the respective surfactants alone. These results can be explained by a theory (11) that PVP-surfactant complexes are formed on alumina. Since it is known (29,30) that PVP and an anionic surfactant can form a polyelectrolyte-like complex by hydrophobic interaction in aqueous solution, it is postulated that the same interaction takes place and a type of surface complex of PVP and surfactant forms at the solid/liquid interface. The anionic surfactant (below the critical micelle concentration) adsorbs much faster on the alumina surface than PVP due to its smaller size and due to the electrostatic attraction force between negatively charged hydrophilic groups of the surfactant and positively charged sites on alumina. The hydrophobic chain of the surfactant extends toward the aqueous solution. Then, PVP attaches to the hydrophobic chain of the adsorbed layer of the anionic surfactant. This model also applies to surfactant concentrations greater than their cmcs, but instead of a bilayer of PVP-surfactant attachments, there might also be patches of hemimicelles to which PVP attaches. As a result, PVP and the surfactant adsorbed on alumina are able to combine with each other by hydrophobic binding, so that more PVP is adsorbed. With increasing concentration of the anionic surfactant, the adsorption of PVP rapidly decreases because PVP-anionic surfactant complexes formed in the bulk are relatively surface inactive and scarcely adsorb at the alumina/solution interface. In addition, the formation of surfactant bilayer on alumina may also prevent the formation of PVP-anionic surfactant complex on alumina. It is interesting to note that at the maximum adsorption of PVP, the amounts of LiDS bound to the PVP are greater than those of LiFOS for both the PVP fixed initial concentrations. These bound values are similar to those in aqueous solutions. Further, the decrease in the adsorption of PVP after maximum adsorption is more marked for the PVP-LiFOS system than for the PVP-LiDS system. This implies that the PVP-surfactant complex is a more favorable energy state for LiFOS than for LiDS in bulk (30).

In order to estimate the change in the conformation of PVP adsorbed on alumina with increasing surfactant concentration, the ESR spectra of spin-labeled PVP on alumina were measured. The ESR signals from the nitroxide labels attached to the polymer chain reflect sensitively the changes in the motion of the adsorbed chain segments arising from the differences in the conformational states (31), whether in the loop, tail, or the train. In order to obtain quantitative data on the conformation of adsorbed polymer from composite spectra, Sakai and Imamura (32) have suggested that any composite spectra can be separated into three components which may be assigned to signals from segments adsorbed in trains, short loops, and long loops or tails. In this study, we obtained three different ESR spectra of PVP which have different degrees of motional freedom. These spectra are shown in Fig.9. Apparently, the chain mobility decreased in the order of (a), (c), and (b). From the observation of the apparent line shape, these three spectra were found to correspond roughly to the three components of the adsorbed PVP. These three spectra were superimposed upon one another with suitable intensity ratios to reproduce the observed spectrum (e). The reproduced spectrum (d) closely fits in the observed line shape. It is worthy to note that the spin labeles do not have a stronger affinity for the alumina surface than the original vinylpyrrolidone monomer. The fraction of train segments in the adsorbed polymer,p , obtained from the integrated intensities of the signal components divided into three parts. The values of p for the spin-labeled PVP on alumina from PVP-LiDS/PVP-LiFOS mixed aqueous solutions are plotted against the anionic surfactant concentration in Figs.10 and 11. The values of p steeply increased with increasing anionic surfactant concentration, and they showed a maximum at the concentration where the adsorption of PVP approached a maximum. This is probably

Downloaded by NORTH CAROLINA STATE UNIV on October 13, 2012 | http://pubs.acs.org
Publication Date: May 5, 1996 | doi: 10.1021/bk-1995-0615.ch008

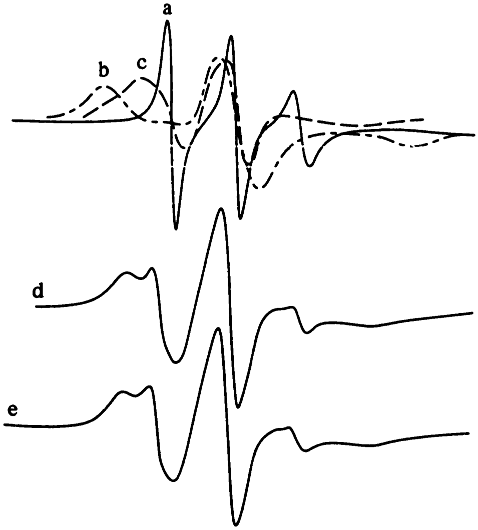

Figure 9 ESR spectra used for simulation of spin-labeled PVP adsorbed on alumina; (a) unadsorbed in water at 10°C, (b) in the adsorbed state at -120°C, (c) in the molten state at 140°C, (d) adsorbed on alumina in water at 25°C, and (e) reproduced by superposition of the above three model spectra.

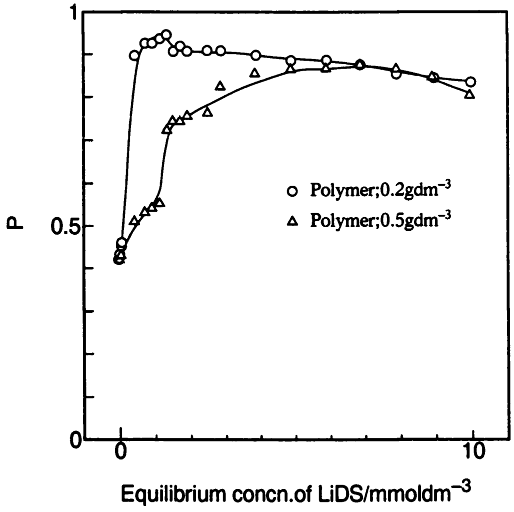

Figure 10 Plots of P value against LiDS concentration.

Downloaded by NORTH CAROLINA STATE UNIV on October 13, 2012 | http://pubs.acs.org
Publication Date: May 5, 1996 | doi: 10.1021/bk-1995-0615.ch008

Downloaded by NORTH CAROLINA STATE UNIV on October 13, 2012 | http://pubs.acs.org
Publication Date: May 5, 1996 | doi: 10.1021/bk-1995-0615.ch008

because the PVP-surfactant complex formed by the interaction between PVP and hydrophobic chains of the anionic surfactant on alumina becomes more rigid. Then, although the amount of PVP adsorbed was remarkably decreased, the values of *p* remained constant with their segments in trains for both PVP-LiDS and PVP-LiFOS systems. It seems likely that PVP attaches to patches of hemimicelles in spite of the anionic surfactant concentration being more than the cmc. In the PVP-LiDS system, the value of *p* was larger in 0.2 g dm^{-3} than in 0.5 g dm^{-3} of PVP at the maximum PVP adsorption. This difference in the *p* is correlated with the bound ratio of between PVP and LiDS adsorbed: The bound ratio of LiDS to PVP in the presence of 0.2 g dm^{-3} PVP is greater than that in the presence of 0.5 g dm^{-3} PVP. Higher values of *p* in the PVP-LiFOS system than those in the PVP-LiDS system over the whole surfactant concentration region can probably be attributed to a rigidity of the fluorocarbon chain of LiFOS (30).

PVP-AOT-alumina

Figure 12 (a)-(c) show the adsorption of AOT and PVP at fixed initial concentrations of PVP (0.5, 1.0 and 2.0 g dm^{-3}, respectively). The adsorption of PVP increased sharply and then decreased gradually with increasing AOT concentration, while the amount of AOT adsorbed also increased steeply at low concentrations and then gradually at high concentrations of AOT. In addition, the saturated amount of AOT in the presence of PVP was slightly lower than that in the absence of PVP. The adsorption of PVP was enhanced with increasing fixed initial concentration of PVP. A similar result has been found in the systems of PVP-LiDS, LiFOS-alumina. However, there is a considerable difference between single-chained and double-chained surfactants: the enhancement in the adsorption of PVP is quite large for the system of PVP-AOT in comparison with the system of PVP-LiDS, LiFOS. This enhancement in the adsorption of PVP is also attributed to formation of PVP-AOT complex. From the measurements of surface tension and ^{13}C-NMR spectroscopy (33), the formation of PVP-AOT complex is confirmed and the basic structure of the complex is almost the same as that of PVP-SDS complex. Further, it is suggested (33) that the large difference in the strength of interaction of PVP with SDS and AOT in aqueous solutions is caused by differences in the degree or extent of hydration of the polar end in the two molecules. These aqueous properties are strongly reflected in the adsorption properties at the solid/liquid interface. It is interesting to note that at the maximum adsorption of PVP, the amounts of surfactants bound to the PVP on alumina are estimated to about 1.0 mole LiDS/mole monomer of PVP and about 0.5 mole AOT/ mole monomer of PVP.

The conformational change of PVP adsorbed on alumina by the adsorption of AOT was also estimated by means of ESR. The *p* value was obtained, and the results are shown in Fig.13. The value of *p* steeply increased with increasing AOT concentration and then almost kept constant. Below the cmc, the *p* value was greater for the PVP-AOT system than for the PVP-LiDS system. This large *p* value suggests that the PVP-surfactant complexes formed by the interaction between PVP and hydrophobic chain of AOT on alumina become more immobile than those formed between PVP and LiDS. In addition, it is likely that since the strength of interaction between PVP and AOT on alumina is stronger than that between PVP and LiDS, the train portion of PVP for the PVP-AOT system on alumina is larger than that for the PVP-LiDS system.

Conclusions

Adsorption of PSS/SDS mixture on positively charged alumina is competitive in nature, where micropolarity in the adsorbed layer is considerably affected by the SDS

Downloaded by NORTH CAROLINA STATE UNIV on October 13, 2012 | http://pubs.acs.org
Publication Date: May 5, 1996 | doi: 10.1021/bk-1995-0615.ch008

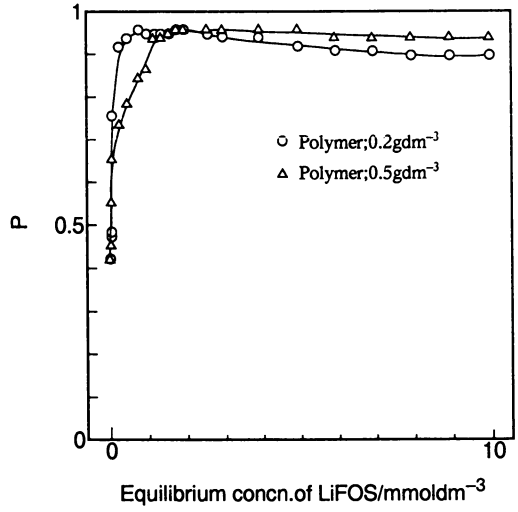

Figure 11 Plots of P value against LiFOS concentration.

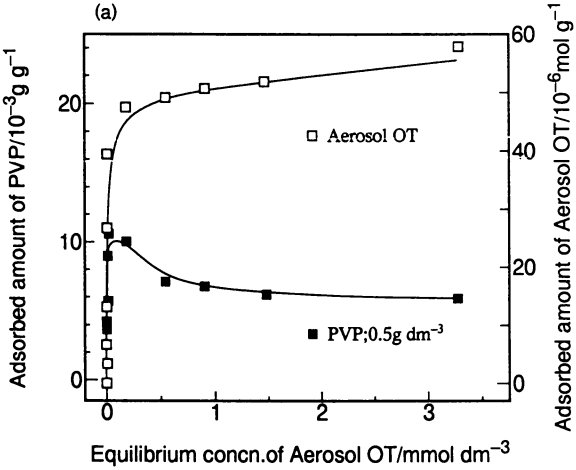

Figure 12 Adsorption of PVP and AOT on alumina from their mixtures at fixed initial concentrations of PVP; (a) 0.5 g dm^{-3}, (b) 1.0 g dm^{-3}, (c) 2.0 g dm^{-3}.

Continued on next page

Downloaded by NORTH CAROLINA STATE UNIV on October 13, 2012 | http://pubs.acs.org
Publication Date: May 5, 1996 | doi: 10.1021/bk-1995-0615.ch008

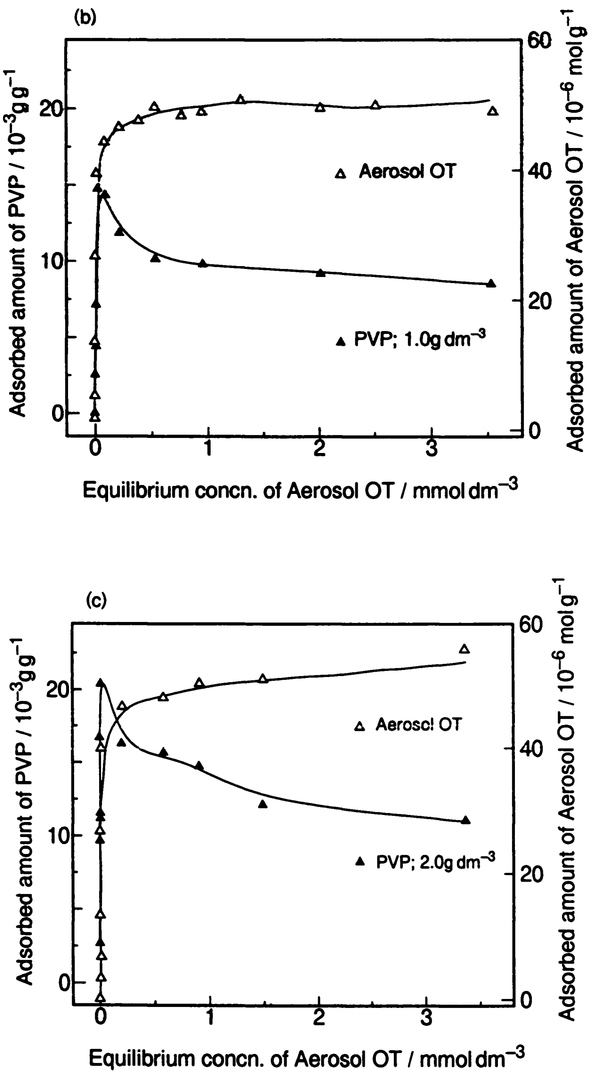

Chapter 12. Continued.

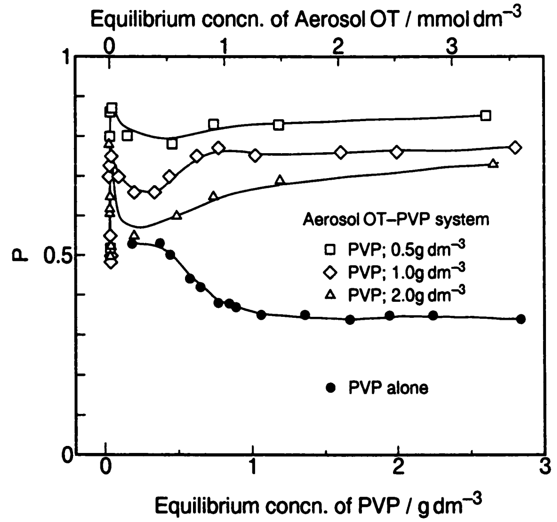

Figure 13 Changes in P value with AOT concentration at fixed initial concentrations of PVP.

adsorption. For PSS/HTAC mixture system, adsorption of HTAC is enhanced by the co-adsorbed PSS through formation of PSS-HTAC complex on the surface of alumina. The PSS/HTAC mixed adsorbed layer provides a much lower micropolarity compared with those of respective layers. For PVP/LiDS, LiFOS, and AOT mixture systems, adsorption of PVP increases sharply at low anionic surfactant concentrations, reaches a maximum, and then decreases with the anionic surfactant concentrations. This sharp increment in PVP adsorption is accompanied by formation of PVP-anionic surfactant complex on alumina, and the co-adsorbed AOT is most effective in enhancing PVP adsorption. In addition, the conformation of PVP adsorbed on alumina estimated using spin-labeled PVP consists mainly of train segments over a wide range of the anionic surfactant concentrations. PVP-LiFOS system shows a larger train portion of PVP adsorbed in comparison with the other systems.

Acknowledgements

The author wishes to acknowledge the assistance of Ms. A. Masuda, Ms. Y. Takaku, and Mr. H. Otsuka for conducting the adsorption studies.

Literature Cited

1 Robb, I. D. in Anionic Surfactants(E. H. Lucassen-Reynders, ed.), Surfactant Science Series, No.11, Marcel Dekker, New York, 1981, pp.109-142.
2 Hayakawa, K.; Kwak, J. C. T. in " Cationic Surfactants " (D. N. Rubingh and P. M. Holland, eds.), Surfactant Science Series, No.37, Marcel Dekker, New York, 1991, pp.189-248.
3 Goddard, E. D. *Colloids Surf.* **1986**, 19, 255.
4 Scheutjens,J. M. H. M.; Fleer, G. J. *J. Phys. Chem.* **1979**,83, 1619.
5 Van der Schee, H. A.; Lyklema, J. *J. Phys. Chem.* **1984**,88, 661.

Downloaded by NORTH CAROLINA STATE UNIV on October 13, 2012 | http://pubs.acs.org
Publication Date: May 5, 1996 | doi: 10.1021/bk-1995-0615.ch008

6 Papenhuijzen, J.; Fleer, G. J.; Bijsterbosch, B. H. *J. Colloid Interface Sci.* **1985**,104, 530.
7 Cosgrove, T.; Obey,T. M.; Vincent, B. *J. Colloid Interface Sci.* **1986**, 111, 409.
8 Somasundaran, P. *J. Colloid Interface Sci.* **1969**, 31, 557.
9 Tadros, Th. F. *J. Colloid Interface Sci.* **1974**,46, 528.
10 Chibowski, S. *J. Colloid Interface Sci.* **1980**, 76, 371.
11 Ma, C.; Li, C. *J. Colloid Interface Sci.* **1989**, 131, 485.
12 Esumi, K.; Oyama, M. *Langmuir*, **1993**,9, 2020.
13 Takahashi, A.; Kawaguchi, M. *Adv. Polym. Sci.* **1982**, 46, 1.
14 Esumi, K.; Yokokawa, M. *J. Jpn. Soc. Colour Mater.* **1992**, 65, 142.
15 Esumi, K.; Masuda, A.; Otsuka, H. *Langmuir*, **1993**,9, 284.
16 Otsuka, H.; Esumi, K. *Langmuir*, **1994**,10, 45.
17 Esumi, K.; Takaku, Y.; Otsuka, H. *Langmuir*, **1994**, 10, 3250.
18 Fox, K. K.; Robb, I. D.; Smith, R. *J.C.S. Faraday Trans 1*, **1974**, 70, 1186.
19 Abott, D. C. *Analyst*, **1962**, 87, 286.
20 Kalyanasundaram, K.; Thomas, J. K. *J. Phys. Chem.* **1977**, 81, 2176.
21 Martinie, J.; Michon, J.; Rassat, A. *J. Am. Chem. Soc.* **1975**, 97, 1818.
22 Ramachandran, C.; Pyter, R. A.; Mukerjee, P. *J. Phys. Chem.* **1982**, 86, 3198.
23 Muller, H.; Krempl, E., *Tenside*, **1968**, 5, 333.
24 Schwuger, M. J. *Kolloid Z.Z. Polym.* **1971**, 243, 129.
25 Hung, Z.; Yan, Z.; Gu, T. *Colloids Surf.* **1989**, 36, 353.
26 Abin, E. B.; Scaiano, J. C. *J Am. Chem. Soc.* **1984**,106, 6274.
27 Esumi, K.; Takehana, K.; Nojima, T.; Meguro, K. *Colloids Surf.* **1992**, 64, 15.
28 Esumi, K.; Okamoto, T. *J. Jpn. Soc. Colour Mater.* **1993**, 66, 592.
29 Murata, M.; Arai, H. *J. Colloid Interface Sci.* **1973**, 44, 475
30 Nojima, T.; Esumi, K.; Meguro, K. *J. Am. Oil Chem. Soc.* **1992**, 69, 64.
31 Robb, I. D.; Smith, R., *Polymer*, **1977**,18, 500.
32 Sakai, H.; Imamura, Y. *Bull. Chem. Soc. Jpn.* **1980**, 53, 3457.
33 Chari, K.; Lenhart, W. C. *J. Colloid Interface Sci.* **1990**, 137, 204.
34 Schwuger, M. J. *J. Colloid Interface Sci.* **1973**, 43, 491.
35 Saito, S. *J. Colloid Interface Sci.* **1967**, 24, 227.

RECEIVED May 3, 1995

Downloaded by NORTH CAROLINA STATE UNIV on October 13, 2012 | http://pubs.acs.org
Publication Date: May 5, 1996 | doi: 10.1021/bk-1995-0615.ch008

Chapter 9

Application of Electron Paramagnetic Resonance Spectroscopy to Surfactants on Surfaces

Martin G. Bakker, Dexter D. Murphy[1], and Brandon Davis

**Department of Chemistry, University of Alabama,
Tuscaloosa, AL 35487–0336**

The application of various EPR experiments to the study of surfactants adsorbed on surfaces from aqueous media is described. Published work using TEMPO and doxyl stearic acid spin-probes is critically reviewed, and new work utilizing spin-labeled cetyltrimethylammonium bromide is discussed to illustrate the use of 100% spin-labeled material to study surfactant aggregation, and the use of paramagnetic broadeners to study surfactant aggregate structure.

Surfactant adsorption on surfaces and solubilization on surfaces result from the interactions of individual surfactant molecules or aggregates of molecules with the surface (*1*). The vast majority of studies of surfactant adsorption on hydrophilic surfaces in aqueous media have focused on measurements of macroscopic properties such as surface area, adsorption isotherm, contact angle and zeta potentials. These provide a macroscopic, average picture of the interaction between the surfactant and the surface, but can not provide details about such questions as the type of binding, the extent of surfactant aggregation, the orientation of the surfactant molecules on the surface and the dynamics of binding and aggregation.

Theoretical studies of surfactant adsorption on surfaces however are increasingly considering the effects of the 'microscopic' nature of surfactant adsorption. That is the size and structure of the surfactant aggregates and the details of the interaction of individual surfactant molecules with the surface. At one extreme Gu and co-workers (*2*), in what they call the small surface aggregate model, postulate surfactant adsorption as occurring through binding of individual surfactant molecules on the strongest binding surface sites followed by growth of surfactant aggregates around these molecules. The model first proposed by Fuerstenau and Somasundaran (*3-5*) postulates adsorption of individual surfactant molecules at low surfactant

---

[1] Current address: Department of Natural Science and Mathematics, Mail Stop 7, Livingston University, Livingston, AL 35470

0097–6156/95/0615–0153$12.00/0

concentrations, formation of hemi-micelles at higher concentrations and bilayers at still higher surfactant concentrations. More recently Schechter and Scamehorn (*6*) and later Schechter and HarwellHarwell (*7,8*) have proposed that bilayered surfactant aggregates called admicelles (*8*) might be important under some conditions.

The microscopic details needed for a fundamental understanding of surfactant adsorption on surfaces requires spectroscopic techniques. The spectroscopic techniques that have the required sensitivity and have been applied to the study of surfactants on surfaces are Fourier Transform Infra-Red (FTIR) spectroscopy (*9,10*), Resonance Raman (*11*), Fluorescence (*12-14*) and EPR (*15-22*). Each technique has different advantages and disadvantages when applied to the study of surfactant aggregates on surfaces (*23,24*). The number of EPR studies of surfactant adsorption is rather small. This is somewhat surprising given the great interest in the structure of these surfactant aggregates and the impact that EPR has had on analogous problems in biochemistry.

The purpose of this contribution is to critically review the existing literature, to report preliminary results illustrating a number of different types of EPR experiment that we are currently developing, and suggest a variety of other EPR experiments possibly applicable to the study of surfactants on surfaces. The combination of such experiments has the potential to give a detailed picture of the structure of the adsorbed surfactant aggregates. The application of EPR to surfaces in general has been recently reviewed in comprehensive fashion by Martini (*25*).

As with a number of other spectroscopic techniques, EPR requires introduction of a probe of some form, ideally as part of the molecule to be studied. This is the approach we have taken with analogs of stearic acid and cetyl trimethylammonium bromide on silica. Failing this the probe molecule added should have properties as similar as possible to those of the surfactant being studied. This was the approach taken by Somasundaran and co-workers (*15,22*) who used stearic acid labeled with a doxyl spin probe to study the behavior of sodium dodecyl sulfate adsorbing on alumina.

EPR Using 100% Labeled Surfactant: Application to Shear-Flocculation

Most EPR experiments use only a small amount of spin-label diluted down with unlabeled surfactant. This is not surprising given the expense of the spin-label. If instead 100% spin-labeled surfactant is used EPR gives information on the extent of surfactant aggregation. When significant amounts of the surfactant are present as individual molecules a three line spectrum will be observed (see Figure 1a). As surfactant aggregation occurs spin-exchange and dipolar broadening lead to a single broad line with a linewidth of approximately 15 Gauss (Figure 1b & c). This effect has been previously reported for surfactant aggregates in solution (*26*) and has more recently been observed for doxyl stearic on alumina (*22*) and on silica (*20*). The composite spectra can be fitted and by numerically doubly integrating each component the relative amounts of surfactant present as aggregates and as individual molecules (or possibly as very small aggregates) can be determined (*20,21*).

We have recently applied this approach to the study of shear-flocculation (*20,21*). Shear-flocculation is a process in which fine particles (<10 μm) are suspended in water when small amounts of surfactant are added and a shear force (typically stirring at speeds of 500-1500 rpm) applied particle aggregation occurs (*27,28*). The aggregated particles are called floccs, and typically of ca. 10 times the diameter of the original particles. The aggregates settle more quickly, and can be floated much more readily than the fine particles. As lower surfactant dosages are required than with alternate particle processing methods, shear-flocculation is a potentially attractive approach.

In our study of shear-flocculation of quartz with spin-labeled cetyltrimethylammonium bromide (*21*), aliquots of the particle suspension were removed over the course of the shear-flocculation experiment and then the EPR spectrum determined. Analysis of the EPR spectra (examples of which are given in Figure 1) gave the relative amounts of the aggregated and non-aggregated forms (expressed as a ratio of aggregated to non-aggregated forms). These are given in Figure 2 superimposed on the mean particle size as determined by an in-line particle size analyzer. From Figure 2 it is clear that increasing surfactant aggregation occurs during the course of the shear-flocculation experiment, and that the particle aggregation and surfactant aggregation processes are related. Further experiments in which the rate of shear was varied over the course of the experiment confirmed that the surfactant aggregation tracked the particle aggregation. When air was excluded the rate of flocculation decreased dramatically, with a much longer time being required to achieve the same mean particle size, the rate of surfactant aggregation however remained constant. This indicates that although the particle aggregation and surfactant aggregation are both altered by the shear force applied and change in parallel they are not necessarily in "lock-step".

Because of the time delay between removal of the aliquots and determination of the EPR spectrum (typically 24 hours) what is being observed is an equilibrium situation. No changes in the EPR spectrum were observed between 24 hours and two weeks. Over the course of the shear-flocculation experiment the ratio of aggregated to non-aggregated surfactant was observed to increase from ca. 10 initially to over 350. The postulated mechanism of shear-flocculation (*27,28*) is that the surfactant forms hydrophobic hemi-micelles on the particle surface and that the shear-force acting to overcome the electrostatic repulsion between the particles results in overlap of the hydrophobic portions of the particle surfaces producing a strong hydrophobic bond. Because the surfactant is in an aggregated form both before and after formation of such hydrophobic bonds, this mechanism does not clearly predict increased surfactant aggregation. However the structure of the surfactant aggregates formed after shear-flocculation is a bilayer form in which all the surfactant head-groups in the bilayer are in contact with a particle surface. The loss of hydrophobic face of the hemi-micelle must correspond to a tighter binding of the surfactant and result in a shift of the aggregated/non-aggregated surfactant equilibrium towards more aggregation. If bilayer structures between particle surfaces are more stable then increases in this form must be at the expense of surfactants adsorbed individually or present in solution. That is the EPR is observing a redistribution of the surfactant between the various surfactant environments. The observed shift in the equilibrium constant is a factor of

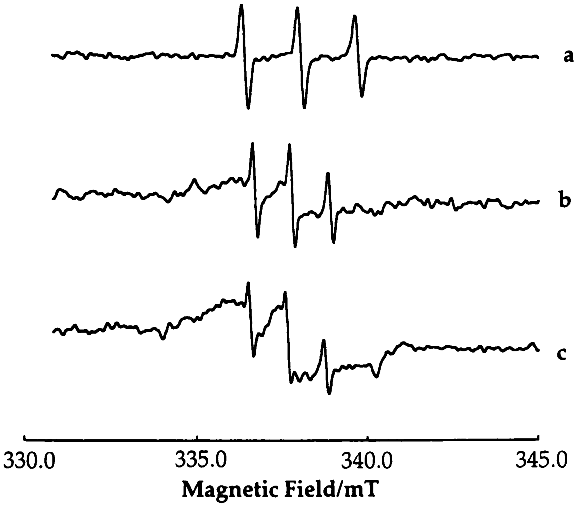

Figure 1. EPR Spectra of Spin-labeled CTAB used in a Shear-Flocculation Experiment. Samples removed (a) 9 seconds, (b) 180 seconds and (c) 840 seconds after surfactant added. CTAB concentration was 10^{-4} M, solution was 2 wt% silica, stirring rate of 1500 rpm. (Adapted from Figure 6 in Ref (21)

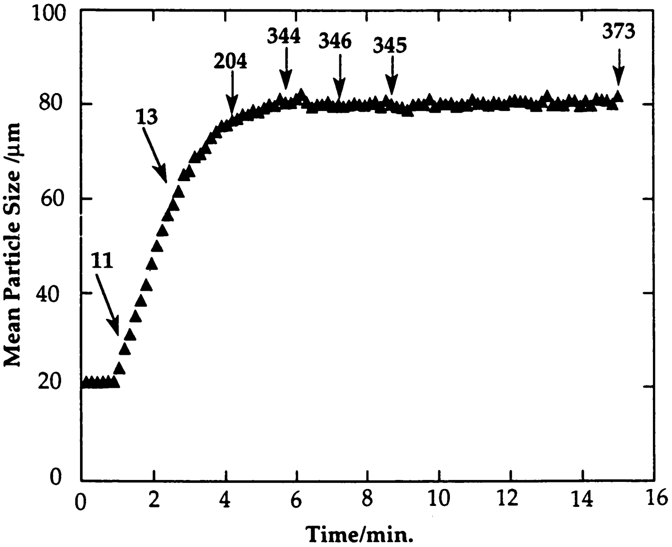

Figure 2. Plot of Mean Particle Size and Ratio of Aggregated to Non-Aggregated Surfactant. During a Shear-Flocculation Experiment. The labels on the figure indicate the ratio of aggregated to non-aggregated surfactant at the times indicated. Conditions as in Figure 1. (Adapted from Figure 5 in Ref(21))

35, this corresponds to a change in free energy, ΔG of approximately 9 kJ mol^{-1}. The change in free energy for removal of a methylene group from water to an alkane phase is reported (*29*) to be ca. 3.0-3.5 kJ mol^{-1} . Removal of a methyl group would be expected to give a somewhat larger change. In forming a bilayer we would be removing two methyl groups from aqueous solution, which would give changes in free energy of about the 9 kJ mol^{-1} observed. our observed change in equilibrium constant is therefore consistent with bilayer formation.

There are a number of considerations to be taken into account in this type of experiment. Firstly, because the aggregated surfactant form is so much broader than the lines of the isolated surfactant it can easily be over looked. increasing the field modulation is one method of decerning the presence of such a spectral component, but care must be taken not to distort the lineshape of the narrow lines. For determination of the relative amounts of the two forms the microwave power must be sufficiently low that no saturation occurs. There are indications of power saturation beginning at 4 mW, but our spectra are run at 0.2 mW. Since the total EPR signal is a function of both the signal amplitude and to the width of the EPR lines, broad signals which appear very weak may in fact correspond to a much larger number of spin-labels than a spectrum with peaks of large amplitude but small linewidth. Care therefore needs to be taken to ensure that the EPR cavity and the particles being used do not give rise to a significant background signal. Many minerals contain intrinsic EPR active centers which give rise to a background signal. When least squares fitting techniques are used, even background signals not detectable by eye can be fitted giving erroneous estimates of the aggregated/non-aggregated ratio.

The experiments described above are done at equilibrium, some time after the shear-flocculation was carried out. Malbrel et al. (*18*) describe an EPR experiment to study the kinetics of adsorption of AOT from cyclohexane onto alumina using doxyl stearic acid as a probe. A small portion of the slurry used is pumped through a flow cell in the cavity of the EPR spectrometer. By holding the magnetic field constant at one position on the EPR spectrum the change in intensity can be used to study kinetics. Care needs to be taken to ensure that no significant changes in microwave frequency or in cavity tuning occurred, particularly if the EPR lines are narrow. Use of a field-frequency lock is ideal to avoid the first problem, and an internal standard allows the second to be detected and compensated for.

EPR Probe Experiments

Polarity Determination. By using only a small amount of a spin-label diluted into a large quantity of surfactant, resolved spectra can be obtained which give information about microscopic polarity and viscosity. It has long been known that the coupling constants of many nitroxide spin-labels are dependent upon the polarity of the environment (*30*), and indeed a class of nitroxide spin labels that can function as pH probes have recently been developed (*31*). This approach has not been widely utilized in studying surfactants on surfaces. It was reported by Esumi and co-workers that there was no detectable change in the coupling constant of TEMPO associated with surfactant aggregates of lithium dodecyl sulfate, lithium perfluorooctane sulfonate on alumina (*16*), of dodecylpyridinium (*17*), cetylpyridinium chloride (*17*) on silica and of binary hydrocarbon-fluorocarbon surfactant aggregates on alumina (*32,33*). Based on work by Mukerjee and co-workers (*30,34,35*) Esumi assumed that the spin-probe was present predominantly in the interfacial region between the surfactant head-groups and the aqueous medium.

The doxyl stearic acids are generally better probes of the surfactant aggregates as they usually align with the surfactant and the position of the doxyl spin-label on the hydrocarbon chain can be varied as a check on the position stearic acid in the surfactant aggregate. However because the doxyl group is part of the backbone of the surfactant the rotation of the spin-label is often substantially slowed when the doxylstearic acid is incorporated into a surfactant aggregate. As a result the anisotropy of the A and g matrices is not totally averaged and it becomes very difficult to determine what the value of the isotropic coupling constant is.

Microviscosity If rotation becomes slowed then the EPR spectra can be used to give information on the microviscosity of the environment of the probe. This can be readily seen in Figure 3, which shows the EPR spectra for cetyltrimethylammonium bromide (CTAB) spin-labeled by replacing one of the methyl groups with a TEMPO group. At concentrations below the CMC three narrow peaks are observed, at concentrations above the CMC broadening characteristic of increased viscosity is observed due to formation of a micelle. In Figure 3 b silica is added to CTAB at concentrations below the CMC, aggregation occurs on the surface and again broadening is observed.

At low viscosity the rotation of the spin label can be described in terms of rotational correlation times τ_b, τ_c. For isotropic rotation $\tau_b = \tau_c$. Equations relating the correlation times to the peak to peak linewidths and peak heights are given in a number of references. (*36,37*) Using these expressions we estimate values of $\tau_b = 2.1 \times 10^{-9}$ s and $\tau_c = 1.1 \times 10^{-9}$ s for CTAB in a micelle and $\tau_b = 2.6 \times 10^{-9}$ s and $\tau_c = 1.1 \times 10^{-9}$ s for CTAB adsorbed in aggregates on the surface. The linewidths used were found by simulating the EPR spectrum using coupling constants of 0.045 mT (6H), 0.031 mT (2H) and 0.049 (2H) found for CTAB in water below the CMC. 'Generic' values (*36*) of A_{XX}, A_{YY}, A_{ZZ}, g_{XX}, g_{YY}, g_{ZZ} were used in this estimate. Clearly appropriate values for CTAB in water are desirable, and we are currently addressing this problem.

Even for these relatively short correlation times it is still advisable to simulate the EPR spectra, this is especially so when the spin-probe being used may partition between two or more environments. The necessity for this can be clearly seen in Figure 4 which shows CTAB adsorbed onto silica. The unusual form of the spectrum is due to CTAB being in two different environments with two different correlation times, coupling constants and g-factor. The narrower lines must correspond to CTAB undergoing free rotation, presumably in solution. The broader lines, which are particularly evident in the high and low field components, must be due to CTAB undergoing slow rotation, presumably due to aggregation. When simulation of this spectrum was attempted using only a Lorentzian or a Gaussian lineshape only very poor agreement with the experimental spectrum could be achieved. When the

In Surfactant Adsorption and Surface Solubilization; Sharma, R.;
ACS Symposium Series; American Chemical Society: Washington, DC, 1996.

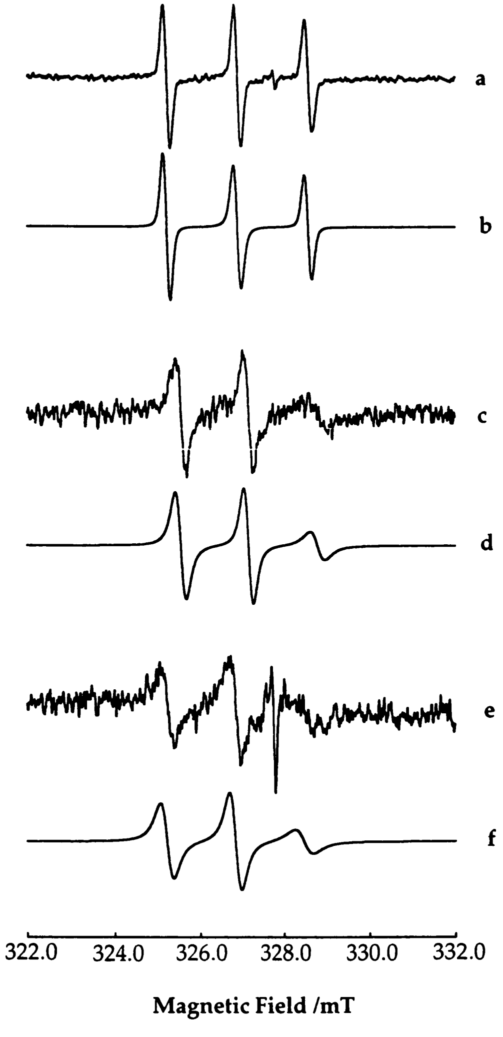

Figure 3. EPR Spectra of 1:100 Spin-labeled:Non-labeled CTAB in aqueous solution (a) 10^{-4} M total CTAB, (b) spectrum fitted using values in text, (c) 10^{-3} M total CTAB, (d) fitted spectrum, (e) 10^{-4} M total CTAB & 2 wt% silica, (f) fitted spectrum

unresolved hyperfine structure was explicitly taken into account the excellent simulation in Figure 4b was obtained. The spectra may not always be as clearly resolved as in this example and it is only when an attempt to fit the shape of the EPR peaks fails that the existence of more than one component may become apparent.

For doxylstearic acids in aqueous media the very low solubility of the stearic acid in water will normally result in strong inclusion into the surfactant aggregates. For TEMPO there is likely to be partitioning between the aqueous and non-aqueous phases, resulting in two overlapping spectra. Even if the two components can not be resolved it is still possible that significant line broadening will occur. This is likely to be most noticeable for the high field line. For example in a spectrum for TEMPO in sodium 4-[2-heptafluoroisopropyl-1,3-bis(trifluoromethyl)-butenoxy]benzene sulfonate reported by Esumi et al. (*33*) in 1991 broadening and asymmetry of the high field can be seen, indicating that two species are present. Careful analysis of this spectrum can give both the partition co-efficient and the desired correlation times. Using only the line heights and linewidths to estimate the rotational correlation times is likely to lead to significant error.

If the rotational correlation times are too long for the approximate forms (above) to be used qualitative information can still be obtained. A good example of this is the work by Chandar et al. (*15*) where various doxyl stearic acids were used to probe the adsorption of sodium dodecyl sulfate from aqueous solution onto alumina. It could be seen clearly that as the spin-label was placed closer and closer to the headgroup the rotational motion became more and more restricted. A more quantitative analysis of such spectra requires detailed simulation of the spectrum using a program such as that of Freed and Schneider (*38,39*).

Use of Paramagnetic Broadeners

An EPR based technique which has been successfully applied in the biochemical area is the use of paramagnetic broadeners. A common, and often inadvertent example of this is failing to remove oxygen from samples, leading to an increase in the linewidth. Other common broadeners are transition metal complexes and other spin-labels (e.g. ^{15}N labeled spin-labels). Broadening can occur through either a spin-exchange mechanism or due to dipolar-dipolar interactions. For transition metals in isotropic solution spin-exchange is the dominant term, but requires the broadener to collide with the spin-label (*40*). Therefore if the broadener is selected so that it is confined to one part of the system (e.g. aqueous solution), then from the absence or presence and the extent of broadening, the position of the spin-label can be inferred. Berner has written a detailed description of a number of different cases that can be encountered, and applied these methods to study the adsorption of stearic acid onto latex (*41*). Some care must however be exercised when applying this method to surfactants adsorbed on surfaces, it is not sufficient that the broadener does not affect the extent of surfactant adsorption. The polarity of the surface, surfactant and broadener must all be considered and how the broadener partitions between the aqueous and surfactant phases must be explicitly determined to avoid erroneous conclusions.

Figure 5a shows the EPR spectrum of 10^{-4} M CTAB with 5 wt% silica present. The three narrow lines from surfactant in solution are prominent because a 1:8 doping ratio was used. Figure 5b is the EPR spectrum when 10^{-3} M of $Fe(CN)_6^{3-}$ broadener has been added. A substantial increase in linewidth is readily apparent accompanied by a substantial decrease in peak height. The peak marked * is due to an intrinsic quartz signal and the two spectra were normalized relative to this peak. Part of the decrease in amplitude may be due to the added broadener increasing surfactant adsorption and aggregation. There is some hint of a broad peak in the lower spectrum. This possibility can be tested by determining the relative concentrations of surfactant in solution by doubly integrating the peaks.

When a similar broadening experiment is carried out using 1:100 doped CTAB the effect is even more dramatic. Figure 6 show the EPR spectra from CTAB adsorbed on a silica surface. In Figure 6b 2 x 10^{-3} M broadener was added, with almost total loss of the EPR spectrum. The surfactant would be expected to adsorb onto the surface with the headgroup down. If the broadener remains in the aqueous phase then no broadening would be expected for the spin-label in contact with the surface. That broadening occurs and that it is sufficient to cause the spectrum to totally disappear implies that the broadener must be adsorbed onto the surface amongst the surfactant headgroups. This is despite the broadener having the same charge as the surface. This type of co-adsorption has been previously postulated by Harwell and Bitting (*42*) based on adsorption isotherm, zeta potential measurements and pH dependence.

It appears that use of other, neutral paramagnetic broadeners would avoid the problem encountered above of the broadener including amongst the headgroups. It should then be possible to study the orientation of the surfactants and determine if at a given concentration the surfactants are present as a monolayer/hemi-micelle or in a bilayer structure, and how much of each form might be present. Because broadening could also be produced if the broadener is adsolubilized care needs to be taken to ensure that this does not occur. Depending upon the type of broadener used the extent of broadening could range from only a Gauss or less to so large that the EPR lines effectively disappear. In the lower range exact simulation of the EPR spectra will be required to allow the broadening to be explicitly determined. In the upper range an apparent decrease in EPR intensity would be seen, this would require accurate quantitation to be carried out, preferably against an internal standard. However in the case of hemi-micelles no broadening would be expected from a broadener in the aqueous phase. Labeling of the surfactant at the tail rather than the head group, coupled with a broadening experiment is then desirable.

Aggregation Number

One experiment that to the best of our knowledge has not yet been attempted for surfactant aggregates is a determination by EPR of the aggregation number. Only a handful of determinations have been carried out using fluorescence for sodium dodecyl sulfate on alumina by Somasundaran and co workers, and for a number of non-ionic surfactants on silica by Levitz and co-workers. If such a determination can be carried out by EPR it would help to fill a void in the literature.

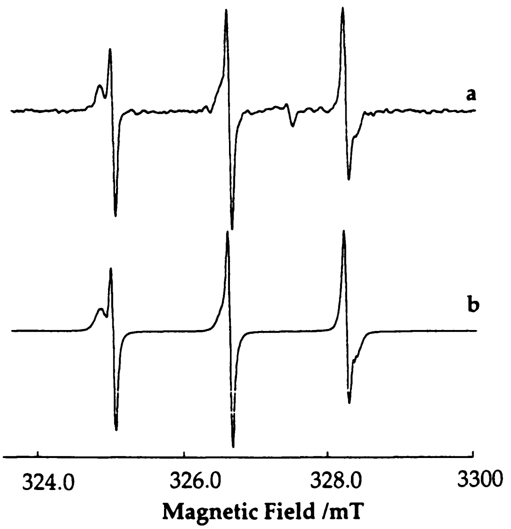

Figure 4. EPR Spectrum of 1:100 Spin-labeled CTAB on High Surface Area Silica. 10^{-4} M CTAB, 2 wt% silica, aqueous solution.

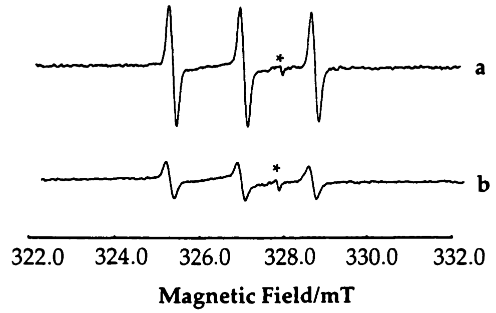

Figure 5. Effect of Paramagnetic Broadener on the EPR Spectrum of Spin-labeled CTAB in aqueous solution. (a) 1:8 Spin-labeled:Non-labeled CTAB, 10^{-4} M, 5 wt% silica, aqueous solution. (b) with 10^{-3} M $K_3Fe(CN)_6$ broadener added.

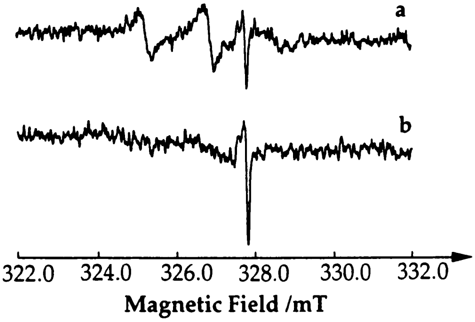

Figure 6. Effect of Paramagnetic Broadener on the EPR Spectrum of CTAB Adsorbed on Silica (a) 10^{-4} M total CTAB, 1:100 doped, 10 wt% silica (b) ca. 2×10^{-3} M $K_3Fe(CN)_6$ M broadener added.

A number of determinations of surfactant aggregation number in micelles have been reported (*43,44*) these both involve determination by EPR of the fraction of label in a micelle and present as monomers in solution. A Poission distribution is then assumed, and from the total amount of label and surfactant present the average aggregation number can be determined. This clearly requires being able to distinguish between the two surfactant environments, and having sufficient signal-to-noise to be able to accurately quantitate both components. Because of the very low concentrations at which surfactant aggregation on surfaces begins (in the case of CTAB on silica, 10^{-4} M) this is problematic. It is possible that by using particles of very high surface area, higher surfactant concentrations could be used with an ensuing improvement in signal-to-noise. This approach does assume that the labeled and un-labeled surfactant incorporate equally into the surfactant aggregate. Our experience with TEMPO labeled CTAB is that there are differences between the labeled and un-labeled forms. We carried out shear-flocculation experiments using both and found about a 7% difference in final mean-particle size. This is something of a worst case, but does indicate that this factor does need to be considered.

An alternative approach which appears more promising is to vary the ratio of labeled to unlabeled surfactant and use the line-broadening to determine the aggregation number. We are not aware of any case in which this approach has been used.

Acknowledgment

This work was supported by the School of Mines and Energy Development at the University of Alabama (MGB) and by a graduate fellowship from the U.S. Bureau of Mines (DDM). Our thanks to Jeff Harwell at the University of Oklahoma for his ideas on the implications of our CTAB/$Fe(CN)_6^{3-}$ broadening experiments.

Literature Cited

1. Clint, J. H. *Surfactant Aggregation*; Blackie & Son: London, 1992, pp 283.
2. Rupprecht, H.; Gu, T. *Colloid Polym. Sci.* **1991**, *269*, 506.
3. Fuerstenau, D. W. *J. Phys. Chem.* **1956**, *60*, 981.
4. Somasundaran, P.; Fuerstenau, D. W. *J. Phys. Chem.* **1966**, *70*, 90.
5. Somasundaran, P.; Healy, T. W.; Fuerstenau, D. W. *J. Phys. Chem.* **1964**, *68*, 3562.
6. Scamehorn, J. F.; Schechter, R. S.; Wade, W. H. *J. Colloid Interface Sci.* **1982**, *85*, 463.
7. Yeskie, M. A.; Harwell, J. H. *J. Phys. Chem.* **1988**, *92*, 2346.
8. Harwell, J. H.; Hoskins, J. C.; Schecter, R. S.; Wade, W. H. *Langmuir* **1985**, *1*, 251.
9. Sperline, R. P.; Song, Y.; Freiser, H. *Langmuir* **1992**, *8*, 2183.
10. Sperline, R. P.; Song, Y.; Freiser, H. *Langmuir* **1994**, *10*, 37.
11. Somasundaran, P.; Kunjappu, J. T.; Kumar, C. V.; Turro, N. J.; Barton, J. K. *Langmuir* **1989**, *5*, 215.
12. Tjipangandjara, K. F.; Huang, Y.-B.; Somasundaran, P.; Turro, N. J. *Colloids Surfaces* **1990**, *44*, 229.
13. Chandar, P.; Somasundaran, P.; Turro, N. J. *J. Colloid Interface Sci.* **1987**, *117*, 31.
14. Levitz, P.; Van Damme, H. *J. Phys. Chem.* **1986**, *90*, 1302.
15. Chandar, P.; Somasundaran, P.; Waterman, K. C.; Turro, N. J. *J. Phys. Chem.* **1987**, *91*, 148.
16. Esumi, K.; Otsuka, H.; Meguro, K. *J. Colloid Interace Sci.* **1989**, *136*, 224.
17. Esumi, K.; Nagahama, T.; Meguro, K. *Colloids Surfaces* **1991**, *57*, 149.
18. Malbrel, C. A.; Somasundaran, P.; Turro, N. J. *J. Colloid Interface Sci.* **1990**, *137*, 600.
19. McBride, M. B. *J. Colloid Interface Sci.* **1980**, *1980*, 393.
20. Murphy, D. D.; Bakker, M. G.; Spears, D. R. *Min. Metal. Proc.* **1994**, *11*, 26.
21. Murphy, D. D.; Spears, D. R.; Bakker, M. G. *Colloids Surfaces A* **1995**, *96*, 143
22. Waterman, K. C.; Turro, N. J.; Chandar, P.; Somasundaran, P. *J. Phys. Chem.* **1986**, *90*, 6828.
23. Somasundaran, P.; Ramachandran, R. In *Flocculation and Dewatering*; Moudgil, B. M., and Scheiner, B. J., Eds.; Engineering Foundation: New York, 1989; pp 21-41.
24. Somasundaran, P.; Kunjappu, J. T. *Min. Metall. Proc.* **1988**, *5*, 68.
25. Martini, G. *Colloids Surfaces* **1990**, *45*, 83.
26. Baglioni, P.; Ottaviani, M. F.; Martini, G.; Ferrani, E. In *Surfactants in Solution*; Mittal, K. L.; Lindman, B. Eds.; Plenum: New York, 1984; Vol. 11, pp 541-557.
27. Warren, L. J. *Chemtech* **1981**, 180.
28. Warren, L. J. *J. Colloid. Inter. Sci.* **1975**, *50*, 307.
29. Clint, J. H.; Walker, T. *J. Chem. Soc., Faraday Trans. I* **1975**, *71*, 946.
30. Mukerjee, P.; Ramachandran, C.; Pyter, R. A. *J. Phys. Chem.* **1982**, *86*, 3189.
31. Khramtsov, V. V.; Vainer, L. M. *Russ. Chem. Rev.* **1988**, *57*, 824.
32. Esumi, K.; Otsuka, H.; Meguro, K. *Langmuir* **1991**, *7*, 2313.

33. Esumi, K.; Otsuka, H.; Meguro, K. *J. Colloid Interface Sci.* **1991**, *142*, 582.
34. Pyter, R. A.; Ramachandran, C.; Mukerjee, P. *J. Phys. Chem.* **1982**, *86*, 3206.
35. Ramachandran, C.; Pyter, R. A.; Mukerjee, P. *J. Phys. Chem.* **1982**, *86*, 3198.
36. Schreier, S.; Polnasczek, C. F.; Smith, I. C. P. *Biochim. Biophys. Acta* **1978**, *515*, 375.
37. Bales, B. L. In *Spin Labeling. Theory and Applications*; Berliner, L. J.; Reuben, J. Eds.; Biological Magnetic Resonance; Plenum: 1989; Vol. 8; pp 77-130.
38. Schneider, D. J.; Freed, J. H. In *Spin Labeling. Theory and Applications*; Berliner, L. J.; Reuben, J. Eds.;Biological Magnetic Resonance; Plenum: New York, 1989; Vol. 8; pp 1-67.
39. Schneider, D. J.; Freed, J. H. In *Lasers, Molecules, and Methods*; Hirschfelder, J. O.; Wyatt, R. E.; Coalson, R. D., Eds.; Advances in Chemical Physics; John Wiley & Sons: New York, 1989; Vol. 63; pp 387-528.
40. Salikhov, K. M.; Doctorov, A. B.; Molin, Y. N.; Zamaraev, K. I. *J. Magn. Reson.* **1971**, *5*, 189.
41. Berner, B. *J. Colloid Interface Sci.* **1982**, *86*, 422.
42. Bitting, D.; Harwell, J. H. *Langmuir* **1987**, *3*, 500.
43. Atherton, N. M.; Strach, S. J. *J. Chem. Soc. Faraday Trans. II* **1972**, *68*, 374.
44. Kwan, C. L.; Atik, S.; Singer, L. A. *J. Am. Chem. Soc.* **1978**, *100*, 4783.

RECEIVED May 3, 1995

Downloaded by NORTH CAROLINA STATE UNIV on October 11, 2012 | http://pubs.acs.org
Publication Date: May 5, 1996 | doi: 10.1021/bk-1995-0615.ch010

Chapter 10

Effectiveness of Surfactants as Steric Stabilizers

Role of Anchor Groups

Paul F. Luckham[1], A. I. Bailey[1], F. Miano[1], and T. F. Tadros[2]

[1]Department of Chemical Engineering and Chemical Technology, Imperial College of Science, Technology and Medicine, Prince Consort Road, London SW7 2BY, United Kingdom
[2]Zeneca Agrochemicals, Jealotts Hill Research Station, Bracknell, Berkshire RG12 6EY, United Kingdom

A comparative study of the effect of three classes of polymeric surfactants on the rheological properties of aqueous carbon black dispersions is reported. The surfactants all contained ethyleneoxide as the hydrophilic group. Three series of surfactants have been examined: nonylphenyl-polyethyleneoxide (NP), nonylphenyl-polypropyleneoxide-polyethyleneoxide (NPE) and polypropyleneoxide-polyethyleneoxide ABA block copolymer (PE), All the surfactants adsorb with their hydrophobic moiety and form a layer around the particles with the polyethyleneoxide chains protruding in water. This configuration provides steric stabilisation to the suspended particles. Rheological and flocculation tests prove that the stability of carbon black dispersions is enhanced when the adsorbing moiety of the polymeric surfactant contains both polar, polypropyleneoxide, and non polar, nonylphenol, functional groups, matching the characteristics of the heterogeneous carbon black surface.

It is well know that polymers, particularly block and graft copolymers are effective colloidal stabilisers (1). The perceived wisdom is that one part of the polymer anchors the polymer to the surface and the other part of the polymer extends sufficiently far into the dispersed phase to prevent the van der Waals interaction between the particles becoming significant. Considerable attention has been paid to the type and molecular weight of the stabilising chain (2). Less attention has been devoted to the chemical nature of the anchor group. The stability of aqueous carbon black suspensions has been studied in our laboratories with the aim of making a comparison between different classes of dispersing agents. The surfactants used were comprised of three functional groups namely: nonylphenol (hydrophobic and non-polar), propyleneoxide

0097–6156/95/0615–0166$12.00/0

(hydrophobic and polar) and ethyleneoxide (hydrophilic). Three series of surfactants have been examined: nonylphenyl-polyethylenoxide (NP), nonylphenyl-poly propyleneoxide polyethylenoxide (NPE) and polypropyleneoxide-polyethyleneoxide ABA block copolymer (PE), Figure 1 reports their chemical structures.

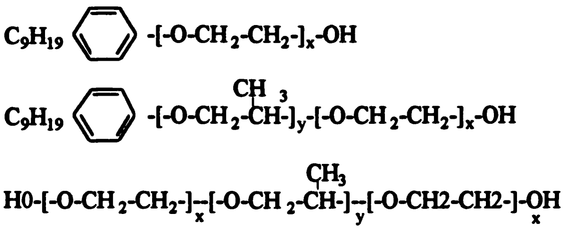

C9H19 -[-O-CH2-CH2-]x-OH
C9H19 -[-O-CH2-CH-]y-[-O-CH2-CH2-]x-OH
CH3
HO-[-O-CH2-CH2-]x-[-O-CH2-CH-]y-[-O-CH2-CH2-]-OH x
CH3

Figure 1: General formula for Synperonic surfactants; from the top NP series, NPE series and PE series. Further details of the NP, NPE and PE structure are reported in Table I.

Preliminary results on individual series have been already published by the present authors (3,4), where a greater emphasis of the molecular weight of the stabilising polyethyleneoxide has been placed. However, the focus of the current paper concerns the role played by different anchoring groups in the adsorption process onto carbon black and in the stabilisation of the resulting dispersions.

Experimental

Materials. The carbon black, used was Elftex 125, kindly supplied by Cabot Chemical Corporation. In appearance it is a fine light black powder whose measured density is 1,400 kg/m^3.

The particle size of Elftex 125 was determined with the aid of Transmission Electrons Microscopy (TEM) and Photon Correlation Spectroscopy (PCS) and was estimated to be 200 nm from both techniques. It was observed that carbon black consists of spherical particles of ~200 nm of diameter, which consist of much smaller ~ 20 nm fused primary carbon particles. It is believed that these aggregates are formed in the flame by flocculation and fusion of the primary particles under high temperature conditions (5). These aggregates cannot be broken into individual particles and hence they have been taken as the particle size determining structures in our analysis. Although the resulting individual particles have a certain degree of anisotropy it has been assumed that the particles are spherical.

Surface area information about carbon black is required for the interpretation of the forthcoming adsorption experiments. Nitrogen adsorption (BET) measurements were carried out with a Carlo Erba automatic analyser giving for Elftex 125 a surface area A_S = 102.5 m^2/g. The porosity of the material was also measured, and resulted 0.165 cm^3/g with pores in the range of 1-2 nm mean size which are presumably inaccessible to the large polymeric molecules used as dispersing agents in the present study. Hence it is necessary to evaluate with another technique the actual surface area available for the adsorption of large molecules from aqueous carbon black dispersions. Therefore, adsorption of the dye, methylene blue, MB, was performed. Adsorption

Downloaded by NORTH CAROLINA STATE UNIV on October 11, 2012 | http://pubs.acs.org
Publication Date: May 5, 1996 | doi: 10.1021/bk-1995-0615.ch010

measurements were carried out in double distilled water by adding MB of different concentrations to a 0.5% (w/w) carbon black suspension and shaking the samples at room temperature for two days until equilibrium was reached. The methylene blue molecule has been assumed to adsorb in a flat configuration on the carbon black surface and thus by knowing the area per molecule of methylene blue, 1.35 nm^2 the available area may be estimated. The wet surface area of carbon black produced an area of 40.5 m^2/g. This area must be compared to that one calculated assuming smooth spheres being the shape of carbon black particles. The radius of the carbon black particles is 100 nm giving a surface area of 21.5 m^2/g. Although less than the wet area, the hard sphere calculated value is consistent with the polydispersity of the carbon black.

The wet surface area has been assumed as the area available for surfactant adsorption in all subsequent experiments

Surfactants. The materials used in the present work as dispersing agents have been chosen from among commercially available nonionic surfactants and polymers with regard to the structure of their hydrophobic groups. The hydrophobic structures of the dispersing agents were nonylphenol and/or polypropylene oxide, whilst the hydrophilic moiety was a polyethylene oxide chain (PEO). For each anchor group, two ethyleneoxide chain lengths, approximately 25 and 150 EO units were studied. Most of the polymers used have been supplied by ICI Petrochemical and Plastic division and their structure are shown schematically in Figure 1. One surfactant, NP 150, was synthesized because it was not available commercially. The chemical structure and nomenclature of the surfactants used are given in Table I.

Table I: Average number of propylene and ethylene oxides groups of Synperonic NP, NPE and PE and their molecular weight

Surfactant	nonylphenol	nPO	mEO	$M_W \times 10^3$
NP20	YES	NO	22	1.2
PE104	NO	56	2 x 25	5.4
NPE1800	YES	13	27	2.2
NP150	YES	NO	143	6.0
PE108	NO	56	2 x 148	16.2
NPEC	YES	13	175	8.7

Adsorption Experiments. Carbon black suspensions (C = 0.35% w/w) were prepared at room temperature in the presence of surfactant solutions of different concentrations. The dispersion was obtained by treatment in an ultrasonic (Branson 9600) bath for 30 minutes and thereafter the equilibrium was reached by rotating the samples end over end for 16 h. Each suspension was centrifuged at 12000 rev min^{-1} (15000 g) for 30 minutes to sediment all the solids, leaving a clear supernatant at the top. We note that for these polymers centrifugation speeds (over the range 3,000 - 12,000 r.p.m.) did not affect the adsorption isotherms. The concentration of the remaining surfactant in the solution was determined using UV spectroscopy at a

Downloaded by NORTH CAROLINA STATE UNIV on October 11, 2012 | http://pubs.acs.org
Publication Date: May 5, 1996 | doi: 10.1021/bk-1995-0615.ch010

Downloaded by NORTH CAROLINA STATE UNIV on October 11, 2012 | http://pubs.acs.org
Publication Date: May 5, 1996 | doi: 10.1021/bk-1995-0615.ch010

wavelength of 276.5 nm, in the absorption region of the phenyl ring for the NP and NPE surfactants. The concentration of PE copolymers in solution was determined by the colorimetric method of Baleux (6). The amount adsorbed was estimated from the difference between the amount of surfactant added and the amount remaining following adsorption.

Rheology Experiments. The aqueous dispersions of carbon black have been prepared simply by mixing the carbon powder with a solution of the required polymeric surfactant of known concentration. The mixture was vigorously stirred with a Silverson mixer for five minutes and then agitated gently for 16 hours to ensure equilibrium. This method was very reliable for making fully dispersed suspensions of moderate concentration (up to ~25% of solids by weight). More concentrated dispersions were obtained by applying a hydrostatic pressure to the above suspensions. After a convenient time the samples were taken for rheological tests.

Rheological measurements were carried out on the carbon black dispersions with a Bohlin VOR instrument, equipped with either the concentric cylinder or cone and plate sample cells. The Bohlin VOR is a shear controlled rheometer capable of the application of rotational shear rates in the range of 10^{-2} -10^{3} s^{-1} and oscillatory strain frequencies in the range of 10^{-2} - 10 Hz. (Note that the Bohlin Rheometer nominally operaters over a shear rate range of 10^{-3} - 10^{3} s^{-1}, however in the current experiments data at the low shear end produced such low shear stresses that the data were unreliable, until a shear rate of 10^{-2} s^{-1} was reached.). Viscosity measurements were performed by choosing a series of shear rates and recording the corresponding τ and η. The oscillatory measurements required a more complex procedure. The first step consisted of the determination of the linear viscoelastic region. This was achieved by a strain sweep measurement whereby the amplitude of the strain was gradually increased from the smallest possible value which can be measured on the system in question, to a point of critical strain where the complex modulus, G*, the elastic modulus, G' and the loss modulus, G" begin to be dependent on the strain. The time taken to determine the linear viscoelastic region was of the order of 30 minutes. This time ensured that the more elastic samples had time to relax to their equilibrium structure following their placement in the rheometer.

Once the linear viscoelastic region was determined, a frequency sweep experiment was carried out by applying a fixed strain of variable frequency within the linear region of viscoelasticity. From these measurements the complex modulus G*, and its in phase and out of phase components, G', the storage modulus, and G", the loss modulus, could be obtained, since:

$$|G^*| = \tau_0/\gamma_0 \qquad (1)$$

$$G' = |G^*| \cos \delta \qquad (2)$$

$$G'' = |G^*| \sin \delta \qquad (3)$$

where τ_0 and γ_0 are the maximum stress and strain respectively and δ is the phase angle between the stress and strain.

Unless otherwise stated, all the measurements, were performed at a constant temperature of 20°C.

Downloaded by NORTH CAROLINA STATE UNIV on October 11, 2012 | http://pubs.acs.org
Publication Date: May 5, 1996 | doi: 10.1021/bk-1995-0615.ch010

Results and Discussion

Adsorption Data The adsorption curves of Synperonic NP, Synperonic NPE and Synperonic PE are reported in the Figures. 2 to 4. All the isotherms reach a plateau value and have a pseudo-Langmuirian shape. The curves are of the high affinity type, typical for polymer and surfactant adsorption. Dilution experiments, showed that desorption of surfactants does not occur over a time of 5 days.

From Figures 2-4, where the adsorption data are presented in weight terms, it can be seen that the longer the section of the ethylene oxide portion of the surfactant, the greater the weight of material adsorbing. However the trend is reversed if one considers adsorption in molar terms (see table II). This indicates that in all cases the nonadsorbing ethyleneoxide is hindering the adsorption of the higher molecular weight surfactants.

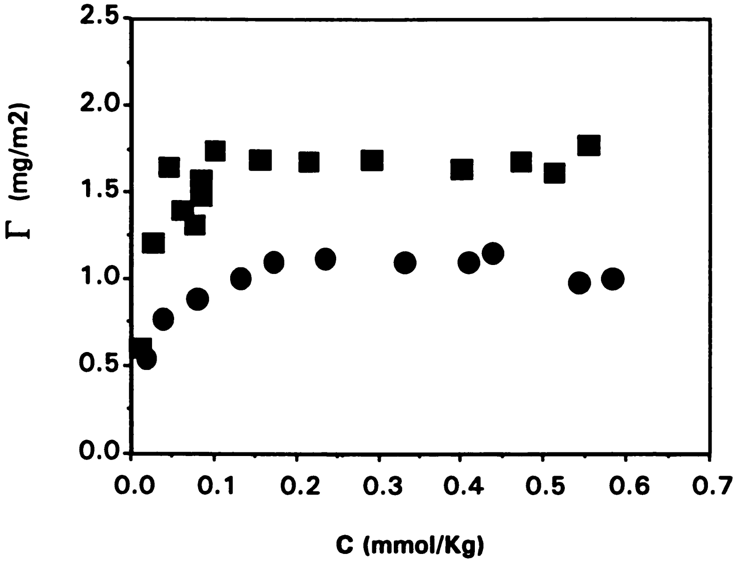

Figure 2: The adsorption isotherm of NP surfactants expressed in weight units. NP 20 = ●, NP 150 = ■.

The interpretation of this trend is more straightforward if we calculate the cross-sectional area σ of the surfactant from the molar surface excess, Γ_m through the relation:

$$\sigma = \frac{1}{\Gamma_m N_A} \quad (4)$$

where N_A is the Avogadro number and Γ_m is the maximum of adsorption in molar units, both Γ_m and σ are reported in Table II. Where for all three classes of surfactant the cross-sectional area occupied per surfactant molecule increases with the size of the PEO chains.

Downloaded by NORTH CAROLINA STATE UNIV on October 11, 2012 | http://pubs.acs.org
Publication Date: May 5, 1996 | doi: 10.1021/bk-1995-0615.ch010

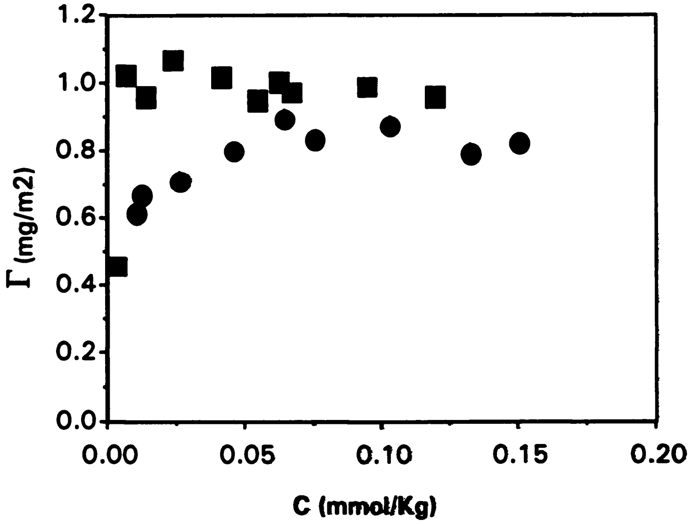

Figure 3: adsorption isotherms of PE10 series of surfactants expressed in weight units. PE 104 = ●,PE 108 = ■.

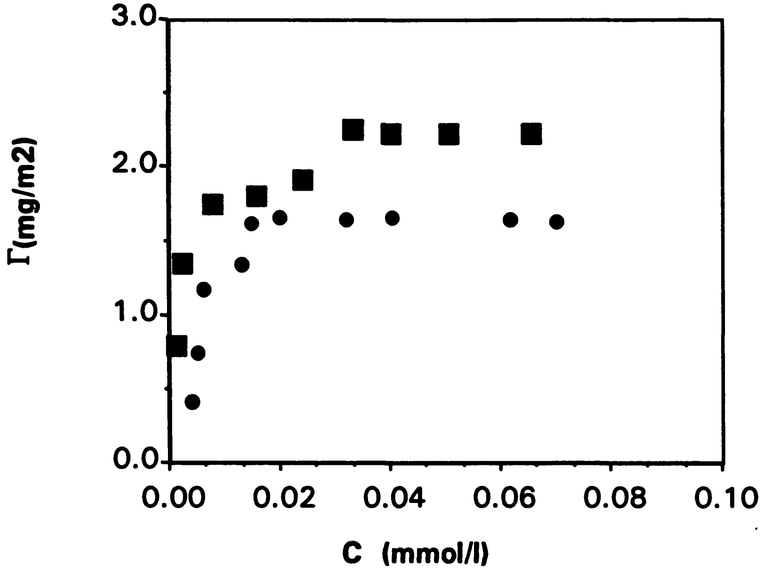

Figure 4: adsorption isotherms of the NPE series of surfactants, expressed in weight units. NPE 1800 = ●, NPE C = ■.

Downloaded by NORTH CAROLINA STATE UNIV on October 11, 2012 | http://pubs.acs.org
Publication Date: May 5, 1996 | doi: 10.1021/bk-1995-0615.ch010

Table II: Maximum of adsorption and cross-sectional area of NP, NPE, and PE series of polymeric surfactants

Surfactant	$\Gamma_{max.}$ (mg m^{-2})	$\Gamma_{max.}$ (μmol. m^{-2})	σ (nm^3)
PE 104	0.84	0.16	10.71
NP 20	1.09	0.90	1.83
NPE 1800	1.67	0.76	2.19
PE108	0.97	0.06	27.68
NP 150	1.69	0.26	6.39
NPE C	2.24	0.26	6.45

Let us now consider the role played by the anchoring group of the surfactants. Let us turn to table II to investigate this effect. For both the high and low molecular weight ethyleneoxide surfactants, the amount of material adsorbed for the Synperonic PE surfactants containing propyleneoxide as the anchor group is the lowest, despite that fact that the Synperonic PE surfactants have the largest anchoring group. When nonylphenol is the anchor group, in the NP series, more surfactant adsorbs. This is as one may expect as the carbon black surface is largely hydrophobic in nature so one would expect the more hydrophobic nonylphenol to adsorb more strongly than the hydrophilic propyleneoxide, which is probably adsorbing on the more hydrophilic oxidised areas of the carbon black dispersion. However, for both the high and low molecular weight surfactants it is when the nonyl phenol anchor and the propyleneoxide group combine in the NPE series that the highest levels of adsorption is noted.

The heterogeneous nature of the carbon black surface enhances the advantage of having a multi- functional surfactant: in the case of NPE surfactants the more hydrophobic nonylphenol is well adsorbed on the hydrocarbon part of the carbon black surface whilst the PPO moiety can be preferentially adsorbed on the oxidised part of the surface.

In addition to the role played by the anchoring group, the stabilising chain also plays a role in determining the number of molecules which are adsorbed to the carbon black surfaces. These data clearly show that more of the lower molecular weight polymers adsorb at the carbon black surface than the higher molecular weight polymers. This indicates that for the higher molecular weight polymers the presence of a high molecular weight stabilising chain adsorbed to the carbon black inhibits further adsorption of the surfactant. Thus the number of molecules adsorbing to the surface is dependent both on the structure of the adsorbing part of the surfactant or copolymer and on the molecular weight of the stabilising part of the molecule as these and other data of ours on similar systems have shown.

Rheology data: Shear Viscosity results. Concentrated dispersions of carbon black containing adsorbed polymers were prepared such that the equilibrium polymer concentration was of the order 1000 parts per million, *i.e.* in the plateau region of the adsorption isotherm. The dispersions were made at a volume fraction of around 10% and concentrated to the required concentration by placing the dispersion in dialysis

Downloaded by NORTH CAROLINA STATE UNIV on October 11, 2012 | http://pubs.acs.org
Publication Date: May 5, 1996 | doi: 10.1021/bk-1995-0615.ch010

bags and applying a hydrostatic pressure. The dispersions showed marked shear thinning behaviour which becomes more evident as the volume fraction of carbon black increases. This trend is well illustrated in Figure 5 where PE 108 has been taken as an example.

The results presented in figure 5, and indeed all the polymers studied in this work are typical of stable dispersions. For most of the carbon black dispersions, the viscosity approaches a lower limiting value at a shear rate above 500 s^{-1}. Thus η (500 s^{-1}) has been taken as the pseudo-Newtonian viscosity or the high shear limit viscosity. When the suspension is very concentrated the high shear limit viscosity could not be found, therefore the lowest viscosity was recorded at the highest experimental shear rate (~750 s^{-1}) and taken for further analysis, unless this seemed physically unreasonable, *i.e.* it was clear that the limiting viscosity was not close to being reached.

The high-shear rate viscosity versus the solid volume fraction for the three classes of surfactant are plotted in figs. 6-8. In all cases the viscosity increases as the carbon black concentration increases. These plots have been compared with two theoretical curves calculated from the Krieger-Dougherty (7) equation which have been set up for dispersions of hard spheres: random packed ($\phi_p = 0.64$) and hexagonal superimposed layers ($\phi_p = 0.608$). We have used these values for the maximum packing of the dispersion as plots of ϕ versus $1/\eta^{0.5}$ was linear with intercepts on the volume fraction axes of 0.58 - 0.64. It was noted that dispersions of volume fractions higher than 0.64 were dilatant.

In all cases the dispersions stabilised by the higher molecular weight surfactant *i.e.* with 150 EO units has a higher viscosity than the dispersions stabilised with the

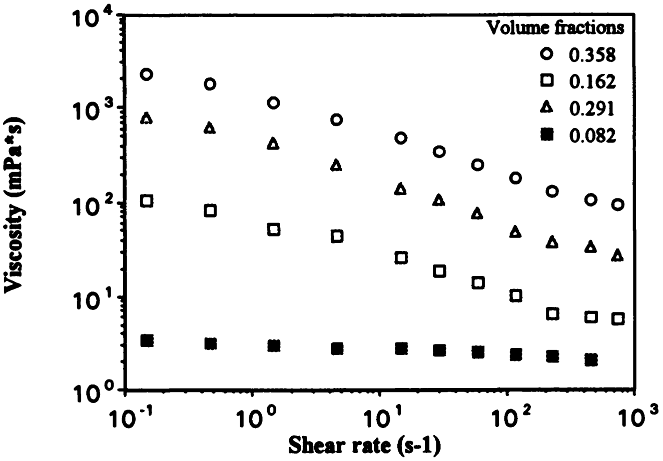

Figure 5: the shear stress versus shear rate of carbon black suspensions in the presence of PE108 at various volume fractions, as indicated in the legend placed inside the graph. The shear thinning behaviour is more enhanced at higher volume fraction.

Downloaded by NORTH CAROLINA STATE UNIV on October 11, 2012 | http://pubs.acs.org
Publication Date: May 5, 1996 | doi: 10.1021/bk-1995-0615.ch010

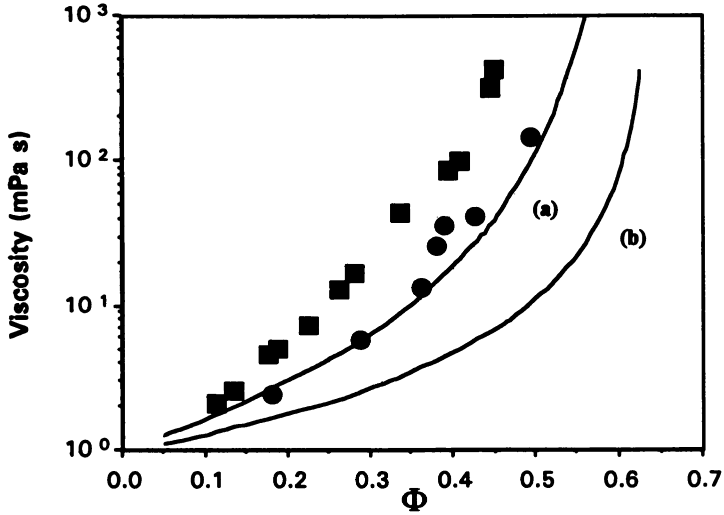

Figure 6: Plot of the high shear rate viscosity of carbon black dispersions in the presence of NP surfactants versus the volume fraction of solids. Symbols are filled circles for NP 20, and squares for NP 150. In the graph are also reported the Krieger-Dougherty equation curves $\phi_p = 0.608$ (a); and for $\phi_p = 0.64$ (b).

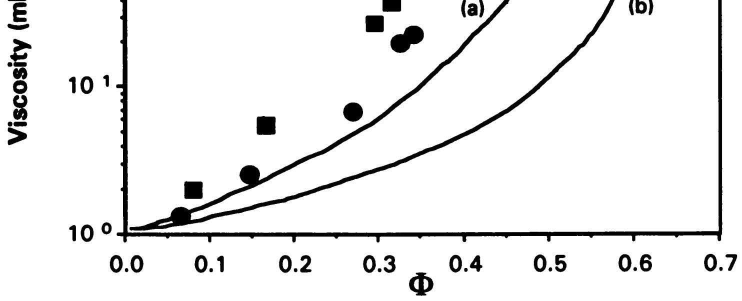

Figure 7: Plot of the high shear rate viscosity of carbon black dispersions in the presence of PE surfactants versus the volume fraction of solids. Filled squares are for PE 104, and filled squares for PE 108. In the graph are also reported the Krieger-Dougherty equation curves for $\phi_p = 0.608$ (a) and for $\phi_p = 0.64$ (b).

Downloaded by NORTH CAROLINA STATE UNIV on October 11, 2012 | http://pubs.acs.org
Publication Date: May 5, 1996 | doi: 10.1021/bk-1995-0615.ch010

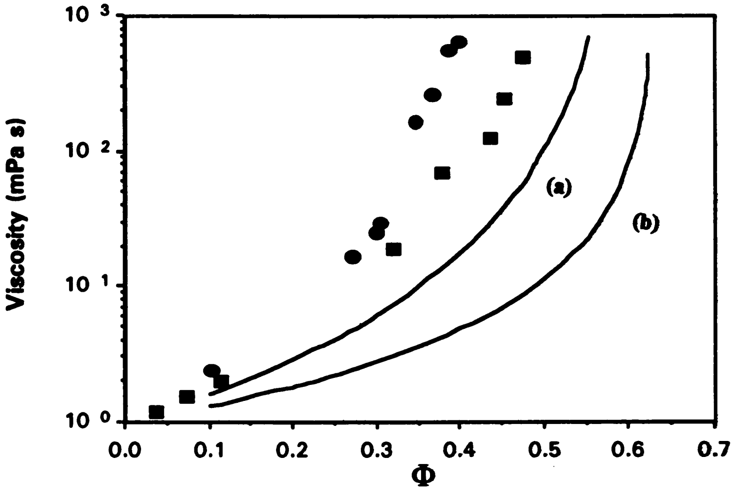

Figure 8: Plot of the high shear rate viscosity of carbon black dispersions in the presence of NPE surfactants versus the volume fraction of solids. Filled circles are for NPE 1800, and filled squares for NPE A. In the graph are also reported the Krieger-Dougherty equation curves for $\phi_p = 0.608$ (a) and for $\phi_p = 0.64$ (b).

shorter surfactant. This is because the effective volume fraction of the surfactant is higher due to the thicker adsorbed polymer layer.

In general, the results of this rheological investigation are in agreement with the general trend of concentrated dispersions. Namely a gradual, followed by a rapid increase in η_r with increase in ϕ is shown in all the series of points referring to each surfactant. However, the common feature of the above graphs is that the experimental curves do not correspond closely to the Krieger-Dougherty functions. In particular, the points appear to be parallel to the $\phi_p = 0.608$ while the $\phi_p = 0.64$ even has a different shape and in all cases the viscosity of all the dispersions at any volume fraction is higher than the predicted viscosity. Moreover, as pointed out earlier, carbon black dispersions stabilised by the higher molecular weight surfactant show a higher viscosity than those stabilised by the lower molecular weight homologues. Part of this discrepancy is due to the fact that the more concentrated dispersions have not reached the high shear limiting viscosity, however this is not he whole story as there are deviations at lower volume fractions where the high shear limiting viscosity has definitely been reached.

This evidence is not surprising since in the above graphs the viscosity was plotted versus the volume fraction of the "core" of carbon black particles. In order to explain the difference between the theoretical and the experimental trend, the adsorbed polymer contribution to the correct hydrodynamic volume fraction should be considered and added.

An estimate of ϕ_m can be obtained by extrapolating $\eta_r^{-1/2}$ versus ϕ to zero. Φ_m is thereafter compared with $\phi_p = 0.64$ and the adsorbed layer thickness δ can be calculated hence (8),

Downloaded by NORTH CAROLINA STATE UNIV on October 11, 2012 | http://pubs.acs.org
Publication Date: May 5, 1996 | doi: 10.1021/bk-1995-0615.ch010

$$\phi_p/\phi_m = [1 + (\delta/R)]^3 \qquad (5)$$

where R is the particle radius (100 nm). The resulting ϕ_m and δ values of the polymeric surfactant studied are reported in Table III. It should be noted that in obtaining the estimate for the adsorbed layer thickness, the data have been fitted at particle volume fractions so as any problems associated with the attainment of the high shear limiting viscosity have been eliminated.

It can be seen that the layer thickness of all the surfactants reported in Table III increases with the number of EO units, as expected from logical considerations; the surfactants are known to be adsorbed through the anchoring group, leaving the PEO chains free to protrude toward the solution. It is worth pointing out that photon correlation spectroscopy experiments were performed on the carbon black dispersions, to estimate the hydrodynamic radius of the particles. These experiments gave the same trends as those obtained from rheology measurements. It was not possible to extract a hydrodynamic thickness for the adsorbed polymers as the carbon black without any added polymer was aggregated.

Table III: Apparent maximum volume fraction and adsorbed layer thickness of carbon black dispersions in the presence of NPE, NP and PE polymeric surfactants

Surfactant	ϕ_m ϕ_p=0.64 $[\eta]\phi_p$=2.0	δ (nm)	δ* (nm)
NP 20	0.538	5.9	4.8
PE 104	0.526	6.8	3.2
NPE 1800	0.522	7.0	5.8
NP 150	0.488	9.4	-
PE 108	0.472	10.7	10.2
NPE C	0.444	12.9	11.5

*hydrodynamic thickness as estimated from earlier experiments by van de Boomgaard (9) on flat surfaces

Viscoelastic results.

Figure 9 shows the variation of G' with frequency ω at various volume fractions of carbon black in the presence of NPE 1800 and the situation pictured in the Figure 9 is typical of all the surfactants studied. In Figure 9 one can see the rapid increase of G' with the frequency at lower volume fractions while the frequency dependence of the storage modulus becomes less pronounced as ϕ is increased. Similar results were obtained for the other series and molecular weight surfactants.

This behaviour is what one would expect from steric stabilised dispersions. As ϕ increases, the adsorbed layers of PEO have a thickness comparable to the average inter-particle distance and the PEO chains come more frequently into contact generating a strong repulsive interaction which gives rise to a more elastic behaviour of the dispersion. At a sufficiently high ϕ (e.g. 0.527), and under low strain, the dispersion behaves like a nearly elastic material. Another observation to emphasise is that it is still possible to measure the viscoelastic properties of a sample whose solid fraction is beyond the limiting volume fraction ϕ_m found by means of high shear rate measurements. In fact, the particles subjected to high shear rate are structured in hexagonally packed layers aligned with the shear plane (10,11). While oscillatory measurements have been carried out without causing the breakdown of the existing particle arrangement present in the dispersion at rest, which would appear to be a random packing arrangement (ϕ_p = 0.64) as discussed earlier. Moreover, under the condition of $\phi > \phi_p$ the viscosity tends to infinity but G' can be still measurable.

Downloaded by NORTH CAROLINA STATE UNIV on October 11, 2012 | http://pubs.acs.org
Publication Date: May 5, 1996 | doi: 10.1021/bk-1995-0615.ch010

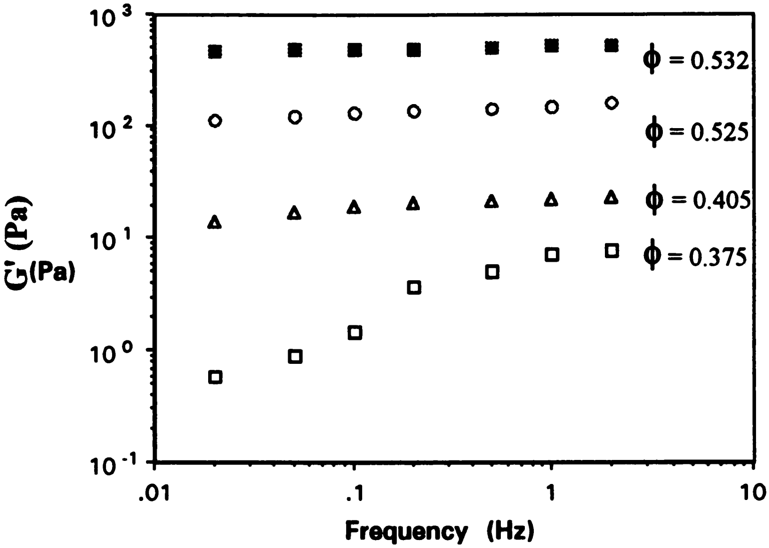

Figure 9: Storage modulus (G') of carbon black dispersion in the presence of NPE 1800 versus the frequency at various volume fraction in the range of 0.375-0.535 at an amplitude of 0.03 mrads. Volume fractions are reported inside the graph.

Figures 10 -12 show the variation of G' and G" (measured at a frequency of 1 Hz) with the volume fraction of the dispersion for all the carbon black-surfactant systems studied. A frequency of 1 Hz was chosen as it is below the resonance frequency of the torque bar used in the experiments. The resonance frequency for the weakest bar, which was used for the most dilute dispersions, was around 7 Hz. Thus the value of 1 Hz was chosen as for most systems, it was the highest accessible frequency and the elastic modulus had reached its high frequency limiting value. The results were obtained at full coverage of the particles by surfactant and represent the most direct method of comparison among the three structures of surfactants investigated.

From the observation of Figs. 10-12, some general features of the carbon black dispersions behaviour can be outlined: first of all, it may be noted that G' are always

Downloaded by NORTH CAROLINA STATE UNIV on October 11, 2012 | http://pubs.acs.org
Publication Date: May 5, 1996 | doi: 10.1021/bk-1995-0615.ch010

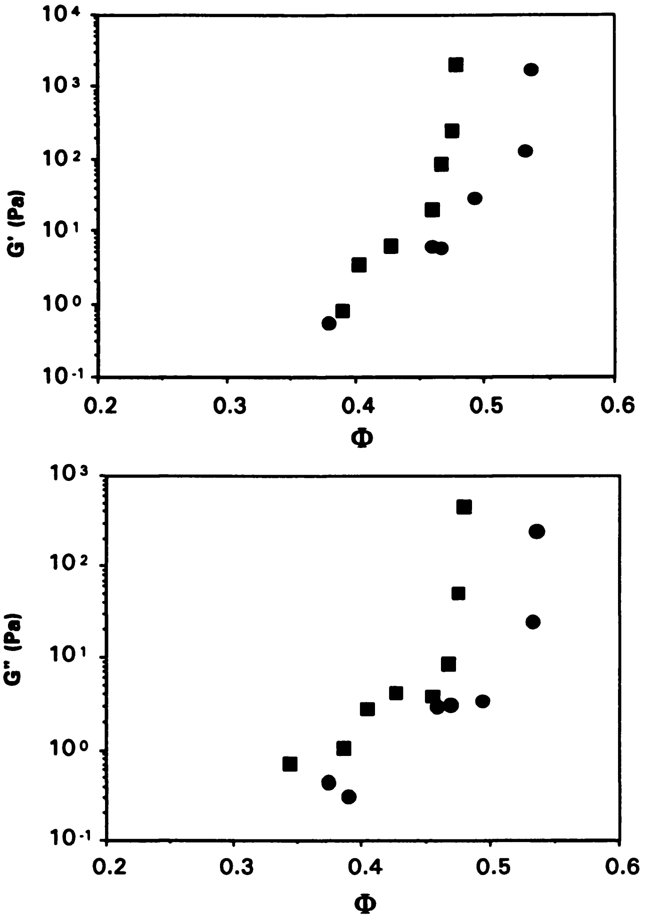

Figure 10: Elastic G' and loss modulus G' versus the volume fraction of carbon black for NP series of surfactants at 20 °C. NP 20 = ●; NP 150 = ■.

higher than G" for volume fractions ϕ in the range of 0.35-0.55. The cross-over of the viscoelastic moduli, *i.e.* the point when G'>G", is related to the occurrence of the onset of particle interactions. In particular, in thses systems, repulsion arises from the entropic and osmotic forces caused by the interactions of the chains of the polymer adsorbed onto the particles surfaces.

It seems, therefore that the particles begin to interact, affecting the viscoelasticity of the dispersion, when the average inter-particle distance is much larger than twice the thickness of the adsorbed polymeric layer. However, the effect of the size of the adsorbed polymer is still important since it may be seen that G' increases at lower ϕ for the higher molecular weight surfactants (with an analogous trend of the plastic viscosity) and this must be the consequence of the increase of adsorbed polymer layer thickness. Moreover, it can be observed that the slope of the G', G" functions versus ϕ reduces with the increase of the number of the EO units per chain adsorbed

Downloaded by NORTH CAROLINA STATE UNIV on October 11, 2012 | http://pubs.acs.org
Publication Date: May 5, 1996 | doi: 10.1021/bk-1995-0615.ch010

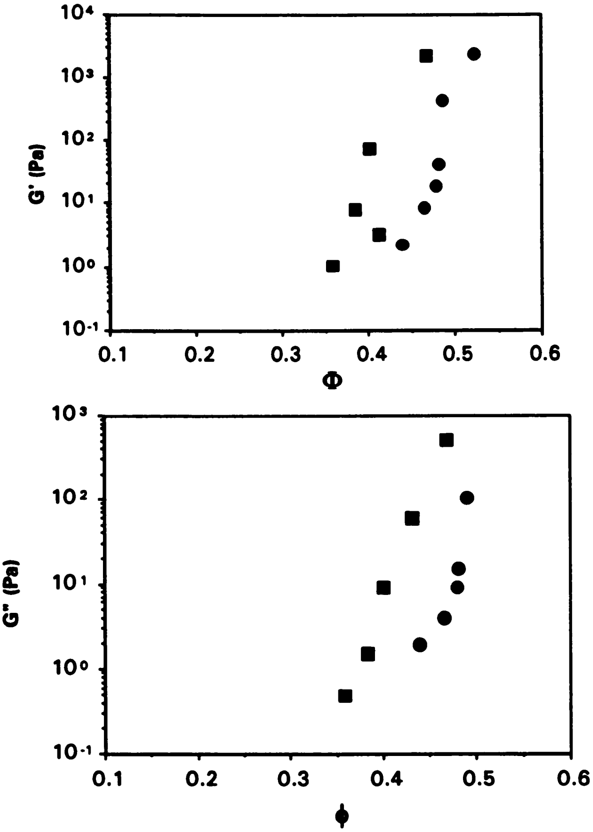

Figure 11: Elastic G' and loss modulus G" versus volume fraction of carbon black for PE series of surfactants at 20 °C. PE 103 = ●; PE 108 =■.

indicating that the surfactants bearing a lower number of EO units are more rigid than the higher ones.

These differences will be discussed in more detail looking now at each single series of polymeric surfactants. In fact, extrapolation of the $1/G'^{1/2}$ data give an estimate of the maximum packing fraction and the adsorbed layer thickness of each surfactant, as reported in Table IV. Comparing the δ values, calculated by the extrapolation of G', to those reported in Table III, it can be observed that the latter are lower in the case of NP and NPE surfactants suggesting that the chains can be reasonably compressed when the suspension is at rest. In the case of PE polymers, however, δ calculated from viscoelastic measurements is slightly higher than the corresponding δ arising from steady shear viscosity, suggesting possibly that some attractive interactions may be the cause of the early rise of G'. These attractive bonds between particles are presumably broken under the effect of high shear rate. Finally, it is worth pointing out that the profiles of both G' and G" versus ϕ are similar to those reported of steric stabilised latex dispersions (10) and differ according to the structure of the surfactants.

Downloaded by NORTH CAROLINA STATE UNIV on October 11, 2012 | http://pubs.acs.org
Publication Date: May 5, 1996 | doi: 10.1021/bk-1995-0615.ch010

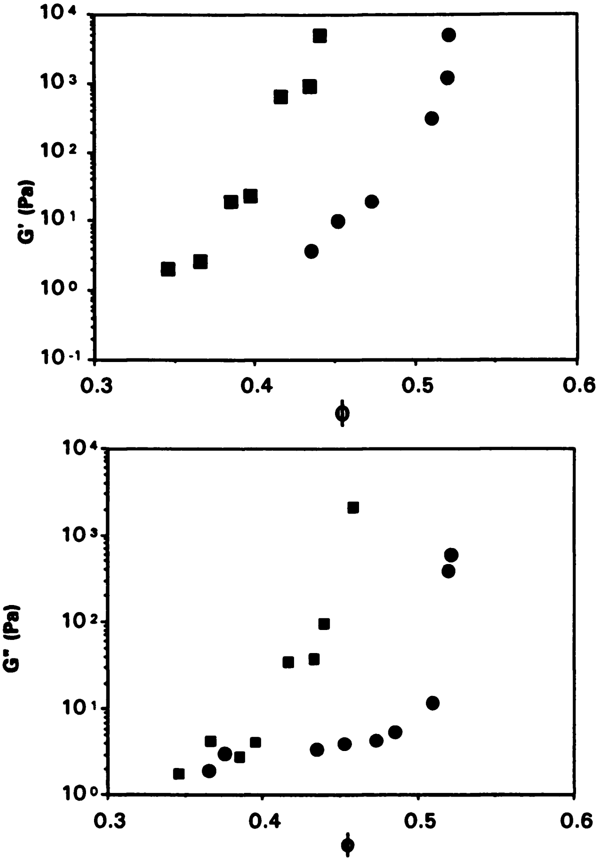

Figure 12: Elastic G' and loss modulus G" versus the volume fraction of carbon black for NPE series of surfactants at 20 °C. NPE 1800 = ●; NPE C = ■.

Table IV: Apparent maximum packing fraction and adsorbed layer thickness for carbon black particles in the presence of NP, NPE and PE series surfactants

Surfactants	ϕ_m	δ (nm)
NP 20	0.540	5.8
PE 104	0.497	8.8
NPE 1800	0.533	6.3
NP 150	0.490	9.3
PE 108	0.468	11.0
NPE C	0.469	10.8

Downloaded by NORTH CAROLINA STATE UNIV on October 11, 2012 | http://pubs.acs.org
Publication Date: May 5, 1996 | doi: 10.1021/bk-1995-0615.ch010

In the case of the NP series a slow increase of G' and G" moduli is observed until $\phi \sim 0.35$ where G" = G' and then a rapid rise of G' occurs which is steeper for the low molecular weight NP 20 and NP 50 surfactants (Figure 10).

PE 104 and PE 108 polymers are able to produce stable dispersions showing a similar behaviour to those prepared using NPE or NP surfactants with an equivalent number of EO units per chain. The results obtained using PE 108 (which contains two PEO chains of 148 units each) are comparable to those obtained using NPE C which contains 175 EO units (see Figure 12). Thus, the onset of the rapid increase of the moduli above a given volume fraction of particles has been shown to be determined by the length of the PEO chain, i.e., by the thickness of the adsorbed layer, only in the case of stable suspensions.

The curves regarding NPE surfactants (Figure 12) show a remarkably similar trend to those obtained for the NP series. Careful inspection of the change of the modulus with ϕ in the region where G' > G" ($\phi \sim 0.34$ for NPE C and 0.45 for NPE 1800), clearly indicates a much steeper increase in G' and G" as the chain length of the PEO moiety becomes smaller. In other words, in the presence of the shortest PEO chain (27 units), the dispersion behaves as a near hard sphere, showing a rapid increase in G' as soon as the PEO chains touch. However with the largest PEO chain (174 units) there is a possibility of denting or compression of the chains and this is reflected in a less steep rise of G' and G" corresponding to a softer interaction. This behaviour is analogous to that already described, for the NP surfactants.

Flocculation studies. In the present investigation the critical flocculation temperatures, C.F.T., of the dispersions have been detected from viscoelastic measurements. The elastic and loss moduli, were recorded at a frequency of 1 Hz as the temperature was increased. Both the modulii increase significantly at the flocculation point (11). Given in table V are the C.F.T., for the six surfactants investigated in this study. It is only for the surfactant which contains both the nonyl phenol and the polypropylene anchor groups that the C.F.T. for the carbon black corresponds to the θ temperature for the stabilising PEO chains, this is particularly apparent for the shorter PEO surfactants.

Table V.: The critical flocculation temperature, C.F.T. of the surfactants studied in 0.1 molar sodium sulfate. Note that the θ temperature for the stabilising PEO chains is 80°C (12)

Surfactants	C.F.T.°C
NP 20	50
PE 104	37
NPE 1800	80
NP 150	74
PE 108	69
NPE C	80

Conclusions

This study shows that in order for the surfactant to act as good steric stabilisers, then strong anchoring to the particle surface is necessary. If the surface of the particles is heterogeneous, which is the case for a carbon black surface, which is largely hydrophobic in nature but contains some hydrophilic surface groups, a heterogeneous anchor group for the surfactant is required

Literature Cited

1. Vincent, B., Adv. Colloid Interface Science, 1974, 4, 193.
2. Luckham, P.F., Adv. Colloid Interface Science, 1991, 34, 191.
3. Miano, F., Bailey, A.I., Luckham, P.F. and Tadros, Th.F., Colloids and Surfaces 1992, 62, 111.
4. Miano, F., Bailey, A.I., Luckham, P.F. and Tadros, Th.F., Colloids and Surfaces 1992, 68, 9.
5. Medalia, A.I. and Heckiman, Carbon, 1969, 7, 567.
6. Baleaux, M.B., C.R. Acad. Sci. Ser. A., 1975, 1617, 274.
7. Kreiger, I.M. and Doughty, M., Trans. Soc. Rheology, 1959, 3, 137.
8. Prestidge, C. and Tadros, Th.F. J. Colloid Interface Sci., 1988, 124, 660
9. Van den Boomgaart, Th., tadros, Th.F. and Lyklema, J., J. Colloid Interface Sci., 1987, 116, 8.
10. Hoffman, R.L., Trans. Soc. Rheology, 1972, 16, 155.
11. Petit, L. and Noetinger, Rheologica Acta, 1988, 27, 437.
10. Liang, W., Tadros, Th.F. and Luckham, P.F. J. Colloid Interface Sci., 1992, 153, 131.
11. Kim, I.T. and Luckham, P.F., Colloids and Surfaces, 1992, 68, 243.

RECEIVED September 14, 1995

Downloaded by NORTH CAROLINA STATE UNIV on October 11, 2012 | http://pubs.acs.org
Publication Date: May 5, 1996 | doi: 10.1021/bk-1995-0615.ch010

Chapter 11

Influence of Polymer End-Group Chemistry and Segment–Substrate Interactions on Polymer Adsorption Kinetics

Case Studies with Polyethylene Oxide

M. M. Santore, M. S. Kelly[1], E. Mubarekyan, and V. A. Rebar

**Department of Chemical Engineering, Lehigh University,
Bethlehem, PA 18015–4791**

The role of molecular architecture and segment-substrate interactions in polymer adsorption is investigated with a combination of dispersion-generated isotherms and Total Internal Reflectance Fluorescence (TIRF) adsorption kinetic studies on the plateau of the isotherm. The work focuses on the water-soluble system of end-modified polyethylene oxide (PEO) and silica and polystyrene substrates. A correlation was found between the rate of adsorption from gentle shearing flow and the apparent adsorption energy of the polymer. Competitive adsorption experiments for two modified PEO's adsorbing onto PS revealed that the more hydrophobic of the PEO samples was preferred on the surface, with the order of introduction having little influence on the ultimate coverage. A convection-diffusion analysis of the TIRF experiments with non-adsorbing polymer agreed with dynamic light scattering results, and revealed that all PEO solutions were dominated by aggregates, ranging in size from 150-300 nm.

Polymer adsorption fundamentals are relevant to a number of technologies including separations, wastewater treatment, rheological modifiers, and coatings additives. These applications have driven research on adsorbed polymer layers, which until recently focused on equilibrium aspects of homopolymers and diblock copolymers. While most of the structure-related issues have been addressed on the fundamental level(*1,2*), a great many questions remain about the kinetic processes involved in building up adsorbed polymer layers, the extent to which such layers equilibrate, and their dynamic properties. Of particular interest are how molecular architecture and segment-substrate interactions influence the equilibration process. Such knowledge would greatly enhance our ability to tailor additives for specific end-use applications.

[1] Current address: Block Drug Company, 257 Cornelison Avenue, Jersey City, NJ 07302

0097–6156/95/0615–0183$12.00/0

The study of the kinetic and dynamic features of adsorbed layers is challenging, because a non-invasive technique is required, and information must be obtained in real time. Therefore, methods such as neutron scattering and reflectivity which provide great molecular-level detail, but where sampling times can exceed several hours, are not generally applicable to kinetic problems. Some of the earliest studies of polymer adsorption and desorption kinetics have exploited ellipsometry, which is sensitive to the total adsorbed mass and the first moment of the mass distribution near the interface. Pioneers such as Fuller(*3*) and Takahashi(*4*) employed ellipsometry to determine that in the homopolymer adsorption process, the layer thickness is first established, and the layer subsequently densifies as chains add at a relatively constant layer thickness. Hydrodynamic methods such as dynamic light scattering(*5*) and capillary flow studies(*6*) have also been used in kinetic studies, but the interpretation of the results requires knowledge of the relationship between layer structure and hydrodynamic thickness, a major complication. ATR-IR was exploited by Granick(*7*) to probe fundamental aspects of desorption and competitive exchange processes. This technique is useful because the adsorbed amount can be quantified from the IR spectra, as can the number of segment-surface contacts in certain systems. The drawback, however, is that the method is apparently difficult to extend to a variety of substrates, as Granick has focused primarily on the surfaces of the IR crystals themselves.

Recently, Total Internal Reflectance Fluorescence, (TIRF), a technique employed in the biotech community to study protein adsorption(*8*), was extended to the study of polymers. Rondelez and coworkers(*9*) were the first to exploit TIRF to document a depletion layer in xanthan solutions(*10*) near a silica surface. These authors also studied adsorption of polymethyl methacrylate onto sapphire(*11*), but have not exploited TIRF to the fullest extent possible to probe dynamic and kinetic features of polymer layers. TIRF is exceptionally powerful, compared to ellipsometry and hydrodynamic methods, because it can be applied to a number of substrates, requiring only optical clarity. TIRF can monitor, in real time, a number of layer features including the adsorbed mass(*12*), the adsorbed chain number(Rebar & Santore, submitted to *Macromol.*), aspects of the molecular configuration(*13*), and the behavior of subpopulations within a sample(*14,18*). The drawback with TIRF is that fluorescent labeling of some fraction of polymer chains is required, and it is essential to establish the extent to which the fluorescent labels alter a polymer's interfacial physics.

In this work we exploit TIRF to study the adsorption kinetics of polyethylene oxide (PEO) onto two model substrates: silica and polystyrene. The work focuses on chemical endgroup modification of the PEO: Fluorescein is added to one end of each PEO chain directly, or via a hydrophobic linking agent. The comparison between samples that vary the attachment of the fluorescein label make it trivial whether or not the fluorescent label itself influences the adsorption kinetics or equilibrium adsorbed amount. Further, the fluorescein label was chosen over other dyes such as rhodamine and anthracene because fluorescein appears to have less impact on the partitioning of PEO between free solution and adsorbed layers. Presented here are case studies which demonstrate the impact of end group chemistry and backbone segment-surface interactions on the adsorption in unchallenged and competitive situations. These examples suggest how isotherm behavior and kinetic effects can be related, and are part of an ongoing systematic study to determine the impact of molecular features and substrate chemistry on polymer dynamics.

Experimental.

Materials. This work employed fluorescently-labeled and hydrophobically-modified PEO (100K, Aldrich, or 97K Polymer Labs), synthesized and purified via procedures already described.(*14*) The two types of samples were Fluorescein-PEO (FPEO), which contained fluorescein on one end of each chain, and Fluoresceinamine-isophoronediisocyanate-PEO (FlAm-IPDI-PEO), which contained a hydrophobic isophorone diisocyanate linker between a fluorescein label and one end of each PEO chain. The chains in the former sample were nearly all labeled, while approximately 75-80% of the chains of the FlAm-IPDI-PEO sample were labeled.

Polystyrene (PS) films, spincast onto microscope slides from a 2% solution of 100,000 molecular weight standard (PolySciences) in toluene, served as a substrate for a flow-adsorption kinetics study. Polystyrene latex (300 nm., provided by Lehigh's Emulsion Polymers Institute) comprised a dispersed analog to the films, which was employed to generate isotherms in a dispersion screening test. Acid-washed microscope slides comprised a second planar substrate for kinetic studies. ESCA analysis of their surfaces revealed only silica. The dispersed analog to the silica flat was 1 μm silica spheres (GelTech), also employed in isotherm screening studies. The intent with these two substrate chemistries was to compare a relatively hydrophobic surface (PS, with a contact angle near 90°) to a hydrophilic one (silica, contact angle very small) capable of hydrogen bonding to the main PEO backbone.

The solvent for adsorption kinetics studies was phosphate-buffered saline (0.147 M NaCl, 0.002M KH_2PO_4, and 0.008M Na_2HPO_4, all from Fisher), necessary to minimize the impact of interfacial conditions (elevated fluorophore concentration and local pH and potential) on the quantum yield of the fluorophores on adsorbed chains(*15*). For the screening isotherm studies involving the PS latex, however, DI (deionized) water was employed. Here the buffer was unnecessary because only the free fluorophores were assayed, and unwanted because buffer flocculates the latex. A previous comparison of FPEO adsorption on PS from buffer and DI water revealed a sharper shoulder in the former, attributed to latex flocculation, but similar plateau coverages for the two solvents.(*14*)

Isotherm Screening Test. Isotherms on PS were generated employing a series of identical latex samples, all 3.23 wt % solids (1 g total in each), into which polymer solutions (10 g each) of varied concentration were added. After agitation for 10 minutes and a 1-hour equilibration period, the latex was centrifuged at 7000 rpm for 1 hour and the serum analyzed for fluorescence to determine the free polymer concentration. Isotherms on silica were generated with a series of polymer solutions (7 g each) of varied concentration, into each of which 1 g. of silica spheres was added. The dispersions were mixed vigorously by hand for several minutes and then left undisturbed. The silica particles settled overnight under gravity, and the serum analyzed by fluorescence for the free polymer. Isotherms were generated from mass balances on the polymer.

Total Internal Reflectance Fluorescence (TIRF). TIRF was employed to measure adsorption kinetics from shearing flow onto PS films and silica, as illustrated in Figure 1, a schematic of the TIRF flow configuration which emphasizes the optical physics. Here, a fluorescently-labeled polymer solution flows in a slit-shear cell past the planar substrate, a PS film on a microscope slide. The flow channel, machined into a black Teflon block, follows the design of Robertson(*8*). The backside of the slide is masked with black spray paint except for a 9-mm diameter window to prevent stray reflections, and then coupled with refractive-index matching oil (Cargille) to a dove prism waveguide (CVI laser). A laser beam (488 nm, Ar+, Coherent) is totally internally reflected inside the substrate, at the PS film-solution interface, to generate an evanescent wave whose intensity, I(y), decays normal to the interface in the y-direction with decay length (or "penetration depth") Λ:

$$I(y) = I_0 e^{-y/\Lambda} \qquad (1)$$

Λ is a function of the refractive indices of the waveguide and polymer solution, and the angle of reflection. In our case, $\Lambda = 65$ nm. As fluorescently-tagged chains diffuse near the surface and adsorb, their labels become fluorescent. The fluorescence detection scheme is not shown in Figure 1; however, the emissions are collected by 2 aspheric lenses (Melles Griot) focused through a sharp cut high-pass filter (Schott, SOG540) onto the photocathode of a PMT (Hammamatsu, R464). The latter is connected to a photon counting system (Stanford Research, SR465). During adsorption, desorption, and exchange experiments, continuous flow was maintained in the cell by a Harvard Apparatus syringe pump. All lines and valves were Teflon, and the syringes were polyethylene.

In experiments such as ours, the evolution of the fluorescent signal tracks the changing fluorophore concentration or number in the evanescent zone (to first order), and hence the adsorption process. The impact of the local environment on the quantum yield (at most a secondary effect in this study) has been documented in a qualitative sense for experimental systems different from ours, and used as a tool to evidence surface relaxations.(*13*)

While a number of techniques have previously been employed to study adsorption kinetics in terms of mass surface excess, TIRF used in conjunction with samples whose labeling densities approach 1 tag/chain (even in polydisperse samples) provides a unique perspective: the evolution of the chain number on the surface. Further, the use of a planar substrate eliminates flocculation-induced complications often encountered in dispersed systems and provides a means, through flow rate adjustments, to control and increase the transport-limited rate of chain arrival at the substrate. Hence, the underlying kinetics can be more readily extracted with this experiment compared with colloidal or non-flow studies.

Analysis of TIRF Data. Two aspects of the TIRF data have been analyzed quantitatively: The relationship between the signal and the surface excess, and from the shapes of some of the kinetic traces, the extraction of the average diffusion coefficient of the dominant adsorbing species.

Internal calibration attempts following the methods of Rondelez(*9*), Andrade(*12*), and Lenhoff(*16*) (or modifications of those methods) have been described elsewhere,(*14*, Rebar & Santore, Submitted to *Macromol.*) for FPEO and FlAm-IPDI-PEO adsorbing onto PS and silica, respectively. In both cases, surface excesses up to a factor of 10 below the expected values were found, for a variety of potential reasons including scattering artifacts, a difference in the quantum yield of the fluorophore on free species and those on adsorbed molecules, and a selectivity of the surface for the high molecular weight species in a polydisperse homopolymer(*17*,*18*). Close investigation revealed no evidence specific to the quantum yield argument (either through direct fluorophore-fluorophore and fluorophore-substrate interactions, or environmental effects)(Rebar & Santore, submitted to *Macromol.*), nor were scattering effects apparent in the y-intercepts of the universal calibration method of Andrade. Run-to-run variations in the relative contributions of the free and adsorbed chains to the TIRF signal, however, suggested scatter effects might have been so large, especially with a PS film substrate, that the inner filter effect was not apparent and the scattering factor mistakenly neglected in our application of Andrade's method(*14*, and Rebar and Santore, submitted to *Macromol.*). Also, a close examination of molecular weight effects in the latex-generated isotherms reveal molecular weight selectivity might exacerbate the calibration inaccuracies, but by no more than a factor of 2.(*17*) For these reasons, we relied on the externally-generated adsorption isotherms to approximate the long-time surface coverage, and assumed linearity between fluorescence signal and surface excess over the range of conditions employed, an assumption typical in TIRF studies.

All of our studies thus far suggest that the TIRF signal is indeed monotonically increasing in surface coverage as expected, although direct linearity has been more difficult to prove conclusively. (Such proof was sought by attempted comparisons of colloidal isotherms and TIRF isotherms; however, history-dependent adsorption confounded this approach over a sufficiently large range of concentrations.) In favor of the linearity argument, we found that on silica, polymer solutions doped with 50% unlabeled chains led to adsorbed layers with half the signal seen for layers adsorbed from completely-labeled samples(*18*). As adsorption on PS films appears well-behaved(*14*), the linearity between the TIRF signal and the surface excess was assumed to apply here as well.

Establishing the linearity of the signal and the surface excess was the first step toward fundamental kinetic studies. In this work, a diffusion-convection analysis(*19-21*) of the slit-flow cell was employed to determine the average diffusion coefficient, and hence the identity, of the adsorbing species (micelles vs. single chains). The particular experiment to extract the diffusivity employed conditions that prevented adsorption. Then a diffusion-convection mass balance in dimensionless form was applied:

$$\frac{\partial C}{\partial \tau} + \eta\,(1 - \eta\,\mathrm{Pe}^{-1/3})\,\frac{\partial C}{\partial X} = \frac{\partial^2 C}{\partial \eta^2} \qquad (2)$$

where C is the dimensionless concentration of the diffusing species, normalized on that of the bulk solution, and τ is dimensionless time. X is the dimensionless flow direction, parallel to the substrate as indicated in Figure 1 and normalized on the distance from the entrance port to the point of observation, $L_\infty = 2.5$ cm. η is the dimensionless distance from the substrate into solution, normalized on the diffusive boundary layer thickness:

$$\eta \equiv \mathrm{Pe}^{1/3}\, y / H_\infty \quad \text{with} \quad \mathrm{Pe} \equiv \frac{\gamma H_\infty^3}{\mathcal{D} L_\infty} \qquad (3a, 3b)$$

H_∞ is the cell depth, in our case 0.5 mm, and the dimensionless Peclet number, Pe, includes the shear rate, γ, and the diffusion coefficient, $\mathcal{D}$. Also, in equation 2, the dimensionless time, τ, is defined:

$$\tau = \frac{t}{L_\infty \mathrm{Pe}^{1/3} / (\gamma H_\infty)} \qquad (4)$$

Initially, the cell contains only flowing solvent, but after a valve turnover, a polymer solution front progresses through the cell with the appropriate local velocity in the X-direction. This gives the initial condition

$$C(\tau{=}0) = 0 \quad \text{for } X > 0 \text{ and } \forall\ \eta \qquad (5a)$$

$$C(X{=}0,\tau{=}0) = 1 \quad \text{for } \forall\ \eta \qquad (5b)$$

and the boundary condition far from the surface:

$$C(\eta \to \infty) = 0 \quad \text{for } \tau < \tau_c \qquad (6a)$$

$$C(\eta \to \infty) = 1 \quad \text{for } \tau \geq \tau_c \qquad (6b)$$

with the contact time τ_c defined:

$$\tau_c = \frac{X}{\eta\,(1 - \eta \mathrm{Pe}^{-1/3})} \qquad (6c)$$

Following the treatment of Lenhoff(*20*), we found it sufficient to apply the condition in equation 6 at $\eta = 4$. Additionally, the condition of no adsorption on the surface leads to

$$\frac{\partial C}{\partial \eta}\Big|_{\eta \to 0} = 0 \qquad \text{for} \quad \forall\, \tau \qquad (7)$$

Equations 2 - 7 were solved numerically to determine the evolution of the free concentration near the surface at the point of observation, $C(\eta=0, X=1)$, as a function of τ, for different values of the Peclet number. The best fit of this model to the data led to an evaluation of $\mathcal{D}$, an average which represents the fluorescently-labeled species in solution. The Stokes-Einstein equation,

$$\mathcal{D} = \frac{kT}{6\pi\ \mu\, R_H} \qquad (8)$$

was employed to determine the hydrodynamic radius, R_H, of the diffusing species. Here k is Boltzman's constant, T is absolute temperature, μ is the viscosity of water.

Results.

The isotherms in Figure 2, for PEO, FPEO, and FlAm-IPDI-PEO adsorbing onto PS latex and silica spheres, demonstrate the impact of fluorescent labeling, hydrophobic end-group modification, and substrate chemistry on the partitioning of PEO between free solution and an adsorbed layer. Comparison of the filled and hollow circles, for a 100%-labeled FPEO sample and the same sample doped with 50% unlabeled PEO chains of approximately the same molecular weight, demonstrates that the fluorescein tag, when attached to PEO via a single thio-urethane linkage, negligibly affects the adsorption behavior on PS. This means that the PEO adsorption to the PS is primarily through interaction of the main backbone with the substrate. The same conclusion concerning the interaction of the main backbone with the surface is reached for PEO adsorbing onto silica: Here the filled and hollow squares on a single isotherm correspond, respectively, to a completely labeled sample and one comprised of labeled chains (50%) and unlabeled chains (50%). One concludes, however, that FPEO adsorbs differently on silica and PS. The ultimate coverage on silica is lower than on PS; however, the initial slope is steeper, perhaps indicating a greater number of PEO-silica contacts per chain due to a higher adsorption energy on silica. Figure 2 also illustrates that in contrast to the impact of the fluorescent label alone, the inclusion of a hydrophobic IPDI unit between the fluorescein and the PEO chain end increases the affinity for a PS surface, seen both by the higher ultimate plateau coverage and by the steeper initial slope for this sample.

Figure 3 illustrates the adsorption kinetics for 150 ppm solutions (on the isotherm plateaus of Figure 2) of FPEO and FlAm-IDPI-PEO adsorbing onto silica and PS substrates. The data for FlAm-IPDI-PEO on PS and FPEO on silica have been shifted upwards to facilitate easy examination. All three experiments can be interpreted as follows: A finite baseline was first established during the continuous flow of

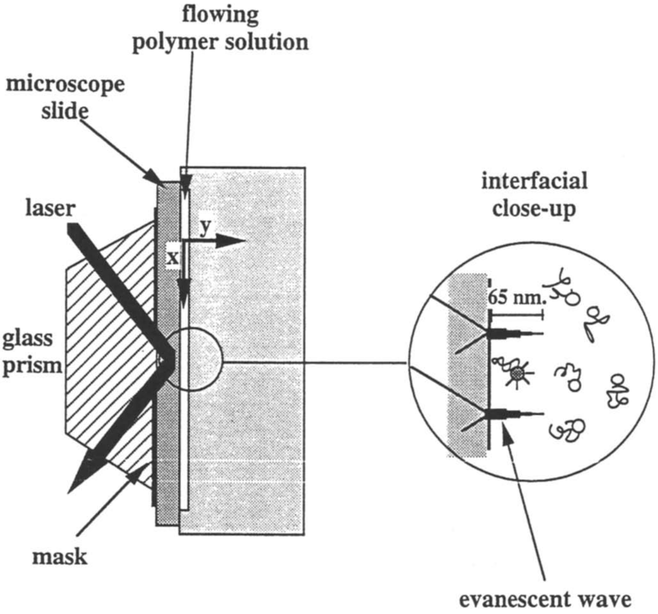
flowing
polymer solution
microscope
slide
laser
y
x
glass
prism
mask
interfacial
close-up
65 nm.
evanescent wave

Figure 1. Schematic of TIRF cell and evanescent wave.

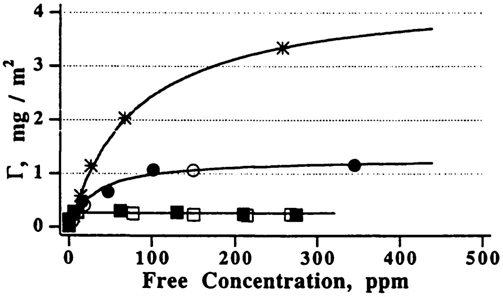

Figure 2. Adsorption isotherms for (•) FPEO on PS; (o) 50-50 mix of FPEO and PEO on PS; (■) FPEO on silica; (❑) 50-50 mix of FPEO and PEO on silica; (*) FlAm-IPDI-PEO on PS.

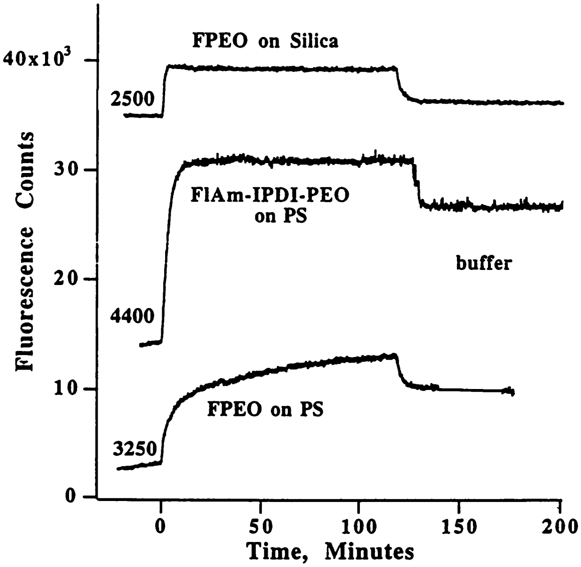

Figure 3. Adsorption kinetics via TIRF.

phosphate-buffered saline (actual values printed). Then at time zero, the polymer solution was injected and the signal rose as adsorption proceeded. After two hours, phosphate-buffered saline without polymer was reinjected and any desorption monitored for the next two hours. The initial rapid signal drop upon buffer reinjection resulted from the removal of free chains from the evanescent zone. (With an evanescent decay length of $\Lambda = 65$ nm., the excitation light reaches fluorophores on adsorbed and free chains when a polymer solution contacts the layer.) The signal remaining after the first few minutes of buffer reinjection comes from the adsorbed layer. Subsequent decreases in signal indicate desorption.

The three experiments in Figure 3 exhibit markedly different behavior. FlAm-IPDI-PEO adsorbs rapidly on PS, and the adsorption process appears nearly complete within 2 hours. Conversely, the adsorption of FPEO on PS is slower, and a gradual signal increase persists for more than two hours. FPEO on silica exhibits a small but reproducible overshoot in the early stages of adsorption, and all but the smallest changes appear complete after 2 hours. This overshoot is discussed in detail elsewhere.(18, and Rebar & Santore, submitted to *Macromol.*)

Figure 4 demonstrates the competitive adsorption characteristics of FPEO and FlAm-IPDI-PEO. Figure 4a is a continuation of the FPEO run in Figure 3. After the FPEO injection and subsequent solvent flush, FlAm-IDPI-PEO was introduced, causing the signal to rise rapidly and level off shortly thereafter. The subsequent solvent flush after 2 hours of FlAm-IPDI-PEO exposure reveals a further increase in coverage, suggesting that the FlAm-IPDI-PEO chains have incorporated into the preadsorbed FPEO layer, or even possibly displaced the original FPEO. In Figure 4B the two polymer samples have been introduced in the reverse order with FPEO chains challenging a preadsorbed FlAm-IPDI-PEO layer. In this case, the FPEO chains exhibit negligible adsorption: Upon buffer reintroduction, the signal drops to nearly the same level it had been prior to the FPEO injection. Also the shape and extent of the signal rise for the FPEO injection in Figure 4B argue against adsorption. The initial rise is rapid and plateaus quickly compared with the kinetics for FPEO on a bare PS surface in Figure 3. The amount of the rise is equal to the bulk signal contribution for 150 ppm FPEO or FlAm-IPDI-PEO, identified in Figure 3. Hence, the surface contribution in Figure 4B is relatively unchanged by the contact of FPEO chains with a FlAm-IDPI-PEO layer, at least for a period of 2 hours.

The second signal rise in Figure 4B, and those in other runs like that in Figure 4B, were exploited to determine the average diffusion coefficient of the dominant fluorescent species (micelles, clusters, or free chains) in the FPEO sample. The analyses, via the model in equations 2 - 7 required that adsorption did not occur when the polymer solution was introduced into the flow channel. In our case, a preadsorbed layer of FlAm-IPDI-PEO prevented FPEO adsorption. Figure 5 illustrates the best-fit comparison between such non-adsorbing flow tracer data and the convection-diffusion model for a 150 ppm solution of FPEO. Here the concentration or fluorescence intensity on the y-axis has been normalized on the maximum, and the time axis is represented without dimensions, as defined by equation 4. The amount by which the data have been shifted on the time axis leads to the diffusivity, here $\mathcal{D} = 7.2 \times 10^{-9}$ cm^2/s, with the best fit found for Pe = 9000, also consistent with this diffusivity value. The Stokes-Einstein equation (8) translates this into a hydrodynamic radius of $R_H = 318$ nm., which is larger than anticipated. Repetition of this experiment revealed hydrodynamic radii between 150 and 350 nm. over 10+ samples. For a single 100,000 molecular weight PEO coil, there are N=1140 statistical segments, each with a length a = 0.4 nm. This leads to a statistical radius $R_g = a(N/6)^{0.5} = 5.5$ nm. in a theta solvent and $R_g = a(N/6)^{0.6} = 9.3$ nm. in a good solvent. Both values are considerably smaller than R_H, suggesting our FPEO samples contain aggregates. Preliminary dynamic light scattering experiments on solutions of unlabeled PEO, FPEO, and FlAm-IPDI-PEO

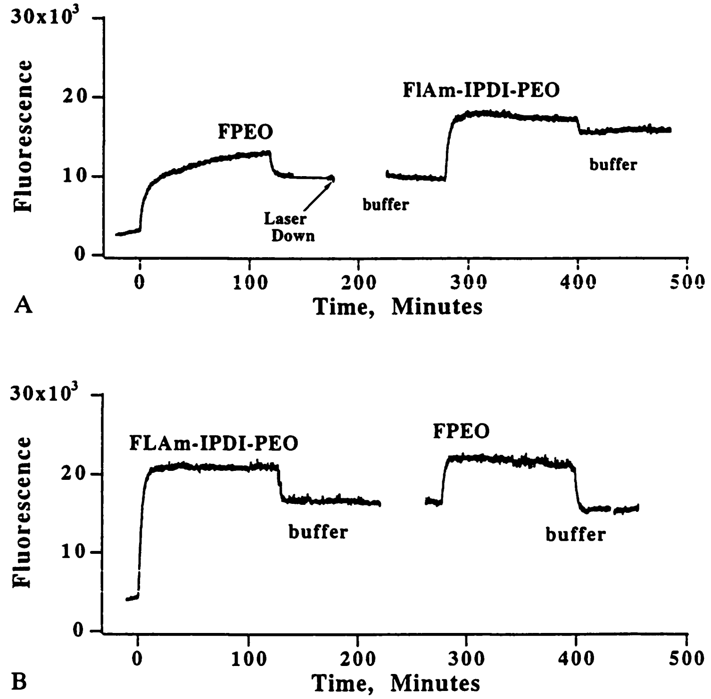

Figure 4. Competitive adsorption between FPEO and FlAm-IPDI-PEO on PS. (A) FPEO introduction is followed by solvent, FlAm-IPDI-PEO, and solvent again. (B) FlAm-IPDI-PEO introduction is followed by solvent, FPEO, and solvent again. (Reproduced with permission from Reference 14. Copyright 1995 Elsevier Science.)

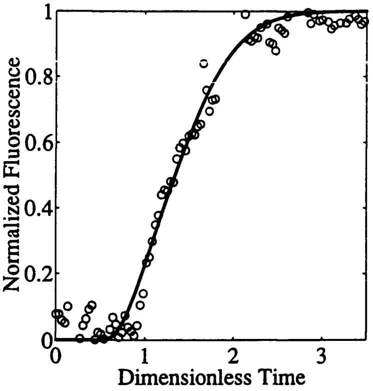

Figure 5. Signal rise for FPEO flowing past a preadsorbed FlAm-IPDI-PEO layer. Line shows best fit to equations 2-7 to determine free species diffusivity.

revealed aggregates in the size range 150-300 nm. for all three samples, in agreement with the TIRF findings for the diffusivity of FPEO.

Discussion.

The adsorption kinetics measured by TIRF in Figure 3 are in accord with the shapes and relative coverages of the isotherms in Figure 2, for analogous dispersed substrates. The initial isotherm slopes, proportional to the adsorption energy (to the extent that equilibrium is achieved in the generation of the isotherms) are ranked: FPEO on PS < FlAm-IPDI-PEO on PS < FPEO on silica, in order of increasing adsorption energy. This ranking roughly parallels the initial adsorption rates measured by TIRF, with the note that the initial slope for FPEO on silica only slightly exceeds that for FlAm-IPDI-PEO on PS, as the transport-limited rate of chain arrival is approached. The weaker adsorption of FPEO on PS is evident in the results of both techniques, though TIRF does indeed reveal good retention of FPEO on PS in buffer.

The overshoot in the adsorption kinetics of FPEO on silica (not seen on PS) may be a result of the stronger binding on silica, where non-equilibrium states exist at short times and the surface becomes temporarily overloaded. The observation that FPEO can achieve just over 1 mg/m^2 on the isotherm plateau for a PS substrate, but reaches less than half of this coverage on the silica isotherm also suggests tighter binding and a denser layer on the latter. A great number of segment surface contacts with silica, evidenced by the initially steep isotherm, would leave few free sites for additional chains, giving a decreased plateau coverage. For silica, if the large number of segment surface contacts does not develop instantaneously, the kinetic overshoots would be explained.

The ultimate relative signal levels measured via TIRF are also in general accord with the relative isotherm plateaus for the dispersed systems, although there is some discrepancy at the quantitative level. For example, approximately 3 times as much FlAm-IPDI-PEO adsorbs on PS compared with FPEO. The TIRF experiment, however, reveals a ratio closer to 2 for the ultimate retained signal from the layers. Such discrepancies may result from unavoidable chemical differences between the planar and dispersed substrates, so perfect agreement is not expected.

The competitive adsorption of FPEO and FlAm-IDPI-PEO on PS films also follows expectations, based on the isotherms measured on PS latex. Here coverage increases when a FPEO layer, preadsorbed from 150 ppm solution, is exposed to a 150 ppm of FlAm-IPDI-PEO. The FlAm-IPDI-PEO should be preferred on the surface because of its hydrophobic end group and, therefore, could potentially displace FPEO even in the presence of FPEO free chains (a situation different from that in Figure 4). For a free concentration of 150 ppm, the adsorbed amount of FlAm-IPDI-PEO should be higher than that of FPEO, and hence it might be expected that FlAm-IDPI-PEO could also incorporate into the FPEO layer without displacing the original FPEO chains. With the information in hand, we can only speculate whether the FPEO is displaced. Notably, the complete retention of FPEO chains during FlAm-IDPI-PEO incorporation would suggest that FlAm-IDPI-PEO can find additional sites (possibly more hydrophobic regions of the surface) on the silica.

The finding that clusters dominate the diffusion of both FPEO and FlAm-IDPI-PEO was not entirely unanticipated. Since dynamic light scattering experiments were in agreement with the TIRF findings for FPEO, and since dynamic light scattering revealed aggregates of the same size in solutions of unlabeled PEO, the clustering appears to be driven by the PEO backbone chemistry and the solvent properties rather than the fluorescein isothiocyanate label in the FPEO. Additionally, the hydrophobic IPDI-linker in the FlAm-IDPI-PEO sample appears not to significantly influence the clustering through the increased hydrophobicity of one end of each chain. Such clustering has been broadly documented for PEO(*22,23*) and has been studied in detail by Polverari(*24*), who found the clusters to be fairly persistent (of slow equilibration time) and removable by filtering.

The implications of PEO aggregation for adsorption kinetics remains an unexplored area. While Gast(*25*) found overshoots in adsorption of copolymers above their CMC, the PEO aggregates are not of the same core-corona structure, so it is not clear if Gast's observations translate to our system. One clearly expects clustering to alter the maximum transport limited adsorption rate attainable with our PEO samples, but without knowing the number of chains per cluster, it is not clear if clustering increases or decreases the transport-limited adsorption rate compared to that of single chains in a good or theta solvent. Also, we have no information about the influence of clusters on the kinetic approach to equilibrium adsorption (dominated by surface processes) or the nature of the equilibrated state (patchy or uniform coverage).

Conclusions.

The adsorption kinetics and relative ultimate surface coverages measured by TIRF for end-modified PEO samples onto planar substrates were in accord with the adsorption behavior identified with dispersed analogs of the planar silica and PS. In particular, the initial isotherm slope, indicative of the adsorption energy, correlated with the initial adsorption rate measured in TIRF, up to the transport-limited rate. For the ultimate plateau coverage it was found, as expected, that hydrophobic modification of a single end group on a PEO chain enhanced adsorption on PS. Also, the steeper initial slope and lower ultimate coverage of FPEO on silica suggested that the PEO backbone binds more tightly to silica than PS. This was borne out in the kinetic traces by overshoots during FPEO adsorption on silica but not on PS.

The use of TIRF to extract an average diffusivity for a polymer solution in a non-adsorbing situation revealed diffusion coefficients and hydrodynamic radii that were in good agreement with dynamic light scattering, building confidence in TIRF as a probe of diffusion. The range of hydrodynamic radii were much larger than anticipated for single chains, suggesting that PEO clusters dominated the solution dynamics. Such clustering was found to be driven by the nature of the PEO backbone and the solvent quality, with minimal influence of the endgroup modification. Whether the clusters increase the transport-limited adsorption rate (important for FPEO adsorbing on silica, and FlAm-IPDI-PEO adsorbing on PS) depends on the number of chains per cluster and the cluster density. It is not thought that the clusters are directly responsible for the overshoots observed for FPEO adsorbing onto silica.

Acknowledgments.

This work was supported by the Exxon Educational Foundation, the National Science Foundation (CTS 9209290), and Lehigh's Polymer Interfaces Center and Chemical Engineering Department. Special thanks go to Luke DeWalt and Daniel Ou-Yang of Lehigh's Physics Department for their dynamic light scattering analysis of our samples.

Literature Cited.

1. Fleer, G.J., Cohen Stuart, M.A., Scheutjens, J.M.H.M., Cosgrove, T., and Vincent, B., *Polymers at Interfaces*; Chapman Hall: New York, NY, 1992.
2. deGennes, P.G., *Adv. Colloid Interface Sci.*, **1987**, *27*, 189-209.
3. Lee, J.-J.,Fuller, G.G., *J. Coll. Int. Sci.* **1985**, *103*, 569-577.
4. Kawaguchi, M., Hayakawa, K., and Takahashi, A., *Macromolecules* **1983**, *16*, 631-635.
5. Garvey, M.J., Tadros, T.F., and Vincent, B., *J. Coll. Int. Sci.* **1976**, *55*, 440-453.
6. Cohen, Y., and Metzner, A.B., *Macromol.* **1982**,*15*, 1425-1429.
7. Kuzmenka, D.J., and Granick, S., *Coll. Surf.* **1988**, *31*, 105-116.
8. Lok, B.K., Cheng, Y.L., and Robertson, C.R., *J. Coll. Int. Sci.* **1983**, *91* 87-103.
9. Rondelez, F., Ausserre, D., and Hervet, H., *Ann. Rev. Phys. Chem.* **1987**, *38*, 317-47.
10. Allain, C., Ausserre, D., and Rondelez, F., *Phys. Rev. Lett.* **1985**, *54*, 1948-1951.
11. Caucheteux, I, Hervet, H, Jerome, R., and Rondelez, F., *J. Chem. Soc. Farad. Trans.* **1990**, *86(9)*, 1369 -1375.
12. Hlady, V., Reineche, D.R., and Andrade, J.D., *J. Coll. Int. Sci.* **1986**, *111*, 555-569.
13. Darst, S.A., Robertson, C.R., and Berzofsky, J.A., *J. Coll. Int. Sci.* **1986**, *111*, 466-474.
14. Kelly, M.S., and Santore, M.M., *Coll. Surf. A: Phys Chem Eng Aspects* **1995**, *96*, 199-215.
15. Rebar, V.A., and Santore, M. M. *J. Coll. Int. Sci.* in press.
16. Shibata, C.T., and Lenhoff, A.M., *J. Coll. Int. Sci.* **1992**, *148*, 469-484.
17. Kelly, M.S., and Santore, M.M. *J. Appl. Polym. Sci.* in press.
18. Santore, M. M., and Rebar, V.A., *Proceedings of the Symposium on Dynamics in Confined Spaces*, *MRS Symp. Proc.* **1994**, *366*.
19. Lok, B.K., Cheng, Y.L., and Robertson, C.R., *J. Coll. Int. Sci.* **1983**, *91* 104 - 116.
20. Shibata, C.T., and Lenhoff, A.M., *J. Coll. Int. Sci.* **1992**, *148*, 485-507.
21. Kelly, M.S., Master's Thesis, Lehigh University, Chemical Engineering, **1993**.
22. Cuniberti, C., *European Polymer Journal* **1974**, *10*, 1175.
23. Polik, W.F., and Bouchard, W., *Macromolecules* **1983**, *16*, 978.
24. Polverari, M., and Van deVen, T., *Langmuir*, in press.
25. Leermakers, F.A.M., and Gast A.P., *Macromol.* **1991** *24* 718-730.

RECEIVED June 16, 1995

Chapter 12

Adsorption Studies on Mixed Silica–Polymer–Surfactant Systems

T. Cosgrove[1], S. J. Mears[1], L. Thompson[2], and I. Howell[2]

[1]Department of Physical Chemistry, School of Chemistry, University of Bristol, Cantock's Close, Bristol BS8 1TS, United Kingdom
[2]Port Sunlight Laboratory, Unilever Research, Quarry Road East, Bebington, Wirral, Merseyside L63 3JW, United Kingdom

Downloaded by NORTH CAROLINA STATE UNIV on October 11, 2012 | http://pubs.acs.org
Publication Date: May 5, 1996 | doi: 10.1021/bk-1995-0615.ch012

Photon correlation spectroscopy measurements have been performed on aqueous silica dispersions containing physisorbed poly(ethylene oxide) in the presence of the surfactant sodium dodecyl sulfate. From the measurements, it appeared that near complete desorption of the polymer occurred around the critical micelle concentration of the pure surfactant. However, at very high surfactant concentrations, the apparent hydrodynamic thickness returned to its initial value in the absence of surfactant. The results are discussed in terms of the specific interactions between the polymer and the surfactant.

Non-ionic polymers such as polyethylene oxide (PEO) and polyvinylpyrolidone (PVP) form self-assembled complexes with anionic surfactants, for example sodium dodecyl sulfate (SDS), in aqueous solution[1,2]. These complexes play an important role in key industrial applications such as colloid stabilization and destabilization, enhanced oil recovery and detergency. Clearly, it is important to identify both the structure of these complexes in solution and any further complexation that may occur on adsorption. Industrially, polymers are used to aid the deposition of silicone emulsions onto skin and hair from shower gel and shampoo formulations. However, this action is subject to interference from the surfactant system which, by virtue of its interaction with the polymer, can either promote or prevent deposition. By studying the interaction between these polymers and surfactants, both in solution and at the interface, the deposition properties can be determined and related to the structure of the interfacial layer.

0097–6156/95/0615–0196$12.00/0

Downloaded by NORTH CAROLINA STATE UNIV on October 11, 2012 | http://pubs.acs.org
Publication Date: May 5, 1996 | doi: 10.1021/bk-1995-0615.ch012

Although adsorption from mixed component systems has been studied extensively [3-5] most of this work has been directed at systems in which both components can adsorb. Changes in adsorption can then occur either because of competitive adsorption or for reasons associated with the polymer/surfactant interactions, making data interpretation more complex. In general, it is the complexation that appears dominant. For example, Ma and Li[3] reported that on the surface of ferric oxide, the adsorption of SDS was almost unaltered by the presence of PVP. The adsorption of PVP however was observed to increase markedly due to the presence of SDS at low concentrations (less than the cmc), followed by a dramatic decrease in adsorption at high SDS concentrations. It was suggested that this was due to complex formation between SDS and PVP, with surface complexes at low SDS concentrations and solution complexes at high SDS concentrations. Similarly, Esumi and Matsui[4] investigated the adsorption of PVP and poly(dimethyldiallylammonium chloride) (PDC) on silica as a function of PVP concentration in the presence of PDC. They reported that the adsorption of PDC decreases with increasing PVP concentration, especially at high concentrations of PDC. Most recently, Schubin[5] has investigated the effect of SDS on the structure of adsorbed layers of the commercial polyelectrolyte Quatrisoft LM 200 on mica. This system differs from the others mentioned above in that only the polymer, not SDS adsorbs onto the substrate. A dramatic decrease in the adsorbed amount around the cmc was reported, so that at an SDS concentration slightly above the cmc, the polymer was almost completely desorbed. Schubin also measured the thickness of the adsorbed layer by ellipsometry, finding that levels of SDS around the cmc led to extended though sparse polymer layers.

In this paper, we discuss the perturbation of the adsorption of the homopolymer PEO by the addition of SDS at the silica/water interface in terms of adsorption and hydrodynamic thickness measurements. This system shares the advantage of Schubin's investigation in that only one of the soluble components adsorbs onto the substrates. PEO readily adsorbs onto silica[6,7], giving high affinity isotherms. Adsorbed amounts tend to be of the order of 1mg m^{-2} but are dependent upon molecular weight[7]. SDS does not adsorb onto silica to any significant extent at neutral pH's since under these conditions both the surfactant and the substrate are of the same charge[8]. It is well documented that PEO interacts with SDS at surfactant concentrations above 2.3×10^{-3}g cm^{-3} to form well defined micelles with an aggregation number of approximately 60 at the critical micelle concentration of the pure surfactant, cmc[1,9]. Cabane[1] has suggested that the structure of these mixed micelles may be represented as the polymer loosely wrapping around the surfactant aggregate. This proposed model has also been described as 'surfactant micelle pearls on a polymer backbone necklace'. It is suggested that the SDS/PEO/water interface retains a certain stoichometric concentration, and when the composition of the solution departs from this stoichometry the mixed micelles resist this change resulting in an excess of either polymer or surfactant in solution. The addition of PEO to an SDS solution lowers the cmc and up until this 'reduced cmc', which is dependent upon the polymer concentration, both the SDS and PEO exist as discrete molecules. However, more recent papers have suggested that there may be some interaction between SDS and PEO molecules at surfactant concentrations as low as 4×10^{-4} mol dm^{-3} (9). There does not appear to be any literature on the SDS/PEO interaction in the presence of a solid/liquid interface.

Downloaded by NORTH CAROLINA STATE UNIV on October 11, 2012 | http://pubs.acs.org
Publication Date: May 5, 1996 | doi: 10.1021/bk-1995-0615.ch012

Experimental Techniques

In photon correlation spectroscopy (PCS), or dynamic light scattering, the scattered light is modulated by the Brownian motion of the diffusing particles. By examining the spectral width of the scattered light particle sizes can be calculated. A correlation function is calculated from these fluctuating electric fields which are incident on the photomultiplier tube. This intensity correlation has an exponential form from Brownian particles, whose time constant τ_c is related to the diffusion coefficient, D *i.e.* $\tau_c = 1/Q^2D$ where Q is the momentum transfer vector. For dilute solutions D is given by the Stokes-Einstein equation;

$$D = \frac{kT}{6\pi\eta a}$$

where a is the particle radius, T is the absolute temperature, k is Boltzmann's constant and η is the solution viscosity. For the case of adsorbed polymer layers the hydrodynamic thickness can be extracted from a knowledge of the particle radius with and without polymer layer. It has been shown in several papers that the hydrodynamic thickness measured in this way is sensitive to polymer segments at the periphery of the adsorbed layer and that these segments may be found at several times the solution radius of gyration of the polymer, from the interface[6]. A Malvern PCS 1000 spectrometer and a laser operating at a wavelength of 514.5 nm were employed. The conventional adsorption isotherms were determined using the tannic acid method[10]. In this technique free polymer is removed from the silica particles by centrifugation, (14,000 r.p.m. for 30 minutes). The PEO concentration in the supernatant is detected colorimetrically by complexation with tannic acid using UV spectrometry and is sensitive to concentrations of the order of 10 ppm.

Downloaded by NORTH CAROLINA STATE UNIV on October 11, 2012 | http://pubs.acs.org
Publication Date: May 5, 1996 | doi: 10.1021/bk-1995-0615.ch012

Materials

The substrate used in this study was the commercial silica Snowtex ZL which has average particle diameters of 90±5 nm (transmission electron microscopy) and 104±1 nm (PCS). This dispersion has an isoelectric point at approximately pH 4 and under the conditions used in this study a pH of approximately 7. Before use, the silica dispersion was dialyzed against double-distilled water. The polymer, polyethylene oxide (PEO) was of molecular weight 200,000 (M_w/M_n = 1.1) and was obtained from Polymer Laboratories Limited, UK, whilst the surfactant, SDS, was from BDH chemicals. These chemicals were of analytical grade and were used as received.

All samples were prepared by adding to a solution of known amount of polymer and surfactant a stock suspension of silica. All dispersions were prepared 24 hours in advance of measurement and solutions containing PEO kept in the dark as much as possible in order to prevent photochemical degradation. All samples containing SDS were discarded after 4 days to ensure only a minimal concentration of the hydrolysis product dodecanol. Those samples required for PCS measurements had a final solids concentration of 1,000 ppm and were corrected for the background viscosity prior to analysis. In the time dependent studies the samples were thoroughly mixed prior to insertion in the spectrometer.

Results and Discussion

Figure 1 shows the conventional adsorption isotherms for PEO in the absence of surfactant. As expected the isotherm is of high affinity and yields saturation coverage of 0.9mg m^{-2} with an equilibrium polymer concentration of 50 ppm. This corresponds well with literature values and the total amount of polymer required for this adsorbed amount was used in all subsequent experiments. Unfortunately, using the tannic acid method[10] (or indeed any other conventional method) it was not possible to obtain reproducible PEO adsorption isotherms in the presence of more surfactant than 30 ppm. This is most probably due to the formation of PEO/SDS aggregates in solution which also bind to the reagent used to determine the PEO concentration. This indicates an interaction between the polymer and surfactant at even lower concentration of SDS than discussed by Ramachandran and Kennedy [9]. Although results were difficult to obtain there was a clear indication that on addition of even very small quantities of surfactant [~ 50 ppm] appreciable PEO desorption took place. However, because of the uncertainty of measuring the absolute PEO concentrations, an isotherm could not be plotted.

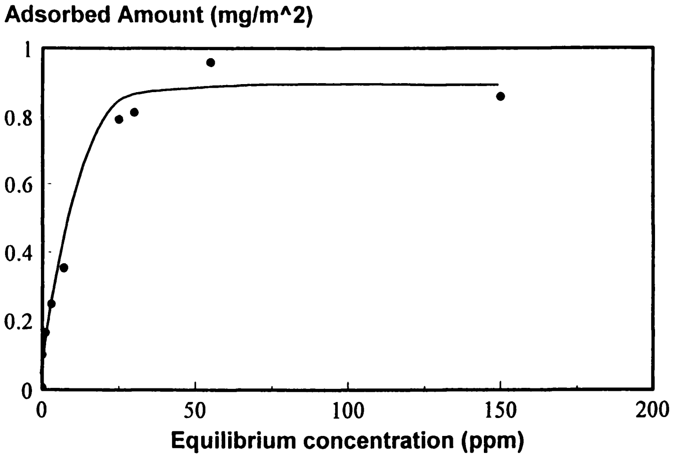

Figure 1. Adsorption isotherms of PEO on silica in the absence of SDS

A measure of the kinetics for equilibration of the adsorbed layer for this system is demonstrated in Figure 2. In these experiments all the components were added simultaneously and thoroughly mixed before measurement. Both the substrate concentration and the polymer concentration remain constant. In the absence of added surfactant the hydrodynamic thickness [δ_H] reaches its final value almost immediately and shows very little change with time, whilst a system containing 1000ppm (3.44 x 10^{-3}mol dm^{-3} i.e. ~ cmc/2[†]) of surfactant requires approximately 15 minutes to reach equilibrium. At the highest surfactant concentration used (11,200 ppm ~ 4 cmc) the final hydrodynamic thickness is only achieved after 10 hr. and for this reason all samples were left to equilibrate for at least 24 hours before use. The slow increase in δ_H with time corresponds to a re-equilibration of the polymer with the surface but presumably as an SDS-PEO complex. This will be discussed further later in the paper. In order to check this last somewhat surprising re-adsorption in the presence of excess SDS the experiment was repeated by using sequential addition. The results are shown in Figure 3. Initially a substantial layer is formed and this was left to equilibrate for 30 minutes. The sample was then mixed with SDS to give 2,700 ppm solution. Almost immediately the adsorbed layer thickness is strongly depressed either by a reduction in the adsorbed amount or by a collapse of the layer. The former proposition is more likely. After a further hour excess SDS was added to increase the concentration to 8000 ppm. Over the next 30 minutes, an effective increase in the adsorbed layer is observed which confirms the previous result in Figure 2. The

---

[†] Where the cmc referred to is that in the absence of polymer.

Downloaded by NORTH CAROLINA STATE UNIV on October 11, 2012 | http://pubs.acs.org
Publication Date: May 5, 1996 | doi: 10.1021/bk-1995-0615.ch012

Downloaded by NORTH CAROLINA STATE UNIV on October 11, 2012 | http://pubs.acs.org
Publication Date: May 5, 1996 | doi: 10.1021/bk-1995-0615.ch012

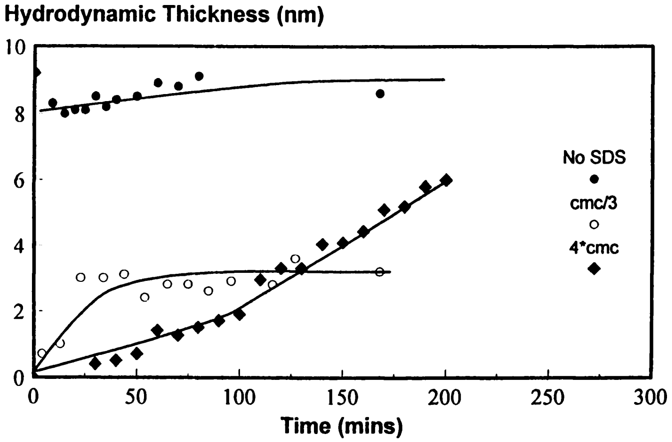

Figure 2. Hydrodynamic thickness versus time for fixed PEO/SDS at different SDS concentrations

increase in viscosity of the solution on addition of this quantity of SDS is of the order of 5% and neither this or scattering from PEO-SDS complexes can account for the observed effects. In the absence of PEO the particle size of silica is independant of SDS concentration throughout the range studied.

Figure 4 shows the hydrodynamic thickness as a function of adsorbed amount for 200,000 molecular weight PEO. As expected, there is a very low thickness at low coverage, followed by a steep increase in the hydrodynamic thickness (δ_H) as the adsorbed amount approaches full coverage. An important point to note from this observation is that the tail segments contribute more to the hydrodynamic thickness than do the train or loop segments. As a result, any variations in hydrodynamic thickness observed are more likely to arise from interactions at the periphery of the molecule than directly at the surface. With SDS the rate of increase of the layer thickness with added polymer is considerably less. At the cmc the thickness is virtually negligible. On increasing the SDS concentration to 2cmc the curve is rising more steeply indicative of re-adsorption of the polymer. However, we have no independent measure of the adsorbed amount and the observed thickness does not necessarily mean that the adsorbed amount approaches that of the pure PEO/silica system.

Figure 5 shows the effect of SDS concentration on the thickness of the adsorbed PEO layer on silica, in the range 0-10,000 ppm SDS at 200 ppm of added polymer. The hydrodynamic thickness goes through a minimum at a surfactant concentration close to the cmc. Our results are not dissimilar to those of Schubin[5] for SDS/cationic polyelectrolyte adsorbed on mica. Schubin's data, show that increasing surfactant induces a steady desorption of material from the interface at above a concentration of 5 ppm SDS. The reduction in adsorption correlates well

Downloaded by NORTH CAROLINA STATE UNIV on October 11, 2012 | http://pubs.acs.org
Publication Date: May 5, 1996 | doi: 10.1021/bk-1995-0615.ch012

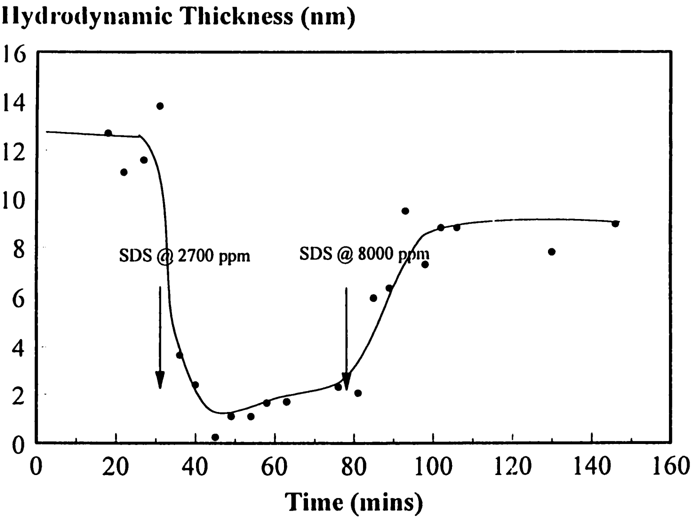

Figure 3 Hydrodynamic thickness versus time for the sequential adsorption of PEO and SDS as indicated.

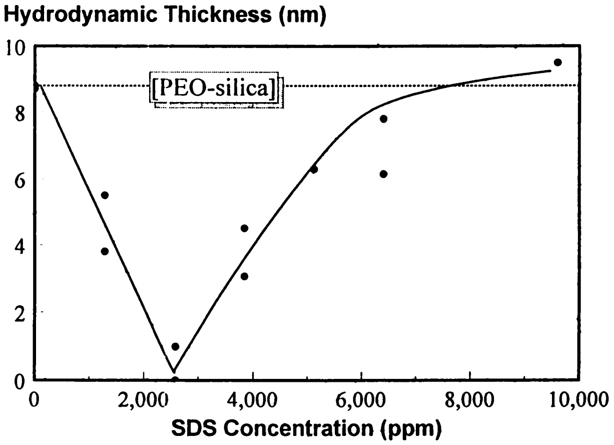

Figure 4. Hydrodynamic thickness as a function of PEO concentration for PEO adsorbed onto silica for different SDS concentrations

Downloaded by NORTH CAROLINA STATE UNIV on October 11, 2012 | http://pubs.acs.org
Publication Date: May 5, 1996 | doi: 10.1021/bk-1995-0615.ch012

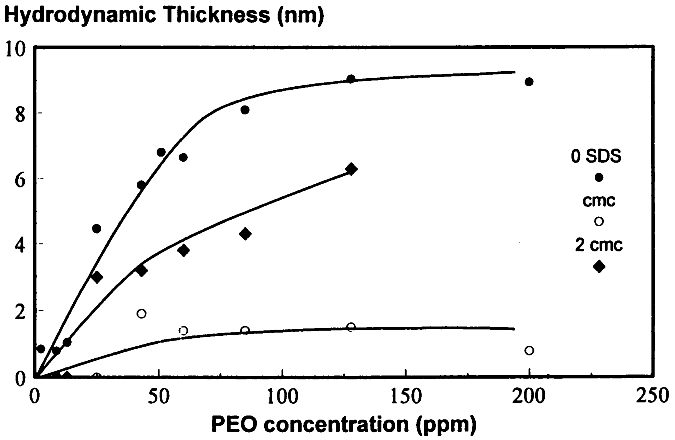

Figure 5. Hydrodynamic thickness versus SDS concentration for PEO adsorbed onto silica in the plateau of the isotherm

with the trend in layer thickness in our data up to 2000 ppm. Between concentrations of 50 ppm and 600 ppm, however, the adsorbed layer in that system becomes substantially more extended. It seems likely that this effect is due to the formation of micelles along the polymer chain, which repel each other, causing the chain to adopt a more extended configuration. In our system, the increase in adsorbed layer thickness occurs at a higher concentration, but this may simply reflect a higher cmc for the SDS/PEO system. The expected trend to polymer desorption at lower surfactant levels is supported by the limited data that we have (Figure 2) but further data are undoubtedly required before we have a complete picture of the situation.

Another possible explanation for the minimum in Figure 5 has been eliminated. This is that a surface active impurity in the surfactant could displace the polymer below the cmc, but is taken into the micelles above the cmc, so that re-adsorption of the polymer could occur. The only such impurity that can be reasonably proposed in this system is dodecanol, a hydrolysis product of SDS. We have added a quantity of dodecanol sufficient to give significant coverage if adsorbed (100Å^2/molecule) to a polymer coated dispersion in the absence of SDS. This quantity, which is about an order of magnitude higher than that likely to be found in practice produced no discernible effect on the PEO layer thickness.

Conclusions

The adsorption of poly(ethylene oxide) from aqueous solutions is markedly affected by the presence of the surfactant SDS. Below the cmc a progressive desorption of PEO is indicated by a rapid decrease in the hydrodynamic thickness.

This was attributed to complexing of the adsorbed PEO making it increasingly negatively charged, which was the same sign as the charge on the particle. At higher concentrations of surfactant, a surprising increase in the layer thickness was seen, which was reversible. The hydrodynamic thickness of this layer does not indicate *per se* that the adsorbed amount reaches that which was found in the absence of polymer but could indicate a very dilute but extended layer comprised of the polymer decorated with micelles. We intend to carry out neutron scattering experiments to define more conclusively the structure of the adsorbed layer.

Downloaded by NORTH CAROLINA STATE UNIV on October 11, 2012 | http://pubs.acs.org
Publication Date: May 5, 1996 | doi: 10.1021/bk-1995-0615.ch012

References

1. Cabane, B.; *J Phys Chem* 1977, **81**, 1639
2. Jones, M.; *Coll. Int. Sci* 1967, **23**, 36
3. Ma, C., Li, C.; *J. Coll. Int Sci* 1989, **132[2]**, 485
4. Esumi, K., Matsui, H.,; *Colloids and Surfaces* 1993, **80**, 273
5. Schubin, V.; *Langmuir* 1992, **10**, 10935.
6. Cohen Stuart, M..A.,Waajen, F. H. W. H., Cosgrove, T., Vincent B., Crowley T. L.; *Macromolecules* 1984, **17**, 1825,
7. Van der Beek, G.P., Cohen Stuart, M.A.; *J. Phys. France* 1988, **49**, 1449
8. Leimbach, J., Rupprecht, H.; *Colloid and Polymer Science* 1993, **271**, 307
9. Ramachandran, R., Kennedy, G. J.; *Colloids and Surfaces* 1991, **54**, 261
10. Nuysink, J., Koopal, L. K.; *Talanta* 1982, **29**, 495

RECEIVED August 16, 1995

Chapter 13

Adsorption of Triblock Copolymers on Nanoparticulate Pharmaceutical Imaging Agents

J. F. Bishop[1], T. H. Mourey[2], and J. Texter[3,4]

[1]Emulsion Processing Division, Manufacturing Research and Engineering, Eastman Kodak Company, Rochester, NY 14652–3701
[2]Analytical Technology Division, Manufacturing Research and Engineering, Eastman Kodak Company, Rochester, NY 14650–2136
[3]Analytical Technology Division, Manufacturing Research and Engineering, Eastman Kodak Company, Rochester, NY 14652–3712

Triiodobenzoate esters (imaging agents) have been introduced as novel nanoparticulate colloids for enhancing x-ray imaging with parenteral administration. BAB-type block copolymer dispersants comprising poly(ethylene oxide) (PEO; B) and poly(propylene oxide) (PPO; A) blocks have been examined in dispersions of these imaging agents. Adsorption isotherms of several BAB-type dispersants (Pluronic F68, F87, and F108) and of an $X(AB)_4$-type dispersant (Tetronic 908) in aqueous dispersions of two imaging agents are reported. Adsorption fits the Langmuir isotherm, binding constants appear correlated with the A-block molecular weight, and saturation adsorption appears inversely correlated with A-block molecular weight and with overall molecular weight. The BAB and $X(AB)_4$ dispersants exhibit markedly different preferential adsorption. The energetics and packing constraints suggest PPO blocks provide the actual binding contacts with the imaging agent surfaces, and the data further indicate that the PPO blocks bind in loops and trains. The free energy of adsorption appears a linear function of the length of PPO segments.

The delivery of aqueous insoluble nanoparticulate pharmaceuticals is an important emerging technology (*1*). A significant area of development in this technology is the delivery of agents useful in x-ray diagnostic medical imaging (*2*). The nanoparticulate system for this application comprises particles of a crystalline organic x-ray contrast agent stabilized by a surface modifier adsorbed on the surfaces. The present study was undertaken to determine the adsorption of various surface modifiers on two candidate x-ray agents.

The aqueous adsorption of a series of Pluronic BAB-type block copolymeric dispersants F-68, F-87, and F-108 (BASF Corporation; hereafter F68, F87, F108, respectively) to nanoparticulate imaging agents was established as the focal point of the present study. Two such imaging agents, **IA1** and **IA2**, were examined in this study. Both of these imaging agents are 2,4,6-triiodo-3,5-bisacetamidobenzoate esters

---

[4]Corresponding author

0097–6156/95/0615–0205$12.00/0

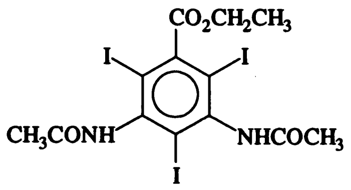

IA1

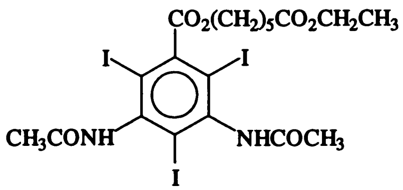

IA2

(*3*). **IA1** is the simple ethyl ester and **IA2** is 6-(ethoxy-6'-oxohexyl)-2,4,6-triiodo-3,5-bisacetamido-benzoate. Hydrolysis of the benzoate ester functionality, between the 2-iodo and 6-iodo substituents is highly sterically hindered. The second ester functionality in **IA2** provides for more rapid hydrolysis in vivo and for more rapid elimination from the body.

The use of nonionic dispersants in pharmaceutical formulation is increasing, particularly because nonionics such as Pluronics (polyoxamers) have low toxicity, a rich phase-behavior in aqueous solution, and efficacy as colloidal stabilizers. Drug release, including lidocaine and indomethacin, from Pluronic micellar solutions and gels has been investigated (*4–9*). The use of Pluronics as passivation against unwanted blood plasma protein adsorption on polystyrene nanoparticles has also been studied (*10,11*). Tan et al. (*11*) found that Pluronic F-108 and Tetronic T-908 were very effective in reducing plasma protein adsorption and increased the blood circulation half-life of 75 nm polystyrene nanoparticles about 40 fold.

The structures of the polymeric dispersants are illustrated in Table I, along with molecular weight and composition data derived from information provided by the vendor (BASF). The Pluronic dispersants are BAB block copolymers of poly(ethylene oxide) (PEO) and poly(propylene oxide) (PPO) oligomers. This Pluronic series varies in overall molecular weight, as well as varying in the formula weight of the PPO block. It is noteworthy that F87 has a lower molecular weight than F68, but a substantially larger (29%) PPO block. The Tetronic dispersant T908 has the largest molecular weight among these nonionic block copolymers.

Experimental Section

The Pluronic F68, F87, and F108 and the Tetronic T-908 dispersants were obtained from BASF Corporation (Wyandotte, MI). The imaging agents **IA1** and **IA2** were synthesized and provided by the Chemicals Development Department, Sterling-Winthrop Pharmaceutical Research Division (Collegeville, PA).

Aqueous nanoparticulate slurries were prepared by roller milling for seven days. An aqueous slurry of each imaging agent was prepared by milling without added dispersant to provide materials of uniform specific surface area. These slurries were milled in a one-gallon ball mill at 65% of critical speed using 1-mm diameter Zircon XR

Table I. Pluronic and Tetronic Dispersants

	Nominal Mol. Wt.	*PPO Mol. Wt.*	*x*	*y*
$(EO)_x(PO)_y(EO)_x$				
F68	8400	1740	76	30
F87	7700	2260	62	39
F108	14600	3250	129	56
$[(EO)_x(PO)_y]_2NCH_2CH_2CH_2CH_2N[(PO)_y(EO)_x]_2$				
T908	25000	--	113	22

media (zirconium silicate). Initial slurry weights were 1.8 kg. As initially formulated, each was 7.5% (w/w) imaging agent, with the balance being water. The resulting slurry of **IA1** was 7.4% **IA1** and yielded 1571 g at pH 8.9. The resulting slurry of **IA2** was 7.1% **IA2** and yielded 1324 g at pH 8.0. The pH obtained are a result of the intrinsic properties of the milling media and imaging agents, and were obtained without adjustment These slurries were kept in a constant convective field by stirring with a magnetic bar to minimize gravitational sedimentation effects during storage.

Scanning electron microscopy was done using a JEOL JSM-35C scanning electron microscope. Specific surface areas of nanoparticulates in these slurries were determined using a NOVA-1000 (Quantachrome Corporation, Syosset, NY) multipoint gas adsorption instrument. Nitrogen adsorption was analyzed using the BET theory (*12*) of multilayer adsorption. Slurries were first freeze dried in order to isolate them for analysis, and freely flowing powders were obtained.

Size-exclusion chromatography (SEC) was used to examine the molecular weight distribution of the nonionic dispersants used in this study, to detect free dispersant in adsorption experiments utilizing imaging agent dispersions, and to characterize the molecular weight distribution and preferential adsorption of adsorbed/free dispersant.

Molecular weight distributions of dispersants were measured in N,N-dimethylformamide (DMF) containing 0.01M lithium nitrate. Two 10.0 x 250 mm Jordi Gel DVB columns were used at near ambient conditions as described previously (*13*). Solid samples were dissolved at a concentration of 2.5 mg/mL in the eluent containing 0.1% acetone as a flow marker. The nominal flow rate was 1.0 mL/min and the injection volume was 100µL. Absolute molecular weight distributions were calculated from the outputs of differential viscometry and differential refractive index (DRI) detectors and application of a universal calibration curve constructed from poly(ethylene oxide) standards between 645 and 1,390,000 MW.

Universal calibration with viscometry detection and the similar specific refractive index increments of the A and B block units in DMF permit accurate measurement of absolute molecular weight distributions using the method described above. This method is, however, unsuitable for aqueous samples because of interferences from water peaks. Instead, the concentration of aqueous phase (unadsorbed) dispersant was determined by aqueous exclusion chromatography using TSK-20, TSK-30 (both 7.8 x 300 mm) and a 7.5 x 75 mm guard columns coupled in series and thermostated at 30.0 °C. The eluent was 0.05 M sodium sulfate (Fisher Scientific) in 5/95 (v/v) ethylene glycol/distilled and, deionized water. Supernatant samples were injected directly into the SEC in a volume of 100µL at a nominal flow rate of 1.0 mL/min. Concentrations of block copolymer were calculated from the integrated peak areas of the DRI chromatograms and calibration curves of DRI peak area versus concentration.

A molecular weight-retention volume calibration curve for the aqueous exclusion column set was constructed from poly(ethylene glycol) standards and used to estimate molecular weights of block copolymer samples in the supernatant. Although not absolute measures, these poly(ethylene glycol) "equivalent" distributions provide a highly precise relative comparison between samples.

Adsorption isotherms of the Pluronic and Tetronic dispersants were measured at 25°C on each of the **IA1** and **IA2** dispersions. Dispersion (2.5–3.2 g), dispersant (50–1000 µL of 0.5% by weight aqueous solution), and make-up water (10–12 g) were combined and equilibrated 16–24 hours in a shaker bath at 25°C. The suspended and continuous phases were then separated by centrifugation at 25°C in a Sorvall RC-5B centrifuge operating at about 19000 rpm for 2–4 hours. Samples of supernatant were then obtained by pipet and analyzed by SEC for dispersant concentration. Adsorption data were fitted to a simple Langmuir adsorption equation (see equation 1) to derive the saturation adsorption amount and a binding constant. This fitting was done by

Table II. Specific Surface Area of Imaging Agent Slurries

Slurry	*SSA (m^2/g)*	*Edge Length of Equivalent Monodisperse Cubes*
IA1	7.6 ± 0.2	0.36 μm
IA2	19.4 ± 0.2	0.15 μm

nonlinear least-squares, using the MINSQ program (MicroMath Scientific Software, Salt Lake City, UT), and error estimates were derived from uncertainties at the 95% confidence limit.

Results

Scanning electron micrographs (SEM) of these **IA1** and **IA2** dispersions prepared without dispersant were obtained after several weeks of aging in a convective field to examine particle morphology as well as to check primary particle size. These micrographs are illustrated in Figures 1(left) and 1(right) for **IA1** and **IA2**, respectively. The **IA1** nanoparticulates are polydisperse in size and parallelepiped in morphology with maximal dimensions on the order of 1 μm and minimal dimensions of about 100 nm. The **IA2** nanoparticulates appear significantly smaller and geometrically more regularly shaped. Dimensions for these **IA2** nanoparticulates range from 100 to 200 nm. Comparisons of these micrographs with examinations made shortly after milling indicated that **IA1** ripened considerably, while the **IA2** nanoparticulates remained essentially unchanged. Initially obtained micrographs of **IA1** indicated these particulates to be more polydisperse in morphology than **IA2**, with dimensions ranging from 100 to 400 nm. Early examinations of **IA2** nanoparticulates indicated a dimensional distribution only very slightly smaller than that illustrated in Figure 1.

A key parameter by which to scale adsorption of dispersant onto particles of imaging agent when judging or comparing dispersants is the specific surface area of the dispersed phase. The dispersions of **IA1** and **IA2**, described above, were lyophilized and analyzed by BET nitrogen adsorption to determine apparent specific surface areas. Average results of replicate determinations are illustrated in Table II. Equivalent cube edge lengths are also indicated for monodisperse cubic particles having specific surface areas of the respective imaging agents. The 0.36 μm equivalent cubic edge length obtained for the **IA1** nanoparticulates is consistent with the 100 nm to 1 μm dimensional range illustrated in the SEM. Similarly, the 0.15 μm equivalent cubic edge length obtained for the **IA2** nanoparticulates is consistent with the 100 to 200 nm dimensional range illustrated in the SEM of Figure 1.

Molecular weight distributions of the dispersants are noticeably bimodal (Figure 2). The molecular weights of the low-molecular weight components illustrated

Table III. Measured Weight-Average Molecular Weights

	F68	*F87*	*F108*	*T908*
Principal Mode				
SEC	8910	7620	18400	28200
Nominal	8400	7700	14600	25000
Apparent BA Di-Block Mode				
SEC	4560	3610	8620	7750
Nominal	5080	4990	8900	6300

and also given in Table III are consistent with BA-diblock impurities. The SEC experiment only measures molecular size and cannot confirm the structure of these impurity molecules. Although their sizes are more consistent with BA diblocks, the presence of homopolymers is also possible. However, preliminary investigations (*14*) using reverse phase liquid chromatography (*15*) indicate that poly(ethylene oxide) homopolymer is not present.

Adsorption isotherm data at 25°C were generated and analyzed according to simple Langmuir adsorption. The most common representation of the Langmuir adsorption isotherm is given according to equation 1,

$$\eta = \frac{bc\eta_s}{bc+1} \qquad (1)$$

where η is the specific adsorption (μmol/m^2), η_s is the saturation ("monolayer") specific adsorption, b is a binding constant,

$$b = e^{-\Delta G_{ads}/RT} \qquad (2)$$

where ΔG_{ads} is the free energy of adsorption, R is the gas constant, and T is temperature, and c is dispersant concentration in the continuous phase (supernatant after centrifugation and phase separation).

Specific surface areas determined by BET adsorption analysis were used to normalize adsorption in terms of area. Results obtained for adsorption of F87 in the **IA1** slurry and for F108 in the **IA2** slurry are illustrated in Figure 3 and are typical of the results obtained for each of these four dispersants with slurries **IA1** and **IA2**. While the adsorption appears Langmuirian, the specific adsorption amounts obtained experimentally were limited to the range of about 50–95% of the saturation values, and the corresponding equilibrium concentrations of dispersant in the supernatant generally spanned a dynamic range of about 5–6. The saturation-specific adsorption and the binding constant parameters, obtained by nonlinear least-squares fitting these adsorption data to equation 1, are summarized in Table IV. The uncertainties illustrated in Table IV were obtained in the numerical nonlinear fitting for estimates at

Table IV. Fitted Binding and Saturation Constants for Adsorption Isotherms[a]

Dispersant	log (b/M^{-1})	η_s	
		(μmol/m^2)	*(mg/g)*
IA1 Slurry			
F68	4.58 (-0.63/+0.25)	0.195 (± 0.064)	12.4
F87	4.85 (-0.08/+0.07)	0.183 (± 0.009)	10.7
F108	5.04 (-0.28/+0.17)	0.130 (± 0.022)	14.4
T908	5.44 (-0.22/+0.15))	0.058 (± 0.006)	11.0
IA2 Slurry			
F68	4.82 (-0.09/+0.07)	0.132 (± 0.008)	21.5
F87	5.29 (-0.12/+0.08)	0.121 (± 0.006)	18.1
F108	5.32 (-0.06/+0.06)	0.087 (± 0.005)	24.6
T908	5.98 (-0.10/+0.07)	0.042 (± 0.018)	20.4

[a] Uncertainties are calculated at the 95% confidence level.

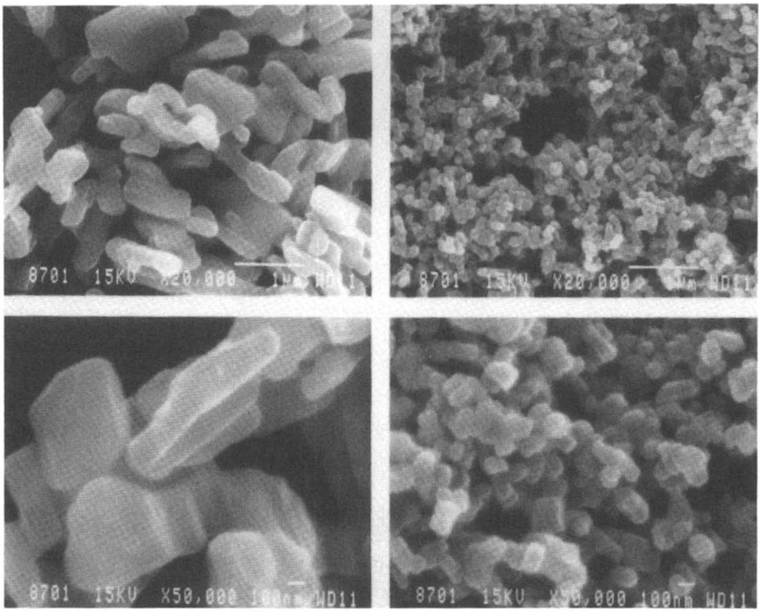
8701 15KU X20,000 1μm WD11
8701 15KU X20,000 1μm WD11
8701 15KU X50,000 100nm WD11
8701 15KU X50,000 100nm WD11

Figure. 1. SEM of (left) IA1 and (right) IA2 dispersion particulates milled without added dispersant; 1 μm (top) and 100 nm (bottom) size bars are illustrated in the micrographs.

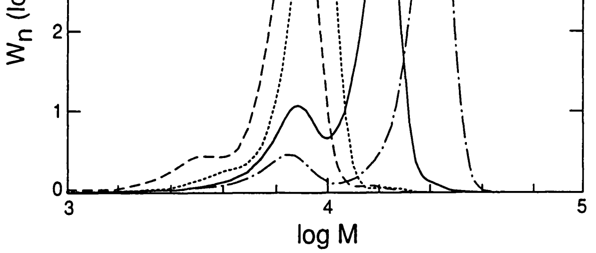

Figure 2. Molecular weight distributions for the Pluronic (F68, F87, and F108) and Tetronic (T908) dispersants. The weight frequency distributions are normalized functions of log(M).

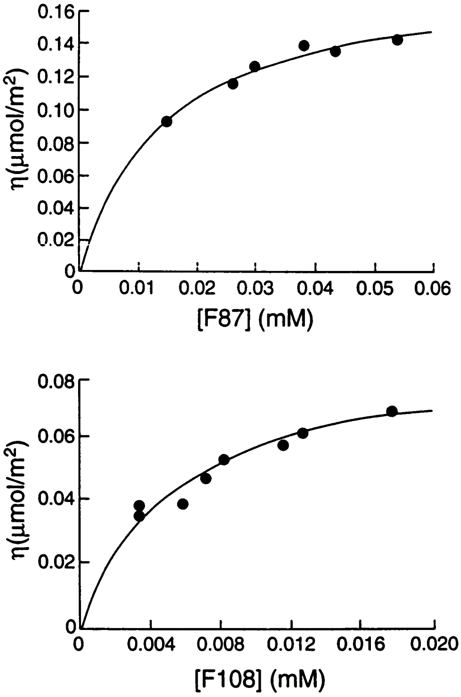

Figure 3. Adsorption at 25°C (top) of F87 in IA1 slurry and (bottom) of F108 in IA2 slurry. Solid curve fitted to data is from Langmuir isotherm, with parameters as listed in Table IV.

the 95% confidence level. The apparently anomalously lower saturation adsorption of F87 relative to F68, on a mg/g weight basis, is a result of the convolution of two factors, a lower specific adsorption (μmol/m^2) *and* a lower overall molecular weight. The lower specific adsorption of F87 is a result of a larger PPO block.

Since there is bi- or trimodal polydispersity in each dispersant, possible preferential adsorption of different molecular weight components was investigated for adsorption of F108 and T908. In the presaturation stages of adsorption, poly(ethylene oxide) equivalent molecular weight distributions of unadsorbed polymeric dispersant in the supernatant were measured by aqueous exclusion chromatography. The poly(ethylene oxide) equivalent distributions in Figure 4 are different in magnitude and shape from the true distributions measured in DMF (Figure 2), but are useful in comparing samples on a relative basis. The unadsorbed polymer in the F108 samples illustrated in Figure 4 (top) from the **IA2** slurry appears slightly shifted to lower molecular weight relative to the F108 control distribution. Marked preferential adsorption of T908 is exhibited in both the **IA1** and **IA2** slurries in Figure 4 (bottom).

Discussion

The Pluronic series of dispersants examined here exhibits an apparent increase in binding affinity with increasing PPO molecular weight (see Tables I and IV), increasing in the order F68 < F87 < F108. While there is statistical overlap from experimental error and fitting uncertainty between pairs of adjacent binding constants in each of these **IA1** and **IA2** series, the same qualitative trend in relative binding affinity is observed for the imaging agents in both of these slurries. This trend is consistent with an adsorption mechanism wherein the PPO blocks stick to the surface and the PEO blocks provide steric stabilization by penetrating the surrounding solvent. PPO-based anchoring has previously been invoked to explain emulsion stabilization (*16*) by such block copolymers, as well as to explain adsorption on hydrophobic (methylated) silica (*17*).

Our results suggest interesting preferential adsorption differences between the Pluronics and the T908 Tetronic. Comparison of results for F108 and T908 in Figure 4 suggests that only minor preferential adsorption occurs for the F108 multicomponent mixture, while marked preferential adsorption of the high molecular weight T908 component, $X(AB)_4$, relative to the corresponding AB diblock. These differences can be understood qualitatively in simple terms that are consistent with the self-consistent field modeling of Evers et al. (*17*). The very marked preferential adsorption exhibited by T908 reflects the competition between a single AB diblock copolymer, and a corresponding star cluster, $X(AB)_4$, having four-fold adsorption capability (four A "stickers" rather than just one). The relatively minor preferential adsorption exhibited by the F108 data of Figure 4 (top) is essentially consistent with the calculated results of self-consistent field theory (*18*). Evers et al. found a proclivity for slight preferential adsorption of A_mB_n diblocks over $B_{n/2}A_mB_{n/2}$ triblocks as a result of greater intermolecular repulsion obtained with the triblocks having two tails.

Presumably, A_mB_k diblocks would adsorb preferentially over A_mB_n diblocks, when $k < n$, due to lower intermolecular repulsion between diblocks having shorter PEO blocks. The results of Evers et al. (*18*; please see Figure 5a therein) indicate that the *weight* of adsorbed diblock increases with increasing A-block length, while the surface concentration decreases slightly and steadily when this weight is scaled for molecular weight. We would therefore expect a slight preferential adsorption (with respect to surface concentration) of $AB_{k/2}$ diblocks over AB_k diblocks because only half as many repulsive EO segments would be available with the $AB_{k/2}$ diblocks.

The contours in Figure 5 of Evers et al. (*18*) suggest that an $A_{56}B_{258}$ diblock would adsorb at about 4.5 effective monolayers, about 50% more than an $A_{56}B_{129}$ diblock, at 3.2 monolayers. This 4.5/3.2 ratio, when scaled for molecular weight (14500/8810), changes to a ratio of 3.1/3.6, and indicates that the surface number

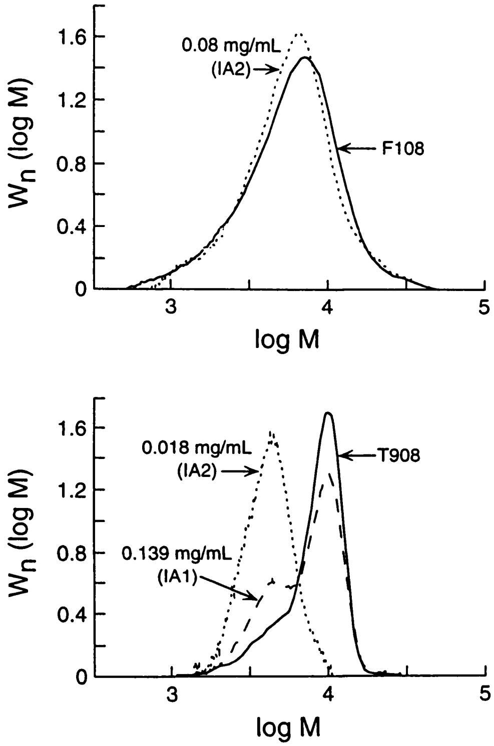

Figure 4. Poly(ethylene oxide) equivalent distributions for (top) F108 adsorption in the IA2 slurry and (bottom) T908 adsorption in the IA1 and IA2 slurries. The solid curves represent the reference or control distribution. The other curves are annotated with the equilibrium dispersant concentration in the supernatant. The differences in these curves represent the preferential adsorption of different molecular weight components.

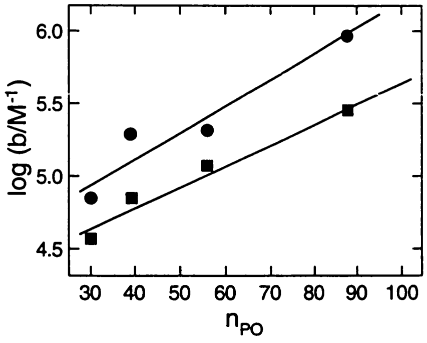

Figure 5. Correlation of free energy of adsorption (log *b/M*$^{-1}$) with the number (n_{PO}) of propylene oxide segments in each dispersant for adsorption on (■) IA1 and (●) IA2. The straight lines are least squares fits with correlation coefficients of 0.99 and 0.96 for the IA1 and IA2 data, respectively.

density of the smaller diblock will be slightly greater. The preferential adsorption of equal molecular weight $A_{100}B_n$ diblocks over $B_{n/2}A_{100}B_{n/2}$ triblocks appears about 10% or less based on Figure 10 of Evers et al. (*18*). An extrapolation of these trends to the F108 adsorption of interest here, assuming an $A_{56}B_{258}$ diblock would preferentially adsorb over a $B_{129}A_{56}B_{129}$ triblock by about 10%, suggests the following: An $A_{56}B_{129}$ diblock would adsorb on a weight basis at about 70% of the $B_{129}A_{56}B_{129}$ triblock, and this translates into a slight preferential adsorption of the diblock, in surface number density terms, by a ratio of 7.9/6.9 (15% greater). The data of Figure 2 indicate the BAB component of F108 is more than four-fold more concentrated, on a weight basis, than the lower molecular weight component. Taking the SEC-measured molecular weights of these components from Table III, the BAB component is more than twice as concentrated in the starting mixtures than is the lower molecular weight component. The very slight preferential adsorption of the triblock components indicated in Figure 4 (top) appears consistent with these predictions of and extrapolations from self-consistent field theory, calling for slight preferential adsorption of diblocks over triblocks (at equal activity or concentration). This very slight preferential adsorption of the BAB component is strong evidence that the lower molecular weight component is not a PEO homopolymer, since PEO is not surface active in these systems. This evidence and interpretation is consistent with the absence of poly(ethylene oxide) homopolymer observed in the reverse phase liquid chromatography of these dispersants (*14,15*).

While the adsorption data appear consistent with a simple Langmuir isotherm, it should be stressed that the dynamic range over which equilibrium block copolymer concentrations were determined was always less than a decade, due to limitations in the ability to determine low concentrations by the SEC-based refractive index detector. It should be mentioned that, in the study of adsorption of PEO-PPO-PEO block copolymers of molecular weight 2700 (PE6200) and 11400 (PE6800) onto methylated silica by Tiberg and coworkers (*17*), adsorption was non-Langmuirian. Similar saturation adsorption limits, on the order of 2–3 mg/m^2, were observed as reported here, however.

The saturation adsorption limits η_s (Table IV) for F68, F87, and F108 appear inversely proportional to A-block (PPO) molecular weight. Inclusion of T908 suggests overall molecular weight, neglecting differences between F68 and F87, may also be significant in controlling saturation. These saturation limits η_s can be converted to equivalent areas per molecule or per PO (propylene oxide) group. On a per molecule basis, these saturation limits from Table IV correspond to 840–1290 Å^2/molecule for F68–T908 adsorption, respectively, onto **IA1** and 1260–1900 Å^2/molecule for F68–T908 adsorption, respectively, onto **IA2**. Miano et al. (*19*) examined the adsorption onto carbon black of a series of BAB block copolymers similar to F108; their copolymers contained A blocks of 56 PO units, as for F108, and contained B-blocks of 16–148 EO (ethylene oxide) units. Their results (*19*) for adsorption of a polymer (PE F108) analogous to F108 yielded a limiting area of about 2500 Å^2/molecule and corresponded to a saturation adsorption of about 6 x 10^{-2} µmol/m^2. A smaller saturation adsorption limit (3.6 x 10^{-2} µmol/m^2) was obtained by Killmann et al. (*20*) for the adsorption of P105 (total molecular weight 6500; PPO block molecular weight 3250, same as F108; PEO blocks only 30% the size of those in F108) onto precipitated silica (having a specific surface area of about 20 m^2/g and average particle diameter of about 200 nm). Comparable saturation limits on macroscopically flat silica surfaces were reported by Malmsten and coworkers (*21*) for PEO (20000 molecular weight) and the Pluronics F127 ($B_{99}A_{65}B_{99}$), F98 ($B_{125}A_{47}B_{125}$), and P75 ($B_{24}A_{35}B_{24}$). These data suggest that these PPO copolymers adsorb more densely onto these imaging agent surfaces than onto carbon black or silica. Carbon black is a very hydrophobic substrate, and silica is very hydrophilic. The presence of the iodine in these imaging agents may tend to make these surfaces more polarizable than those of carbon black and silica and result in stronger adsorption energetics. Additionally, surface corrugation involving the ester chains of these imaging agents may tend to induce preferential alignment in the adsorption of trains, thereby increasing the saturation limits (22).

In a very recent report (*23*) of Pluronic (P105, F68, F88, F108) adsorption onto polystyrene latices (69–272 nm in diameter), it was concluded that the (saturation adsorption) surface concentration is controlled by the A-block size. In the present study of F68, F87, and F108 (Table IV), saturation adsorption *decreases* as A-block size *increases*. However, Li et al. (*23*) report *lower or nominally equal* surface concentrations (molecules per unit area) for F68 than for F108, while in the present study we find the surface concentration (η_s) of F108 to be only 2/3 that of F68 for both **IA1** and **IA2**. The reason for this discrepancy is not apparent, since F68 is roughly about 60% of F108 in various block dimensions. Perhaps the differences are assignable to the different substrates in the two studies. The magnitude of surface concentration determined (*23*) for F68 and F108 of 800–1600 Å^2/molecule is comparable to that found here (850–1900 Å^2/molecule). The relative rank ordering are different, however. The ranking derived in the present study appears consistent with the steric packing concepts developed by Evers et al. (*18*).

The apparent qualitative correlation of binding affinity with A-block molecular weight mentioned above is examined quantitatively in Figure 5, where log(b/M^{-1}) values of Table IV are correlated with the total number of PO segments in each of the dispersants. In this analysis, interestingly, the T908 data, with n_{PO} = 88, appear co-linear with the Pluronic data.

On a per PO group basis, these saturation limits for the adsorption of the Pluronics on **IA1** yield 25 ± 3 Å^2/PO group. For adsorption on **IA2** this limiting area is 37 ± 4 Å^2/PO group. At present, these limits for adsorption onto **IA1** seem too small, since the cross-sectional area of aliphatic chains adsorbed vertically in monolayers is approximately 26–28 Å^2/molecule. It is likely therefore that not all the PO groups are adsorbed onto **IA1** surfaces; the higher limiting area for adsorption onto **IA2** surfaces may indicate a smaller percentage of PO groups are adsorbed. These results support the hypothesis that the PO blocks adsorb in loops and trains, as pictured by Tan et al. (*11*) for adsorption onto polystyrene surfaces. More work is needed to characterize the geometry and packing of these adsorbed segments.

Acknowledgments. The authors are indebted to Karen Maskasky for preparing the imaging agent slurries. The SEC analyses of dispersant molecular weight and concentration were done with the assistance of Trevor Bryan and Brian Owens. Anne West provided scanning electron microscopy. Bella VanPelt and Ed Voll provided BET measurements. This work was motivated by problems raised by Nats Rajagopalan of Sterling-Winthrop Pharmaceutical Research and Development (SWPRD) and was funded by contract No. 177-55510-91007 from SWPRD. Critical comments and suggestions by Nats Rajagopalan given in the preparation of this manuscript are gratefully acknowledged.

Literature Cited

(*1*) Liversidge, G.; Cundy, K. C.; Bishop, J. F.; Czekai, D. A., *U.S. Patent 5,145,684* (1992).

(*2*) Liversidge, G.; Cooper, E. R.; Shaw, J. M.; McIntire, G. L., *U.S. Patent 5,318,767* (1992).

(*3*) Bacon, E. R.; Daum, S. J.; Spara, P. P. *U.S. Patent 5,322,679* (1994).

(*4*) Chen-Chow, P.-C.; Frank, S. G. *Int. J. Pharm.*, **1981**, *8*, 89–99.

(*5*) Gilbert, J. C.; Hasdgraft, J.; Bye, A.; Brookes, L. G. *Int. J. Pharm.*, **1986**, *32*, 223–228.

(*6*) Lin, S.-Y. and Kawashima, Y. *Pharm. Acta Helv.*, **1985**, *60*, 345–350.

(*7*) Miyazake, S.; Yokouchi, C.; Nakamura, T.; Hashiguchi, N.; Hou, W.-M.; Takada, M. *Chem. Pharm. Bull.*, **1986**, *34*, 1801–1808.

(*8*) Lin, S.-Y. and Kawashima, Y. *Pharm. Acta Helv.*, **1985**, *60*, 339–344.

(*9*) Lin, S.-Y. and Kawashima, Y. *J. Parenteral Sci. Tech.*, **1987**, *41*, 83–87.

(*10*) Tan, J. S.; Martic, P. A. *J. Colloid Interface Sci.*, **1990**, *136*, 415–431.

(*11*) Tan, J. S.; Butterfield, D. E.; Voycheck, C. L.; Caldwell, K. D.; Li, J. T. *Biomaterials*, **1993**, *14*, 823–833

(*12*) Adamson, A. W. *Physical Chemistry of Surfaces*, Fifth Edition, John Wiley & Sons, New York (1990); pp. 609–617.

(*13*) Mourey, T. H.; Bryan, T. G. *J. Liq. Chromatogr.*, **1991**, *14*, 719-732.

(*14*) Schunk, T. C. unpublished results (1995).

(*15*) Schunk, T. C. *J. Chromatography A*, **1993**, *656*, 591–615.

(*16*) Napper, D. H.; Netschey. A. *J. Colloid Interface Sci.*, **1971**, *37*, 528–535.

(*17*) Tiberg, F.; Malmsten, M.; Linse, P.; Lindman, B. *Macromolecules*, **1991**, *7*, 2723–2730.

(*18*) Evers, O. A.; Scheutjens, J. M. H. M.; Fleer, G. J. *J. Chem. Soc. Faraday Trans.*, **1990**, *86*, 1333–1340.

(*19*) Miano, F.; Bailey, A.; Luckham, P. F.; Tadros, Th. F. *Colloids Surfaces*, **1992**, *68*, 9–16.

(*20*) Killmann, E.; Maier, H.; Baker, J. A. *Colloids Surfaces*, **1988**, *31*, 51–71.

(*21*) Malmsten, M.; Linse, P.; Cosgrove, T. *Macromolecules*, **1992**, *25*, 2474–2481.

(*22*) Texter, J.; McMillan, M.; Minter, J. R. unpublished x-ray and electron diffraction results (1994).

(*23*) Li, J.-T.; Caldwell, K. D.; Rapoport, N. *Langmuir*, **1994**, *10*, 4475–4482.

RECEIVED July 24, 1995

Downloaded by NORTH CAROLINA STATE UNIV on October 11, 2012 | http://pubs.acs.org
Publication Date: May 5, 1996 | doi: 10.1021/bk-1995-0615.ch014

Chapter 14

Fluorescence Probe Studies of Self-Assembled Monolayer and Multilayer Films from *n*-Alkyltrichlorosilanes

Shaun H. Chen and Curtis W. Frank

Department of Chemical Engineering, Stanford University, Stanford, CA 94305–5025

The fluorescence intensity of mixed monolayers containing a pyrene-labeled probe n-alkyltrichlorosilane in an n-alkyltrichlorosilane host matrix was used to determine the dependence of the energetics of the self-assembly process on the adsorbate chain length. The negative entropic segmental contribution of the hydrocarbon tailgroup was found to be the dominating factor. Fluorescence quenching experiments were performed on the pyrene-doped monolayers and on multilayers with aqueous solutions of nitromethane which quenches the pyrene fluorescence via a dynamic process. The effective diffusivity is decreased for monolayers with pyrene groups located near the film-solution interface, consistent with the pyrene probe becoming more enclosed by the hydrocarbon chain packing. For pyrene probes incorporated in the bottom layer of a multilayer assembly the effective quencher diffusivity remained at a minimum value, demonstrating the barrier effectiveness of one full monolayer.

Organized organic monolayers formed on solid substrates by spontaneous adsorption of amphiphilic molecules from solution, known as self-assembled monolayers (SAMs) have received a great deal of attention recently *(1-6)*. Previous workers have shown that the hydrocarbon chains in these films are well-ordered and closely packed with structures closely resembling those of Langmuir-Blodgett (LB) monolayers. The capability of molecular-level structure control in fabricating the SAMs provide a good means of "molecular engineering" materials for specific purposes and as model systems in electrical *(7,8)*, physical*(9)*, chemical *(10,11)* and mechanical *(12)* experiments.For many applications such as nonlinear optical devices *(13,14)* and chemical sensors *(13,15)* it is necessary to introduce extrinsic chemical groups into the films. In some cases the whole film can be constructed of the active molecule, while in others the active compound can be introduced into the films as a guest molecule. When anchored or enclosed in an organized structure, a chemical functional group may possess a different character from that of a similar group in the bulk. Sagiv and coworkers *(16)* studied the reactivity of intrinsic alkene groups within monolayer films with oxidizing agents penetrating into the films. They found that the penetrability of the enclosed groups decreased as the packing density of the hydrocarbon chains of the molecules is increased. Rubinstein *et al.* also constructed SAMs containing electroactive ligands on Au electrodes and showed that these electrodes are ionic size-selective *(17)*.

0097–6156/95/0615–0217$12.00/0

Downloaded by NORTH CAROLINA STATE UNIV on October 11, 2012 | http://pubs.acs.org
Publication Date: May 5, 1996 | doi: 10.1021/bk-1995-0615.ch014

In investigating systems containing small guest components, spectroscopic techniques are desirable because of their non-destructive nature. UV/Vis absorption and fluorescence spectroscopic probe techniques have been used to study the structure of dye-containing SAMs *(18)* and to study the chemical reactivity of active amphiphilic compounds forming *(19)* or incorporated into *(20)* Langmuir films. The various fluorescent probe methods can provide molecular-level information about local structure (configuration and molecular association around the probe), microenvironment (polarity and viscosity around the probe) and dynamics (probe-probe interaction). These have also been demonstrated for a variety of other type of systems, e.g., micelles and bilayers *(21)*, polymers *(22)* and Langmuir-Blodgett films *(23)*.

In previous studies *(6)*, we incorporated amphiphilic pyrene-containing fluorescent probes as the guest molecules into alkanoic acid SAMs. The fine structure of pyrene emission reflects the molecular-scale environment surrounding the probe, and the fluorescence quenching experiments manifest the interaction between the surface-bound pyrene groups with substances in the surroundings. The fluorescence ratio I_1/I_3 was measured as a function of the variation in probe location. The fluorescence intensity variation with relative probe/host concentration in the adsorbing solution was used to obtain kinetic and thermodynamic information. Results from fluorescence quenching of the surface-bound pyrene probes showed the effect of film packing on the diffusion of external quencher molecules in the vicinity of the probes. In this work, we extend the use of fluorescence probe techniques to study the guest-containing organized alkylsiloxane monolayer and multilayer SA films. Particular focus is given to the mechanistic differences of adsorption between the alkanoic acid and the alkyltrichlorosilanes.

Experimental Section

Materials. The adsorbates consisted of a series of n-alkyltrichlorosilanes with different hydrocarbon chain lengths, including n-decyltrichlorosilane (abbreviated C_{10}TCS), n-dodecyltrichlorosilane (C_{12}TCS), n-octadecyltrichlorosilane (C_{18}TCS) and n-eicosyltrichlorosilane (C_{20}TCS), which were obtained from Petrarch Systems, Inc. The methyl ester-terminated trichlorosilane molecule methyl 17-trichlorosilyl heptadecanoate (ME-C_{17}TCS), used for multilayer film preparation, was synthesized according to similar literature procedures *(24,25)*.

The pyrene tagged alkyltrichlorosilane, (4-pyrenebutyl) 11-trichlorosilyl undecanoate (PyBu-C_{11}TCS) was synthesized using the following scheme:

$$\text{1-Py(CH}_2\text{)}_3\text{COOH} \xrightarrow{\text{LiAlH}_4} \text{Py(CH}_2\text{)}_4\text{OH}$$

$$\text{1-Py(CH}_2\text{)}_4\text{OH} + \text{CH}_2\text{=CH(CH}_2\text{)}_8\text{COCl} \rightarrow \text{1-Py(CH}_2\text{)}_4\text{OOC(CH}_2\text{)}_8\text{CH=CH}_2$$

$$\text{1-Py(CH}_2\text{)}_4\text{OOC(CH}_2\text{)}_8\text{CH=CH}_2 + \text{SiHCl}_3 \xrightarrow{\text{H}_2\text{PtCl}_6} \text{1-Py(CH}_2\text{)}_4\text{OOC(CH}_2\text{)}_{11}\text{SiCl}_3$$

1-Pyrenebutyric acid was obtained from Kodak Chemical Co. and was recrystallized from ethanol/toluene mixed solvent. The reducing reagent was 1M $LiAlH_4$/THF solution, obtained from Aldrich Chemical Co. The reduction was carried out at room temperature in anhydrous THF solvent distilled from Na; the yield was typically 80-90%. The esterification reaction was carried out at room temperature in dry CH_2Cl_2 solvent distilled from P_2O_5 with a yield typically >90%. The intermediate product, 1-Py$(CH_2)_4$OOC$(CH_2)_8$CH=CH_2, was isolated by n-hexane elution through a silica gel column. The hydrosilation reaction was carried out by refluxing for ca. 4 hr. in dry $CHCl_3$ solvent distilled from P_20_5. Chloroplatinic acid (Kodak Chemical Co.) was used as the catalyst as 0.1 g/ml solution in isopropanol. The product was isolated by vacuum-distillation. The reagent-grade solvents were obtained from either Aldrich Chemical Co., Sigma Chemical Co., or J. T. Baker, Inc. Distilled and deionized water was used for substrate cleaning.

The quartz substrates used were strips of ca. 1 cm in width cut from wafers obtained from Shin-Etsu, Inc. The substrates were cleaned by immersing in hot (120°C) 4:1 H_2SO_4/H_2O_2 solution for 20 min., followed by rinsing with water, ethanol, and acetone, and finally blow-drying with a nitrogen stream.

Sample Preparation. Solutions of the host monolayer constituent alkyltrichlorosilanes were prepared in 0.01M hexadecane (HD) solution. The fluorescent probe 1-PyBu-C_{11}TCS was dissolved in toluene also to 0.01M. Solutions were then prepared by mixing the 1-PyBu-C_{11}TCS toluene solutions with a host silane solution to the desired molar ratios. The solutions were then diluted with HD to give a final total silane concentration of 0.001M in solvent mixtures containing 0.1-0.4% by volume of toluene in HD and having small fractions of 1- PyBu-C_{11}TCS probe among the silane adsorbate (probe host molar fraction = 0.05% - 0.5%). Monolayer films were prepared at 22°C. The substrates were immersed in the solutions for a predetermined period of time, removed, sonicated in n-hexane and acetone consecutively, rinsed with hexane and acetone, and then blown dry with nitrogen.

Fluorescence Measurement and Sample Characterization. Fluorescence spectra were obtained with a Spex Fluorolog 212 spectrofluorometer, equipped with a 450 W Xenon arc lamp and a Hammamatsu R928 photomultiplier. The spectra were taken in the front-face mode, using 2mm-width slits. Excitation light of 343 nm was used when collecting the emission spectra, while emission wavelengths of 377 nm or 475 nm were used when collecting the excitation spectra. Fluorescence quenching experiments *(6,26)* were used to study the interaction between the surface-bound fluorophore groups and the surroundings. The surface-bound film is immersed in a liquid phase containing the nitromethane quencher, which will partition into the film phase, diffuse to the vicinity of the pyrene fluorophore and quench the fluorescence. Mixed SAMs containing the pyrene probes were immersed in aqueous CH_3NO_2 solutions of specified concentrations in a fluorescence cell and the fluorescence spectra were taken. In order to optimize the spectrophotometer output for the solid-in-cell geometry, the optical path for the excitation light was modified to focus on the sample surface. For additional characterization of the monolayer films, a Rame-Hart contact-angle goniometer was used to measure the contact angles of HD and water on film surfaces, a Gaertner ellipsometer with a He-Ne laser source was used to measure the film thickness, and a Perkin-Elmer 1710 FTIR spectrometer was used to obtain the transmission or ATR-IR spectra of the films.

Results

Characterization of SA Monolayers and Multilayers. We used a number of conventional methods to characterize the pyrene probe-containing SA monolayers. The results were very similar to those reported earlier *(1,3,10,11)* for pure n-alkylsiloxane SAMs. For C_{18}TCS host monolayers containing 1-PyBu-C_{11}TCS probes prepared from 0.05% - 0.4% probe solutions, the water and hexadecane advancing contact angles were 118+/-3° and 48+/-2°, respectively. These values were identical to those obtained for pure C_nTCS monolayers. Similarly, the CH_2 stretch peaks (2850 and 2920 cm^{-1}) for all 1-PyBu-C_{11}TCS/CnTCS mixed monolayers were identical to those of the pure C_nTCS monolayers. These characterization results seem to indicate that the quality of the SAMs was not significantly altered by the incorporated pyrene groups. The only

Downloaded by NORTH CAROLINA STATE UNIV on October 11, 2012 | http://pubs.acs.org
Publication Date: May 5, 1996 | doi: 10.1021/bk-1995-0615.ch014

spectroscopic measurements that could be used to monitor the pyrene probes directly, however, were the fluorescence techniques, as will be discussed in the following.

Fluorescence of Monolayers Containing Pyrene Labeled Probes. Mixed monolayers containing the fluorescence probe 1-PyBu-C_{11}TCS in host monolayers of C_{10}TCS, C_{12}TCS, C_{18}TCS, C_{20}TCS and ME-C_{17}TCS, were prepared by adsorption from solutions containing mostly the host silane and 0.05 to 0.4 mol % of the probe silane. A typical fluorescence emission spectrum of a 1-PyBu-C_{11}TCS/C_{18}TCS mixed monolayer prepared from a solution of 0.0001M total acid, 1% of which is 1-PyBu-C_{11}TCS, is shown in Figure 1. The features of the spectrum are similar to the usual pyrene emission, with peaks between 370 and 430 nm assignable to the pyrene monomer, and the broad band at ca. 475 nm assignable to the pyrene excimer. The relative content of pyrene monomer and excimer florescence emission varies significantly with the solution probe mole fraction.

Fluorescence excitation spectra of samples of relatively high excimer/monomer I_E/I_M values were examined in order to determine whether there were any ground state interactions, which would cause the peaks in the excitation spectra measured at the excimer emission peak to be shifted compared to those measured at the monomer emission peak. However, for all mixed alkylsiloxane monolayer samples, the excitation spectra monitored at the monomer and excimer emission show no shift in peak position. This indicates that the probe molecules adsorb onto the substrate surface individually, ruling out the possibilities of either solution-state or adsorbate-state phase separation.

The excimer contribution to the fluorescence emission of 1-PyBu-C_{11}TCS/C_nTCS mixed monolayers is significantly higher than those of the pyrene-containing n-alkanoic acid monolayers previously reported *(6)*. Although the latter were prepared on Al substrates while the former were deposited on quartz, the general shape of the spectra of the two types should be similar since they both contain end-tagged pyrene groups. For the alkyltrichlorosilane system, the relative adsorption tendency of the 1-PyBu-C_{11}TCS probe to the host molecules C_nTCS is stronger than the Py-CnCOOH probe to the host CnCOOH molecules in the alkanoic acid system. Although the solution probe fractions were at about the same level, the surface probe fraction may be quite different in the two systems.

Dependence of Fluorescence Intensity of Probe-Containing Monolayers on Host Length. Figure 2(a) shows the 377 nm pyrene monomer emission peak intensity (I_1) of mixed monolayers prepared at equilibrium from solutions of 0.05 to 0.4% tagged probes in 0.001M total concentration. The intensity increased with the molar fraction of 1-PyBu-C_{11}TCS in solution, up to about 0.2%, but leveled off or decreased as the hydrocarbon chain length of the host silane molecule is increased. The decrease in the pyrene monomer emission intensity is due to the formation of excited state pyrene excimers. However, if the total integral emission intensity of the mixed monolayers was plotted instead, a continuous increase with the solution probe fraction was observed. The total integral intensity also exhibited a continuous decrease as the host silane chain length increased.

To account for the effect of the different excimer and monomer fluorescence quantum yields on the overall fluorescence intensity, the combined intensity is calculated with the following equation:

$$I = I_M + (2\Phi_M/\Phi_E)I_E \qquad (1)$$

Downloaded by NORTH CAROLINA STATE UNIV on October 11, 2012 | http://pubs.acs.org
Publication Date: May 5, 1996 | doi: 10.1021/bk-1995-0615.ch014

Downloaded by NORTH CAROLINA STATE UNIV on October 11, 2012 | http://pubs.acs.org
Publication Date: May 5, 1996 | doi: 10.1021/bk-1995-0615.ch014

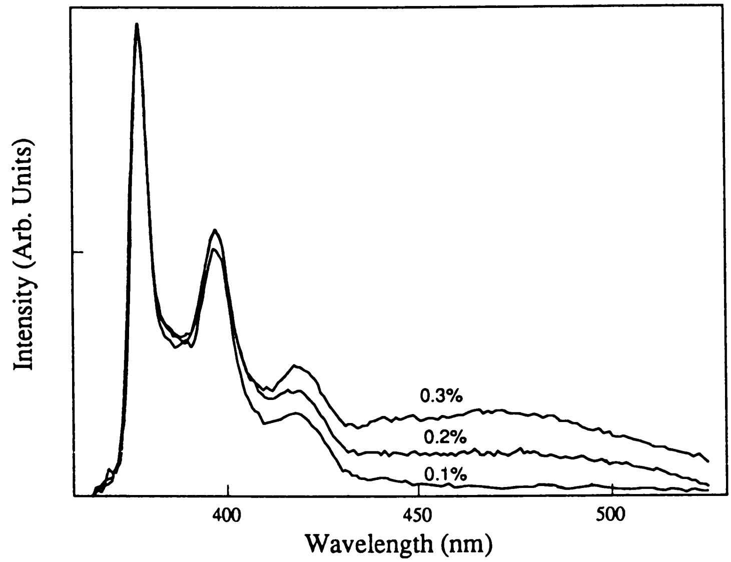

Figure 1. Typical fluorescence spectra of 1-PyBu-C_{11}TCS/C_{18}TCS mixed monolayers on quartz substrate as a function of the probe content.

Downloaded by NORTH CAROLINA STATE UNIV on October 11, 2012 | http://pubs.acs.org
Publication Date: May 5, 1996 | doi: 10.1021/bk-1995-0615.ch014

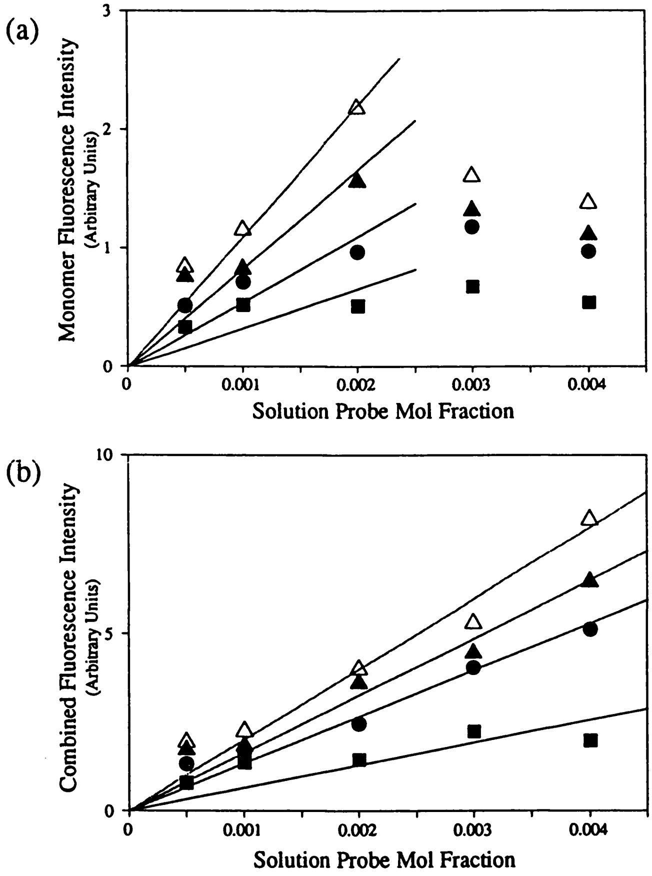

Figure 2. Dependence of monomer fluorescence intensity I_1 (a) and combined fluorescence intensity I (b) on solution mole fraction of 1-PyBu-C_{11}TCS mixed with C_{10}TCS (■), C_{12}TCS (●), C_{18}TCS (▲) and C_{20}TCS (△).

where I_M and I_E are the integral fluorescence intensities, and Φ_M and Φ_E are the monomer and excimer quantum yields. Exact values of Φ_M and Φ_E for the mixed monolayer systems are not available. However, a literature value *(6)* of $\Phi_E/\Phi_M = 2.36$ for pyrene in a nonpolar solvent cyclohexane, which is a case similar to those in the SAMs, may be used for approximate evaluations. The combined intensity calculated in this manner, as shown in Figure 2(b), increased with the solution probe fraction and decreased with the host molecular chain length. The trend of change in I, unlike that of I_1, is not affected by the higher excimer content for the samples prepared at higher probe mole fractions, indicating that the above method of calculation of combined intensity has approximately counterbalanced the excimer effect. The combined intensity can thus be used as a measure of the probe population in the monolayers.

Incorporation of Fluorescence Probes in Multilayers. As demonstrated previously *(11)*, multilayers can be built up by repeated deposition of ME-C_{17}TCS and chemical activation of the surface functionality. The key step in this procedure is the complete reduction of the methyl ester groups to alcohol groups. We also used the same method to embed probe molecules in multilayers prepared from ME-C_{17}TCS. Since the 1-PyBu-C_{11}TCS probe molecule also contains an ester linkage, it may also be susceptible to chemical reduction when exposed to $LiAlH_4$. When the probe molecules are anchored in an SAM, however, the ester linkages are located within a distinctive environment of ordered hydrocarbon chain packing. Under this condition, the enclosed ester linkages may have different reactivity than those of the surface methyl ester groups. The low permeability of an organized layer should then significantly reduce the rate of reaction between a liquid-phase component and enclosed groups, as has been demonstrated by aqueous $KMnO_4$ oxidation of alkene groups *(16)* and by aqueous CH_3NO_2 fluorescence quenching *(27)*.

The reduction of the ester groups in 1-PyBu-C_{11}TCS molecules enclosed in ME-C_{17}TCS monolayers during $LiAlH_4$/ THF reduction can be easily monitored by fluorescence spectroscopy, since the pyrene-tagged fluorescent species would be detached if the ester linkage were reduced. Typical results are listed in Table I. For probes in a full monolayer (i.e., of unity surface coverage), the extent of reduction of the ester linkage is quite small. During a reduction time of 3 min., the typical standard cycle used for ME-C_{17}TCS monolayer reduction, the fluorescence intensity is virtually unchanged. The majority of the enclosed 1-PyBu-C_{11}TCS probe molecules clearly remained intact. The reduction of the probe ester linkage was not substantial even after prolonged (30 min.) reduction treatment. It is of interest, however, that the I_E/I_M ratio increased slightly upon reduction of the monolayer. The increased probability in excimer formation is likely due to the decrease in the host chain length that gives the terminal pyrene groups a slight increase in conformational freedom necessary for excimer formation. For comparison, in a partial mixed monolayer (low surface coverage), the extent of reduction of the probe ester linkage was significantly higher than that in a complete monolayer. This is reasonable since the less ordered structure of the incomplete monolayer would be less effective in preventing the penetration of the reducing agent. For probe molecules enclosed in the bottom layer of a two-layer system, the reduction of the exterior surface had no effect on the interior ester groups.

As demonstrated above, it is possible to prepare alkylsiloxane monolayers or multilayers containing probes located at desired levels. The deposition of a subsequent alkylsiloxane monolayer onto a previously deposited and activated monolayer surface usually proceeds to full extent, with the coverage of the upper layers comparable to that of the first layer. For probe-containing mixed monolayers, the space taken by probes can be considered to be defects with respect to the reduction and subsequent adsorption of a second monolayer. After ME-C_{17}TCS multilayers were deposited under suitable

Downloaded by NORTH CAROLINA STATE UNIV on October 11, 2012 | http://pubs.acs.org
Publication Date: May 5, 1996 | doi: 10.1021/bk-1995-0615.ch014

Downloaded by NORTH CAROLINA STATE UNIV on October 11, 2012 | http://pubs.acs.org
Publication Date: May 5, 1996 | doi: 10.1021/bk-1995-0615.ch014

conditions onto a reduced 1-PyBu-C_{11}TCS/ME-C_{17}TCS mixed monolayer, both FTIR and contact angle measurements indicate that the upper layer(s) were of the same quality as a complete monolayer. Apparently higher alkylsiloxane monolayers can bridge over defect spaces generated by individual probe molecules previously deposited. This self-healing mechanism *(11)* for the SA alkylsiloxane films is especially useful in reducing defects in monolayers and multilayers.

Table I. Fluorescence of Mixed Monolayers

System	I_1	I_E/I_M
1 Partial probe-containing monolayer	0.32	1.7
1 Partial monolayer, reduced	0.35	2.2
1 Full probe-containing monolayer	1.0	0.5
1 Full monolayer, reduced	0.94	0.55
2 Layers, probe in first layer	1.23	0.23
2 Layers, reduced	l1.15	0.25

First layers prepared from approximately *5%/95%* 1-PyBu-C_{11}TCS/ME-C_{17}TCS O.OOlM solution. Second layers prepared from 0.001M C_{18}TCS solution.

Fluorescence Quenching of Probe-Containing Monolayers and Multilayers. The most frequently observed type of fluorescence quenching is the dynamic quenching process, in which a quencher molecule collides with the excited chromophore and causes non-radiative energy loss that reduces the fluorescence emission *(26)*. On the other hand, the static quenching process involves the formation of a non-fluorescent complex between the quencher and the fluorophore. Dynamic quenching has been observed for the CH_3NO_2/pyrene systems *(23)*. For a dynamic quenching system, the Stern-Volmer equation (2) describes the fluorescence intensity variation:

$$I_0/I = 1 + K_D\,[Q] \qquad (2)$$

where I_0 and I are the unquenched and quenched fluorescence emission intensity, K_D is the dynamic quenching constant, and [Q] is the quencher concentration. The bimolecular quenching constant k_q, a molecular parameter, is related to K_D by

$$k_q = K_D/\tau_0 \qquad (3)$$

where τ_0 is the unquenched fluorescence lifetime.

To compare the quenching effect on probes incorporated in various configurations, we prepared various types of organized probe-containing SAMs and studied them in fluorescence quenching experiments. The configurations included a full 1-PyBu-C_{11}TCS/ME-C_{17}TCS monolayer (surface concentration ≈ 8.5×10^{-10} mol/cm^2, determined by FTIR *(6)*), a partial 1-PyBu-C_{11}TCS/ME-C_{17}TCS monolayer of ca. 30% of a full monolayer surface coverage (determined by FTIR), a C_{18}TCS second-layer coated on a reduced 1-PyBu-C_{11}TCS/ME-C_{17}TCS (abbreviated as C_{18}Si[PyBu-C_{11}Si/-

O-C_{17}Si]) two-layer film, a C_{18}TCS[-O-C_{17}Si]-[PyBu-C_{11}TCS/-O-C_{17}Si] three-layer, and a C_{18}TCS-[-O-C_{17}Si]-[-O-C_{17}Si]-[PyBu-C_{11}Si/-O-C_{17}Si] four-layer. The upper layers of the multilayer samples were all complete layers, and a C_{18}TCS top-most layer was used to create a uniform CH_3 group external film surface. For the two-, three- and four-layer films with the C_{18}TCS top-most layer, the water contact angles measured were all 122+/-2°, clearly indicating the formation of fully covered CH_3 surfaces.

CH_3NO_2 solutions of concentration up to 1M significantly quenched the fluorescence emission of 1- PyBu-C_{11}TCS probe-containing monolayers. All followed the Stern-Volmer dynamic quenching relationship, as shown in Figure 3. The apparent dynamic quenching constant K_D (based on the aqueous phase CH_3NO_2 concentration), or the slope of the lines, was different between different film systems. K_D was the highest for the partial 1-PyBu-C_{11}TCS/ME-C_{17}TCS monolayer, decreased for the full 1-PyBu-C_{11}TCS/ME-C_{17}TCS monolayer, and was at approximately the same low value for the multilayers containing the 1-PyBu-C_{11}TCS probe in the bottom layer.

Discussion

Determination of Relative Adsorption Rate Constants. For competitive adsorption from mixed solutions, because of the irreversible nature of the monolayer formation process, the relative amount of adsorbed moieties depend only on the relative adsorption rate constant k and the solution concentrations. The fractional coverage of the guest molecule, Θ_g, can be expressed as

$$\Theta_g = c_g k_g/(c_g k_g + c_h k_h) \approx I \qquad (4)$$

where k_g and k_h are the adsorption rate constants for the guest molecule 1-PyBu-C_{11}TCS and the host silane, respectively, and I is the fluorescence intensity. Under the experimental conditions used, $c_g << c_h$, $\Theta_h >> \Theta_g$ and Equation (4) reduces to

$$\Theta_g = c_g k_g/c_h k_h \qquad (5)$$

The rate constant k_g for the guest molecule is unknown, leading to unknown absolute probe concentrations in the films, as mentioned above. However, this problem can be circumvented by taking the ratio of the slopes of any two lines in Figure 3, which equals the ratio of the k_h constants between host molecules (such as $k_h(C_{10}TCS)/k_h(C_{20}TCS)$, etc.). The adsorption rate ratios determined in this manner are shown in Figure 4. Expressed as the adsorption rate relative to that for C_{10}TCS, the k_h values of the alkyltrichlorosilanes decreased monotonically with the tailgroup chain length.

The dependence of the adsorption rate constant on the thermodynamic parameters of the adsorption reaction can be expressed as

$$k \propto \exp(-\Delta G/RT) \qquad (6)$$

Since $\Delta G = \Delta H - T\Delta S$

$$k \propto \exp(\Delta S/R)\exp(-\Delta H/RT) \qquad (7)$$

$$k \propto \exp(\Delta S/R)\exp(-E_a/RT) \qquad (8)$$

Downloaded by NORTH CAROLINA STATE UNIV on October 11, 2012 | http://pubs.acs.org
Publication Date: May 5, 1996 | doi: 10.1021/bk-1995-0615.ch014

Downloaded by NORTH CAROLINA STATE UNIV on October 11, 2012 | http://pubs.acs.org
Publication Date: May 5, 1996 | doi: 10.1021/bk-1995-0615.ch014

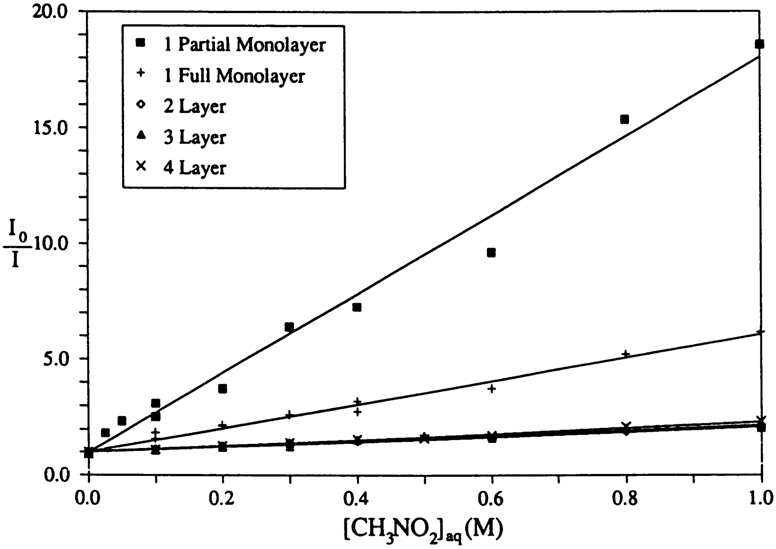

Figure 3. Stern-Volmer plots of aqueous CH_3NO_2 quenching of 1-PyBu-C_{11}TCS embedded in partial and full monolayers as well as in multilayer systems with the probe molecule dispersed in the bottom layer.

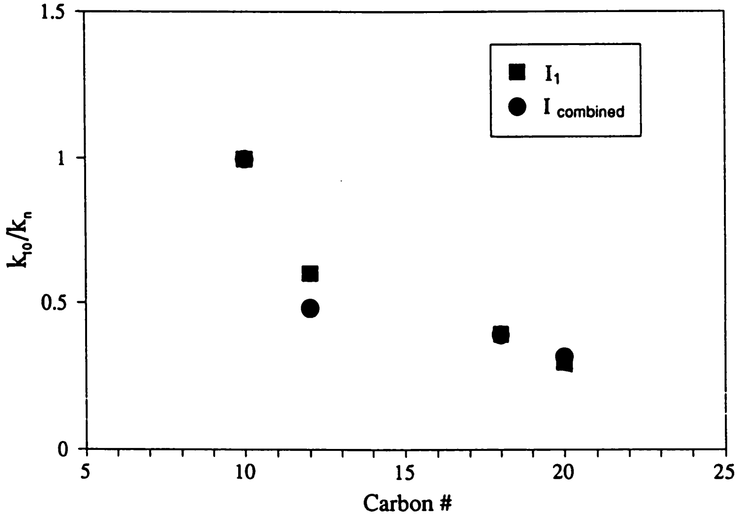

Figure 4. Adsorption rate ratios for various various alkyltrichlorosilanes normalized to the rate for C_{10}TCS.

Downloaded by NORTH CAROLINA STATE UNIV on October 11, 2012 | http://pubs.acs.org
Publication Date: May 5, 1996 | doi: 10.1021/bk-1995-0615.ch014

The ratio between the rate constants of two molecules (denoted by the superscripts 1 and 2) can be expressed as

$$k^1/k^2 = \exp\,[(\Delta S^1 - \Delta S^2)/R]\,\exp[(E_a^2 - E_a^1)/RT] \qquad (9)$$

If W_S and W_H are defined as the entropic and enthalpic (for the energy of activation) contributions of each methylene unit to the adsorption reaction based on energy additivity, then the rate constant ratio is

$$k^1/k^2 = \exp(W_S\,\Delta n/R)\,\exp(-W_H\Delta n/RT) \qquad (10)$$

where Δn is the difference between the hydrocarbon chain lengths of the two molecules.

From an exponential fit to the data of Figure 3 an overall energetic relationship per methylene unit may be established as Equation (11)

$$\Delta n\,(W_S T - W_H) \approx -0.12RT \text{ cal/mol} = -71.5 \text{ cal/mol} \qquad (11)$$

The negative value of the overall segmental (i.e., per unit methylene chain) adsorption energetic contribution indicates that the entropic effect for the alkyltrichlorosilane adsorption rate, which is negative due to the loss of configurational degrees of freedom, dominates over the enthalpic one, which is positive as a result of the associative van der Waals inter-chain attraction.

A correlation between the energy of activation E_a and the enthalpy of reaction for exothermic reactions, given by Semenov *(27)* is

$$E_a = 48.1 - 0.75\Delta H \text{ kJ/mol} \qquad (12)$$

Thus, the adsorption energetic relationship can be rewritten as

$$\Delta n(W_S T - 0.75W_H) \approx -71.5 \text{ cal/mol} \qquad (13)$$

Calculation of Effective Quencher Diffusivity. The fluorescence quenching data can be used to obtain information on the quencher mobility in the neighborhood of the fluorophore. The bimolecular quenching constant k_q is related to the diffusion coefficient by the Smoluchowski-Einstein equation:

$$k_q = 4\Pi N_A D_Q R\gamma/1000 \qquad (14)$$

where N_A is Avogadro's number, D_Q is the effective quencher diffusion coefficient, R is the sum of the collisional radii of the quencher and the fluorophore, and γ is a proportionality constant.

To perform such further analysis, two complicating factors have to be considered. The first is the partitioning of the CH_3NO_2 quencher between the aqueous solution and the hydrocarbon film phases. The situation is completely analogous to the partitioning of a solute between two unlike solvating phases. We measured this partition constant with long chain alkanes, including a liquid (hexadecane) and a solid (octadecane), in equilibrium with aqueous CH_3NO_2 solutions using FTIR and UV absorption measurements. A numerical value for the partition coefficient, defined as the

Downloaded by NORTH CAROLINA STATE UNIV on October 11, 2012 | http://pubs.acs.org
Publication Date: May 5, 1996 | doi: 10.1021/bk-1995-0615.ch014

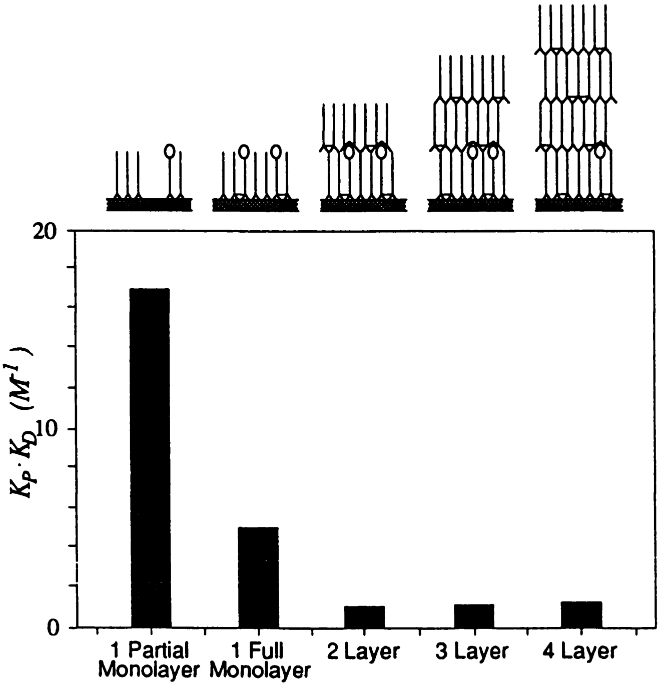

Figure 5. Dynamic quenching constant K_D multiplied by the probe partition coefficient K_P = 0.08 for partial and full monolayers as well as multilayer systems with the probe molecule dispersed in the bottom layer.

Downloaded by NORTH CAROLINA STATE UNIV on October 11, 2012 | http://pubs.acs.org
Publication Date: May 5, 1996 | doi: 10.1021/bk-1995-0615.ch014

CH_3NO_2 concentration ratio between the hydrocarbon phase and the aqueous phase, was obtained:

$$K_P = [Q]_{HC}/[Q]_{AQ} = 0.08 \qquad (15)$$

The quenching constant data can then be used to calculate the effective quencher diffusivity according to Equation (14). To do this, we compared our data to the literature data *(28)* of k_q=3.04 x 10^9 l/mol-sec and D_Q =1.4 x 10^{-5} cm^2/sec for CH_3NO_2 pyrene in aqueous systems. The CH_3NO_2 effective diffusivity in the vicinity of the pyrene groups thus obtained are shown in Figure 5, in which D_Q is plotted for pyrene groups embedded in a partial monolayer, in a full monolayer, and in multilayer systems. For the maximally exposed pyrene case, i.e., in a partial monolayer, the calculated D_Q is much higher than in other systems. As the host chain length is increased, D_Q decreases, indicating that the hydrocarbon chain packing somehow "blocks" the diffusion of CH_3NO_2. For a full monolayer, the pyrene groups are probably partially enclosed by a organized film, leading to a lower D_Q value. For the totally enclosed pyrene (in 2, 3 and 4 multilayers) D_Q remain at a small value, which can be thought of as the diffusivity within the hydrocarbon packing. The results demonstrate the protective effect of the monolayers on the accessibility and reactivity of the surface-anchored or embedded chemical groups.

Summary

Fluorescence probe techniques were used to study guest groups incorporated into organized self-assembled n-alkylsiloxane monolayers and multilayers formed by spontaneous adsorption from n-alkyltrichlorosilane solutions. The fluorescence intensity of mixed monolayers containing a probe 1-PyBu-C_{11}TCS in host CnTCS molecules was used to obtain information on the dependence of the energetics of the C_nTCS self-assembly process on the adsorbate chain length. The negative entropic segmental contribution of the hydrocarbon tailgroup was found to be the dominating factor. Fluorescence quenching experiments were performed on the pyrene-doped monolayers and multilayers with aqueous solutions of nitromethane, CH_3NO_2. The relative diffusivity of CH_3NO_2 in the vicinity of the pyrene groups was determined from the fluorescence quenching constant. For pyrene probes incorporated in the bottom layer of multilayers, the effective quencher diffusivity was low, demonstrating the effectiveness of a full monolayer in reducing the rate of transport of matter.

Acknowledgement

This work was supported by the Chemistry Program of the Office of Naval Research.

References

1. Maoz, R.; Sagiv, J. *J. Colloid Interface Sci.* **1984**, *100*, 465; Gun, J., Iscovici, R., Sagiv, J. *J. Colloid Interface Sci.* **1984**, *101*, 201; Gun, J., Sagiv, J. *J. Colloid Interface Sci.* **1986**, *112*, 457.
2. Allara, D. L.; Nuzzo, R. G. *Langmuir* **1987**, *3*, 1034.
3. Maoz, R.; Sagiv, J. *Langmuir* **1987**, *3*, 1034.
4. Nuzzo, R. G.; Fusco, F. A.; Allara, D. L. J. *Am. Chem. Soc.* **1987**, *109*, 2358.
5. Troughton, E. B.; Bain, C. D.; Whitesides, G. M.; Nuzzo, R. G.; Allara, D. L.; Porter, M. D.,*Langmuir* **1988**, *4*, 365; Strong, L., Whitesides, G. M. *Langmuir* **1988**, *4*, 546.

6. Chen, S. H.; Frank, C. W. *Langmuir* **1989**, *5*, 978; Chen, S. H., Frank, C. W. *ACS Symp. Ser.*, No. 447, Scheuing, D. R., ed. p. 160, 1990.
7. Sabatani, E.; Rubinstein, I.; Maoz, R.; Sagiv, J. J. *Electroanal. Chem.* **1987**, *219*, 365.
8. Widrig, C.; Majda, M. *Langmuir* **1989**, *5*, 689.
9. Cohen, S. R.; Naaman, R.; Sagiv, J. *Phys. Rev. Lett.* **1987**, *58*, 1208; *J. Chem. Phys.* **1988**, *88*, 2757.
10. Wasserman, S. R.; Tao, Y.; Whitesides, G. M. *Langmuir* **1989**, *5*, 1074.
11. Tillman, N.; Ulman, A.; Elman, J. F. *Langmuir* **1989**, *5*, 1020.
12. DePalma, V.; Tillman, N. *Langmuir* **1989**, *5*, 868.
13. Swalen, J. D.; Allara, D. L.; Andrade, J. D.; Chandross, E. A.; Garoff, S., Israelachvili, J.; McCarthy, T. J.; Murray, R.; Pease, R. F. W.; Rabolt, J. F.; Wynne, K. J.; Yu, H. *Langmuir* **1987**, *3*, 932.
14. Swalen, J. *Electron.* **1985**, *2*, 155.
15. Tafusa, I.; Kurihara, K. *Jpn. Kokai Tokkyo Koho JP* 62209350, 1987; *Chem. Abs.*, 1989, 110: 150918j.
16. Maoz, R.; Sagiv, J. *Langmuir* **1987**, *3*, 1034; *Langmuir* **1987**, *3*, 1045.
17. Rubinstein, I.; Steinberg, S.; Tor, Y.; Shanzer, A.; Sagiv, J. *Nature* **1988**, *332*, 426.
18. Sagiv, J. *J. Am. Chem. Soc.* **1980**, *102*, 92. *Israel J. Chem.* **1979**, *18*, 339. *Israel J. Chem.* **1979**, *18*, 346.
19. Grieser, F.; Drummond, J. *J. Phys. Chem.* **1988**, *92*, 5580.
20. Whitten, D. G.; Frederick, R. H.; Quina, F. H.; Sprintschnik, G.; Sprintschnik, H. W. *Pure Appl. Chem.* **1977**, *49*, 379.
21. Jay, J.; Johnston, L. J.; Scaiano, J. C. *Chem. Phys. Lett.* **1988**, *148*, 517. Somasundaran, P.; Turro, N. J. *Macromol.* **1988**, *21*, 950.
22. Chander, P.; Somasundaran, P.; Turro, N. J.; Waterman, K. C. *Langmuir* **1987**, *3*, 298; Avnir, D.; Busse, R.; Ottolenghi, M.; Wellner, E.; Zachariasse, K. A. *J. Phys. Chem.* **1985**, *89*, 3521.
23. Murakata, T.; Miyashita, T.; Matsuda, M. *Langmuir* **1986**, *2*, 786; Tamai, N.; Yamazaki, T.; Yamazaki, I. *J. Phys. Chem.* **1987**, *91*, 841; Tamai, N.; Yamazaki, T.; Yamazaki, I. *J. Phys. Chem.* **1987**, *91*, 3572.
24. Barraud, A.; Rosilio, C.; Raudel-Teixier, A. *J. Colloid Interface Sci.* **1977**, *62*, 509.
25. Tillman, N.; Ulman, A.; Penner, T. L. *Langmuir* **1989**, *5*, 1020.
26. Lakowicz, J. R. *Principles of Fluorescence Spectroscopy,* Plenum Press, New York, 1983.
27. Semenov, N.N. Some Problems in Chemical Kinetics and Reactivity, Chap. 1, Pergamon Press, London, 1958.
28. Arora, K. S.; Turro, N. J. *J. Polym. Sci., Polym. Chem.* **1987**, *25*, 259.

RECEIVED August 18, 1995

Downloaded by NORTH CAROLINA STATE UNIV on October 11, 2012 | http://pubs.acs.org
Publication Date: May 5, 1996 | doi: 10.1021/bk-1995-0615.ch014

Chapter 15

Nonionic Surfactant Systems and Surface Solubilization of Oil at the Silica–Water Interface

Fredrik Tiberg and Johanna Brinck

**Physical Chemistry 1, Chemical Centre, Lund University, Box 124,
S–221 00 Lund, Sweden**

The present paper deals with the interfacial behaviour of nonionic surfactant systems at silica studied by ellipsometry. The technique is shown to be an excellent tool for the investigation of the adsorption of surfactants, since it allows fast and non destructive *in situ* measurements of the mean thickness and the refractive index of thin interfacial films. The independent determination of these properties means that it is possible to obtain information on the surface excess as well as the structure of the adsorbed layer. Few other techniques, if any, allow such measurements with the relevant time-resolution. Ellipsometry measurements are shown to reveal a great deal about how adsorbed surfactant layers are built up and disintegrated with time during adsorption and desorption, respectively. We discuss the behaviour observed for monodisperse polyethylene glycol monoalkyl ether (C_nE_m) systems. In addition, new results on the adsorption and desorption of mixed surfactant-surfactant and surfactant-oil systems are presented. The findings from these studies are important for the understanding of the adsorption of polydisperse surfactants and copolymers and the phenomenon of surface solubilisation.

The importance of surfactant behaviour at interfaces can hardly be overestimated. Adsorption of surfactants from aqueous solution is critical for processes ranging from lubrication, cleaning, paint technology, water treatment to enhanced oil recovery. The main effects of adsorbed amphiphilic compounds are to be found in the modified surface energetics (promoting spreading, wetting, cleaning, etc.) and in the stabilisation of colloids. Fundamental research on the self-assembly properties of amphiphilic molecules has traditionally been focused on the solution behaviour, whereas relatively few studies treat the phenomenon in the presence of an interface. Nevertheless, during recent years the adsorption (or surface self-assembly) of surfactants has been subjected to increasing experimental and theoretical work, see for instance reviews (*1-4*).

In this paper, some specific features of the adsorption of nonionic polyethylene glycol monoalkyl ethers (C_nE_m) systems are discussed. The

0097–6156/95/0615–0231$12.00/0

experimental data presented are obtained by a novel ellipsometric methodology developed for characterising the nature of thin adsorbed films on solid substrates (*5*). The major advantage of ellipsometry is its ability to monitor adsorbed layer properties, i.e. the mean thickness and the refractive index, with the relevant time-resolution. It is possible to follow the evolution of these properties during adsorption as well as desorption. Therefore, ellipsometric data provides unique information for the understanding of for example (i) the mechanism of adsorption, (ii) the kinetics of adsorption and desorption processes, and (iii) the molecular architecture of the adsorbed layers. In recent studies, different C_nE_m systems are investigated with regards to both kinetic and equilibrium aspects (*6-8*).

Adsorption of surfactants is in many cases best described as a self-assembly process influenced by the presence of the interface. We present results showing the characteristics of this process for monodisperse C_nE_m systems. Studies of the desorption also show how the adsorbed layers are disintegrated with time. The parameters determining the rates of these processes are elucidated. Moreover, for monodisperse surfactant systems a kinetic model that quantitatively accounts for the observed time-dependence during adsorption and desorption is discusssed. In addition to the adsorption of neat surfactants, we also examine the interfacial behaviour of mixed surfactant systems. These studies are important for a future understanding of polydisperse surfactant and copolymer systems. We show that the framework developed for understanding the behaviour of monodisperse systems also provides the basis for the comprehension of the interfacial behaviour of mixed systems, although theoretical modelling of the kinetics observed in the latter is more complex. Finally, some results connected with the surface solubilisation of alkanes in adsorbed surface aggregates of C_nE_m surfactants are considered.

Ellipsometry and Materials

Measures of the mean thickness (d), refractive index (n), and the surface excess (Γ) are obtained by means of in situ null ellipsometry. The instrument used in this study is an automated Rudolph Research thin-film ellipsometer, type 43603-200E, equipped with high precision step motors from Berger-Lahr, type VRDM 566, and controlled by a personal computer. The ellipsometer is operating with a wavelength of 401.5 nm and an angle of incidence of 67.5°. The experimental set-up as well as a description of the procedure for in situ characterisation of thin films adsorbed on layered substrates are given in (*5*).

In brief, first we determine the optical properties of the oxidised silicon substrate. This is done by measurements (by so called four-zone null averaging) of the substrate in different ambient media, having different refractive indices (e.g. air followed by water). The data resulting from these measurements are then used to calculate the complex refractive index ($N_2=n_2-jk_2$) of the bulk silicon as well as the thickness (d_1) and refractive index ($N_1=n_1$) of the silica layer. Typical values of these parameters are: $n_2=5.500\pm0.005$, $k_2=-0.3\pm0.05$, $n_1=1.480\pm0.03$ and $d_1\approx300$Å (the latter varying somewhat from batch to batch).

After the characterisation of the substrate is performed, a controlled amount of the surfactants under study is added to the temperature controlled cuvette (25±0.1°C), and the ellipsometrical angles ψ and Δ are subsequently monitored as a function of time. The parameters ψ and Δ are not recorded simultaneously, which introduces some errors during fast changes of the adsorption. However, the time-delay ($\approx$1 second) between the recordings of these parameters has in this work been taken into account in the further analysis of the data. The adsorption measurements are usually only performed in one zone, since corrections for optical imperfections already have been carried out in water. The maximum time resolution of our ellipsometer is about 2 seconds. Stirring is performed by a magnetic stirrer at 300 rpm and rinsing achieved after steady state conditions have been established by a continuous flow (10 ml·min^{-1}) of preheated double distilled Millipore water (DD-MP). From the ellipsometrical angles ψ and Δ, the average refractive index (n) and the mean layer thickness (d) are determined numerically by means of an optical four layer model. It is noteworthy that the mean optical thickness is calculated under the assumption of layer uniformity. The uniform layer model applies well for adsorbed layers of nonionic surfactants (*5, 7, 8*). For qualitative interpretations of ellipsometry data in terms of segment density profiles, it may be useful to compare the ellipsometrical measurements with thickness measurements performed by different techniques. The adsorbed layer thickness of nonionic surfactants has been studied by other techniques in a few cases, e.g., for $C_{12}E_5$ and $C_{12}E_6$. For these surfactants, it is observed that the thickness measured with ellipsometry agrees within a few Ångström with the thicknesses obtained by neutron and X-ray scattering (*9-11*), as well as with PCS and streaming potential measurements (*12*).

The mean optical thickness and refractive index were finally used to calculate the common ellipsometric measure of their combination in terms of the surface excess (Γ) according to de Feijter et al. (*13*). The values of Γ are mainly presented in terms of μmol m^{-2}. For the mixed systems, the calculations are based on approximating the composition by ideal solution theory, which may induce small errors in Γ presented. We have estimated the maximal error due to this approximation to ±5%.

Surface Self-Assembly in Monodisperse Nonionic Surfactant-Water-Silica Systems.

We begin this section with a brief presentation of some central features of the interfacial behaviour of nonionic surfactants adsorbed at silica. For a complete narration, c.f. (*4, 7 and 8*). Adsorption of nonionic surfactants on hydrophilic surfaces is a highly co-operative process governed by weak attractive interactions between the ethylene oxide chain of the surfactant unimers and the surface. The adsorption is hence limited (< 0.2 mmol m^{-2}) at low bulk concentrations. However, as the interfacial concentration exceeds a certain value, due to the small surface affinity of the surfactants to the surface, surfactant aggregates begin to form in the interfacial region. The resulting effect is the drastic rise of the surface excess observed at a bulk concentration below but close to the cmc in Figure 1.

The bulk concentration where the sharp rise is first observed is here referred to as the critical surface aggregation concentration, csac. At this point, surface aggregates with a well-defined thickness normal to the surface are first formed. Above csac, the adsorbed layer thickness is virtually constant, while the surface excess continues to rise until the cmc is reached, cf. (*8*). Along with the stabilisation of the surfactant chemical potential around the cmc, the surface excess reaches a plateau. For dodecyl surfactants with short ethylene oxide chains a step-like increase of the surface excess is observed after csac ($m \leq 5$), whereas for surfactants with longer ethylene oxide chains, a more gradual increase is observed. Hence, the ratio csac/cmc decreases with increasing ethylene oxide chain length. At plateau conditions above the cmc, C_nE_m surfactants with relatively long ethylene oxide chain ($m > 8$ for dodecyl surfactants) adsorb relatively sparsely at silica ($\Gamma < 0.2 \mu$mol m^{-2}). These surfactants form small surface micelles, while those with short ethylene oxide chains assemble into larger disc-like surface micelles or more extended bilayer structures (*8*).

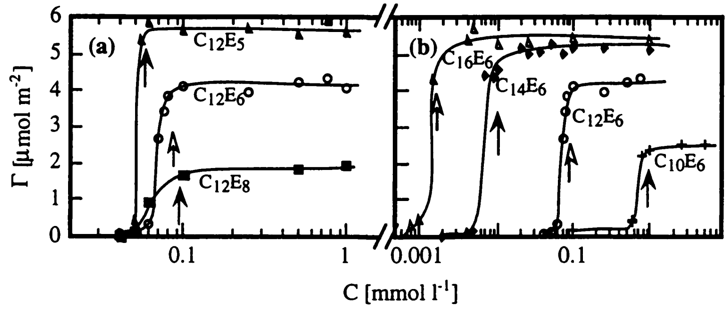

Figure 1. Adsorption isotherms for (a) polyethylene glycol monododecyl ethers, $C_{12}E_m$, m=5, 6 and 8, and (b) hexaethylene glycol monoalkyl ethers, C_nE_6, n=10, 12, 14 and 16. Cmc's are indicated by filled and hollow arrows respectively.

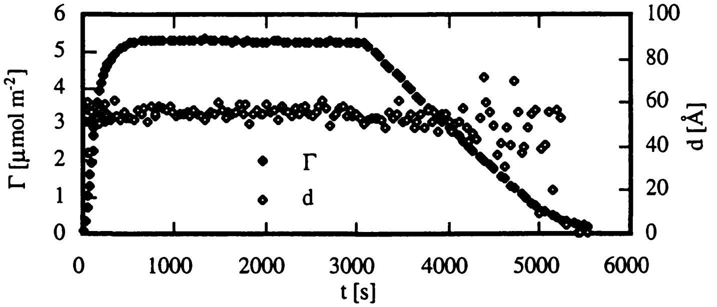

Figure 2. The adsorbed amount (Γ) and the mean adsorbed layer thickness measured during an adsorption-desorption cycle for $C_{16}E_6$ (C=0.025 mmol l^{-1}). The surfactant is injected prior to t=0 and continuous rinsing is started at t≈3000 s.

The dynamic of the adsorption and desorption of nonionic surfactants has not been studied extensively in the past. This is mostly due to the difficulty of following the rapid processes with conventional adsorption techniques. However, ellipsometry allows studies of the mean thickness, the refractive index and the surface excess with the relevant time-resolution. This means that by using this technique we can follow the time-evolution of both the structural features of the adsorbed layer and the mass transfer to and from the interface. Figure 2 shows a typical adsorption-desorption cycle for $C_{16}E_6$. Five different kinetic regimes are identified during an adsorption and desorption cycle of a nonionic surfactant (7):

(i) Initially, the adsorption progresses linearly with time. The rate of this process is affected by the bulk surfactant concentration both below and above the cmc, with a smaller dependence in the concentration region below the cmc. The linear increase of adsorption with time is due to a local equilibrium, keeping the surfactant chemical potential more or less constant in the immediate vicinity of the

adsorbed layer. This is also true in the bulk solution, since the total amount of surfactant in the interfacial region is negligible compared to that present in the bulk solution. The transport to the interfacial layer proceeds by diffusive flow of monomers and micelles (when present) from the bulk solution through a stagnant layer. Apart from the monomer and micellar diffusion through the stagnant layer, there are also a continuous dissociation and build up of micelles in the stagnant layer region.
We further observe that the mean thickness reaches plateau values much faster than the adsorbed amount, i.e. $\Gamma/\Gamma_{plateau}$ values around 0.2. We conclude from such measurements that surface micelles with well-defined dimension normal to the surface are present throughout most of the adsorption process.

(ii) After some time, adsorption starts to level off. The rate of adsorption begins to decrease, due to crowding of surface micelles in the interfacial region and a subsequent increase of the surfactant chemical potential just outside this region. This results in a decrease of the chemical potential gradient over the stagnant layer and consequently in a decrease of the adsorption rate.

(iii) A stable plateau is reached as equilibrium conditions are established between the adsorbed layer and the bulk solution. The adsorbed layer properties in this regime were discussed above.

(iv) As rinsing is initiated, the surface excess remains unaffected until cmc is reached just outside the adsorbed layer region. Rinsing is initiated after 3000 (±100) seconds. Desorption is generally observed in the interval 50-200 seconds after rinsing is initiated (see Figures 2, 4 and 5). Then the surface excess begins to decrease more or less linearly with time. Here, as in the first adsorption regime, the desorption proceeds with a rate that is proportional to the surfactant concentration just outside the adsorbed layer. This is kept constant ≈csac, through a local equilibrium existing between the surface micelles and the surrounding monomers within the interfacial region. The bulk concentration of surfactants outside the stagnant layer is ≈0 as this regime is entered, due to effective material exchange in the ellipsometric cuvette. Hence, the higher the csac (or cmc) the faster is the desorption (see Figures 1, 2, 4 and 5).

(v) The flow of monomers will, however, lead to a reduction of the concentration of surface micelles. As the number of surface micelles descends below a critical value, the flow of surfactant monomers away from the interfacial region will no longer be able to keep the surfactant concentration just outside the adsorbed layer fixed ≈csac. The desorption rate will instead be determined by the dissociation rate of the surface micelles. This diffusive decay is probably comparable to the corresponding dissociation of micelles in bulk solution, apart from the fact that the surface hinders the flow of monomers in one direction. The dissociation of surface micelles will therefore proceed somewhat slower than that in bulk solution.
Finally, the mean thickness is more or less constant in regime (iv) and the major part of regime (v), indicating again that surface micelles are present down to low surface coverages.

A kinetic model that explains the observed rates of the adsorption and desorption for monodisperse nonionic surfactants is developed, but presented elsewhere (*7*). Using this model, properties such as the monomer and micellar diffusion coefficients, stagnant layer thicknesses, critical surface aggregation concentrations and the half-life of surface micelles were calculated.

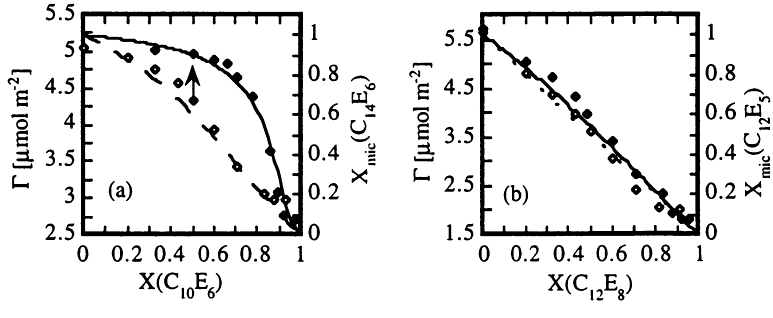

Figure 3 a. Total adsorbed amount (Γ) and the calculated molar fraction of $C_{14}E_6$ in the mixed micelles, $X_{mic}(C_{14}E_6)$, as a function of the total fraction of $C_{10}E_6$ in the solution, $X(C_{10}E_6)$. The measurements are performed at two different constant bulk concentrations of $C_{14}E_6$, where open diamonds and solid diamonds represent the evolution of Γ at 0.1 mmol l^{-1} and 1 mmol l^{-1}, respectively. The evolution of $X_{mic}(C_{14}E_6)$, calculated by ideal solution theory (*15*). at the corresponding bulk concentrations is given by the solid and the dashed curve, respectively. Figure 3 b shows comparative behaviour in the mixed $C_{12}E_5$-$C_{12}E_8$ system.

Some Observations in Mixed Nonionic Surfactant Systems.

On the basis of the discussion of the interfacial behaviour of monodisperse surfactants, we will now go on to and look at the equilibrium and kinetic features observed in mixed nonionic surfactant systems.

Adsorption of a Mixture of Two Monodisperse Surfactants. The isotherms and adsorbed layer structure observed for one component monodisperse surfactants show that there is a strong correlation between the surfactant bulk properties and those observed at the interface. In fact, adsorption to silica is best described as a self-assembly process in the presence of an interface. In solution, ideal solution theory is applicable for estimating micellar compositions and the cmc's of mixed nonionic surfactant systems (*14*).

We have studied the surface excess of two component C_nE_m systems ($C_{14}E_6$-$C_{10}E_6$ and $C_{12}E_5$-$C_{12}E_8$) as a function of the bulk fraction of the surfactants and the total surfactant concentration. The pairs were chosen so that the surface excess of the different neat surfactants differ significantly, in order to show the mixing effects clearly (see Figures 3a and b).

Figure 3a and b show how the surface excess changes with the bulk molar ratios $X(C_{10}E_6)$ and $X(C_{12}E_8)$ in the mixed $C_{14}E_6$-$C_{10}E_6$ and $C_{12}E_5$-$C_{12}E_8$ systems, respectively. They also show how the bulk micellar composition $X_{mic}(C_{10}E_6)$ and $X_{mic}(C_{12}E_8)$ varies with the same quantities. The addition of a more hydrophilic surfactant lowers the adsorbed amount. Also, the path going from one pure system to the other depends on the total bulk surfactant concentration and the cmc's of the different surfactants. There is an evident correlation between the calculated bulk micellar composition and the surface excess of the mixed system. This further indicates that there is a similar evolution of the micellar composition in the bulk micelles and the surface aggregates on changing the bulk surfactant composition or total surfactant concentration.

We shall now discuss the kinetics, in particular the desorption kinetics, observed in mixed systems. The rates of adsorption and desorption of a monodisperse surfactant are constant with time during the major part of these processes. They are further proportional to the chemical potential gradient over the stagnant layer and inversely proportional to the thickness of this layer (*7*). The latter can be assumed constant in the measurements presented in this work.

The processes of adsorption and desorption become much more complex in the case of a mixed system and this is intimately related to behaviour shown in Figures 3a and b. Figure 4 shows an adsorption-desorption cycle for a $C_{14}E_6$-$C_{10}E_6$ system adsorbed from a 1mmol l^{-1} bulk solution with a $C_{10}E_6$ molar ratio of 0.5. It also displays the comparative evolution of the pure surfactants adsorbed from solutions well above the cmc. We will here focus on the desorption regime. A surprising effect is that the surface excess observed in the mixed system initially increases upon rinsing and then reaches a maximum. The mode and rates of desorption after this maximum are nearly the same as observed for the neat $C_{14}E_6$ system. We can understand this by studying Figure 3a. In the beginning of the desorption process, the bulk concentration outside the stagnant layer is lowered. This means that we shift the equilibrium surface excess to higher Γ values (see arrow in Figure 3a). Similarly, we shift the equilibrium composition in the surface aggregates towards more and more $C_{14}E_6$. Therefore, a deficit of $C_{14}E_6$ will arise in the interfacial region. Together with the faster masstransfer of the high solubility compound away from surface region through the stagnant layer, this results in a chemical potential gradient in the stagnant layer region giving rise to a net diffusive counterflow of $C_{14}E_6$ towards the surface. This effect is only observed in cases where the low cmc (or csac) compound adsorbs to a larger extent than the compound with high cmc. If the surfactants have similar csac or cmc values, the rate of desorption is the same as that of any of the two surfactants alone. An example of this is shown in Figure 5, in which an adsorption-desorption cycle for the $C_{12}E_5$-$C_{12}E_8$ pair is shown together with the curves obtained for the corresponding neat surfactant systems.

Another situation that may arise is when the adsorption of the low solubility compound is lower than that of the high solubility compound. This is a less common situation and results in a relatively rapid desorption that decays during some time and finally the mode of desorption follows that of the low solubility compound alone (results not shown). An understanding of these rather complex phenomena exhibited in mixed surfactant systems are vital for understanding polydisperse surfactant and copolymer systems. We have here shown some examples of these phenomena, but a more complete description is the scope for a future publication. A theoretical model for explaining the phenomena described above is now being formulated.

Coadsorption of Nonionic Surfactants and Oil. Figure 6 shows how the adsorption-desorption cycle obtained for a water rich $C_{12}E_5$-water-oil microemulsion and a neat $C_{12}E_5$ system, respectively. Note that the adsorbed amount and the concentrations are given in mass units in this sub-section.

As can be seen by comparing the curves of the $C_{12}E_5$ system with that of the $C_{12}E_5$-decane system in Figure 6, the effects of added oil are large and most noticeable in the equilibrium properties of the adsorbed layer and in the mode of desorption. At these surfactant concentrations (C_b>>cmc), the adsorption proceeds rapidly, mainly facilitated through diffusive flow of swollen micelles to the surface through the stagnant layer. This is manifested by the rapid approach to equilibrium adsorption values. The drop in adsorption noticed after the initial adsorption is out of the scope of this presentation, but we note that it is related to the redistribution of oil and surfactants within the interfacial region. The adsorbed amount at equilibrium conditions is much larger for the system with decane than without, while the thickness increase due to the added oil is much smaller. The refractive index ≈1.45, measured for the C_nE_m-decane system at plateau

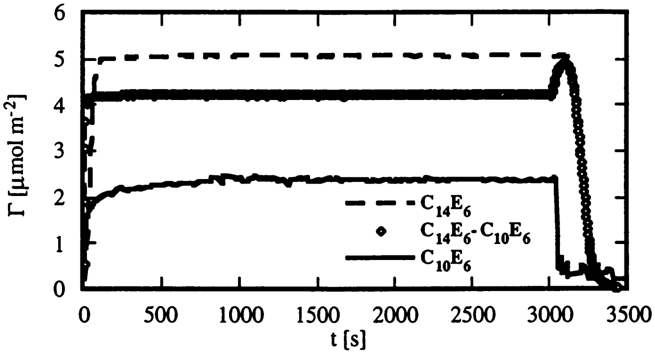

Figure 4. The surface excess (Γ) measured during adsorption-desorption cycles for a mixed $C_{14}E_6$-$C_{10}E_6$ system, $X(C_{12}E_8)=0.5$, as well as monodisperse $C_{12}E_5$ and $C_{12}E_8$ systems. The surfactant mixture is injected prior to t=0 and continuous rinsing is started at about t≈3000 s. The total surfactant concentration is in all systems > cmc.

conditions, compares well with that expected for a complete surfactant bilayer with oil in the interior.

As mentioned, a large effect of added oil is also manifested in the change of the mode of desorption. For the C_nE_m-water system, the adsorbed amount (Γ) decreases linearly with time and the layer thickness remains more or less constant during the major part of the desorption process. However, desorption from the mixed surfactant-oil layer occurs in strikingly different two-step fashion. Initially, the desorption rate is the same as for the pure $C_{12}E_5$ system ($d\Gamma/dt \approx -0.08$ mg $m^{-2}s^{-1}$), but after a while, we enter second linear regime where the desorption rate has slowed down by almost two orders of magnitude ($d\Gamma/dt \approx -0.0007$ mg $m^{-2}s^{-1}$). The difference in the slopes of the two linear regimes is well correlated to the difference in monomer solubility of $C_{12}E_5$ and decane. The desorption is, hence, initially dominated by diffusive flow of monomer surfactants away from the surface through a stagnant layer. As the concentration of free surfactant in the interfacial region starts to approach zero, desorption slows down and is instead controlled by the diffusive flow of decane through the stagnant layer. A very important consequence of this is that from the adsorbed amount obtained at the extrapolated breakpoint between the two linear desorption regimes, it is possible to estimate the fraction of oil and surfactant present in the layer prior to rinsing. Finally, we note that the thickness of the layer increases strongly on desorption. Due to the decreasing surfactant to oil ratio during desorption, emulsion droplets are formed at the surface. Eventually, as more and more oil is transferred away from the interface, these start to become smaller and finally disappear.

Summary

We have tried to illustrate different interfacial phenomena related to self-assembly of nonionic surfactant systems at hydrophilic surfaces in aqueous solution that can (and have been) studied by ellipsometry. The aim of this paper is to give some flavour of the world of surface self-assembly of surfactants at solids and present a technique suited for studies of these phenomena.

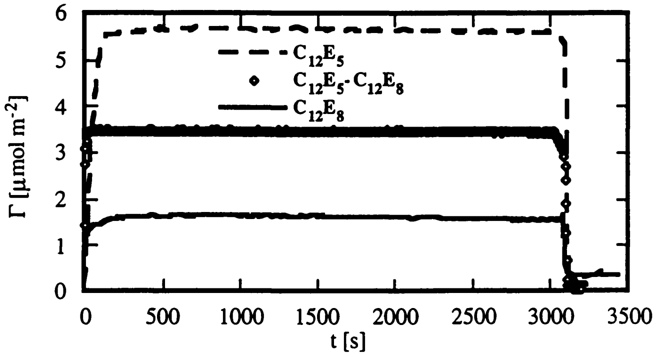

Figure 5. The surface excess (Γ) measured during adsorption-desorption cycles for a mixed $C_{12}E_5$-$C_{12}E_8$ system, $X(C_{12}E_8)=0.5$, as well as monodisperse $C_{12}E_5$ and $C_{12}E_8$ systems, respectively. The surfactant mixture is injected prior to t=0 and continuous rinsing is started at about t≈3000 s. The total surfactant concentration is in all systems >cmc.

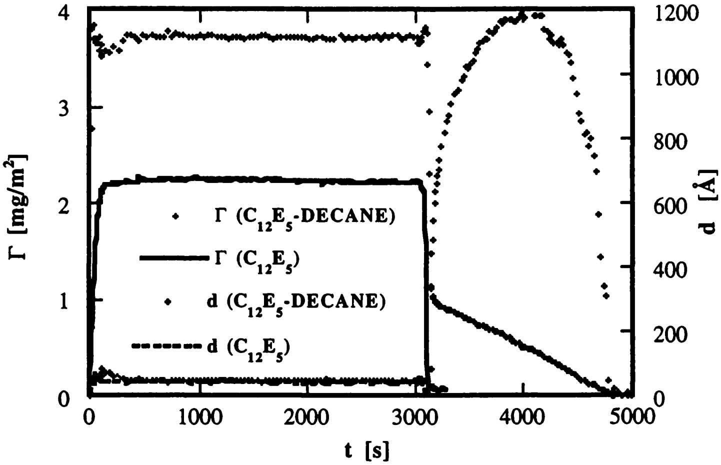

Figure 6. Ellipsometric measurement of the evolution of the total excess (Γ) and the mean thickness (d) with time during adsorption of pure $C_{12}E_5$ and $C_{12}E_5$-decane (3:1) systems. The experiments were both carried out at concentrations >> cmc. The surfactant and surfactant-oil samples were injected at t=0 and rinsing initiated at t=3000 s.

References

1. Clunie, J. S.; Ingram, B. T. In *Adsorption from Solution at the Solid/Liquid Interface*; G. D. Parfitt and C. H. Rochester, Ed.; Academic Press: New York, 1983; pp 105-152.
2. von Rybinsky, W.; Schwuger, M. J. In *Surfactant Science Series*; M. J. Schick, Ed.; Marcel Dekker: New York, 1987; Vol. 23.
3. Cases, J. M.; Villieras, F. *Langmuir* **1992**, *8*, 1251.
4. Levitz, P. *Langmuir* **1992**, *7*, 1595.
5. Tiberg, F.; Landgren, M. *Langmuir* **1993**, *9*, 927.
6. Tiberg, F.; Lindman, B.; Landgren, M. *Thin Solid Films* **1993**, *234*, 478.
7. Tiberg, F.; Jönsson, B.; Lindman, B. *Langmuir* **1994**, *10*, 3714.
8. Tiberg, F.; Jönsson, B.; Tang, J.; Lindman, B. *Langmuir* **1994**, *10*, 2294.
9. Gellan, A.; Rochester, C. H. *J. Chem. Soc., Faraday Trans. 1* **1985**, *81*, 2235.
10. Cummins, P. G.; Staples, E.; Penfold, J. *J. Phys. Chem.* **1990**, *94*, 3740.
11. Cummins, P. G.; Penfold, J.; Staples, E. *J. Phys. Chem.* **1992**, *96*, 8092.
12. Böhmer, M. R.; Koopal, L. K.; Janssen, R.; Lee, E. M.; Thomas, R. K.; Rennie, A. R. *Langmuir* **1992**, *8*, 2228.
13. de Feijter, J. A.; Benjamins, J.; Veer, F. A. *Biopolymers* **1978**, *17*, 1759.
14. Clint, J. H. *J. Chem. Soc. Faraday. 1* **1975**, *71*, 1327.
15. Tiberg, F. PhD Thesis, Lund University, 1994.

RECEIVED August 29, 1995

Chapter 16

Interactions Between Pentadecylethoxylated Nonylphenol and Tetradecyltrimethylammonium Chloride Mixtures at the Alumina–Water Interface

L. Huang, C. Maltesh, and P. Somasundaran

Langmuir Center for Colloids and Interfaces, School of Engineering and Applied Science, Columbia University, New York, NY 10027

Adsorption behavior of surfactants in mixtures was studied using tetradecyltrimethylammonium chloride (TTAC) and pentadecylethoxylated nonyl phenol (NP-15). In the single surfactant system, only the cationic TTAC was found to adsorb at the alumina-water interface at pH 10. In the mixed surfactant system, the cationic tetradecyltrimethylammonium chloride (TTAC) was found to induce significant coadsorption of the nonionic NP-15. This was attributed to hydrophobic interactions between the TTAC and NP-15. The adsorption behavior varied with the ratio of the two surfactants in the mixture. In TTAC rich mixtures, adsorption of NP-15 was higher and the adsorption isotherms of NP-15 shifted to lower concentrations. On the other hand, in NP-15 rich mixtures adsorption of TTAC was suppressed due to competitive adsorption and steric hindrance by the larger NP-15 molecules. Zeta potential measurements also showed that with the increase of NP-15 in the mixtures, TTAC molecules could not reach the alumina-water interface easily as their positive charge was partially screened by the co-adsorbed NP-15. Regular solution theory has been used to understand the nature of the interaction between surfactants in the mixtures and the relation between the monomer concentration and adsorption behaviors.

Adsorption of surfactants at solid-liquid interfaces plays a critical role in many important industrial processes. In many of these processes, the use of mixed surfactant systems can significantly improve the performance over that of single component systems. In applications such as enhanced oil recovery processes, surfactant adsorption is not desirable and mixed surfactant systems, if properly designed, may offer some promising advantages over pure components in this regard and reduce the adsorption. In other cases the adsorption of surfactants from mixtures can be higher and past work has clearly shown that the adsorption behavior is much more complex than that of single surfactants (1-3).

0097–6156/95/0615–0241$12.00/0

Surfactant adsorption from solution is related to the chemical potential of the surfactant molecules in the solution, and the nature of solid. It is widely accepted that surfactant mixtures can form mixed micelles in the solution and that the CMC of a surfactant mixture varies with the mixture composition. This may in turn reduce the chemical potential of the monomers from that for the single surfactant system, thereby reducing its adsorption as well. But on the other hand, the hemimicelle concentration (HMC) may also vary with the mixture composition. It is clear that adsorption from solution containing mixtures of surfactants can be understood only by taking into account the equilibrium among monomers, micelles and hemimicelles. So far the interaction of surfactants in bulk solutions have been studied for many cases (4-8). Literature on the solution behavior of surfactant mixtures suggests significant deviation from ideal mixing behavior. Generally, mixtures of surfactants with similarly charged head groups behave more ideally in solutions, and very large deviations from ideality are observed for mixtures of oppositely charged surfactants in solutions. However, there is very little information on mixed surfactant interactions at solid/liquid interface, particularly for the case of cationic- nonionic surfactant mixtures . Regular solution approximation has been used to treat nonideal mixing micelles in solution and this approach has been extended to model also adsorption at interface (9-10). Although regular solution theory has been criticized by some researchers (11), it has provided a very useful way to describe the behavior of mixed surfactant aggregates. In this work, the adsorption of binary mixtures of the isometrically pure cationic tetradecyltrimethylammonium chloride(TTAC) and pentadecylethoxylated nonylphenol (NP-15) at alumina-water interface was investigated. The effects of synergism and steric hindrance in this mixed system are discussed, and the possible relationship between adsorption behaviors and monomer concentrations is discussed using regular solution approximation.

Materials and Experimental Procedure

Alumina. Linde A alumina was purchased from Union Carbide Corp. It was specified to be 90% α-Al_2O_3 and 10% γ-Al_2O_3 and to have a mean diameter of 0.3μm. The specific surface area was measured to be 15 m^2/g by N_2 BET adsorption using a Quantasorb system.

Surfactants: The cationic surfactant, n-tetradecyltrimethylammonium chloride, $[CH_3(CH_2)_{13}N(CH_3)_3]Cl$ (TTAC), from American Tokyo Kasei, Inc., and the nonionic pentadecylethoxylated nonylphenol, $C_9H_{19}C_6H_4O(CH_2CH_2O)_{15}H$ (NP-15), from Nikko Chemicals, Japan were used as received.

Reagents: NaCl, used for controlling the ionic strength, was purchased from Fisher Scientific Co. and was of A.C.S. grade certified (purity >99.9%). NaOH, used for adjusting the pH, was purchased from Fisher Scientific Co. and was certified as the volumetric standard solution(0.1M). Water used in all experiments was triple distilled water. Conductivity of triple distilled water was measured to be in the range of $(1\text{-}2)\times10^{-6}\Omega^{-1}$.

Adsorption: Adsorption experiments were conducted in capped 20-mL vials. First, 2g of alumina and 10ml of 0.03 M NaCl solution were mixed and conditioned for 1 hour and then the pH value was adjusted as desired and allowed to equilibrate at the room temperature (22±2 °C) for 1 hour. Then, 10 ml of 0.03M NaCl solution containing the surfactants was added, and the samples were allowed to equilibrate at room temperature (22±2 °C) for 15 hours. pH measurements were then made and, if necessary, adjusted using 0.1 M NaOH. The change in pH during equilibration was usually between 0.2 and 0.4 units. The samples were allowed to equilibrate for about 3 hours after the final pH adjustment, and then centrifuged for 25 min at 5000 rpm. About 20 ml of the supernatant was pipetted out for analysis.

Surfactant analyses: Tetradecyltrimethylammonium chloride (TTAC) concentration was measured by a two-phase titration technique(12). Pentadecylethoxylated nonylphenol (NP-15) concentration was analyzed by UV absorbance using a Shimadzu UV-1201 UV-Vis spectrophotometer. Wavelength scans of NP-15 solution shows two absorbance peaks at 223nm and 275nm. NP-15 concentrations can be measured at either of these wavelengths.

Surface tension: Surface tension was measured using a Fisher Model 20 ring tensiometer. A 15-20 ml portion of the solution was poured into a 25 ml beaker at room temperature (22±2 °C). Three minutes were allowed for equilibration before surface tension measurements.

Electrokinetic measurements: Zeta potential measurements were made using a PEN KEM, Inc. Laser zee meter model 501 system.

Results and Discussions

Interactions between tetradecyltrimethylammonium chloride (TTAC) and pentadecyl ethoxylated nonylphenol (NP-15) in solution

In an attempt to correlate changes in monomer concentrations of the individual surfactants in the mixtures with their adsorption behavior, mixtures of tetradecyltrimethylammonium chloride (TTAC) and pentadecyl ethoxylated nonylphenol (NP-15) were studied using surface tensiometry and regular solution theory (9). Results obtained for the surface tension of aqueous solutions of pure tetradecyltrimethylammonium chloride (TTAC) and pure pentadecylethoxylated nonylphenol (NP-15) showed, as expected, the CMC of the nonionic NP-15 to be lower than that for the TTAC, but the results obtained for mixtures showed them to be not as surface active as the nonionic surfactant. The critical micelle concentrations (CMC) of the mixtures are plotted in figure 1 as a function of NP-15 composition. Regular solution model was used to fit these data (figure 1) and an interaction parameter (β) between -1.5 and -1.2 was obtained. A considerable number of binary mixed micellar system have been studied using this procedure (4-8) and the interaction parameters obtained are about -25.5 for cationic-anionic systems (4), -4.6 to -1.0 (16-17) for cationic-nonionic mixtures, and -0.2 for cationic-cationic mixtures (6). Compared with these, the interaction parameter obtained for the present system is not very large. Nevertheless, the adsorption behavior of these surfactants was modified measurably as a result of these interactions. This will be discussed later in this paper.

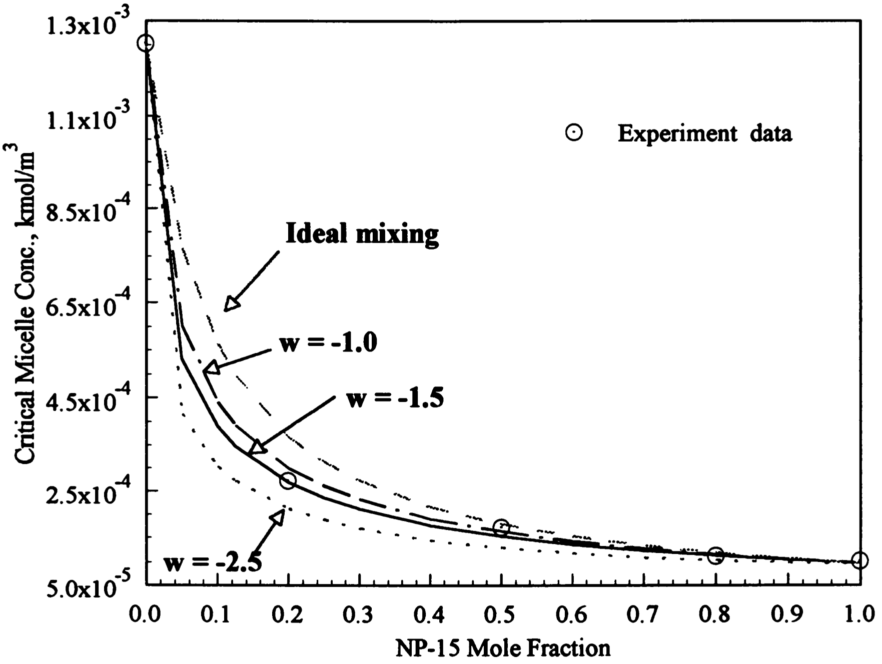

Figure 1 Measured CMC values of mixtures of tetradecyltrimethylammonium chloride (TTAC) and pentadecylethoxylated nonylphenol (NP-15) and their relation to ideal mixing and regular mixing theories.

<ins>Adsorption of surfactant mixtures</ins>

The adsorption isotherm of TTAC on alumina at pH 10 is shown in figure 2. It is observed that TTAC adsorbs significantly at the alumina-water interface at pH 10. At this pH the alumina surface is negatively charged(isoelectric point of alumina is pH 8.5-9.0) and the electrostatic attraction with the cationic TTAC will be dominant. There is a sharp increase in the adsorption density around 5x10^{-4} kmol/m^3 which is attributed to the formation of surfactant aggregates(solloids) at the solid-liquid interface. The maximum adsorption density of TTAC on alumina at pH 10 is about 2.5x10^{-6}mol/m^2. This translates to roughly 66A^{o2}/molecule which is similar to the molecular area at air/solution interface(61A^{o2}) reported in the literature (15). This suggests that the adsorption layer on alumina is composed mainly of a monolayer than a bilayer or micelles.

Tests with nonionic pentadecylethoxylated nonylphenol (NP-15) showed it not to adsorb at the alumina-water interface. In a study on the adsorption of

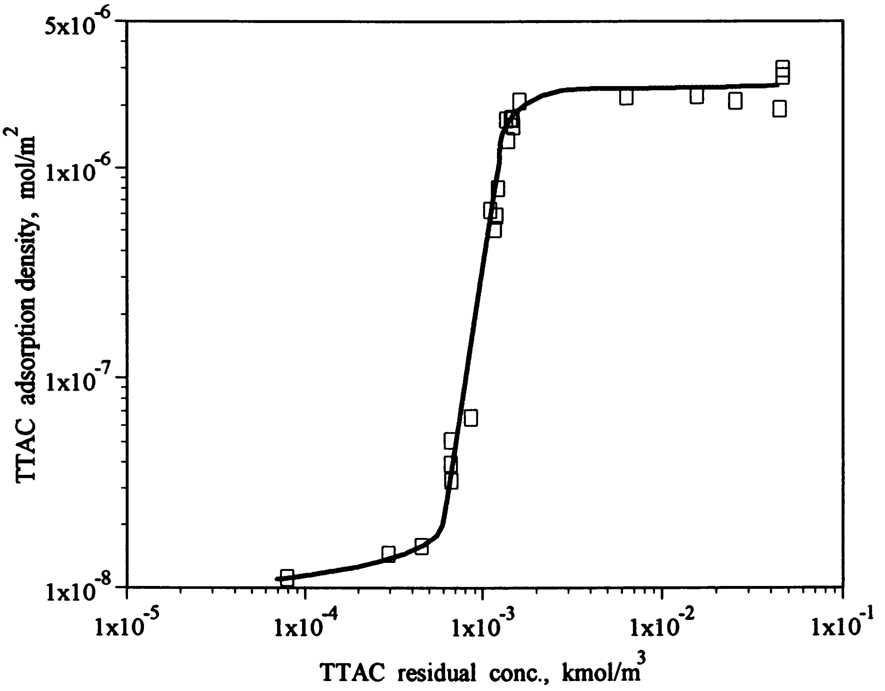

Figure 2 Adsorption of tetradecyltrimethylammonium chloride (TTAC) alone on alumina at pH 10, 0.03M NaCl.

polyethoxylated monolaurate (ML-n) and polyethoxyl lauryl ether (LE-n) on titania, Fukushima and Kumagai (13) concluded that for adsorption on polar surfaces it is necessary that the nonionic surfactant have a radical which has sufficient adsorption force to overcome the strong interaction between water molecules and the ethylene oxide groups. This observation is similar to that in the literature on the adsorption of polyethylene oxide (PEO) on different minerals (14). It has been reported that PEO adsorbs on silica but not on alumina or hematite. It was proposed that for PEO to adsorb on oxide surfaces, the polymer has to displace enough water molecules bonded to the solid surface and create a strong entropic effect. In the case of the strongly hydrated alumina surface the polymer molecule is unable to adsorb on it to displace sufficient number of water molecules from the interface. It is reasonable then that NP-15 does not adsorb on the alumina-water interface. Experiments conducted with mixtures show that in the presence of TTAC, NP-15 is forced to adsorb at the alumina-water interface. The adsorption of NP-15 is plotted in figure 3 as a function of TTAC residual concentration. In this series of experiments, the initial NP-15 concentration was the same for all the tests.

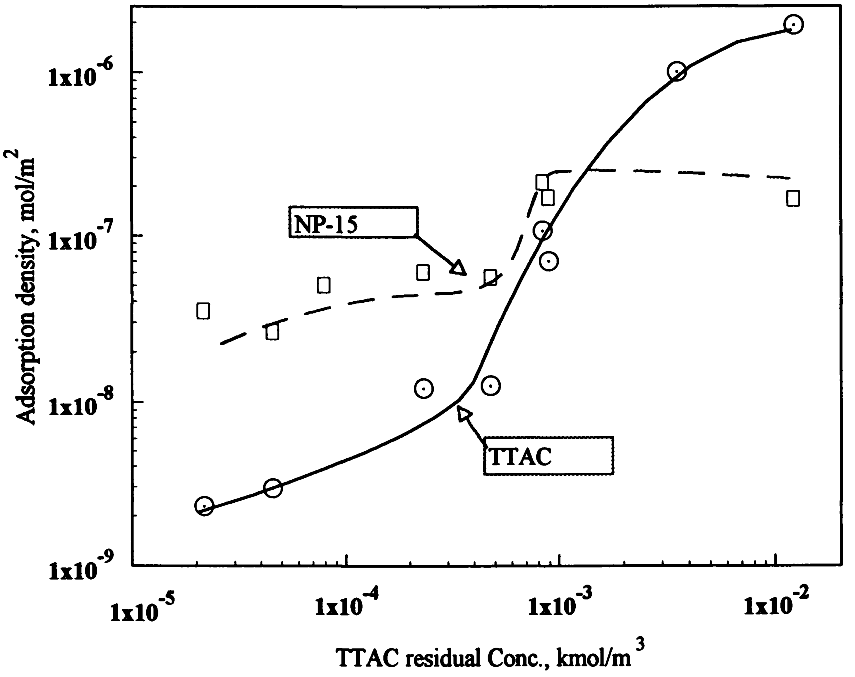

Figure 3 Adsorption of pentadecylethoxylated nonylphenol (NP-15) as a function of tetradecyltrimethylammonium chloride (TTAC) residual concentration, NP-15 initial concentration 2.13x 10^{-3} kmol/m^3.

It can be seen that adsorption of NP-15 increases with increase in TTAC concentration. It is also to be noted that when TTAC molecules form hemimicelles at the interface, NP-15 adsorption increased markedly. Above the hemimicelle concentration however, there is no further effect of any increase in the TTAC adsorption density on the adsorption of NP-15.

Figure 4 shows the adsorption isotherms of pentadecylethoxylated nonylphenol with pre-adsorbed TTAC on it along with one isotherm for adsorption of it when added along with TTAC. It is noted that tetradecyl trimethylammonium chloride(TTAC) does force the adsorption of NP-15 on alumina. Pre-adsorbed TTAC molecules function as anchors for the adsorption of NP-15. With an increase in TTAC initial concentration, the adsorption of NP-15 increases and the isotherm is shifted to lower NP-15 concentrations. The results also show that the order of addition of the surfactants has a marked effect on the adsorption of NP-15. If NP-15 and TTAC are pre-mixed and added to the alumina suspension, the adsorption density of NP-15 is markedly higher below the saturation coverage. This indicates that NP-15 adsorption from mixtures with TTAC is not completely reversible, but is controlled by the nature of molecular packing at the interface. Although NP-15 itself does not adsorb on alumina, coadsorbed NP-15 does affect the adsorption of TTAC as shown in figure 5.

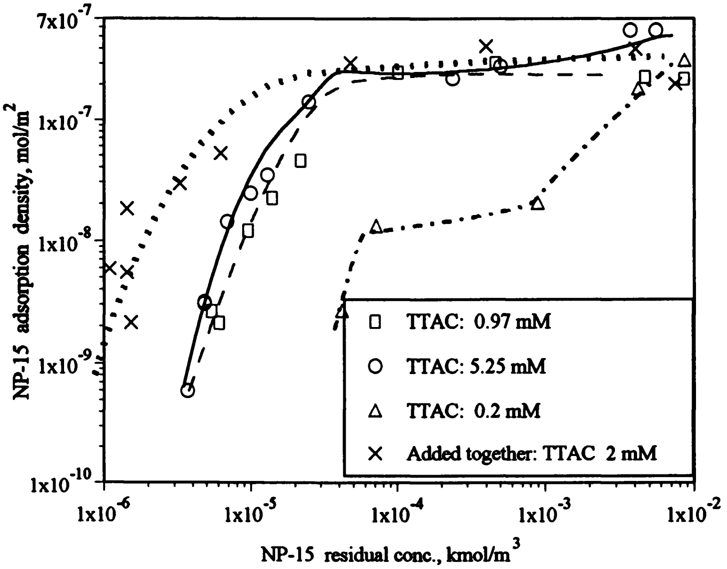

Figure 4 Adsorption of NP-15 on alumina in the presence of preadsorbed TTAC or when added together with TTAC. pH 10, 0.03M NaCl.

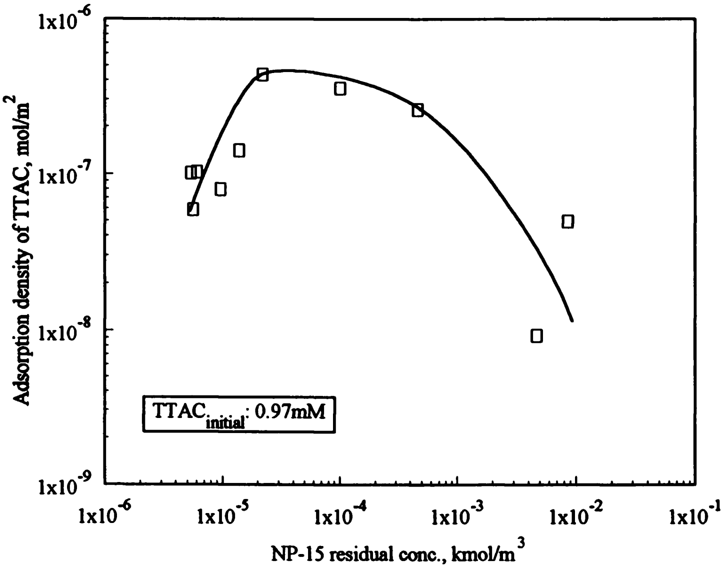

Figure 5 Effect of coadsorbed NP-15 on the adsorption of TTAC. pH 10, 0.03M NaCl

In this experiment pre-adsorbed TTAC amounts are the same for all the samples, but with the increase of NP-15 concentration the adsorption of TTAC first increased, reached a maximum, and then decreased. This suggests both cooperation and competitive interactions between TTAC and NP-15 can take place depending on the concentration region.

The adsorption isotherms of TTAC in the presence of different amounts of NP-15 are shown in figure 6 along with that in the absence of it. In all these experiments, the tetradecyl trimethyl ammonium chloride (TTAC) and pentadecylethoxylated nonyl phenol (NP-15) were pre-mixed and then equilibrated with alumina for 15 hours at pH 10. It is seen that tetradecyltrimethylammonium chloride (TTAC) solloid aggregation occurs at lower TTAC concentrations in the presence of the nonionic NP-15 but only at the 4:1 and 1:1 TTAC:NP-15 ratios. For the 1:4 ratio, however, the sharp increase in adsorption density corresponding to such aggregation is not observed. It is to be noted that the plateau adsorption density decreases continuously upon the addition of the nonionic surfactant. This is attributed to the steric hinderance and competition provided by the bulky nonionic pentadecylethoxylated nonylphenol (NP-15) for the adsorption sites.

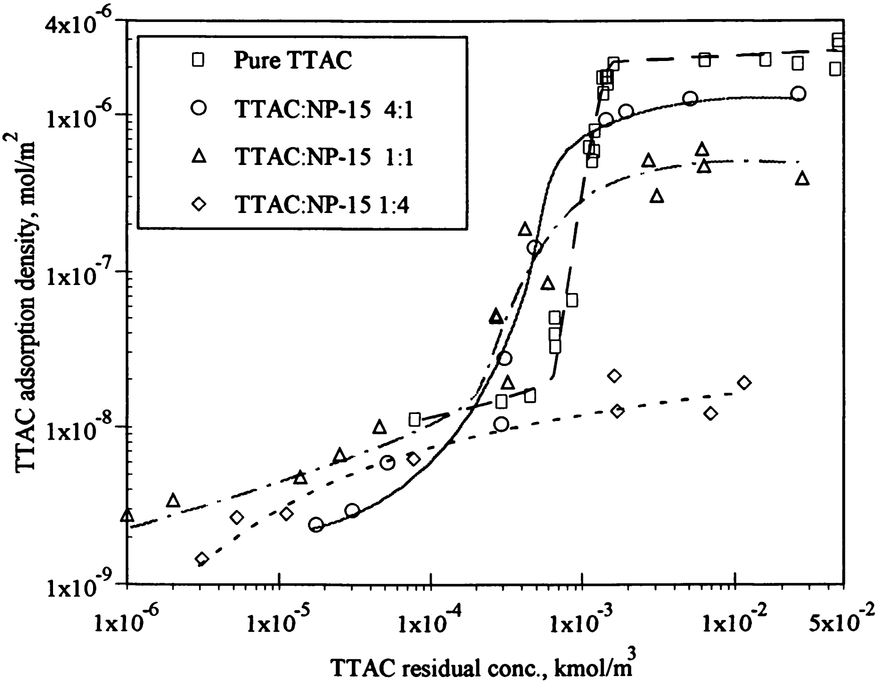

Figure 6 Adsorption of tetradecyltrimethylammonium chloride (TTAC) in the presence and absence of pentadecylethoxylated nonylphenol (NP-15), pH 10, 0.03M NaCl

The adsorption isotherms of NP-15 from different mixtures with TTAC are shown in figure 7. As mentioned earlier whereas the pure nonionic surfactant NP-15 did not adsorb on alumina, the presence of TTAC causes significant adsorption of the NP-15. With an increase in TTAC content in the mixtures, the adsorption of NP-15 is enhanced significantly, and the adsorption isotherms are shifted to lower concentration ranges.

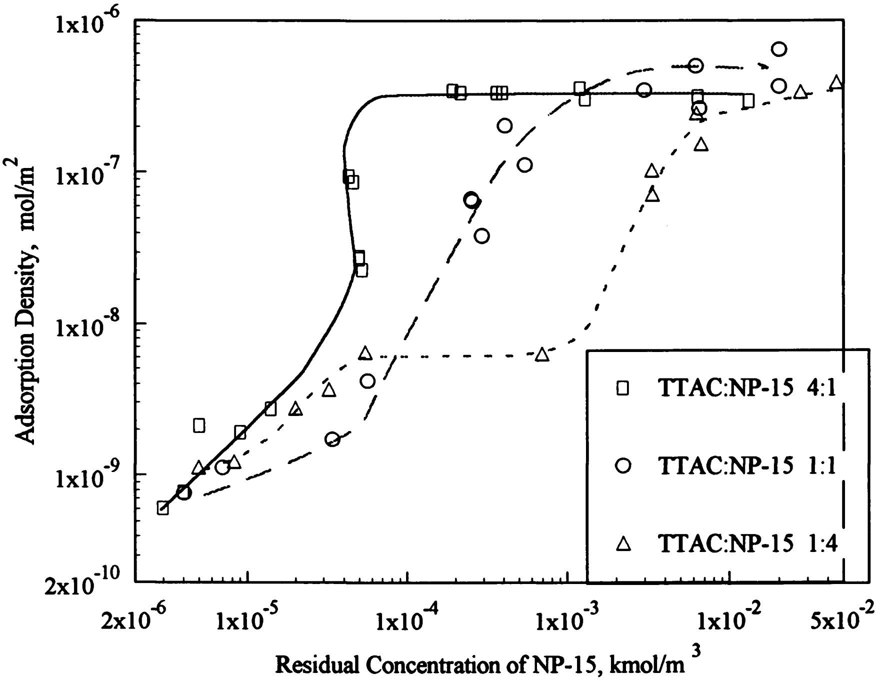

Figure 7 Adsorption of pentadecylethoxylated nonylphenol (NP-15) on alumina in the presence of different amounts of tetradecyltrimethylammonium chloride (TTAC), pH 10, 0.03M NaCl.

The peculiar S-shape isotherm obtained for NP-15 adsorption as a function of its residual concentration should be noted and is in agreement with our previous work (2). This is attributed to the more effective coadsorption of NP-15 as the number of TTAC solloids at the alumina-water interface increase, since the concentration of tetradecyl trimethyl ammonium chloride (TTAC) does vary from point to point along the NP-15 adsorption isotherm.

The NP-15 molecules are much larger than the TTAC molecules and the adsorbed NP-15 molecules will occupy more area than the TTAC spaces thus reducing the area available for TTAC. The structure of the solloids and micelles will be different in the single surfactant and the mixed surfactant systems and the charge of the ionic head of the tetradecyl trimethyl ammonium chloride (TTAC) will be shielded by the NP-15 as its content in the mixtures increases. This in turn will reduce electrostatic attraction between the negatively charged alumina surface and the positively charged TTAC molecules thereby reducing the TTAC adsorption density. This hypothesis was tested by measuring the zeta potential after adsorption and the results are shown in figure 8. The zeta potential of alumina particles will be decided mainly by the adsorption of the oppositely charged TTAC molecules, even though the adsorbed nonionic species can also contribute to reduction in zeta potential by masking the surface and by shifting the shear plane

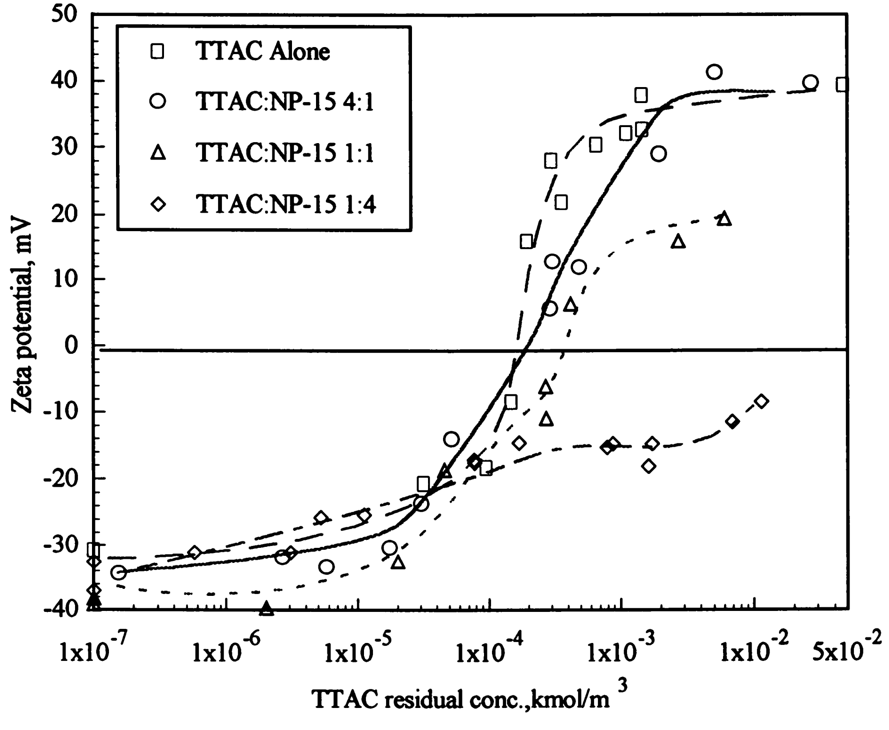

Figure 8 Zeta potential of alumina particles after adsorption of TTAC:NP-15 mixtures of different composition.

From figure 8 it is seen that with an increase of NP-15 in the mixture, the zeta potential of alumina decreases drastically, especially in the high concentration range. This is in agreement with the adsorption isotherms of TTAC and NP-15 in figures 6 & 7 respectively. Comparing the isoelectric point (IEP) for alumina in the presence of mixtures to that in the presence of TTAC alone it can be seen that the IEP is shifted to higher TTAC concentrations with an increase in the NP-15. Upon examining the adsorption density of TTAC at the isoelectric point, it is evident that the adsorption density of TTAC from mixtures is higher than that for TTAC alone. This means that the effect of TTAC in mixtures on zeta potential reduction is less than that of TTAC when present alone. It can be concluded that the positive charge of the TTAC ionic head is partially screened by the co-adsorbed nonionic NP-15 molecule. The fact that adsorption of the cationic tetra decyl trimethyl ammonium chloride (TTAC) continues to take place leading to monolayer coverage even after the particles have become similarly charged (figure 2) suggests the predominating role of hydrophobic interactions between the hydrocarbon tails in causing adsorption. On the other hand, lack of adsorption of the nonionic pentadecylethoxylated nonyl phenol (NP-15) without the synergism of the cationic TTAC shows the essential role of the electrostatic interaction as well.

The ratio of adsorption densities of TTAC and NP-15 at the alumina-water interface is examined in figure 9 as a function of the total residual concentration. It can be seen that the ability of the two surfactants to cooperate/compete at the alumina-water interface keeps changing over the entire concentration range. This suggests that the monomer composition and adsorption mechanism are changing over the concentration range studied.

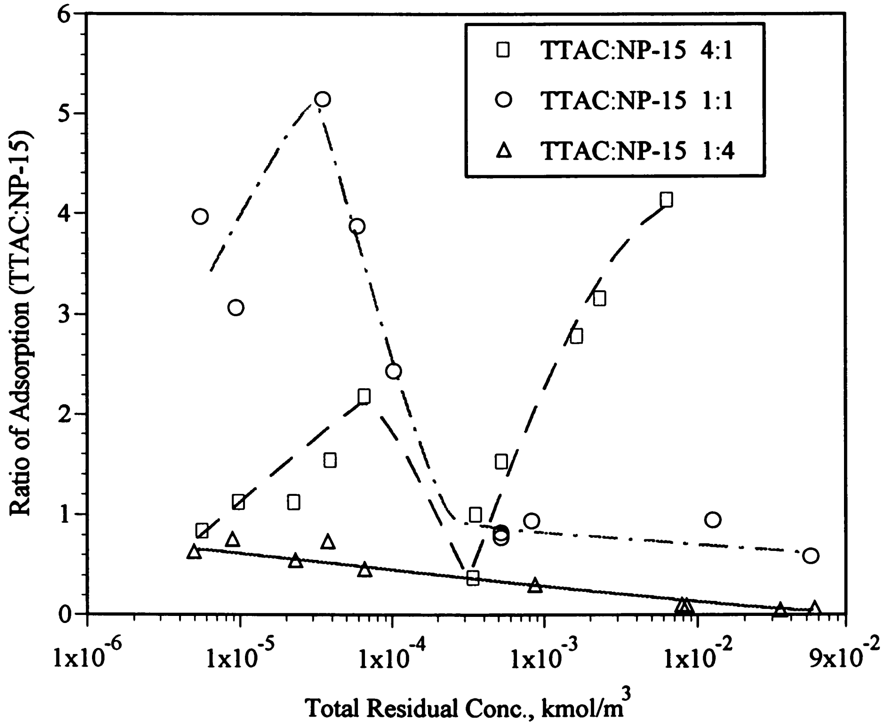

Figure 9 Ratio of adsorption densities of TTAC:NP-15 for different surfactant mixtures.

To better understand the relation between the adsorption mechanism and the monomer concentrations, the monomer concentrations of solutions of different mixtures in this system were calculated using the regular solution theory with an interaction parameter of -1.5. The results are shown in Figures 10 and 11.

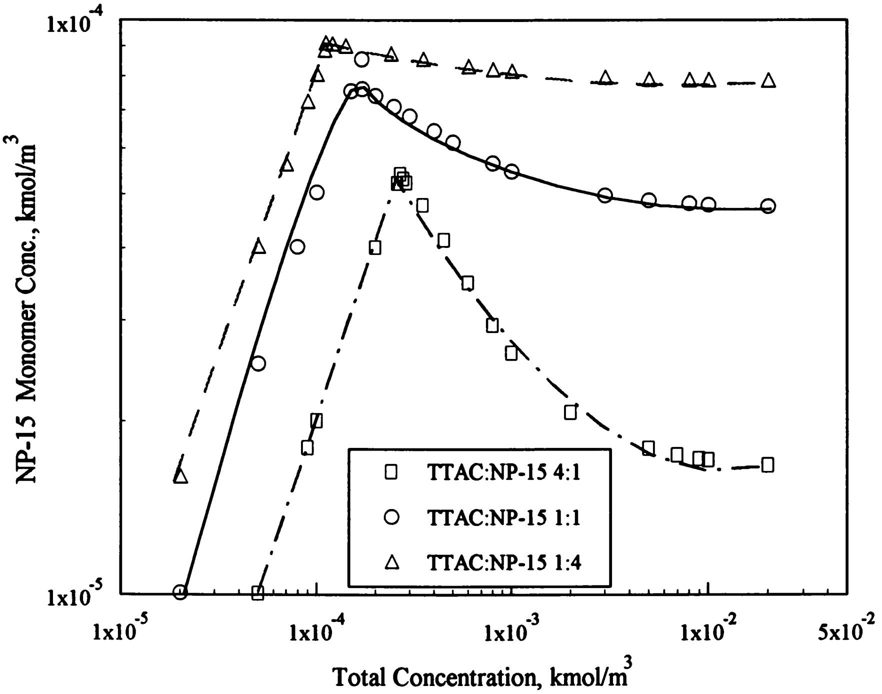

Figure 10 Monomer concentrations of NP-15 in different TTAC:NP-15 mixtures calculated from regular mixing theory with interaction parameter β=-1.5

Although the initial mixed ratio of studied surfactant system will have some changes after adsorption, it is still interesting to compare the adsorption isotherms in Figures 6 and 7 with the results for the monomer concentrations, which were calculated from regular solution with initial mixed ratio. It can be found that the adsorption of NP-15 does not depend upon its monomer concentrations in the feed mixtures. For example, the adsorption of NP-15 in 4:1 TTAC:NP-15 mixture is the highest in all these mixtures, but its monomer concentrations are the lowest. This further confirms that the adsorption of NP-15 is very much controlled by the pre-adsorbed TTAC as anchors. For the adsorption of TTAC, the adsorption quantities corresponds to its monomer concentrations in the mixtures. The higher the monomer concentration, the higher is the adsorption density. On examining the synergistic and competitive effects in this system, it becomes evident that these phenomena are decided mostly by the relative as well as the absolute quantities of NP-15. Only when the relative and absolute quantities of NP-15 are low, synergism between these two surfactants can be seen, and the maximum exhibited in Figure 8 is attributed to this behavior. There is no this kind of maximum exhibited in the case of 1:4 TTAC:NP-15 mixture because the relative quantity of NP-15 is too high. In the high concentration range the absolute quantity of NP-15 is higher, and steric hindrance will be dominant thus suppressing the adsorption of TTAC.It will be interesting to determine the monomer concentrations experimentally using suitable techniques to confirm the results of regular solution theory.

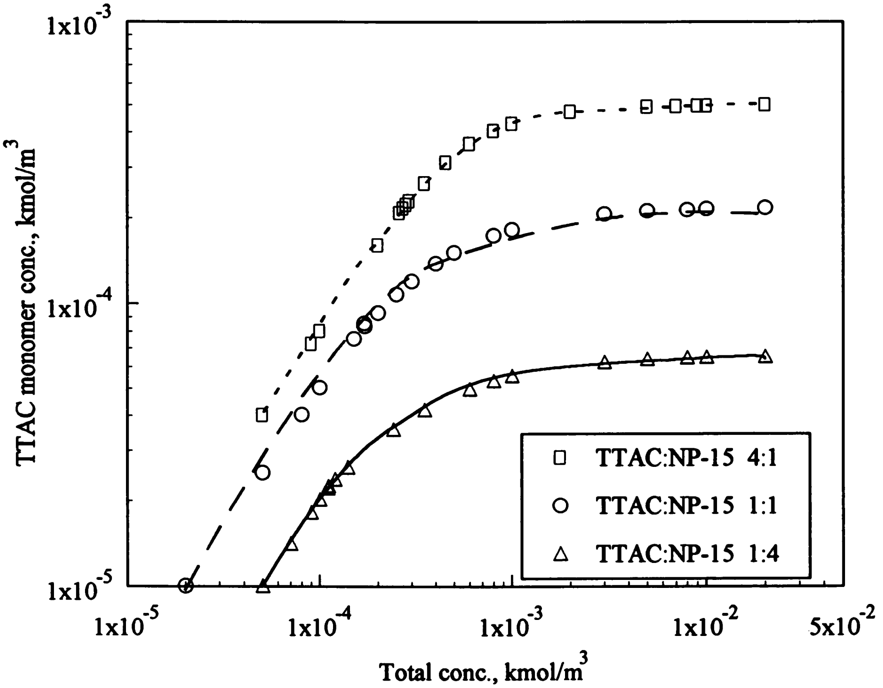

Figure 11 Monomer concentrations of TTAC in different TTAC:NP-15 mixtures calculated from regular mixing theory with interaction parameter β=-1.5

SUMMARY & CONCLUSIONS

Interactions between a cationic surfactant and a nonionic surfactant were studied using tetradecyl trimethylammonium chloride and pentadecylethoxlated nonylphenol. The interaction parameter determined using the regular solution theory indicated the molecular level associations between tetradecyl trimethyl ammonium chloride (TTAC) and pentadecylethoxylated nonyl phenol (NP-15) to be much weaker than those between an anionic surfactant and a nonionic surfactant. Nevertheless, the adsorption behavior of the nonionic NP-15 was modified significantly as a result of these interactions. Presence of TTAC in this system forced adsorption of NP-15 on alumina where the latter does not normally adsorb. The adsorption density of both TTAC and NP-15 could be varied by altering the composition of the surfactant mixture. Presence of coadsorbed NP-15 lowered the adsorption of TTAC due to competition and steric hindrance. As a result of mixed aggregation between the nonionic and the cationic surfactant, electrostatic attraction between TTAC and the negatively charged alumina surface was reduced which also contributed to the lower adsorption of TTAC from its mixtures with NP-15. Importantly the adsorption of NP-15 on alumina was not dependent on its monomer concentration but on the [TTAC]:[NP-15] ratio. The mode of addition of the TTAC:NP-15 mixture also had a significant effect on the adsorption densities of both surfactants. Adsorption was higher when the two surfactants were premixed than when the TTAC was preadsorbed. This is attributed to more favorable interactions and more possible ways to arrange surfactants coaggregates at the alumina-water interface.

Acknowledgments: Support of the Department of Energy (DE-AC22-92BC14884) and the National Science Foundation (CTS-9212759) is gratefully acknowledged.

REFERENCES

1. Harwell, J. H., Roberts, B. L., and Scamehorn, J. F., *Colloids and Surfaces* **1988**, vol. 32, pp.1
2. Somasundaran, P., Fu, E., and Xu, Q., *Langmuir* **1992**,vol. 8, pp. 1065
3. Esumi, K., Sakamoto, Y., and Meguro, K., *J. Colloid Interface Sci.* **1990**,vol. 134, pp.283
4. Zhu, B. Y., and Rosen, M. J., *J. Colloid Interface Sci.* **1984**,vol. 99, pp.435
5. Holland, P. M., and Rubingh, D. N., *J. Phys. Chem.*.**1983**,vol. 87, pp.1984
6. Nguyen, C. M., Rathman, J. F., and Scamehorn, J. F., *J. Colloid Interface Sci.* **1986**, vol. 112, pp.438
7. Rathman, J. M., and Scamehorn, J. F., *Langmuir* **1987**,vol. 3, pp. 372
8. Shinoda, K., *J. Phys. Chem.* **1954**, vol. 58, pp.541
9. Rubingh, D. N., in "Solution Chemistry of Surfactants."(K. L. Mittal , ed.), Plenum Press. New York, 1979 Vol. 1, pp.337,
10. Rosen, M. J., and Hua, X. Y., *J. Colloid Interface Sci.***1982**, vol. 86, pp. 164
11. Hall, D.G., and Huddleston, R. W., *Colloids and Surfaces,* **1985**,vol. 13, pp.209
12. Li, Z., and Rosen, M. J., *Anal. Chem.* **1981**,vol. 53, pp. 1516
13. Fukushima, S., and Kumagai, S., *J. Colloid Interface Sci.* **1973** vol. ,42, pp. 539
14. Koksal, E., Ramachandran, R., Somasundaran, P., and Maltesh, C., *Powder Tech.*, **1990**, vol. 62, pp.253
15. Venabl, R. L., and Naumann, R. V., *J. Phys. Chem.***1964**, vol. 68, pp.3498
16. Lange, H., and Beck, K. H., *Koll. -z.u.Z. Polym.***1973**, vol. 251, pp.424
17. Rosen, M. J., in "Phenomena in Mixed Surfactant System" (J.F. Scamehorn, ed.) ACS. Symposium Series 1986 Vol. 311, pp. 144

RECEIVED May 3, 1995

Chapter 17

Surfactant and Polymer Adsorption: Atomic Force Microscopy Measurements

Simon Biggs[1] and Paul Mulvaney[2]

[1]School of Chemistry, University of Newcastle, Callaghan, Newcastle,
New South Wales 2308, Australia
[2]Advanced Mineral Products Research Centre, School of Chemistry,
University of Melbourne, Parkville, Victoria 3052, Australia

The Atomic Force Microscope (AFM) is a versatile tool for the study of interaction forces due to the virtually unlimited choice of substrates. The adsorption of surfactants, dispersants or polymers at the solid/liquid interface is often used for the stabilisation of colloidal dispersions. Such adsorbed molecules can give rise to a range of additional short range forces not predicted by the standard DLVO theory of colloid stability. Results for the adsorption of CTAB onto gold and long chain poly(acrylic acid) onto zirconia are presented.

The atomic force microscope (AFM) was initially developed in 1986 (*1*) as an instrument for atomic imaging of non-conducting substrates. However, it has recently been shown by Ducker et al. that the AFM can also be used to directly measure interfacial forces between colloid particles and flat substrates (*2*). Until now, almost all such interfacial force measurements have been carried out using the Surface Forces Apparatus (SFA) (*3-5*). Measurements with the SFA have largely confirmed the main features of the DLVO theory of colloid stability. However, in addition, various other forces have been observed including solvation (*6*) and hydration (*7*) forces. A limitation of the SFA is the need for atomically smooth surfaces in order to obtain accurate force data. This has meant that almost all of the reported data have been obtained using freshly cleaved mica as a substrate. The advent of atomic force microscopy permits the extension of these surface force studies to a much broader range of substrates.

In an AFM force experiment the deflection of a microfabricated cantilever is measured as a function of its separation from a surface. Modification of the end of this cantilever spring by the attachment of a micron sized sphere allows accurate control of both the physical dimensions of the interacting unit as well as its surface chemistry. This so-called "colloid probe" (*2*) can then be brought up to a flat surface and the forces which act upon it determined as a function of separation. The first practical demonstration of this was by Ducker et al. (*2, 8*) who monitored silica-silica interaction forces as a function of salt concentration and solution pH, their data being in qualitative agreement with theory (*9*). Since this initial report a wide range of substrates have been examined including gold (*10*), titania (*11*), zirconia (*12*), polystyrene latex (*13*) and zinc sulphide (*14*). Mixed surface interactions have also

0097–6156/95/0615–0255$12.00/0

been reported between silica and titania (*15*). These studies have generally focussed on the electrostatic aspects of the interparticle forces, although some information on van der Waals interactions has also been reported (*16*). We have begun using atomic force microscopy to examine the effects of adsorbed species, particularly surfactants (*10*) and polymers (*17,18*), on interparticle forces. The aim of this work is to identify the origin of some of the short range forces present in colloidal systems which are not predicted by the standard DLVO theory (*8*). We present here an overview of the type of force data obtained with the AFM for systems where the surfaces have been modified by the presence of adsorbates. The experiments to be reported were carried out with either gold or zirconia substrates.

Experimental Procedures

Reagents, Colloid Probes and Surface Preparation. All chemicals used were of analytical grade or better and were not purified further. Water was distilled and then purified to Millipore Milli-Q quality (surface tension=72 mN/m). The exact methods used to prepare the colloid probes have been detailed elsewhere (*2,8,11*). To prepare gold probes, a tungsten sphere was glued to the cantilever and the substrate was then sputter coated with a 300 nm thick gold layer. Zirconia probes were prepared from spray dried agglomerates of 300 nm primary zirconia particles that had been calcined at >850°C. The agglomerates were spherical and typically had radii > 5μm. The radii of all the colloids were determined by optical microscopy, using 1μm diffraction gratings as calibrants. SEM micrographs of the gold probes revealed no evidence of surface roughness down to 10nm. BET results on the zirconia particles showed them to be non-porous, and HRTEM micrographs also revealed no signs of significant surface roughness.

All measurements reported here were performed against flat plates. Gold plates were 24 carat gold (purity > 99.999%) and were polished to optical smoothness. Whilst optical polishing leads to a macroscopic smoothness of order $\lambda/10$, over a 1 μm^2 area AFM imaging consistently yielded an RMS roughness of ±1nm. These plates were cleaned by soaking in chromic acid for 15 min and then washing in an excess of water. This renders the surface of gold hydrophilic. The zirconia plates used here were polished surfaces of pure zirconia ceramic. These plates were cleaned by soaking in 0.1 M KNO_3 for 24 h followed by steaming for 3 h and rinsing in pure water. The plates were used immediately after cleaning.

Force Measurements. Force-distance information was obtained from a Nanoscope III AFM (Digital Instruments) which was operated in the "force mode." In this operating mode the X-Y raster motion of the sample on the scanning piezoelectric crystal is suspended and the substrate is moved towards and away from the cantilever in the Z direction by the application of a sawtooth voltage. In a typical experiment, the colloid probe was mounted into the AFM liquid cell after being washed with ethanol. The solution for study was then pumped into the liquid cell from a sealed, bulk reservoir using a peristaltic pump. In all cases, the force-distance experiments were performed in a closed environment using the commercial liquid cell (Digital Instruments) and the solution conditions were accurately controlled with respect to additive concentration, salt concentration and pH. The surfaces employed were always freshly cleaned immediately prior to assembly of the liquid cell. Any changes to the additive concentration, background electrolyte concentration and pH were carried out in the bulk reservoir under a nitrogen atmosphere whilst circulating the fluid through the AFM with the peristaltic pump. After a suitable equilibration time had elapsed the peristaltic pumping was suspended and the force-distance data for those conditions was then collected.

AFM Data Analysis. Cantilever deflections are monitored by recording the changes in voltage from a split photodiode, onto which is focused a laser beam that is reflected from the rear of the cantilever. The raw data of voltage change versus piezo displacement is converted into real force versus separation data following the principle of Ducker et al. (2), which requires the definition of a position of zero force and a position of zero separation. Zero force is defined as being at large separations where a change in the crystal position has no effect on cantilever deflection. Zero separation is defined as the point where a change in crystal position causes an equal change in the cantilever displacement, the so-called region of constant compliance. From a knowledge of these two positions and the slope of the region of linearity at constant compliance the force can be calculated as a function of true separation.

In this study, the reported data were collected with V-shaped cantilevers having quoted spring constants of between 0.06 N/m and 0.36 N/m. In all cases the cantilevers were independently calibrated using either the method outlined by Cleveland et al. or Sader et al.(*19*). The spring constants used here are given in the figure legends. The best fits to the experimental data were calculated by solution of the non-linear Poisson-Boltzmann equation and assuming either a constant surface charge or a constant surface potential (*20*). The van der Waals constants used here were calculated from dielectric data according to the technique described by Larson et al. (*11*). The Hamaker constant for zirconia was calculated to have a value of 6.0x 10^{-20} J whilst for gold the Hamaker constant was determined to be 2.5 x 10^{-19}J (*16*).

Clean Surface Interactions.

A pre-requisite for any study of the interaction forces in the presence of adsorbed additives is a knowledge of the force-distance curves for the bare surfaces when brought together with no additives present. The primary reason for this is, of course, to have a blank measurement against which any differences can be assessed. However, other reasons are that it provides some information on the cleanliness of the surfaces and also the importance of surface roughness can be assessed. Data for gold-gold interactions across pure water are given in Figure 1. It is clear that the surfaces are attractive under these conditions, the data being well fitted by a van der Waals interaction with a composite Hamaker constant of A=2.5 x 10^{-19} J. It may also be seen that in the contact region the data points are effectively registered as a hard wall, with little or no deviation from the apparent zero distance. The implication of this is that the surfaces have contacted at a single point, that they are relatively incompressible and that there are no surface contaminants. Unwanted surface contaminants appear as a soft, steric layer at initial contact before the attainment of a hard compliance at higher contact pressures. In the same way, multiple contacts were observed as random steps in the contact and pull-off regions. In both these cases, further information is gained from the retraction curve, where a single, clean contact is seen to give rise to strong, sharp adherence with a single pull-off point. Surface contamination usually leads to a decrease in the strength of this attraction and may also lead to a protracted pull-off that extends out some nanometres from the surface. Multiple contacts almost invariably lead to multiple pull-off points. Thus, the quality of this contact zone offers a sensitive measure of the bare surface contacts and if it is found to be inadequate then the surface and probe are recleaned and re-tested before proceeding.

For surfaces which carry an inherent charge, for instance mineral oxides, a further verification of the surface cleanliness is available from measurement of the long range electrostatic forces under controlled electrolyte and pH conditions. In Figure 2 force-distance data for zirconia-zirconia interactions at two electrolyte concentrations and a single pH are shown. Larson et al (*11*) have demonstrated that

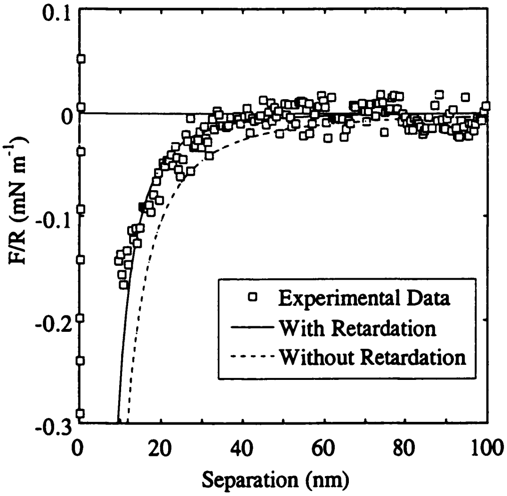

Figure 1. Force-distance data for the interaction of a 3.3 μm radius gold sphere with a flat gold plate in water at 20°C. Best fits to the data were calculated using a Hamaker constant of 2.5 x 10^{-19}J. pH = 6.3, spring constant = 0.32 N/m.

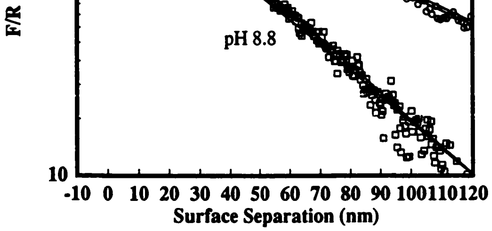

Figure 2. Force-distance data for a zirconia probe of 10 μm radius under two different solution conditions: (i) pH= 8.8, ψ_{afm}=47 mV, 10^{-4} M KNO_3, κ^{-1}= 31 nm; (ii) pH= 8.4, ψ_{afm}=72 mV, 2 x 10^{-5} M KNO_3, κ^{-1}= 58 nm. In each case the solid lines correspond to the best fits to the DLVO theory at the limits of constant charge (upper line of each pair) and constant potential (lower lines): The spring constant = 0.24 N/m, Hamaker constant = 6 x 10^{-20}J.

the apparent surface potentials determined from the best fits to these AFM data are equal to the zeta potentials determined under the same solution conditions for dispersions of the same material. If we know the salt concentration we can determine the expected decay length from theory. Thus, comparison of both the potential and the decay length of the experimental force-distance data, determined from the best fits to these data, with the theoretical decay length and the zeta potential will give an indication as to whether the surfaces are behaving as expected. Interestingly, the force-distance curves for the zirconia surfaces employed here all showed an additional, short-range repulsion in alkaline solutions at separations where the van der Waals attractive interaction should dominate. Such a short range force has been seen previously for other mineral oxide surfaces, for example silica and titania (*6, 8, 11*). This extra, short-range barrier to flocculation has been attributed to hydration layers at the solid/liquid interface.

Adsorption of Surfactants and Dispersants.

CTAB Adsorption on Gold. After confirmation that the surfaces for study are clean, the effects of surface adsorption can be investigated. Data for the interaction of gold surfaces in the presence of cetyltrimethylammonium bromide (CTAB) are given in Figures 3 and 4. In Figure 3 the data were collected for a gold sphere of radius 3.3 μm whilst in Figure 4 the conditions are exactly the same although the probe is now a gold coated cantilever tip having an effective radius of 0.1 μm. CTAB is a cationic surfactant that is known to form a coating on surfaces at concentrations above the critical micelle concentration (cmc) (*21*). In the case of gold surfaces adsorption will give rise to some electrostatic stabilisation of the surfaces and the formation of a double layer extending into solution.

In both cases the observed data are well fitted at longer range by the electrostatic component of the DLVO theory. At small separations, however, there are considerable differences between the two sets of data. At < 3nm the attractive van der Waals component of the overall force-distance profile should begin to dominate. In the case of the gold sphere there is no attractive well, the data showing a repulsive force all the way into contact. This suggests that the contact distance corresponds to contact of the surfactant headgroups. The fits to these force curves were therefore calculated by offsetting the plane of the van der Waals interaction from the plane of the surface electrostatic charge by 3nm, which is equal to the thickness of a CTAB monolayer (1.5-1.7nm) on each surface. We also assumed that the contribution of the surfactant layers to the overall Hamaker constant was negligible. The best fits to the data calculated in this way are shown in Figure 3. The decay length was found to be 10.2 nm which is close to the predicted value of 9.8 nm. The calculated surface potential of 90 ± 5 mV agrees well with previous experiments for CTAB adsorption at mineral surfaces. With this offset, we can easily rationalise the lack of an attractive interaction at small separations. The adsorption of the surfactant leads to both electrostatic and steric stabilisation of the gold surfaces. It should be noted that the Hamaker constant for gold is one of the largest known and so the strength of the dispersion interaction for gold surfaces will also be large. This implies that most other surfaces will also be sterically stabilised by adsorbed CTAB. Indeed, even shorter adsorbates should be sufficient to completely mask the attractive part of the total interaction force. It is worth noting that CTAB stabilized gold sols have been found to be stable for months, as would be predicted from the AFM force curve in Figure 3.

The data for the sharper, gold coated tip shown in Figure 4 are also well fitted with a decay length of 10.2 nm and a surface potential of 90 ± 5mV. In this case however there is a clear attractive interaction at small separations before the region of constant compliance is attained. The apparent jump-in distance was found to be

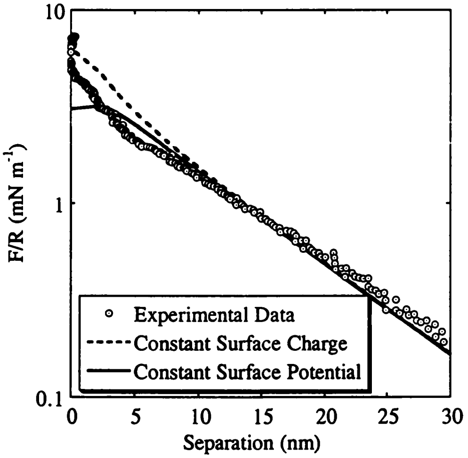

Figure 3. Force-distance data for the interaction of a 3.3 μm radius gold sphere with a flat gold plate in a 1.5 mM CTAB solution at 20°C. Best fits to the DLVO theory at the limits of constant charge (upper line of each pair) and constant potential (lower lines) calculated using ψ_{afm}= 90 mV, κ^{-1}= 10.2 nm and a Hamaker constant of 2.5 x 10^{-19}J. The plane of charge was put at a distance of 3 nm equal to the thickness of two CTAB monolayers: pH = 6.3, spring constant = 0.32 N/m.

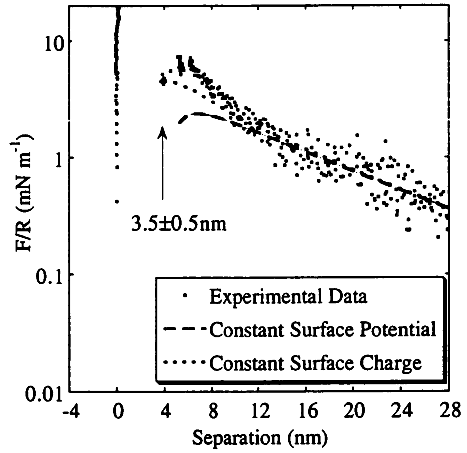

Figure 4. Force-distance data for the interaction of a 0.1 μm radius gold coated tip with a flat gold plate in a 1.5 mM CTAB solution at 20°C. Best fits to the DLVO theory at the limits of constant charge (upper line of each pair) and constant potential (lower lines) calculated using ψ_{afm}= 90 mV, κ^{-1}= 10.2 nm and a Hamaker constant of 2.5 x 10^{-19}J. The plane of charge was put at a distance of 3 nm equal to the thickness of two CTAB monolayers: pH = 6.3, spring constant = 0.32 N/m.

approximately 3.5 nm, i.e. about the size of two surfactant layers. A jump such as this in the data is conventionally attributed to the van der Waals interaction between the probe and the surface. In this case we consider it to be due to the penetration of the adsorbed surfactant bilayers by the sharper AFM tip, which has an effective radius about 15 times smaller than the radius of the gold sphere used in the previous experiment. We therefore assume that the compliance or contact region corresponds to contact between the gold surfaces and not the bilayers as before. The theoretical fits to the force curves were again calculated using a van der Waals offset of 1.5nm but assuming the compliance region to correspond to metal-metal contact. The fact that the 15 fold increase in pressure is sufficient to disrupt the surfactant coating means that care must be taken when comparing AFM force curve data with coagulation data for colloid systems where the particle size is much smaller than the AFM colloid probe.

Citrate Adsorption on Gold. Gold sols are typically prepared in the laboratory by the reduction of gold(III)chloride with citrate anions in aqueous solution (*22*). It is accepted that the gold colloids formed in this way are stabilised by the adsorption of excess citrate anions at the gold surface. In Figure 5 data are presented for the interaction of a gold sphere (radius = 4.2 μm) with a flat gold plate at three different concentrations of trisodium citrate and at a pH of 6.3. The decay length and the diffuse layer potential are seen to decrease with increasing salt concentration, as expected from theory. It is clear from these data that citrate adsorption to gold surfaces does indeed give rise to the observed electrostatic repulsion between the surfaces.

The form of the data at small separation distances is particularly interesting. At citrate concentrations below 1 x 10^{-5}M the surfaces were seen to jump directly into a hard wall contact of the type seen for the bare gold surfaces (c.f. Figure 1). At higher concentrations the surfaces were also seen to jump towards contact at separations predicted well by theory. However, prior to attaining a hard-wall contact some form of short-range steric barrier was always seen. The data for the contact region at these concentrations showed a varying response with increasing load on the surfaces. Short, periodic steps were observed which may be due to the squeezing out of small molecules from between the surfaces (*23*). The size of these steps was determined to be 8 ±1 Å, which corresponds well to the predicted size for a citrate anion (*24*). Thus, it appears that the adsorbed citrate anion is able to offer a short range steric barrier as well as electrostatic stabilisation to gold surfaces.

Adsorption of Polymeric Stabilisers. When a polymer adsorbs to a surface it can give rise to a range of possible interaction forces. Amongst these are steric, electrosteric and bridging forces (*25*). In Figure 6 force data obtained during the interaction of a 10 μm zirconia probe with a flat plate of polished zirconia ceramic after the adsorption of polyacrylic acid (MW=750K) are shown. The surfaces were equilibrated for 24 h with a solution of 30 μg/L PAA before any force measurements were made. The background electrolyte concentration for these measurements was 10^{-3}M KNO_3. All measurements reported here were performed at a pH of 5 which is well below the average pK_a of 6.3 for high molecular weight PAA. Thus, the polymer will only be weakly dissociated, theoretical predictions suggesting < 25% dissociation (*26*). The radius of gyration, R_G, for such a weakly dissociated PAA (MW=770K) has been previously determined to be 56 nm (*27*). Data for both the compression and decompression of the surfaces are given. The measured force when compressing the surfaces is seen to increase monotonically from an apparent separation of around 180 nm until the surfaces are only about 20 nm apart. The onset of repulsion at about 180 nm corresponds to approximately $4R_G$ and is thus in line with theoretical predictions for interacting adsorbed polymer layers (*28*). At around

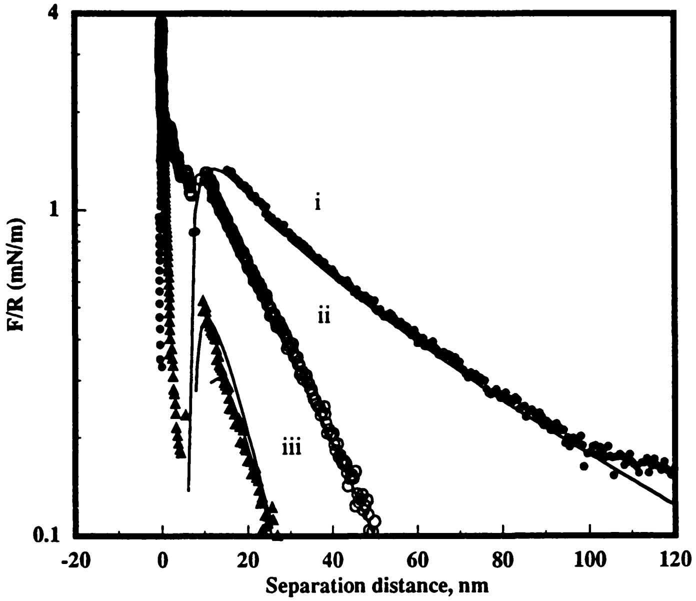

Figure 5. Force-distance data for the interaction of a 4.2 μm radius gold sphere with a flat gold plate in aqueous trisodium citrate solutions at 20°C. Best fits to the DLVO theory at the limits of constant charge (upper line of each pair) and constant potential (lower lines) calculated using the following information: (i) ψ_{afm}= 125 mV, κ^{-1}= 58.8 nm, 6 x 10^{-6}M; (ii) ψ_{afm}= 84 mV, κ^{-1}= 15.3 nm, 1 x 10^{-4}M; (iii) ψ_{afm}= 53 mV, κ^{-1}= 8.9 nm, 3 x 10^{-4}M. Hamaker constant = 2.5 x 10^{-19}J, pH = 6.3, spring constant = 0.32 N/m.

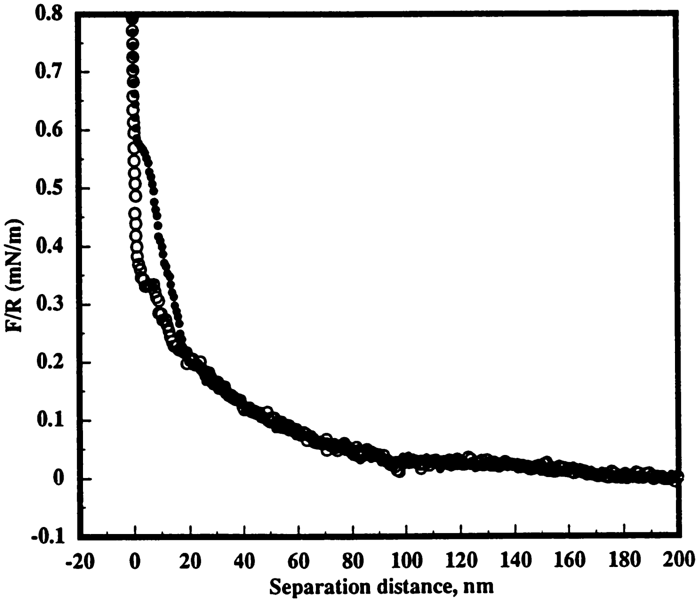

Figure 6. Force-distance data for the interaction of a 10 µm radius zirconia sphere with a flat zirconia plate in an aqueous solution of 30 µg/L Polyacrylic acid. Background electrolyte is 10^{-3}M KNO_3 and the equilibration time for the polymer with the surfaces was 24 h. Filled symbols correspond to the compression data, open symbols are for the decompression.

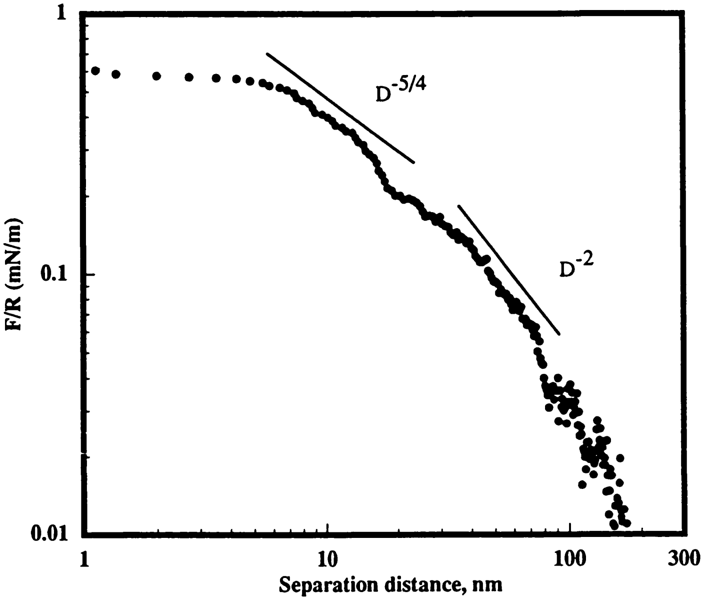

Figure 7. Force-distance data on a double logaritmic scale for the compression data given in Figure 6. Solid lines correspond to interaction energies that scale as $D^{-5/4}$ and D^{-2} at short and long ranges respectively.

20nm a more steeply repulsive force is observed until a region of constant compliance is achieved. This region of constant compliance only corresponds to pseudo-zero separation since polymer must remain between these surfaces at all times, and therefore in this region the adsorbed polymer layers are in a collapsed, incompressible conformation. Evidence for the presence of polymer between the surfaces at all times is gained from the decompression curves where the main features of the compression curves are exactly reproduced, implying that as the pressure is reduced the polymer can expand back between the surfaces with only a little hysteresis. If the polymer desorbs as the surfaces are brought together then a much stronger, adhesive retraction curve would be expected and this was not observed. There was however a small region of hysteresis between 0 and 20 nm for the compression and decompression data. This is explained by an initial, slow relaxation of the polymer into the gap as the pressure is released during the decompression cycle. The polymer is present after compression as a highly compressed coil at the surface, and as the pressure is released it is unable to expand at an equivalent rate, leading to an effective segment density decrease between the plates relative to the concentration at the same distance during compression. Thus, the repulsion is lower during decompression because there is a lower concentration of polymer segments in the gap. Plotting the compression data on a log-log scale allows comparison with equilibrium polymer theory as shown in Figure 7. According to scaling theories (*28*) any interaction energy E(D) at a distance D will be minimised with respect to the polymer segment density profile f(z) away from the surface. By assuming interaction at a constant surface coverage of polymer it is predicted that the interaction energy for a homopolymer will vary as D^{-2} at long range and as $D^{-5/4}$ at small surface separations. There is therefore good agreement between the scaling theory predictions and the experimental data for this particular system.

Conclusions

The results presented here on the effects of surfactant and polymer adsorption reveal several important features. The first is that the tip geometry is crucial, and that it may not be correct to deduce the interfacial behaviour of nanosized particle systems from the interaction of micron-sized spheres with flat plates. Unless the applied loads for various probes are comparable, completely different interaction curves may result. The AFM data suggest that an octadecyl surfactant will electrosterically stabilize even particles with high Hamaker constants against collapse into the primary minimum. Perhaps more importantly, the results show that direct measurement of the kinetics of interfacial processes such as adsorption and desorption and double layer relaxation is possible. In fact, the rate at which the double layer builds up on gold surfaces during citrate reduction has already been measured by this technique (*10*).The force curves obtained in the presence of the long-chain polyacrylic acid demonstrate in addition that changes in polymer conformation during the approach and separation of two surfaces can be measured directly by AFM. Finally, we note that the observation of short range repulsive forces in the presence of the citrate anion suggests that these forces are far more widespread and important to the stability of colloids than is generally recognized.

Acknowledgments. The authors are grateful to the Advanced Mineral Products Research Centre, a special research centre of the ARC, for supporting this work. PM is also the recipient of a QE II Fellowship from the ARC. We would also like to express thanks to Prof. T.W.Healy, Dr. F.Grieser and Dr. D.Y.C. Chan for their assistance and helpful criticism of this work.

Literature Cited

1. Binnig, G.; Quate, C.F.; Gerber, C. *Phys. Rev. Lett.* **1986**, *56*, p.930.
2. Ducker, W.A.; Senden, T.J.; Pashley, R.M. *Nature* **1991**, *353*, p.239.
3. Israelachvili, J.N.; Adams, G.E. *JCS Faraday I*, **1978**, *74*, p.975.
4. Tabor, D.; Winterton, R.H.S. *Proc. Royal Soc.* **1969**, *A 312*, p.435.
5. Horn, R.G.; Israelachvili, J.N. *Chem. Phys. Lett.* **1980**, *71*, p.192.
6. Pashley, R.M. *J.Colloid Inter. Sci.* **1981**, *83*, p.531.
7. Pashley, R.M. *J.Colloid Inter. Sci.* **1981**, *80*, p.153.
8. Ducker, W.A.; Senden, T.J.; Pashley, R.M. *Langmuir* **1992**, *8*, p.1831.
9. Israelachvili, J.N. *Intermolecular and Surface Forces* ; 2nd edn, Academic Press, London, 1991.
10. Biggs, S.; Mulvaney, P.; Zukoski, C.F.; Grieser, F. *J. Am. Chem. Soc.*, **1994**, *116*, p.9150.
11. Larson, I.; Drummond, C.J.; Chan, D.Y.C.; Grieser, F. *J. Am. Chem. Soc.*, **1993**, *115*, p.11885.
12. Prica, M.; Biggs, S.; Grieser, F; Healy, T.W. *Colloids and Surfaces*, (in press).
13. Li, Y.Q.; Tao, N.J.; Pan, J.; Garcia, A.A.; Lindsay, S.M. *Langmuir* **1993**, *9*, p.637.
14. Atkins, D.T.; Pashley, R.M. *Langmuir* **1993**, *9*, p.2232.
15. Larson, I.; Drummond, C.J.; Chan, D.Y.C.; Grieser, F. *J. Phys. Chem.* **1995**, *99*, p.2114.
16. Biggs, S.; Mulvaney, P. *J.Chem.Phys.* **1994**, *100*, p.8501.
17. Biggs, S. *Langmuir* **1995**, *11*, 156.
18. Biggs, S.; Healy T.W. *J. Chem. Soc. Fara. Trans.* **1994**, *90*, p.3415.
19. (a) Cleveland, J.P. ; Manne, S.; Bocek, D.; Hansma, P.K. *Rev. Sci. Instr.* **1993**, *64*, p.403.
    (b)Sader, J.; Larson, I.; Mulvaney, P.; White, L.R. *Rev. Sci. Instr.* (in press).
20. Chan, D.Y.C.; Pashley, R.M.; White, L.R. *J. Coll. Inter. Sci.* **1980**, *77*, p.283.
21. Drummond, C.J.; Senden, T. *J. Am. Chem. Soc.*, (submitted).
22. Enüstün, B.V.; Turkevich, J. *J. Am. Chem. Soc.* **1963**, *85*, p.3317.
23. Biggs, S.; Scales, P.; Leong, Y.K.; Healy, T.W. *J. Chem. Soc. Fara. Trans* . (in press).
24. Kielland, J. *J. Am. Chem. Soc.* **1937**, *59*, p.1675.
25. Napper, D.H. *Polymeric Stabilisation of Colloidal Dispersions*; Academic Press, London, 1983.
26. Fleer, G. In *Food Polymers, Gels and Colloids;* Dickenson, E., Ed.; RSC: London, 1991, Special Publication no.82.
27. Orofino, T.A.; Flory, P.J. *J.Phys.Chem* . **1959**, *63*, p.283.
28. De Gennes, P.G. *Adv. Coll. Inter. Sci.* **1987**, *27*, p.189.

RECEIVED September 15, 1995

Chapter 18

Adsorption Kinetics of Demulsifiers to an Expanded Oil–Water Interface

Patrick J. Breen

**Baker Performance Chemicals, Inc., 3920 Essex Lane,
Houston, TX 77027**

Relaxation of interfacial tension was recorded for the sudden expansion of a water droplet in the presence of a heptane or toluene solution of a number of demulsifier polymers prototypical of products used in industry to demulsify crude oil. Adsorption kinetics were found in all cases to be non-diffusion controlled. Increasing the polyoxyethylene content within the demulsifiers resulted in slower relaxation rates. This effect was much stronger in heptane than in toluene suggesting that polyoxypropylene-type polymers would be better candidates for demulsifying light, waxy crude oil emulsions.

Much has been written concerning the specific chemical mechanisms involved in demulsification[1-7]. Much of this work addresses the behavior of polymers at an oil-brine interface or in thin films. What has generally been ascertained is that the demulsification process involves the displacement of emulsifying entities such as asphaltenes, natural surfactants or solids at the interface by a surface-active demulsifier which then also causes changes in the rheological properties of the interface. Such changes favor rapid coalescence between converging droplets of dispersed aqueous phase by increasing the rate at which the continuous oil phase can drain.

More specifically, as dispersed phase water droplets approach each other and flatten to form a thin film of continuous oil phase between them, the outward drainage flow of the film can create gradients in interfacial tension which then oppose and slow such drainage (Marangoni-Gibbs effect)[8,9]. The presence of a demulsifier in the continuous phase, which rapidly adsorbs to prevent the formation of gradients at the interface, speeds drainage and coalescence[4]. In effect, the demulsifier serves to impart a lower elasticity, or dynamic film modulus, to the interface by minimizing changes in

0097–6156/95/0615–0268$12.00/0

interfacial tension, $\Delta\sigma$, when the interface is expanded or stretched. This is illustrated by Equation 1 for the Gibbs elasticity, E:

$$E = \frac{d\sigma}{d\ln A} = \left(\frac{d\sigma}{dt}\right)\cdot\left(\frac{dt}{d\ln A}\right) \qquad (1)$$

Where σ is the dynamic interfacial tension, A is the area of the interface and t is time. For situations where dt/dlnA is constant, the elasticity will vary with the rate at which the dyamic interfacial tension changes with time ($d\sigma/dt$). Thus, the kinetics of adsorption and the resultant dynamic elasticity of the interface are prime factors to consider in attempting to understand and predict demulsifier performance.

Much work has been published concerning the relaxation kinetics of aqueous solutions of various alcohols and polyethylene glycols[10-17]. Comparably little work has been devoted to examining the adsorption behavior of oil-soluble demulsifying polymers, such as polypropylene glycols or oxyalkylated phenolic resins, to water/oil interfaces, although Wasan et al.[18] and Tambe et al.[19] have recently been active in this area. Work has also been published on some oil-soluble surfactants such as cholesterol[20] and some organic diols[21,22] in which adsorption was found to be non-diffusion controlled.

In this work, the overall relaxation kinetics of an expanded oil-water interface in the presence of various prototypical demulsifiers are examined. Data is presented that shows the interfacial tension relaxation process to be non-diffusion controlled and dependent on such structural factors as MW and hydrophobicity.

Experimental

Organic oil phases were HPLC-grade toluene and heptane, purchased from Aldrich and used without further purification. Water was ultra-purified using a Barnstead Nanopure ultrapure water system. Polypropylene glycols, triols and oxyalkylated phenolic resins were obtained from Arco Chemicals and Baker Performance Chemicals. Polypropylene polyethylene glycols were obtained from BASF. Five oxyalkylated resins were used, and are described chemically in Table 1. Prototypical structures are illustrated in Figure 1. Percent ethylene oxide content of the polymers was as given by the manufacturer.

All glass surfaces were cleaned by soaking in fresh aqua regia followed by extensive rinsing with ultrapure water. Relaxation kinetics were measured using an expanded drop tensiometer, similar to others described in the literature[23,24], depicted in Figure 2. A low pressure differential pressure transducer (obtained from Micro Switch, Inc. a division of Honeywell) with an operating range of 0-0.18 psi was connected with a plastic tee to a 25 μl gastight syringe on one end and a glass capillary, with an inner diameter of 0.45 mm and a wall thickness of 3.09 mm, on the other end. The syringe, tee, capillary and transducer cell were filled with pure water. The transducer was interfaced to a computer for easy data aquisition. The

Table 1. Characteristics of Phenolic Resins

	MW	Phenol	% Propylene Oxide	% Ethylene Oxide
Resin A	5,400	p-nonyl	0.0	100.0
Resin B	9,400	p-nonyl	26.0[†]	74.0[†]
Resin C	10,450	p-tert-butyl	100.0	0.0
Resin D	5,500	p-tert-butyl	61.0[†]	39.0[†]
Resin E	8,600	p-nonyl	62.0	38.0

[†] Mixed oxide copolymer

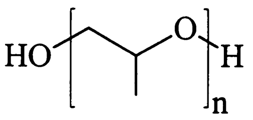

Polyproplyene Glycol

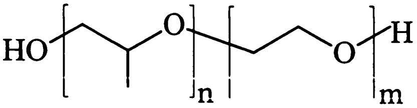

Polypropylenepolyethylene Glycol

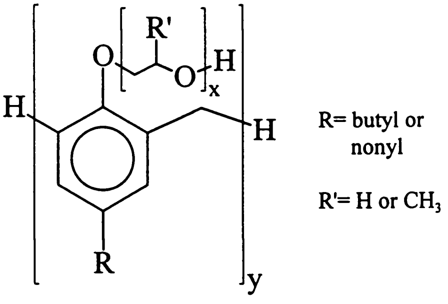

Oxyalkylated Phenolic Resin

Figure 1. Representative demulsifier structures.

relationship between pressure and interfacial tension is described by the equation of Young and Laplace[25],

$$\Delta P = \frac{2\sigma}{R} \tag{2}$$

where ΔP is the capillary pressure, σ is the interfacial tension, and R is the radius of curvature of the droplet. The tip of the capillary was immersed in the organic phase and allowed to equilibrate for several minutes. Data collection was then initiated and the plunger of the syringe quickly depressed to create a roughly hemispherical droplet at the tip of the capillary. This sudden expansion to the maximum radius of curvature results in a sudden, sharp increase in the internal droplet pressure in the blank sample (pure liquids), with no subsequent changes. This control experiment was conducted prior to every measurement to ensure that contamination was minimal; if surface active contaminants were present in the water or organic phases to any significant extent, they would adsorb to the freshly formed interface and cause the interfacial tension, and detected droplet pressure, to decrease over time.

It was observed early on that it was extremely difficult to obtain a stable drop at the tip of the capillary, since the drop tended to slowly spread across the face of the capillary. This problem was solved by soaking the capillary tip for several hours in a 50/50 mixture of chlorotrimethylsilane and 1,1,1,3,3,3-hexamethyldisilazane, which made the glass surface hydrophobic and effectively prevented spreading. With such treated tips, steady unchanging interfacial tensions were observed after expansion of the droplet using the pure phases (control experiment).

Adsorption kinetics were measured for each demulsifier by adding, via microliter syringe, a set amount of demulsifier directly to the oil phase, which was then stirred several minutes with a magnetic stirrer (also cleaned with aqua regia). The demulsifiers were added from stock solutions (1000 ppm) in toluene. The capillary was then lowered into the oil phase, allowed to equilibrate for several minutes, and expanded. In most cases the resultant data could be easily fit to an exponential, allowing the calculation of a rate constant to describe the approximate rate of relaxation. For display purposes the data was plotted as a function of $\Delta\sigma/\Delta\sigma_0$ vs. time, where $\Delta\sigma$ is the difference in the dynamic interfacial tension at time t and at equilibrium, and $\Delta\sigma_0$ is the difference in the dynamic interfacial tension at initial time t t = 0 and at equilibrium.

Plots of static interfacial tension as a function of demulsifier concentration were prepared using a Fisher semi-automated du Nouy ring tensiometer. The surfactant was added to 50 ml of heptane in a 100 ml graduated cylinder to which 35 ml of water were added. The cylinder was capped and shaken, and the contents poured into an 8 cm dish. The dish was covered and the contents allowed to equilibrate overnight, whereupon the interfacial tension was measured.

Results and Discussion

Representative plots of $\Delta\sigma/\Delta\sigma_0$ as a function of time following a sudden expansion are presented in Figures 3, 4 and 5 for a series of polypropylene glycols, triols and oxyalkylated phenolic resins, respectively, at $1\text{x}10^{-6}$ M, in heptane at 24°C. The solid lines in these figures show the good fit of the data to single exponential decays. For a diffusion controlled process, the dynamic interfacial tension should vary with time according to equation 3[26]:

$$\Delta\sigma(t) = \Delta\sigma_o \exp\left(\frac{t}{\tau_D}\right) erfc\sqrt{\frac{t}{\tau_D}} \qquad (3)$$

where $\Delta\sigma(t)$ is the difference between the interfacial tension at time t and at equilibrium, $\Delta\sigma_0$ is the difference between the interfacial tension at time t = 0 and at equilibrium, and where τ_D is the diffusion relaxation time as defined by equation 4,

$$\tau_D = \frac{1}{D}\left(\frac{d\Gamma}{dC}\right)^2 \qquad (4)$$

where D is the diffusion coefficient, Γ the adsorption and C the bulk concentration. This expression fails to describe the relaxation data in Figures 3-5 for polypropylene glycols triols and oxyalkylated phenolic resins in heptane, and also fails to describe the corresponding relaxation data in toluene. Polypropylene polyethylene glycols also exhibit exponential relaxation kinetics.

As mentioned earlier, non-diffusion controlled adsorption has been reported for other oil-soluble surfactants[19-21] adsorbing to an expanded oil-water interface, so a non-diffusion controlled relaxation is not altogether unexpected. To further bolster such a conclusion, the total time frame for the relaxation in a diffusion controlled situation can be estimated[20,21] from the first term of Ward and Tordai's equation[27] describing the adsorption of a surfactant to an expanded interface. The first term of this expression describes the inward diffusive flow of the surfactant, and is presented as equation 5:

$$\Gamma = 2C_o\left(\frac{Dt}{\pi}\right)^{1/2} \qquad (5)$$

Using the Gibbs equation (equation 6), values for Γ can be obtained from the slope of a plot of the static interfacial tension as a function of ln C:

$$\Gamma = -\frac{1}{RT}\left(\frac{d\sigma}{d\ln C}\right) \qquad (6)$$

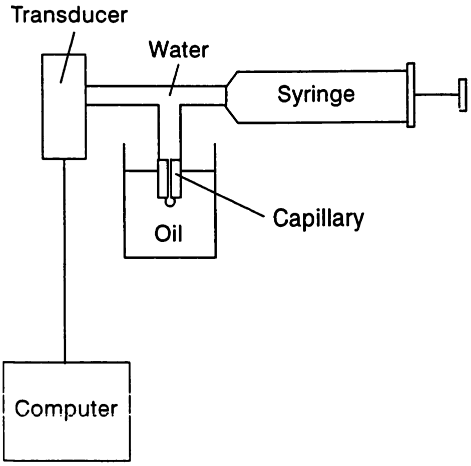
Transducer
Water
Syringe
Capillary
Oil
Computer

Figure 2. Expanded Drop Apparatus.

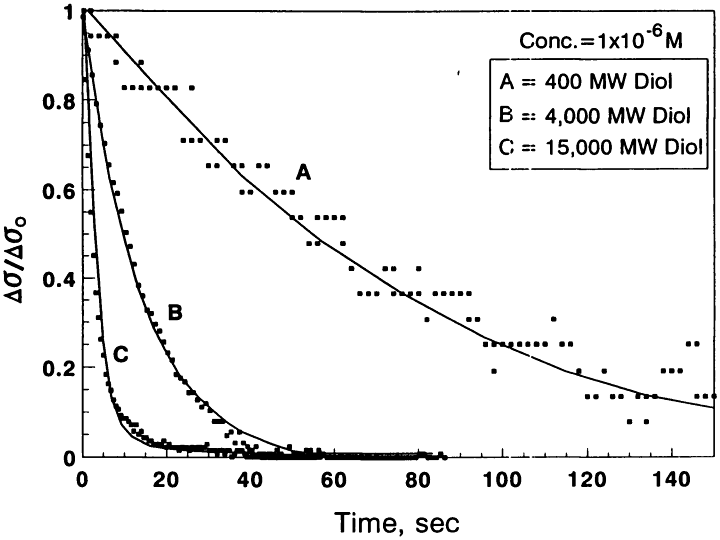

Figure 3. Relaxation kinetics and exponential fits for polypropylene glycols of varying molecular weight, at 1x10^{-6} M in heptane at 24°C.

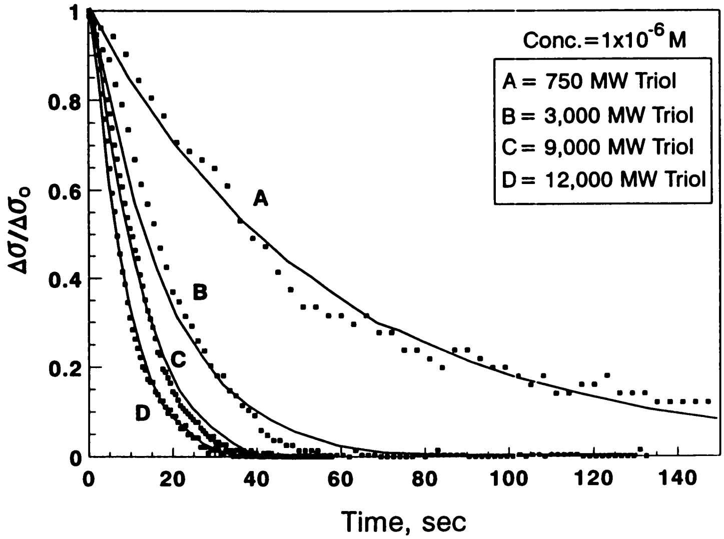

Figure 4. Relaxation kinetics and exponential fits for polypropylene triols of varying molecular weight, at 1x10^{-6} M in heptane at 24°C.

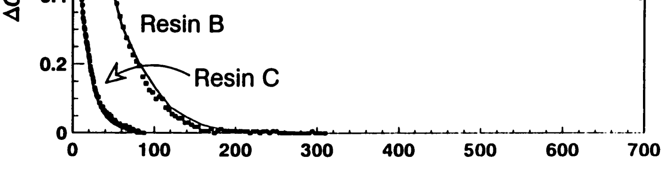

Figure 5. Relaxation kinetics and exponential fits for oxylakylated phenolic resins, at 1x10^{-6} M in heptane at 24°C.

Plots of static interfacial tension as a function of ln C for three of the diols are presented in Figure 6. Values for Γ obtained from these plots are listed in Table 2. Estimating the diffusion coefficient to be on the order of $1x10^{-6}$ cm^2/s, based on reported values[11,15] for polyethylene glycols, and taking the measured values of Γ listed in Table 2, estimates of the approximate time for the relaxation were calculated and are also listed in Table 2. As can be seen, these values are much smaller than the time frames of the relaxations observed. This can be taken as further evidence that the relaxation is not diffusion controlled.

Relaxation lifetimes, defined as the reciprocal of the fitted exponential rate constant, are presented in Table 3 for all of the demulsifiers examined in this work. Each of the values reported in Table 3 are averages of lifetimes obtained for at least three separate data traces. Standard deviations were found to vary from 5-10%. This data, along with the data in Figures 3 and 4 illustrate that the relaxation rate increases significantly with increasing molecular weight. Thus higher MW glycols and triols will be more effective at maintaining a low interfacial elasticity than low MW glycols and triols, due to faster relaxation kinetics, which should result in faster film drainage and coalescence due to more efficiently suppressed Marangoni-Gibbs effects.

It is interesting from an industrial, economic point of view to consider a comparison of relaxation rates based on an equal mass, or ppm, basis rather than a molar one. Figure 7 shows the relaxation data for the 400 and 15,000 molecular weight glycols at a concentration of 2 ppm. The relaxation for the 400 MW glycol is noticably faster than the 15,000 MW glycol. As a result it might be tempting to conclude that at an equal cost per pound, the 400 MW glycol would be the demulsifier of preference. This is not true, however, because of the poor adsorption thermodynamics of the 400 MW glycol as compared to the 15,000 MW glycol as illustrated in Figure 6 and Table 2. Figure 8 illustrates that in a draining thin film between water droplets, if Γ is small, interfacial gradients may not be entirely suppressed even if relaxation kinetics are rapid. Alternatively, if Γ is large, a reverse gradient in interfacial tension could be created which would push in the same direction as the outward flow, speeding it even more.

It is interesting to consider the effect of changing the nature of the organic oil phase from aliphatic (heptane) to aromatic (toluene). The data in Table 3 include lifetimes for three glycol block polymers of varying polyethylene oxide (PEO) content, obtained in heptane and toluene at $1x10^{-6}$ M. Increased PEO content leads to longer relaxation times in heptane, whereas in toluene the effect is greatly reduced. These solvent effects correspond to the relative solubilities of the polyethers in heptane and toluene. It is possible, for example, to prepare 10 percent weight solutions of the polypropylene glycols in heptane or toluene, with no visible turbidity. In contrast, as increasing amounts of PEO are incorporated into the polymer, visible turbidity appears at lower and lower concentrations in heptane. A 10 percent weight solution of the 2650 MW glycol containing 30 percent PEO in toluene is clear, for example, while noticable turbidity exists in a 100 ppm solution of the same polymer in heptane[28], indicating an aggregation of the polymer. The slower relaxation rates observed for the PEO-containing polyols may be due to a rate-limiting dissociation of the polymer segments from such aggregates.

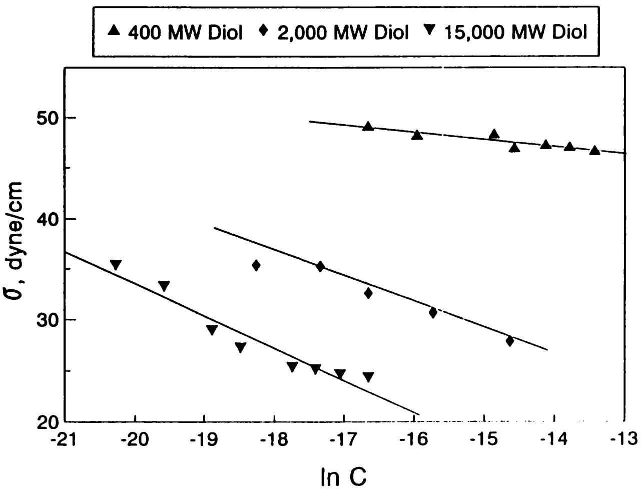

Figure 6. Static interfacial tension of a water-heptane interface as a function of ln C for PPO glycols, at 24°C. The slope of the lines was used to calculate the adsorption, Γ.

Table 2. Absorption and Calculated Diffusion Relaxation Times for Glycols

SAMPLE	Γ, mol/cm^2	t, sec[‡]
400 MW Glycol	2.9×10^{-11}	6.6×10^{-4}
2000 MW Glycol	9.0×10^{-11}	6.4×10^{-3}
15,000 MW Glycol	1.3×10^{-10}	1.3×10^{-2}

[‡] Diffusion Coefficient $=1\times10^{-6}$ cm^2/s

Table 3. Relaxation Lifetimes for Demulsifiers

	OIL PHASE	
SAMPLE	HEPTANE	TOLUENE
400 MW Glycol	74.4 sec	---
2000 MW Glycol	42.0	47.3 sec
4000 MW Glycol	12.7	13.2
15,000 MW Glycol	2.9	4.2
750 MW TRIOL	63.0	42.3
3000 MW TRIOL	22.7	35.5
6000 MW TRIOL	10.5	17.5
9000 MW TRIOL	10.9	12.5
12,000 MW TRIOL	8.0	11.6
2000 MW Glycol, 10% EO	37.4	39.9
2750 MW Glycol, 20% EO	52.9	39.7
2650 MW Glycol, 30% EO	69.2	48.6
Resin A	868.0	14.2
Resin B	76.3	34.7
Resin C	13.0	11.5
Resin D	27.3	8.2
Resin E	140.1	78.5

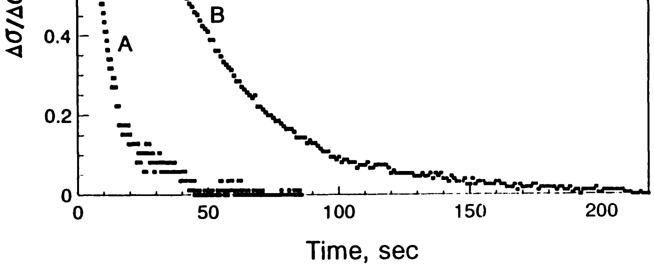

Figure 7. Relaxation kinetics at 2 ppm for the 400 and 15,000 MW PPO glycols.

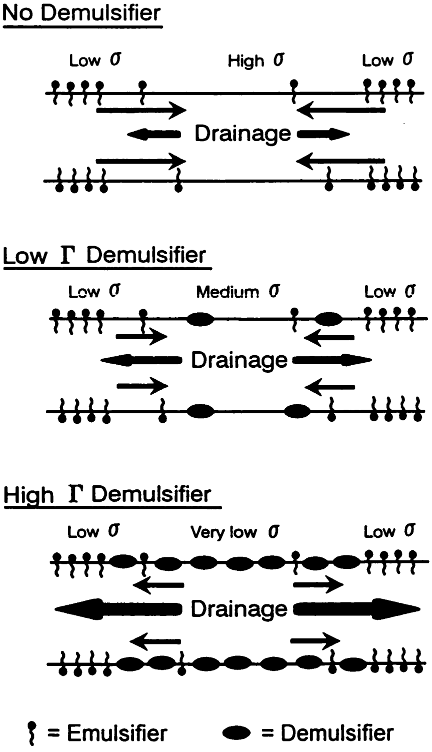

Figure 8. Effects of demulsifier Γ on ability to quench the Marangoni-Gibbs effect.

The effect of increased PEO content on relaxation rates in heptane is even more dramatic for the oxyalkylated resins. Lifetimes presented in Table 3 show a definite increase in relaxtion lifetime in heptane, as compared to toluene, for resins with PEO segments. The comparisons between resins are, unfortunately, not perfect, since there are other structural variations as well (e.g.; p-nonyl phenol vs. tert-p-butyl phenol), but the fact remains that the only resin with approximately equal relaxation rates in both heptane and toluene contained no PEO segments (Resin C), and showed the fastest relaxation in heptane. Conversely, the resin with the greatest difference in relaxation rate between heptane and toluene contained only PEO segments (Resin A) and showed the slowest relaxation in heptane.

The data in Table 3 illustrate that demulsifiers containing hydrophilic PEO segments are less suited for aliphatic oil emulsions than polypropylene glycols and triols, since the slower relaxation kinetics will allow a higher degree of elasticity at the interface. This is consistent with empirical observation and field experience.

Summary

Adsorption kinetics of prototypical demulsifiers from a hydrocarbon phase to a water/hydrocarbon interface have been shown to be non-diffusion controlled.

Measurements of relative relaxation rates for a series of polypropylene glycol and triol homologues have demonstrated that, on a per molecule basis, high molecular weight polypropylene glycols and triols yield the fastest relaxation kinetics, favoring rapid coalescence. Kinetic comparisons need to be made on an equimolar basis: comparisons based on an equal mass or ppm basis should not be used to predict performance.

The longer relaxation times observed in heptane for demulsifiers containing PEO segments indicate that the hydrophilic content should be minimized for optimum performance in aliphatic oil emulsions.

References

1. Krawczyk, M.A.; Wasan, D.T.; Shetty, C.S. *Ind. Eng. Chem. Res.* **1991**, *30*, 367.
2. Berger, P.D.; Hsu, C.; Arendell, J.P. Proceedings SPE International Symposium on Oilfield Chemistry, **1985**, *Paper 16285*.
3. Thompson, D.G.; Taylor, A.S.; Graham, D.E. *Colloids Surf.* **1985**, *15*, 175.
4. Jones, T.J.; Neustadter, E.L.; Whittingham, K.P. *J. Can. Pet. Tech.* **1978**, *April-June*, 100.
5. Sjöblom, J.; Söderlund, H.; Lindblad, S.; Johansen, E.J.; Skjärvo, I.M. *Colloid Polym. Sci.* **1990**, *268*, 389.
6. Shetty, C.S.; Nikolov, A.D.; Wasan, D.T. *J. Disp. Sci. Tech.* **1992**, *13*, 121.
7. Wasan, D.T.; Shah, S.M.; Aderangi, N.; Chan, M.S.; McNamara, J.J. *Soc. Pet. Eng. J.* **1978**, *18*, 409.
8. Zapryanov, Z; Malhotra, A.K.; Aderangi, N.; Wasan, D.T. *Int. J. Multiphase Flow* **1983**, *9*, 105.
9. Malhotra, A.K.; Wasan, D.T. *Chem. Eng. Comm.* **1987**, *55*, 95.
10. Van Hunsel, J.; Bleys, G.; Joos, P. *J. Colloid Interface Sci.* **1986**, *114*, 432.
11. Lucassen, J.; Giles, D. *J. Chem. Soc., Faraday Trans. I* **1975**, *71*, 217.
12. Nakamura, M.; Takeuchi, S. *Bull. Chem. Soc. Jpn.* **1978**, *51*, 2776.
13. Lunkenheimer K.; Serrien, G.; Joos, P. *J. Colloid Interface Sci.* **1990**, *134*, 407.
14. Hansen, R.S. *J. Colloid Sci.* **1961**, *16*, 549.
15. Sauer, B.B.; Yu, H. *Macromolecules* **1989**, *22*, 786.
16. Van Hunsel, J.; Joos, P. *Colloids Surf.* **1987**, *25*, 251.
17. Tsonopoulos, C.; Newman, J.; Prausnitz, J.M. *Chem. Eng. Sci.* **1971**, *26*, 817.
18. Kim, Y.H.; Wasan, D.T.; Breen, P.J. *Colloids Surf.* in press.
19. Tambe, D.; Paulis, J.P.; Sharma, M.M. *J. Colloid Interface Sci.* in press.
20. Van Hunsel, J.; Bleys, G.; Joos, P. *J. Colloid Interface Sci.* **1986**, *114*, 432.
21. Joos, P.; Bleys, G.; Petre, G. *J. Chim. Phys.* **1982**, *79*, 387.
22. Bleys, G.; Joos, P. *J. Phys. Chem.* **1985**, *89*,1027.
23. Clint, J.H.; Neustadter, E.I.; Jones, T.J. *Developments in Petroleum Science* **1981**, *13*, 135.
24. Nagarajan, R.; Wasan, D.T. *J. Colloid Interface Sci.* **1993**, *159*, 164.
25. Adamson, A.W. *Physical Chemistry of Surfaces* John Wiley & Sons, New York, NY, 1982, pp. 6-11.
26. Joos, P.; Bleys, G. *Colloid Polym. Sci.* **1983**, *261*, 1038.
27. Ward, A.F.H.; Tordai, L. *J. Chem. Phys.* **1946**, *14*, 453.
28. Breen, P.J. unpublished observations.

RECEIVED May 3, 1995

Chapter 19

Kinetic Study of the Adsorption of Nonionic and Anionic Surfactants and Hydrophobically Modified Water-Soluble Polymers to Oil–Water Interfaces

Christopher J. Rulison[1] and Robert Y. Lochhead

[1]Department of Polymer Science, University of Southern Mississippi, SS Box 10076, Hattiesburg, MS 39406

The use of polymers as primary stabilizers for oil-in-water emulsions has been widely studied.[1,2,3,4,5,6] One mechanism by which a polymer may act to stabilize an emulsion against coalescence is steric stabilization. The term steric stabilization refers to inter-droplet repulsive forces that are caused by osmotic and entropic effects as a consequence of polymer molecules adsorbed at the interface between the droplets and the continuous phase.[7] Figure 1 is a schematic representation of the repulsive forces of steric stabilization. When droplets containing adsorbed polymer diffuse to close proximity due to Brownian motion and the continuous phase is dilute in the polymer adsorbed, an unfavorable chemical potential to mixing of the adsorbed chains can be developed in the region between the droplets due to an increase in polymer concentration. The result is that disperse phase coalescence does not occur.

There are several factors to consider in the design of effective polymeric steric stabilizers. For oil-in-water emulsion systems, hydrophilic polymers which have low levels of hydrophobic modification are typically employed. The hydrophobic portions of such polymers serve as anchors for adsorption of the polymer to the disperse oil phase, while the hydrophilic portions extend from the surface to provide the effects of steric stabilization. The primary factors to consider in specifying the polymer structure further are as follows: (1) The polymer must be interfacially active. In other words, it must be thermodynamically driven to the oil/water interface. (2) The polymer must firmly anchor to the interface, so that polymer desorption is not a thermodynamic alternative as droplets approach one another. (3) The conformation of the polymer at the interface and the breadth of its extension into the continuous phase must be substantial enough to cause osmotic and entropic effects, as described above, which more than compensate for van der Waals attractive forces between the droplets. (4) During the actual process of emulsion formation, the kinetics of adsorption of the polymer to developing oil/water interfaces must be favorable relative to the kinetics of unstabilized droplet coalescence.

---

[1]Current address: Kruss U.S.A., 9305–B Monroe Road, Charlotte, NC 28270–1488

0097–6156/95/0615–0280$15.50/0

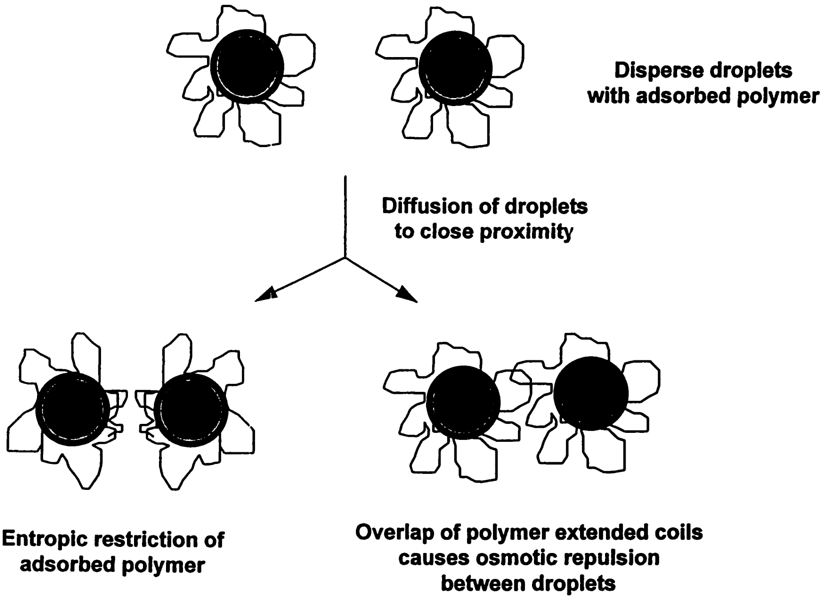
Disperse droplets with adsorbed polymer
Diffusion of droplets to close proximity
Entropic restriction of adsorbed polymer
Overlap of polymer extended coils causes osmotic repulsion between droplets

Figure 1. Mechanisms of Steric Stabilization

Each of these factors are important, but all of them must be simultaneously satisfied for steric stabilization to be achieved. For example, characterization of the equilibrium interfacial tensions for aqueous solutions of select hydrophobically-modified poly(acrylic acids) and hydrophobically-modified hydroxyethylcelluloses has shown that the latter are more interfacially active than the former.[8] However, no steric stabilization ability was observed for the hydroxyethylcelluloses whereas the poly(acrylic acids) were found to be highly effective steric stabilizers, based on emulsion phase diagram work. Obviously, there is a need to investigate the other relevant factors if predictive structure/property relationships are to be elucidated which can be used to guide the synthesis of novel polymeric emulsion stabilizers.

The focus of the research presented here is the development of methods to quantitatively study the kinetics of adsorption of polymers to liquid/liquid interfaces, factor (4) above. The necessity to study these kinetics stems from the fact that high molecular weight polymers are typically of interest for steric stabilization purposes. The necessity of a large extension from the oil/water interface by the hydrophilic portion of a sterically stabilizing polymer effectively dictates this. At the same time polymers with large hydrodynamic volumes diffuse relatively slowly through solution compared with, for example, interfacially active small molecule surfactants. The former have typical Brownian diffusion coefficients on the order of 10^{-12} to 10^{-13} m^2/s. The latter have Brownian diffusion coefficients in the range 10^{-9} to 10^{-10} m^2/s. It is, therefore, conceivable that a polymer could (a) have a high interfacial activity, (b) be capable of firm adsorption to an oil/water interface, (c) have an extension from the surface which is conducive to steric stabilization, and (d) still be ineffective as a steric stabilizer simply because the kinetics of its adsorption to oil/water interfaces does not compete favorably with the natural coalescence of droplets during the emulsion formation process.

Early theory on the coalescence of unstabilized disperse droplets, simply due to random droplet collisions owing to Brownian motion, is due to Smoluchowski[9]. From Smoluchowski theory it can be calculated that the half-life for coalescence of an unstabilized emulsion containing 10^{22} droplets per liter of continuous phase is on the order of 10^{-9} seconds. 10^{22} drops/liter is a reasonable number of droplets for a commercial emulsion system[10] and the theoretical work of Smoluchowski has been verified to represent experimental findings within a factor of approximately two by Lips[11], Honig[12], and Lichtenbelt[13]. This further justifies the need to explore the kinetics of the process of polymer adsorption to liquid/liquid interfaces for purposes of further understanding steric stabilization.

Here, we describe the use of drop volume techniques[14,15,16,17], and a method of combining dynamic interfacial tension data obtained from such experimentation with existing Fick's law based theory, to determine "adsorption/diffusion" coefficients for interfacially polymers and surfactants diffusing to liquid/liquid interfaces. This, combined with independent determinations of the Brownian diffusion coefficients for these materials in aqueous solution, provides a means of elucidating the kinetics of diffusion and adsorption of interfacially materials to liquid/liquid interfaces.

Materials

Interfacially Active Materials

The diffusion and adsorption of ten interfacially active solutes from aqueous solution to oil/water interfaces has been studied. The nonionic small molecule surfactant $C_{12}H_{25}(OCH_2CH_2)_4OH$ and the anionic small molecule surfactant $C_{12}H_{25}OSO_3^-Na^+$ have been studied as controls for the polymer work. The $C_{12}H_{25}(OCH_2CH_2)_4OH$ used for this study was obtained in 95% purity from ICI Specialty Chemicals (who sells it commercially under the trade name BRIJ®30) and used without purification. It shall, for the remainder of this text, be referred to as $C_{12}E_4$. The recognized impurity in BRIJ®30 is mainly the $C_{14}E_4$ analogue, and the distribution of ethyleneoxide head group size for the surfactant is reported to be narrow.[18] The critical micelle concentration of the $C_{12}E_4$ in aqueous solution was determined to be $1.9x10^{-3}$ g/L, by performing Wilhelmy plate based surface tension measurements using a Krüss model K-12 tensiometer. The water used in preparation of the $C_{12}E_4$ solutions for the surface tension work was doubly distilled from potassium permanganate (Aldrich #22,346-8, 99% pure) solution and had a surface tension in the absence of added solute of 71.7±0.3mN/m at 25°C. The generally accepted value for the surface tension of pure water at 25°C under ideal conditions is 71.97mN/m.[19] Water prepared in this manner was used throughout this study as a solvent. It will be henceforth referred to as DDW. The $C_{12}H_{25}OSO_3^-Na^+$ (sodium dodecylsulfate) used in this research was obtained in 98% purity from Aldrich Chemical (#86,201-0) and used without purification. It will be referred to as SDS throughout the remainder of this paper. Surface tension experimentation, analogous to that reported above for $C_{12}E_4$, showed that the critical micelle concentration for the SDS in aqueous solution at 25°C is 2.4 g/L. All of the diffusion and adsorption work reported in this text was performed at concentrations below the critical micelle concentration for each of the surfactants, so that what is being studied is the diffusion and adsorption of discrete non-aggregated molecules to the oil/water interface. The Brownian diffusion coefficients for $C_{12}E_4$ and SDS have been reported[20] under these conditions. The values are given in Table 1 along with the critical micelle concentrations (cmc values) for the surfactants.

A hydrophobically-modified hydroxyethylcellulose (HMHEC) and a control unmodified hydroxyethylcellulose (HEC) were also studied. Both were obtained from Aqualon Inc., and their trade names are Natrosol® Plus Modified Hydroxyethylcellulose and Natrosol® Hydroxyethylcellulose, respectively. HMHEC is reported to contain cetyl hydrophobes, at an average level of incorporation of one hydrophobe for every 30 anhydroglucose units along the backbone.[21] The molecular weights of both HEC and HMHEC have been determined based on solution viscometry in DDW to be approximately $4.0x10^5$g/mole.[8] The critical overlap concentrations (c*'s) of these polymers in DDW have been determined to be 1.6g/L and 1.9g/L, respectively, through the use of viscometric techniques and the formation of Huggins plots as described elsewhere.[8] Dynamic light scattering was performed on the polymers in DDW at concentrations equal to c*/10 to determine the average hydrodynamic diameter of the polymer coils and the Brownian diffusion coefficients for the polymers under dilute conditions. A Brookhaven instrument at a scattering angle of 90° was employed. All measurements were made at 25°C. The distributions in hydrodynamic diameter were found to be Gaussian. Sample preparation included pre-filtration of DDW through a 0.02μm inorganic membrane filter (Whatman, Anotop 10), dilution of the polymer studied in such water, and filtration of the polymer solution through a 1.2μm membrane filter (Gelman, low protein binding Acrodisc® brand). The Brookhaven light scattering sample cells used were washed with aqua regia and rinsed with copious amounts of filtered DDW prior to use. The hydrodynamic diameters and Brownian diffusion coefficients which were determined are reported in Table 1.

Six poly(acrylic acid) based polymers were used in this work. Two are commercially available from the BF Goodrich Company and have trade names of Pemulen™ TR-2 Emulsifier and Carbopol® 980 Resin. These polymers are referred to as HMPAA (hydrophobically-modified poly(acrylic acid)) and PAA (unmodified poly(acrylic acid)), respectively, throughout this discussion. Both are reported to be lightly covalently crosslinked and have an average molecular weight of 5×10^6 g/mole.[22] HMPAA is hydrophobically modified by the incorporation of approximately 1 mole% of long chain C_{10}-C_{30} acrylates.[23]

The remaining four modified poly(acrylic acids) studied are model copolymers which were synthesized and characterized with respect to their precise incorporation of hydrophobic modification and crosslinking. They are copolymers of pyreneacrylamide (PYA) and acrylic acid (AA). Details of synthesis and general characterization of these copolymers has been reported elsewhere[24,25]. The PYA units serve as the hydrophobic modification in these copolymers. It has been proven that the PYA units are incorporated in a random fashion into the four copolymers discussed here.[24] Table 1 provides relevant characterization information on the PYA/AA copolymers. The nomenclature used to describe each is based on the relative molar incorporations of PYA and AA in the copolymers. For example, copolymer PYA/AA 1/340 contains 1 monomeric unit of PYA for every 340 monomeric units of AA. Two of the copolymers (PYA/X/AA 1/0.9/230 and PYA/X/AA 1/0.6/150) are lightly crosslinked with 1,6 hexanediol diacrylate (X). The crosslinked copolymers contain one monomeric unit of X per 250 monomeric units of AA. The nomenclature used for the crosslinked copolymers, however, is analogous to that used for the non-crosslinked copolymers, so that the molar ratio of X reported in the nomenclature is based on unit PYA monomer incorporation. For example, PYA/X/AA 1/0.9/230 is a copolymer which has 1 monomeric unit of PYA for every 0.9 monomeric units of X and 230 monomeric units of AA.

Table 1 shows the approximate molecular weight for each PYA/AA copolymer. These values were determined by viscometry techniques as reported elsewhere.[8,25]

The c* values for these copolymers, as well as those for HMPAA and PAA, in pH=5.5 NaOH-neutralized DDW are also reported in Table 1. These values have been determined by viscometry experimentation and the formation of Huggins plots. This technique has been described previously.[8]

All of the work discussed in this text for the modified poly(acrylic acid) based polymers was performed on aqueous solutions of the polymers in DDW

Table 1 - Solute Characteristics

Solute	Molecular Weight (g/mole)	cmc or c* (g/L)	Average Hydrodynamic Diameter (Å)	D (m^2/s)
$C_{12}E_4$	362	1.9×10^{-3}	---	8.6×10^{-10}
SDS	288	2.4	---	1.5×10^{-9}
HMHEC	4.0×10^5	1.9	690	7.0×10^{-12}
HEC	4.0×10^5	1.6	723	6.7×10^{-12}
HMPAA	5.0×10^6	0.37*	3635**	1.3×10^{-12}**
PAA	5.0×10^6	0.55*	3124**	1.6×10^{-12}**
PYA/AA 1/340	1.0×10^6	0.89*	1603**	3.0×10^{-12}**
PYA/AA 1/150	1.2×10^6	0.58*	2405**	2.0×10^{-12}**
PYA/X/AA 1/0.9/230	1.2×10^6	0.67*	2009**	2.4×10^{-12}**
PYA/X/AA 1/0.6/150	1.1×10^6	0.85*	1842**	2.6×10^{-12}**

* In NaOH neutralized aqueous solution (pH = 5.5)

** In NaOH neutralized aqueous solution (pH = 5.5) and at concentration = c*/10 neutralized to pH=5.5 with NaOH (Fisher, Scientific grade pellets). Dynamic light scattering studies were performed on the poly(acrylic acids) in DDW at pH=5.5 and at concentrations of c*/10. The procedure for these studies was analogous to that reported above for the hydroxyethylcelluloses. For each of the poly(acrylic acids) the distribution of hydrodynamic diameters was found to be Gaussian. The average hydrodynamic diameter and the Brownian diffusion coefficient for each poly(acrylic acid) are also reported in Table 1.

Other Materials

The cyclohexane used was Fisher, Certified A.C.S. Scientific grade. This cyclohexane was determined to have a density of ρ=0.77392g/cm^3 using a Paar DMA 58 density meter and an interfacial tension against DDW of 51.7±0.1mN/m using a Krüss model K-12 tensiometer and the duNouy ring method.[26] The white mineral oil used for this work was obtained from the Shell Development Company. It was determined to have a density of ρ=0.86582g/cm^3 and an interfacial tension against DDW of 49.4±0.1mN/m by the same techniques.

Theory and Experimental Techniques

Equilibrium Interfacial Tension Measurements

The interfacial activity of the polymers and surfactants toward oil/water interfaces was evaluated as a function of concentration by equilibrium interfacial tension measurements. In the case of the poly(acrylic acids) all reported measurements are for the aqueous polymer solutions neutralized with NaOH to pH=5.5 against cyclohexane. In the case of the hydroxyethylcelluloses and the small molecule surfactants studied no NaOH was added to the aqueous solutions. Equilibrium interfacial tensions were evaluated using a Krüss model K-12 tensiometer which determines interfacial tension by the duNouy ring method.[26] The process involves filling a sample holder with a known quantity of DDW (neutralized to pH=5.5 for the poly(acrylic acid) based polymer work), covering the DDW with a layer of oil, and then dosing specific quantities of an aqueous polymer solution (neutralized to pH=5.5 for the poly(acrylic acids)) into the aqueous layer while measuring the interfacial tension between the two layers. After each dose of polymer solution the polymer took time to disperse throughout the aqueous layer, as well as to reach equilibrium adsorption at the oil/water interface. For these studies, the equilibrium interfacial tension was defined at the point in time, after a dose, when five consecutive measurements of interfacial tension, each taking approximately 90 seconds, fell within a standard deviation of 0.01 mN/m. In other words, equilibrium was defined as a situation in which the interfacial tension did not change more than 0.01 mN/m for approximately 450 seconds. Using this criterion, it took anywhere from two to fifteen hours for a polymer to come to equilibrium at the interface once the aqueous phase concentration was altered by a dose of polymer solution. It was observed during this experimentation that, in general, equilibrium took longer to develop for the poly(acrylic acid) based polymers than for the hydroxyethylcelluloses. The reason for this has been elucidated by the dynamic interfacial tension work as is discussed below.

Tate's Law and Drop Volume Theory

In order to accurately study the diffusion of interfacially solutes from a homogenous aqueous solution to an oil/water interface, an apparatus was designed and built based on the Tate drop volume method of determining interfacial tension.[14,15,16,17] The general procedure for drop volume analysis of interfacial tension between two liquid phases is to form drops of the denser liquid at the end of a tube which is submerged in the less dense liquid. The forming droplets increase in size until they disconnect themselves from the end of the tube and become droplets in the less dense continuous phase. Tate's law[27], derived from a balance of forces acting on a forming droplet, states that the volume (V) of each droplet, when it disconnects, is given by:

$$V \cdot \frac{2\pi r \gamma}{\Delta\rho\, g}$$

where r = the radius of the tube, γ = the interfacial tension between the two phases, $\Delta\rho$ = the difference in density between the two liquids, and g = the force of gravity.

In practice, Tate's equation typically needs to be modified by a factor of "f" to account for three fundamental considerations of the detachment of the drop from the tip. On detachment, (a) even for the most well defined tips, the drop does not completely leave the tip, but rather necks somewhat near the tip and leaves a portion of the droplet behind, (b) the interfacial tension forces seldom act precisely vertically, and (c) there exists a pressure differential across the curved droplet surface.[28]

Tate's law thus becomes:

$$V \cdot \frac{2\pi r \gamma f}{\Delta\rho\, g}$$

Intuitively, one might expect the "f" factor to be a function of the tip design and the nature of the two liquids used in the experiment, particularly in terms of viscosity. However, the "f" factor has been well characterized by, Harkins and Brown[29] and also Lando and Oakley[30], to be only a function of $r/V^{1/3}$, and independent of the nature of the liquids studied, providing that neither liquid has a significant yield stress and the tip employed meets certain design criteria, which include it not being spontaneously wetted by the drop phase. This determination is based on calculation of the "f" factor from drop volume experiments between several sets of liquids for which the interfacial tension has been determined by an independent method. The majority of drop volume tensiometry studies reported in the literature [31,32,33,34] use these correction factors without experimental verification. Most commonly the correction factors of Harkins and Brown are used, since Harkins and Brown also showed that the same "f" factors apply to the liquid/air surface tensiometry.

While the drop volume technique certainly provides a means of determining the ***equilibrium*** interfacial tension between two pure liquids, or the surface tension of any pure liquid, it also provides the capability of determining *dynamic* interfacial tensions for systems in which one of the liquids contains a surface active solute. This is depicted schematically in figure 2, for the case in which the interfacially active solute is in the more dense of the two liquids. In this schematic the small squares represent molecules of the interfacially active solute (in the case of this research a hydrophobically-modified water soluble polymer or a small molecule surfactant in aqueous solution). The tip on which the drops are formed can be connected to a precision pump, so that drops can be formed at precise rates. When a droplet is formed rapidly, these will be little time for the interfacially active solute within it to diffuse to and adsorb at the liquid/liquid interface (in the case of this research either an aqueous/white mineral oil or an aqueous/cyclohexane interface). The result is that the drop will be relatively large on detachment, because the interfacial tension between the two phases will be high(γ_H) and near its value between the two pure liquids in the absence of the interfacially active solute. Conversely, if a drop is formed more slowly, the interfacially active material will have time to diffuse to and adsorb at the liquid/liquid interface. As a result, the interfacial tension will be lower (γ_L), as evidenced by smaller droplet size at detachment. In forming a drop over a infinite time frame, with respect to the rate of diffusion and adsorption of the solute to the interface, the interfacial tension realized will be the equilibrium interfacial tension between the solution and the liquid, and would be expected to match this value, in the case of our experiments, as determined by ring tensiometry.

Drop Volume Apparatus Design and Characterization

The drop volume apparatus used for this work is shown schematically by figure 3. It was designed so that the aqueous solution under study was dropped from a 0.230 cm diameter poly(tetrafluoroethylene) (PTFE) tip submerged in a test tube containing the oil phase. A detailed diagram of the tip is shown in the inset of figure 3. The drop flow rate of the aqueous solution was controlled very accurately by a Metrohm® 665 dosimat. The test tube is fitted with an infrared motion detector so that the time between drops can be detected to the accuracy of 0.01 sec, with the aid of a Televideo TS800A computer.

The time between drops is converted to drop volume with knowledge of the drop flow rate from the dosimat. This volume is then used in the modified Tate's law equation (Eq. 2), along with the known radius of the tip, the acceleration due to gravity (taken as 9.806 m/s^2) and the difference in density between the two liquid phases. (Densities of the aqueous polymer and surfactant solutions studied were also

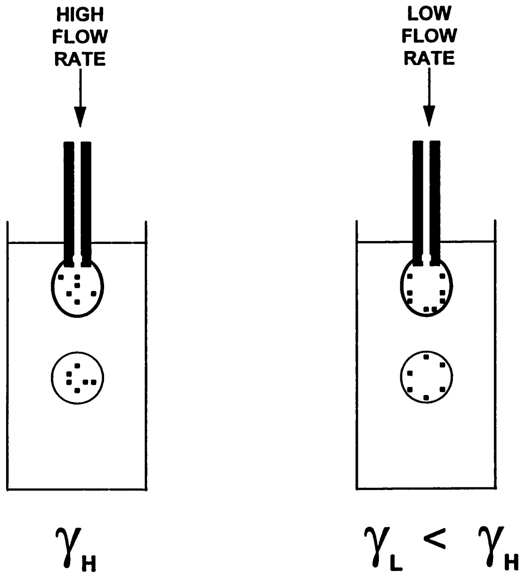
HIGH FLOW RATE
LOW FLOW RATE
γ_H
$\gamma_L < \gamma_H$

Figure 2. Schematic of Polymer Adsorption at the Droplet Interface at Fast & Slow Flow Rates

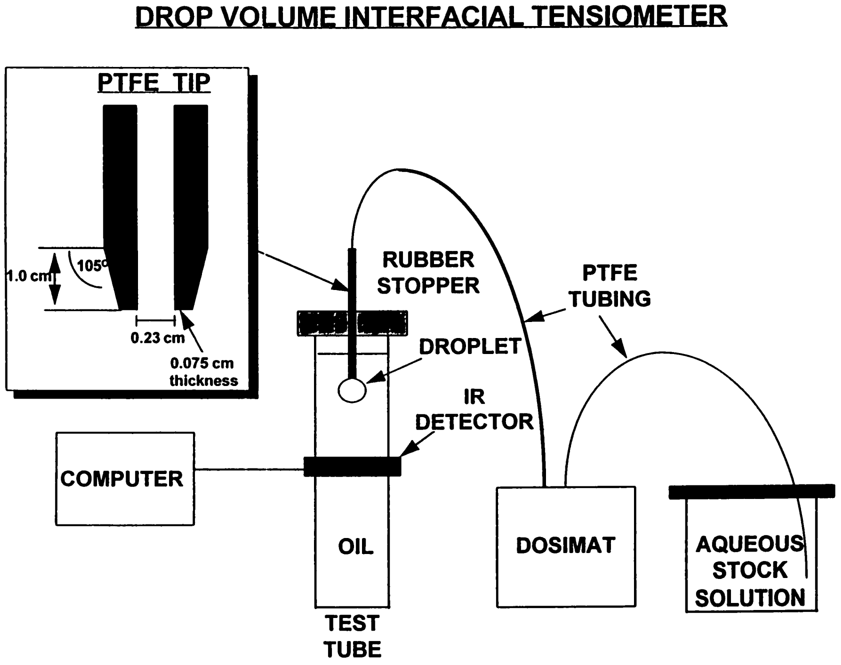
DROP VOLUME INTERFACIAL TENSIOMETER
PTFE TIP
1.0 cm
105°
0.23 cm
0.075 cm thickness
RUBBER STOPPER
PTFE TUBING
DROPLET
IR DETECTOR
COMPUTER
OIL
TEST TUBE
DOSIMAT
AQUEOUS STOCK SOLUTION

Figure 3. Schematic of the Dynamic Drop-Volume Apparatus

determined using a Paar DMA 58 density meter, which determines density accurate to 0.00001 g/cm^3.) With this information the interfacial tension, multiplied by the f factor, can be determined for any dilute polymer or surfactant solution against any oil at a variety of solution drop rates.

In order to deconvolute the f factor from this data, and thus achieve a dynamic interfacial tension value, an average of the "f" factors suggested by Harkins and Brown[29] and Lando and Oakley[30] was calculated from experimental values of $r/V^{1/3}$ and used. The validity of this is discussed below.

In the case of pure liquids it is possible to determine the "f" factor directly, because equilibrium interfacial tension will be equal to dynamic interfacial tension. Therefore, values of equilibrium interfacial tension determined by ring tensiometry can be used in the modified Tate's law equation. Experiments have been performed to directly determine the "f" factor for pure DDW drops formed on our tip in cyclohexane and in white mineral oil. The equilibrium interfacial tension values between cyclohexane and DDW, and white mineral oil and DDW, have been reported above. Note that for drop volume experiments on pure liquids neither the "f" factor nor the drop volume should be a function of drop rate, since interfacial tension is not a function of drop rate. This was indeed found to be the case for DDW droplets formed in cyclohexane and white mineral oil, in our apparatus, at the drop rates of interest throughout this research, which are in the range of 0.005ml/min to 2ml/min. The "f" factors determined were 0.750±0.003 for cyclohexane/DDW, and 0.858±0.004 for white mineral oil/DDW.

Shown in figure 4 is a graphical representation of the theoretical values for "f" based on the work of Harkins and Brown and Lando and Oakley. Superimposed on this plot are the values reported above, as a function of the $r/V^{1/3}$ values determined for the pure liquids by the same experiments. As can be seen from this figure, an independent determination of "f" factors for DDW dropping into cyclohexane and white mineral oil, yielded factors consistent with the values of previous workers. In the case of the cyclohexane work, an $r/V^{1/3}$ value of 0.228±0.001 was found over the range of flow rates studied. The Harkins and Brown (H&B) theory predicts an "f" value, based on this value of $r/V^{1/3}$, of 0.753, while the Lando and Oakley (L&O) theory predicts 0.749. The average of these is 0.751, which corresponds almost perfectly with our experimental value of 0.750±0.003. In the case of the white mineral oil work, an $r/V^{1/3}$, value of 0.190±0.001 is determined experimentally over the range of flow rates studied. As can be seen in figure 4, the H&B and L&O theories for prediction of the "f" factor based on the value of $r/V^{1/3}$ deviate from one another most substantially below a $r/V^{1/3}$ value of approximately 0.22. At $r/V^{1/3}=0.190$ the H&B theory predicts a value of "f" of 0.872, and the L&O theory predicts 0.850. The average of these values is 0.861 which is also very close to our experimental determination of 0.858±0.004.

It is believed that the above findings for pure liquids justify the use of "f" factors averaged from the H&B and L&O theories to deconvolute the drop volume data compiled in this research into dynamic interfacial tension values. Recall that H&B and L&O both report that the "f" factor is only a function of $r/V^{1/3}$ and not of the nature of the liquids studied, or their viscosity, so long as neither liquid has a yield stress. This limits the usefulness of the drop volume technique to the study of dilute solutions of interfacially active material, if the "f" factors of H&B and L&O are to be used. The dynamic interfacial tension work reported in the remainder of this text respects this limitation and focuses on interfacially active polymers below their c*'s, and small molecule surfactants below their critical micelle concentrations.

Dynamic Interfacial Tension Measurements

A rather rigorous procedure was used in collection of the dynamic interfacial tension data presented in this paper. Here the procedure is described briefly using the work on the non-ionic surfactant $C_{12}E_4$ as an example. Drop volume interfacial tension work was performed on aqueous solutions of $C_{12}E_4$ at five different drop rates. Three different concentrations were studied, which were prepared by dissolving the surfactant in DDW in a glass container which was pre-washed with copious amounts of concentrated aqueous HCl and/or aqua regia and pre-rinsed with copious quantities of DDW. This represents the general procedure for preparation of solutions to be studied by drop volume throughout this work, whether polymer or small molecule surfactant. It is important that contamination of the samples by interfacially active materials, in particular small molecule organics, is eliminated.

It is also necessary, prior to each experiment, to be sure that the apparatus is free of contamination. The PTFE tubes and tip, and the glass syringe, associated with the precision pump used to dose the interfacially-active solute-containing phase in these experiments, were, prior to each change of sample solution, washed thoroughly with 0.5 molar aqueous HCl and rinsed by pumping 500ml (at minimum) of DDW through the system. After each system cleaning, of this type, a drop volume experiment, consisting of a minimum of five drops, was performed at a flow rate of 0.005ml/min on pure DDW into the oil phase. In cases where this experiment did not yield the proper interfacial tension for the pure liquids, within the experimental errors reported above, the system was re-cleaned until this was the case. In cases, where the proper pure liquid interfacial tension was obtained, the system was deemed clean enough for use, and 50ml of the solution to be studied was pumped through the system prior to beginning the experiment. The test tube which holds the oil phase, in our apparatus, was washed by the same procedure reported above for the sample containers, and additionally rinsed twice (at minimum) with the oil to be studied prior to each experiment. The same experimental procedure was used for all the drop volume work reported in this text.

The results of the $C_{12}E_4$ work are presented in figure 5 as a function of drop rate, in comparison with the values of equilibrium interfacial tension as a function of concentration, which were obtained by the duNouy method as described above. Each drop volume interfacial tension data point reported in this plot is an average calculated from fifteen experimental drops. The general procedure of obtaining this data, for each solute concentration studied, was to: (1) run five drops at each of the rates (in the case of the $C_{12}E_4$ studies, five drops at 0.05ml/min, then five at 0.01ml/min etc.) all consecutively, from the same solution, and without breaking down the apparatus for cleaning, (2) break down and completely clean the apparatus

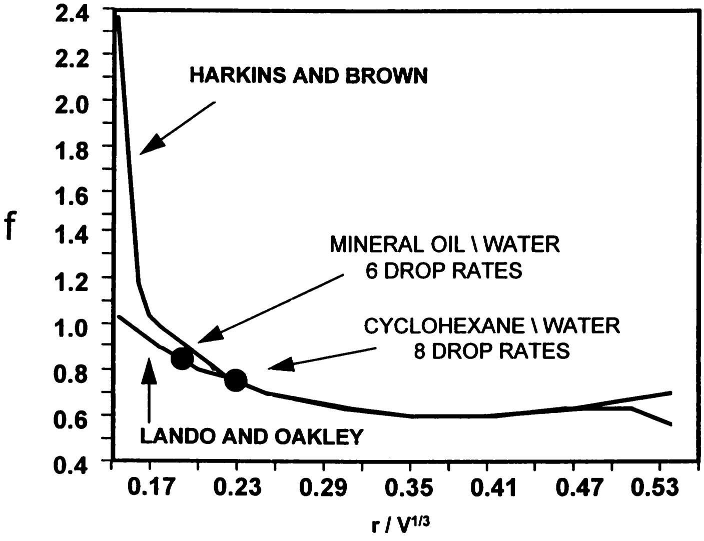

Figure 4. The 'f' Correction Factor According to Harkins & Brown and Lando & Oakley

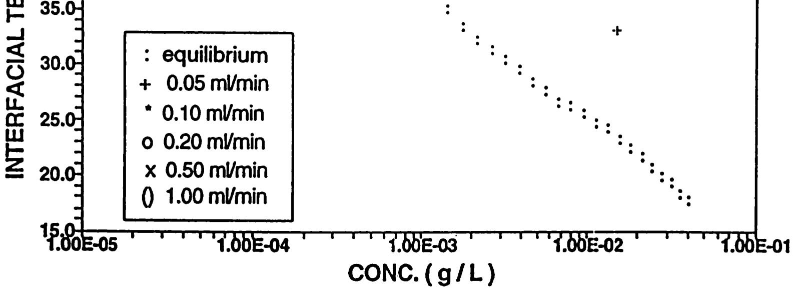

Figure 5. Dynamic Interfacial Pressure for Aqueous C12E4 Solution/Cyclohexane

to specifications discussed above and prepare a new sample solution, also using procedures discussed above, (3) repeat steps 1 and 2 twice more, so that a total of fifteen drops, at each rate and concentration, are obtained, (4) calculate an interfacial tension based on each drop, (5) average the fifteen values of interfacial tension to produce one point on a plot such as figure 5. This was the procedure used throughout this research for the small molecule surfactants, as well as the polymers studied. In all cases the standard deviation of the fifteen interfacial tensions obtained did not exceed 1mN/m. However, the standard deviation with a polymer, as the interfacially active solute, was often in the range 0.5 to 0.9mN/m, whereas it did it not exceed 0.6mN/m at any point for the surfactants studied. Thus, error bars do not appear in figure 5 or similar figures throughout this text. The error bars are, therefore, smaller than the symbols shown in the figures.

Results and Discussion

Surfactants

It can be seen from figure 5 that at a concentration of $9\text{x}10^{-4}$ g/L, none of the drop formation rates studied is low enough to give $C_{12}E_4$ sufficient time to adsorb substantially to the cyclohexane/water interface. This is evidenced by the fact that even at the slowest rate (0.05ml/min) the dynamic interfacial tension was still about 48mN/m, compared with 51.7mN/m for the pure cyclohexane/water interface, and an equilibrium interfacial tension value, at this concentration, of 38.5mN/m. As the bulk concentration was increased to $2\text{x}10^{-3}$ g/L and $1.5\text{x}10^{-2}$ g/L, the dynamic interfacial tension at each rate decreased, as expected. Further, in all cases the dynamic interfacial tension was found to increase with increasing drop rate, at any given concentration. This is expected, since forming drops more quickly gives the surfactant less time to diffuse to and adsorb at the cyclohexane/water interface prior to droplet detachment. It is evident that in order to observe an interfacial tension approaching the equilibrium interfacial tension, at any of the concentrations studied for $C_{12}E_4$, much lower rates of droplet formation would need to be explored.

Van Voorst Vader and coworkers[35] have proposed that equation 3, a modification of Fick's second law of diffusion, applies to the case of an interfacially active solute diffusing from one bulk phase to a spherically growing interface, based on prior theoretical work by Ward and Tordai[36], which applied to the same situation, but with an interface that expands as a plane.

$$\frac{\partial C}{\partial t} - \theta z \frac{\partial C}{\partial z} . D \frac{\partial^2 C}{\partial z^2} \qquad \text{(EQ.3)}$$

In equation 3, C = bulk solute concentration, t = time over which the interface expands, z = a coordinate normal to the growing interface, θ = dilation (1/A dA/dt, where A = droplet surface area), and D = the diffusion constant for the interfacially active material. This equation applies directly to drop volume experimentation, in so far as the drops grow spherically, which has been shown by Lando and Oakley[30], to be a good assumption. However, Van Voorst Vader never strictly solved the equation for the spherical system.

The solution, only possible under three very important assumptions, is due to Joos and Rillaerts[32] and is shown below.

$$\Pi \;.\; 2\,R\,T\,C_o\left(\frac{3\,D_A\,t}{7\,\pi}\right)^{1/2} \qquad \text{(EQ.4)}$$

In equation 4, Π = interfacial pressure = $\gamma_o - \gamma$ (where γ_o is the interfacial tension between the two pure phases considered, and γ is the interfacial tension after adsorption of solute molecules to the interface), C_o = bulk solute concentration in the phase that contains the solute, t = interface formation time (the time from the start of droplet growth to the point of droplet detachment, in a drop volume experiment), D = the diffusion constant of the solute through the bulk phase in which it is contained initially, and R is the gas constant and T, the absolute temperature.

Based on equation 4, if dynamic interfacial tension data such as that shown in figure 5 for $C_{12}E_4$ adsorbing to the cyclohexane/water interface, is plotted in the form of interfacial pressure (Π) as a function of (bulk concentration (C_o) x the square root of drop time ($t^{1/2}$)) it would be expected to yield a straight line with a slope = 2RT ($3D/7\pi$). A value for D can be calculated from the slope. D is the diffusion coefficient of the solute through the phase in which it is initially dispersed. This is, however, not strictly true, due to the assumptions used in the derivation of equation 4.

The first, and least important assumption, which has been proven experimentally by McBain and Swain[37], is that interfacial or surface pressure decreases logarithmically with the excess concentration of the solute at the interface relative to the bulk. This is known as the Gibbs adsorption isotherm.[38] The second, more important assumption is that the "sub-interface concentration is zero for all time".[32] This is equivalent to assuming that once an interfacially active solute molecule adsorbs at the interface it "disappears", or more precisely that the interface is, throughout the experiment, free of barriers to solute adsorption based on possible adsorption sites being pre-filled by the solute molecules that adsorbed at a earlier time. This assumption will be valid only in the initial stages of adsorption (low interfacial pressures), until enough solute is absorbed to the interface that such a barrier to adsorption begins to develop. The third, and most important assumption in terms of this work, is that adsorption is purely diffusion controlled. In other words, the effectiveness of approaches of the solute to the interface in leading to adsorption is 100%. There is no activation energy associated with the adsorption process.

Under these assumptions, dynamic interfacial tension data can still be evaluated quantitatively using equation 4, and plots of Π versus ($C_o * t^{1/2}$). However, two results may be expected. One, the entire plot will not be linear, since at high values of interfacial pressure there must exist barriers to continued solute interfacial adsorption, due to the presence of already adsorbed solute at the interface. In this case, further adsorption is only possible based on surface rearrangement of the already adsorbed solute. Thus, it might be expected that an ionic repulsion between an adsorbed polyion and an adsorbing polyion, would present a barrier to adsorption of the latter. Two, if the plot is found to be linear at low Π values, the diffusion coefficient calculated from the slope in this region may not equal the Brownian diffusion coefficient of the solute molecule in solution. Rather, the diffusion coefficient obtained may be lower than the Brownian diffusion coefficient owing to the fact that there may exist an activation energy barrier to adsorption, which is not accounted for in the derivation of equation 4. For example, consider a hypothetical solute molecule having a Brownian diffusion coefficient of 2 hypothetical units. Assume an activation energy barrier to this solute's adsorption exists. The barrier is of a magnitude such that the efficiency of approaches of the solute to the interface in leading to adsorption is 50%. Under these conditions the diffusion coefficient for the solute, as calculated by drop volume experimentation and the theory described above, will be 1 hypothetical unit. To distinguish diffusion coefficients calculated from interfacial tension studies from Brownian diffusion coefficients determined by dynamic light scattering, throughout the remainder of this text, the former will be referred to as "adsorption diffusion coefficients" and signified by "D_A", and the latter will be signified by their common symbol of "D".

Figure 6 shows dynamic interfacial pressure data for $C_{12}E_4$ plotted in the form which allows for the determination of D_A for $C_{12}E_4$ diffusion to and adsorption at the cyclohexane/water interface. Figure 6 is based on the drop volume data presented in figure 5. The first twelve data points on this diagram fit a straight line (line coefficient (r) = 0.997). The slope of this line (in units of J*m / mol*s$^{1/2}$) is shown on the figure, along with the calculated adsorption diffusion coefficient (8.9×10^{-10} m^2/s) for $C_{12}E_4$ diffusing to and adsorbing at a cyclohexane/water interface. As expected, at higher Π values equation 4 is not longer valid (the slope of the plot changes). The slope at high values of Π may well have some significance in terms of rearrangement controlling adsorption of the surfactant to the interface. However, this significance is not unequivocal, and it should be realized that, at higher values of Π, this plot must reach an asymptote as the interface becomes saturated with solute to the point that the chemical potential drive for adsorption is eliminated. This research places no significance on the slope of the "line" at high values of Π and in the case of figure 6, as well as other plots of this type, which appear herein, the line is drawn tentatively only to show that the slope has changed from its value at lower values of Π.

The experimental value for the Brownian diffusion of discrete $C_{12}E_4$ molecules in aqueous solution was reported above to be 8.6×10^{-10} m^2/s.[20] Estimation of the error associated with the adsorption diffusion coefficient reported above is complicated mathematically by the process of determining the value, but is believed

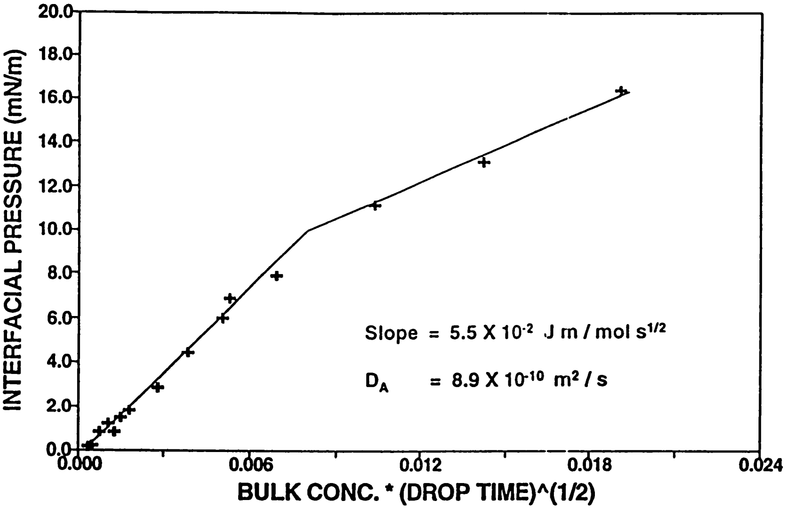

Figure 6. Dynamic Interfacial Pressure for Aqueous C12E4 Solution/Cyclohexane

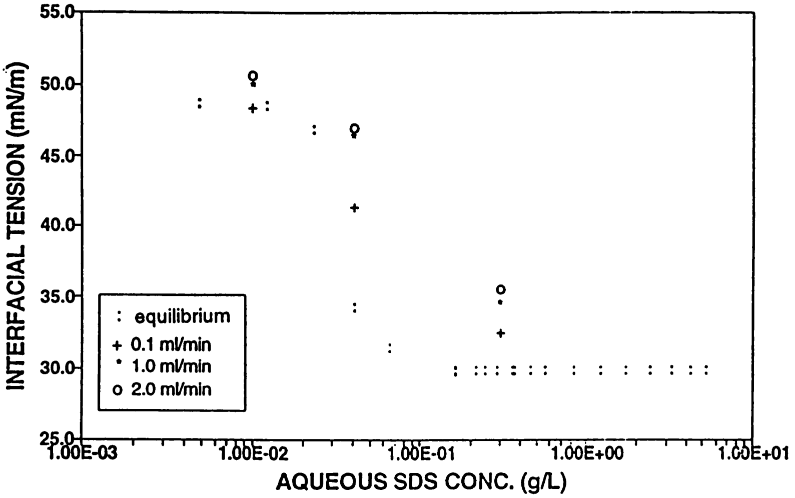

Figure 7. Dynamic Interfacial Tension for Aqueous SDS Solution/Cyclohexane

to be $1x10^{-11}$ m^2/s. The error associated with the Brownian value is unreported. A ratio of these diffusion coefficients is $D/D_A = 0.97$ (or based on experimental errors ≈ 1), which indicates that the adsorption of $C_{12}E_4$ to cyclohexane/water interfaces is free of energy barriers and completely diffusion controlled.

The reason for studying a nonionic surfactant, as part of this research, is that diffusion controlled adsorption is exactly what was expected in this case. Davies and Rideal[39], Bendure[31] and Van Voorst Vader and coworkers[35] have each shown that nonionic surfactant adsorption to the air/water interface is controlled by diffusion alone. Davies and Rideal studied the adsorption of various alkylethylene glycol monoethers to the air/water interface by the maximum bubble pressure method. Bendure studied alkylphosphine oxides by the same technique. Van Voorst Vader used a modified Langmuir trough, in conjunction with the modified Fick's second law theory of Ward and Tordai[36], pertaining to planar interfaces, to calculate adsorption diffusion coefficients, for $C_{12}E_5$ and 1,2 dodecanediol.

Ward and Tordai[36] have reported that the surface adsorption of ionic surfactants is not purely diffusion controlled. They reported that the diffusion coefficient of the sodium salt of nonanoic acid, determined through studies of its diffusion to the air/water interface by the maximum bubble pressure method, was "at minimum a order of magnitude smaller than expected". Figures 7 and 8 show the results of drop volume dynamic interfacial tension work which has been performed on aqueous SDS solutions against cyclohexane. These results indicate that the D_A for SDS diffusing to and adsorbing at the cyclohexane/water interface is $3.4x10^{-11}$ m^2/s. Based on the Brownian diffusion coefficient for SDS in aqueous solution ($D=1.5x10^{-9}$ m^2/s) the D/D_A ratio for SDS in this situation equals 44. The adsorption of SDS to the cyclohexane/water is a factor of 44 times slower than diffusion controlled. These findings for SDS are not surprising based on the work of Ward and Tordai. An electrostatic barrier is presumably developed by the initial adsorption of an ionic surfactant to an interface, so that further adsorption of the surfactant is not purely diffusion controlled. Further adsorption is inhibited kinetically by electrostatic repulsion between the ionic head groups of the pre-adsorbed surfactant and the head groups of the surfactant molecules that are diffusing to the proximity of the interface at later times. The adsorption to oil/water interfaces of the polyelectrolytic poly(acrylic acid) based polymers studied in this research seems to be governed by the same types of considerations when compared to the adsorption behavior of the hydroxyethylcelluloses.

Hydroxyethylcelluloses

Figure 9 shows drop volume dynamic interfacial tension data for HMHEC solutions of variable concentration against cyclohexane. Concentrations studied were 0.1g/L and below, which is a factor of nineteen below the determined c* of HMHEC in aqueous solution, so that HMHEC can be assumed to diffuse to the cyclohexane/water interface as discrete (non-aggregated) molecules. As would be expected, the dynamic interfacial tensions at each HMHEC concentration decreased as the rate of droplet formation decreased. A typical drop size, throughout the polymer studies, is approximately 0.2ml, so that drops formed at a rate of

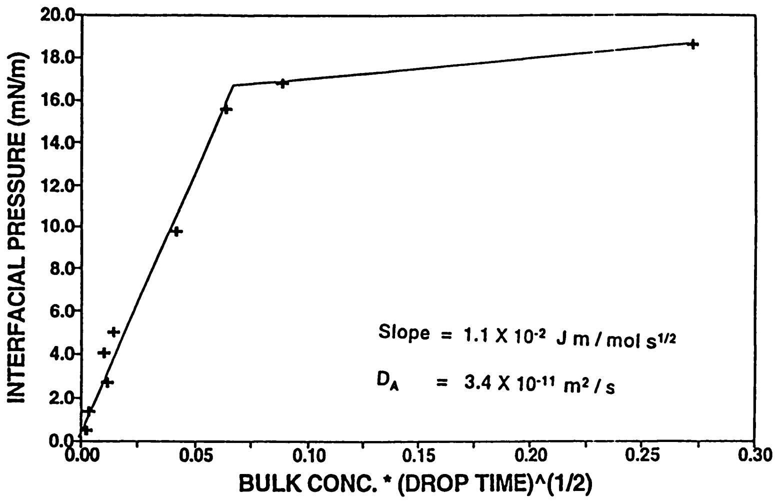

Figure 8. Dynamic Interfacial Pressure for Aqueous SDS Solution/Cyclohexane

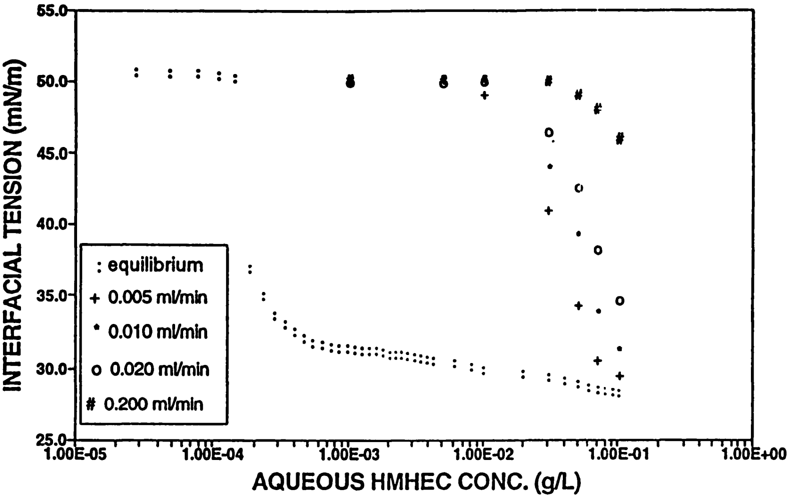

Figure 9. Dynamic Interfacial Tension for Aqueous HMHEC Solution/Cyclohexane

In Surfactant Adsorption and Surface Solubilization; Sharma, R.;
ACS Symposium Series; American Chemical Society: Washington, DC, 1996.

0.2ml/min allow approximately one minute for the polymer to diffuse to and adsorb at the cyclohexane/water interface before the drop detaches from the tip. The slowest rate studied (0.005ml/min) allows approximately forty minutes for the same phenomenon to occur. For example, focusing on the highest HMHEC concentration studied (0.1g/L) in the figure above, it can be seen that over an approximately one minute period of time for droplet formation (rate = 0.2ml/min) only enough polymer adsorbs to the cyclohexane/water interface to decrease the interfacial tension between the cyclohexane and the HMHEC solution to about 46mN/m. Forming droplets of 0.1g/L HMHEC solution in cyclohexane over an approximately 40 minute period (rate = 0.005ml/min) allows enough time for HMHEC to adsorb at the cyclohexane/water interface to the point where the dynamic interfacial tension decreases to approximately 30mN/m- nearly its equilibrium value, as determined by duNouy ring tensiometry of *circa* 29mN/m.

Figure 10 is a plot of this same data in the form of (bulk polymer concentration x (drop time)$^{1/2}$) versus dynamic interfacial pressure. Using Joos' solution[32] to Van Voorst Vader's modified Fick's law equation a value of $2.2x10^{-12}$ m^2/s can be calculated for the absorption diffusion coefficient (D_A) of HMHEC diffusing to the cyclohexane/water interface from the initial slope of figure 10. Figures 11 and 12 represent analogous data for HMHEC solutions against white mineral oil. The D_A calculated from this data is $2.3x10^{-12}$ m^2/s, which is in agreement with the value of D_A determined for HMHEC diffusing to the cyclohexane/water interface. This indicates that the diffusion and absorption efficiency of HMHEC to the oil/interface is relatively independent of whether the white mineral oil/water interface or the cyclohexane/water interface is studied.

Figures 13 and 14 represent drop volume dynamic interfacial tension data for HEC diffusing to the white mineral oil/water interface. The maximum aqueous phase HEC concentration studied was c*/16 (0.1g/L). This data indicates that the D_A for HEC diffusing and adsorbing to the cyclohexane/water interface is $9.3x10^{-13}$ m^2/s- a lower value than that observed for HMHEC. The actual diffusion coefficient, D, can be determined from dynamic light scattering, and compared with the value, D_A, formed from dynamic interfacial tension measurement. The structural difference between HEC and HMHEC is the hydrophobic modification of the latter, which causes the hydrophobic/hydrophilic interface adsorption efficiency of HMHEC to be greater than that of HEC. $D/D_A=7.2$ for the diffusion and adsorption of HEC to the white mineral oil/water interface. While D/D_A values of 3.0 and 3.2 are obtained for the diffusion and adsorption of HMHEC to the cyclohexane/water interface and the white mineral oil/water interface, respectively.

Poly(acrylic acids)

Figures 15-18 represent the dynamic interfacial tension results for HMPAA and PAA diffusing to the cyclohexane/water interface from NaOH-neutralized pH=5.5 aqueous solution. Under these conditions the poly(acrylic acids) are polyelectrolytes in aqueous solution. The HMPAA and PAA concentrations studies were below the respective c* values for each of the polymers under pH=5.5

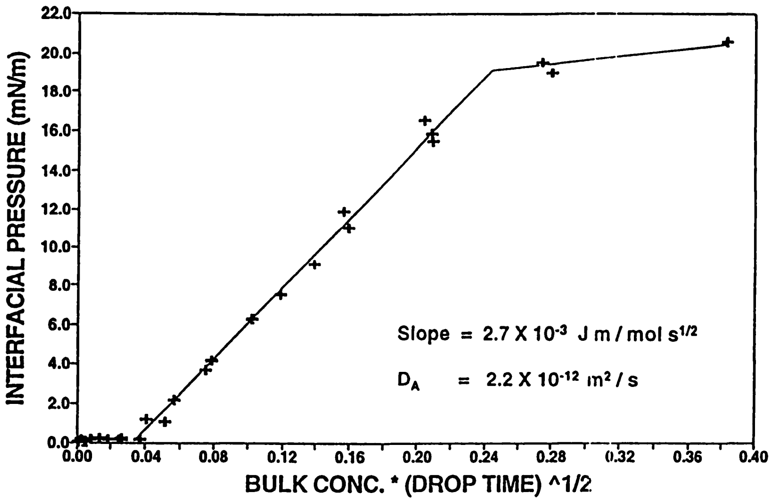

Figure 10. Dynamic Interfacial Pressure for Aqueous HMHEC Solution/Cyclohexane

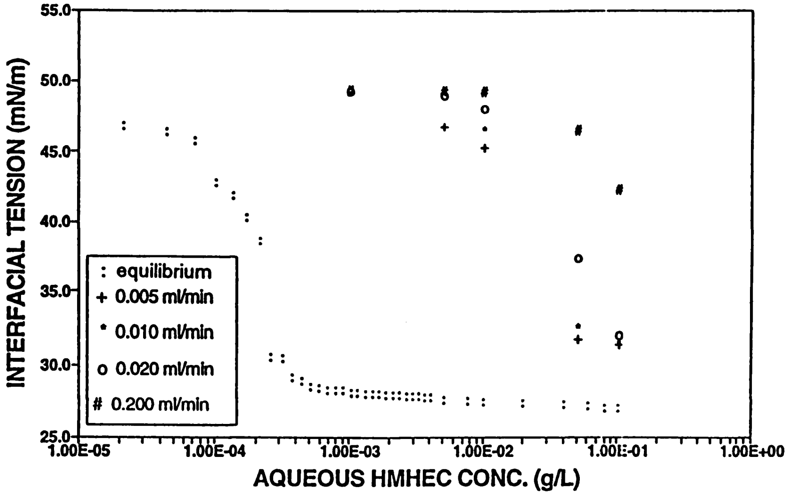

Figure 11. Dynamic Interfacial Tension for Aqueous HMHEC Solution/Mineral Oil

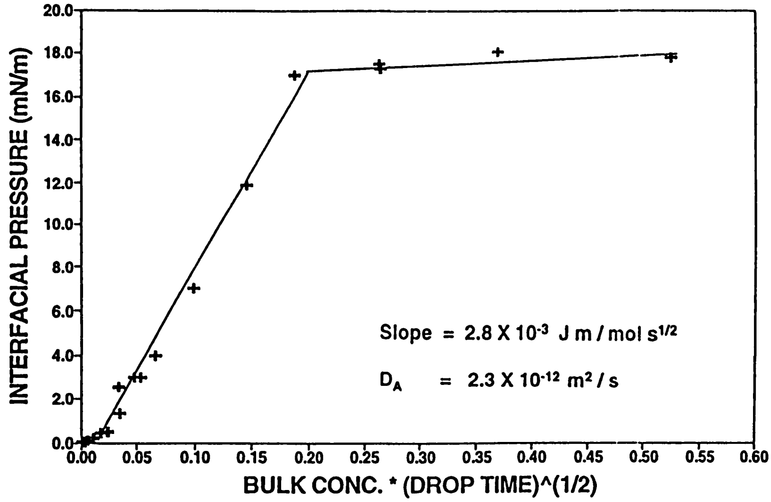

Figure 12. Dynamic Interfacial Pressure for Aqueous HMHEC Solution/Mineral Oil

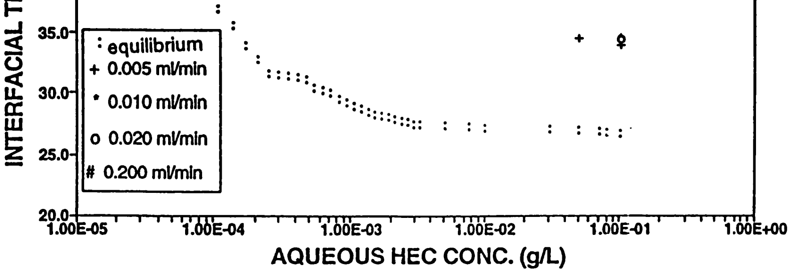

Figure 13. Dynamic Interfacial Tension for Aqueous HEC Solution/Mineral Oil

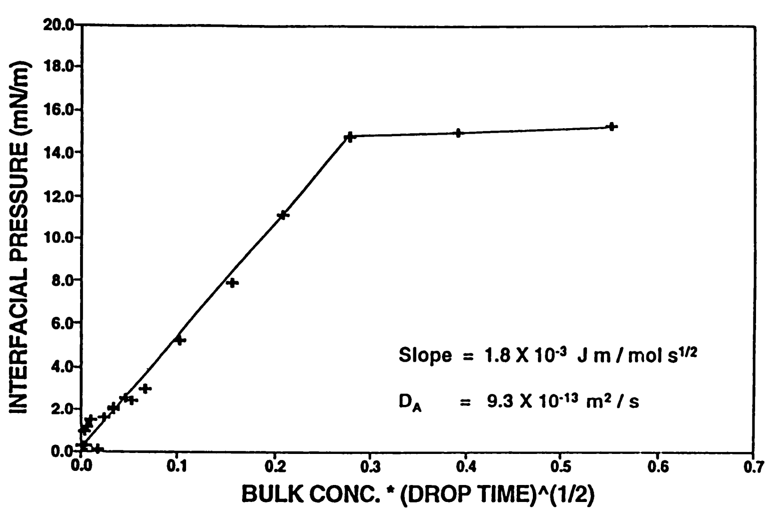

Figure 14. Dynamic Interfacial Pressure for Aqueous HEC Solution/Mineral Oil

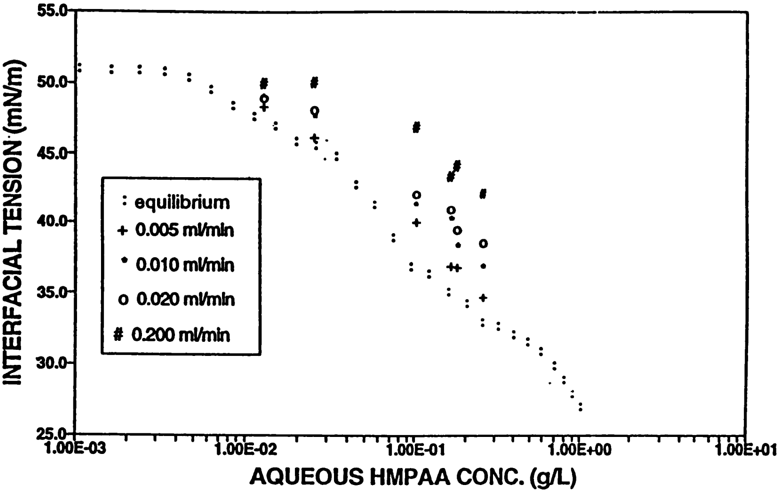

Figure 15. Dynamic Interfacial Tension for Aqueous HMPAA Solution/Cyclohexane

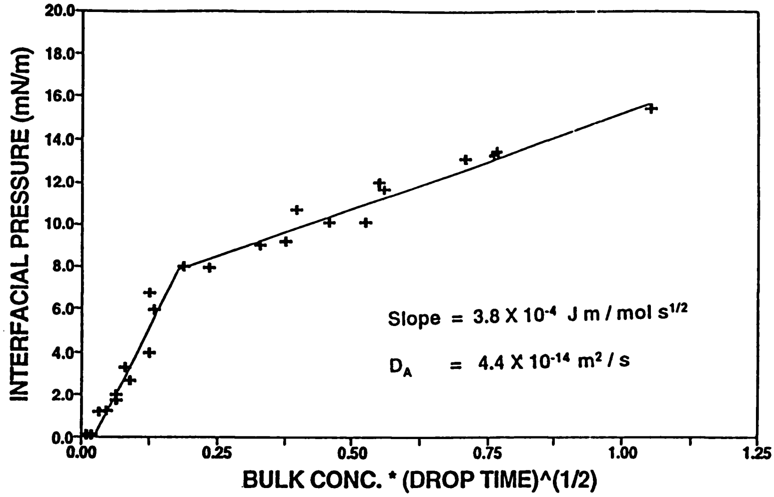

Figure 16. Dynamic Interfacial Pressure for Aqueous HMPAA Solution/Cyclohexane

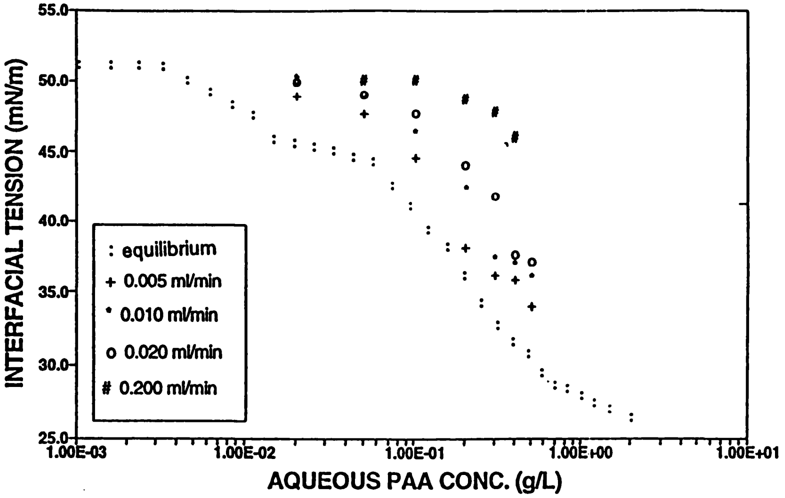

Figure 17. Dynamic Interfacial Tension for Aqueous PAA Solution/Cyclohexane

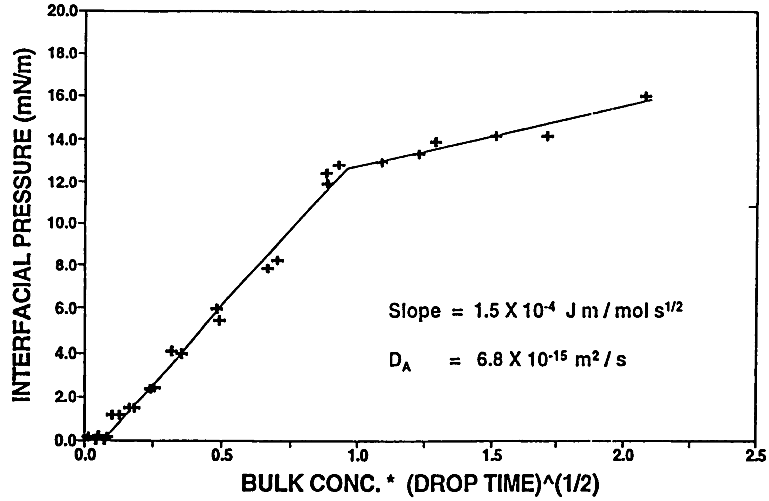

Figure 18. Dynamic Interfacial Pressure for Aqueous PAA Solution/Cyclohexane

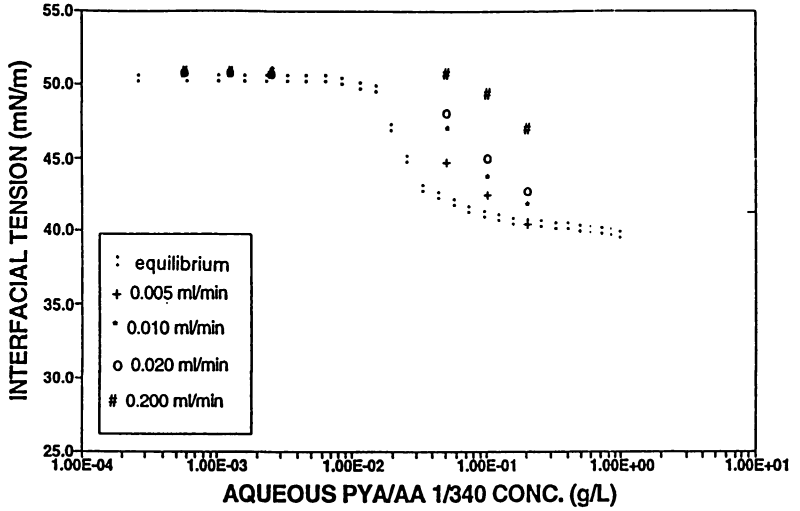

Figure 19. Dynamic Interfacial Tension for PYA/AA 1/340/Cyclohexane

conditions. A D/D_A ratio of 30 for HMPAA diffusing to and adsorbing at the cyclohexane/water interface can be calculated from this data and Brownian diffusion coefficient data presented in Table 1. This value is much larger than the values obtained for either HEC or HMHEC. This is believed to be due to the polyelectrolytic nature of HMPAA under these conditions and the subsequent development of an electrostatic barrier to adsorption. This is analogous to the D/D_A ratio being greater for SDS diffusion and adsorption to the cyclohexane/water interface relative to the D/D_A ratio for $C_{12}E_4$ diffusion and adsorption to the cyclohexane/water interface. For PAA a D/D_A ratio of 240 was obtained under these conditions. This decreased adsorption efficiency relative to HMPAA is believed to be due to the lack of hydrophobic modification in PAA. Hydrophobic modification would be expected to increase the efficiency of adsorption for interfacially active polymers because hydrophobes are expelled from water structure due to entropic considerations[40] and, therefore, effectively act as anchors for the adsorption of the polymer to the oil/water interface. The same trend of increased adsorption efficiency with hydrophobic modification was observed for the hydroxyethylcelluloses studied, as reported above.

The four pyreneacrylamide/acrylic acid copolymers discussed above were synthesized for use as model polymeric emulsifiers in the investigation of the effects of extent of hydrophobic modification and crosslinking on (i) the emulsification ability of modified poly(acrylic acids), (ii) the conformation and hydrophobic interactions of poly(acrylic acid) based emulsifiers in aqueous solution, and (iii) the precise extent of adsorption of poly(acrylic acid) emulsifiers onto hydrophobic/hydrophilic interfaces. However, it appears that the adsorption of HEC and HMHEC to oil/water interfaces is kinetically more efficient than the adsorption of PAA and HMPAA under conditions in which the latter are ionically charged. Therefore, it was of interest to study the kinetics of adsorption of the pyreneacrylamide/acrylic acid copolymers to the cyclohexane/water interface from NaOH-neutralized pH=5.5 aqueous solution. This research serves two purposes. First, it broadens the drop volume techniques described herein by applying them to copolymers for which the degree of hydrophobic modification has been precisely characterized. Second, it provides for an understanding of the effects of crosslinking on the kinetics of interfacially active polymer adsorption to hydrophobic/hydrophilic interfaces.

Figures 19-26 represent the dynamic interfacial tension results for PYA/AA 1/340, PYA/AA 1/150, PYA/X/AA 1/0.9/230, and PYA/X/AA 1/0.6/150 diffusing to the cyclohexane/water interface from NaOH-neutralized pH=5.5 aqueous solutions. Each polymer was only studied at concentrations below its c* value under pH=5.5 conditions.

Table 2 summarizes the D/D_A ratios obtained for these polymers diffusing to the cyclohexane/water interface under the conditions described, as well as all of the D/D_A ratios reported for the various polymers and surfactants discussed in this text. The values of D used in the calculation of these D/D_A ratios are those reported in Table 1.

For the pyreneacrylamide/acrylic acid copolymers which were synthesized in the absence of added crosslinker (PYA/AA 1/340 and PYA/AA 1/150) the D/D_A

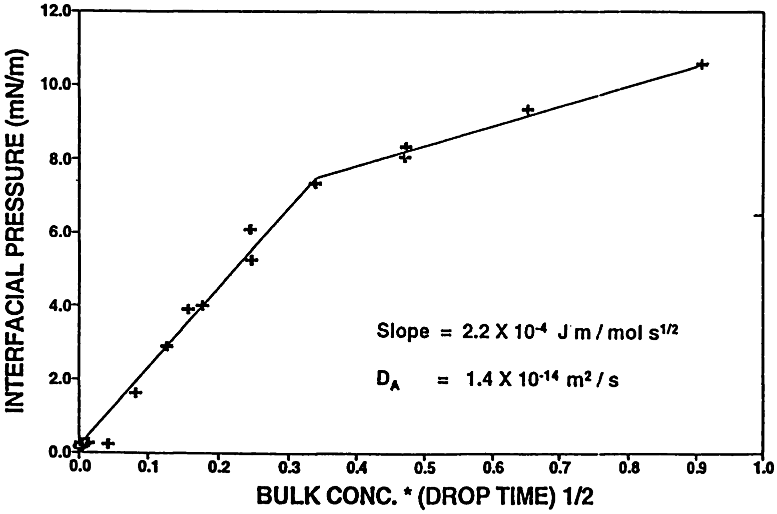

Figure 20. Dynamic Interfacial Pressure for PYA/AA 1/340/Cyclohexane

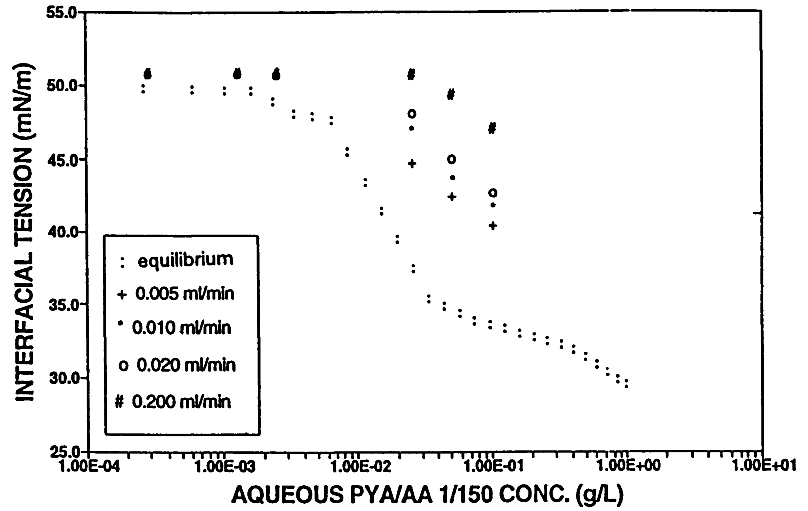

Figure 21. Dynamic Interfacial Tension for PYA/AA 1/150/Cyclohexane

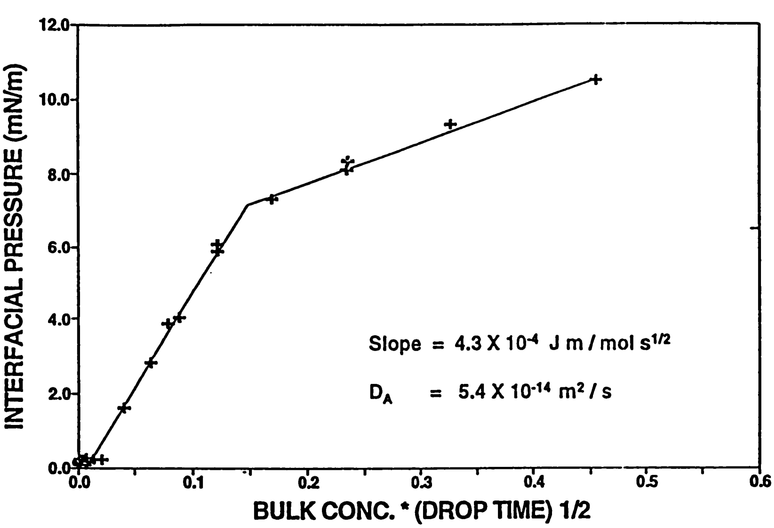

Figure 22. Dynamic Pressure Tension for PYA/AA 1/150/Cyclohexane

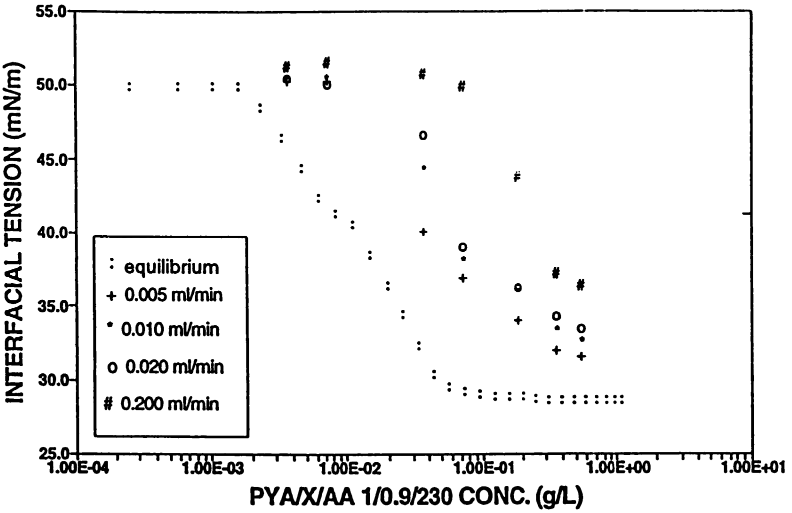

Figure 23. Dynamic Interfacial Tension for PYA/X/AA 1/0.9/230/Cyclohexane

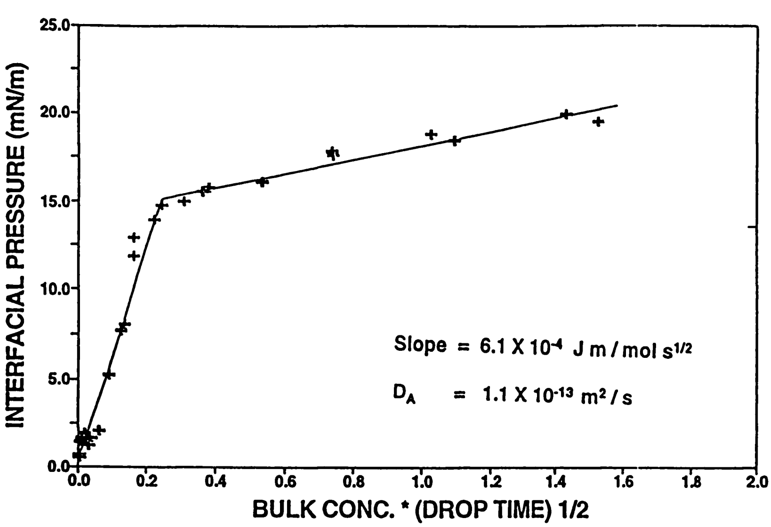

Figure 24. Dynamic Interfacial Pressure for PYA/X/AA 1/0.9/230/Cyclohexane

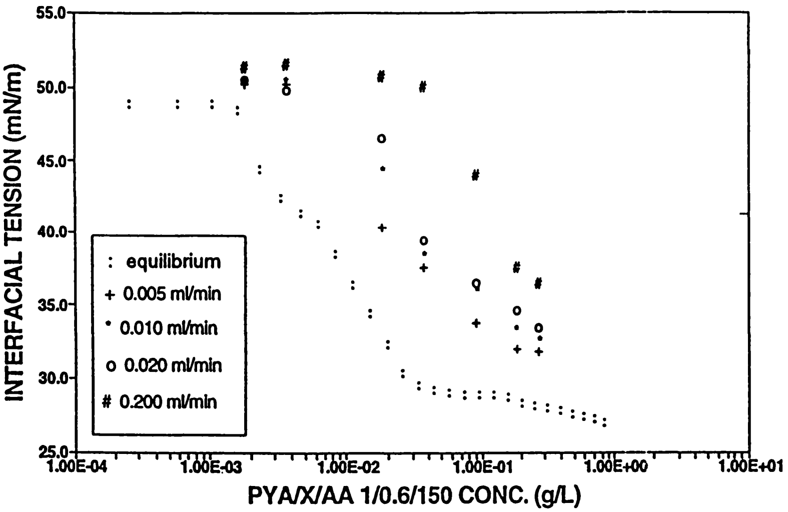

Figure 25. Dynamic Interfacial Tension for PYA/X/AA 1/0.6/150/Cyclohexane

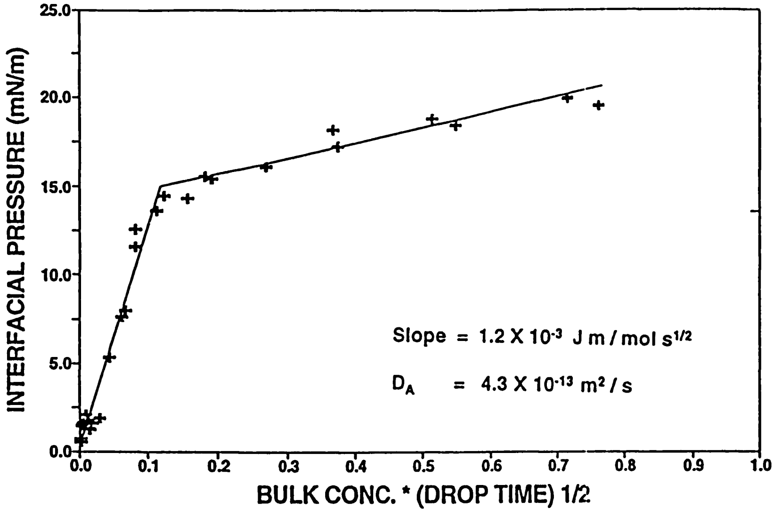

Figure 26. Dynamic Interfacial Pressure for PYA/X/AA 1/0.6/150/Cyclohexane

Table 2 - Comparison of Brownian and Adsorption Diffusion Coefficients

Solute / Oil	D/D_A
$C_{12}E_4$ / Cyclohexane	0.97
SDS / Cyclohexane	44
HMHEC / Cyclohexane	3.0
HMHEC / Mineral Oil	3.2
HEC / Mineral Oil	7.2
HMPAA / Cyclohexane	30
PAA / Cyclohexane	240
(PYA/AA 1/340) / Cyclohexane	210
(PYA/AA 1/150) / Cyclohexane	37
(PYA/X/AA 1/0.9/230) / Cyclohexane	22
(PYA/X/AA 1/0.6/150) / Cyclohexane	6.0

*The values reported here are statiscally significant to at least 95% confidence levels.

ratio decreases from 210 to 37, as the degree of hydrophobic monomer incorporation is increased by a factor of 340/150. This corresponds to the trend established previously between the D/D_A ratios for HMPAA and PAA, and suggests that increasing hydrophobic modification does increase the efficiency of polymer/interface encounters (or close approaches) in leading to interfacial adsorption for hydrophobically modified polyelectrolytes. Neither PYA/AA 1/340 nor PYA/AA 1/150 comes within an order of magnitude (diffusion coefficient-wise) of exhibiting diffusion controlled adsorption which is expected based on their polyelectrolytic natures under the conditions of the study.

Comparison of the D/D_A ratios of PYA/AA 1/150 (D/D_A = 37) and PYA/X/AA 1/0.6/150 (D/D_A = 6.0) indicates that crosslinking of a hydrophobically modified poly(acrylic acid) containing a specific degree of hydrophobic modification has the effect of increasing the efficiency of the polymer's hydrophobic/hydrophilic interfacial adsorption. This could be due to a decrease in the conformational entropy for the polymer in solution, so that the decrease in polymer conformational entropy associated with a polymer's adsorption to an interface is not as substantial for the adsorption of a crosslinked polymer to an interface relative to the adsorption of a non-crosslinked polymer to an interface. However, since the crosslinker employed in this work (1,6 hexanediacrylate) is hydrophobic, the effects of increased hydrophobe incorporation into the polymer are not deconvoluted from the effects of crosslinking on the polymer, when comparing the kinetic efficiencies for the adsorptions of PYA/AA 1/150 and PYA/X/AA 1/0.6/150.

By assigning each of the 16 carbons in a pyrene moiety and each of the 6 aliphatic carbons in 1,6 hexanediacrylate the same hydrophobicity value, it can be calculated that PYA/X/AA 1/0.9/230 is less hydrophobic, overall, than PYA/AA 1/150. That D/D_A = 22 for PYA/X/AA 1/0.9/230 and D/D_A = 37 for PYA/AA 1/150 suggests that crosslinking does, independent of added hydrophobicity, increase the efficiency of adsorption of a modified poly(acrylic acid) to cyclohexane/water interfaces.

A comparison of the D/D_A ratios for the PYA/X/AA 1/0.9/230 (D/D_A = 22) and PYA/X/AA 1/0.6/150 (D/D_A = 6.0) shows again that increasing hydrophobic monomer incorporation increases the efficiency of interface/polymer encounters (or close approaches) in leading to adsorption. Recall that PYA/X/AA 1/0.9/230 and PYA/X/AA 1/0.6/150 possess the same mole percentage of crosslinker.

Conclusions

Four important conclusions can be drawn from this study.

(1) The hydroxyethylcelluloses studied diffuse to and adsorb at cyclohexane/water interfaces and mineral oil/water interfaces more rapidly than do the poly(acrylic acids) studied. This indicates that the inability of the hydroxyethylcelluloses studied to sterically stabilize oil-in-water emulsions is not caused by their adsorption to the oil/water interface being kinetically unfavorable. The inability of HEC and HMHEC to sterically stabilize oil-in-water emulsions may

be due to the adsorbed polymers not providing for a substantial steric barrier to emulsion coalescence.

(2) The D/D_A value of $C_{12}E_4$ is very close to unity, indicating a purely diffusion-controlled adsorption. It must be noted, however, that $C_{12}E_4$ will have a finite solubility in the oil phase, and therefore, the process may involve partitioning between the two phases as well as adsorption at the oil\water interface.

The D/D_A ratio for HMHEC was found to be of the order of 3. It is expected that the kinetic mechanism of adsorption must involve rearrangement and packing of these large molecules at the interface and, thus, it may be concluded that the adsorption of HMHEC is essentially a diffusion-controlled process. The D/D_A ratio for PAA and HMPAA was extremely high, indicating the presence of a large kinetic barrier to diffusion. Increasing levels of hydrophobe on the polymer leads to lower values of D/D_A and thus it appears that adsorption is facilitated by hydrophobic modification of these polymers.

(3) Ionic interfacially active solutes seem to adsorb much less efficiently to oil/water interfaces than nonionics. The poly(acrylic acids) studied, at pH =5.5, have been found, in general, to have large D/D_A ratios, relative to those of the hydroxyethylcelluloses studied. Also, the small molecule ionic surfactant SDS has been shown to have a D/D_A ratio of 44 for adsorption to the cyclohexane/water interface, while the adsorption of the nonionic surfactant $C_{12}E_4$ has been found to be diffusion controlled (D/D_A = 0.97). These findings suggest that when an ionic interfacially active material adsorbs at an interface, charge/charge repulsion between the molecules that adsorb at the interface first and those that diffuse toward the still unsaturated interface at later times causes the kinetics of adsorption to be somewhat less than diffusion controlled.

(4) Studies performed on the pyreneacrylamide/acrylic copolymers suggest that crosslinking a hydrophobically modified poly(acrylic acid), in and of itself, increases the efficiency of the polymer's adsorption at oil/water interfaces. This may be due to crosslinking decreasing the conformational entropy of the polymer in aqueous solution, thus decreasing the polymer's entropic favorablity for solution rather than adsorption.

References

1. Lochhead, R.Y.; Chapter 6 of Polymers as Rheology Modifiers, ACS Symposium Series 463, E.D. Glass, editor, (1991).
2. Chu, K.W.; Masters Thesis, University of Cinncinnati, (1990).
3. Lochhead, R.Y.; Rulison, C.J.; *Colloids and Surfaces A*, **88**(1), 27, (1994).
4. Rulison, C.J.; Lochhead, R.Y.; *Polymer Preprints*, **33**(2), (1992).
5. Rulison, C.J.; Lochhead, R.Y.; Bui, H.S.; Pierce, T.D.; *Polymer Preprints*, **34**(1), (1993).
6. Rulison, C.J.; Lochhead, R.Y.; *Polymer Preprints*, **34**(2), (1993).
7. Vincent, B.; Whittington, S.; In Colloid and Surface Science; Matifevic, E., editor; Plenum, (1982).
8. Lochhead, R.Y.; Rulison, C.J.; *Colloids and Surfaces A*, **88** (1), 27, (1994).
9. Israelachvili, J.N., Adams, G.E.; *Nature (London)*, **262**, 774, (1976).

10. Von Smoluchowski, M.; *Physik Z.*, **17**, 557, 585, (1916), **92**, 129, (1917).
11. Napper, D.H.; Polymeric Stabilization of Colloidal Dispersions, Academic Press, (1983).
12. Lips, A., Smart, C., Willis, E.; *Trans. Faraday Soc.*, **67**, 2979, (1971).
13. Honig, E.P., Roberson, G.J., Wiersema, P.H.; *J. Colloid Interface Sci.*, **36**, 97, (1971).
14. Lichtenbelt, J.W.Th., Pathmamanoharan, C., Wiersema, P.H., *J. Colloid Interface Sci.*, **49**, 281, (1974).
15. Jho, C. and Burke, R.; *J. Colloid Interface Sci.*, **95**(1), 61, (1983).
16. Tornberg, E.; *J. Colloid Interface Sci.*, **60**(1), 50, (1977).
17. Hua, X.Y. and Rosen, M.J.; *J. Colloid Interface Sci.*, **124**(2), 652, (1988).
18. Van Hunsel, J.; Bleys, G.; Joos, P.; *J. Colloid Interface Sci.*, **114**(2), 432, (1986).
19. Correspondence with ICI technical service department, Wilmington, DE (302) 886-3000.
20. Shaw, D.J.; Introduction to Colloid and Surface Chemsitry, Third Edition, 149, (1980).
21. Longworth, L.G.; *J. Amer. Chem. Soc.*, **75**, 5705, (1953).
22. Steiner, C.A., Dualeh, A.J.; *Macromolecules*, **23**, 252, (1990).
23. BF Goodrich Company, Carbopol Water-Soluble Polymers, (1991).
24. Lochhead, R.Y.; p. 375 in ACS Symposium Series 213, Schulz, D.N. and Glass, J.E., editors, American Chemical Society, Washington, DC, (1986).
25. Rulison, C.J.; Ph.D. Dissertation, University of Southern Mississippi, pg. 61-75, (1994).
26. Rulison, C.J.; Ph.D. Dissertation, University of Southern Mississippi, pg. 48-77, (1994).
27. Shaw, D.J.; Introduction to Colloid and Surface Chemsitry, Third Edition, 68, (1980).
28. Adamson, A. W.; Physical Chemistry of Surfaces, Fifth edition, pg. 21-22, (1990).
29. Boucher, E.A.; Evans, M.J.B.; *Proc. Royal Soc.*, **A346**, 349, (1975).
30. Harkins, W.D.; Brown, F.E.; *J. Amer. Chem. Soc.*, **41**, 499, (1919).
31. Lando, J.L.; Oakley, H.T.; *J. Colloid Interface Sci.*, **25**, 526, (1967).
32. Bendure, R.; *J. Colloid Interface Sci.*, **35**, 2, 247, (1971).
33. Joos, P.; Rillaerts, E.; *J. Colloid Interface Sci.*, **79**, 1, 96, (1981).
34. Carroll, B.J.; Doyle, P.J.; *Jour. Chem. Soc., Faraday Trans. 1*, **81**, 2981, (1985).
35. Tornberg, E.; "Interfacial Behavior of Food Proteins Studied by Drop Volume Method", Chapter 40 of Proteins at Interfaces, (1987).
36. Van Voorst Vader, F.; Erkens, Th. F.; Van Den Tempel, M.; *Trans. Faraday Soc.*, **60**, 1170, (1964).
37. Ward, A.F.H.; Tordai, L.; *Jour. of Chem. Phys.*, **14**, 7, 453, (1946).
38. McBain, J.W.; Swain, R.C.; *Proc. Royal Soc.*, **A154**, 608, (1936).
39. Haydon, D.A.; Phillips, J.N.; *Trans. Faraday Soc.*, **54**, 698, (1958).
40. Davies, J.T.; Rideal, E.K.; Interfacial Phenomena, pg. 165-177, Academic Press, New York, (1963).

41. Tanford, C.; The Hydrophobic Effect, Wiley Interscience, New York, (1973).
42. Rulison, C.J.; Ph.D. Dissertation, University of Southern Mississippi, pg. 131-214, (1994).
43. Rulison, C.J.; Ph.D. Dissertation, University of Southern Mississippi, pg. 271-279, (1994).

RECEIVED August 18, 1995

Chapter 20

Vibration Spectroscopy of Surfactants in Solution and at the Air–Water Interface

L. J. Fina

Department of Mechanics and Materials Science, College of Engineering, Rutgers University, Piscataway, NJ 08855

This chapter examines the current status of the research in the area of vibrational spectroscopy of surfactants in solution. The treatment of surfactants in this chapter is divided into five main areas covering first, the influence of the concentration of the surfactant near the critical micelle concentration (CMC) and what can be learned about structural changes through the CMC. The second area involves micellular formations. Thirdly, a considerable amount of vibrational spectroscopic work has been done on mixed micelles and the use of one of the components as a probe molecule. This will be reviewed. Fourthly, the recent work on the use of infrared spectroscopy to probe phospholipid bilayers has yielded new quantitative information on conformational defects. Finally, the current status of the use of infrared spectroscopy in the reflection mode at the air-water interface will be covered. In all areas, the use of vibrational spectroscopy as a tool to probe the molecular structure and interactions is highlighted.

Most of the work in this area involves Fourier transform infrared (FTIR) spectroscopy rather than Raman spectroscopy, due to the inherently stronger absorption process in infrared as compared to Raman scattering. However, the absorption of water in the infrared is often prohibitively strong. Researchers have used several methods to compensate for this problem in order to look at surfactants in aqueous environments. Among them are: 1) the use of infrared peaks that are not in regions of water absorption; 2) subtraction of water bands; 3) substitution of deuterium

0097–6156/95/0615–0316$13.50/0

oxide for water; and 4) combining the surfactant of interest with a small amount of water.

The term surfactants is used here in the most general sense, where it refers to the materials as used for detergents, surface tension modifiers, etc., and also refers to amphiphilic molecules such as phospholipid molecules.

Micellular Structures

Concentration Variations through the Critical Micelle Concentration. The majority of studies which characterize the transition from isolated molecules to micelles in surfactants conducted with vibrational spectroscopy focus on three characteristics of the spectroscopic peaks, the intensity, frequency and half-width. In some cases interpretations related to molecular structure are straight forward and unambiguous, while in other cases conclusions must be considered speculative. Most spectroscopists examine relative simple surfactant molecules, i.e., straight chain methylene-based molecules, since data interpretation is somewhat more straightforward.

One of the earlier vibrational studies of concentration variations through the critical micelle concentration (CMC) was conducted with sodium hexanoate ($CH_3(CH_2)_5COO^-Na^+$) in aqueous solutions(*1*). Sodium hexanoate has a relatively high CMC, and therefore the transition lends itself to spectroscopic analysis. FTIR spectral information on the hexanoate was obtained by a subtraction with the spectrum of pure water. The following bands were used for investigation: asymmetric methyl stretch (~2960 cm^{-1}); antisymmetric methylene stretch (~2934 cm^{-1}); symmetric carboxylate stretch (~1410 cm^{-1}); and antisymmetric carboxylate stretch (~1548 cm^{-1}). Figures 1 and 2 show the variation in frequency and bandwidth, respectively, for the four bands. The frequency shifts with concentration are similar for three of the bands, i.e., constant below 0.75 M, a nonlinear change for the 0.75-1.75 M region, and a linear change above 1.75 M. In the dilute concentration range, the surfactant exists primarily as isolated surfactant molecules. The frequency shifts are probably due to a small amount of molecular association and solvation changes accompanying association. The frequency changes of the methylene stretches are not attributed to conformational changes due to the internal mode character. The nonlinear changes in slope are due to premicellular aggregation, which appears to be complete at 1.75 M. At this concentration, a transition occurs from a heterogeneous system (monomers, aggregates, micelles) to a homogeneous system (micelles). Acyl mode bandwidth changes above 1.25 M are attributed to an increase in solute-solute interactions. The increase in bandwidth of the carboxylate modes at higher concentrations (Fig.2) are attributed to counterion association.

The vibrational properties through the CMC were also studied with resonance Raman spectroscopy, albeit on a surfactant with a more complex

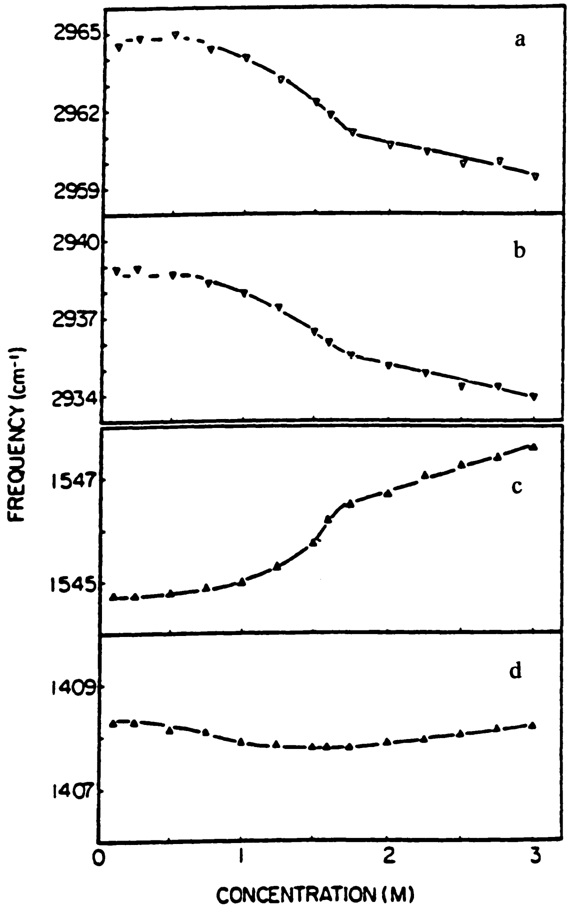

Figure 1. Concentration dependence of the infrared frequencies of aqueous sodium *n*-hexanoate: (a) asymmetric CH_3 stretching mode; (b) antisymmetric CH_2 stretching mode; (c) antisymmetric COO^- stretching mode; (d) symmetric COO^- stretching mode. (Reprinted by permission from reference *1*)

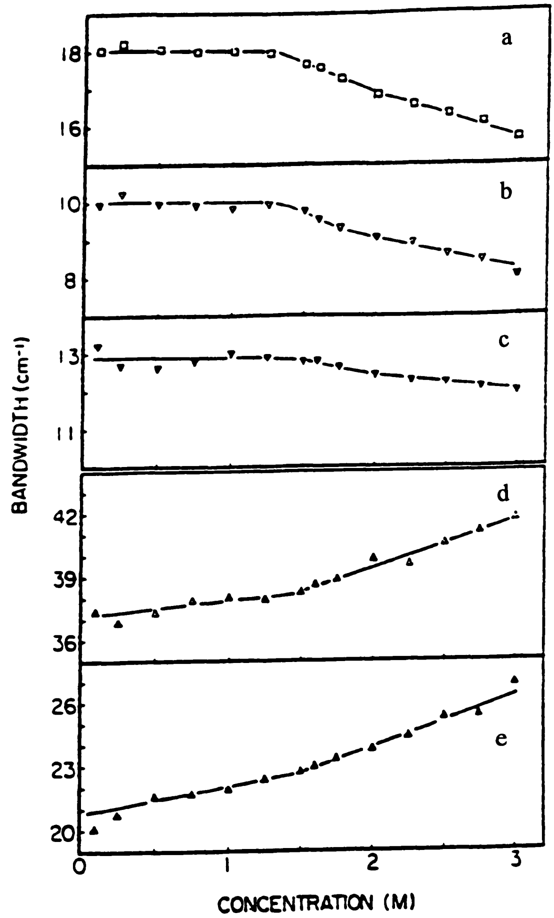

Figure 2. Concentration dependence of the bandwidths of the infrared absorption bands of aqueous sodium *n*-hexanoate: width of the asymmetric CH_3 stretching mode (a) at half-height and (b) at nine-tenths of the peak height; width of the antisymmetric CH_2 stretching mode (c) at nine-tenths of the peak height; and half-widths of the (d) antisymmetric and (e) symmetric COO^- stretching modes. (Reprinted by permission from reference *1*)

head group(*2*). The surfactant is disodium 5-(acetylamino)-3-{(4-dodecylphenyl)azo}-4-hydroxy-2,7-naphthalenedisulfonate (a.k.a. BRBS or Brilliant Red) and the structure is:

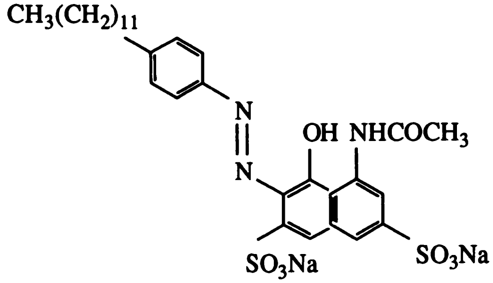

The azo and hydrazone forms exist in equilibrium. The above form is the azo form. At neutral pH, the hydrazone form predominates. At pH 6.2, the Raman spectra show that the hydrazone predominates both above and below the CMC. However, at pH 13.2, the Raman and electronic absorption spectra dramatically change above and below the CMC. Above the CMC, the hydrazone form exists and below, the azo.

Studies of the influence of chain length have lead to an understanding of the role of the acyl chain in micellation. In one such infrared analysis, the chain length in sodium *n*-alkanoates was varied from C_3 to C_{10}, and the concentrations of each were varied through the CMC(*3*). Frequency and bandwidth plots as a function of concentration were produced for the asymmetric methyl, the antisymmetric methylene and the antisymmetric carboxylate stretches. In sodium propionate and butyrate, no micellular aggregation occurs as evidenced by the smooth changes in the frequency and bandwidth with concentration. The pentanoate through decanoate show different behavior from shorter chains. At low concentrations, frequencies and bandwidths versus concentrations are constant indicating the existence of isolated monomers. As the concentration increases, the frequencies and bandwidths change. The rate of change is dependent on the chain length. The smaller chain lengths have a premicellular transition region width of ~2 M while the longer chains have a width of 0.2 M. In other words, the transition becomes progressively sharper as the chain length increases. The data support premicellular aggregation in pentan-, hexan- and heptanoates, while in octan-, nonan- and decanoates, the transition is essentially an abrupt phase transition. Figures 3 and 4 show the antisymmetric carboxylate and methylene stretching frequencies, respectively. In Figure 3, the frequency of the antisymmetric carboxylate stretch at low and high concentrations is relatively independent of the acyl chain length. It follows that the carboxylate frequencies are determined by the state of aggregation and not by the chain length. Contrarily, the monomeric and micellular frequencies of the acyl chain depend on the chain length. At the lowest concentrations in Figure 4, the chain length dependence in the monomeric state is

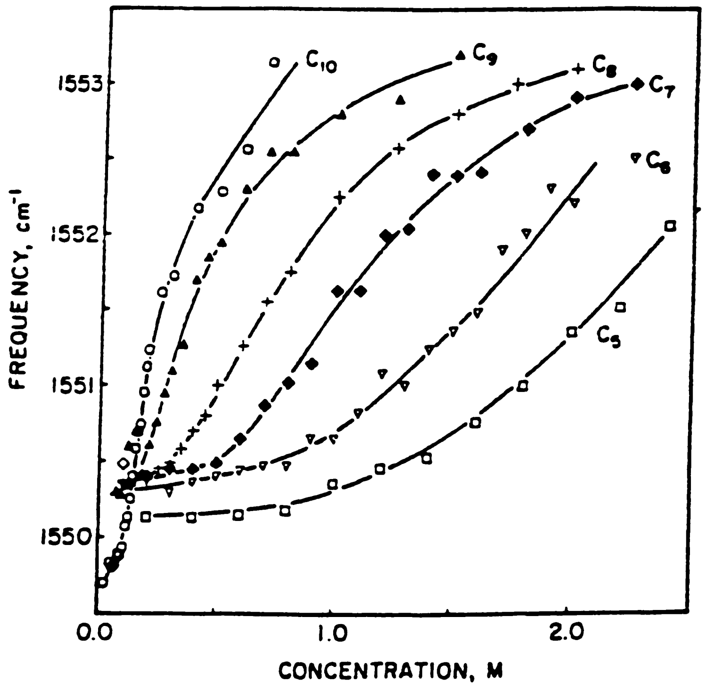

Figure 3. Concentration and acyl chain length dependence of the frequency of the antisymmetric COO^- stretching bands of deuterium oxide solutions of sodium *n*-pentanoate through *n*-decanoate. (Reprinted by permission from reference *3*)

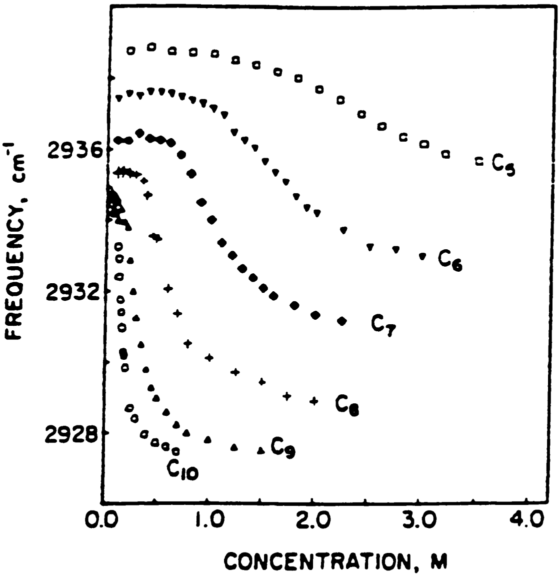

Figure 4. Concentration and acyl chain length dependence of the frequency of the antisymmetric methylene stretching bands of the deuterium oxide solutions of sodium *n*-pentanoate through *n*-decanoate. (Reprinted by permission from reference *3*)

attributed to the inductive effects of the carboxylate end group. In the micellular phase , the acyl frequency decreases with increasing chain length. Two explanations are offered: greater conformational disorder in the micelles of the shorter alkanoates; and a more aqueous environment in micelles of the shorter alkanoates.

A very similar infrared study was done on hexane to nonane sulfonates(*4*), where methylene and sulfonate stretching modes were examined. The methylene stretching frequencies are comparatively and bandwidths are large in the isolated monomeric state. The opposite occurs in the micellular state. Below the CMC, methylene stretching frequencies were found to linearly decrease with concentration. Conformational changes and premicellular aggregation are probably causes. The change in bandwidth can be attributed to a decrease in motion of the chains in the micelles. Close to the CMC, the bandwidth goes through a maximum due to the combined environments of micelles and premicellular species.

In the same work[4], the frequency and bandwidth of the sulfonate modes are shown to depend on counterion binding and hydration. Whereas below the CMC the frequencies of the symmetric and asymmetric sulfonate stretching modes are constant, above the CMC, the asymmetric mode frequency increases and the symmetric decreases. A specific location of the counterion with respect to the sulfonate group accounts for the frequency changes. Below the CMC, the ratio of symmetric to asymmetric sulfonate stretching intensities is constant, whereas above CMC the ratio increases (~12%). As in the bandwidth changes, the intensity changes are attributed to counterion binding in the micellular state.

In a Raman study of sodium decyl and dodecyl sulfate, and of lithium tetradecyl sulfate, the spectra above and below CMC were compared and no major differences were found. This leads to the conclusion that no premicellular aggregates occur in these materials(*5*). Difference spectroscopy was used to highlight subtle frequency shifts and intensity changes. Using the fact that the all-*trans* methylene chain has depolarized methylene stretching modes and a conformationally random chain has polarized modes, spectra were collected with the incident laser polarized perpendicular to the detection optics (total polarization collected) and parallel (depolarized modes only). The two polarizations were collected above and below the CMC and subtracted. All three surfactant systems show methylene stretching frequency shifts upon transition from micelles to monomers. It is suggested that frequency shifting in the methylene stretching modes of the surfactants is due to intermolecular methylene vibrational coupling.

Micelles and Phases in Concentrated Solution. Variations in temperature of micellular phases produces transitions. The phase transition between the micelle and coagel phase is known as the Kraft point or critical micelle temperature (CMT). In the coagel phase, the surfactant molecules are poorly hydrated, multilamellar and polycrystalline. Cameron et al.(*6*) studied the CMT of sodium laurate, sodium oleate and 2,2,12,12,12-pentadeuterio sodium laurate, the former of which has a Kraft point at 19°C and the latter two below 20°C. Bands used in the analysis are methyl and methylene stretching, methylene bending, and carboxylate stretching. In the C-H stretching region, the laurate and the oleate spectra are invariant with temperature between 0 and 20°C (coagel phase). In the coagel spectrum of the laurate, the asymmetric methyl stretching vibrational peak is split indicating restricted mobility. At the CMT, large frequency and half-width increases of the bands show the introduction of *gauche* conformers and disorder. In the carboxylate stretching region, the peaks are also invariant with temperature in the coagel phase. The antisymmetric COO^- peak broadens in half-width through the CMT and shows the presence of two components. The narrow high frequency component corresponds to those of anhydrous carboxylate soaps. Therefore, the coagel phase in this material is one of low hydration. In the higher temperature coagel phase, the antisymmetric COO^- peak has a relative large half-width due to the increase in mobility and a range of interactions with cations, water, etc. In the methylene bending region, a 1468 cm^{-1} peak occurs in both the coagel and micelle phases, indicating the presence of all-*trans* methylene chains outside of well-organized crystalline structures.

The micelle-coagel transition was also studied in sodium and potassium decanoates(*7*). Micellular solutions were prepared in D_2O (15 wt%) with the pH was adjusted to 10. Figure 5 shows the major differences which result between the micelle (30°C) and the coagel (4°C) in sodium decanoate solutions. The CO^- stretching of the carboxylate group at 1409 cm^{-1} in the micelles shifts to 1428 cm^{-1} in the coagel and decreases in intensity due to the coupling between the CO^- and the α-methylene bend in the coagel (α to the carboxylate). This coupling also results in a large increase in the methylene band at 1449 cm^{-1} in the coagel. The very large CO^- stretch and very small methylene stretch in the micelle indicates a weak coupling between the two species and therefore a disordered structure.

Hydrostatic pressure can induce first order phase transitions in aqueous surfactants. Spectral changes occur which are descriptive of the phase transition. Below a critical pressure, the micellular phase exists and infrared bands are broad due to conformational and orientational disorder. Figures 6 and 7 show the frequency characteristics of the methylene stretching and bending modes of sodium decanoate (NaC_{10}) and potassium decanoate (KC_{10}) with pressure(*7*). The critical pressure for a transition in the sodium decanoate from micelles to a coagel is 21.2 kbar, and 22.5 kbar in the potassium decanoate. In the micellular phase increases in pressure lead to an increase in conformational disorder, as evidenced by methylene bandwidth broadening. The carboxylate head groups are not affected by increases in pressure in the micellular phase. In the coagel phase, the half-width of all methylene bands decreases indicating that the chains become extended and ordered. In sodium decanoate the methylene bending peak splits into two peaks (see Figure 7) due to crystal field splitting of

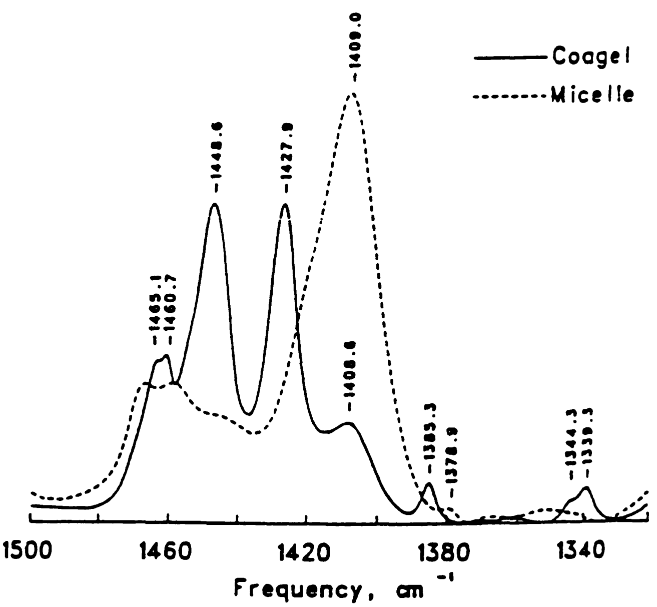

Figure 5. Infrared spectra of the micellular and coagel phases of sodium decanoate (15 wt% in deuterium oxide) measured at atmospheric pressure at 30° and 4°C, respectively. (Reprinted by permission from reference 7)

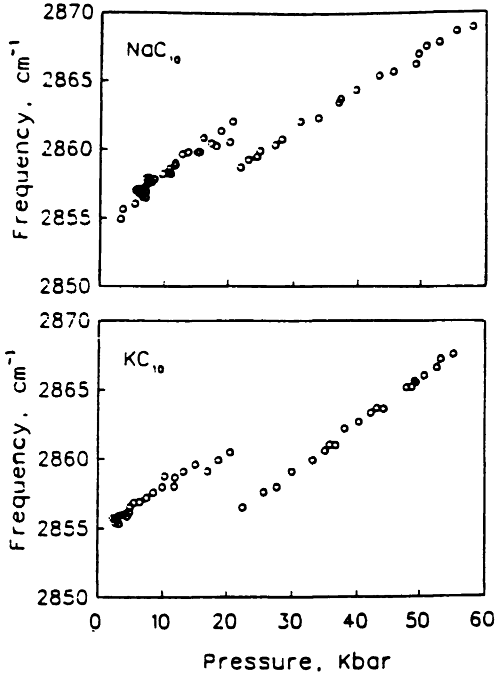

Figure 6. Pressure dependence of the frequencies of the symmetric methylene stretching bands of NaC_{10} and KC_{10}. (Reprinted by permission from reference 7)

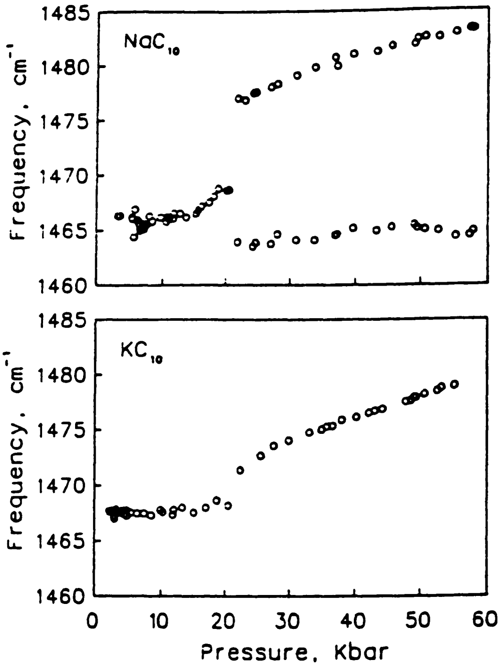

Figure 7. Pressure dependence of the frequencies of the symmetric methylene bending bands of NaC$_{10}$ and KC$_{10}$. (Reprinted by permission from reference 7)

orientationally nonequivalent chains in the lattice. The methylene bending peaks in the potassium decanoate do not split so there is only one chain in the spectroscopic unit cell.

The *gauche* defect content of methylene chains in micelles of sodium dodecyl sulfate (SDS) was studied by Holler and Callis(*8*). The work was based on that of Snyder(*9,10*) who gave detailed assignments to the conformational defect modes in the methylene bending region of alkanes. Three bands were used in this study, the 1341 (end *gauche*), 1354 (double *gauche*) and 1376 cm^{-1} (kink, *g-t-g*). These are localized vibrations, the intensities which are proportional to the number of segments in that conformation. The intensities (or areas) of these peaks can be used to predict the conformational distribution with the use of Flory's rotational isomeric state model(*11*) using alkane spectra as a reference. In 10% SDS in water at room temperature, the conformational distribution was found to be 0.36 end *gauche*, 0.77 double *gauche* and 0.68 kink conformers per molecule.

Infrared studies on aqueous dispersions of dioctadecyldimethyl ammonium chloride (DODAC) were done in the -10 to +56°C temperature range by Umemura et al.(*12*) The antisymmetric stretching modes show two distinct and sharp phase transitions at 35.5 and 45.5°C corresponding to the coagel-gel and gel-liquid crystal phase transitions. The amount of *gauche* increases at each transition.

The transition from disk micelles to rod micelles was studied in concentrated aqueous solutions of sodium decyl sulfate and decanol(*13*). From the methylene stretching modes, the high temperature rod micelles are found to be conformationally disordered in comparison to the low temperature phase. The methyl bending peak shows a large shift (1399 cm^{-1}, low temp. phase, 1379 cm^{-1}, high temp. phase) due to environmental and interchain interaction changes.

Mixed Micelles. The advantage to the use of infrared spectroscopy to probe the structure of mixed micelles is that often head groups of two species in a mix have distinguishable peaks in the spectrum. Thus, the structural features of the individual components can readily be determined. Also, by perdeuteration of one of the components, infrared spectroscopy can be used to distinguish the aliphatic environments.

Sodium dodecyl sulfate (SDS) and dodecyltrimethylammonium chloride (DTAC) is a strongly interacting mixture. The properties of the micelles of this mixture were studied by varying the mole fractional composition(*14*). The frequency of the antisymmetric and symmetric methylene stretching modes decreases as the mole fraction approaches 1:1 from either concentration direction. Also, the methylene stretching modes are lower in frequency than in the micelles of either components alone. Therefore, more conformational order exists in the mixtures. Changes in the head group packing occur when both components are present and the sulfonate stretching modes reflect this. In DTAC-rich mixtures, the asymmetric sulfonate stretching mode is split into two bands due to the perturbation of the C_{3v} symmetry of the sulfonate group. In SDS-rich mixtures, the asymmetric stretching mode resembles that of pure SDS, with one mode of the split dominating the spectra.

In other strongly interacting mixtures, different behavior has been noted. Hexadecyltrimethylammonium bromide (C_{16}TAB) or dodecyltrimethylammonium bromide (C_{12}TAB) were mixed with sodium xylene sulfonate (SXS) and the phase transition behavior was studied as a function of temperature(*15*). The methylene stretching region of these mixtures shows that the critical micelle temperature (CMT, spherical to rod-like micellular transition) of the C_{16}TAB-SXS mixture is 18°C and the C12TAB-SXS mixture, 29°C. Figure 8 shows the fingerprint region of the C_{16}TAB-SXS mixture. The methylene bending modes appear as a doublet at temperatures below 20°C. The doublet occurs due to the orthorhombic subcell packing in the coagel phase. At the CMT the doublet becomes a single peak representative of the chains in a hexagonal subcell. At high temperatures, the frequency decreases as *gauche* bonds are introduced.

Also shown in Figure 8 is a split of the asymmetric sulfonate stretching peaks at 1214 and 1187 cm^{-1}, as opposed to a singlet in pure SXS solutions. In these mixtures, the sulfonate head group is surrounded by C_{16}TAB neighbors. The strong electrostatic interactions lower the C_{3v} symmetry and split the asymmetric mode. Bands due to the ammonium head group of C_{16}TAB undergo significant changes at the CMT. Below the CMT, the CH_3-N^+ asymmetric deformation mode occurs at 1486 cm^{-1} with a small shoulder at 1482 cm^{-1}. At 20°C the frequency of the doublet separation increases; the bands are at 1490 and 1480 cm^{-1}. This implies the non-equivalence of the three methyl groups of C_{16}TAB.

Mixtures of dodecyltrimethylammonim bromide (DTAB) and didodecyltrimethylammonim bromide (DDAB) behave ideally in that the interaction energy is close to zero. However, infrared spectroscopy shows that some level of interaction is present. A straight-forward method was determined to test the frequency shifting that occurs when the above surfactants are mixed together(*16*). The spectra of the pure components were digitally added together in a variety of ratios. This represents the ideal case where the resulting frequencies are that of the non-interacting mixture. Figure 9 shows this simulation as the solid line. The experimental data points are also shown. Above 0.65 mole fraction DTAB, the mixture behaves ideally, while below, a phase change occurs from micelles to bilayers and the data deviates from the prediction.

Several studies have been done in Casal's laboratory on the extent of water penetration into micelles. The incorporation of guest molecules in low concentration that reside in the micelles and are capable of hydrogen bonding to water serve as spectral probe molecules. In one such study, several different host surfactants were used. Aliphatic ketones were incorporated at concentrations that do not disturb the native micelle structure(*17*). In the spectra of 0.018 M 6-undecanone (probe) in 0.25 M

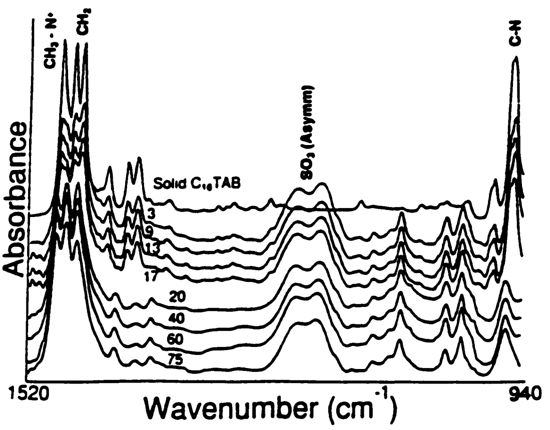

Figure 8. Spectra of C_{16}TAB/SXS mixture at various temperatures, and a reference spectrum of solid C_{16}TAB. (Reprinted by permission from reference *15*)

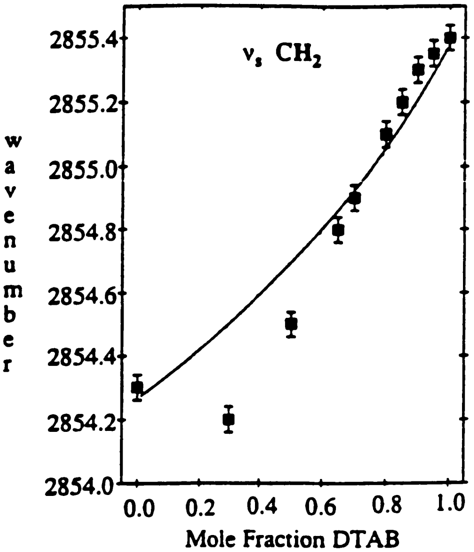

Figure 9. Frequency shifts of the composite methylene symmetric stretching band in spectra of actual mixtures and synthetic spectra. The squares are data points obtained from actual spectra, while the line is derived from synthetic spectra. (Reprinted by permission from reference *16*)

SDS, two carbonyl bands exist, 1720 cm^{-1} from free carbonyls and 1698 cm^{-1} from hydrogen bonded carbonyls. These result from the ketone residing in micelles that are protected from the aqueous environment and exposed to it, respectively. When the ketone chain length is less than or equal to the surfactant chain length, varying the chain length of the surfactant from C_8 to C_{16} while the surfactant chain length is constant causes a ten-fold increases in the ratio of H-bonded to free carbonyl groups. An increase in chain length therefore leads to a smaller amount of water in the micelles. When the ketone chain length is longer than the surfactant molecules, three carbonyl peaks arise from: free carbonyls (1720 cm^{-1}); a 1:1 carbonyl to water ratio (1705 cm^{-1}); and a 1:2 ratio (1698 cm^{-1}).

In another study from Casal's laboratory, a carbonyl group was incorporated into the hydrophobic part of a surfactant molecule, i.e., sodium 7-oxooctanoate. This molecule was used as a probe in micelles of sodium octanoate(*18*). In this mixture, there is considerable chemical similarity between the host surfactant and the probe, and minimal structural disturbance of the micelles is expected. Earlier work with this mixture had shown that water penetrates the micelle up to position seven along the chain(*19*). When pressure was used as a variable, both the carboxylate stretching modes (from the host) and the carbonyl (from the probe) shows discontinuous frequency shifts at about 17 kbar, indicating the micelle to coagel transition (critical micelle pressure). Below the critical micelle pressure, the ketone peak position is constant (1697 cm^{-1}), while above, the ketone splits into two peaks at 1720 and 1707 cm^{-1}. In the micelles (low pressure), the keto group is in contact with water, and the latter penetrates to position seven along the aliphatic chain. In the coagel phase, the two carbonyl bands are due to free (1720 cm^{-1}) and monohydrated (1707 cm^{-1}) ketones. The contact with water is diminished at position seven in the coagel.

Probe molecules in micelles of dodecyl sulfate were also used to analyze the water penetration as affected by different counterions(*20*). In all counterion tested (sodium, lithium, tetraethylammonium, tetramethylammonium) two overlapping carbonyl bands are seen corresponding to free and hydrogen-bonded carbonyls. Since the absorptivities of these two species are approximately equal, the intensity ratio is a measure of the quantity of each. In micelles composed of 0.1 M lithium dodecyl sulfate with 0.008 M 7-undecanone, a considerably higher amount of water is bound at position seven along the chain as compared to the other three counterions, implying a more "open" micellular surface. In the more hydrophobic counterion systems (alkylammoniums), the binding to the surface sulfate head groups is stronger than in sodium, and thus the ratio of bound to free guest carbonyls decreases due to limited water penetration.

Lipid Bilayers

Extensive work has been done with infrared spectroscopy of lipid bilayers since the latter are the primary component of biological membranes. Lipid bilayers act as a structural matrix for a variety of proteins in cell membranes which control the transport properties of all living cells. The study of phase transitions in these materials is of great relevance to membrane functioning. This work was recently reviewed by Mantsch and McElhaney(*21*). Work done since this review will be emphasized here. The primary variable that has been studied in lipid bilayers in conjunction with vibrational spectroscopy is temperature and its relationship to phase transitions and structure. Many studies have been done in this regard and only a collection of the most relevant work will be covered here.

Aqueous dispersions of double acyl chain ammonium amphiphiles having the general formula $2C_{12}$-L-Glu-$C_nN^+X^-$ where n=2, 6 and 11 were studied by Nakashima et al.(*22*) The temperature was varied during the infrared scanning and the following vibrational modes were monitored: methylene bending and stretching, carbonyl of the Glu component, amide I and II of the Glu, and the asymmetric C-O-C stretch, also of Glu. The antisymmetric methylene stretching mode of the n=2 compound show a linear increase with temperature indicating no phase transitions. In the n=6 and 12 compounds, the frequency abruptly increases at 5-10 and 30-35°C, respectively, and corresponds to the gel-liquid crystal phase transition. The methyl and symmetric methylene stretching peaks show the same behavior. The ester carbonyl frequency shows a variation with temperature similar to the above bands. Two explanations are offered for this behavior: 1) conformational changes around the ester group; and 2) a suppression of the polarization of the carbonyl group.

In another temperature study of lipid bilayers, Shimada et al.(*23*) studied the temperature dependence of the interaction of the protein gramicidin D and two bilayer forming amphiphiles, dioctadecamethylammonium bromide ($2C_{18}N^+$-$2C_1Br$) and 1,2-dipalmytoyl-L-α-phosphatidylcholine (DPPC). Gramicidin D is a linear polypeptide of 15 hydrophobic amino acids. It forms ion channels in a membrane and displays selectivity for small monovalent cations. Figure 10 shows the methylene symmetric stretching region of the aqueous bilayer $2C_{18}N^+$-$2C_1Br$ as a function of temperature between 22 and 55°C. The frequency shifts to higher frequencies with temperature and decreases in intensity corresponding to the introduction of *gauche* conformers. Between 40 and 45°C the frequency abruptly shifts corresponding to the gel to liquid crystal transition. A similar transition is seen in the gramicidin D-containing bilayers, except that the transition region is over 38-43°C. A parallel temperature response is observed in the half-width of the amide I band (from the gramicidin D), i.e., an maximum rate of change occurs at the same temperatures, suggesting that the gramicidin D is associated with the alkyl regions of the membrane.

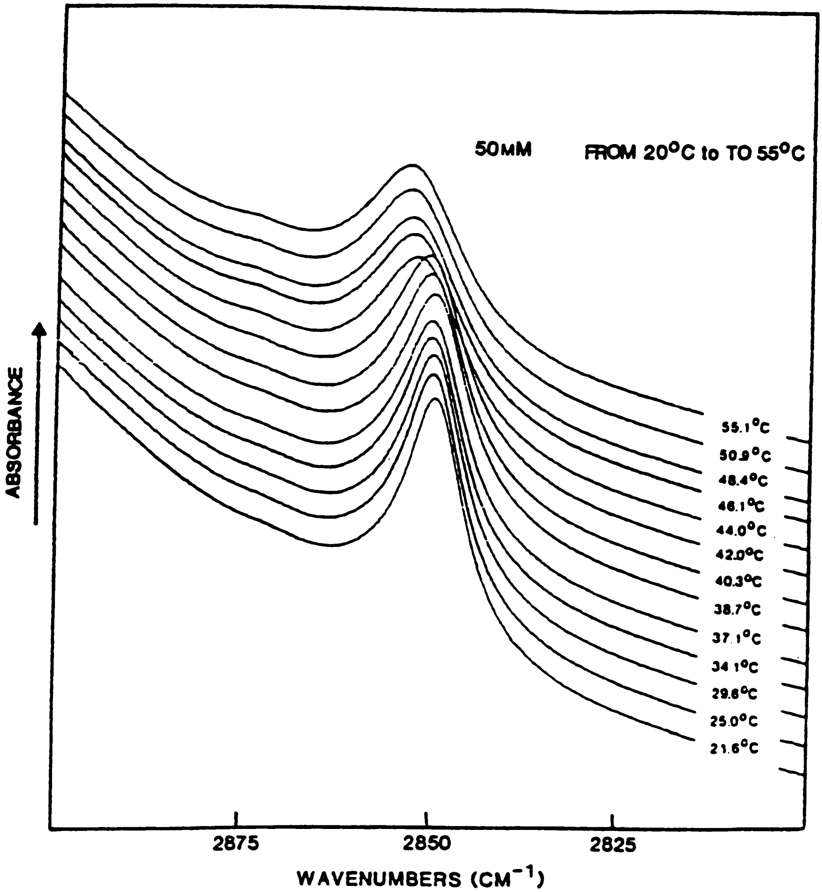

Figure 10. Temperature dependence of the methylene stretching band of bilayers composed of $2C_{18}N^{+}2C_1Br^{-}$. (Reprinted by permission from reference *23*)

The phosphatidylserine 1[1'-^{13}C]palmitoyl-2-palmitoyl-*sn*-glycero-3-phospho-L-serine (DPPS) was synthesized and studied with infrared spectroscopy(*24*). Three metal ions were complexed with DPPS: NH_4^+; Li^+; and Ca^{++}. The temperature dependent gel to liquid crystal transition of DPPS can easily be seen in the frequency response of the symmetric methylene stretching peak when complexed to NH_4^+ and Li^+ (53 and 86°C, respectively). In contrast, the Ca^{++} complex shows no transition between 30 and 90°C. With NH_4^+ as the counterion, in the gel phase the two carbonyl peaks at 1737 and 1700 cm^{-1} have low frequency shoulders. Deconvolution reveals that the higher frequency *sn*-2 C=O band is actually composed of two species at 1741 and 1730 cm^{-1}, assignable to the two *sn*-carbonyl types. A strong band at ~1623 cm^{-1} is due to the antisymmetric carboxylate stretching vibration of the serine moiety. From the frequency of occurrence, it follows that the serine carboxylate in DPPS-NH_4^+ is fully hydrated above and below the phase transition. In DPPS-Li^+, the level of hydration is quite different. From the frequency of the carboxylate groups, they are completely dehydrated up to 80°C. At 86°C, the shift of the carboxylate peak to 1627 cm^{-1} demonstrates hydration. However, even at this temperature, some of the carboxylate groups remain dehydrated, an indication of the strong binding of Li^+ to DPPS. Detailed assignments to all carbonyl groups are given in this work.

A body of work has come from the laboratory of Casal using probes molecules to explore the structure of lipid bilayers, similar to his work on micelles. He used the probe molecules 8-pentadecanone, 9-heptadecanone, and 10-nonadecanone in bilayers of 1,2-dihexadecyl-*sn*-glycero-3-phosphocholine (DHPC)(*25*). DSC shows that the probes molecules do not form separate phases in the bilayers. In 0.1M DHPC in D_2O (12 parts DHPC to 1 part 9-heptadecanone), three carbonyl bands exist, a 1719 cm^{-1} band due to free, unhydrogen bonded groups, and two bands, 1706 and 1699 cm^{-1}, due to hydrogen bonding to D_2O. The areas of the bands indicate that the ratio of bound to free carbonyls at 26°C is 0.2, at 38°C it is 0.5, and at 46°C, 0.3. The increase at the "pretransition" (33.3°C) is thought due to water penetration. The water content of these lipid bilayers is found to be considerably less than micelles of similar structure.

Further work on the above lipid bilayer system has been done and compared with potassium stearate dispersions, the latter of which do not form bilayers(*26*). Potassium stearate solutions were prepared from 0.012 M D_2O with the probe molecules 5-oxo-potassium stearate, 12-oxo-potassium stearate or 9-heptadecanone. Liposomes of DHPC were also prepared with the stearate probe molecules in low concentration. In the methylene stretching peaks of the potassium stearate solutions, no change is observed at the coagel to gel transition, and the frequencies are characteristic of all-*trans* chains. Abrupt frequency shifts are observed at the gel to micelle transition. Unlike with the methylene stretching modes, spectral changes are observed in the methylene bending region at the coagel to gel transition in the stearate solutions. A small shoulder on the high frequency side of the 1466 cm^{-1} peak appears in the coagel which is absent in the gel phase, suggesting crystal field splitting at the lower temperatures.

Mendelsohn and coworkers have done a series of experiments on lipid bilayers to quantify the defect content in lipid bilayers. Initial work involved the spectra of alkanes, where they found that the methylene wagging bands due to end-*gauche* and double-*gauche* linearly increased with temperature in the 20-80°C temperature range(*27*). On the other hand, the wagging band due to kink defects actually decreases slightly with temperature, contrary to the predictions of Flory's rotational isomeric state model (RIS)(*11*). In a study of DPPC and DPPE (1,2-dipalmitoylphosphatidylcholine), the spectra were also collected as a function of temperature. The methylene wagging region of DPPC bilayers shows a very much reduced double-*gauche* defect peak from room temperature to 45°C, as compared to liquid hexadecane or the predictions of the RIS model. This is due to the conformational restrictions in the bilayers. The spectra between 45 and 80°C show a greater degree of conformational freedom. In the DPPE lipids, the amount of double-*gauche* species are reduced by a factor of 2-3 as compared to DPPC.

In other studies Mendelsohn and coworkers focused on specific-site deuteration of DPPC(*28-30*). The methylene rocking modes are used to explore conformational defects. With the deuteration of positions 6 and 13 along the acyl chains, at room temperature most to the intensity of the CD_2 rocking mode goes to the C-C-C *trans-trans* peak at 622 cm^{-1}. When the temperature is raised to 50°C, 2 higher frequency peaks appear (or increase in intensity) at 646 and 652 cm^{-1} due to the introduction of *gauche* defects. Also, at 50°C, the 4, 10 and 13 positions of the liquid crystal phase show about 20% *gauche*. On the other hand, nearer to the bilayer center, the 14-15 bond has about 40% disorder (at 50°C). With the addition of cholesterol to the aqueous bilayers, a large reduction in the amount of *gauche* occurs at all measured positions along the chain.

In a further study of lipid bilayers, Mendelsohn and coworkers(*31*) varied the acyl chain length in DPPC-like molecules and added cholesterol. The low temperature phase is well ordered, permitting a study of the methylene wagging progression, which is a sensitive measure of the existence of the all-*trans* form in phospholipids. In aqueous dispersions (4:1wt%::H_2O:lipid), the subtraction of a phosphate peak which covers the wagging progression, nicely reveals the progression. The combined intensities of the k=1-4 modes of the progression in DPPC decrease in intensity with temperature, and dramatically so at the melting point (T_m) of the bilayers. The behavior parallels the increase in frequency of the symmetric methylene stretching peak. The intensity of the progression series decreases with temperature below the T_m because of the introduction of a small amount of disorder. In DPPC/cholesterol mixtures, sufficient conformational order exists in the DPPC chains so that the wagging progression is visible. At 20 mole% cholesterol, a monotonic decrease is seen in the k=1 intensity between 15 and 39°C followed by a phase transition with a rapid loss of the $k=1$ intensity. At 33 mole%, the progression intensity slowly decreases throughout the whole temperature range studied (20-60°C) with no T_m observed. There is a substantial residual progression intensity at 60°C in the 33 mole%, indicating the persistence of order. In DPPC/androsten mixtures, the presence of androsten decreases the $k=1$ intensity by about one-half throughout the whole temperature range.

As in the case of micelles, lipids respond to pressure by displaying conformational changes and phase transitions. Pressure combined with infrared spectroscopic studies has lead to new information on lipid structure. Auger et al.(*32*) studied the barotropic behavior of aqueous dispersions of sodium 1,2-dimyristoyl-*sn*-glycero-3-phospho-L-serine (DMPS) and sodium 1,2-dioleoyl-*sn*-glycero-3-phospho-L-serine (DOPS). Both acyl chains contain a rigid *cis* double bond in the middle. No significant variations in the carbonyl stretching peak occurred in DMPS from 0.001-25 kbar. In DOPS, the carbonyl peak shows a 10 cm^{-1} decrease in the half-width at 6.1 kbar, indicative of a liquid crystal to gel transition. An abrupt drop in methylene stretching frequencies also occurs at 6.1 kbar. In DMPS, a correlation field splitting occurs in the methylene bending modes above 3.7 kbar indicating an orientational nonequivalence of all-*trans* chains. In DOPS, no splitting occurs, i.e., the acyl chains are parallel. In this same study, the anesthetic tetracaine was added to the bilayers. The shape and intensity of the tetracaine carbonyl can be used to monitor the environment of tetracaine(*33*). In the bilayer environment, the carbonyl peak is weak and broad whereas in the aqueous environment, the peak is intense and narrow. The spectra establish that at 2.1 kbar (pH=5.5) the tetracaine is expelled (by the pressure) to the aqueous environment. Although the expulsion is somewhat surprising because DMPS is negatively charged and the anesthetic is positively charged, the charges probably cause the anesthetic to reside close to the surface, and therefore, more easily expelled.

Barotropic variation has also been used to study the behavior of the cyclohexyl phosphatidylcholines 1,2-di-14-cyclohexyltetradecanol-*sn*-glycero-3-phosphocholine (14cyPC) and 1,2-di-13-cyclohexyltetradecanol-*sn*-glycero-3-phosphocholine (13cyPC)(*34*). These type of saturated fatty acids occur in some thermo-acidophilic bacteria. The bacteria can function under extreme environments such as pH=1-3 and 50-90°C. An increase in pressure of 0.4-21 kbar results in no phase transition, i.e., they remain in the gel state. In the methylene bending region at low pressures, the existence of a 1468 cm^{-1} band is characteristic of straight chain molecules not organized into orthorhombic or monoclinic crystals. The behavior of the odd and even lipids is quite different. The odd shows very little changes in the methylene bending region with pressure, while the even shows a correlation splitting. As pointed out by Snyder(*35*), the ratio of the integrated intensities of the rocking mode crystal field splitting peaks is related to the angle between neighboring chains. Since the same behavior can be expected for the methylene bending region, Hübner et al.(*34*) used this to show that increases in pressure (4-20 kbar) converts the almost perpendicular arrangement to a parallel one in the even phospholipid (14cyPC).

Surfactants at the Air-Water Interface

The above research done on surfactants in solution serves as a basis for the work involving the structure and properties of surfactant molecules which reside at the air-water interface. A considerable amount of work has been done at the air-water interface with a variety of techniques. For example, fluorescence microscopy has lead to the observation of phase domains(*36-38*), synchrotron x-ray reflectivity has been used to define the relationship between the monolayer thickness, the orientation and the surface-pressure isotherms(*39-41*), and sum-frequency generation and optical second harmonic generation have lead to the characterization of conformational and orientational order(*42-46*). However, very little work has been done at the air-water interface with vibrational spectroscopy. Dluhy(*47*) pioneered the use of reflection-absorption infrared spectroscopy in insoluble monolayers for isotropic systems. Work followed which highlighted the conformation and phase transitions at the air-water interface in phospholipids monolayers(*48-50*).

The isotropic-based models for the calculation of infrared reflection properties were extended to oriented monolayers by Fina et al.(*51,52*). Three additional models have appeared in the literature. Gericke et al.(*53*) presented a treatment which included an integration of the optical constants with depth. Hsu et al.(*54*) derived expressions for the transition moment angle and the absorption coefficient. Buontempo and Rice(*55*) included unrestricted rotation about the chain axis in their derivation. All treatments are used for the measurement of the methylene chain orientation in all-*trans* chains.

The sensitivity of reflection-absorption infrared spectroscopy to conformation, orientation and concentration requires that these variables be constant with time. The time dependence of the reflection-absorption signal can be monitored to insure "vibrational" equilibrium. In the adsorption process of sodium dodecyl sulfonate ($C_{12}S$), the molecules initially adsorb from the bulk solution to the air-water interface and show relatively high methylene stretching frequencies of absorption. Therefore, a high content of *gauche* conformers is present. At concentrations near the CMC, the methylene stretching frequencies quickly decrease to values consistent with all-*trans* methylene chains when equilibrium is established.

Reflection-absorption infrared spectra of $C_{12}S$ monolayers as a function of bulk concentration are shown in Figure 11. All spectra are collected with bulk concentrations below the CMC, so molecules are either isolated or collect in premicellular aggregations. The top three spectra are at bulk concentrations below the linear region of the surface tension-(log)

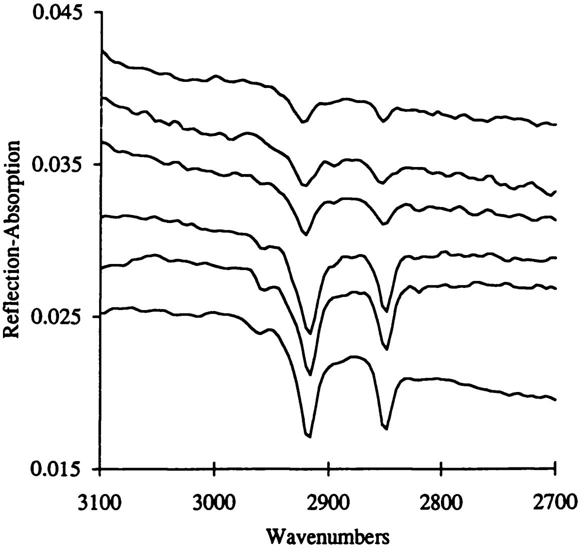

Figure 11. Reflection-absorption *p*-polarized infrared spectra of sodium dodecyl sulfonate monolayers on a water substrate. Bulk concentrations from bottom to top are: $1x10^{-2}$, $5.60x10^{-3}$, $3.58x10^{-3}$, $2.28x10^{-3}$, $1.49x10^{-3}$,$1.18x10^{-3}$M.

bulk concentration plots, while the bottom three are in the linear region. The constancy of the intensity and peak position of the spectra in the linear region establishes that the surfactant conformation, concentration and orientation are unchanging. In the top three spectra, an abrupt change in intensity and frequency occurs, consistent with the introduction of conformational and orientational disorder, and a phase transition.

The intensities of the *p*- and *s*-polarized methylene stretching peaks can be used to calculate the orientation and absorption coefficients of the all-*trans* methylene chains in the linear region of the surface tension isotherm. The average chain tilt angle (from the surface normal) is found to be 39.8±0.97° and the average k_{max} (absorption coefficient) value (where $k_{max} = 3k_{isotropic}$) for the asymmetric methylene stretch (~2917 cm^{-1}) is 0.544±0.014. The angle is (perhaps fortuitously) in good agreement with that found in a hydrated crystal of $C_{12}S$, i.e. 40° (*56*). The k_{max} value can be converted to a surface concentration (Γ) for the purpose of comparison with the Γ value predicted from a surface tension analysis, the latter of which is known to be an accurate measure. Following a procedure described elsewhere (*52*), the two dimensional concentration of $C_{12}S$ monolayers is found to be 3.28×10^{-10} mol/cm^2. This value is in reasonably good agreement with that found in a surface tension analysis, 2.90×10^{-10} mol/cm^2 (*57*).

Literature Cited

(1) Umemura, J.; Cameron, D. G.; Mantsch, H. H. *J. Phys. Chem.* **1980**, *84*, 2272.

(2) Takahashi, H.; Umemura, J.; Takenaka, T. *J. Phys. Chem.* **1982**, *86*, 4660.

(3) Umemura, J.; Mantsch, H. H.; Cameron, D. G. *J. Coll. Interface Sci.* **1981**, *83*, 558.

(4) Kawai, T.; Umemura, J.; Takenaka, T. *Coll. Polym. Sci.* **1984**, *262*, 61.

(5) Kamogawa, K.; Tajima, K.; Hayakawa, K.; Kitagawa, T. *J. Phys. Chem.* **1984**, *88*, 2494.

(6) Cameron, D. G.; Umemura, J.; Wong, P. T. T.; Mantsch, H. H. *Coll. Surf.* **1982**, *4*, 131.

(7) Wong, P. T. T.; Mantsch, H. H. *J. Coll. Interface Sci.* **1989**, *129*, 258.

(8) Holler, F.; Callis, J. B. *J. Phys. Chem.* **1989**, *93*, 2053.

(9) Snyder, R. G. *J. Chem. Phys.* **1967**, *47*, 1316.

(10) Snyder, R. G.; Schachtchneider, J. H. *Spectrochim. Acta* **1963**, *19*, 85.

(11) Flory, P. J. *Statistical Mechanics of Chain Molecules*; Hanser Publishers: New York, 1989.

(12) Umemura, J.; Kawai, T.; Takenaka, T.; Kodama, M.; Ogawa, Y.; Seki, S. *Mol. Cryst. Liq. Cryst.* **1984**, *112*, 293.

(13) Hui, Y. W.; Labes, M. M. *J. Phys. Chem.* **1987**, *91*, 6066.

(14) Scheuing, D. R.; Weers, J. G. *Langmuir* **1990**, *6*, 665.

(15) Scheuing, D. R.; Weers, J. G. *Coll. Surf.* **1991**, *55*, 41.

(16) Weers, J. G.; Scheuing, D. R. *J. Coll. Interface Sci.* **1991**, *145*, 563.

(17) Casal, H. L.; Martin, A. *Can. J. Chem.* **1989**, *67*, 1554.

(18) Casal, H. L.; Wong, P. T. T. *J. Phys. Chem.* **1990**, *94*, 777.

(19) Casal, H. L. *J. Am. Chem. Soc.* **1988**, *110*, 5203.

(20) Abuin, E. B.; Lissi, E.; Casal, H. L. *Photochem. Photobiol. A: Chem.* **1991**, *57*, 343.

(21) Mantsch, H. H.; McElhaney, R. N. *Chem. Phys. Lipids* **1991**, *57*, 213.

(22) Nakashima, N.; Yamada, N.; Kunitake, T.; Umemura, J.; Takenaka, T. *J. Phys. Chem.* **1986**, *90*, 3374.

(23) Shimada, I.; Ishida, H.; Ishitani, A.; Kunitake, T. *J. Coll. Interface Sci.* **1987**, *120*, 523.

(24) Hübner, W.; Mantsch, H. H.; Paltauf, F.; Hauser, H. *Biochem.* **1994**, *33*, 320.

(25) Casal, H. L. *J. Phys. Chem.* **1989**, *93*, 4328.

(26) Muga, A.; Casal, H. L. *J. Phys. Chem.* **1990**, *94*, 7265.

(27) Senak, L.; Davies, M. A.; Mendelsohn, R. *J. Phys. Chem.* **1991**, *95*, 2565.

(28) Davies, M. A.; Schuster, H. F.; Brauner, J. W.; Mendelsohn, R. *Biochem.* **1990**, *29*, 4368.

(29) Mendelsohn, R.; Davies, M. A.; Brauner, J. W.; Schuster, H. F.; Dluhy, R. A. *Biochem.* **1989**, *28*, 8934.

(30) Mendelsohn, R.; Davies, M. A.; Schuster, H. F.; Xu, Z.; Bittman, R. *Biochemistry* **1991**, *30*, 8558.

(31) Senak, L.; Moore, D.; Mendelsohn, R. *J. Phys. Chem.* **1992**, *96*, 2749.

(32) Auger, M.; Smith, I. C. P.; Mantsch, H. H.; Wong, P. T. T. *Biochem.* **1990**, *29*, 2008.

(33) Auger, M.; Jarrell, H. C.; Smith, I. C. P.; Wong, P. T. T.; Siminovitch, D. J.; Mantsch, H. H. *Biochem.* **1987**, *26*, 8513.

(34) Hübner, W.; Wong, P. T. T.; Mantsch, H. H. *Biochim. Biophys. Acta* **1990**, *1027*, 229.

(35) Snyder, R. G. *J. Mol. Spectrosc.* **1961**, *7*, 116.

(36) Möhwald, H. *Thin Solid Films* **1988**, *159*, 1.

(37) Kjaer, K.; Als-Nielsen, J.; Helm, C. A.; Laxhuber, L. A.; Möhwald, H. *Phys. Rev. Lett.* **1987**, *58*, 2224.

(38) Helm, C. A.; Möhwald, H.; Kjaer, K.; Als-Nielsen, J. *Biophys. J.* **1987**, *52*, 381.

(39) Kim, M. W.; Sauer, B. B.; Yu, H.; Yazdanian, M.; Zografi, G. In *Materials Research Society Symposium Proceedings, Macromolecular Liquids*; C. R. Safinya, S. A. Safran and P. A. Pincus, Ed.; Materials Research Society: Pittsburgh, 1990; Vol. 177; pp 405-410.

(40) Kjaer, K.; Als-Nielsen, J.; Helm, C. A.; Tippmann-Krayer, P.; Möhwald, H. *Thin Solid Films* **1988**, *159*, 17.

(41) Schlossman, M. L.; Schwartz, D. K.; Kawamoto, E. H.; Kellogg, G. J.; Pershan, P. S.; Ocko, B. M.; Kim, M. W.; Chung, T. C. In *Materials Research Society Symposium Proceedings, Macromolecular Liquids*; C. R. Safinya, S. A. Safran and P. A. Pincus, Ed.; Materials Research Society: Pittsburgh, 1990; Vol. 177; pp 351-361.

(42) Grubb, S. G.; Kim, M. W.; Rasing, T.; Shen, Y. R. *Langmuir* **1988**, *4*, 452.

(43) Rasing, T.; Shen, Y. R.; Kim, M. W.; Grubb, S. G. *Phys. Rev. Lett.* **1985**, *55*, 2903.

(44) Rasing, T.; Shen, Y. R.; Kim, M. W.; Valint, J., P.; Bock, J. *Phys. Rev. A* **1985**, *31*, 537.

(45) Vogel, V.; Mullin, C. S.; Shen, Y. R.; Kim, M. W. *J. Chem. Phys.* **1991**, *95*, 4620.

(46) Sionnest, P. G.; Hunt, J. H.; Shen, Y. R. *Phys. Rev. Lett.* **1987**, *59*, 1597.

(47) Dluhy, R. A. *J. Phys. Chem.* **1986**, *90*, 1373.

(48) Mitchell, M. L.; Dluhy, R. A. *J. Am. Chem. Soc.* **1988**, *110*, 712.

(49) Dluhy, R. A.; Reilly, K. E.; Hunt, R. D.; Mitchell, M. L.; Mautone, A. J.; Mendelsohn, R. *Biophys. J.* **1989**, *56*, 1173.

(50) Pastrana, B.; Mautone, A. J.; Mendelsohn, R. *Biochem.* **1991**, *30*, 10058.

(51) Fina, L. J.; Tung, Y. S. *Appl. Spectrosc.* **1991**, *46*, 986.

(52) Tung, Y. S.; Gao, T.; Rosen, M. J.; Valentini, J. E.; Fina, L. J. *Appl. Spectrosc.* **1993**, *47*, 1643.

(53) Gericke, A.; Michailov, A. V.; Hühnerfuss, H. *Vib. Spectrosc.* **1993**, *4*, 335.

(54) Hsu, S. L. *personal comm.* **1993**.

(55) Buontempo, J. T.; Rice, S. A. *J. Chem. Phys.* **1993**, *98*, 5825.

(56) Lingafelter, E. C.; Jensen, L. H. *Acta Cryst.* **1950**, *3*, 257.

(57) Dahanayake, M.; Cohen, A. W.; Rosen, M. J. *J. Phys. Chem.* **1986**, *90*, 2413.

RECEIVED June 6, 1995

Chapter 21

Structure of Surfactant Monolayers at the Air–Water Interface Determined by Neutron Reflection

J. R. Lu and R. K. Thomas

Physical Chemistry Laboratory, South Parks Road, Oxford OX1 3QZ, United Kingdom

The determination of the structure of a soluble surfactant monolayer, hexadecyl trimethyl ammonium bromide (C_{16}TAB), using isotopic substitution in conjunction with neutron reflection is described. The roughness of the layer has been determined as has the separation of the various parts of the molecule in the normal direction. The molecule is strongly tilted with respect to the surface normal and the outer part of the molecule is more tilted than the inner part. The roughness is comparable with the projection of the molecule on the surface normal direction. In different C_nTABs with n = 12 to 18 the thickness of the chain region of the monolayer is found to be almost independent of chainlength at 16 – 17 Å. In monolayers of $C_{12}E_m$, where E_m is an ethylene glycol chain of *m* units, the thickness of the ethylene glycol chain region varies from about 8 Å for *m* = 2 to 19 Å when *m* = 8.

Neutron specular reflection is a recently developed technique for exploring composition and density profiles normal to the surface for a variety of different types of interface (e.g. (*1*)). The intrinsic spatial resolution of the experiment is not very good but the systematic use of isotopes to label different parts of the layer can increase the resolution so that structure can be probed at the Å level (*2*). There is no restriction to any particular type of interface, the only condition for the feasibility of the experiment being that one of the bulk phases on either side of the interface is transparent to neutrons. In this paper we explore the structure of equilibrium monolayers of surfactants adsorbed at the air/water interface.

The main characteristic of an equilibrium monolayer that distinguishes it from an artificially spread monolayer is that the limiting area per molecule is usually much larger than the cross sectional area of the hydrophobic chain part of the surfactant. Thus, for a typical limiting coverage of a soluble surfactant at the air/water interface the area per molecule, *A*, is about 45 Å^2, whereas *A* would be 20 – 25 Å^2 for a typical spread monolayer. The extra space available in the

0097–6156/95/0615–0342$12.00/0

equilibrium monolayer is expected to lead to tilting of the molecule with respect to the surface normal and possibly to a significant incidence of chain defects, orientational disorder of the chains, and disorder in the direction normal to the surface, i.e. roughness (*3*). At the air/water interface there will be a further contribution to disorder from thermal excitations (capillary waves). Until now, no experiment has been able to characterize all these features for a surfactant monolayer. The first part of this paper describes the extent to which neutron reflection and isotopic labelling can yield this information.

In the second part of the paper we compare the structural parameters obtained by neutron reflection for two types of chain in equilibrium monolayers of surfactants at the air/water interface, hydrocarbon chains in the series of alkyl trimethyl ammonium bromides (the C_nTABs), and ethylene oxide chains in the series of monododecyl ethers of ethylene glycols ($C_{12}E_m$).

Neutron Reflection from $C_{16}TAB$

There are two key structural quantities that can be determined, the width (in the normal direction) of the average distribution of a given fragment *i* of the surfactant, which we will denote by σ_i, and the separation between the centres of the distributions of any pair of fragments in the layer, which we will denote δ_{ij} where *i* and *j* identify the two fragments. The way the width may be determined is illustrated by the following example for $C_{16}TAB$ (*3*).

We suppose that we wish to determine the width of the distribution of the outer butyl group of the hexadecyl chain. This is achieved approximately by measuring the reflectivity of $C_4D_9C_{12}H_{24}N(CH_3)_3Br$ ($dC_4hC_{12}hTAB$ for short) in a 9:1 mixture of H_2O and D_2O. Because protons and deuterons scatter neutrons with opposite phases, an H_2O/D_2O mixture of this proportion has a neutron refractive index the same as air and therefore does not reflect neutrons. We refer to this composition of water as null reflecting water (n.r.w.). The head group is also null reflecting because the contributions of the N, C, and Br nuclei cancel out the contribution from the protons, which is of opposite sign, and a similar effect approximately operates for the $C_{12}H_{24}$ group. The latter can be exactly matched to air by the inclusion of a small amount of $C_{12}D_{24}$ to make dC_4"0"$C_{12}hTAB$ and this has been done for all the results described below. The reflected signal from $dC_4hC_{12}hTAB$ in n.r.w. is then only from the labelled butyl group.

The reflectivity can be written approximately (*4*)

$$R(\kappa) = \frac{16\pi^2}{\kappa^2} b_f^2 h_{ff} \qquad (1)$$

where κ is the momentum transfer defined in terms of the grazing angle of incidence and the wavelength of the neutron ($\kappa = 4\pi\sin\theta/\lambda$), b_f is the empirical scattering length of the fragment (known independently), and h_{ff} is the partial structure factor of the fragment, given by

$$h_{ff} = |n_f(\kappa)|^2 \qquad (2)$$

where $n_f(\kappa)$ is the Fourier transform of the number density profile of the fragment in the direction normal to the surface. Generally, a Gaussian distribution is found to be a good representation of the surfactant fragments, in which case, h_{ff} becomes

$$h_{ff} = \frac{1}{A^2}\exp(-\kappa^2\sigma_f^2) \tag{3}$$

where A is the area per molecule at the surface and σ_f is the full width at 1/e of the maximum of the distribution. We have not justified the assumption of a Gaussian distribution because, at this stage, the exact nature of the distribution is not important for the arguments that follow.

When neutron reflection is done on C_{16}TAB, on either a labelled C_4 group at any position in the chain, or on the labelled head group, the resulting h_{ff} is the same within error, that is, the head group or any chosen C_4 fragment distributions all have exactly the same width. The average h_{ff} for these groups is shown as points in Figure 1. The continuous line is the best fit of equation 3 with $\sigma = 14 \pm 2$ Å. This dimension is much greater than the fully extended length of the fragments (7 – 10 Å) and indicates that much of the width is generated by roughness. We can determine the roughness directly as follows.

We increase the length of the fragment visible to neutrons, i.e. the length of the deuterated fragment, by studying the series of compounds $C_{16-n}H_{33-2n}$–C_nD_{2n}dTAB as a function of n, in null reflecting water. Since the neutron reflection experiment then only observes the labelled fragment the measured width in each case is the width of the labelled part of the molecule only, not of the whole molecule. The width depends on the relative contributions of the roughness and the average intrinsic projection of the labelled fragment along the surface normal. The latter will dominate when it becomes significantly larger than the roughness, i.e. as the length of the labelled fragment increases. In Figure 2 we plot σ^2 for this series of compounds against n^2. The reason for plotting the square of the width is that the convolution of two Gaussians to give a composite width gives the relation

$$\sigma^2 = (nl)^2 + w^2 \tag{4}$$

where nl is the projection of the fragment on the surface normal and w the roughness. For the shorter fragments this gives a linear extrapolation to n = 0, where the value of σ^2 is the square of the roughness. Because there must also be some contribution to the length from the head group we actually use $(n+1)^2$ rather than n^2, but this only has a slight effect on the extrapolated value of w. For C_{16}TAB w is found to be 14 ± 1 Å. Values in the range 10 – 14 Å have been deduced for other surfactants in a less direct way (*5–8*). This is, however, the first direct measurement.

The slope of the plot of Figure 2 is determined by the increase in the length of the normal projection of the chain as each CD_2 group is added. That a straight line is obtained up to $n \simeq 10$ indicates that the chain remains fairly straight, although the value of the gradient indicates that it must be tilted away from the surface normal. At higher n the plot flattens off indicating that the end part of the chain is on average tilted more strongly away from the surface normal than the lower part. However, Figure 2 is not a sensitive means of determining the chain orientation or any disorder within the chain. This is better done by determining the separation between two fragments of the chain.

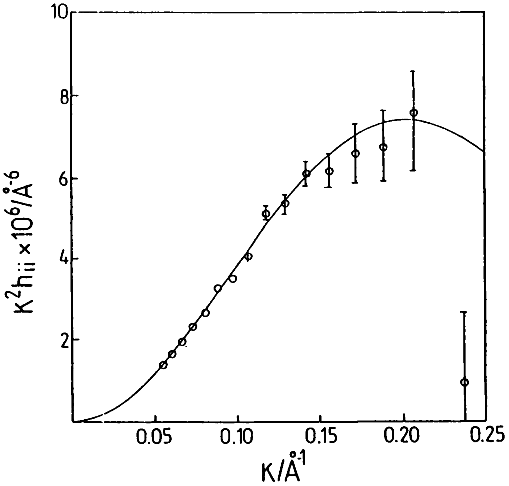

Figure 1. Partial structure factor for the "smallest" unit of C_{16}TAB averaged over measurements on "0"C_{16}dTAB, dC_4"0"C_{12}hTAB, and "0"C_{12}dC_4hTAB. The continuous line is calculated using equation 3 with $\sigma = 14 \pm 1$ Å and $A = 45 \pm 2$ Å^2

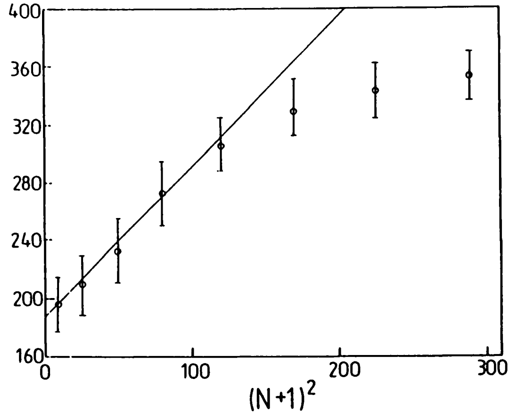

Figure 2. Plot of the square of the width against the square of the number of labelled carbon atoms in the series $C_{16-n}H_{33-2n}C_nD_{2n}$dTAB. The straight line is the best linear fit to this region of the curve (see text).

If we study the reflectivity of a $C_{16}TAB$ species labelled with deuterium in such a way that there is one dC_4 fragment and the head group is deuterated, e.g. $dC_4hC_{12}dTAB$, in n.r.w. the reflectivity is determined by three partial structure factors:

$$R(\kappa) = \frac{16\pi^2}{\kappa^2}(b_{c4}^2 h_{c4c4} + b_h^2 h_{hh} + 2b_{c4}b_h h_{c4h}) \qquad (5)$$

where h_{c4c4} and h_{hh} denote the self partial structure factors of the dC_4 fragment and the head group, and h_{c4h} denotes the cross partial structure factor between C_4 and the head. The two self partial structure factors can be determined directly from measurement of the appropriate reflectivity using labelled compounds where either the dC_4 group or the head group is the only deuterated fragment and everything else is null reflecting. Application of equation 1 then gives the self partial structure factor directly. If a third reflectivity measurement is made, where both dC_4 and head group are deuterated, then application of equation 5, with the known two self partial structure factors, gives the cross partial structure factor h_{c4h}. The special feature about this partial structure factor is that it can be written, to a very good approximation, as

$$h_{c4h} = \pm (h_{c4c4}h_{hh})^{1/2}\cos\kappa\delta_{c4h} \qquad (6)$$

where δ_{c4h} is the separation between the centres of the labelled C_4 and the head group distributions (*5,9*). Since everything except δ is known in equation 6, δ can be deduced directly from the data without any need for Fourier transformation or model fitting.

We have made a whole series of labelled compounds and done the appropriate reflectivity measurements to measure the separations of each of the four C_4 groups constituting the C_{16} chain, both from each other and from the head group (*3*). The fitting of equation 6 to the data is shown for the four cross partial structure factors in Figure 3. The values of δ_{c4h} were found to be 2.5, 7.5, 7.5, and 12.0 ± 1 Å for the C_4 groups nearest to furthest from the head respectively. We have made a similar set of measurements to determine the separations of the 8 constituent C_2 groups of the C_{16} chain from the head (*3*).

From these data it is possible to derive a shape for the whole chain distribution, which is approximately independent of any model. To do this we take the distributions of the individual C_2 or C_4 units and superimpose them at the appropriate distances δ from each other. In the present case the eight different C_2 units and four different C_4 units have exactly the same width because they are determined predominantly by the roughness of the layer. This makes the calculation particularly simple. The result, where the C_2 units are taken to be Gaussian distributions, is shown in Figure 4a. The resolution of the neutron experiment is too low to distinguish whether each C_2 unit is best described as Gaussian or as a uniform layer. However, if we use the alternative distribution of a uniform layer for each C_2 fragment to reconstruct the whole chain distribution using the same values of δ, we obtain a profile that also looks distinctly Gaussian (Figure 4b). The reason is that the shape of the chain profile is affected more by the δ values, which are obtained independently of the shape of the individual units using equation 6, than by the shape of the units themselves. In any case, the uniform layer becomes an increasingly inappropriate distribution as the size of the fragment decreases because,

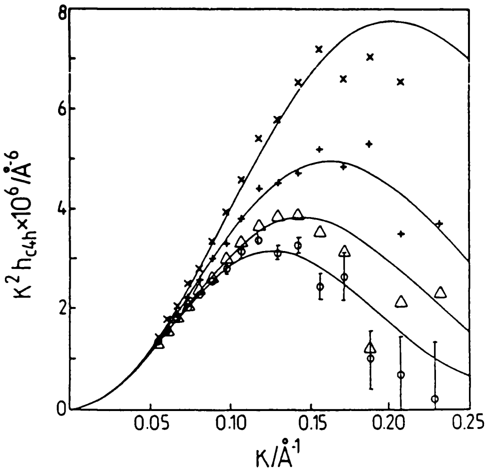

Figure 3. The four partial structure factors, $h_{c4h}(1–4)$ of the compounds dC_4"0"$C_{12}dTAB$ (x), "0"C_4dC_4"0"C_8dTAB (+), "0"C_8dC_4"0"C_4dTAB (Δ), and "0"$C_{12}dC_4dTAB$ (o) in n.r.w. The continuous lines are the best fits of equation 6 to the data.

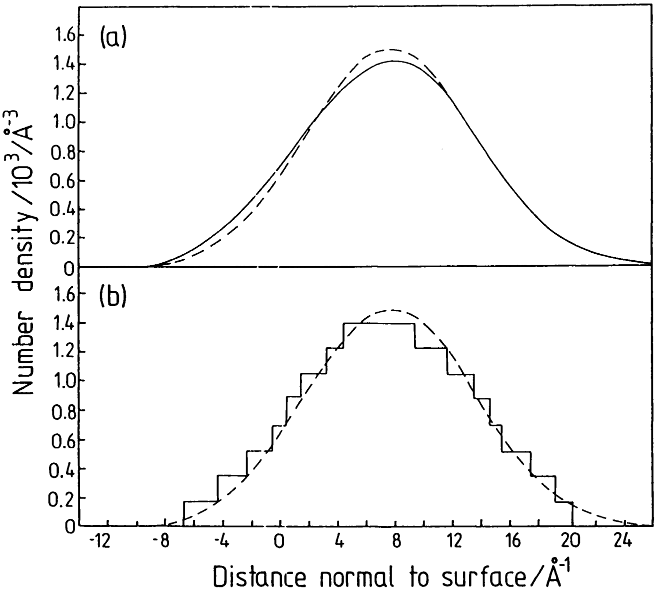

Figure 4. Chain distributions of $C_{16}TAB$ combined from (a) a set of Gaussians and (b) a set of uniform layers. The dashed lines are from the direct measurement of the whole C_{16} chain with $\sigma = 16.5 \pm 1$ Å and $A = 45 \pm 2$ Å^2.

ultimately, it must be determined by capillary wave roughness, which will give a Gaussian distribution. Thus, without making any *a priori* assumptions as to whether the chain as a whole is better represented by a uniform layer or by a Gaussian, it is at least reasonable to assume that the individual small fragments are well represented by Gaussians.

An equation similar to equation 5 can be written for the reflectivity when only the water and a fragment of the chain are considered

$$R(\kappa) = \frac{16\pi^2}{\kappa^2}\left(b_{c4}^2 h_{c4c4} + b_w^2 h_{ww} + 2b_{c4}b_w h_{c4w}\right) \tag{7}$$

A set of three isotopic measurements can again lead to the three partial structure factors in equation 7. The partial structure factor for the water, h_{ww}, gives information about the width of the water distribution across the interface. For all surfactant systems so far studied this is about twice the width for a clean water surface but whether this results from capillary wave roughening of the surface or from an intrinsically greater width is not yet clear. The separation of each of the C_4 fragments from the centre of the water distribution can be determined from an equation similar to equation 6 (*5*):

$$h_{c4w} = \pm\,(h_{c4c4}h_{ww})^{1/2}\sin\kappa\delta_{c4s} \tag{8}$$

Once again, since the self terms are already known, the various values of δ may be determined without recourse to any models. These results confirm those determined above and give the additional information of the position of the surfactant relative to the water. The centre of the distribution of the head groups of C_{16}TAB at its critical micelle concentration is found to be 0.7 Å on the air side of the centre of the water distribution. A more subtle consequence of the agreement between the two separate determinations of the fragment positions is that it implies that the roughness of the layer (the 14 Å determined above) applies to the whole layer including the water.

Figure 4 showed the distribution of the chain as a whole in the direction normal to the interface. However, with some assumptions it is possible to deduce more detail about the chain orientation and internal structure from the δ values for the separation of the different fragments (*3*). We first note that the δ values are not affected by the roughness of the surface. In Figure 5 the δ values are plotted on the vertical axis and the solid points represent the fully extended lengths between the centre of each fragment. Thus, if all the fragments have the same orientation in the layer, which is not necessarily the case, this diagram represents the average tilt of the chain fragment in the surface layer. It can be seen from the Figure that the lower part of the chain is oriented more closely to the surface normal, that the chain tends to kink at around the fourth carbon from the head group and again at about 8, and that it is strongly tilted away from the surface normal. An interesting observation is that the roughness of 14 Å, as determined separately above, is greater than the projection of the chain length along the surface normal.

The most direct way of assessing the structure of a surfactant layer is in terms of the number distribution of the various components. This is done in Figure 6 for the highest concentration of C_{16}TAB with a computer simulation of C_{16}TACl done at the same area per molecule by Böcker et al. (*10*). The agreement in the relative positions of the distributions of the three components is

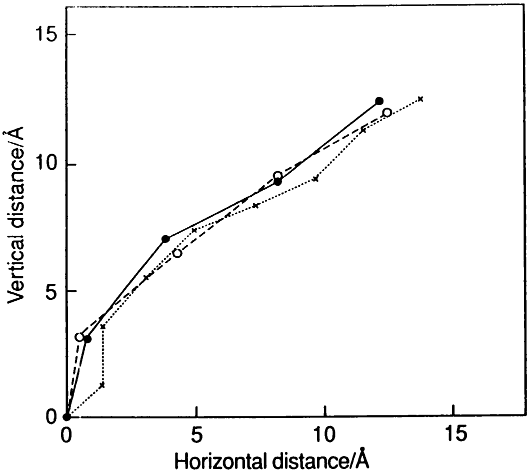

Figure 5. The mean structure of the hexadecyl chain of C_{16}TAB using least squares parameters drived from the cross distances between the C_2 and C_4 fragments in reference (*1*) and their known extended lengths. The solid circles show the positions of the centres of the C_4 groups and crosses the C_2 groups. The open circles show the positions of the C_4 groups based on the structure determined only from the C_4 labelling scheme.

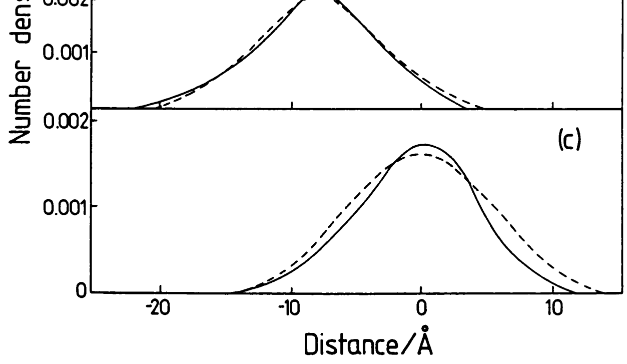

Figure 6. Number density distributions of (a) the solvent, (b) the head and (c) the chain of C_{16}TAB (dashed lines) in comparison with those of computer simulation of C_{16}TACl (solid lines).

excellent. The simulated width of the head group distribution also agrees well with experiment and shows clearly that roughness makes an important contribution to this width. The only disagreement between simulation and experiment is that the experimental chain width is greater by about 25%. Note that we have used the composite chain distribution, given by Figure 4, in Figure 6, which is slightly skewed in the same sense as in the simulation. This skewness is as would be expected from the orientation of the chain fragments as given by Figure 5. Thus the distribution is wider on the water side of the interface because this part of the chain is more vertical. The discrepancy between the simulation and experiment may well result from the limited sample size not accounting for all of the capillary wave roughness.

There are no direct measurements of the surface roughness for the air/water interface of surfactant solutions, although roughness is often incorporated as a fitting parameter when uniform layer models are used to fit specular reflectivity data. However, off–specular scattering has been used to examine the roughness of pure liquids and, in particular, the roughness of pure water has been determined to be 3 Å, close to that predicted from the capillary wave model (*11*). Since the capillary wave roughness varies inversely as the square root of the surface tension we can calculate what it should predict for the surfaces of C_{16}TAB solutions. Allowing for a factor of 2.3 because of difference in our definition of the roughness we obtain a value of 8.5 Å for comparison with our value of 14 Å. Thus the capillary wave prediction falls significantly short of the observations. If the roughness and the intrinsic width in the absence of roughness are taken to add in quadrature, which is appropriate for Gaussian distributions, it is found that there is an additional 11 Å roughness not accounted for by the simple theory.

Comparison of different surfactant layers

So far we have been considering the detailed interfacial structure of one surfactant at one concentration. It is interesting, however, to investigate the effects of chain length of the surfactant on the structure. We have shown above that, for the C_{16}TAB layer, a Gaussian (equation 3) is a good representation of the chain distribution. We can then most easily determine the thickness of a particular part of the layer by determining h_{ff} and plotting $\ln h_{ff}$ against κ^2 because, from equation 3,

$$\ln h_{ff} = -2\ln A - \kappa^2\sigma_f^2 \qquad (9)$$

In Figure 7 we show the results of doing this for C_{12}TAB and C_{18}TAB at approximately the same area per molecule. It is quite difficult to ensure that sets of measurements on different surfactants are made at the same value of *A*. For the C_nTABs the value of *A* at the c.m.c. is almost exactly the same for $n = 14$, 16, and 18. For C_{12}TAB a value of *A* of about 44 Å^2 was achieved by the addition of sodium bromide. The almost identical plots for the different chainlengths demonstrate that *A* is indeed the same, as it should be, but also show that the thicknesses of the layers are the same, a most unexpected result. The thicknesses given for these two compounds in Table 1 differ by 1 Å. These are the original values quoted in references (*6*) and (*8*). The best fitted thicknesses actually led to a difference of 0.6 Å, but rounding of the values to the nearest

0.5 Å has increased the difference to 1 Å, which, however, is within the experimental error. This observation is supported by data for the whole series, given in Table 1. We have included an estimated result for C_{10}TAB, whose layer cannot be compressed to the value of 44 $Å^2$, but its thickness at $A = 60$ $Å^2$ is already 16 Å and, in this series of surfactants, the layers always thicken as A decreases. We discuss this set of observations in more detail below.

Table 1
Miscellaneous experimentally determined parameters of the C_nTABs

Property	C_{10}	C_{12}	C_{14}	C_{16}	C_{18}
$\sigma_h \pm 3$ Å	11.0	12.5	13.0	14.0	14.0
l_c	14.2	16.7	19.2	21.7	24.2
$\delta_{ch} \pm 1$ Å	6.0	6.5	6 ± 1.5	8.5	9.0
$\sigma_c \pm 1$ Å	16.0	16.0	16.0	16.5	17.0
$2\delta_{ch}$/Å	12	13	12	17	18

The alkyl chain part of the surfactant layer protrudes into the vapour phase. In a certain sense it can be said to be in a poor solvent (air). It is interesting to compare the behaviour of the alkyl chains of different length with that of ethylene oxide chains in water, i.e. the behaviour of chains in good solvent conditions. Figure 8 shows the use of equation 9 to determine the thickness of $C_{12}E_m$ layers, where m varies from 2 to 8, at the air water interface at a constant area per molecule of about 55 $Å^2$ (*12*). Now the slopes increase substantially with m, showing that the EO chain thickness does increase with length, as one would expect. The actual values are given in Table 2.

Table 2
Structural parameters of $C_{12}(EO)_m$ as a function of EO length
(area per molecule of about 55 $Å^2$)

Property	E_2	E_3	E_4	E_6	E_8
$\sigma_e \pm 2$ Å	8.0	11.0	14.5	16.5	19.0
l_e	7.2	10.8	14.4	21.6	28.8
$\delta_{ce} \pm 1$ Å	6.0	6.5	6.5	9.0	10.5
$\sigma_c \pm 2$ Å	14.0	14.5	14.5	16.0	15.0

Some interesting comparisons may be made of the structural parameters in Table 1. The most remarkable feature is that the width of the chain distribution for these four molecules is almost identical within experimental error, although the length of the fully extended chain (l_c) increases substantially with n. From the observations on C_{16}TAB above the width of the head group is approximately the same as the roughness and this increases very slightly with n. When allowance for this is made in considering the width of the chain regions it can be

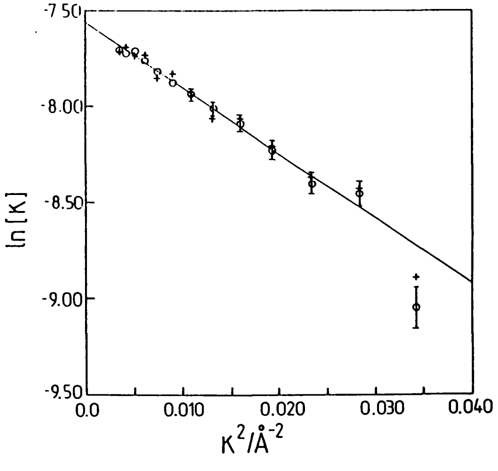

Figure 7. Plots of ln[h_{ii}] versus κ^2 for the alkyl chains of C_{12}TAB (o) and C_{18}TAB (+). Both have the width of 16.5 ± 1 Å and area of 45 ± 2 Å².

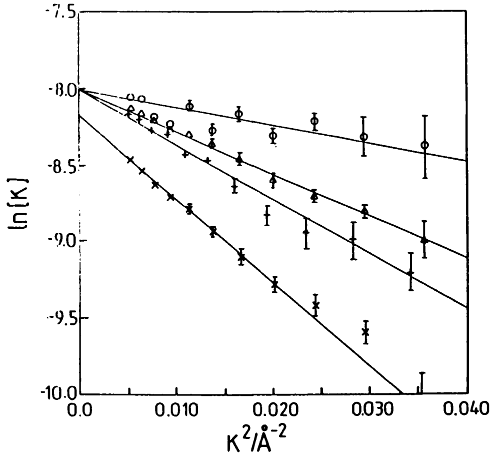

Figure 8. Plots of ln[h_{ii}] versus κ^2 for the ethylene oxide groups of $C_{12}E_n$, where n = 2 (o), 4 (Δ), 6 (+) and 8 (x). The values of σ are 8, 14.5, 16.5, 19 ± 1 Å and the area is 55 ± 3 Å² for the three lower ethylene oxide groups and 62 ± 3 Å² for n = 8.

seen that the intrinsic chain length must actually *decrease* slightly as the length of the fully extended chain increases. This trend is continued for C_{10}TAB, for which the values in Table 1 were obtained at an larger area per molecule of about 60 Å^2. The thickness of the chain always decreases as A increases so the value of 16 Å for σ is less than it would be if the C_{10}TAB layer could be compressed to the same area per molecule as the other members of the series. The explanation of this behaviour must be that the chains on average are more tilted away from the surface normal as their length increases. That the explanation must be a little more complicated can be seen from an examination of the δ_{ch} values. If the tilt is constant throughout the length of a chain and if only the tilt varies down the series, δ would also be approximately constant. It, however, *increases* in a way that suggests that the tilts of those parts of the chains closest to the head group do not vary across the series. It should be emphasized that the disorder in these layers is such that there will be contributions to the structural parameters from static and dynamic disorder and the description given in terms of tilts above is necessarily over simplified.

For close–packed alkyl chains, of the type that form insoluble monolayers, the observation has generally been that the chains are fully extended and that they may be uniformly tilted with respect to the surface normal (see, for example (*13*)). This would mean that the thickness of the layer should increase with the length of the alkyl chain unless the tilt also increases. There is no systematic study of the effects of chainlength on layer thickness to give any guidance on this possibilty. For soluble monolayers the cross sectional area at the surface is almost double that of a typical insoluble monolayer, leading to very loose packing. Furthermore, the fact that the surfactant is completely soluble in the subphase means that, unlike the insoluble monolayers, the head group/water interactions must play as important a part in determining the possible orientations of the molecule as the chain–chain interactions. The combination of these two factors should lead to considerable disorder in the layer and this has been substantiated by computer simulation (*10*). The results that we have so far obtained for the C_nTAB series of molecules suggest that the molecules are tilted away from the surface normal, that there is some disorder in the *internal* chain conformation, and that the roughness of the layer is not very different from its intrinsic thickness. The lack of variation of the thickness of the layer with chain length would then seem to be associated with a tendency of the chains to cohere more strongly as their length increases. Given the large area per molecule this can only be achieved by the longer chains tilting more strongly away from the surface normal. This increasing tilt apparently compensates for the change in chain length. One study of the relation between chainlength and layer thickness has been made on a series of spread polymer monolayers, which gives some support to the present observations, although the nature of the layer is such that it falls in between a typical insoluble monolayer and a soluble surfactant monolayer (*14*). The thicknesses of spread layers of poly (N–alkyl–4–vinylpyridinium bromide) with alkyl chain lengths of 8, 10, 12, 14, 16, 18, 20, and 22 carbon atoms were measured at areas per segment of 30 – 40 Å^2 by x–ray reflection. The ratio of the observed thickness (modelled by uniform layers) to the fully extended chain length *decreased* from 1.3 at C_8 to 0.7 at C_{16} and C_{18} before increasing to 0.8 at C_{20} and C_{22}. Although these are insoluble monolayers, an important factor in the layer structure is the polymer backbone and it is this that competes with the alkyl chain interactions. The parallel with the C_nTAB layers is that the attractive alkyl chain interactions are not able to overcome the roughness of the polymer backbone until there are more than 18 carbon atoms.

Up to about C_{16} or C_{18} this roughness, which is related to the effective head group substrate interaction, dominates over the alkyl chain interaction. Thus we might expect that, depending on the strength and nature of the head group solvent interaction, the transition from disordered to ordered chains will occur somewhere between C_{14} and C_{20}. It may well be that this transition strongly parallels the Krafft point, the temperature above which micelles may form, which is also very dependent on the nature of the head group (see data in (*15*)).

Similar studies on the series of the non–ionic surfactant series, monododecyl oligoethylene ethers, $C_{12}E_m$ (*10*) show that the behaviour of hydrophilic chains is quite different from the hydrophobic chains above. Table 2 shows that the E_m chain increases systematically with *m*. At low *m* this behaviour is masked a little by the contribution from roughness, but the ratio of both σ_e and δ_{he} to the fully extended length l_e suggests that the hydrophilic chains are, like the hydrophobic alkyl chains, strongly tilted away from the surface normal. However, the rather slow increase of thickness with chainlength suggests that they are not fully extended (see (*16*)) and that they may not necessarily all be tilted similarly.

Literature Cited

(*1*) Lu, J.R.; Hromadova, M.; Thomas, R.K.; Penfold, J., *Langmuir*, **1993**, *9*, 2417.

(*2*) Lu, J.R.; Lee, E.M.; Thomas, R.K., *Acta Cryst.* (in press)

(*3*) Lu, J.R.; Li, Z.X.; Smallwood, J.; Thomas, R.K., *J. Phys. Chem.* (in press)

(*4*) Crowley, T.L., D. Dhil. Thesis, University of Oxford, 1984.

(*5*) Simister, E.A.; Lee, E.M., Thomas, R.K.; Penfold, J., *J. Phys. Chem.*, **1992**, *96*, 1373.

(*6*) Lu, J.R.; Hromadova, M.; Simister, E.A.; Thomas, R.K.; Penfold, J, *J. Phys. Chem.*, **1994**, *98*, 11519.

(*7*) Lu, J.R., Simister, E.A., Thomas, R.K., Penfold, J., *J. Phys. Chem.* **1993**, *97*, 6024.

(*8*) Lyttle, D.J.; Hromadova, M.; Lu, J.R.; Thomas,R.K.; Penfold, J., *Langmuir* (in press)

(*9*) Simister, E.A.; Lee, E.M.; Thomas, R.K; Penfold, J, Macromolecular Reports, 1992, *A29*, 155.

(*10*) Böcker,J.; Schlenkrich, M.; Bopp, P.; Brickmann, J., *J. Phys. Chem.* , **1992**, *96*, 9915.

(*11*) Schwartz, D.K.; Schlossman, M.L.; Kawamoto, E.H.; Kellogg, G.J.; Pershan, P.J.; Ocko, B.M., *Phys. Rev. A.*, **1990**, *41*, 5687.

(*12*) Lu, J.R; Li, Z.X.; Thomas, R.K.; Staples, E.J.; Thompson, L.; Tucker, I.; Penfold, J.;, *J. Phys. Chem.*, **1994**, *98*, 6559.

(*13*) Böhm, C.; Leveiller, F.; Jacquemain, D.; Möhwald, H.; Kjaer, K.; Als–Nielsen, J.; Weissbuch, I.; Leiserowitz, L., *Langmuir*, **1994**, *10*, 830.

(*14*) Styrkas, D.A.; Thomas, R.K.; Adib, Z.A.; Davis, F.; Hodge, P.; Liu, X.H., *Macromolecules*, **1994**, *27*, 5504.

(*16*) Mukerjee, P.; Mysels, K.J., *Critical Micelle Concentrations of Aqueous Surfactant Systems*, NSRDS–NBS 36, National Bureau of Standards, **1971**.

(*17*) Nikas, Y.J.; Puvvada, S.; Blankschtein, D., *Langmuir*, **1992**, *8*, 2680.

RECEIVED May 3, 1995

Chapter 22

Prepolymerized Langmuir–Blodgett Films of *n*-Octadecylsiloxane Monolayers

Atul N. Parikh[1], Jonathan Wood[2], Ravi Sharma[2], and David L. Allara[1]

[1]**Departments of Materials Science and Chemistry, Pennsylvania State University, University Park, PA 16802**
[2]**Materials Science and Engineering Division, Eastman Kodak Company, Rochester, NY 14650–2158**

Monolayers of *n*-octadecylsiloxane (ODS) have been prepared by Langmuir-Blodgett film transfer of pre-polymerized films onto oxidized silicon substrates at a surface pressure of 20 mN.m^{-2}. Characterization by infrared spectroscopy, single-wavelength ellipsometry, and contact angle measurements show that highly organized structures are formed which are nearly identical to those reported for ODS films made by solution self-assembly. Atomic force microscopy images reveal that the macroscopic structure of the LB film consists of large, dense domains on the size scale of ~10 μm.

Recently it has been shown(1) that densely packed, polymerized *n*-alkylsiloxane [$RSiO_x(OH)_y$] monolayer films, usually prepared by self-assembly from hydrocarbon solution,(2, 3) can be obtained by Langmuir-Blodgett film transfer from the air-water interface. In the above study,(1) *n*-octadecyltriethoxysilane [OTE; $H_3C(CH_2)_{17}Si(OC_2H_5)_3$] was spread at the air-water interface and LB films subsequently transferred onto mica substrates to yield polymerized *n*-octadecylsiloxane(ODS) monolayers. Characterization by wetting, ellipsometry, and surface force measurements showed the films to be quite hydrophobic and formed at high coverages. While these observations suggest a highly organized molecular packing, no direct structural evidence of the molecular structure was obtained. In this paper, we present preliminary results in which a combination of ellipsometry, wetting, atomic force microscopy (AFM), and infrared spectroscopic (IRS) measurements are applied to characterize details of the structures of ODS LB monolayers. In order to simplify the optical characterizations, oxidized silicon surfaces were used instead of mica, while mica was used in the parallel AFM measurements. This combination of characterization tools allows a direct comparison of the LB film structure with that reported previously for ODS monolayers prepared by self-assembly techniques.(4)

0097–6156/95/0615–0355$12.00/0

Experimental Section

Materials. Highly polished silicon wafers were used as film substrates for IRS, contact angle and ellipsometry measurements while freshly-cleaved mica sheets were used as substrates for AFM measurements. For IRS measurements the wafers (Harrick Scientific; Ossining, NY) had wedged faces to minimize interference fringes. The materials *n*-octadecyltriethoxysilane (OTE; Petrarch-Hüls America, Bristol, PA),ethanol (Quantum, Tuscola, IL), chloroform (Kodak, Rochester, NY) and methanol (Baker Analyzed, G. T. Baker) were used as recieved. For all cleaning and deposition procedures, deionized water (18.2 MΩ) was used. All glassware was cleaned by the sequence: 20-25 min. immersion in an ultrasonic bath contining 2% RBS solution (Phosphate-free RBS, Pierce, Rockford, IL) at 50 °C, extensive rinsing in deionized water, at least 1 hr soaking in fuming nitric acid (Reagent grade, Kodak, Rochester, NY), thorough rinsing in deionized water followed by ethanol, and finally air drying. For the Langmuir film preparation, the 0.01 M HNO_3 sub-phase was prepared by diluting 0.1 N HNO_3 (pre-packaged ampoules; J. T. Baker, Philipsburg, NJ) in the required proportions of deionized water.

Isotherm Measurements and Langmuir-Blodgett Film Deposition. All isotherm measurements and LB depositions were conducted on a commercial KSV 5000 (Helsinki, Finland) Langmuir trough. The procedures followed those described elsewhere(1). An acidic sub-phase was chosen since this condition leads to rapid hydrolysis of the triethoxy head-group to $-Si(OH)_3$ groups but relatively slow formation of Si-O-Si crosslinks(5). A 45 µL aliquot of 2 $mg.ml^{-1}$ OTE in chloroform/methanol (95/5 v/v) was spread drop-wise onto a freshly aspirated surface of the sub-phase. The solution was allowed to stand for ~40 min. in order to allow complete solvent evaporation and subsequent hydrolysis and polymerization of the triethoxy head-group. A 30 min. standing time allows complete evaporation of solvent and headgroup crosslinking at ~ 0 mN m^{-1} barrier pressure. Considerably longer standing times do not change the isotherm characteristics in any noticeable way. The sub-phase temperature during the isotherm run was held constant between 21 and 22 °C to an accuracy of ±0.1 °C. Multiple runs were made in order to ensure isotherm reproducibility and accuracy and the actual LB monolayer depositions were performed under identical conditions. Prior to monolayer deposition, silicon substrates were cleaned and oxidized using a combination of chemical (immersion in peroxysulfuric acid at ~110 °C for 10-15 min.) and photochemical (UV/ozone treatment; cleaning unit purchased from Boekle Industries, Philadelphia, PA) methods.(4) Mica substrates were freshly cleaved and then rendered highly hydrophilic by plasma treatment as described earlier.(1) The depositions were carried out by the upward drawing method at a constant substrate withdrawal rate of 5 mm $min.^{-1}$ with surface pressures (Π) of 20 mN m^{-1}. The final LB films were obtained by curing at ~100 °C for ~2 hrs in a vacuum oven. All films were stored in a dry atmosphere between use.

Contact angle measurements. Advancing and receding contact angle measurements were conducted by the sessile drop and captive drop methods using a Ramé-Hart Model 100 contact angle goniometer in which the chamber was maintained at 21.0 ±

0.5°C and saturated with the test-liquid vapor. Details can be found elsewhere.(4) Advancing angles of decane, dodecane, tetradecane, and hexadecane were used to assess the critical surface tension (γ_c) values using the standard extrapolation method of Zisman.(6)

Single-Wavelength Ellipsometric Measurements. Ellipsometry measurements (632.8 nm; 70° angle of incidence) were performed using a null-ellipsometer (Rudolph AutoEL-II, Fairfield, NJ). The experimental and analyses procedures are only summarized below since full details can be found elsewhere.(4) The measurement protocol for each sample involved the sequential measurement of the polarization parameters(7), Δ and Ψ, at three arbitrarily chosen spots on each sample immediately following substrate pre-cleaning and at variable times after film transfer. The overall, film thickness errors, in terms of sample-to-sample variations, are within ±1 Å.

Thickness were calculated from Δ and Ψ using a model of parallel, homogeneous layers with sharp, planar interfaces. The optical functions (refractive index or dielectric constant) of the initial SiO_2/Si substrates were derived from the Δ and Ψ values of bare substrates using a pseudo-two-medium **[SiO_2-Si]/air** model and subsequently applied to film thickness calculations using a three-medium **air/$RSiO_x$/SiO_2-Si** model in which the ODS film was treated as optically anisotropic in order to account rigorously for the effects of alkyl chain orientation.

Transmission Infrared Spectroscopy. Infrared spectra were collected in the transmission mode using a Fourier transform spectrometer (Bomem Model MB-100, Québec , Canada) operating at 2 cm^{-1} resolution with an unpolarized beam striking the sample at normal incidence. Details can be found elsewhere.(4) All spectra are reported as $-\log(T/T_0)$, where T and T_0 are the emission power spectra of each sample and its corresponding clean substrate obtained prior to deposition, respectively.

Atomic Force Microscopy (AFM) Measurements. AFM measurements were conducted in air in a clean, laboratory environment using a commercial Topometrix (Model TMX-2010) instrument with a nominal spring constant of ~0.12 N m^{-1}. The integrated perimeter, Si_3N_4 probe tips were obtained from Digital Instruments. Measurements were performed on ODS films deposited at 20 mN m^{-1} onto mica substrates, chosen to provide large-scale flat terraces for optimum AFM characterization. Because of the high flatness and comparable water wettability of the mica and SiO_2/Si substrates it is expected that highly comparable ODS films are formed.(4). Images were collected for low magnifications (50 μm x 50 μm) in a constant force mode.

Results and Discussion

Langmuir Isotherms. A representative compression isotherm obtained at ~21 °C is shown in Figure 1. Three distinct regions in the isotherm are easily distinguished: I.) a flat portion with the average area per molecule, A_m, ranging from ~45 to ~24 $Å^2$ $molecule^{-1}$ at $\Pi \leq 0.3$ mN m^{-1}, II.) a rapidly increasing portion with $24 \geq A_m \geq 17$ $Å^2$

molecule^{-1} and III.) a region of ultimate film collapse for $\Pi \geq 50$mN m^{-1}. These data are in excellent agreement with a previously reported isotherm collected under similar conditions(1) and are also in general qualitative agreement with isotherms reported(8,9) for Langmuir films prepared from the identical chain-length silanes, $CH_3(CH_2)_{17}NHCOCONHSi(OC_2H_5)_3$ and $CH_3(CH_2)_{17}SiCl_3$ (OTS), under conditions of sub-phase pH and temperature similar to the present experiments.

Several salient features of the phase behavior of the present OTE Langmuir films can be derived from the above data. First, the observation of the steep rise in region I indicates that upon compression the monolayer structure undergoes only a single significant phase transition before collapse. Based on A_m ~24 Å^2.molecule^{-1} at the transition, (to the left of the dashed line in Fig. 1), it appears that a liquid-condensed (LC) phase structure forms. Drawing on an analogy with typical C_{18} alkyl chain surfactant behavior,(10) the absence of an intermediate liquid-expanded (LE) phase indicates that the sub-phase temperature of ~20 °C is well below the triple point temperature [the simultaneous LC, LE and gas (G) co-existence point] above which the LE phase can exist. This conclusion is strongly supported by the recent observation that for analogous ODS monolayers self-assembled on SiO_2/Si substrates(4,11) a critical temperature (T_c) of 28 (±5)°C exists below which no general LC phase character is observed in the ODS film. Further support is obtained from grazing incidence X-ray diffraction measurements of ODS Langmuir monolayers at the air/water interface(9) which show that the monolayer structure in region II of the isotherm consists of alkyl chains in a hexagonal arrangement, although with short correlation lengths. Second, the observation of no appreciable rise in surface pressure at A_m ~24 Å^2 molecule^{-1} suggests that at A_m >24 Å^2 molecule^{-1}, the monolayer is composed of structurally uncorrelated, polymerized islands randomly placed on the sub-phase surface. Assuming the existence of only the G phase between the domains, the average degree of polymerization is estimated to be ~45-60, and consequently, an average size of a condensed domain would be ~200-270 Å. This value is lower than the size of ~700 Å estimated from the reported degree of polymerization equal to 155 for ODS Langmuir monolayers prepared using OTS precursor molecules(9). The above inference is consistent with the fact that the overall polymerization rate of the -$Si(OC_2H_5)$ head-group of OTE is significantly slower than the -$SiCl_3$ group of OTS molecules(12). The structure of these polymers must be quasi-two dimensional since the formation of a single linear oligomer of such a large degree of polymerization is difficult owing to the steric constrains on the Si-0-Si bond-angles and distances imposed by the pendant alkyl chain of 4.5-5.0 Å diameter(13). It is quite plausible, however, that the G phase domains themselves are not single, polymerized oligomers but are composed of loosely correlated aggregations of cyclic trimers or tetramers. Extrapolation of the isotherm curve in region II to zero surface pressure yields a value of A_{m0} ~22 Å^2 molecule^{-1}. This value falls in the range of 20-25 Å^2 molecule^{-1} which has been reported for single-chain *n*-alkanoic acid Langmuir monolayers(14) for which a film structure composed of closely spaced, highly organized islands has been observed. Finally, the high collapse pressure of ~50 mN m^{-1} in region III of Fig. 1 indicates the appearance of a significantly enhanced stability in these ODS monolayers compared to typical single alkyl chain surfactant layers(15) where typical collapse pressures of ~30-40 mN.m-1 are observed. This stability is consistent with the presence of intermolecular cross-linking or polymerization in the present ODS monolayers.

Transferred LB films on SiO_2/Si Substrates. Monolayer films were prepared at Π = 20 $mN.m^{-1}$ and a transfer ratio of ~1 was obtained in all depositions. The films always emerged completely dry (autophobic) from the sub-phase during the pull-up process.

Wetting measurements revealed a water contact angle of 113(±3)°, in quantitative agreement with that reported previously for mica(1) and for a self-assembled ODS monolayer on SiO_2/Si.(4) Hydrocarbon wetting measurements led to γ_c = 20.6 (±0.5) mN m^{-1}, in good agreement with the value of 20.5 mN m^{-1} reported for self-assembled ODS films(4,11).

Ellipsometry measurements led to a film thickness value of 24.2(±1) Å. A value of ~22 Å is estimated from the isotherm intercept, A_{m0} ~ 22 $Å^2$ $molecule^{-1}$, by using a theoretical maximum film coverage of 5.42 chains nm^{-2} together with a 26.2 Å maximum chain extension.(16) On the latter basis, the ellipsometric thickness of 24.2 Å corresponds to an equivalent coverage of 92%. The latter value is in excellent agreement with that of 87-95% obtained for self-assembled ODS monolayers.(4) Figure 2 shows the IRS spectrum in the C-H stretching mode frequency region. The spectrum is characterized by the presence of three distinct peaks at ~2848, ~2916.1, and ~2957 cm^{-1} which are assigned(17) to the methylene C-H symmetric (d^+) and antisymmetric (d^-) stretching modes and the methyl C-H antisymmetric stretching modes, respectively. Based on previous correlations,(18, 19) the values of the d^- and d^+ frequencies lead to the conclusion that an average alkyl chain in the ODS film is highly conformationally ordered, close to an all-*trans* state, and exists in a crystalline-like environment.

Atomic Force Microscopy Data. Figure 3 shows an AFM image (50 μm x 50 μm) of an OTE LB film transferred onto a companion, plasma-treated mica substrate at Π=20 mN m^{-1}. The image clearly reveals a large number of interconnected domains or islands of distorted circular shapes with smooth edges. The average domain sizes, ignoring the bridge regions, occur in a remarkably narrow distribution of ~12.5 ±1.2 μm and the height difference between the inter-domain boundary region and the domain surfaces is ~12±3 Å.(20) The observation of distorted shapes of closely spaced, often touching domains is entirely consistent with the crystalline-like organization of chains shown by the IRS data. We note that the estimated 12 Å domain height is significantly lower than the ellipsometrically determined film thickness of ~24 Å. This difference is consistent with a film structure in which islands of conformationally ordered all-*trans* extended chains are separated by boundary regions of disordered chains at reduced densities (G phase). This mixed morphology is reminiscent of the LC-G phase co-existence which obtains for equilibrium Langmuir films at arbitrary surface-pressures below the LC-LE-G triple point temperature(21).

Thermally Induced Structural Changes. The previous sections show that the LB films transferred at Π=20 $mN.m^{-2}$ are densely-packed with their alkyl chains in nearly all-*trans* conformational sequences. It would be expected that such a dense structure

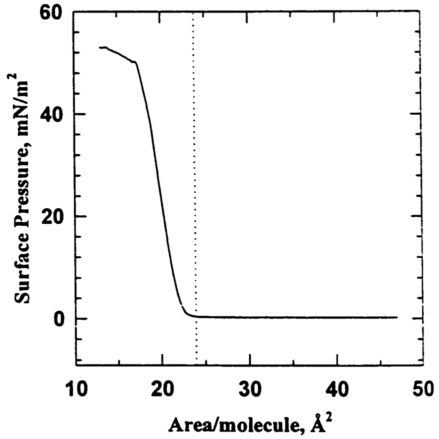

Figure 1. Surface pressure vs average area per molecule for an octadecylsiloxane film at the air-water interface with an acidic sub-phase at 21 °C.

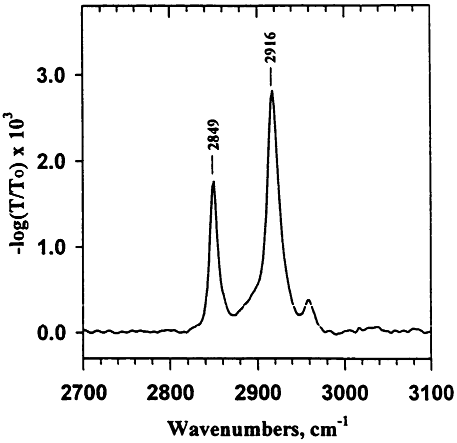

Figure 2. A representative transmission infrared spectrum in the C-H stretching region of an octadecylsiloxane Langmuir-Blodgett film withdrawn at a surface pressure 20 mN.m^{-2} onto an oxidized silicon substrate.

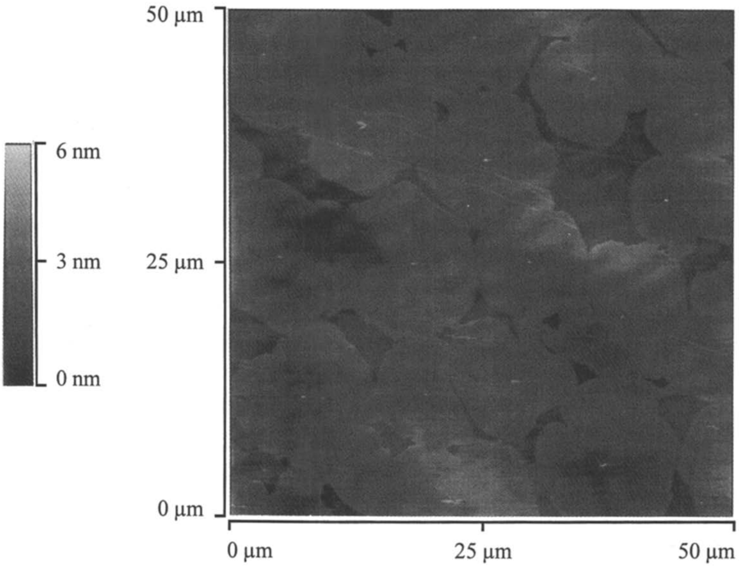

Figure 3. An atomic force microscopy image (50 μm scale) of a Langmuir-Blodgett film of an octadecylsiloxane Langmuir-Blodgett film withdrawn at a surface pressure of 20 mN.m^{-2} onto mica substrates.

would lead to a lack of response to thermal stress. Analysis of IRS spectra taken at room temperature and 160 °C reveal that the d^+ and d^- peak positions shift upward by ~2.6 and ~4.9 cm^{-1}, respectively, upon heating. This shift is accompanied by a slight but progressive increase in the peak-widths. While these changes are consistent with increasing *gauche* content in the film, the small magnitude of the changes are quite noteworthy when compared with reported changes observed in bulk *n*-alkane crystals(22) and other monolayer alkyl chain assemblies of comparably high organizations. For example, for *n*-alkanethiolate monolayers on Au(111) surfaces heated over the same temperature range,(23) the d^+ and d^- peak positions shift upward by ~4 and 8 cm^{-1}, respectively. The relatively smaller shifts of the ODS films can be taken as evidence for a smaller available space within the LB chain assemblies for accommodation of increasing chain disorder as compared to the alkanethiolate/Au SAMs.

Conclusion

The characterization of ODS Langmuir films transferred to hydrophilic substrates at a high surface pressure of 20 $mN.m^{-2}$ shows that a highly organized film structure is obtained which closely approaches the limit of LC Langmuir phases of *n*-alkyl surfactant films and is quite similar to that obtained from solution self-assembly methods. Atomic force microscopy images reveal an islanded structure of large domains which indicates that intermolecular polymerization at the air-water interface is a relatively slow process which does not significantly hinder formation of highly organized, dense structures.

Acknowledgment

This work was supported in part by the National Science Foundation (Grant No. DMR-900-1270; for DLA and ANP).

References

1 Wood, J.; Sharma, R. *Langmuir* **1994**, 10, 2307-2310.
2 For example, see: A. Ulman, *Introduction to Ultra-thin Organic Films: From Langmuir Blodgett to Self-Assembly*; Academic, San Diego, CA 1991.
3 Maoz, R. and Sagiv, J. *J. Colloid Interface Sci.* **1984**, 100, 465-496.
4 Parikh, A. N.; Allara, D. L.; BenAzouz, I.; Rondelez, F. *J. Phys. Chem.* **1994,** 98, 7577-7590.
5 Devreux, F.; Boilot, J. P.; Chaput, F.; Lecomte, A. *Phys. Rev. A* **1990**, 41, 6901-6909.
6 Zisman, W. A. *Adv. Chem. Ser.* **1964**, No. 43, 1-51.
7 See, for example: Azzam, R. M. A.; Bashara, N. M. *Ellipsometry and Polarized Light;* North-Holland : Amsterdam, The Netherlands 1977.
8 Ariga, K.; Okahata, Y. *J. Am. Chem. Soc.* **1989**, 111, 5618-5622.
9 Barton, S. W.; Goudot, A.; Rondelez, F. *Langmuir* **1991**, 7, 1029.

10 Kellner, B. M. J.; Muller-Landau, F.; Cadenhead, D. A. *J. Colloid Interface Sc.* **1978**, 66, 3.

11 Brzoska, J. B.; Shahidzadeh, N.; Rondelez, F. *Nature* **1992**, 360, 719-721.

12 Pluedemann, E. P. *Silane Coupling Agents;* Plenum: New York, 1990.

13 Ulman, A.; *Adv. Mater.* **1990**, 2, 573-582

14 See, for example: Deamer, D. W.; Meek, D. W.; Cornell, D. G. *J. Lipid Res.* **1967**, 8, 255.

15 Gaines, G. L., Jr. *Insoluble Monolayers at Liquid-Gas Interfaces;* Interscience: New York, 1966.

16 Wasserman, S. R.; Tao, Y.-T.; Whitesides, G. M. *Langmuir* **1989**, 5, 1074.

17 Dubois, L. H.; Nuzzo, R.G.; Allara, D. L. *J. Am. Chem. Soc.* **1990**, 112, 558-569.

18 (a) Snyder, R. G.; Schachtschneider, J. H. *Spectrochim. Acta* **1963**, 19, 85-116 (b) MacPhail, R. A.; Strauss, H. L.;Snyder, R. G.; Elliger, C. A. *J. Phys. Chem.* **1982**, 88, 334-341 (c) Snyder, R. G.; Hsu, S.L.; Krimm, S. *Spectrochim. Acta Part A* **1978**, 34, 395-406. (d) Hill, I. R.; Lewin, I. W. *J. Chem. Phys.* **1979**, 70, 842-581.

19 Snyder, R. G.; Strauss, H. L.; Elliger, C. A. *J. Phys. Chem.* **1982**, 86, 5145-5150.

20 The above images are in strong contrast to those obtained in independent AFM studies of self-assembled ODS films on SiO_2/Si substrates where polygonal islands are observed with several tens of nanometer lateral spans [Allara, D.L.; Parikh, A.N.; Coulman, D.; Rondelez, F. manuscript submitted for publication]. These contrasting observations suggest that pre-polymerization at the air-water interface leads to much larger LC domains than do self-assembly conditions. This difference most likely arises because of more extensive relaxation of domain structures at the air-water interface than directly on solid substrates.

21 See, for example: Knobler, C. M. *Science* **1990,** 249, 870-876.

22 Snyder, R.G.; Maroncelli, M.; Strauss, H. L.; Hallmark, V. M. *J. Phys. Chem.* **1986**, 90, 5623-5630.

23 (a) Nuzzo, R.G.; Korenic, E. M.; Dubois, L. H. *J. Chem. Phys.* **1990**, 93, 767-773 (b) Dubois, L. H.; Zegarski, B. R.; Nuzzo, R. G. *J. Electron Spec. Rel. Phenom.* **1990**, 54/55, 1143-1152.

RECEIVED September 7, 1995

Chapter 23

Surface Charging Effects at Gelatin–Silica Interfaces

D. T. Smith[1] and Ravi Sharma[2]

[1]Ceramics Division, National Institute of Standards and Technology, Gaithersburg, MD 20899
[2]Materials Science and Engineering Division, Eastman Kodak Company, Rochester, NY 14650–2158

An experimental technique based on the Surface Force Apparatus is used to study contact electrification at the interface between amorphous silica and photographic gelatin coated on mica. Results are presented of the charge transferred from one surface to the other in non-sliding contact for several gelatin compositions containing different surfactants. In addition, the decay of surface charge in dry and humid environments is reported. Significant variation in both the charge transfer and charge decay behavior of the gelatins as a function of surfactant additive is observed.

When two different materials come into contact, electric charge often transfers from one to the other, resulting in two equally, but oppositely, charged surfaces (contact electrification) (*1,2*). The precise reasons why and the mechanisms whereby this occurs are not always clear, particularly with insulating materials, but in broad terms the effect can be explained as the movement of charge from one material to the other so as to equalize the Fermi levels of the two materials. This effect is enhanced when the surfaces slide over each other (tribocharging), and can be particularly problematic in manufacturing, where resulting high potential differences can damage electronic circuits and generate gas discharges that are capable of fogging film or causing explosions. Alternatively, tribocharging can be desirable in applications such as photocopying and laser printing, where toner particles are deliberately charged through contact with larger particles of another material.

Recently, contact electrification has been studied between mica and silica (*3*) and between treated and untreated silica surfaces (*4*) using a Surface Force Apparatus (SFA) modified to incorporate two *in situ* electrometers (*5*). The instrument provides a means of measuring both the surface charge and the true area of contact, thus enabling accurate determination of surface charge density. It also allows measurement

0097–6156/95/0615–0364$12.00/0

of the attractive force between the surfaces during separation of the charge double layer. In the earlier work (*3,4*), it was observed that charge densities as high as 20 mC/m^2 could be created in the simple, non-sliding contact of cleaved mica and smooth silica surfaces. These high densities resulted in a work of adhesion of the interface (*i.e.*, the integral of the measured force between the surfaces as they are moved from contact to large separation) of several J/m^2, comparable to the cohesive energies of the individual solids. They also created electric fields and potential differences in the gap during separation that were high enough to cause dielectric breakdown of the intervening nitrogen gas.

In this report we present results, obtained using the same apparatus, on contact electrification between silica and photographic gelatin. Of particular interest were the effects of several surfactants, commonly added to gelatin as coating aids or antistats, on charge transfer and charge decay. Silica was chosen as a reference contact surface for the experiments because of its high surface smoothness and low electrical conductivity (described below). The experiments were performed both in dry nitrogen gas and in air at 33% relative humidity, and the rates of decay of charge for the two conditions are noted.

Experimental Technique

The Surface Force Apparatus. The experimental system is based on the SFA, a device developed primarily by Israelachvili (*6*) to measure the forces between molecularly smooth solid surfaces in a variety of environments including dry air or nitrogen, partial pressures of other vapors, or bulk liquids. The specimens to be studied are prepared as thin sheets (typically 2 μm to 10 μm thick) that are coated on their back surfaces with 50 nm of silver vacuum deposited by evaporation, and glued to cylindrical lenses of radius $R \approx 10$ mm. The lenses are then mounted in the SFA with their axes at right angles. Two mechanical stages and a final piezo-electric stage are used to control the surface separation to better than 0.1 nm. The force between the surfaces is determined by measuring the deflection of a double cantilever spring that supports the lower lens.

Optical interferometry is used to determine the separation profile of the two surfaces; white light is incident on the crossed-cylinder system from below, as shown in Figure 1, and light that passes through the interferometer formed by the silver layers is collected by a microscope objective and focused on the entrance slit of a spectrometer. At the output of the spectrometer, Fringes of Equal Chromatic Order (FECO) are observed and recorded; they are analyzed to yield the surface separation profile and the thicknesses of the dielectric films between the silver layers (*7*). Resolution in surface separation of 0.1-0.2 nm is possible. When the surfaces touch, they form a flattened, approximately circular contact area. This flattening is the result of elastic deformation in the glue supporting the substrates; the glue is substantially softer than the mica and silica substrates. An external load is not required to create the flattened contact area; attractive forces between the surfaces create contact areas with typical diameters, ϕ, in the range $75\mu m \le \phi \le 150\mu m$. Larger diameters can be obtained by adding an external load. This contact area can be clearly seen and measured using FECO and, when combined with the surface charge measurement described below, enables the accurate determination of surface charge density.

Preparation of Surfaces.

Silica. One of us (DTS) has developed a technique for preparing silica surfaces of sufficient smoothness and cleanliness for use in the SFA. The technique, described more fully elsewhere (*8*), involves blowing a thin bubble of molten silica (Suprasil F100, Heraeus-Amersil, Buford, GA) that cools rapidly and solidifies under tension. (Certain trade names and products of companies are identified in this paper to adequately specify the materials and equipment used in this research. In no case does such identification imply that the products are necessarily the best available for the purpose or that they are recommended by NIST.) Atomic force microscopy and talystep profilometry measurements made at NIST show an average surface roughness for the silica of less than 0.5 nm.

Gelatin Coatings on Mica. Mica sheets were used as substrates for deposition of the gelatin coatings. Mica is the material most often chosen for use in the SFA, because it can easily be cleaved into smooth, thin transparent sheets. Mica specimens used in this work were approximately 5 μm thick, and were prepared by cleaving thin, step-free pieces from thicker samples of Muscovite mica. The mica was freshly cleaved, silvered and glued to the glass disks used in the surface force apparatus.

Photographic grade lime-processed gelatin (Eastman Gelatin, isoelectric point ≈ pH 5) was used without further purification, as was Bis(vinylsulfonyl)methane (BVSM), a crosslinking agent commonly used to harden gelatin. BVSM was used in all gelatin formulations. The surfactant additives, which included alkanol xc (AXC, DuPont), fluorinated alkyl quaternary ammonium iodide (FC135, 3M), and polyethylene oxide (9 units) - tridecyl alcohol (PEO(9)TDA, Trycol 5944 from Henkel) were also used without further purification. Water was double-distilled before being further purified by a Milli-Q water polishing unit to give a final resistivity of 18 MΩ·cm. A freshly prepared gelatin solution in deionized water (2 wt% gelatin) containing BVSM (0.35 mg/g gelatin) was pipetted over the glued mica sheets so as to completely cover the surface. The sample was then spun at 2000 RPM for 20 s, and allowed to dry in a laminar flow hood for 3 hours. Surfactants were added to the gelatin solution in the following quantities: AXC, 0.008 wt%; FC135, 0.004 wt%; and PEO(9)TDA, 0.02 wt%. The gelatin coatings were cured at room temperature in a sealed container for a period of 4 days before being used. The gelatin was hardened so that it would be less tacky, thereby minimizing adhesive transfer of gelatin to the opposing surface upon separation. Coating thicknesses were typically 2–3 μm.

Electrical Connection. In addition to creating the interferometric cavity needed to measure surface separation and contact area, the silver layers behind each substrate were also used as part of an electrometer circuit (described below) to measure net surface charge. Electrical contact to each silver layer was accomplished by attaching a #40 copper wire to the layer using indium just above its melting point as solder (see Figure 1). Contact resistances were typically less than 1 Ω; silver layer resistance was on the order of 1 Ω/square.

Measurement of Surface Charge. When charge is transferred from one surface to the other during the contact of two dissimilar materials in the SFA, it is desirable to measure that charge *in situ*, without having to remove the surfaces and use an external probe. The presence of the silver layer on the back side of each substrate used in the SFA presents the means for making that *in situ* measurement. The technique, shown schematically in Figure 2, and described in detail elsewhere (*5*), relies on the fact that if a double layer of charge (Q_s) forms at the contact interface (Figure 2a) and is separated by pulling the surfaces apart (Figure 2b), the potential of the (electrically isolated) silver layer will shift in response to the field from the layer of surface charge. Conversely, if the silver layer is held at fixed (typically ground) potential during separation, through an electrometer circuit for example, a current will flow into or out of the silver layer (resulting in charge $\pm Q_{Ag}$ in Figure 2a); this method of measuring surface charge is commonly referred to as a "proof plane" technique. If the surfaces are pulled quickly apart to large separation (relative to the substrate thickness), the integral of the current into or out of each silver layer will be, to a very good approximation, equal to the amount of charge on the surface of each substrate. Figure 2 shows only the section of the surfaces which contact; their shape changes during separation, from parallel plates to cylindrical curvature, but because they are moved to what is effectively infinite separation, and because the curvature is slight compared with the sample thickness, the small change in geometry is not a source of error.

The primary measurement made in each experiment involved moving the surfaces in and out of contact several times with the piezo-electric tube until subsequent contacts transferred no further charge (typically 5 to 10 contacts), then pulling the surfaces from contact to large separation (greater than 500 μm) in approximately 2 s. This separation resulted in sharp steps in the integrator output voltages, the heights of which were proportional to the charge remaining on the surfaces. Voltage-vs-time data during this process were digitized and stored, and measurements of the FECO fringes were made when the surfaces were in contact, so that the contact diameter could be accurately determined. Surfaces could be moved relative to one another without opening the apparatus, allowing measurements to be made at new locations on each surface well removed from areas where previous contacts had been made.

As discussed above, the surfaces are extremely smooth and the contact area can be measured directly from the interferometry fringes; therefore, the true surface charge density in the contact area can be determined to a relatively high degree of precision. In addition, the time required to make the measurement is limited only by the time required to separate the surfaces, typically one to two seconds. Consequently, electrometer drift (the integration of error currents within the electrometer itself) is not a problem for the surface charge measurement.

Measurements were made both in dry nitrogen gas and in air with 33% relative humidity. Relative humidity was controlled by placing approximately 5 mL of a saturated $MgCl_2$ solution (*9*) in a beaker inside the SFA, which has an internal volume of 0.4 L; room temperature was regulated at 21 °C ± 0.5 °C.

Measurement of Charge Decay. When it is desirable to monitor surface charge for longer periods of time, as in a charge decay measurement, electrometer drift very

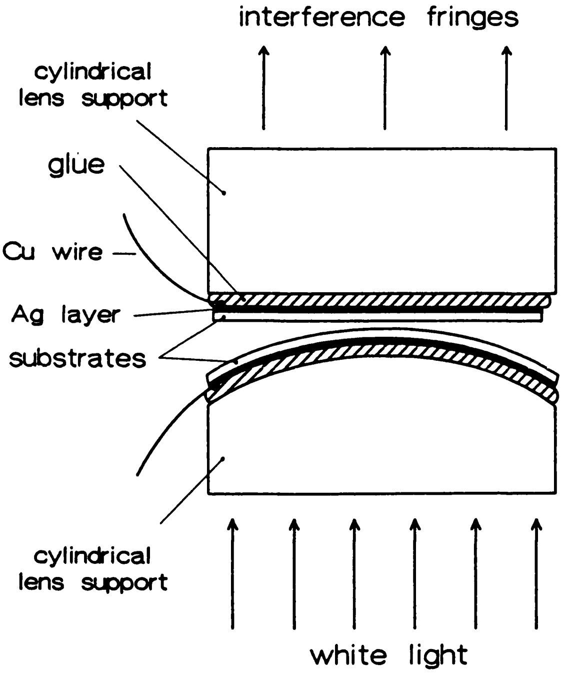
interference fringes
cylindrical lens support
glue
Cu wire
Ag layer
substrates
cylindrical lens support
white light

Figure 1. Schematic cross-section of the crossed cylinders. The drawing is not to scale; the thicknesses of the substrates/specimens, silver layers and glue are exaggerated for visibility. (Adapted from ref. 5.)

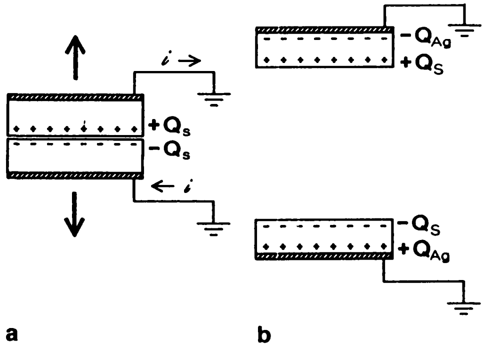
i →
+Q$_s$
−Q$_s$
← i
−Q$_{Ag}$
+Q$_S$
−Q$_S$
+Q$_{Ag}$
a
b

Figure 2. Schematic representation of the separation of two insulating surfaces with grounded metal backing layers, showing the surfaces (a) in contact and (b) after separation. (Adapted from ref. 5.)

quickly becomes a significant source of error. In this situation, an alternate technique that measures *changes* in surface charge relative to some initial value is employed.

A straightforward analysis of the electric field strength resulting from the separation of the transferred double layer at the interface gives the relationship between the charge measured on the silver layer, Q_{Ag}, and the actual charge on the surface, Q_s, as a function of surface separation D, as $Q_{Ag} = DQ_s/[(Y_1/K_1)+(Y_2/K_2)+D]$, where Y_1 (Y_2) and K_1 (K_2) are respectively the thickness and dielectric constant of the first (second) substrate. This analysis assumes that the system behaves as an infinite parallel-plate capacitor within the contact area, a good approximation here because substrate thicknesses are on the order of 5 μm, while contact diameters are typically 75 to 150 μm. In the limit of D large compared to the quantity $(Y_1/K_1)+(Y_2/K_2)$, the equation above reduces to the expected result that the full charge Q_s appears on each silver layer; a separation of only 200 μm results in $Q_{Ag} = 0.99Q_s$ for 5 μm-thick substrates. In the limit of D small, however, the charge seen on the silver layer depends linearly on both D and Q_s. It is possible, therefore, to monitor changes in surface charge using small changes in D.

In practice, the surfaces are moved quickly (within 1 s) from contact to a separation of 270 nm (at the closest point) and are held there. A small (~ 10 nm) 1 kHz modulation of the separation is generated by superposing an AC voltage on the DC piezo voltage that controls the separation. The magnitude of the electrometer AC response, detected using a lock-in amplifier, is directly proportional to the surface charge density, but also depends on the average surface separation, so a constant average separation must be maintained.

Results

Observed Surface Charge Densities. The primary results of this study are presented in Table I, which shows the net charge density on each gelatin surface following contact with silica in both dry nitrogen and air at 33% relative humidity. The total charge on each surface was measured by quickly pulling the surfaces from contact to large separation and observing the amount of charge moving into or out of each silver layer,

Table I. Surface charge density on gelatin surfaces following contact with silica

Gelatin Composition (all with BVSM)	*σ_s (mC/m^2) Dry Nitrogen*	*σ_s (mC/m^2) Air at 33% RH*
Gelatin	5.3 – 5.9	3.3 – 3.8
Gelatin + AXC	5.8 – 6.3	2.0 – 2.2
Gelatin + FC135	4.2 – 4.5	3.0 – 3.2
Gelatin + AXC + FC135	3.4 – 4.4	2.4 – 2.7
Gelatin + PEO(9)TDA	1.3 – 1.5	0.9 – 1.1

as described above. In each case, the gelatin surface was positive after contact, and a charge equal in magnitude but opposite in sign was observed on the silica surface, as expected. Charge density was determined by dividing that charge by the area of the contact circle prior to separation. The charge densities observed varied somewhat from position to position, and to a lesser extent from contact to contact at the same position, within the ranges shown in the table. This variability is common in charge transfer experiments, and is usually attributed to slight inhomogeneities in one or both surfaces. It is the largest source of uncertainty in the measurement. The uncertainty in individual measurements is typically on the order of 5%; most is the result of the accuracy with which the contact area can be determined from the FECO.

Table I reveals several important features of the charging behavior of the gelatin/surfactant systems. First, the added surfactants have a clear influence on the ability of the coating to charge (or to resist charging, depending on one's perspective), with FC135 and PEO(9)TDA both significantly reducing surface charging relative to gelatin with BVSM alone. Addition of AXC alone has little effect in dry nitrogen, but lowers charging when used in conjunction with FC135. Second, the presence of water vapor at 33% RH reduces contact charging of most of the gelatins to 0.6–0.7 of the value seen under dry conditions. The exception to this is gelatin+AXC, for which the charge drops by more than half; this may in part be due to an experimental artifact related to charge decay rate that is discussed below.

Interfacial Electrostatic Adhesion. In addition to measuring the surface charge density in these systems, it is also possible to measure the work of adhesion that results from the separation of the charge double layer. The force between the surfaces is measured from contact to separations larger than the range of the force (typically 2–3 μm), and is integrated to obtain the total work required to separate the surfaces. This approach has been used in several systems where charge densities comparable to those for gelatin–silica system are observed (*3,4*). Because of the strength and the long range of the attractive interaction (relative to a van der Waals interaction, for example), works of adhesion for systems like mica–silica (*3*) in dry N_2 are in the range 5–7 J/m^2, comparable to the cohesive energy of either of the individual materials. In this work, the adhesion was measured for the silica–plain gelatin system and was found to be 1.6 J/m^2, significantly higher than would be observed in the absence of charge transfer. The van der Waals attraction in this system, for example, would result in a work of adhesion on the order of only 50 mJ/m^2 (*10*).

Observed Charge Decay. Charge decay in dry nitrogen and air at 33% relative humidity is shown in Figures 3 and 4 respectively. Plotted is the surface charge at time t, $\sigma(t)$, normalized by the charge $\sigma(0)$ at t=0, the moment of surface separation. Note the differences in scale between the two figures. The irregularities in the curves are the result of manual adjustments to the piezo tube DC voltage required to keep the separation constant, and are particularly pronounced on the expanded scale in Figure 3.

Within the error of the measurement, little or no systematic difference in the decay of charge in the dry environment is observed among the varying gelatin compositions; after 200 s in dry nitrogen, all gelatin systems retained more than 0.98 of their initial surface charge. At 33% RH, however (Figure 4), the systems show dramatically

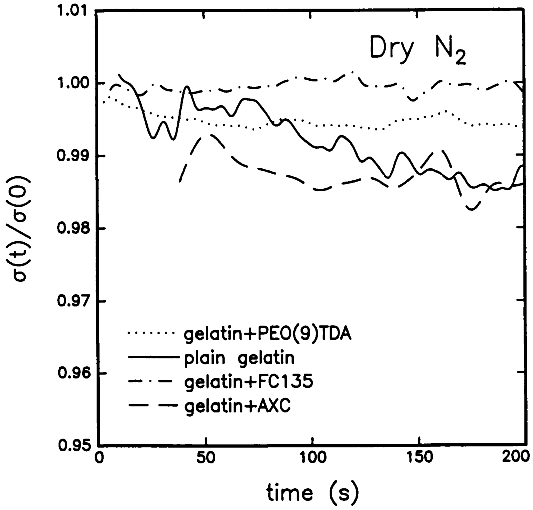

Figure 3. Rate of decay of surface charge, measured in dry nitrogen gas, for silica contact with gelatin. Each plot shows the net surface charge density σ(t) normalized by the charge density at the instant of separation, σ(0).

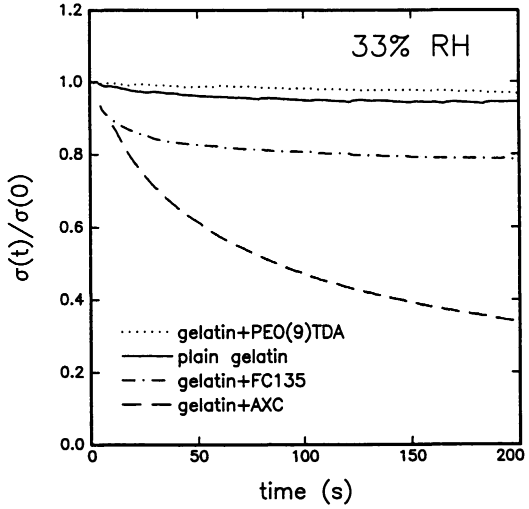

Figure 4. Rate of decay of surface charge, measured in air at 33% relative humidity, for silica contact with gelatin. Note the difference in the y-axis range between Figures 3 and 4.

different decay behavior, with gelatin+AXC decaying most rapidly and gelatin+PEO(9)TDA most slowly. The rapid decay seen for gelatin+AXC may in part explain the low value of the surface charge density observed in that system at 33% RH; some of the charge may decay in the time it takes to make the density measurement (typically 2 s).

A quantitative analysis of the decay data presented in Figure 4 is quite complex and has not yet been successfully completed; each electrometer responds to the combined decay of charge on both surfaces, and determining *where* the net charge is going (*e.g.*, leaking away through increased surface or bulk conductivity, or being neutralized by ions in the vapor) is not straightforward. The decay curves do not in general fit simple exponential functions. Furthermore, during the decay measurement the electric field within the gelatin is reduced significantly by the presence of the charge on the nearby silica surface. If the gelatin conductivity is field dependent, decay rates on isolated gelatin surfaces will be higher than those shown in Figures 3 and 4. Despite the ambiguities in the measurement, however, the comparison of the decay rates for the different formulations is still informative, since the silica used is common to all the measurements. Surface force measurements in aqueous salt solutions (*11*) show that the density of surface hydroxyl groups on this silica is only 2 per nm^2. Water does not wet these surfaces well (we observe an advancing wetting angle of 41°– 45°), and the surface conductivity for relative humidities below 50% is low (*12*). This makes it reasonable to assume that the differences in the combined decay shown in Figure 4 are the result of differences in the conductivity of the gelatin formulations. Gelatin, even under very dry conditions, typically contains some water incorporated into its structure, but in a bound form (*13*). When the humidity is increased to 11%, the additional water is believed to still exist in a bound form, and contributes little conductivity. When the humidity reaches 33%, however, the water absorbed by the gelatin is freer to move, in analogy to observations by Nomura et al (*14*) on the related protein collagen. Sheppard *et al.* (*13*) report a thousandfold increase in gelatin conductivity when changing from 11% to 33% RH. The surfactant additives appear to have a strong effect on the water mobility and consequent conductivity of the gelatin formulations, but the mechanism for this interaction is not understood.

Summary

We report measurements of the charge transfer and decay at the interface between silica and several gelatin surfaces. Due to the exceptional smoothness of the surfaces, intimate molecular contact is achieved, and surface charge densities as high as 6 mC/m^2 are observed following contact in the silica–gelatin system. This charge transfer results in a work of adhesion for the interface of 1.6 J/m^2, comparable to the cohesive energy of the individual solids. The decay of surface charge is also measured in the silica–gelatin system, and is seen to increase dramatically in some of the gelatin systems when the humidity is increased, presumably because the absorbed water is free to move within the gelatin structure. These results may prove useful in understanding the tribocharging behavior of gelatin-coated systems (*e.g.*, photographic film) during manufacturing and use.

Literature Cited

[1]Harper, W.R. *Contact and Frictional Electrification;* Oxford Univ. Press, Oxford, 1967.

[2]Lowell, J.; Rose-Innes, A.C. *Adv. Phys.* **1980**, *29,* 947.

[3]Horn, R.G.; Smith, D.T. *Science* **1992**, *256,* 362.

[4]Horn, R.G.; Smith, D.T. *Nature* **1993**, *366*, 442.

[5]Smith, D.T. *J. Electrostat.* **1991**, *26*, 291.

[6]Israelachvili, J.N.; Adams, G.E. *J. Chem. Soc. Faraday Trans. 1* **1978**, *74*, 975.

[7]Horn, R.G.; Smith, D.T. *Appl. Opt.* **1991**, *30*, 59.

[8]Horn, R.G.; Smith, D.T.; Haller, W. *Chem. Phys. Lett.* **1989**, *162*, 404.

[9]Greenspan, L. *J. Res. N. Bureau Stands,–A, Phys. and Chem.* **1977**, *162,* 89, and references therein.

[10]Israelachvili, J.N. *Intermolecular and Surface Forces;* Academic Press: New York, NY, 1991; Second edition.

[11]Grabbe, A. *Langmuir* **1993**, *9*, 797.

[12]For mica and glass surface conductivity data see Jonscher, A.K.; Chaudhry, M.A.; Goel, T.C. *IEEE Transactions on Electrical Insulation* **198823**, *23*, 397.

[13]Sheppard, S.E.; Houck, R.C.; Dittmar, C. *J. Phys. Chem.* **1940**, *44*, 185.

[14]Nomura, S.; Hiltner, A.; Lando, J.B.; Baer, E. "Interactions of Water with Native Collagen," in *Biopolymers;* 16; Wiley: New York, NY, 1977; pp 231-246.

RECEIVED July 24, 1995

Chapter 24

Determination of Ultralow Interfacial Tension by Axisymmetric Drop-Shape Analysis

D. Y. Kwok[1], P. Chiefalo[1], B. Khorshiddoust[1], S. Lahooti[1], M. A. Cabrerizo-Vilchez[2], O. del Rio[1], and A. W. Neumann[1]

[1]Department of Mechanical Engineering, University of Toronto, 5 King's College Road, Toronto, Ontario M5S 1A4, Canada
[2]Departamento de Fisica Aplicada, Universidad de Granada, Campus de Fuentenueva, 18071 Granada, Spain

It is shown that Axisymmetric Drop Shape Analysis (ADSA) is well-suited to study ultra-low interfacial tensions down to at least the order of 10^{-3} mJ/m^2: The technique is not restricted to equilibrium interfacial tensions, it is also suitable for measuring the time dependence of ultra-low interfacial tensions in the presence of surface active materials. The capability of ADSA to measure ultra-low interfacial tensions is shown by forming inverted sessile drops for two liquid-liquid surfactant systems: Oleic acid in olive oil with aqueous solution of NaCl and NaOH and Dioctyl Sulfosuccinate (AOT) in aqueous solution of NaCl/water and *n*-heptane.

Many techniques have been developed to measure interfacial tensions and detailed descriptions of the methods can be found in Padday (*1*), Ambwani and Fort (*2*), Adamson (*3*), and Neumann and Good (*4*). Among the commonly used methods for interfacial tensions, drop shape methods are very promising; they are based on the idea that the shape of a sessile or pendant drop is determined by a combination of surface tension and gravity effects. When gravitational and surface tension effects are comparable, one can, in principle, determine the surface tension from the measurements of the shape of the drop or bubble. A general procedure is to form the drop or bubble under static conditions and then to make certain measurements of its dimensions, for example, from a photograph.

The advantages of using pendant and sessile drop methods are as follows. First, only small quantities of liquid are required. Second, they can be used to study both liquid-vapour and liquid-liquid interfacial tensions. The methods have been applied to materials ranging from organic liquids to molten metals and from

0097–6156/95/0615–0374$12.00/0

pure solvent to concentrated solutions. Equally satisfactory, both methods have been applied at low and high temperatures, at high pressures and under vacuum conditions. Since the profile of the drops can be rapidly recorded, these methods are used to determine the surface tension of aging systems, i.e., systems where the properties are changing with time.

Despite the experimental simplicity in using sessile and pendant drops for determining interfacial tension and contact angle, there are doubts remaining whenever high precision and consistency are needed. Usually, the cases of sessile and pendant drops are treated separately, and the experimental information has to be interpreted with different sets of tables. Such tables are those of Bashforth and Adams (*5*) for sessile drops, and of Fordham (*6*) for pendant drops, as well as other tables (*7*). The use of the tables is limited to drops of a certain size range and drops of a certain shape range. Hartland and Hartley collected numerous solutions for determining the interfacial tensions of axisymmetric liquid-fluid interfaces of different shapes and presented the results in tabulated form (*8*). A serious and perhaps major source of error in these methods is connected with input data selection. The description of the whole surface of the drop is reduced to the measurements of a few preselected critical points which are compatible with the use of the tables. These points are critical since they must be determined with high precision.

More recently, Rotenberg *et al.* (*9*) have developed a drop shape technique called Axisymmetric Drop Shape Analysis (ADSA). It relies on a numerical integration of the Laplace equation of capillarity (see below). This numerical procedure unifies both the method of the sessile drop and the method of the pendant drop. There is no need for any table nor is there any restriction on the applicability of the method. It is a powerful and versatile methodology in interfacial energetics; it has been applied to drop size dependence of contact angles and line tension (*10*), contact angle measurements with an accuracy exceeding other methods by an order of magnitude (*11*), the pressure dependence of liquid/liquid interfacial tensions (*12*), film balance experiments with insoluble films (*13*) and a variety of studies on the time dependence of liquid/fluid interfacial tensions in the presence of surface active materials (*14-16*). ADSA has also been employed by other laboratories (*17,18*).

Theoretically, a drop profile can be generated from a known interfacial tension value, by numerical integration of the Laplace equation of capillarity. This procedure can be thought of as the reverse of ADSA, where ADSA determines the interfacial tension based on a given drop profile. It should be noted that determining the interfacial tension from a given drop profile by using ADSA is more complicated: it requires both numerical integration of the Laplace equation and least square optimization between the theoretical and experimental drop profiles (see later).

The purpose of this paper is to illustrate the applicability of ADSA to study ultra-low interfacial tensions. We began by looking for a system with very low interfacial tension from Adamson (*3*). It was found in the literature (*19*) that the interfacial tension of oleic acid in olive oil and aqueous solution of NaCl and

NaOH should be very low, approximately in the order of 10^{-3} mJ/m^2. However, using ADSA as the experimental technique, we found that the interfacial tension of this system appears to be two order of magnitude larger than that published by Harkins and Zollman (*19*). Doubts arose on whether ADSA can be used to measure ultra-low interfacial tensions. To investigate this further, we tried to find other independent means to estimate an interfacial tension based on another drop shape analysis, proposed by Malcom and Elliott (*20*). The interfacial tensions calculated from the scheme given by Malcom and Elliott (*20*) are of the same order of magnitude as our interfacial tension values.

As an alternative to an experimental test, we have generated a mathematically computed drop profile based on a given low interfacial tension; coordinates points were then taken from this profile as input data for ADSA. The output interfacial tension was found to be in excellent agreement with the input interfacial tension (see later). We, therefore, concluded that ADSA can be used to measure ultra-low interfacial tensions and that the interfacial tension values reported by Harkins and Zollman (*19*) are incorrect. More interfacial tension measurements were performed on Dioctyl Sulfosuccinate (AOT) in aqueous solution of NaCl/water and *n*-heptane for three different concentrations.

Theory of Axisymmetric Drop Shape Analysis

Axisymmetric Drop Shape Analysis (ADSA) is a technique to determine liquid-fluid interfacial tensions and contact angles from the shape of axisymmetric menisci, i.e., from sessile as well as pendant drops (*9*). The strategy employed is to fit the shape of an experimental drop to a theoretical drop profile according to the Laplace equation:

$$\Delta P = \gamma \left(\frac{1}{R_1} + \frac{1}{R_2} \right) \tag{1}$$

where R_1 and R_2 are the principal radii of curvature of the drop, and ΔP is the pressure difference across the curved interface. The surface tension γ is then computed from the best numerical fit to the Laplacian curve using non-linear least-squares optimization techniques. Figure 1 shows a typical theoretical sessile drop profile with a number of coordinates from an experimental profile. As described above, ADSA determines the operative surface tension by finding a best fit between the two profiles.

Apart from local gravity and densities of liquid and fluid phases, the only information required by ADSA is several arbitrary but accurate coordinate points selected from the drop profile. To achieve rapid and accurate data acquisition and preprocessing, an automatic digitization technique utilizing recent developments in digital image acquisition and analysis has been used (*21,22*). Computer software has been developed to implement this method and computational results provide the values of interfacial tension, drop volume, surface area, radius of curvature at the apex and, in the case of a sessile drop, contact angle and the radius of the three phase contact line.

Materials and Experimental Set-Up

Materials.

Oleic Acid in Olive Oil and Aqueous Solution of NaCl and NaOH. Oleic acid and olive oil were supplied from Sigma Co. with 99% purity and with a "highly refined" purity (Cat. No. 015000), respectively. A concentration of 1 mM of oleic acid in olive oil was used to form an inverted sessile drop in 0.15 M of NaCl, (Fisher Sci. Co.) and 1 mM of NaOH, (BDH Chem. Ana.).

Dioctyl Sulfosuccinate (AOT) in Aqueous Solution of NaCl/Water and *n*-Heptane. Dioctyl Sulfosuccinate (AOT) was supplied by Aldrich Co. with 98% purity. A stock solution (0.001 mole/litre) of AOT in aqueous solution of 0.0513 M NaCl/water was always used. Three different AOT concentrations were used: 0.415 mM, 0.410 mM and 0.420 mM in aqueous solution of NaCl/water were produced by dilution from the stock solution and subsequently used to form inverted sessile drops in *n*-heptane (Aldrich Co., 99% purity). Pendant drops or inverted pendant drops are very difficult to work with at very low interfacial tensions because the drops detach very easily from the capillary. The advantage of using an inverted sessile drop is that it is easier to manipulate than a sessile drop when the interfacial tension is very low.

Experimental Set-Up. A block diagram of the experimental set-up for ADSA is shown in Figure 2. As shown in this diagram, a Cohu 4800 monochrome camera is mounted on a Wild-Heerbrugg M7S microscope. The video signal of the pendant drop is transmitted to a digital video processor, which performs the frame grabbing and digitization of the image with 256 gray levels for each pixels, where 0 represents black and 255 represents white. A SPACRstation 10 computer is used to acquire images from the image processor and to perform the image analysis and computation. The rate of image acquisition for the present experiment is one image every two to five seconds.

Figure 3 shows the experimental apparatus for ultra-low interfacial tension measurements. As can be seen, an inverted sessile drop of liquid 1 with lower density can be formed from a steel capillary onto a glass surface inside a quartz cuvette containing liquid 2 with higher density. For the AOT system, AOT in aqueous solution of NaCl/water is liquid 1 and *n*-heptane is liquid 2; for the oleic acid system, oleic acid in olive oil is liquid 1 and aqueous solution of NaCl and NaOH is liquid 2.

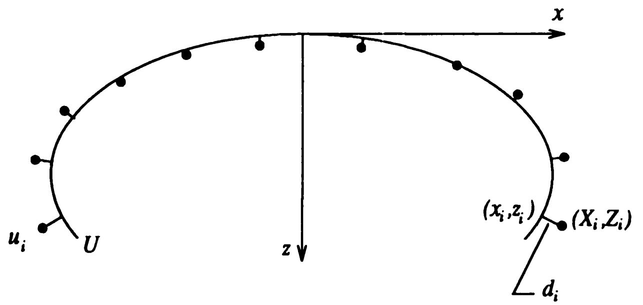
x
u_i
U
z
(x_i,z_i)
(X_i,Z_i)
d_i

Figure 1. A schematic sessile drop profile (solid line) with a number of coordinates from an experimental drop profile (circles). The best fit between the two profiles identifies the operative interfacial tension. d_i is the perpendicular distance between the experimental and theoretical coordinates.

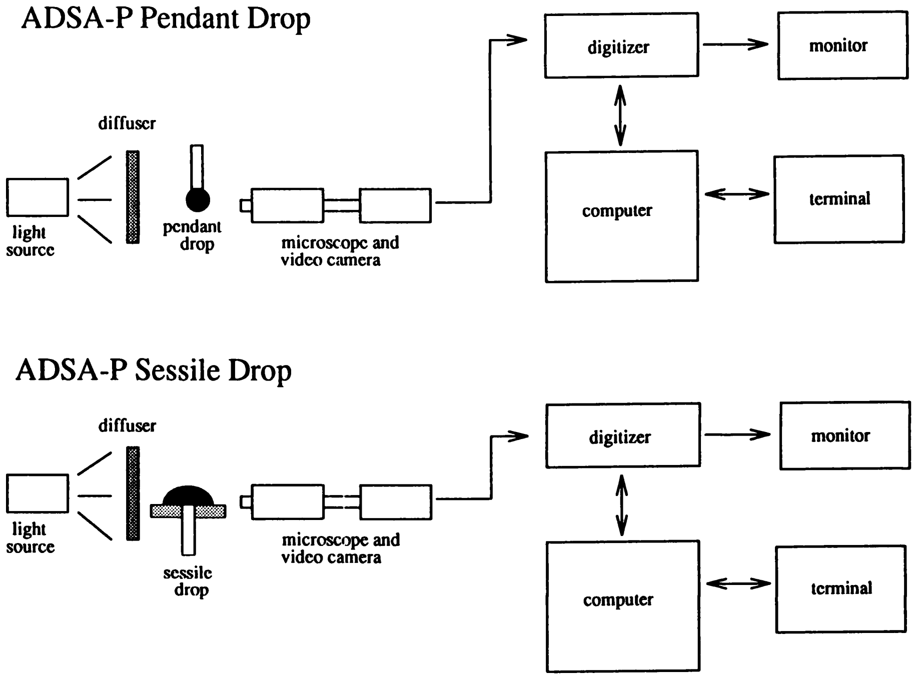
ADSA-P Pendant Drop
diffuser
light source
pendant drop
microscope and video camera
digitizer
monitor
computer
terminal
ADSA-P Sessile Drop
diffuser
light source
sessile drop
microscope and video camera
digitizer
monitor
computer
terminal

Figure 2. A schematic of an experimental set-up for pendant drop and sessile drop experiments.

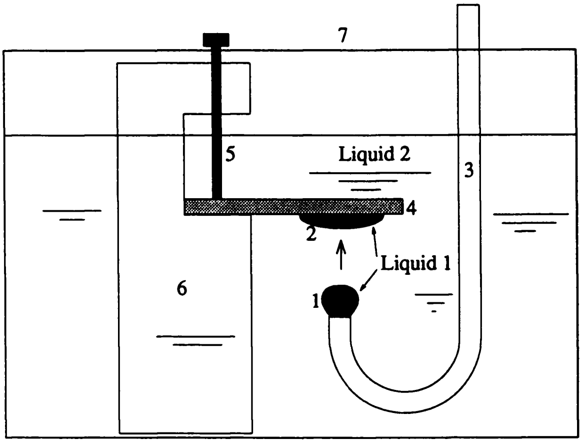

1. Inverted Pendant Drop
2. Inverted Sessile Drop
3. Steel Capillary
4. Glass Surface
5. Teflon Screw
6. Teflon Support
7. Quartz Cuvette

System 1:
Liquid 1: AOT in Solution of NaCl/Water
Liquid 2: n-Heptane

System 2:
Liquid 1: Oleic Acid in Olive Oil
Liquid 2: Solution of NaCl and NaOH

Figure 3. A schematic of an apparatus to form inverted sessile drops for ultra-low interfacial tension measurements.

Results and Discussion

Oleic Acid in Olive Oil and Aqueous Solution of NaCl and NaOH. Figure 4 shows the results of 1 mM oleic acid in olive oil with 0.15 M of NaCl and 1 mM of NaOH. A picture of an inverted sessile drop for this experiment is shown in Figure 5. As can be seen in Figure 4, the interfacial tension decreases from about 0.8 mJ/m^2 to 0.2 mJ/m^2 in 10 minutes. It should be noted that this time dependent behaviour cannot be readily studied by the conventional ultra-low interfacial tension technique, i.e., the spinning drop method.

The result of this experiment was compared with the interfacial tension values in the literature (*19*). It was found that our interfacial tension values are two orders of magnitude larger than those published by Harkins and Zollman (*19*). We, therefore, investigated an alternative, independent means to estimate the interfacial tension from the drop shape: The scheme proposed by Malcolm and Elliott (*20*) to estimate interfacial tension requires knowledge of the height and diameter of the sessile drop with a contact angle of 180°. It was found that the interfacial tensions calculated from the scheme given by Malcolm and Elliott (*20*) are of the same order of magnitude as our interfacial tension values shown in Figure 4, with a discrepancy ranging from 9% to 27%: the interfacial tensions calculated from the scheme of Malcolm and Elliott tends to decrease as the contact angle decreases from 180°; the interfacial tensions obtained from ADSA are very consistent and, of course, independent of the contact angle values.

We have also calculated a mathematically computed sessile drop profile based on a low interfacial tension value. Figure 6 shows such computed sessile drop profile generated by the numerical integration of the Laplace equation of capillarity, using an interfacial tension value of 0.001 mJ/m^2 and a density difference $\Delta\rho$ between the liquid and fluid phases of 0.05 g/cm^3. Using drop profile coordinates from Figure 6 as input parameters, ADSA yielded an output interfacial tension value of 0.001 mJ/m^2, which is, of course, in perfect agreement with the input value of interfacial tension used for the mathematical generation of the drop. In view of this, ADSA should, in principle, be able to measure ultra-low interfacial tensions. We concluded that the interfacial tension values reported by Harkins and Zollman (*19*) are incorrect.

Dioctyl Sulfosuccinate (AOT) in Aqueous Solution of NaCl/Water and *n*-Heptane. Figure 7 shows the interfacial tension results of 0.410 mM of AOT in aqueous solution of 0.0513 M NaCl/water and *n*-heptane. As shown in this figure, the interfacial tension decreases from about 0.25 mJ/m^2 to 0.06 mJ/m^2 in 3 minutes. It can be seen that an equilibrium of the interfacial tension cannot be reached in this period. A picture of an inverted sessile drop for 0.41 mM of AOT in aqueous solution of NaCl/water and *n*-heptane is shown in Figure 8.

The same type of experiment was performed for 0.415 mM of AOT in aqueous solution of NaCl/water and *n*-heptane. Figure 9 shows the result of this experiment: The interfacial tension decreases from about 0.05 mJ/m^2 to an equilibrium value of 0.01 mJ/m^2 in 12 minutes.

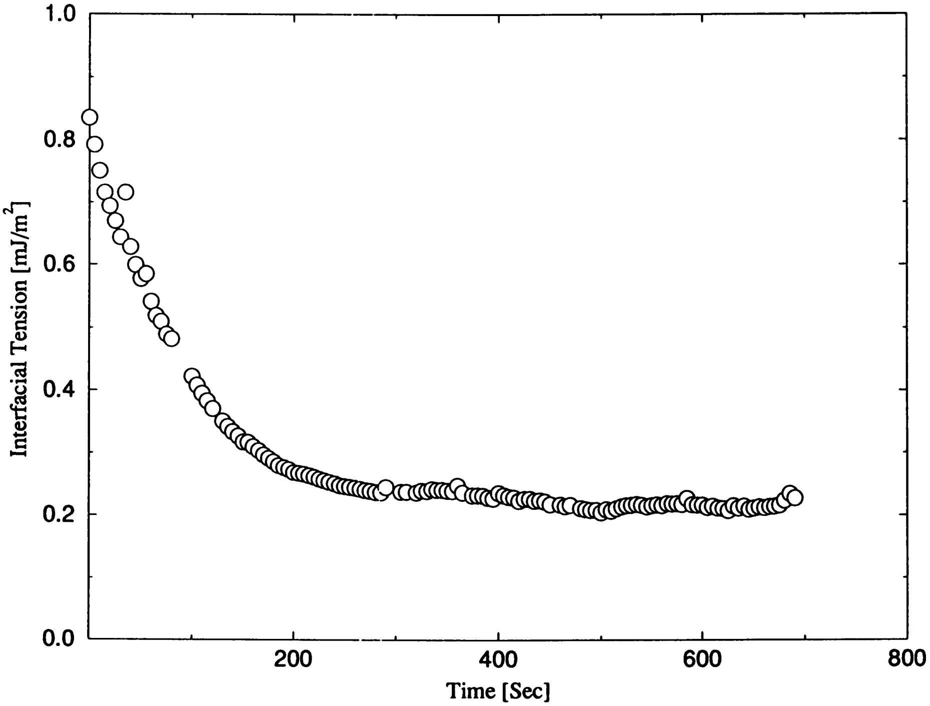

Figure 4. Interfacial tension vs. time for 1 mM of oleic acid in olive oil in the aqueous solution of 0.15 M of NaCl and 1 mM of NaOH.

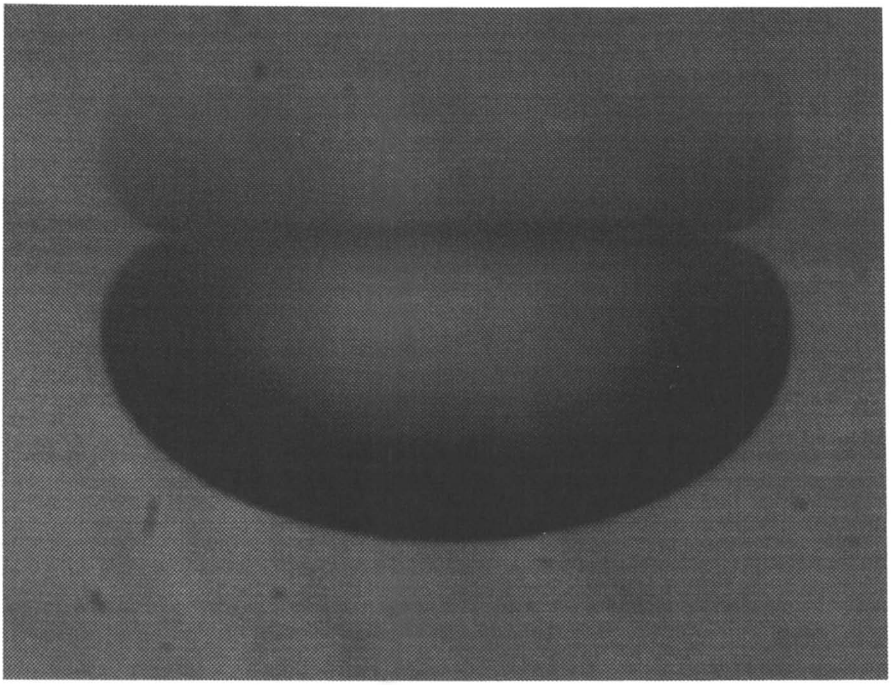

Figure 5. A picture of an inverted sessile drop for 1 mM of oleic acid in olive oil in the aqueous solution of 0.15 M of NaCl and 1 mM of NaOH. The upper part of the picture is a reflection of the actual drop due to mirror image effect of the glass surface. The contact diameter of this drop is 0.150 cm.

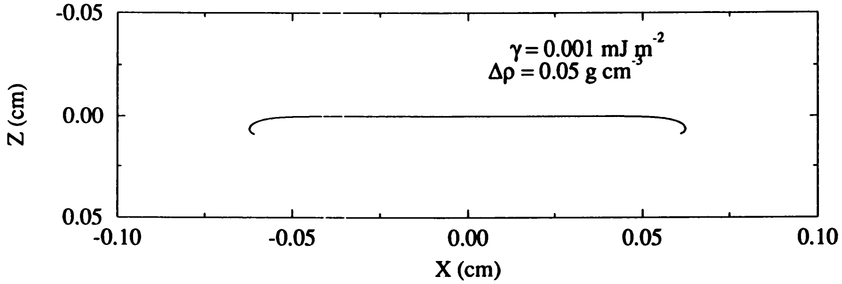

Figure 6. A theoretical sessile drop profile generated by using an interfacial tension of 0.001 mJ/m^2 and a density difference of 0.05 g/cm^3.

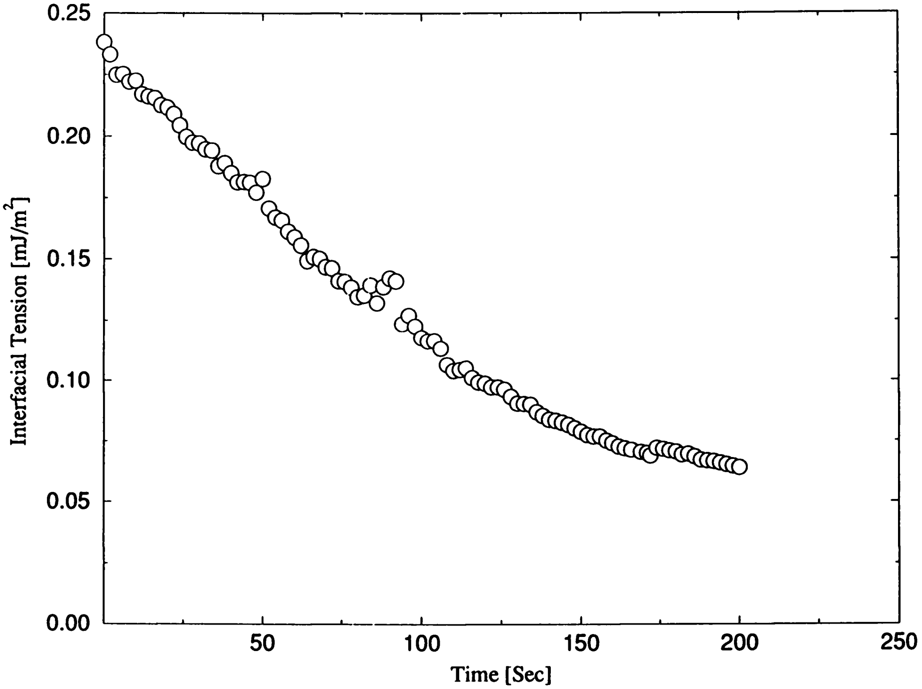

Figure 7. Interfacial tension vs. time for 0.410 mM of AOT in aqueous solution of 0.0513 M of NaCl/water and *n*-heptane.

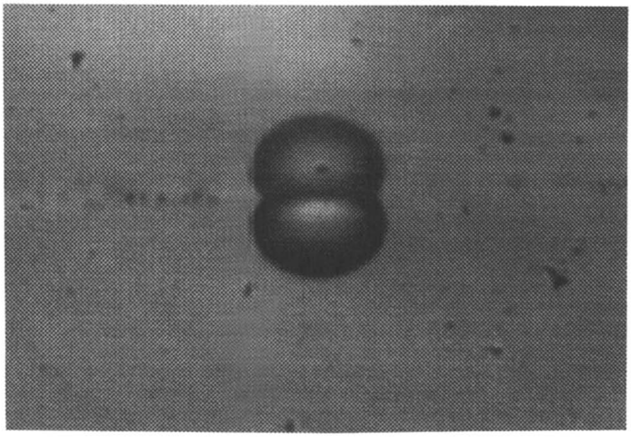

Figure 8. A picture of an inverted sessile drop for 0.410 mM of AOT in aqueous solution of 0.0513 M of NaCl/water and *n*-heptane. The upper part of the picture is a reflection of the actual drop due to mirror image effect of the glass surface. The contact diameter of this drop is 0.035 cm.

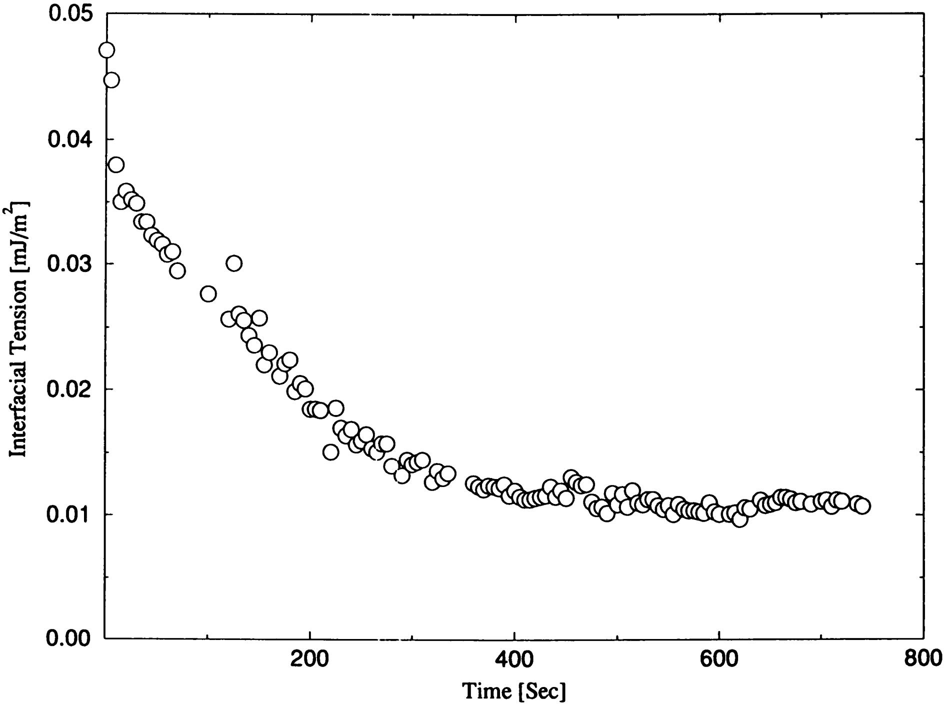

Figure 9. Interfacial tension vs. time for 0.415 mM of AOT in aqueous solution of 0.0513 M of NaCl/water and *n*-heptane.

Figure 10 shows the results of 0.420 mM of AOT in aqueous solution of NaCl/water and *n*-heptane. It can be seen that the interfacial tension decreases from about 0.026 mJ/m^2 to 0.006 mJ/m^2 in 2 minutes: Increasing the AOT concentration decreases both the interfacial tension value and the time required to reach equilibrium.

The above results suggest that not only can ADSA be used to determine ultra-low interfacial tension down to the order of 10^{-3} mJ/m^2, it can also be employed to study time dependent behaviour of such systems in the presence of surface active materials. Since the results shown in Figure 7 did not reach equilibrium, only the results shown in Figures 9 and 10 could be compared with those published by Aveyard *et al.* (*23*) who used the spinning drop technique: The interfacial tension values reported by Aveyard *et al.* (*23*) were estimated from their graph to be ≈ 0.01 mJ/m^2 and ≈ 0.003 mJ/m^2, respectively, for 0.415 mM and 0.420 mM of AOT in the aqueous solution of 0.0513 M NaCl/water and *n*-heptane, in good agreement with the results shown in Figures 9 and 10.

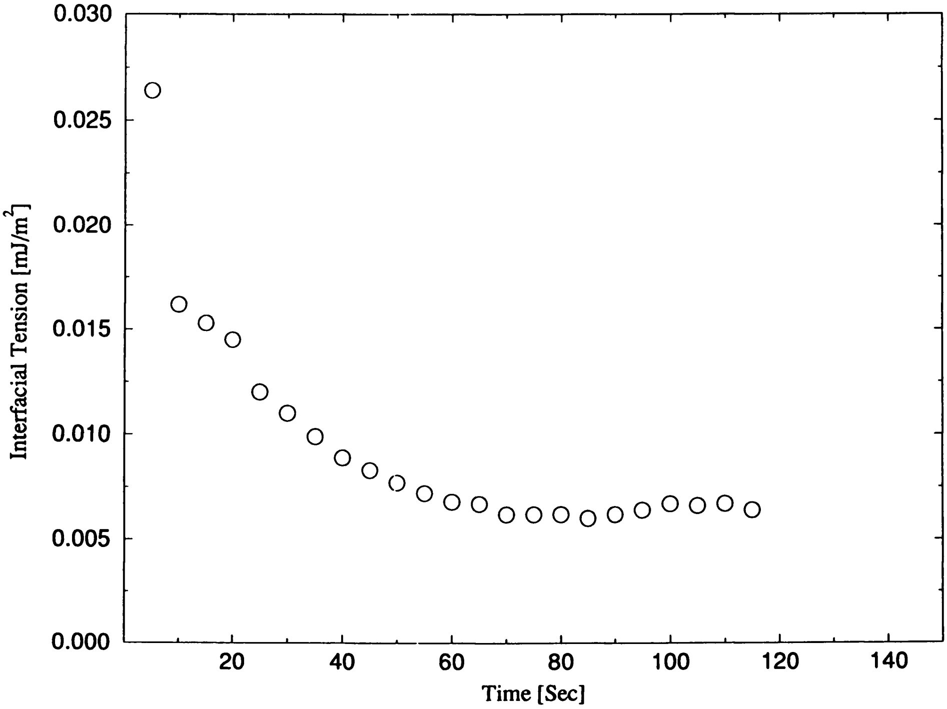

Figure 10. Interfacial tension vs. time for 0.420 mM of AOT in aqueous solution of 0.0513 M of NaCl/water and *n*-heptane.

Conclusions

Axisymmetric Drop Shape Analysis (ADSA) is a novel experimental technique which can be used to study ultra-low interfacial tensions. We have shown that ADSA can be used to determine ultra-low interfacial tension down to the order of 10^{-3} mJ/m^2. Not only the equilibrium values, but also the time dependence of ultra-low interfacial tensions in the presence of surface active materials can be studied.

Acknowledgments

This research was supported by the Natural Science and Engineering Research Council of Canada (No. A8278), and a University of Toronto Open Fellowship (D.Y.K). One of the authors (M.A.C) would like to thank the Dirección General de Investigación Científica y Técnica (DGICYT) PR 94-047 for financial support.

Literature Cited

1. Padday, J.F., In *Surface and Colloid Science*, Editor, Matijevic, E., Ed.; Wiley, New York, 1986, Vol. 1; p.101.

2. Ambwani, D.S. and Fort, Jr. T., In *Surface and Colloid Science*, Editor, Good, R.J. and Stromberg, R.S., Eds.; Plenum Press, New York, 1979, Vol. 11; p.93.

3. Adamson, A.W., In *Physical Chemistry of Surfaces*, John Wiley & Sons, New York, 1990, 5th Ed.

4. Neumann, A.W. and Good, R.J., In *Surface and Colloid Science*, Editor, Good, R.J. and Stromberg, R.S., Eds.; Plenum Press, New York, 1979, Vol. 11, p.31.

5. Bashforth, F. and Adams, J.C., In An Attempt to test the Theories of Capillary Action, Cambridge Univ. Press and Deighton Bell & Co, Cambridge, 1883.

6. Fordham, S., *Proc. Ro. Soc. London*, **1948**, *194A*, p.1.

7. Padday, J.F., In *Surface and Colloid Science*, Editor, Matijevic, E. and Eirich, F.R., Eds; Wiley-Interscience, New York, 1969, Vol. 1, p.151.

8. Hartland, S. and Hartley, R.W., In *Axisymmetric Fluid-Liquid Interfaces*, Elsevier, Amsterdam, 1976.

9. Rotenberg, Y., Boruvka, L., and Neumann, A.W., *J. Colloid Interface Sci.*, **1983**, *93*, pp.169-183.

10. Gaydos, J.A., and Neumann, A.W., *J. Colloid Interface Sci.*, **1987**, *120*, pp.76-86.

11. Li, D., and Neumann, A.W., *J. Colloid Interface Sci.*, **1992**, *148*, pp.190-200.

12. Susnar, S.S., Hamza, H.A., and Neumann, A.W., *Colloids & Surfaces A: Physicochemical and Engineering Aspects*, **1994**, *89*, pp.169-180.

13. Kwok, D.Y., Vollhardt, D., Miller, R., Li, D., and Neumann, A.W., *Colloids & Surfaces A: Physicochemical and Engineering Aspects*, **1994**, *88*, pp. 51-58.

14. Voigt, A., Thiel, O., Williams, D., Policova, Z., Zingg, W., and Neumann, A.W., *Colloids & Surfaces*, **1991**, *58*, pp.315-326.

15. Miller, R., Sedev, R., Schano, K-H., Ng, C., and Neumann, A.W., *Colloids & Surfaces*, **1993**, *69*, pp.209-216.

16. Miller, R., Policova, Z., Sedev, R., and Neumann, A.W., *Colloids & Surfaces A: Physicochemical and Engineering Aspects*, **1993**, *76*, pp.179-185.

17. Busscher, H.J., van der Vegt, W., Noordmans, J.M., Schakenraad, J.M., and van der Mei, H.C., *Colloids & Surfaces*, **1991**, *58*, p.229.

18. van der Vegt, W., van der Vegt, H.C., and Busscher, H.K., *J. Colloid Interface Sci.*, **1993**, *156*, p.129.

19. Harkins, W., and Zollman, H., *Amer. Chem. Soc.*, **1926**, *48*, pp.69-80.

20. Malcolm, J.D., and Elliott, C.D., *Can. J. Chem.*, **1980**, *58*, pp.151-153.

21. Cheng, P., Li, D., Boruvka, L., Rotenberg, Y., and Neumann, A.W., *Colloids & Surfaces*, **1990**, *43*, pp.151-167.

22. Cheng, P., Ph. D. Thesis, University of Toronto, Toronto, Canada, 1990.

23. Aveyard, R., Binks, B.P., Lawless, T.A., and Mead, *J., Can. J. Chem.*, **1988**, *66*, pp.3031-3037.

RECEIVED May 3, 1995

Author Index

Allara, David L., 355
Bailey, A. I., 166
Bakker, Martin G., 153
Biggs, Simon, 255
Bishop, J. F., 205
Breen, Patrick J., 268
Brinck, Johanna, 231
Cabrerizo-Vílchez, M. A., 374
Chen, Shaun H., 217
Chiefalo, P., 374
Cosgrove, T., 196
Davis, Brandon, 153
del Rio, O., 374
Esumi, Kunio, 138
Fina, L. J., 316
Frank, Curtis W., 217
Goloub, Tanya, 78
Gumkowski, Michael J., 22
Harwell, Jeffrey H., 49
Howell, I., 196
Huang, L., 241
Kelly, M. S., 183
Khorshiddoust, B., 374
Koopal, Luuk K., 78
Krishnakumar, S., 104
Kunjappu, Joy T., 104
Kwok, D. Y., 374
Lahooti, S., 374
Lobban, Lance L., 67
Lochhead, Robert Y., 280
Lu, J. R., 342
Luckham, Paul F., 166
Maltesh, C., 241
Mears, S. J., 196
Miano, F., 166
Monticone, V., 36
Mourey, T. H., 205
Mubarekyan, E., 183
Mukerjee, Pasupati, 22
Mulvaney, Paul, 255
Murphy, Dexter D., 153
Neumann, A. W., 374
O'Haver, John H., 49
Parikh, Atul N., 355
Pyter, Richard A., 22
Rebar, V. A., 183
Rulison, Christopher J., 280
Santore, M. M., 183
Sharma, Ravi, 1,22,355,364
Smith, D. T., 364
Somasundaran, P., 104,241
Tadros, T. F., 166
Texter, J., 205
Thomas, R. K., 342
Thompson, L., 196
Tiberg, Fredrik, 231
Treiner, C., 36
Wood, Jonathan, 355
Yu, Chung-Ching, 67

Affiliation Index

Abbott Laboratories, 22
Baker Performance Chemicals, Inc., 268
Columbia University, 104,241
Eastman Kodak Company, 1,22,205,355,364
Imperial College of Science, Technology, and Medicine, 166
Lehigh University, 183
Lund University, 231
National Institute of Standards and Technology, 364
Pennsylvania State University, 355
Pfizer Central Research, 22
Physical Chemistry Laboratory, 342
Rutgers University, 316
Science University of Tokyo, 138

Downloaded by 89.163.35.42 on October 11, 2012 | http://pubs.acs.org
Publication Date: May 5, 1996 | doi: 10.1021/bk-1995-0615.ix001

Stanford University, 217
Unilever Research, 196
Universidad de Granada, 374
Université Pierre et Marie Curie, 36
University of Alabama, 153
University of Bristol, 196
University of Melbourne, 255
University of Newcastle, 255
University of Oklahoma, 49,67
University of Southern Mississippi, 280
University of Toronto, 374
University of Wisconsin, 22
Wageningen Agricultural University, 78
Zeneca Agrochemicals, 166

Subject Index

A

Acidic zwitterionic surfactants, 2
Admicellar catalysis, 67–76
  acidic hydrolysis, 67–75
  adsolubilization, 69–74
  adsorption measurement procedure, 68–69
  buffer concentration vs. rate constant, 74,75*f*
  critical micelle concentration, 70,71*f*
  description, 67–68
  experimental procedure, 68–70
  kinetics measurement procedure, 69–70
  pH vs. rate constant, 72–73
  previous studies, 68
Admicelles
  description, 3,68
  formation, 3,50
  solubilization capacity, 13
  structure, 50
Adsolubilization, 49–66
  alcohols, 55,57–65
  alkanes into SDS admicelles, 50–56
  applications, 13–14,50
  comparison to solubilization, 50,51*f*,64,66
  description, 36
  evidence for surfactant aggregate occurrence, 12–13
  expected results, 50–56
  future work, 66
  2-naphthol on hexadecylpyridinium chloride adsorbed aggregates, 36–47
  oil, silica–water interface, 231–239
  role on rate constant of admicellar catalysis, 74
Adsolubilization—*Continued*
  two-state model, 12–13
  unexpected results, 55,57–65
Adsolubilization constant, 69
Adsorbed amphiphilic compounds, 231
Adsorbed layer structure, self-consistent field lattice theory for association and adsorption, 79–80
Adsorption
  AFM measurements, 255–265
  cationic surfactants, effects of porosity, 36–42
  definition, 272
  determination of role of anchor group of surfactant in effectiveness as steric stabilizers, 166–181
  ionic surfactants
    charged solids, 3–4
    solid surfaces, 78–79
    uncharged hydrophobic surfaces, 4–5
  mixed silica–polymer–surfactant systems, 196–203
  PEO–PPO–PPO on nanoparticulate pharmaceutical imaging agents, 205–215
  polymer(s), studies, 138–139
  polymer and surfactant at solid–liquid interface, 104
  polymer and surfactant from binary mixtures on alumina, 138–151,197–203,241,275–276*t*
  surfactants in mixtures, 241–254
Adsorption density, calculation, 108
Adsorption kinetics
  block copolymers, 11–12
  liquid–liquid interface, 11

Downloaded by 89.163.35.42 on October 11, 2012 | http://pubs.acs.org
Publication Date: May 5, 1996 | doi: 10.1021/bk-1995-0615.ix001

Stanford University, 217
Unilever Research, 196
Universidad de Granada, 374
Université Pierre et Marie Curie, 36
University of Alabama, 153
University of Bristol, 196
University of Melbourne, 255
University of Newcastle, 255
University of Oklahoma, 49,67
University of Southern Mississippi, 280
University of Toronto, 374
University of Wisconsin, 22
Wageningen Agricultural University, 78
Zeneca Agrochemicals, 166

Subject Index

A

- Acidic zwitterionic surfactants, 2
- Admicellar catalysis, 67–76
  - acidic hydrolysis, 67–75
  - adsolubilization, 69–74
  - adsorption measurement procedure, 68–69
  - buffer concentration vs. rate constant, 74,75*f*
  - critical micelle concentration, 70,71*f*
  - description, 67–68
  - experimental procedure, 68–70
  - kinetics measurement procedure, 69–70
  - pH vs. rate constant, 72–73
  - previous studies, 68
- Admicelles
  - description, 3,68
  - formation, 3,50
  - solubilization capacity, 13
  - structure, 50
- Adsolubilization, 49–66
  - alcohols, 55,57–65
  - alkanes into SDS admicelles, 50–56
  - applications, 13–14,50
  - comparison to solubilization, 50,51*f*,64,66
  - description, 36
  - evidence for surfactant aggregate occurrence, 12–13
  - expected results, 50–56
  - future work, 66
  - 2-naphthol on hexadecylpyridinium chloride adsorbed aggregates, 36–47
  - oil, silica–water interface, 231–239
  - role on rate constant of admicellar catalysis, 74

Adsolubilization—*Continued*
  - two-state model, 12–13
  - unexpected results, 55,57–65
- Adsolubilization constant, 69
- Adsorbed amphiphilic compounds, 231
- Adsorbed layer structure, self-consistent field lattice theory for association and adsorption, 79–80
- Adsorption
  - AFM measurements, 255–265
  - cationic surfactants, effects of porosity, 36–42
  - definition, 272
  - determination of role of anchor group of surfactant in effectiveness as steric stabilizers, 166–181
  - ionic surfactants
    - charged solids, 3–4
    - solid surfaces, 78–79
    - uncharged hydrophobic surfaces, 4–5
  - mixed silica–polymer–surfactant systems, 196–203
  - PEO–PPO–PPO on nanoparticulate pharmaceutical imaging agents, 205–215
  - polymer(s), studies, 138–139
  - polymer and surfactant at solid–liquid interface, 104
  - polymer and surfactant from binary mixtures on alumina, 138–151,197–203,241,275–276*t*
  - surfactants in mixtures, 241–254
- Adsorption density, calculation, 108
- Adsorption kinetics
  - block copolymers, 11–12
  - liquid–liquid interface, 11

Downloaded by 89.163.35.42 on October 11, 2012 | http://pubs.acs.org
Publication Date: May 5, 1996 | doi: 10.1021/bk-1995-0615.ix002

Adsorption kinetics—*Continued*
  measurement, 11
  nonionic and anionic surfactants and hydrophobically modified water-soluble polymers to oil–water interface, 280,283–311
  polymer, *See* Polymer adsorption kinetics
  role of polymer end-group chemistry, 183–194
  small-molecule surfactants to air–water interface, 11
Adsorption properties
  structure of surface aggregates, 3–4
  studies, 2–3
Aerosil, adsorption of dodecylpyridinium chloride, 96–99
Aerosil 200, hexadecylpyridinium chloride adsorption, 40–42*f*
Aerosol OT, adsorption, spectroscopic characterization, 104–135
Aggregation number
  calculation, 106
  determination using EPR, 161,163
Air–water interface
  adsorption, 7,11
  neutron reflectivity measurements of monolayers of styrene–maleic anhydride copolymers, 7
  second harmonic generation of molecular arrangement of poly(acrylonitrile-*co*-4-vinylpyridine) monolayer, 7
  structure of surfactant monolayers using neutron reflection, 342–354
  vibration spectroscopy of surfactants, 316–339
n-Alkyltrichlorosilanes, fluorescence probe studies of self-assembled monolayer and multilayer films, 217–229
Alkylsilanated silicon oxide surface, segregation of poly(deuterostyrene-*b*-2-vinylpyridine), 10–11
Alon, micellar exclusion, 30
γ-Alumina, adsorption of SDS and polyethoxylated nonylphenol, 5–6
Alumina
  adsorption, 6,138–151
  spectroscopic characterization, 104–135
Alumina–water interface, pentadecylethoxylated nonylphenol–tetradecyltrimethylammonium chloride mixture interactions, 241–254
Amorphous silica, surface charging effects, 364–372
Amphiphilic molecules, self-assembly property studies, 231
Amphoteric zwitterionic surfactants, 2
Anchor group of surfactant, role in determining effectiveness as steric stabilizers, 166–181
  adsorption data, 170–172
  experimental procedure, 166–169
  flocculation data, 181
  rheological experimental procedure, 169
  shear viscosity data, 172–176
  surfactant structures, 167–168
  viscoelastic data, 176–187
Anionic surfactants
  adsorption kinetics at oil–water interface, 280–311
  description, 2
Antagonism, surfactant solutions, 5
Aqueous insoluble nanoparticulate pharmaceuticals, importance of delivery, 205
Atomic force microscopic measurements
  applications, 255
  cetyltrimethylammonium bromide adsorption on gold, 259–261
  citrate adsorption on gold, 261,262*f*
  clean surface interactions, 257–259
  colloid probe, 255-256
  experimental procedure, 256–257
  polymeric stabilizer adsorption, 261,263–265
  prepolymerized Langmuir–Blodgett films of *n*-octadecylsiloxane monolayers, 359,361–362
  previous studies, 255–256
  procedure, 357
Axisymmetric drop shape analysis
  description, 375
  theory, 376–378*f*
  ultralow interfacial tension determination, 374–385

Downloaded by 89.163.35.42 on October 11, 2012 | http://pubs.acs.org
Publication Date: May 5, 1996 | doi: 10.1021/bk-1995-0615.ix002

B

Basic zwitterionic surfactants, 2
Bilayers
  1,2-dihexadecyl-*sn*-glycero-3-phosphatidylcholine, vibration spectroscopy, 334–335
  solubilization in adsorbed layers, 32–34
Bimolecular quenching constant
  definition, 224
  determination, 227
Binary mixtures, adsorption of polymer and surfactant, 138–151
Binding constant, definition, 209
Block copolymers
  adsorption kinetics, 11–12
  PEO–PPO–PEO adsorption on nanoparticulate pharmaceutical imaging agents, 205–216
Brush layer thickness scales, diblock copolymers, 8
Brushes, description, 8
Buffer concentration, role on rate constant of admicellar catalysis, 74,75*f*

C

Capillary pressure, calculation, 271
Cationic surfactants
  description, 2
  effects of porosity on adsorption at silica–water interface, 36–47
  interactions with nonionic surfactants, 241–253
Cetylpyridinium chloride, micellar exclusion, 31
Cetyltrimethylammonium bromide adsorption on gold, AFM measurements, 259–261
Charged surfaces, exclusion of micelles, 28–31
Charging effects at gelatin–silica interfaces, surface, *See* Surface charging effects at gelatin–silica interfaces
Citrate adsorption on gold, AFM measurements, 261,262*f*
Coadsorption
  2-naphthol, effects of porosity, 36–47
  See also Adsolubilization
Coalescence of unstabilized disperse droplets, theory, 282
Complex modulus, determination, 169
Contact angle measurements, 356–357
Contact electrification, description, 364
Contact time, definition, 188
Copolymers
  adsorption at interface between immiscible polymers and polymer–nonpolymer interface, 9–10
  block, adsorption on nanoparticulate pharmaceutical imaging agents, 205–216
Critical micelle concentration, vibration spectroscopy in solution and at air–water interface, 317–323
Critical micelle temperature, studies, 323–328
Cross partial structure factor, 346–348
Cross-sectional area of surfactant, calculation, 170
Cyclohexylphosphatidylcholines, vibration spectroscopy, 336–337

D

Dapral GE 202, *See* Maleic anhydride α-olefin copolymer
Demulsification, description, 268
Demulsifier, function, 268–269
Diblock copolymers, adsorbed configuration, 8
1,2-Dicyclohexyltetradecanol-*sn*-glycero-3-phosphatidylcholine, vibration spectroscopy, 336–337
Didodecyltrimethylammonium bromide, vibration spectroscopy, 329
Diffusion coefficient, calculation, 198
Diffusion relaxation time, definition, 272
Dimensionless time, definition, 187
Dimethylbenzyltetradecylammonium chloride, adsorption on silicas, 37–41

Downloaded by 89.163.35.42 on October 11, 2012 | http://pubs.acs.org
Publication Date: May 5, 1996 | doi: 10.1021/bk-1995-0615.ix002

Downloaded by 89.163.35.42 on October 11, 2012 | http://pubs.acs.org
Publication Date: May 5, 1996 | doi: 10.1021/bk-1995-0615.ix002

Dioctadecyldimethylammonium chloride, vibration spectroscopy, 328
Dioctyl sulfosuccinate, ultralow interfacial tension determination by axisymmetric drop shape analysis, 380,383–385
1,2-Dipalmitoylphosphatidylcholine, vibration spectroscopy, 335
1,2-Dipalmitoylphosphatidylcholine–cholesterol mixtures, vibration spectroscopy, 335–336
Dipole moment, calculation, 108
Distance from substrate into solution, determination, 187
Dodecylpyridinium chloride, adsorption on Aerosil, 96–99
Dodecyltrimethylammonium bromide, vibration spectroscopy, 329
Dodecyltrimethylammonium chloride, vibration spectroscopy, 328–329
Dolomite, spectroscopic characterization of oleate adsorption, 104–135
Double acyl chain ammonium amphiphiles, vibration spectroscopy, 332
Drop shape analysis, axisymmetric, *See* Axisymmetric drop shape analysis
Drop shape method for interfacial tension measurement, description, 374
Drop volume
  apparatus, 288–292
  theory, 287–288
Dynamic interfacial tension
  definition, 272
  measurement procedure, 291–293
Dynamic light scattering, description, 198

E

Electron paramagnetic resonance to study surfactants adsorbed on surfaces, 153–163
  aggregation number, 161,163
  completely labeled surfactant, 154–157
  experimental objectives, 154
  probe experiments, 157–162
  use of paramagnetic broadeners, 160–163*f*
Electron spin resonance spectroscopy, characterization of surfactant and polymer solloids at solid–liquid interface, 104–135
Ellipsometry, self-assembly of surfactants at silica–water interface, 231–239
End-functionalized polymers segregating to impenetrable wall, self-consistent field lattice theory for association and adsorption, 10–11
End-group, polymer, role in adsorption kinetics, 183–194
Energy gap, calculation, 106
Equilibrium interfacial tension measurement, procedure, 286–287
Equilibrium monolayer, characteristics, 342

F

f correction factors, determination, 290–292*f*
Flocculation, determination of role of anchor group of surfactant in effectiveness as steric stabilizers, 166–181
Fluorescence probe studies of self-assembled monolayer and multilayer films from *n*-alkyltrichlorosilanes, 217–229
  characterization of self-assembled monolayers and multilayers, 219–220
  effective quencher diffusivity calculation, 227–229
  experimental materials, 218–219
  fluorescence intensity of probe-containing monolayers on host length, 220,222–223
  fluorescence of pyrene-labeled probes containing monolayers, 220,221*f*
  fluorescence quenching of probe-containing monolayers and multilayers, 224–225,226*f*
  incorporation of fluorescence probes in multilayers, 223–224
  relative adsorption rate constant determination, 225–227

Downloaded by 89.163.35.42 on October 11, 2012 | http://pubs.acs.org
Publication Date: May 5, 1996 | doi: 10.1021/bk-1995-0615.ix002

Fluorescence spectroscopy, characterization of surfactant and polymer solloids at solid–liquid interfaces, 104–135
Fluorescently labeled species in solution, determination, 188
Fluorinated surfactants, applications, 2
Fluorocarbon surfactants, adsorption to Graphon, 23–28
Fractional coverage of guest molecule, determination, 225
Francolite, spectroscopic characterization of oleate adsorption, 104–135

G

Gelatin–silica interfaces, surface charging effects, 364–372
Gibbs elasticity, definition, 269
Gold
  cetyltrimethylammonium bromide adsorption, 259–261
  citrate adsorption, 261,262*f*
Gramicidin D, vibration spectroscopy, 332–333
Graphon, description, 22

H

Hemimicelles
  description, 3,68
  formation, 3
  verification of existence, 12
Hexadecylpyridinium chloride, adsorption on Sorbsil C30 and Aerosil 200, 40–42*f*
Hexadecyltrimethylammonium bromide
  structure at air–water interface using neutron reflection, 342–354
  vibration spectroscopy, 329
Hexadecyltrimethylammonium chloride–sodium poly(styrenesulfonate)–alumina system, adsorption, 138–151
Hexane, solvent properties, 6–7
Hydrocarbon surfactants, adsorption to Graphon, 23–28
Hydrocarbon–water distribution coefficient, definition, 32
Hydrodynamic thickness, measurement, 198
Hydrophobic groups, substitution into hydrocarbon backbone, 2
Hydrophobically modified water-soluble polymers, adsorption kinetics at oil–water interfaces, 280–311
(Hydroxyethyl)celluloses, adsorption kinetics, 297–302,310–311
Hydroxyl-terminated 1,4-polyisoprene, structure at air–water interface, 7

I

Imaging agents, pharmaceutical, adsorption of PEO–PPO–PPO, 205–216
Immiscible polymers and polymer–nonpolymer interface, adsorption of copolymers, 9–10
Intensity
  calculation, 220
  determination, 185–186
  monomer emissions, calculation, 106
Interaction forces, AFM measurements, 255–265
Interfacial behavior, nonionic surfactant systems at silica–water interface, 321–239
Interfacial force measurement, 255
Interfacial tension
  axisymmetric drop shape analysis, ultralow, *See* Ultralow interfacial tension determination by axisymmetric drop shape analysis
  measurement techniques, 374
Ionic surfactants
  adsorption on uncharged hydrophobic surfaces, 4
  self-assembly on mineral oxides, 78–100
IR spectroscopy, characterization of surfactant and polymer solloids at solid–liquid interfaces, 104–135
Isomeric surfactant adsorption at interfaces, spectroscopic characterization, 104–135
Isotherm measurements, procedure, 356–357

K

Kinetics of nonionic and anionic surfactant and hydrophobically modified water-soluble polymers to oil–water interfaces, adsorption, *See* Adsorption kinetics of nonionic and anionic surfactant and hydrophobically modified water-soluble polymers to oil–water interfaces
Kraft point, description, 323

L

Langmuir–Blodgett film deposition, procedure, 356–357
Langmuir–Blodgett films of *n*-octadecylsiloxane monolayers, *See* Prepolymerized Langmuir–Blodgett films of *n*-octadecylsiloxane monolayers
Langmuir isotherms, prepolymerized Langmuir–Blodgett films of *n*-octadecylsiloxane monolayers, 357–360*f*
Lipid bilayer
  quantification of defect content, 335
  vibration spectroscopy in solution and at air–water interface, 332–337
Liquid–liquid interface, adsorption interface, 11
Liquid–solid interface, *See* Solid–liquid interface
Lithium dodecyl sulfate–lithium perfluorooctanesulfonate–PVP–alumina system, adsorption, 138–151
Loss modulus, determination, 169

M

Maleic anhydride α-olefin copolymer, adsorption at solid–liquid interface, 104–135
Marangoni–Gibbs effect, description, 268
Mean ionic activity, calculation, 26
Methyl benzoate, adsolubilization constants, 74
Micellar catalysis, product isolation problems, 67
Micellar exclusion from charged surfaces
  Alon, 30
  cetylpyridinium chloride, 31
  example, 28,29*f*
  experimental description, 28,30
  implications, 28
  previous studies, 28,30
Micelle(s)
  solubilization function, 50
  solubilization in adsorbed layers, 32–34
  vibration spectroscopy in solution and at air–water interface, 323–328
Micelle–water distribution coefficient, definition, 32
Microviscosity, determination using EPR, 158–160,162*f*
Mineral oxides, self-assembly of adsorbed ionic surfactants, 78–100
Mixed micelles, vibration spectroscopy in solution and at air–water interface, 328–331
Mixed surfactant adsorption on alumina, spectroscopic characterization, 104–135
Mixed surfactant systems, advantages, 241–242
Monodisperse surfactants, adsorption at silica–water interface, 236–239*f*
Monolayer and multilayer films from *n*-alkyltrichlorosilanes, fluorescence probe studies, 217–229
Mushrooms, description, 8

N

Nanoparticulate pharmaceutical imaging agents, adsorption of PEO–PPO–PEO block copolymers, 205–216
2-Naphthol, effects of porosity on coadsorption at silica–water interfaces, 36–47
Neutron reflection, structure of surfactant monolayers at air–water interface, 342–354
Neutron reflectivity, polymer conformation study, 6–7

Downloaded by 89.163.35.42 on October 11, 2012 | http://pubs.acs.org
Publication Date: May 5, 1996 | doi: 10.1021/bk-1995-0615.ix002

Downloaded by 89.163.35.42 on October 11, 2012 | http://pubs.acs.org
Publication Date: May 5, 1996 | doi: 10.1021/bk-1995-0615.ix002

Nonamphoteric zwitterionic surfactants, 2
Nonionic block copolymers, 2
Nonionic dispersants, advantages for use in pharmaceutical formulation, 206
Nonionic poly(ethylene glycol) monoethers, adsorption–desorption kinetics at silica–water interface, 11
Nonionic polymer–anionic surfactant self-assembled complexes, adsorption studies, 196–203
Nonionic surfactants
  adsorption kinetics at oil–water interfaces, 280–311
  description, 2
  interactions with cationic surfactants, 241–253
  interfacial behavior at silica–water interface, 231–239
Nonylbenzenesulfonate, adsorption on rutile, 91–96
Nonylphenylpoly(ethylene oxide) surfactant, role of anchor group in effectiveness determination as steric stabilizers, 166–181
Nonylphenylpoly(propylene oxide)–PEO surfactant, role of anchor group in effectiveness determination as steric stabilizers, 166–181
Number of probes per micelle, calculation, 106

O

n-Octadecylsiloxane monolayers, prepolymerized Langmuir–Blodgett films, 355–362
Oil, surface solubilization at silica–water interface, 231–239
Oil–water interfaces, adsorption kinetics of nonionic and anionic surfactant and hydrophobically modified water-soluble polymers, 280–311
Oleate adsorption on dolomite and francolite, spectroscopic characterization, 104–135
Oleic acid, ultralow interfacial tension determination by axisymmetric drop shape analysis, 380–382*f*
Orange OT
  description, 30
  in micelles and bilayers, solubilization in adsorbed layers, 32–34
Order parameter, calculation, 107

P

1-[1'-^{13}C]Palmitoyl-2-palmitoyl-*sn*-glycero-3-phospho-L-serine, vibration spectroscopy, 334
Paramagnetic broadeners, role in EPR to surfactants on surfaces, 160–163*f*
Partial structure factor of fragment, definition, 343–344
Partition coefficient
  coadsorption of 2-naphthol on hexadecylpyridinium chloride adsorbed aggregates, 43–47
  definition, 227,229
Patchy bilayer structure, structure of surface aggregates, 3
Pendant and sessile drop methods for interfacial tension measurement, 374–375
Pentadecylethoxylated nonylphenol–tetradecyltrimethylammonium chloride mixture interactions at alumina–water interface
  experimental procedure, 242–243
  interactions in solution, 243–244
  surfactant mixture adsorption, 244–254
pH, role on rate constant of admicellar catalysis, 72–73
Pharmaceutical imaging agents, adsorption of PEO–PPO–PPO block copolymers, 205–216
Phases, vibration spectroscopy in solution and at air–water interface, 323–328
Photographic gelatin, surface charging effects, 364–372
Photon correlation spectroscopy, 198
Pluronic BAB-type block copolymeric dispersants, aqueous adsorption to nanoparticulate imaging agents, 205–215

Polarity, determination using EPR, 157–158
Poly(acrylic acids)
  adsorption kinetics, 299,302–311
  on zirconia, polymeric stabilizer adsorption, 261,263–265
Poly(acrylonitrile-*co*-4-vinylpyridine) monolayer molecular arrangement at air–water interface, second harmonic generation, 7
Poly(deuterostyrene-*b*-2-vinylpyridine, segregation of alkylsilanated silicon oxide surface, 10–11
Poly(dimethylsiloxane)
  adsorption at air–water interface, 7
  applications, 2
Polyethoxylated nonylphenol, adsorption on γ-alumina, 5–6
Poly(ethylene oxide)–PPO–PEO triblock copolymers, structure of adsorbed layers, 9
Poly(ethylene oxide)–PPO–PPO on nanoparticulate pharmaceutical imaging agents, adsorption, 205–216
Poly(ethylene oxide)–SDS–silica systems, adsorption, 196–203
Polymer(s)
  as primary stabilizers for O/W emulsions, mechanisms, 280
  use as colloidal stabilizers, 166
Polymer adsorption
  at solid–liquid interface, 7–8
  AFM measurements, 255–265
  from binary mixtures on alumina, 138–151
  kinetics, 183–194
  role in technologies, 183
  total internal reflectance fluorescence concept, 185–186,189*f*
Polymer end-group chemistry, role in polymer adsorption kinetics, 183–194
Polymer–silica surfactant systems, adsorption, 196–203
Polymer–solid systems, spectroscopic characterization, 127–133
Polymer solloids, spectroscopic characterization at solid–liquid interfaces, 104–135
Polymer–surfactant aggregates adsorption at interfaces, spectroscopic characterization, 104–135
Polymer–surfactant interactions in aqueous solutions, influencing factors, 138
Polymer–surfactant–solid systems, spectroscopic characterization, 134
Polymer stabilizer adsorption, AFM measurements, 261,263–265
Polymeric steric stabilizers, design consideration, 280,282
Polymeric surfactant adsorption, 2–14
Poly(methylmethacrylate), structure of adsorbed layers, 8–9
Poly(propylene oxide)–PEO ABA block copolymer surfactant, role of anchor group in effectiveness as steric stabilizers, 166–181
Polystyrene, structure of adsorbed layers, 8–9
Polystyrene–PEO copolymer on polystyrene latex particles, adsorption kinetics, 12
Polystyrene–poly(vinylpyridine) on silver, adsorption kinetics, 12
Poly(styrenesulfonate)–SDS–alumina system, adsorption, 138–151
Poly(vinylpyrrolidone)–lithium dodecyl sulfate–lithium perfluorooctane-sulfonate–alumina system, 138–151
Poly(vinylpyrrolidone)–sodium bis(2-ethylhexyl)sulfosuccinate–alumina system, adsorption, 138–151
Porosity
  effects on cationic surfactant adsorption at silica–water interfaces, 37–42
  effects on coadsorption of 2-naphthol at silica–water interfaces, 40,42–47
Potassium decanoate, vibration spectroscopy, 324–328
Prepolymerized Langmuir–Blodgett films of *n*-octadecylsiloxane monolayers
  AFM, 359,361–362
  discovery, 355
  experimental procedure, 355–356
  Langmuir isotherms, 357–360*f*

Downloaded by 89.163.35.42 on October 11, 2012 | http://pubs.acs.org
Publication Date: May 5, 1996 | doi: 10.1021/bk-1995-0615.ix002

Prepolymerized Langmuir–Blodgett films of *n*-octadecylsiloxane monolayers—*Continued*
  thermally induced structural changes, 362
  transferred films on SiO_2/Si substrates, 359,360*f*

R

Raman spectroscopy, characterization of surfactant and polymer solloids at solid–liquid interface, 104–135
Reflection–absorption IR spectroscopy, surfactants at air–water interface, 337–339
Reflectivity, determination, 343,346–348
Relative adsorption rate constant, determination, 225–227
Relaxation lifetimes, 275,277*t*
Reverse orientation model, structure of surface aggregates, 3
Rutile, adsorption of nonylbenzenesulfonate, 91–96

S

Second harmonic generation, molecular arrangement of poly(acrylonitrile-*co*-4-vinylpyridine), 7
Sedimentation field-flow fractionation and ESR, structure of adsorbed layers, 9
Segment–substrate interactions, role in polymer adsorption kinetics, 183–194
Self-assembled monolayers from *n*-alkyltrichlorosilanes, fluorescence probe studies, 217–229
Self-assembly
  ionic surfactants adsorbed on mineral oxides, 78–101
    constant charge surfaces, 87,89–91
    constant potential surfaces, 83–88
    dodecylpyridinium chloride adsorption on Aerosil, 96–100
    experimental procedure, 80–81
    nonylbenzenesulfonate adsorption on rutile, 91–96
Self-assembly—*Continued*
    self-consistent field lattice theory for association and adsorption, 81–83
  surfactants at silica–water interface
    experimental procedure, 231–233
    mixed nonionic surfactant systems, 236–239*f*
    surface self-assembly in monodisperse nonionic surfactant–water–silica systems, 233–235
Self-consistent field lattice theory for association and adsorption
  application, 79
  concept, 81–83
  parameter choice, 82
  role of heterogeneity, 79
  self-assembly of ionic surfactants adsorbed on mineral oxides, 80–100
Self-consistent mean field theory, end-functionalized polymers segregating to impenetrable wall, 10-11
Shear flocculation, application of EPR using 100% labeled surfactant, 154–157
Shear viscosity, determination of role of anchor group of surfactant ineffectiveness as steric stabilizers, 166–181
Silica(s), adsorption of dimethylbenzyltetradecylammonium chloride, 37–41
Silica–gelatin interfaces, surface charging effects, 364–372
Silica–PEO–SDS systems, adsorption, 196–203
Silica–polymer–surfactant systems, adsorption, 196–203
Silica–water interfaces
  adsorption–desorption kinetics of nonionic poly(ethylene glycol) monoethers, 11
  effects of porosity on adsorption of cationic surfactants and coadsorption of 2-naphthol, 36–47
  nonionic surfactant systems and surface solubilization of oil, 231–239
Single-wavelength ellipsometric measurements, procedure, 357

Downloaded by 89.163.35.42 on October 11, 2012 | http://pubs.acs.org
Publication Date: May 5, 1996 | doi: 10.1021/bk-1995-0615.ix002

Downloaded by 89.163.35.42 on October 11, 2012 | http://pubs.acs.org
Publication Date: May 5, 1996 | doi: 10.1021/bk-1995-0615.ix002

- Small-molecule surfactant(s)
  - adsorption kinetics, 11–12
  - adsorption properties, 2–11
  - description, 2
  - surface solubilization, 12–14
- Sodium bis(2-ethylhexyl)sulfosuccinate adsorption, spectroscopic characterization, 104–135
- Sodium bis(2-ethylhexyl)sulfosuccinate–poly(vinylpyrrolidone)–alumina system, adsorption, 138–151
- Sodium decanoate, vibration spectroscopy, 324–327
- Sodium 1,2-dimyristoyl-*sn*-glycero-3-phospho-L-serine, vibration spectroscopy, 336
- Sodium 1,2-dioleoyl-*sn*-glycero-3-phospho-L-serine, vibration spectroscopy, 336
- Sodium dodecyl sulfate
  - adsorbed on solid surfaces, admicellar catalysis, 67–75
  - adsorption on γ-alumina, 5–6,104–135
  - vibration spectroscopy, 328
- Sodium dodecyl sulfate–PEO–silica systems, adsorption, 196–203
- Sodium dodecyl sulfate–PSS–SDS–alumina system, adsorption, 138–151
- Sodium laurate, adsorption on alumina, 6
- Sodium poly(styrenesulfonate)–hexadecyltrimethylammonium chloride–alumina system, adsorption, 138–151
- Solid–liquid interface
  - polymer adsorption, 7–8
  - spectroscopic characterization of surfactant solloids, 104–135
  - surfactant adsorption, 3–4
- Solid surfaces, adsorption of ionic surfaces, 78–79
- Solloids
  - description, 3,104–105
  - spectroscopic characterization at solid–liquid interface, 104–135
- Solubilization
  - comparison to adsolubilization, 50,51*f*,64,66
  - in adsorbed layers, 31–34
  - on surfaces, cause, 153

Solubilization—*Continued*
  - studies, 49
  - surface, oil at silica–water interface, 231–239
  - *See* Adsolubilization
- Sorbsil C30, hexadecylpyridinium chloride adsorption, 40–42*f*
- Specific adsorption, definition, 209
- Spectroscopic characterization of surfactant and polymer solloids at solid–liquid interface, 104–135
  - adsorption of SDS on alumina
    - ESR spectroscopy, 111,115–116
    - fluorescence spectroscopy, 109–114
    - isotherm, 109,110*f*
    - Raman spectroscopy, 116–118
  - experimental description, 104–105
  - isomeric surfactants at interface, fluorescence spectroscopy, 119–121*f*
  - maleic anhydride α-olefin copolymer at solid–liquid interface, 129,132–133*f*
  - mixed surfactants on alumina, Raman spectroscopy, 125,127,128*f*
  - oleate on dolomite and francolite, FTIR spectroscopy, 125,126*f*
  - polymer–surfactant aggregates at interface, fluorescence, 134,135*f*
  - sodium bis(2-ethylhexyl)sulfosuccinate
    - ESR spectroscopy, 119,123–125
    - IR spectroscopy, 119,121–122*f*
  - theory
    - ESR spectroscopy, 106–107
    - fluorescence spectroscopy, 105–106
    - IR spectroscopy, 107–108
    - Raman spectroscopy, 108–109
- Steric stabilization, repulsive forces, 280,281*f*
- Steric stabilizers, role of anchor group of surfactant in determination of effectiveness, 166–181
- Storage modulus, determination, 169
- Stretching frequency, calculation, 107
- Structure
  - surface aggregates, controversy, 3–4
  - surfactant monolayers at air–water interface, 342–354

Styrene–maleic anhydride copolymers at air–water interface, neutron reflectivity measurements, 7
Substrate–segment interactions, role in polymer adsorption kinetics, 183–194
Sugar surfactants, description, 2
Surface aggregates, structure controversy, 3–4
Surface charging effects at gelatin–silica interfaces
  charge decay measurement procedure, 367,369
  electrical connection procedure, 366
  experimental description, 364
  gelatin coating on mica surface, 366
  interfacial electrostatic adhesion, 370
  observed charge decay, 370–372
  observed surface charge densities, 369–370
  silica surface preparation, 366
  surface charge measurement, 367,368*f*
  surface force apparatus, 365–366,368*f*
Surface force apparatus
  description, 365–366,368*f*
  function, 364–365
  interfacial force measurement, 255
  limitation, 255
Surface micelles, formation, 3
Surface solubilization of oil at silica–water interface, 231–239
Surface tension, effect of surfactant concentration, 6
Surfactant(s)
  adsorption in mixtures, 241–254
  adsorption kinetics, 11–12
  adsorption properties, 2–11
  classification according to head-group type, 2
  definition, 317
  hydrophobic group substitution, 2
  interface studies, 1
  ionic, self-assembly on mineral oxides, 78–100
  nonionic, interfacial behavior at silica–water interface, 231–239
  on surfaces, studied with EPR, 153–163
  role of anchor group in determination of effectiveness as steric stabilizers, 166–181
Surfactant(s)—*Continued*
  structure–adsorption capacity relationship, 1–2
  surface solubilization, 12–14
  technological applications, 1
  types, 2
  vibration spectroscopy in solution and at air–water interface, 316–339
Surfactant adsorption
  adsolubilization, 12–14
  AFM measurements, 255–265
  at solid–liquid interface, 3–4,104–135
  from solution, influencing factors, 242
  isotherm, 49–51
  kinetics, 11–12
  on surfaces, 153–163
  properties, 2–11
  solubilization in adsorbed layers, 23–34
Surfactant aggregate, evidence for occurrence, 12–13
Surfactant and polymer for binary mixtures on alumina, adsorption, 138–151
Surfactant behavior at interfaces, importance, 231
Surfactant concentration, effect on surface tension, 6
Surfactant monolayers at air–water interface, structure, 342–354
Surfactant–solid systems, spectroscopic characterization, 109–128
Surfactant solloids, spectroscopic characterization at solid–liquid interfaces, 104–135
Surfactant systems, silica–polymer, adsorption 196–203
Synergism, surfactant solutions, 5

T

Tetradecyltrimethylammonium chloride–pentadecylethoxylated nonylphenol mixture interactions at alumina–water interface, *See* Pentadecylethoxylated nonylphenol–tetradecyltrimethylammonium chloride mixture interactions at alumina–water interface

Downloaded by 89.163.35.42 on October 11, 2012 | http://pubs.acs.org
Publication Date: May 5, 1996 | doi: 10.1021/bk-1995-0615.ix002

Total internal reflectance fluorescence, 184–189

Transmission IR spectroscopy, 357–358

Tribocharging, description, 364

Trimethylorthobenzoate, acidic hydrolysis, 67–75

U

Ultralow interfacial tension determination by axisymmetric drop shape analysis
  - dioctyl sulfosuccinate in aqueous solution of NaCl–water and *n*-heptane, 380,383–385
  - experimental setup, 375–379
  - oleic acid in olive oil and aqueous solution of NaCl and NaOH, 380–382
  - theory of axisymmetric drop shape analysis, 376–378*f*

Uncharged hydrophobic surfaces, adsorption of ionic surfactants, 4–5

V

Vibration spectroscopy of surfactants in solution and at air–water interface, 337–339
  - lipid bilayers, 332–337
  - micellar structures, 317–331

Viscoelasticity, determination of role of anchor group of surfactant in effectiveness as steric stabilizers, 166–181

W

Water–air interface, *See* Air–water interface

Water–oil interface, *See* Oil–water interface

Water–silica interface, *See* Silica–water interface

Water-soluble polymers, hydrophobically modified, adsorption kinetics at oil–water interfaces, 280–311

Z

Zirconia, poly(acrylic acid) adsorption, 255–265

Zwitterionic surfactants, description, 2

Downloaded by 89.163.35.42 on October 11, 2012 | http://pubs.acs.org
Publication Date: May 5, 1996 | doi: 10.1021/bk-1995-0615.ix002